Lecture Notes in Electrical Engineering 506

Ming Jiang
Nathan Ida
Alfred K. Louis
Eric Todd Quinto *Editors*

The Proceedings of the International Conference on Sensing and Imaging

Springer

Lecture Notes in Electrical Engineering

Volume 506

**** Indexing: The books of this series are submitted to ISI Proceedings, EI-Compendex, SCOPUS, MetaPress, Springerlink ****

Lecture Notes in Electrical Engineering (LNEE) is a book series which reports the latest research and developments in Electrical Engineering, namely:

- Communication, Networks, and Information Theory
- Computer Engineering
- Signal, Image, Speech and Information Processing
- Circuits and Systems
- Bioengineering
- Engineering

The audience for the books in LNEE consists of advanced level students, researchers, and industry professionals working at the forefront of their fields. Much like Springer's other Lecture Notes series, LNEE will be distributed through Springer's print and electronic publishing channels.

For general information about this series, comments or suggestions, please use the contact address under "service for this series".

To submit a proposal or request further information, please contact the appropriate Springer Publishing Editors:

Asia:

China, *Jessie Guo, Assistant Editor* (jessie.guo@springer.com) (Engineering)

India, *Swati Meherishi, Senior Editor* (swati.meherishi@springer.com) (Engineering)

Japan, *Takeyuki Yonezawa, Editorial Director* (takeyuki.yonezawa@springer.com)
(Physical Sciences & Engineering)

South Korea, *Smith (Ahram) Chae, Associate Editor* (smith.chae@springer.com)
(Physical Sciences & Engineering)

Southeast *Asia, Ramesh Premnath, Editor* (ramesh.premnath@springer.com)
(Electrical Engineering)

South Asia, *Aninda Bose, Editor* (aninda.bose@springer.com) (Electrical Engineering)

Europe:

Leontina Di Cecco, Editor (Leontina.dicecco@springer.com)
(Applied Sciences and Engineering; Bio-Inspired Robotics, Medical Robotics, Bioengineering; Computational Methods & Models in Science, Medicine and Technology; Soft Computing; Philosophy of Modern Science and Technologies; Mechanical Engineering; Ocean and Naval Engineering; Water Management & Technology)

(christoph.baumann@springer.com)
(Heat and Mass Transfer, Signal Processing and Telecommunications, and Solid and Fluid Mechanics, and Engineering Materials)

North America:

Michael Luby, Editor (michael.luby@springer.com) (Mechanics; Materials)

More information about this series at http://www.springer.com/series/7818

Ming Jiang • Nathan Ida • Alfred K. Louis
Eric Todd Quinto
Editors

The Proceedings of the International Conference on Sensing and Imaging

Springer

Editors
Ming Jiang
School of Mathematical Sciences
Peking University
Beijing, China

Alfred K. Louis
Institute of Applied Mathematics
Saarland University
Saarbrücken, Germany

Nathan Ida
Department of Electrical and
Computer Engineering
The University of Akron
Akron, OH, USA

Eric Todd Quinto
Department of Mathematics
Tufts University
Medford, MA, USA

ISSN 1876-1100 ISSN 1876-1119 (electronic)
Lecture Notes in Electrical Engineering
ISBN 978-3-319-91658-3 ISBN 978-3-319-91659-0 (eBook)
https://doi.org/10.1007/978-3-319-91659-0

Library of Congress Control Number: 2018950659

Printed on acid-free paper

This Springer imprint is published by the registered company Springer Nature Switzerland AG
The registered company address is: Gewerbestrasse 11, 6330 Cham, Switzerland

Foreword

Sensing and imaging is an interdisciplinary field involving a number of science, technology, and engineering disciplines, such as optics, electricity, magnetism, heat, sound, mathematics, and computing technology, among others. It has diversified applications that have significantly changed our lives.

Our university, Chengdu University of Information Technology (CUIT), is jointly sponsored by the Sichuan Provincial Government and Meteorological Bureau of China with a history since 1951. It is specialized in atmospheric science and information technology and focuses on research and teaching for meteorological, industrial, and medical applications, etc. Our mission is to train students and have them prepared for their future career development. With atmospheric science and information technology as the core, we provide multidisciplinary programs in science, technology, engineering, management, together with economics, literature, law, and art in 17 colleges of CUIT. There are a number of interdisciplinary institutes or centers in CUIT for graduate students to develop their potentials.

Because of the interdisciplinary nature of sensing and imaging, and to promote the interdisciplinary research and teaching in our university, we are happy to have the opportunity to hold the International Conference on Sensing and Imaging 2017 (ICSI 2017) in our university, Chengdu University of Information Technology, Chengdu, Sichuan, China, on June 5–7, 2017.

I thank the co-chairs of the conference, Prof. Ming Jiang and Prof. Eric Todd Quinto, for their efforts in co-chairing the conference, and Prof. Nathan Ida and Prof. Alfred K. Louis for joining Profs. Jiang and Quinto to edit the proceedings of the conference. I would also like to thank Prof. Quinto for leading the publication of a special issue from nine selected submissions to the conference. Special thanks to all the local organizers and volunteers for their efforts in supporting this conference, especially to Prof. Jia He and Dr. Yongqing Zhang. I thank all the invited speakers,

session chairs, and participants for coming to CUIT and participating in this conference. It is the efforts of all the aforementioned ones that made this conference successful.

General Chair of ICSI 2017 Prof. Dr. Jiliu Zhou
President of Chengdu University
of Information Technology (CUIT)
Chengdu, China

Preface

The International Conference on Sensing and Imaging 2017 (ICSI 2017) was the third of our conference series on sensing and imaging. The previous two were held at Chifeng, Inner Mongolia, China, in 2015, and Taiyuan, Shan Xi Province, China, in 2016.

With the success of the previous two conferences, and because of the suggestions from peers and requests from participants, we decided to publish the proceedings for ICSI 2017.

This conference was held at Chengdu University of Information Technology, Chengdu, Sichuan Province, China, on June 5–7, 2017, and was sponsored and organized by CUIT. We have received 79 submissions for ICSI 2017. After the first round review, we accepted 66 submissions for presentation at the conference. Among them, there were 22 invited talks.

The review and publication of these proceedings are unlike most conference proceedings. All submissions were first reviewed to see if they could be suitable for presentations at the conference and were accepted after revisions. Unlike other proceedings of conferences, after the conference, all revised submissions underwent another round of revision so the authors could incorporate discussions at the conference. They were reviewed again for final acceptance in the proceedings, and some submissions were rejected. We understand that proceedings are different from journal submissions, but we hope the two rounds of revisions improve the quality of submissions without delaying the publication.

For the publication of the work presented at the conference, nine submissions were selected to be published in the special issue entitled "Recent Developments in Sensing and Imaging" in the journal *Sensing and Imaging* of Springer Nature. Each selected manuscript has been extended to a full-length regular paper with significant extension from its conference version and reviewed under the normal reviewing process of the journal *Sensing and Imaging*. This special issue has been edited by Profs. Eric Todd Quinto, Mark Anastasio, Tingting Jiang, and Yu Shang, and has been published.

For the proceedings, we have 35 papers including 5 invited chapters. There are four parts in the proceedings: Part I for invited chapters, Part II for sensing technologies, Part III for imaging and image processing technologies, and Part IV for sensing and imaging applications.

We thank Christopher T. Coughlin, Publishing Editor of Springer Nature, for his prompt agreement and coordination to publish the proceedings in Lecture Notes in Electrical Engineering (LNEE), so that authors could prepare their manuscript for this publication opportunity. We thank all the reviewers for their timely responses and comments for authors to improve the quality of manuscripts. We thank all the authors for their participation in ICSI 2017 and their understanding and patience for the two rounds of revisions. We thank the authors of the five invited contributions for their effort in preparing the invited chapters. Finally, we thank Marie Josephine, Jeffrey Taub, HoYing Fan, and Divyaa Veluswamy of the editorial team of Springer Nature for their help and support during our editing of the proceedings.

Beijing, China — Ming Jiang
Akron, OH, USA — Nathan Ida
Saarbrücken, Germany — Alfred K. Louis
Medford, MA, USA — Eric Todd Quinto

Contents

Part I
Invited Chapters

Sensing and Actuation: A Case for Multidisciplinary Engineering Education

Nathan Ida

1 Introduction

The importance of sensors and actuators in design and operation of modern systems cannot be overstated. Almost every device or system one comes in contact with in industry, in transportation, in the home, or in medicine makes use of sensors and actuators, often in staggering numbers. The humblest of cars may contain many dozens of these devices, and some cars may contain literally hundreds of sensors and actuators. A quick read of the OBD-II (On Board Diagnostics) list shows that a car central processing unit monitors hundreds of sensors and actuators to comply with pollution control [1], safety, and operational requirements of the modern car. But sensors and actuators can be found in more mundane places affecting everybody's daily life. From thermostats in the kitchen to voice-actuated toys, to accelerometers in telephones, to entertainment, and to medical tests in laboratories and hospitals, the average person comes in contact with dozens of sensors and actuators every day, often unknowingly, almost always casually. Does the average driver know where the oxygen sensors in a car are, how many of them the car possesses, exactly what function they perform, and how they perform that function? And if an accident should occur, the driver is confident the airbag system will protect him or her. But does the driver know that to do so, the system uses an array of accelerometers as sensors and an explosive charge as a chemical actuator to generate the gas that fills the bag? But, as a whole, the public has accepted sensors and actuators as part of modern systems and is comfortable with their presence even if their location and function is not known or understood. Indeed, the idea of sensing and actuation may be viewed as an extension of natural sensing by living organisms, and much

N. Ida (✉)
Department of Electrical and Computer Engineering, The University of Akron, Akron, OH, USA
e-mail: ida@uakron.edu

M. Jiang et al. (eds.), *The Proceedings of the International Conference on Sensing and Imaging*, Lecture Notes in Electrical Engineering 506,
https://doi.org/10.1007/978-3-319-91659-0_1

of the efforts in modern sensing and actuation can be summarized in attempts to mimic and, in some cases, improve on natural sensing. In many areas of sensing and actuation, existing sensors far surpass anything that may have existed as natural sensors. But in others much remains to be done. For example, current chemical sensors are very far from being able to mimic the nose of a dog, let alone surpass it and the dexterity of a hand has no match in modern actuators.

One tends to think of sensors and actuators as a product of the information age and of the rapid development of electronics associated with it. Indeed, as far as the sheer number and variety of sensors available and their sophistication, this attitude is justified. But sensors existed before electronics, before the transistor, before the vacuum tube, or even before electricity. The first thermocouples date to 1826 when Antoine Becquerel first used them to measure temperature. The Peltier effect that allowed refrigeration and heating in space and then found its way into consumer products dates back to 1836 and has been in use in thermoelectric generators from the 1890s. The RTD (resistance temperature detector) was developed in 1871 by William Siemens. The photoelectric sensor existed as a device since the early 1930s. Aircraft use Pitot tubes to measure their speed, a device invented in 1732 by Henri Pitot for the mundane function of measuring water flow in rivers. And, perhaps more than any other sensor, the magnetic needle or compass dates back to at least 1100 CE and by some sources to 2400 BCE. Modern actuators can be easily dated as starting with Michael Faraday's invention of the motor in 1824. But actuation occurred before, back into times lost to memory. The use of steam for actuation can be dated to the work of Hero of Alexandria (10–70 CE) [2]. The use of water and water wheels existed before 250 CE and probably much before that [3]. Wind harvesting can be dated to at least the work of Hero [2] and probably earlier.

In addition, man has made use of animal senses (as well as animal power) to improve his lot. In tenth-century France, salamanders were kept in water sources to detect poisoning and later fish served the same purpose. To this day, truffles are harvested with the help of pigs who can detect their smell. The canary in the coal mine has become an adage, and in reality it saved lives of coal miners well into the 1990s. Plants as well have joined this quest; rose bushes have been used for early detection of phylloxera – a fungus that devastated the wine industry in Europe in the late 1880s. The quest for new sensors and sensing mechanism in the modern age can be viewed as a continuation of human efforts to improve its lot by better sensing its environment and, by extension, and by better interacting with it. This nobble quest and the less noble but equally important industrial need for sensing and actuation have fueled the rapid development of sophisticated sensors and actuators.

It is therefore not surprising that engineering education has responded by introducing programs in sensors and to a much lesser extent in actuators either as part of existing offerings or as new disciplines. Here too, the variety of approaches mirrors the extent and variety of devices and the needs. Many approaches to teaching sensors and actuators stem from the research environment and hence follow the same degree of specialization. These tend to be focused on particular classes of devices such as MEMs, nanosensors, biosensors, wireless sensors, and many other specialized topics. Others view sensors and to a degree actuators as

complementary to other primary topics such as control, environmental engineering, physics, aerospace, transportation, and others, focusing on those aspects of sensing and actuation that are of interest to the discipline and are often bundled with the primary subject. The topics exposed are cherry-picked to fit the subject and may be supplemented with topics in signal processing or microprocessor control as needed. Still others, particularly training offerings, focus on classes of devices of interest to an industry, a company, the military, or a branch of government. A course of study of this type may focus entirely on a single class of sensors or a few related classes such as accelerometers, temperature sensors, capacitive sensors, or pH sensing, as examples. The focus is typically narrow and often intended to popularize the use of these devices or to stimulate research. On the other extreme of the spectrum stand "catch all" classes attempting to cover all topics related to sensors and/or actuators following some logical groupings, necessarily minimizing the details to allow broad coverage of the topics. In most cases, course offerings focus on sensors alone, but there are also approaches that take into account the intended use of sensors and hence deal with applications, interfacing, and related issues. Discussion of actuators is less common, but, nevertheless, offerings exist either as separate subjects or in combination with sensors. A quick search on the internet will produce many offerings in each category complete with outlines and rationale.

The books and textbooks that have been publish to support teaching of sensors and, again, to a smaller extent, actuators reflect and in many cases drive the type of offerings available. The two most common types are handbooks [4–8] and monographs [9–14]. Handbooks, by their nature, are inclusive but shallow and are often written as cooperative efforts by many contributors, each focusing on subjects of their expertise. Some are very broad in coverage [4–6], some more focused [7, 8], but in all cases they make for very poor textbooks. Indeed, their very intent is as references not as textbooks. Monographs tend to be loaded with research results, ideally suited as references but, in general, not suitable for teaching. There are a few publications that qualify as textbooks in the classical sense [15–17]. Unfortunately there are few of these, and some are specialized [15, 17] or at a low level, not really suited for university-level teaching [16]. This is not surprising. Very often a textbook will follow a course, and it is only practical for a publisher to invest in a good textbook once the subject has received wide support in academia. The teaching of sensors and actuators is not at that stage, that is, most classes are taught as electives and are driven by local interest rather than by broad discipline requirements. The fact that the topic itself is interdisciplinary contributes to this state.

2 Proposed Course of Study

2.1 The Sensor-Actuator Ensemble

Sensors and actuators serve many purposes, but, on the whole, sensors may be viewed as input to systems; these are devices that collect information needed for the system to operate. The outputs of systems are connected to actuators of various types and levels of sophistication and produce an output action of some sort – from the simplest to the most sophisticated imaginable. In between, interfacing between sensors and actuators is a processor, again of various levels of sophistication as needed. This view of sensors and actuators broadens the scope of sensing and actuation and emphasizes the link between the two classes of devices. In effect, any input device, from switches to gyroscopes, becomes a sensor, and any output, from a flashing LED to a multi-MW motor or the entire power grid, becomes an actuator. The processors themselves can be trivial or utterly complex. Turning on the lights involves a switch (sensor), a lamp (actuator), and the wiring harness (processor). Of course, it can be much more complex than this. One can use a motion sensor to turn on the lights and a microprocessor or timer to turn them off. The processor may be a microprocessor, a computer, or a network of computers acting together to affect processing of input data and producing output of some sort.

The three components of a system that involves sensors, actuators, and processors must be studied together since these are interrelated. Sensors must be capable of interfacing with microprocessors a need that affects their design. Many sensors are designed specifically with this in mind affecting their operation, power needs, sensitivities, and other properties such as the addition of purely digital functions including buses, digital output communication links, and other circuits. Actuators as well must be interfaced requiring compatibility with microprocessors. This may be done by directly driving small, low power actuators or, more often, by additional circuitry allowing microprocessor to control actuators. The most common interfacing element, the microprocessor, has itself evolved to accommodate these inputs and outputs, and it is not surprising to find that microprocessors contain the basic circuit elements needed to interface to sensors and actuators. Sensors and actuators often use similar principles, and many devices are dual – they can serve as both sensors and actuators. Because of that, it is possible and perhaps desirable to describe them together. The processor linking the two is at the center of the system, and its role in achieving a successful sensing system must be addressed in conjunction with sensors and actuators. In addition, basic electronic circuits needed for interfacing or to operate the devices must be part of the study. These include amplifiers, comparators, digital gates, bridge circuits, oscillators, and power supply and management circuits. As a result, a comprehensive approach must address the following:

Sensors
Actuators
Interfacing circuits
Microprocessors

2.2 The Nature of Sensors and Actuators

The vast majority of sensors and actuators are electrical devices in the sense that output of sensors and input to actuators is electrical. However, most devices encompass principles and techniques that involve other disciplines. For example, many pressure sensors are semiconductor devices, and as such they belong squarely in the realm of electrical engineering. But their operation is based on strain in the semiconductor, and understanding of their operation, properties, limitations, and possible uses all involve knowledge of mechanical properties of materials and structures. The same types of sensors are highly sensitive to temperature variations. Understanding of the errors due to temperature variations and possible compensation of errors involves heat transfer issues such as heat capacity. Many sensors as well use multiple principles in arriving at the intended function. The principles come from all disciplines, sometimes from corners of science that engineering students know little or nothing about. Table 1 shows a selection of effects commonly used in sensing and actuation. Some are common engineering principles and well known to students, some less so. There are in fact over dozens of effects and laws that are being used, and they hail from disciplines ranging from quantum electronics to mechanics and everything in between.

The sensors and actuators an engineer is expected to understand, develop, and use are governed by physical laws. The understanding of these physical laws is crucial to understanding sensors and actuators. Again, these laws encompass all areas of engineering and science. Some of the more important in sensing and actuation are listed in Table 2.

In light of what sensors and actuators are and how they operate, the student needs to have at least cursory knowledge of the following:

Solid state physics and atomic structure
Quantum theory and effects
Semiconductor physics, band gaps, energy states, and semiconductor processing
Thermodynamics, heat transfer principles, conduction, and radiation
Optics, spectral response, and optical effects
Materials science, material properties, statics, and dynamics
Wave propagation in materials, stresses, strains, acoustics, and ultrasound
Electromagnetics, magnetic materials, laws, and electromagnetic wave propagation
Chemistry and electrochemistry

In addition, the use, calibration, and analysis of data from sensors and actuators require elements of the following:

Table 1 A selection of physical effects used in sensing and actuation

Avalanche effect	Magnetoresistive effect
Barkhausen effect	Magnetostrictive effect
Cherenkov effect	**Magnus effect**
Compton effect	Mateucci effect
Coriolis effect	Meissner effect
Doppler effect	Miller effect
Edison effect	Mössbauer effect
Einstein effect	Nernst effect
Electrooptic effect	Peltier-Seebeck effect
Electrocaloric effect	Photoconductive effect
Electrochemical effect	Photoelastic effect
Electron-cloud effect	Photoelectric effect
Electrostrictive effect	Photomagnetic effect
Faraday effect	Photorefractive effect
Ferroelectric effect	Photothermal effect
Giant magnetoresistance	Piezoresistive effect
Gibbs-Thomson effect	Sagnac effect
Gunn effect	Proximity effect
Haas effect	Relativistic Doppler effect
Hall effect	Reverse Cerenkov effect
Hypersonic	Rusty bolt effect
Inverse Doppler effect	Schottky effect
Inverse Faraday effect	Skin effect
Joule's effect	Stefan-Boltzmann law
Josephson effect	Thermoelastic effect
Joule-Thomson effect	Thermoelectric effect
Kelvin effect	Thermomagnetic effect
Kerr effect	Thermooptic effect
Magneto-optic effect	Transformer effect
Magneto-optic Kerr effect	Triboelectric effect
Magnetoelectric effect	Venturi effect
	Wiedemann effect
	Zeeman effect

Electronics and electric circuits and power electronics
Microprocessors and programming
Error analysis and statistics
System integration

3 A Proposed Approach to Teaching Sensors and Actuators

It is not likely that students will be proficient in all areas of science and engineering involved in sensing and actuation. The very fact that sensors are used and taught across all disciplines indicates that most students will only be knowledgeable in a subset of the topics needed, perhaps a small subset. It is therefore imperative that the topics necessary for understanding be taught as part of the offering in sensors and

Table 2 A short list of laws, principles, and constants governing operation of sensors and actuators

Ampere's law	Faraday's law
Avogadro's hypothesis	Faraday's laws of electrolysis
Bernoulli's equation	Gauss' law
Biot-Savart law	Hooke's law
Blackbody radiation	Huygens' principle
Bode's law	Ideal gas constant
Boyle's law	Ideal gas laws
Bragg's law	Joule's laws
Brewster's law	Kirchhoff's law of radiation
Carnot's theorem	Kirchhoff's laws
Causality principle	Lambert's laws
Charles' law	Lenz's law
Cherenkov radiation	Mach's principle
Conservation laws	Maxwell's equations
Coulomb's law	Newton's laws of motion
Curie-Weiss law	Ohm's law
Dalton's law of partial pressures	Pascal's principle
de Broglie wavelength	Planck radiation law
Planck constant	Snell's laws
Dulong-Petit law	Stefan-Boltzmann constant
Einstein field equation	Thermodynamic laws
Equivalence principle	Wave-particle duality
Faraday constant	Wiedemann-Franz law

actuators at a level that is appropriate. One cannot expect to teach and the students cannot be expected to learn all necessary topics in depth. Rather, the presentation should be at a level that allows understanding at present and serves as the basis for further study should specialization be needed in the future. Because sensors and actuators cover a vast number of devices, the focus should be on principles based on a rational classification of devices. Here too there are many approaches, all with some logical choices behind them. However, for a general purpose, interdisciplinary course in sensors and actuators, the choice must be on physical principles. The proposed course of study divides sensors and actuators into nine sections based on the following physical principles.

3.1 Temperature Sensors and Thermal Actuators

Topics include thermo-resistive sensors including metal resistance temperature detectors (RTDs), silicon-resistive sensors and thermistors, thermoelectric sensors and actuators, metal junction and semiconductor thermocouples as well as Peltier cells (both as sensors and as actuators), PN junction temperature sensor, and thermo-mechanical devices as thermal actuators. Bimetal sensors with applications in thermostats and thermometers serve to introduce the concept of duality between sensing and actuation.

3.2 Optical Sensing and Actuation

The photo-conducting effect is the first optical principle that found its way into sensing, and hence it is a good starting point. Silicon-based sensors including photodiodes, transistors, and photovoltaic sensors allow the introduction of quantum principles and basic semiconductor theory. Photoelectric, photomultipliers, and CCD sensors are followed by thermal-based optical sensors including thermopiles, infrared sensors, pyroelectric sensors, and bolometers. Most optical actuators rely on MEMs principles and are therefore delayed to a special section on MEMs and smart devices.

3.3 Electric and Magnetic Sensors and Actuators

A large number of devices fall into this class, and as a consequence, the discussion is more extensive. It starts with capacitive devices followed by magnetic devices. A variety of sensors and actuators including position, proximity, and displacement sensors, as well as magnetometers, velocity, and flow sensors, are introduced. The principle involved including the Hall effect and magnetostrictive effect are discussed side by side with more common effects. A rather extensive discussion of motors and solenoids covers many of the principles of magnetic actuation, but capacitive actuators are discussed as well.

3.4 Mechanical Sensors and Actuators

Many sensors and actuators are mechanical in nature or respond to mechanical quantities. The classical strain gauge is featured as a generic method of measuring forces and the related quantities of strain and stress. But it is also used in accelerometers, load cells, and pressure sensors. Accelerometers, force sensors, pressure sensors, and inertial sensors are some of the more common sensors in industry. Mechanical actuators are exemplified by the bourdon tube, bellows, and vacuum motors.

3.5 Acoustic Sensors and Actuators

By acoustics are meant sensors and actuators based on elastic, sound-like waves. These include microphones and hydrophones based on magnetic, capacitive and piezoelectric principles, the classical loudspeaker, ultrasonic sensors and actuators, piezoelectric actuators, and surface acoustic wave (SAW) devices. Thus, although

acoustics may imply to many sound waves, the frequency range of acoustic sensors is from near zero to many GHz. As in other classes of sensors, the distinction between sensors and actuators is based on function and size rather than principles and some exhibit duality. A loudspeaker is not different than a microphone except for function and size, and ultrasonic transducers are almost always dual sensors/actuators.

3.6 Chemical Sensors and Actuator

Chemical sensors and actuators are some of the most common, ubiquitous, and, unfortunately, least understood devices by most engineers. A fairly large section of the existing chemical sensors including electrochemical and potentiometric sensors, thermochemical, optical, and mass sensors are covered. Chemical actuation is not neglected either, and again, it is much more prevalent than normally thought. Actuators include catalytic conversion, electroplating, cathodic protection, and others.

3.7 Radiation Sensors and Actuators

Aside from classical ionization sensors, this category includes non-ionizing, microwave radiation as well. Sensors are based on reflection, transmission, and resonant methods, and, since any antenna can radiate power, it can serve as an actuator to affect specific tasks such as cauterization during surgery, low-level treatment for cancer, or hypothermia, not to mention microwave cooking and heating.

In addition to the discussion of principles, the comprehensive approach proposed includes the following topics to supplement and complement the discussion on sensors and actuators:

3.8 Microelectromechanical (MEM) Sensors and Actuators

Microelectromechanical sensors and actuators as well as smart sensors form an important part of available devices. Necessarily, methods of sensor/actuator production are an important aspect of these devices. Some of the methods of production are first given, followed by a number of common classes of sensors and actuators including inertial and electrostatic sensors and actuators, optical switches, valves, and others. In the context of smart sensors, issues associated with wireless transmission, modulation, encoding, and sensors networks are emphasized.

3.9 Performance Characteristics Sensors and Actuators

The discussion of the performance characteristics of sensors and actuators is important in design and in applications. The transfer function, span, sensitivity and sensitivity analysis, errors, nonlinearities as well as frequency response, accuracy, and other properties including issues of reliability, response, dynamic range, and hysteresis are discussed early in general terms and through examples of actual sensors and actuators, and all sensor and actuator characteristics are repeated and discussed in conjunction with specific sensors throughout the course of study.

3.10 Interfacing Methods and Circuits

With few exceptions sensors or actuators cannot operate on their own and require electronic circuits to operate and interface. The circuits discussed start with the operational amplifier and its many applications followed by power amplifiers and pulse width modulation circuits for use with actuators. The A/D and D/A in their various forms, including voltage to frequency and frequency to voltage converters, follow these prior to discussion of bridge circuits and data transmission methods. Excitation circuits including linear and switching power supplies, current and voltage references, and oscillators are also discussed. Noise and interference issues were also deemed part of interfacing although some issues of noise were introduced in the section on performance characteristics.

3.11 Interfacing to Microprocessors

The microprocessor and its role in interfacing sensors and actuators do not need introduction or justification. It is a fact that most sensors and actuators are interfaced using microprocessors. The emphasis is on 8-bit microprocessors to keep the discussion simple, but the issues addressed are general and pertain to all microprocessors. The architecture, memory, and peripherals of the microprocessor, the general requirements for interfacing, properties of signals, resolution, and errors are introduced and their role in interfacing emphasized.

3.12 Units

Engineering students are familiar with the SI system of units, but the scope of topics in sensors and actuators is so wide that they need to deal with many derived units they are not used to and perhaps would never have used otherwise. A short discussion on units is included as part of the introduction to the course.

Each of the subjects *A* through K is allocated about 3.5 h on the average and includes a few detailed examples per subject. The material in each section is supplemented by a set of problems that allow the student to reinforce knowledge. Some are classical problem where a student is asked to come up with a definite answer, but many are open-ended questions that can easily be extended into projects of considerable scope, within or out of class. The use of examples and problems is particularly important in a course of this type as it allows the student to review unfamiliar material in disciplines in which he or she is not proficient. To this end, a generous supplement of material is being made available ranging from the table of elements, through summaries on theoretical issues in radiation, electromagnetics, acoustics, mechanics, and electrochemistry to data sheets and application notes. The latter serve not only to supplement the class but also to take it beyond fundamentals and keep it practical and current.

As was mentioned in the introduction, one of the missing links in sensors and actuators is a modern, comprehensive textbook to complement a course of study such as the one proposed. Undoubtedly that will happen, and in the future the student will have access to a selection of good textbooks to help focus the study of sensors and actuators.

4 A New Direction in Teaching

Most of the engineering curriculum tends to be narrowly focused with specific subjects taught individually and later integrated through electives and in many cases through a capstone project. This means that a student really only needs a handful of topics, closely related to his/her discipline. An electrical engineering student will rarely have recourse to stress analysis, and a mechanical engineering student probably will never hear of Maxwell's equations. The teaching of sensors and actuators takes a decisively different turn and broadens the scope of teaching. The student now is exposed to a very broad range of issues in many disciplines allowing for a better understanding of systems and, indeed, for a broader education. In the current environment in industry, where design and work is done in interdisciplinary teams, this approach to teaching serves as a means of tighter cooperation between disciplines or, at the very least, a better understanding of each other's views and needs.

5 Conclusions

The teaching of sensors and actuators is different than other areas in engineering in the inherent broad base in principles. The proposed course of study touches on some of the most important principles involved and links sensors and actuators through processors. The proposed course is interdisciplinary in nature although, by

necessity, it is based on electrical engineering principles with additions from all other disciplines in engineering and many in sciences. A comprehensive approach based on fundamentals is taken throughout with examples and problems anchoring it in the application world and ensuring it is current. Central to the approach proposed here is the microprocessor, viewed as a general-purpose tool for interfacing. Hence an integral part of the course of study is electronic circuits needed for interfacing and elements of microprocessor interfacing.

References

1. http://epa.gov/obd/
2. Hero (or Heron) of Alexandria (10–70 AD), Pneumatica (see for example: The Pneumatics, Hero of Alexandria, www.history.rochester.edu/steam/hero/translator.html)
3. (1976) The Perachora Waterworks: Addenda, R A Tomlinson. Annu Br Sch Athens 71:147–148
4. Fraden J (2010) Handbook of modern sensors, physics, designs, and applications. Springer, New York
5. Wilson JS (2004) Sensor technology handbook. Newness
6. Soloman S (2009) Sensors handbook, 2nd edn. McGraw-Hill
7. Webster JG (1999) The measurement, instrumentation, and sensors handbook. CRC Press, Boca Raton
8. Xiao Y, Chen H, Li FH (eds) (2010) Handbook on sensor networks. World Scientific
9. Cooper J, Cass T (2004) Biosensors a practical approach. Oxford University Press, New York
10. Brauer JR (2006) Magnetic actuators and sensors. Wiley
11. Alciatore DG, Histand MB (2007) Introduction to mechatronics and measurement systems. McGraw-Hill Education (India) Pvt Ltd
12. Janocha H (2010) Actuators: basics and applications. Springer
13. Nesbit B Handbook of valves and actuators: valves manual international. Rols and Associates
14. Pons JL (2005) Emerging actuator technologies: a micromechatronic approach. Wiley
15. De Silva CW (2007) Sensors and actuators: control system instrumentation. CRC Press
16. Carstens JR (1993) Electrical s*ensors* and transducers. Regents/Prentice-Hall
17. Benedict RP (1984) Fundamentals of temperature, pressure, and flow measurements. Wiley

Advances in Reconstruction Algorithms for Diffuse Correlation Spectroscopy and Tomography

Yu Shang

Abbreviations

BFI	Blood flow index
CSF	Cerebrospinal
DCS/DCT	Diffuse correlation spectroscopy/tomography
DOS/DOT	Diffuse optical spectroscopy/tomography
FE	Finite element
PDE	Partial differential equation
RBC	Red blood cell
S-D	Source-detector

1 Introduction

As an essential substance involved in the biological metabolism, the oxygen carried in the blood is vital to the tissue health. Over the years, various technologies have been developed to monitor the oxygen status in the tissue. Among these, near-infrared diffuse optical spectroscopy/tomography (DOS/DOT) is one category used most widely to detect the blood oxygenation level in bulk tissue [15, 20, 39], owing to the features of noninvasiveness, portability, and inexpensive instrumentation. DOS/DOT utilizes the light intensity change at multiple source-detector separations, as well as the phase change (when frequency-modulated light is applied), to probe

Y. Shang (✉)
Shanxi Provincial Key Laboratory for Biomedical Imaging and Big Data, North University of China, Taiyuan, China
e-mail: yushang@nuc.edu.cn

M. Jiang et al. (eds.), *The Proceedings of the International Conference on Sensing and Imaging*, Lecture Notes in Electrical Engineering 506,
https://doi.org/10.1007/978-3-319-91659-0_2

oxygenation parameters, including oxyhemoglobin ([HbO_2]), deoxy-hemoglobin ([Hb]), and total hemoglobin concentrations (THC), as well as oxygen saturation (StO_2) [6, 13]. While the tissue oxygen parameters reflect the balance between the oxygen supply and oxygen consumption, they are unable to comprehensively evaluate the oxygen kinetics in the tissue [13, 34].

Blood flow is a dynamic parameter indicating how fast the oxygen in the blood is supplied to the biological tissue. Additionally, blood flow reflects the vasodilation and vasoconstriction features of the vessel, which is helpful to diagnose vasculature diseases [6, 30]. Furthermore, combination of the blood flow and oxygen information (taken together as hemodynamic parameters) allows for estimation of tissue metabolic rate [28, 32], thus proving comprehensive assessment of oxygen kinetics and physiology. Measurement of blood flow in deep tissue, however, is not a routine task in the past, due to the limitation in the technology. Ultrasound Doppler can measure the blood flow in large vessel [38], but not able to assess microvasculature blood flow. Laser Doppler is a technology to detect microvasculature blood flow [29], but only in superficial tissue, up to 2 mm. There exist some large instruments for probing the blood perfusion in deep tissue, such as perfusion MRI or Xenon CT [41]. However, the high cost and low portability restrict them for use in routine clinic, such as in the bedside or surgical rooms.

A relatively new technology for blood flow measurement, namely, diffuse correlation spectroscopy (DCS) [5, 7, 18, 24], has gained rapid development in recent years. While DCS also utilizes the light in near-infrared (NIR) range, the temporal autocorrelation of light electric field, rather than the light intensity, is quantified in DCS to extract the blood flow information in deep tissue [3, 18]. DCS for tissue blood flow measurement has been validated against a variety of flow techniques, including ultrasound Doppler [28], laser Doppler [30], perfusion MRI [41], as well as fluorescent microsphere flow measurement [43]. Moreover, the DCS has been applied in clinic, for therapeutic monitoring of the microvasculature blood flow that are relevant to various diseases, such as ischemic stroke [31], peripheral arterial disease [40], head-neck tumor, and breast tumor [8, 12]. The successful applications of DCS also promote the development of diffuse correlation tomography (DCT) [9, 23, 44], an extension of DCS for blood flow imaging.

Apart from instrumentation, the reconstruction algorithm of DCS/DCT also contributes greatly to the accuracy and robustness of BFI values as well as the detective sensitivity of diagnostic outcomes. In the next sections, we will briefly describe the basic principle and hardware components of DCS/DCT. We will then review the conventional algorithms used to reconstruct the blood flow information from the measured data of DCS/DCT. The fast and wide applications of DCS/DCT to the physiological studies and clinic triggered the developments of a few advanced algorithms, which will be the focus in this paper. Finally, we will discuss the future prospective of the DCS/DCT reconstruction algorithm and anticipate these technologies for clinical implications.

2 Principle and Instrumentation of DCS/DCT

The details of the DCS/DCT are described elsewhere [3, 7, 18, 23, 44]. Briefly, NIR light is emitted by the long-coherent lasers (source) into biological tissue. The light experiences multiple scattering events within the tissue, and a small portion of photons eventually reach the detectors placed on the tissue surface millimeters to centimeters away from the source. There are temporal changes in the light electric field, which is due to the moving scatterers (mainly the red blood cells (RBC) in the tissue). The autocorrelation function of light electric field with respect to delay time is calculated, so as to quantify the RBC motions (i.e., blood flow) based on the mathematical models specified below [4, 22, 24, 25]:

$$g_1\left(\vec{r},\tau\right)=\frac{\left\langle E\left(\vec{r},0\right)E^*\left(\vec{r},\tau\right)\right\rangle}{\left\langle\left|E\left(\vec{r},0\right)\right|^2\right\rangle}=\int_0^\infty P(s)\exp\left(-\frac{1}{3}k_0^2<\Delta r^2(\tau)>\frac{s}{l^*}\right)ds \tag{1}$$

Here $E\left(\vec{r},0\right)$ and $E^*\left(\vec{r},\tau\right)$ denote the electric field of scattered light at time 0 and its conjugation at time τ, respectively. $\vec{r}$ denotes the position relative to the source. $P(s)$ is the normalized distribution of the detected photon path length s. k_0 is the wave vector magnitude of the light in the medium. l^* is the photon random-walk step length, with the value equal to $1/\mu_s{}'$ ($\mu_s{}'$ is the medium reduced scattering coefficient).

To comply with the principle of DCS/DCT, basic hardware components of the instrument include a few long-coherent (>5 m) lasers in NIR range, a few single-photon-detectors, a digital correlator, as well as a computer for data records and analyses. Because the light electric field ($E(0)$ and $E^*(\tau)$) cannot be directly measured, the light intensity ($I(0)$ and $I(\tau)$) was collected by the detector instead, and the temporal autocorrelation of light intensity is calculated as:

$$g_2\left(\vec{r},\tau\right)=\frac{\left\langle I\left(\vec{r},0\right)I\left(\vec{r},\tau\right)\right\rangle}{\left\langle\left|I\left(\vec{r},0\right)\right|^2\right\rangle} \tag{2}$$

There exists a Siegert relation that associates the electric field autocorrelation with light intensity autocorrelation [27]:

$$g_2\left(\vec{r},\tau\right)=1+\beta\left|g_1\left(\vec{r},\tau\right)\right|^2 \tag{3}$$

One pair of source (S) and detector (D) permits extracting a single value of BFI from the measured DCS data, by assuming that the tissue is homogeneous within the volume covered by the S-D pair. A few S-D pairs at different separations enable to extract the blood flow in tissue with relative heterogeneity (e.g., layered

tissue). Furthermore, an S-D array, i.e., numerous S-D pairs aligned in regular pattern, allows for three-dimensional tomography/imaging of blood flow by using reconstructed algorithm.

3 Conventional Reconstruction Algorithms for DCS and DCT

The conventional algorithm for DCS is based on the analytical solution of a partial differential equation (PDE), which is derived by combing the integral form of autocorrelation function and the point spread function of time-domain DOT [26]. Ultimately, the unnormalized autocorrelation of light $G_1\left(\vec{r},\tau\right) = \left\langle E\left(\vec{r},0\right)E^*\left(\vec{r},\tau\right)\right\rangle$ satisfies the following form of PDE [23, 26, 44]:

$$\left(D\nabla^2 - v\mu_a - \frac{1}{3}v\mu_s^{'}k_0^2\langle\Delta r^2(\tau)\rangle\right)G_1\left(\vec{r},\tau\right) = -vS\left(\vec{r}\right) \tag{4}$$

The analytical solution of PDE is dependent on the geometry of the tissue and usually has complicated mathematical forms. For the purpose of readily implementation, the tissue geometry is often assumed as semi-infinite, and accordingly, the below solution is obtained [7, 18]:

$$G_1(\rho,\tau) = \frac{vS_0}{4\pi D}\left(\frac{e^{-K(\tau)r_1}}{r_1} - \frac{e^{-K(\tau)r_2}}{r_2}\right) \tag{5}$$

where ρ is the source-detector separation, S_0 is source light intensity, $K^2(\tau) = 3\mu_a\mu_s^{'} + \mu_s^{'2}k_0^2\alpha\langle\Delta r^2(\tau)\rangle$, $r_1 = \sqrt{\rho^2 + (z-z_0)^2}$, $r_2 = \sqrt{\rho^2 + (z+z_0+2z_b)^2}$, $z_0 = \frac{1}{\mu_s^{'}}$, $z_b = \frac{2}{3\mu_s^{'}}\left(\frac{1+R_{eff}}{1-R_{eff}}\right)$, $R_{\text{eff}} = -1.440n^{-2} + 0.710n^{-1} + 0.668 + 0.0636n$, and n is the refraction coefficient.

The term $\alpha < \Delta r^2(\tau) >$ contained in $K^2(\tau)$ is the blood flow index (BFI) that we aim to reconstruct. The form of $<\Delta r^2(\tau)>$ varies according to different flow models being considered. For example, a diffuse model, i.e., $<\Delta r^2(\tau)> = 6D_{\text{B}}\tau$, was found to fit experimental data well in large range of tissues [7, 18]. Here, D_B is the effective diffusive coefficient. To account for the fact that some scatterers are not "moving" in the tissue, a factor α, denoting the ratio of "moving" scatterers to the total number of scatterers, is added to $<\Delta r^2(\tau)>$ (so that $<\Delta r^2(\tau)> = 6\alpha D_{\text{B}}\tau$). The combined term, αD_{B}, is referred to as blood flow index (BFI) in biological tissues.

The BFI is extracted by fitting the measured DCS data with the analytical solution, which aims to minimize the sum of the squared errors over all delay times (τ), as specified below:

$$\min_{\alpha D_B}\sum_k\left[g_{1,\text{mea}}\left(\vec{r},\tau_k\right) - g_{1,\text{cal}}\left(\vec{r},\tau_k\right)\right]^2 \tag{6}$$

Here $g_{1,\mathrm{mea}}$ and $g_{1,\mathrm{cal}}$ represent the measured data of normalized autocorrelation function and the one calculated by the analytical solution (Eqs. 3 and 5), respectively.

The solution of BFI by fitting the autocorrelation data to the analytical solution can be numerically implemented via simplex approach, wherein the BFI (i.e., αD_{B}) is the only unknown variable during the searching process. A few attempts have been made to improve the fitting procedures. For example, the parameter β is conventionally calculated via the Siegert relation prior to the calculation of BFI, in other words, solving the two variables sequentially. As an alternative method, the solution to fit the two unknowns (BFI and β) simultaneously was proposed and was shown to have good performance [11]. The methods to fit more than two unknowns (e.g., BFI and absorption coefficient u_{a} and reduced scattering coefficient u_{s}') were also developed and validated by experiments [14]. Despite the progress, fitting multiple variables with simplex method is highly theoretical and sometime may fail to find the minimum, thus has not gained widely applications.

Apart from the semi-infinite solution, there are analytical solution to the PDE (i.e., Eq. 4) for other regular tissue geometries, such as cylinder and sphere [2, 4]. However, those solutions are rarely adopted for practical applications, due to the complicated and tedious mathematical expression.

Similar to DCS, the conventional algorithm to reconstruct BFI in DCT is also based on the analytical solution to PDE (Eq. 4), with the following expression [9, 42]:

$$\ln\left(\frac{g_1\left(\vec{r}_{\mathrm{si}},\vec{r}_{\mathrm{di}},\tau\right)}{g_{1,0}\left(\vec{r}_{\mathrm{si}},\vec{r}_{\mathrm{di}},\tau\right)}\right)=\sum_{j=1}^{N}W_{ij}\left(\vec{r}_{\mathrm{si}},\vec{r}_{\mathrm{di}},\vec{r}_{\mathrm{j}},\tau\right)\Delta\left(\alpha D_{\mathrm{B}}\left(\vec{r}_{j}\right)\right) \tag{7}$$

Here $g_0\left(\vec{r}_{\mathrm{si}},\vec{r}_{\mathrm{di}},\tau\right)$ and $g_1\left(\vec{r}_{\mathrm{si}},\vec{r}_{\mathrm{di}},\tau\right)$ are the normalized autocorrelation data in homogeneous background and the heterogeneous tissue, respectively, both collected at the ith source-detector pair of $\left(\vec{r}_{\mathrm{si}},\vec{r}_{\mathrm{di}}\right)$. $\Delta\left(\alpha D_{\mathrm{B}}\left(\vec{r}_{j}\right)\right)$ is the perturbation of BFI relative to the homogeneous flow. $\vec{r}_{j}$ is the location of j voxel. $W_{ij}\left(\vec{r}_{\mathrm{si}},\vec{r}_{\mathrm{di}},\vec{r}_{\mathrm{j}},\tau\right)$ is the weight of flow contributions at jth voxel to the perturbation of autocorrelation function at pair of $\left(\vec{r}_{\mathrm{si}},\vec{r}_{\mathrm{di}}\right)$. The form of $W_{ij}\left(\vec{r}_{\mathrm{si}},\vec{r}_{\mathrm{di}},\vec{r}_{\mathrm{j}},\tau\right)$ depends on the tissue geometry and usually consists of Green's functions. The perturbation of BFI (i.e., $\Delta\left(\alpha D_{\mathrm{B}}\left(\vec{r}_{j}\right)\right)$) relative to homogeneous background is extracted by solving the linear equation group Eq. (7), with incorporation of regularization method.

In 2003, the DCT was first utilized to image the cerebral blood flow in rat during cortex spreading experiment [9]. The reconstruction algorithm was further improved by considering the noise effect, and it was adopted in rat experiments [44].

4 Recent Progress in DCS/DCT Reconstruction Algorithms

While the analytical solutions of PDE are able to quantify the BFI temporal change or spatial contrast and have been utilized for diagnosis or therapeutic monitoring of various diseases, this sort of algorithms requires the tissue to have simple and regular geometries (such as semi-infinite). Most of biological tissues or organs (e.g., brain, limb, breast) have irregular geometry, which can be quantified by medical imaging modalities. The assumption of regular geometry would lead to the error in extracting the BFI values. It was reported that the semi-infinite solution leads to up to 18% error in estimation of BFI in homogeneous tissue, dependent on the curvature of the tissue being measured [33]. Besides the geometry, the analytical solution generally assumes the tissue to be homogeneous, which is also inconsistent with most of real tissues. In recent years, many efforts have been made to improve the conventional algorithms. For example, a solution with geometry of multilayered slabs was proposed and used to investigate the brain cortex activities [19]. Similarly, an algorithm of "modified Beer-Lambert law" for blood flow was proposed to quantify the blood flow change in slab-layered tissue [1].

Although tremendous progress was made as mentioned above, the analytical solution, by nature, cannot account for arbitrary geometry of the tissue. This problem was well resolved through introduction of finite element (FE) method, according to Eq. (4). In FE method for Eq. (4), the variable to be reconstructed is $\mu_a + 2\mu_s' k_0^2 \tau \alpha D_B$. When assuming μ_a and μ_s' are homogeneous and fixing a value of delay time τ, the value of αD_B is extracted [23]. The concept of FE solution for DCT was borrowed from that of DOT, and the combined term (i.e., $\mu_a + 2\mu_s' k_0^2 \tau \alpha D_B$) is called "effective μ_a" [23], because it is equivalent to variable μ_a in DOT reconstruction. As such, there is an established FE package for DOT (e.g., Nirfast [10]) which can be readily adapted for DCT flow reconstruction.

In both phantom and in vivo experiments, the FE method exhibited good efficiency in reconstruction of BFI contrast [23] and has been used for diagnosis of the diseases such as breast cancer [17]. As seen from Eq. (4), the BFI is largely affected by the variation of μ_a when using the FE method. Moreover, only the $g_1(\tau)$ at single delay time, as described in last paragraph, is utilized in FE method. Although the $g_1(\tau)$ data at multiple delay times could be used to denoise the curve and select a stable single $g_1(\tau)$ value, the FE method, in principle, insufficiently utilizes the DCT measured data (i.e., the $g_1(\tau)$ at multiple delay times).

For sufficient use of the DCT data, we proposed a new mathematical approach, namely, the *N*th-order linear algorithm (i.e., NL algorithm) for extracting BFI value. Unlike the analytical solution or FE method, the NL algorithm does not seek for the solution of PDE. Instead, it starts with combination of an *N*th-order Taylor polynomial with the integral form of $g_1(\tau)$. After a series of mathematical procedures, the BFI is extracted by iteration of linear regressions, ultimately reaching the following expressions:

$$g_1(\tau, j) - 1 = \tau \sum_{i=1}^{n} A(i, j)\ \alpha D_B(i) \tag{8}$$

$$g_1(\tau, j) - 1 - \sum_{k=2}^{N} \frac{\sum_{p=1}^{Q} w(p, j) \left(-2 \sum_{i=1}^{n} k_0^2(i) \alpha D_B(i) s\left(i, p, j\right) \mu_s'(i) \right)^k}{k!} \tau^k$$

$$= \tau \sum_{i=1}^{n} A(i, j)\ \alpha D_B(i) \tag{9}$$

Equations (8) and (9) are called first-order and Nth-order linear (NL) algorithm, respectively. Here $\alpha D_B(i)$ is the BFI of the ith tissue component; $w(p,j)$ is the normalized weight of photon package collected by jth detector; and $s(i, p, j)$ is the path length of pth photon packet traveled within ith tissue component and collected by jth detector. The coefficient of matrix $A(i, j)$ has the following expression:

$$A(i, j) = \sum_{p=1}^{Q} -2w(p, j) k_0^2(i) s(i, p, j) \mu_s'(i) \tag{10}$$

The key parameter contained in Eqs.(8), (9), and (10) is $s(i, p, j)$, which is determined by the tissue geometry and heterogeneity, indicating that both of these two features are fully taken into consideration in NL algorithm. The accuracy of NL algorithm on various geometries and tissue heterogeneity was validated in DCS, through computer simulations as well as animal experiment [33, 35].

As an example, we compared the performance of NL algorithm and the conventional semi-infinite solution in reconstruction of the BFI in layered model of human head. For this purpose, the human head was modeled as an ideal sphere, with four layers including, in order from the outer to inner, the scalp, skull, cerebrospinal (CSF), and brain (Fig.1a). Different BFI values were assigned to each layer of head except CSF, which is considered as non-scattering tissue and does not contain RBCs. The forward problem of DCS (i.e., generating autocorrelation function $g_1(\tau)$) was implemented through Eq. (1), with the assigned BFI values and optical properties (e.g., μ_a and μ'_s) at different layers. Additionally, realistic noise was added to the DCS data according to the relevant theory of photon statistics [11, 21]. The inverse problem (i.e., reconstruction of BFI from noisy $g_1(\tau)$ data) was solved through analytical solution (Eqs. 5 and 6) and NL algorithm (Eqs. 8, 9, and 10), respectively. Due to the noise in DCS data, the reconstructed values of BFIs at different layers tend to be difficult to separate, which is referred to as "cross-talk," also commonly found in NIRS for oxygenation calculation [36]. The "cross-talk" becomes more evident when the photon signals at different layers are unbalanced. As shown in Fig. 1b, when small S-D separation (2.0 cm) is utilized, the mean photon path

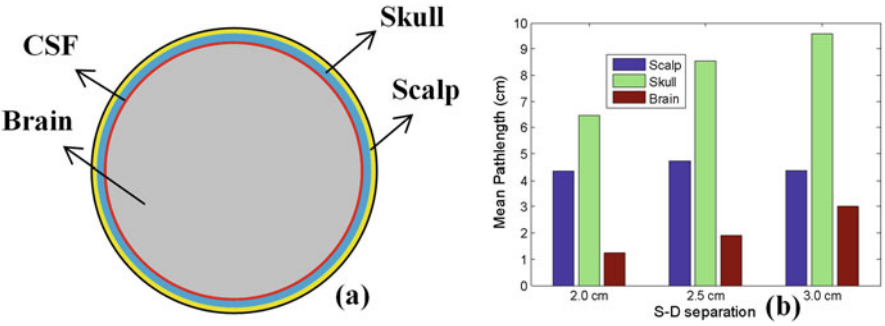

Fig. 1 (**a**) Four-layered model of human head including, in order from the outer to inner, the scalp, skull, cerebrospinal (CSF), and brain; the BFI values of the scalp, skull, and brain are assigned to be 0.5, 0, and 1.0×10^{-8} cm^2/s, respectively. (**b**) The mean path length of photons traveled in the scalp, skull, and brain, collected at different S-D separations (i.e., 2.0, 2.5, and 3.0 cm)

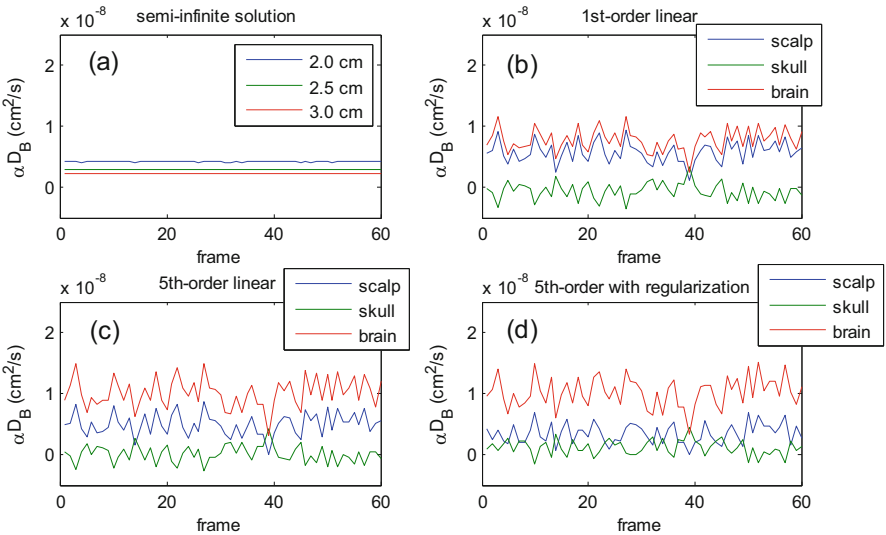

Fig. 2 Time course of BFI values at different layers, extracted by (**a**) semi-infinite solution, (**b**) first-order and (**c**) fifth-order linear algorithm, as well as the (**d**) fifth-order linear algorithm combined with regularization approach. The noisy DCS data were generated by computer simulation on layered sphere human head through Eq. (1) as well as the theory of photon statistics

length (MPL, representing the photon signals) at shallow layers (scalp and skull) is much longer than that in deep layer (brain), leading to larger signal unbalance. With increase in S-D separation (e.g., 3.0 cm), the "cross-talk" effect is greatly alleviated.

In this comparison, we also introduced the Tikhonov regularization [16, 37] to the NL algorithm, with aim to reduce the "cross-talk" among BFIs at different layers. Figure 2 shows the reconstructed value of BFI at the three layers (scalp, skull, and brain) reconstructed by semi-infinite analytical solution, NL algorithm, as well as

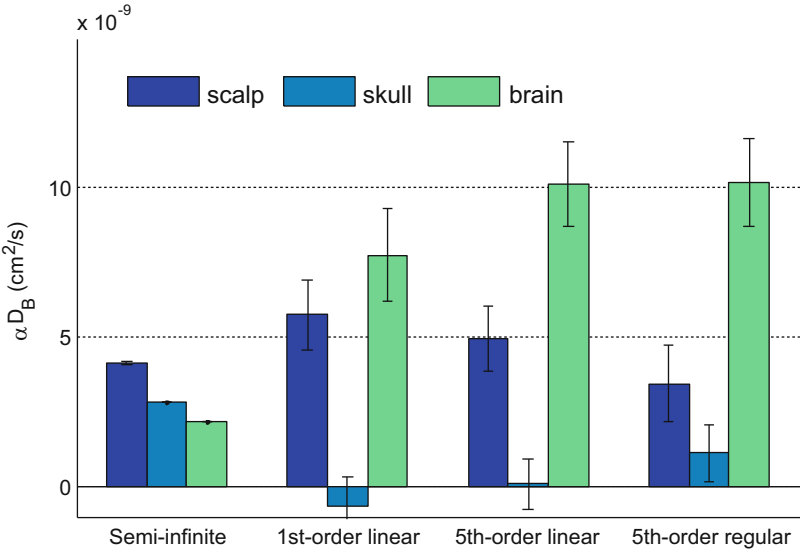

Fig. 3 The mean value and the standard derivation of BFIs in different layers, extracted by semi-infinite solution, first-order and fifth-order linear algorithm, as well as the fifth-order linear algorithm combined with regularization approach. Note that with semi-infinite solution, the BFI values extracted from 2.0, 2.5, and 3.0 cm represent flow in the scalp, skull, and brain, respectively. The two horizontal dashed lines indicate the true values of BFI in the scalp and brain (i.e., 0.5 and 1.0×10^{-8} cm^2/s, respectively). According to Fig. 1 caption, the true value of BFI in skull is 0 cm^2/s

the NL algorithm with Tikhonov regularization. Because the analytical solution can only extract a single value of BFI, the ones extracted from the small, medium, and large S-D separation (i.e., 2.0, 2.5, and 3.0 cm) data represent the BFI of the scalp, skull, and brain, respectively. Compared with the true values, the analytical solution generates the largest errors (up to 78% error in brain flow, see Fig. 3), while it is little affected by the noise, evidenced by the smallest variations (Fig. 2a). The BFI values at different layers were elegantly reconstructed by the NL algorithm, with accuracy dependent on the order of linear algorithm (Fig. 2a–d). First-order linear algorithm generates around 22.6% error in brain flow, while the error was reduced to 1.3% with fifth-order algorithm (Fig. 3). However, the noisy DCS data makes the separation of BFI values at shallow (scalp and skull) and deep (brain) layers unclear, as exhibited in Fig. 2b, c. By use of Tikhonov regularization, the BFIs at superficial layers (in blue and green) and deep layer (in red) were better separated, and the data robustness was enhanced (Fig. 2d). However, the regularization term, aiming to reduce the condition number of matrix in Eqs. 8, 9, and 10, also decreases the overall accuracy of BFI (Fig. 3). Therefore, investigations on regularization form and parameter selection are needed for future studies.

It is possible to adapt the NL algorithm for use in DCT flow imaging. With this aim, the entire tissue is discretized into numerous voxels (or elements) by

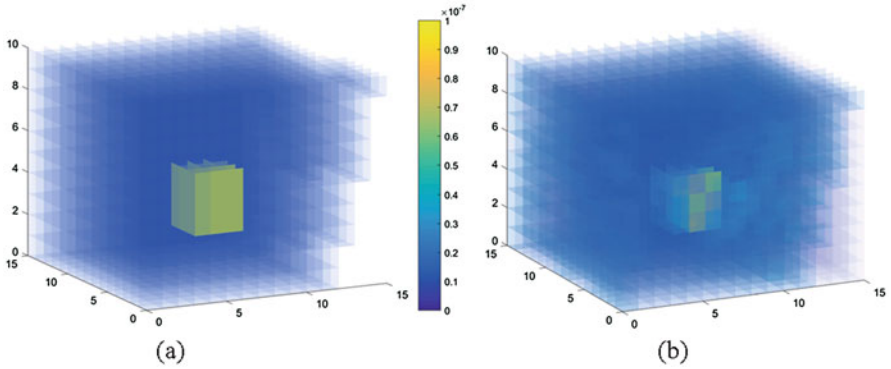

Fig. 4 The pilot outcome of DCT flow imaging by NL algorithm. (**a**) Setup of flow spatial distribution in a flat tissue, in which the flow value in a cube-shape anomaly is set as 1.0×10^{-7} cm^2/s, ten times of the background flow. The tissue contains 2250 ($15 \times 15 \times 10$) elements in a volume of $30 \times 30 \times 30$ mm^3. (**b**) Three-dimensional flow images reconstructed by NL algorithm. The autocorrelation data were collected from a 9×22 S-D array placed on the tissue surface (bottom side)

meshing, and only the BFI within the same voxel is considered homogeneous. As such, the "*i*th" in Eqs. (8)–(10) represents the number of voxel (or element) rather than the tissue component. Similar to DOT, the DCT is also an ill-posed problem requiring a few mathematical techniques to maintain the solution fidelity and robustness. Here we present a pilot outcome of DCT flow imaging by NL algorithm, for a flat tissue in a volume of $30 \times 30 \times 30$ mm^3. The Tikhonov regularization mentioned above was adopted by us as well for flow reconstruction. The autocorrelation data were collected by a 9×28 S-D array placed on the tissue surface. To establish the DCT model, the flat tissue was meshed with 2250 elements ($15 \times 15 \times 10$), as shown in Fig. 4a. The tissue contains a cube-shape anomaly with BFI value at 1.0×10^{-7} cm^2/s, ten times of the surrounding tissue. Figure 4b exhibits three-dimensional imaging of flow reconstructed by NL algorithm and Tikhonov regularization approach. Generally, the anomaly was well reconstructed and the outline is clearly visible. Due to the large unbalance between the numbers of unknowns (i.e., 2250 elements) and that of measurements (i.e., 252 S-D pairs), however, the reconstructed flow images tend to be homogenized, when compared to the true contrast shown in Fig. 4a. More approaches for image reconstructions (e.g., algebraic reconstruction technique (ART), total variation (TV)) could be considered as the potential method to improve the quality of flow imaging, which is one target of our ongoing research projects.

5 The Future Prospective of the DCS/DCT Reconstruction Algorithms

While the applications of DCS and DCT to physiological studies and clinic are remarkably increasing in recent years, there are technical challenges, particularly in reconstruction algorithms. The first challenge is how to process the noisy autocorrelation data, in order to enhance the accuracy and robustness of BFI value. As mentioned in Sect. 3, by use of the analytical solution, the BFI was extracted through minimizing the sum of squared errors between the analytical $g_1(\tau)$ value and measured data (also referred to as least-squares method), which is based on L_2 norm minimization. The L_2 norm minimization, however, is susceptible to the noisy data, or in other words, the target value is influenced more by the data with larger error than that by the smaller one. The L_2 norm minimization is also applied to the procedure of linear regression in NL algorithm that we proposed. In the past decade, there are increasing studies on L_1 norm minimization, which exhibits advantages in denoising and robustness for image reconstruction. In addition to the L_1 norm minimization, the progress in classification or cluster methods (such as the support vector regression) provides alternative solutions to the fitting optimization. Hence, introduction of advanced optimization approaches into DCS/DCT reconstruction algorithm is one of the potential future studies.

For extraction of the BFIs at multiple layers (or tissues) using NL algorithm, an important factor affecting the BFI value is the parameter selection. For example, we used L-curve method to determine the parameter value in Tikhonov regularization for the outcomes presented in Fig. 2. However, we found that the L-curve is not ideal in parameter selection when the noise level is high, and manual adjustment of parameter value is thus required. Furthermore, for any reconstruction approach (e.g., Tikhonov regularization, ART, or TV), development of mathematical techniques that incorporate both solution fidelity and data noise will be a worthwhile target of future research.

How to improve the temporal and spatial resolution of DCS/DCT would be another possible research direction in field of reconstruction algorithm. Compared with the morphological imaging modalities such as CT or MRI, the diffuse optical technologies (DOT and DCT) have limited measured data, leading to low spatial resolution in reconstructed images. Adding more S-D pairs to the optical system is the most straightforward solution, which, however, substantially increases the instrumentation cost. Maximizing the spatial resolution with limited measured data would be a realistic solution, which is also a study focus for other image technologies, such as CT or MRI. A few optimization methods proposed for those image technologies, such as the compressed sensing or deep learning, could also be translational to improve the spatial resolution of DCT flow imaging. Moreover, the method could also be used to improve the temporal resolution of DCS, which is particular critical for real-time monitoring of acute diseases such as ischemic stroke.

Acknowledgments This work is partially supported by the National Natural Science Foundation of China (61771433), National Key Research and Development Program of China (2016YFC0101602), and Shanxi Scholarship Council of China (2016-087).

Conflicts of Interest The author declares no conflict of interest.

References

1. Baker WB, Parthasarathy AB, Busch DR, Mesquita RC, Greenberg JH, Yodh AG (2014) Modified beer-Lambert law for blood flow. Biomed Opt Express 5:4053–4075
2. Boas D (1996) Diffuse photon probes of structural and dynamical properties of turbid media: theory and biomedical applications. Department of Physics. University of Pennsylvania, Philadelphia, pp 1–244
3. Boas DA, Campbell LE, Yodh AG (1995) Scattering and imaging with diffusing temporal field correlations. Phys Rev Lett 75:1855–1858
4. Boas DA, Yodh AG (1997) Spatially varying dynamical properties of turbid media probed with diffusing temporal light correlation. J Optical Soc Am Optics Image Sci Vision 14:192–215
5. Busch DR, Lynch JM, Winters ME, McCarthy AL, Newland JJ, Ko T, Cornaglia MA, Radcliffe J, McDonough JM, Samuel J, Matthews E, Xiao R, Yodh AG, Marcus CL, Licht DJ, Tapia IE (2016) Cerebral blood flow response to hypercapnia in children with obstructive sleep apnea syndrome. Sleep 39:209–216
6. Cheng R, Shang Y, Hayes D, Saha SP, Yu G (2012) Noninvasive optical evaluation of spontaneous low frequency oscillations in cerebral hemodynamics. NeuroImage 62:1445–1454
7. Cheung C, Culver JP, Takahashi K, Greenberg JH, Yodh AG (2001) In vivo cerebrovascular measurement combining diffuse near-infrared absorption and correlation spectroscopies. Phys Med Biol 46:2053–2065
8. Choe R, Putt ME, Carlile PM, Durduran T, Giammarco JM, Busch DR, Jung KW, Czerniecki BJ, Tchou J, Feldman MD, Mies C, Rosen MA, Schnall MD, DeMichele A, Yodh AG (2014) Optically measured microvascular blood flow contrast of malignant breast tumors. PLoS One 9:e99683
9. Culver JP, Durduran T, Furuya T, Cheung C, Greenberg JH, Yodh AG (2003) Diffuse optical tomography of cerebral blood flow, oxygenation, and metabolism in rat during focal ischemia. J Cereb Blood Flow Metab 23:911–924
10. Dehghani H, Eames ME, Yalavarthy PK, Davis SC, Srinivasan S, Carpenter CM, Pogue BW, Paulsen KD (2009) Near infrared optical tomography using NIRFAST: algorithm for numerical model and image reconstruction. Commun Numer Methods Eng 25:711–732
11. Dong L, He L, Lin Y, Shang Y, Yu G (2013) Simultaneously extracting multiple parameters via fitting one single autocorrelation function curve in diffuse correlation spectroscopy. IEEE Trans Biomed Eng 60:361–368
12. Dong L, Kudrimoti M, Cheng R, Shang Y, Johnson EL, Stevens SD, Shelton BJ, Yu G (2012) Noninvasive diffuse optical monitoring of head and neck tumor blood flow and oxygenation during radiation delivery. Biomed Opt Express 3:259–272
13. Durduran T, Choe R, Baker WB, Yodh AG (2010) Diffuse optics for tissue monitoring and tomography. Rep Prog Phys 73:076701
14. Farzam P, Durduran T (2015) Multidistance diffuse correlation spectroscopy for simultaneous estimation of blood flow index and optical properties. J Biomed Opt 20:055001
15. Ferrari M, Muthalib M, Quaresima V (2011) The use of near-infrared spectroscopy in understanding skeletal muscle physiology: recent developments. Philos Trans A Math Phys Eng Sci 369:4577–4590

16. Hansen PC, Jensen TK, Rodriguez G (2007) An adaptive pruning algorithm for the discrete L-curve criterion. J Comp Appl Math 198:483–492
17. He L, Lin Y, Huang C, Irwin D, Szabunio MM, Yu G (2015) Noncontact diffuse correlation tomography of human breast tumor. J Biomed Opt 20:086003
18. Irwin D, Dong L, Shang Y, Cheng R, Kudrimoti M, Stevens SD, Yu G (2011) Influences of tissue absorption and scattering on diffuse correlation spectroscopy blood flow measurements. Biomed Opt Express 2:1969–1985
19. Jaillon F, Skipetrov SE, Li J, Dietsche G, Maret G, Gisler T (2006) Diffusing-wave spectroscopy from head-like tissue phantoms: influence of a non-scattering layer. Opt Express 14:10181–10194
20. Jobsis FF (1977) Noninvasive, infrared monitoring of cerebral and myocardial oxygen sufficiency and circulatory parameters. Science 198:1264–1267
21. Koppel DE (1974) Statistical accuracy in fluorescence correlation spectroscopy. Phys Rev A 10:1938–1945
22. Li T, Lin Y, Shang Y, He L, Huang C, Szabunio M, Yu G (2013) Simultaneous measurement of deep tissue blood flow and oxygenation using noncontact diffuse correlation spectroscopy flow-oximeter. Sci Rep 3:1358
23. Lin Y, Huang C, Irwin D, He L, Shang Y, Yu G (2014) Three-dimensional flow contrast imaging of deep tissue using noncontact diffuse correlation tomography. Appl Phys Lett 104:121103
24. Maret G, Wolf PE (1987) Multiple light-scattering from disordered media – the effect of Brownian-motion of Scatterers. Zeitschrift Fur Physik B-Condensed Matter 65:409–413
25. Pine DJ, Weitz DA, Chaikin PM, Herbolzheimer E (1988) Diffusing-wave spectroscopy. Phys Rev Lett 60:1134–1137
26. Pine DJ, Weitz DA, Zhu JX, Herbolzheimer E (1990) Diffusing-wave spectroscopy – dynamic light-scattering in the multiple-scattering limit. J Phys 51:2101–2127
27. Rice SO (1954) Mathematical analysis of random noise. In: Wax N (ed) Noise and stochastic processes. Dover, New York, p 133
28. Roche-Labarbe N, Carp SA, Surova A, Patel M, Boas DA, Grant RE, Franceschini MA (2010) Noninvasive optical measures of CBV, StO(2), CBF index, and rCMRO(2) in human premature neonates' brains in the first six weeks of life. Hum Brain Mapp 31:341–352
29. Saumet JL, Kellogg DL, Taylor WF, Johnson JM (1988) Cutaneous laser-Doppler Flowmetry – influence of underlying muscle blood-flow. J Appl Physiol 65:478–481
30. Shang Y, Chen L, Toborek M, Yu G (2011a) Diffuse optical monitoring of repeated cerebral ischemia in mice. Opt Express 19:20301–20315
31. Shang Y, Cheng R, Dong L, Ryan SJ, Saha SP, Yu G (2011b) Cerebral monitoring during carotid endarterectomy using near-infrared diffuse optical spectroscopies and electroencephalogram. Phys Med Biol 56:3015–3032
32. Shang Y, Gurley K, Symons B, Long D, Srikuea R, Crofford LJ, Peterson CA, Yu G (2012) Noninvasive optical characterization of muscle blood flow, oxygenation, and metabolism in women with fibromyalgia. Arthritis Res Ther 14:R236
33. Shang Y, Li T, Chen L, Lin Y, Toborek M, Yu G (2014) Extraction of diffuse correlation spectroscopy flow index by integration of Nth-order linear model with Monte Carlo simulation. Appl Phys Lett 104:193703
34. Shang Y, Li T, Yu G (2017) Clinical applications of near-infrared diffuse correlation spectroscopy and tomography for tissue blood flow monitoring and imaging. Physiol Meas 38:R1–R26
35. Shang Y, Yu G (2014) A Nth-order linear algorithm for extracting diffuse correlation spectroscopy blood flow indices in heterogeneous tissues. Appl Phys Lett 105:133702
36. Strangman G, Franceschini MA, Boas DA (2003) Factors affecting the accuracy of near-infrared spectroscopy concentration calculations for focal changes in oxygenation parameters. NeuroImage 18:865–879
37. Tikhonov AN, Arsenin VY (1977) Solutions of ill-posed problems. Winston & Sons, Washington, D.C

38. Tschakovsky ME, Shoemaker JK, Hughson RL (1995) Beat-by-beat forearm blood-flow with Doppler ultrasound and strain-gauge plethysmography. J Appl Physiol 79:713–719
39. Wolf M, Ferrari M, Quaresima V (2007) Progress of near-infrared spectroscopy and topography for brain and muscle clinical applications. J Biomed Opt 12:062104
40. Yu G, Durduran T, Lech G, Zhou C, Chance B, Mohler ER, Yodh AG (2005) Time-dependent blood flow and oxygenation in human skeletal muscles measured with noninvasive near-infrared diffuse optical spectroscopies. J Biomed Opt 10:024027
41. Yu G, Floyd TF, Durduran T, Zhou C, Wang JJ, Detre JA, Yodh AG (2007) Validation of diffuse correlation spectroscopy for muscle blood flow with concurrent arterial spin labeled perfusion MRI. Opt Express 15:1064–1075
42. Zhou C (2007) In-vivo optical imaging and spectroscopy of cerebral hemodynamics. University of Pennsylvania, Philadelphia, pp 1–325
43. Zhou C, Eucker SA, Durduran T, Yu G, Ralston J, Friess SH, Ichord RN, Margulies SS, Yodh AG (2009) Diffuse optical monitoring of hemodynamic changes in piglet brain with closed head injury. J Biomed Opt 14:034015
44. Zhou C, Yu G, Furuya D, Greenberg JH, Yodh AG, Durduran T (2006) Diffuse optical correlation tomography of cerebral blood flow during cortical spreading depression in rat brain. Opt Express 14:1125–1144

Steady and Transient Flow CFD Simulations in an Aorta Model of Normal and Aortic Aneurysm Subjects

R. Vinoth, D. Kumar, Raviraja Adhikari, S. Vijayapradeep, K. Geetha, R. Ilavarasi, and Saravanakumar Mahalingam

1 Introduction

The aorta is the biggest artery in cardiovascular system; it serves as the medium for transmission of blood from heart to all organs in the body. An aortic aneurysm (AA) is a regional bulging of the aorta. It represents the progressive weakening of aortic wall in aneurysm region. Thoracic aortic aneurysm (TAA) and abdominal aortic aneurysm (AAA) are the major subclasses of aortic aneurysm. TAA occurs in the thoracic region of aorta and AAA occurs in the abdominal region of aorta. The aneurysm may rupture if it is not treated timely, and it can be treated by medical procedure and surgery. Aortic aneurysm is standing at fifteenth and tenth position as leading cause of death and top ten killers for men older than 55 years, respectively, according to the Society for Vascular Surgery. Abdominal aortic aneurysm is identified as the 18th leading cause of death in patients of all age groups and the

R. Vinoth
Division of Nanotechnology, Department of Electronics and Communication Engineering, Periyar Maniammai University, Thanjavur, Tamil Nadu, India

Department of Electronics and Communication Engineering, Manipal Institute of Technology, Manipal University, Udupi, Karnataka, India

D. Kumar (✉) · S. Vijayapradeep · K. Geetha · R. Ilavarasi
Division of Nanotechnology, Department of Electronics and Communication Engineering, Periyar Maniammai University, Thanjavur, Tamil Nadu, India
e-mail: headnano@pmu.edu

R. Adhikari
Department of Mechanical and Manufacturing Engineering, Manipal Institute of Technology, Manipal University, Udupi, Karnataka, India

S. Mahalingam
Honeywell Technology Solutions, Bengaluru, Karnataka, India

M. Jiang et al. (eds.), *The Proceedings of the International Conference on Sensing and Imaging*, Lecture Notes in Electrical Engineering 506,
https://doi.org/10.1007/978-3-319-91659-0_3

15th leading cause of death in the age group more than 65 years [1]. Every year in the United States (USA), more than 15,000 patients die due to aneurysm dissection and rupture [2]. The rupture or dissection of aortic aneurysm may happen when aneurysm's diameter reaches value in the range of 6–7 cm [3]. The maximum aneurysm diameter criteria are used for the predication of aneurysm's rupture and advising the aneurysm patients to undergo medical procedure or surgery [4–6]. Darling et al. [7] described that the aneurysm with large diameter may not rupture. Choksy et al. [8], Nicholls et al. [9] and Hall et al. [10] have reported that the aneurysm with small diameter could also rupture. The maximum aneurysm diameter criteria for the predication of rupture are unreliable [11]. The maximum diameter criteria do not convinced the researchers in predicting the rupture of aneurysms. The medical procedures and surgery for treating the aneurysms are high in price with high mortality risks. Since the medical treatment expenses and mortality rate are high, using the diameter of aneurysm as basis for advising the patients for aneurysm repair is incompatible. It is essential to detect new parameters to predict the aneurysm's rupture and dissection. The diseases are to be found to exist in cardiovascular system due to flow conditions in blood vessels [12]. Since the flow of blood through vessel changes haemodynamic forces acting on the blood vessel wall, the investigation on flows in aorta is crucial. The occurrence of aneurysm in blood vessel mainly depends on the relationship between haemodynamic forces and corresponding changes in layers of blood vessel wall [13]. Therefore, it is believed that the interaction between haemodynamic forces and physiological conditions of blood vessel wall plays a major role in the aneurysm formation, its progression and rupture. Computational fluid dynamics (CFD) technique has been widely used for simulating the blood flow in blood vessels.

In the present work, computational fluid dynamics approach is used for the simulation of blood flow through an aorta model of normal subject and patient-specific aortic aneurysm model. The bifurcations, curvature of arteries and branches could result in the complex flow regions in the abdominal aorta [14]. Shahcheraghi et al. [15] reported the effect of aortic branches on the flow. The aortic branches considered by Shahcheraghi et al. in their model are included in the present study. The brachiocephalic artery, common carotid artery, left subclavian artery, celiac artery, renal arteries, superior mesenteric artery, inferior mesenteric artery and common iliac arteries are included in the present study. The other branches and arteries are not included in the present model to reduce the computational time.

The blood has a non-Newtonian nature, but it adopts Newtonian nature when the shear rate is more than 100 s^{-1} [16, 17]. The blood as a Newtonian fluid is an acceptable condition for large arteries like aorta [16, 18, 19]. In unsteady flow analysis, the non-Newtonian nature of blood influences the flow when the shear rate is less than 100 s^{-1} [16]. Yu Lei et al. [20] reported that the non-Newtonian nature of blood plays a crucial role in the transportation of oxygen and low-density lipoproteins (LDL) and the Newtonian blood rheology underestimates the wall shear stress. Some authors reported that the non-Newtonian assumption for flow simulation in large blood vessels is essential [21–23], while a few other authors concluded that it is a noncrucial assumption [24, 25].

The purpose of this study is to compare the blood flow pattern of aorta model of normal subject with blood flow pattern of patient-specific aortic aneurysm. The steady and transient analyses of flow were carried out. The haemodynamic parameters like wall pressure, wall shear stress (WSS) and velocity distribution were estimated during the analysis.

2 Methodology

2.1 Generation of Geometry

The generation of aortic geometry was described in our previous publication [26], and it is depicted again in this section. The subject of normal case was a 36-year-old female, and AAA case was a male aged 79 years. The heart rate and blood pressure of subjects were normal. The study approved by the Institutional Ethics Committee-Clinical Studies (Apollo Hospitals, Chennai, India) and obeyed to the declaration of Helsinki. A 320-slice computed tomographic (CT) scanner (Aquilion one, Toshiba Medical System) was used to obtain sectional images of the aneurysmal and normal aorta. The pixel size and slice thickness were 0.5 mm. The 3D geometry of subjects was reconstructed from CT image using Mimics v17.0 (Materialise, Belgium). The reconstructed geometry of aneurysmal aorta is shown in Fig. 1, and the reconstructed geometry of aorta of normal subject was shown in our previous publication [26].

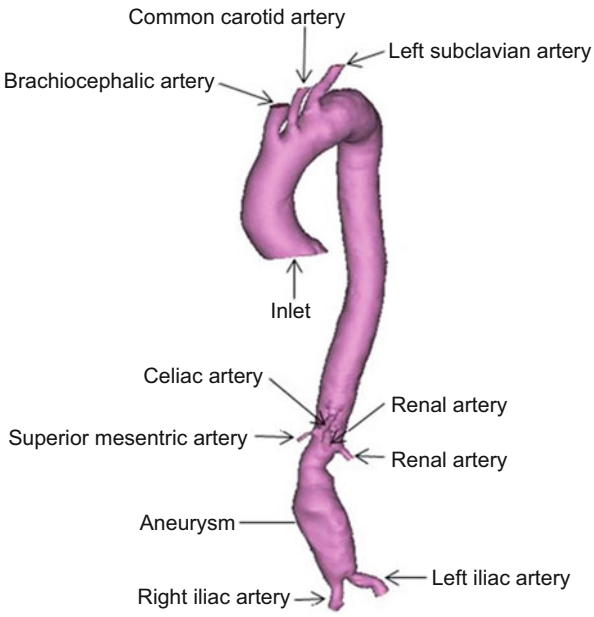

Fig. 1 Geometry of aneurysmal aorta

2.2 Flow and Boundary Conditions

Steady State

The three-dimensional blood flow is governed by the Navier-Stokes and continuity equations. The solutions of these governing equations were computed by using a volume-based solver

ANSYS CFX (v15, ANSYS, Inc.). The laminar model was employed for the flow simulation. The value of 10^{-4} was taken as maximum RMS residual value for controlling the accuracy of solution. To attain convergence in simulation, the minimum iteration was kept as 100, and maximum iteration was set at 500 in convergence control. The Reynolds number considered for the flow analysis was 1,350 [27]. The velocity of 0.225 m/s was set as the inlet boundary condition for aorta, which is calculated from the Reynolds number. The opening boundary conditions were considered with static pressure of 120 mmHg at the outlet of all the branches and iliac arteries. The aortic wall was taken as rigid, and no-slip boundary condition was used at the aortic wall. The assumption of Newtonian model for blood is a satisfactory assumption for aorta [16, 18, 19]; hence, the blood flow was assumed to be Newtonian, homogeneous and incompressible. The density and dynamic viscosity of blood were to be 1050 kg m^{-3} and 0.0035 Ns m^{-2}, respectively [16, 18, 28].

Transient State

The transient analysis was carried out to investigate the pulsatile nature of flow through an aorta and a patient-specific aortic aneurysm. The time-varying velocity and pressure profiles were obtained from Olufsen et al. [29]. The velocity profiles at the inlet of aorta and pressure profile at the outlet of iliac arteries were enforced in simulation. The velocity profile for aneurysmal aorta is shown in Fig. 2. The velocity profile for normal subject and pressure profile were shown in our previous publication [26]. In the present work, five cardiac cycles were employed with a step of 0.002 s. The fifth cycle was taken as the final solution to estimate the haemodynamic parameters from the aorta models. The pressure waveforms enforced for both subject are the same. The cardiac cycle period was taken as 1 s and the flow reaches its peak value at 0.14 s. A 15% of the inlet flow volume was considered at brachiocephalic artery, and 5% of the inlet flow volume was assumed for left subclavian artery and common carotid artery [15]. A 10% of the thoracic mass flow was set at renal arteries [30], and pressure was assumed at other branches. The blood was assumed to be a non-Newtonian fluid. The Casson fluid model was recommended for non-Newtonian fluids by Casson [31], and the Casson fluid model was used in the simulations to approximate the non-Newtonian nature of flow. The dynamic viscosity of the Casson fluid model is given by Eq. (1) [32].

$$\sqrt{\mu} = \sqrt{\frac{\tau_Y}{\dot{\gamma}}} + \sqrt{K} \tag{1}$$

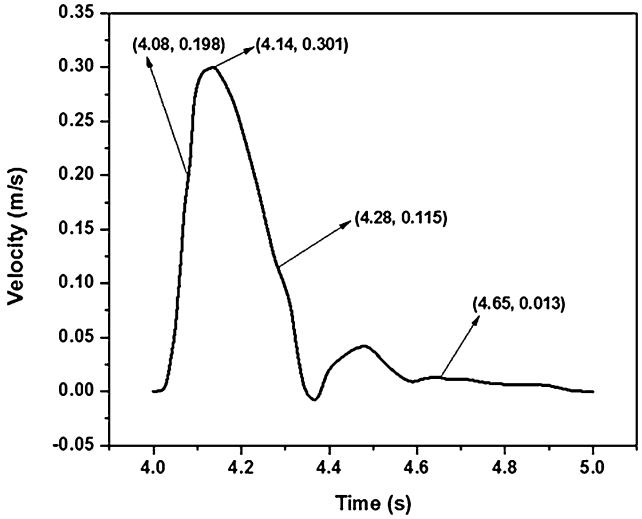

Fig. 2 Velocity profile. The fifth cardiac cycle of inlet velocity waveform of aneurysmal subject

Table 1 Mesh sensitivity test for aneurysmal aorta model

Mesh	Number of mesh elements	Wall shear stress in Pa	Difference in %
Coarse mesh	546,087	17.684	
			54.61
Medium mesh	1,148,858	27.343	
			30.45
Fine mesh	1,488,499	35.67	

where μ is the dynamic viscosity, τ_Y is the yield stress, $\dot{\gamma}$ is the shear strain rate and K is the viscosity consistency. The yield stress was assumed as 0.004 Pascal [33]. The other boundary conditions and properties were the same as that of steady-state analysis.

2.3 Meshing and Mesh Sensitivity Test

The fluid domain geometry of aorta models was discretised into tetrahedral elements by using ANSYS Workbench (v15, ANSYS, Inc.). Three tetrahedral meshes (coarse, medium and fine mesh) were generated for the fluid domain geometry of each model. The mesh sensitivity test was carried out by steady-state analysis with maximum wall shear stress (WSS) value as reference for comparison in the model. Table 1 shows the details of mesh sensitivity test of aneurysmal model. The mesh sensitivity test for normal subject was shown in our previous publication [26]. It is

observed that the difference in maximum WSS between fine and medium mesh was lesser than the same between medium and coarse mesh. Hence, the fine mesh was considered for analyses.

3 Results and Discussion

3.1 Steady State

The velocity, wall pressure and wall shear stress distributions in the models were estimated from this analysis. Figure 3 shows velocity streamline of the aorta models. The flow in aorta model of normal subject is highly stable. The flow in aneurysmal aorta model is unstable and recirculation encounters in aneurysm region. This recirculation makes the bits of protoplasm in prolonged contact with the aneurysm lumen surface, and it induces the platelets deposition in the lumen surface [34]. The platelets deposition contributes to the thrombus formation, and it may lead to aneurysm rupture. The high velocity of flow has occurred at the branches of aortic arch. The peak velocity of the aneurysmal model (1.068 m/s) was greater than the same of the aorta model of normal subject (0.671 m/s). The results depict that the

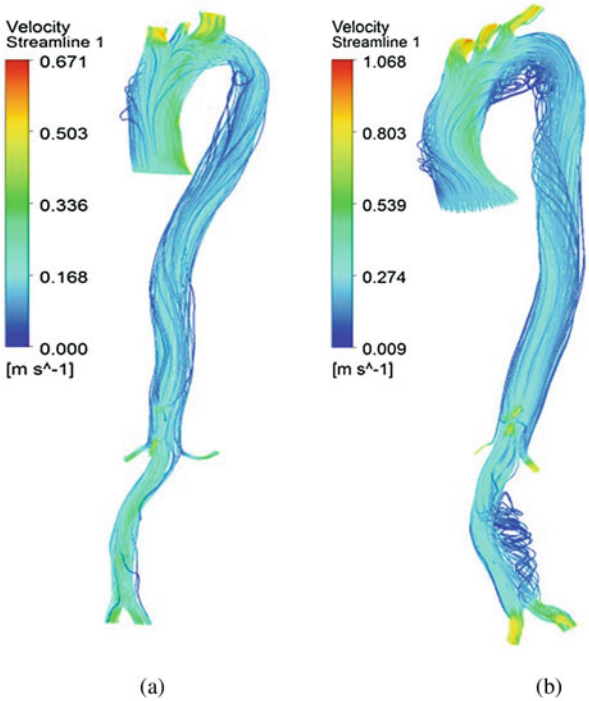

Fig. 3 Velocity streamline. (**a**) Normal (**b**) Diseased

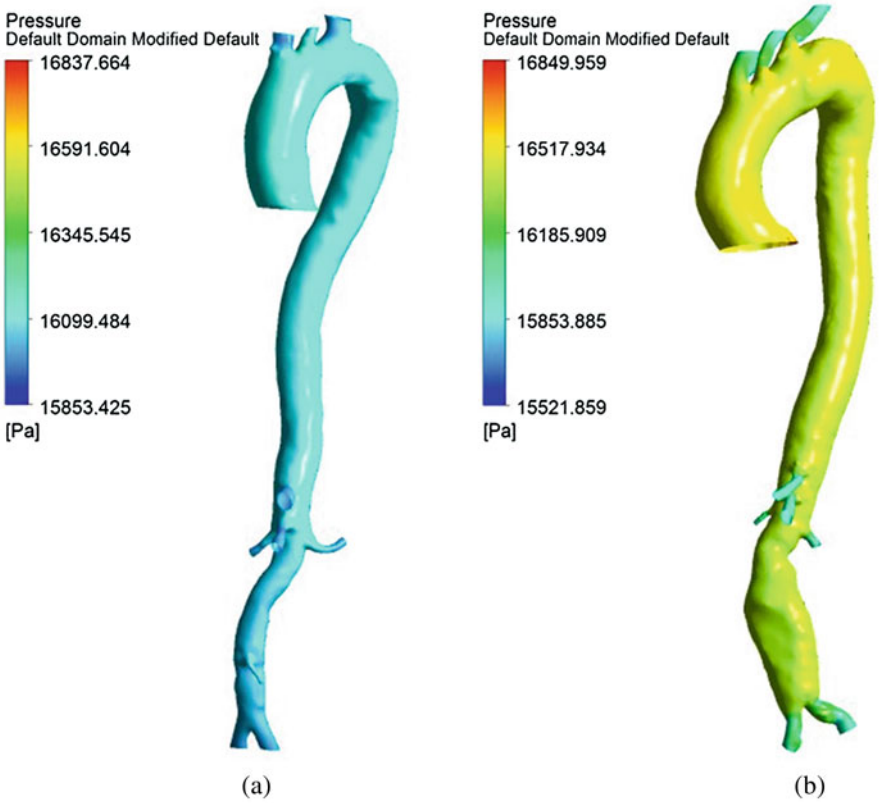

Fig. 4 Wall pressure. (**a**) Normal (**b**) Diseased

flow was streamline in aorta model of normal subject but the flow was unstable in the aneurysmal aorta model due to recirculation. The flow pattern within the lumen surface depends on the geometrical arrangement of lumen. These results propose that the aneurysm may cause severe threats to the patients. The wall pressure distribution of the aorta models is shown in Fig. 4. The wall pressure was distributed uniformly in the aorta model of normal subject, but there was a nonuniformity in wall pressure distribution in the aneurysmal aortic model. The peak pressure of the aneurysmal model (16,849.959 Pa) was more than the same in the aorta model of normal subject (16,837.664 Pa). The pressure distribution result reveals that the variation in the flow dynamics within the aneurysm region may increase aortic wall pressure. Figure 5 presents the wall shear stress (WSS) distribution in aorta models. The WSS is a stress component, and it is a tangential force acting on the lumen surface due to blood flow. The wall shear stress can be converted into biological signals by mechanoreceptor, and this signal acts on the endothelial cells as stimulator to change the cellular functions of the vessel wall [35, 36]. The platelet deposition along the aneurysm region is related with the WSS distribution along the

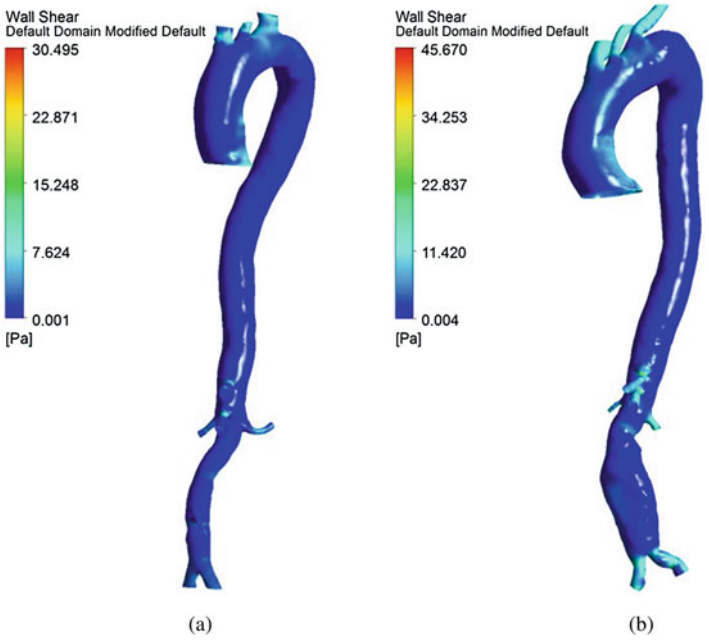

Fig. 5 Wall shear stress. (**a**) Normal (**b**) Diseased

aneurysmal wall. The WSS is distributed comparatively uniform in both models. The high magnitude of wall shear stresses appeared at the branches of aorta and bifurcation. The peak value of WSS in aneurysmal model (45.670 Pa) was more than the peak value of WSS from aorta model of normal subject (30.495 Pa).

3.2 Transient State

The velocity, wall pressure and WSS were estimated at four different time instants during the cardiac cycle from transient analysis. These four time instants ($t = 4.08$ s (maximum acceleration), 4.14 s (peak systole), 4.28 s (maximum deceleration) and 4.65 s (mid-diastole)) represent the important phases of the cardiac cycle. The velocity streamlines of the aorta models are shown in Fig. 6. The streamlines show that each model has a unique flow pattern according to the shape of aorta. At all-time instants, the peak velocity of aorta model of normal subject was higher than the peak velocity of aneurysmal aorta. At $t = 4.08$ s, the flow was uniform in both models. The peak velocity occurred at branches of aorta. At $t = 4.08$ s and $t = 4.14$ s, the velocity decreased in the aneurysm region. At $t = 4.14$ s, the velocity increased in the descending region of aorta of normal subject, and flow became retrograde in the aneurysm region. At $t = 4.28$ s, the velocity has reached its peak value at

the bifurcation, and the velocity increased in aneurysm region. The recirculation of flow and vortices occurred in aneurysm cavity. At $t = 4.65$ s, the flow velocity increased in aortic arch and aneurysm region. The flow in aneurysmal model became

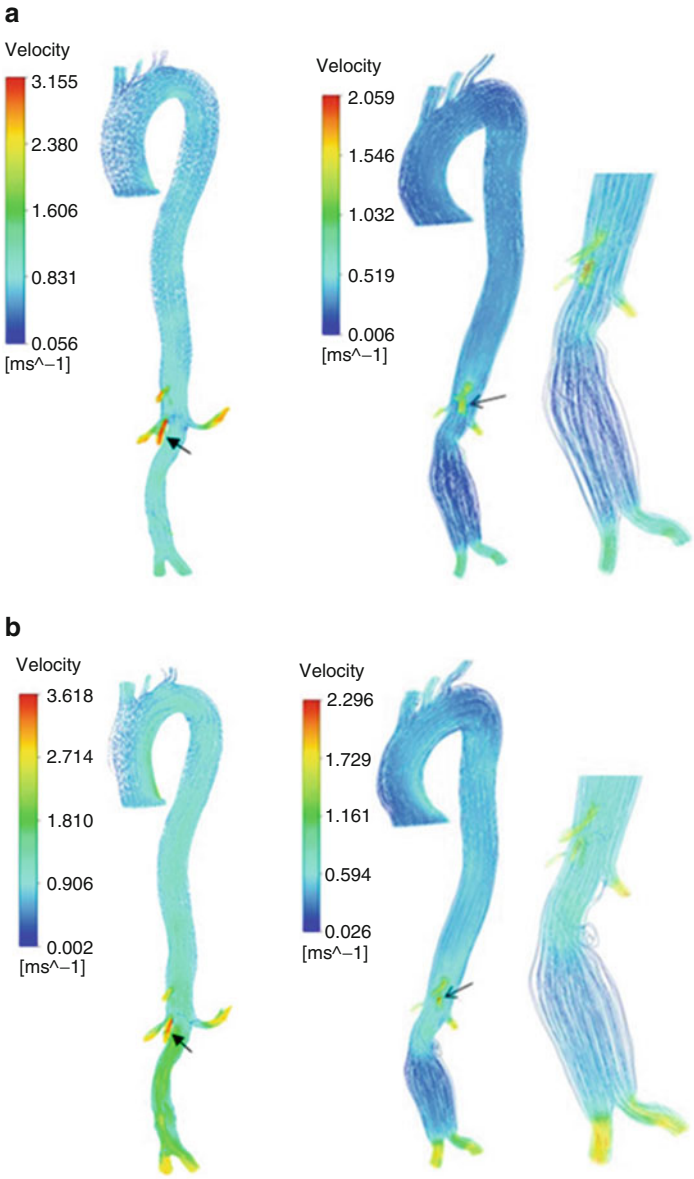

Fig. 6 Velocity streamlines. (**a**) $t = 4.08$ s (**b**) $t = 4.14$ s (**c**) $t = 4.28$ s (**d**) $t = 4.65$ s. Arrows indicate the peak value. Magnified image is displayed on the right side

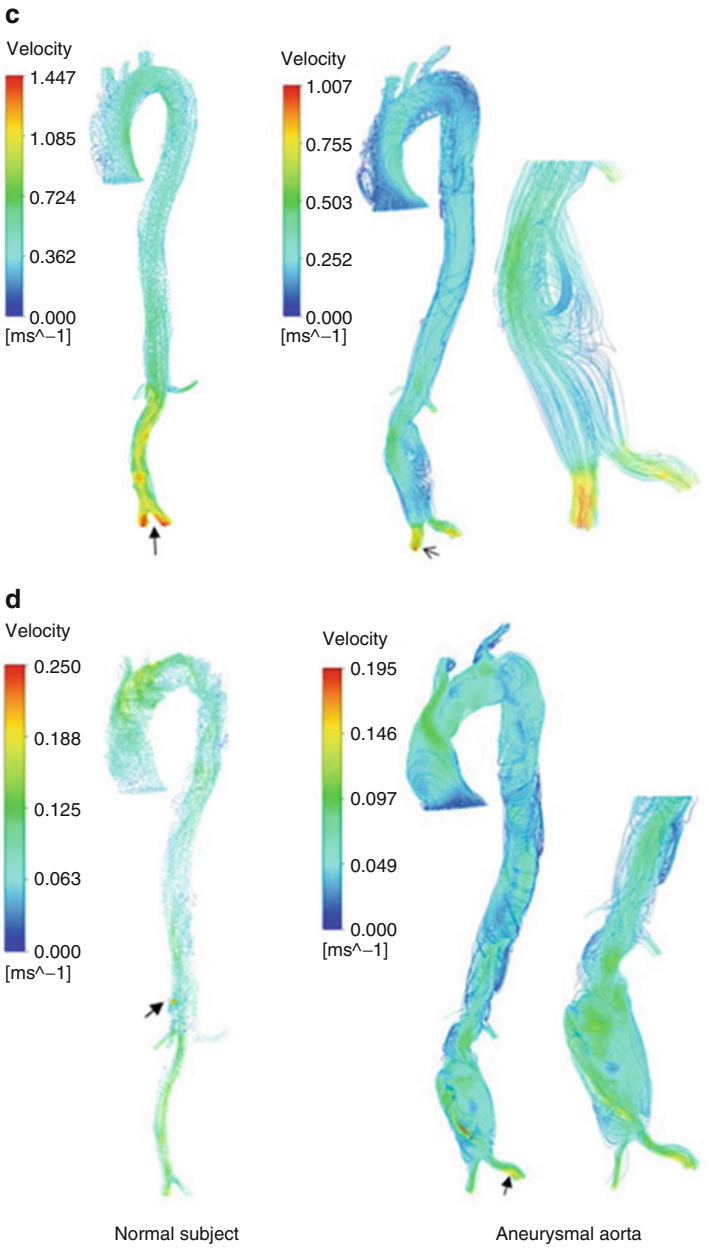

Fig. 6 (continued)

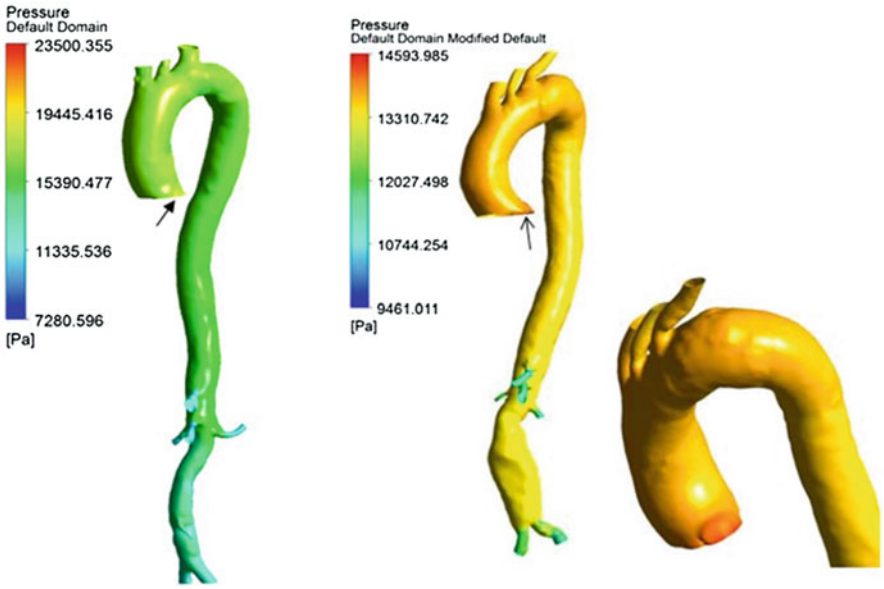

Fig. 7 Wall pressure at peak velocity. Arrows indicate the peak value. Magnified image is displayed on the right side

worse. The recirculation may increase the deposition of platelets. This promotes the thrombus renewal and it may cause aneurysm rupture. Figure 7 depicts the pressure distribution at aortic walls at peak velocity. The higher-pressure value was observed in the aorta model of normal subject. This occurs due to degree of complexity in shape of aorta. The pressure decreased in the descending region of aorta in normal subject. The pressure in aneurysm cavity was comparatively lower than the pressure in the aortic arch. There was no change in radial pressure within the aneurysm region.

The wall shear stress distribution in aorta models is presented in Fig. 8. At $t = 4.08$ s, very low WSS is distributed in the aorta models, and a little higher shear stress appeared at the branches of abdominal aorta. At peak systole, the WSS attains its peak value. A few patches of low WSS (62.476–124.926 Pa) appeared in the abdominal aorta region of normal subject. A little higher WSS occurred at the bifurcation of aneurysmal aorta. At $t = 4.28$ s, some patches of low WSS were distributed in ascending aorta, arch of aorta and descending aorta. The high WSS appeared at the bifurcations. At mid-diastole, the intensity level of low WSS patches has increased in the aortic arch and abdominal regions. The abnormal low and high shear stress regions are observed in the aneurysm region. The abnormal low and high wall shear stress patterns play an important role in the formation of thrombus and aneurysm rupture.

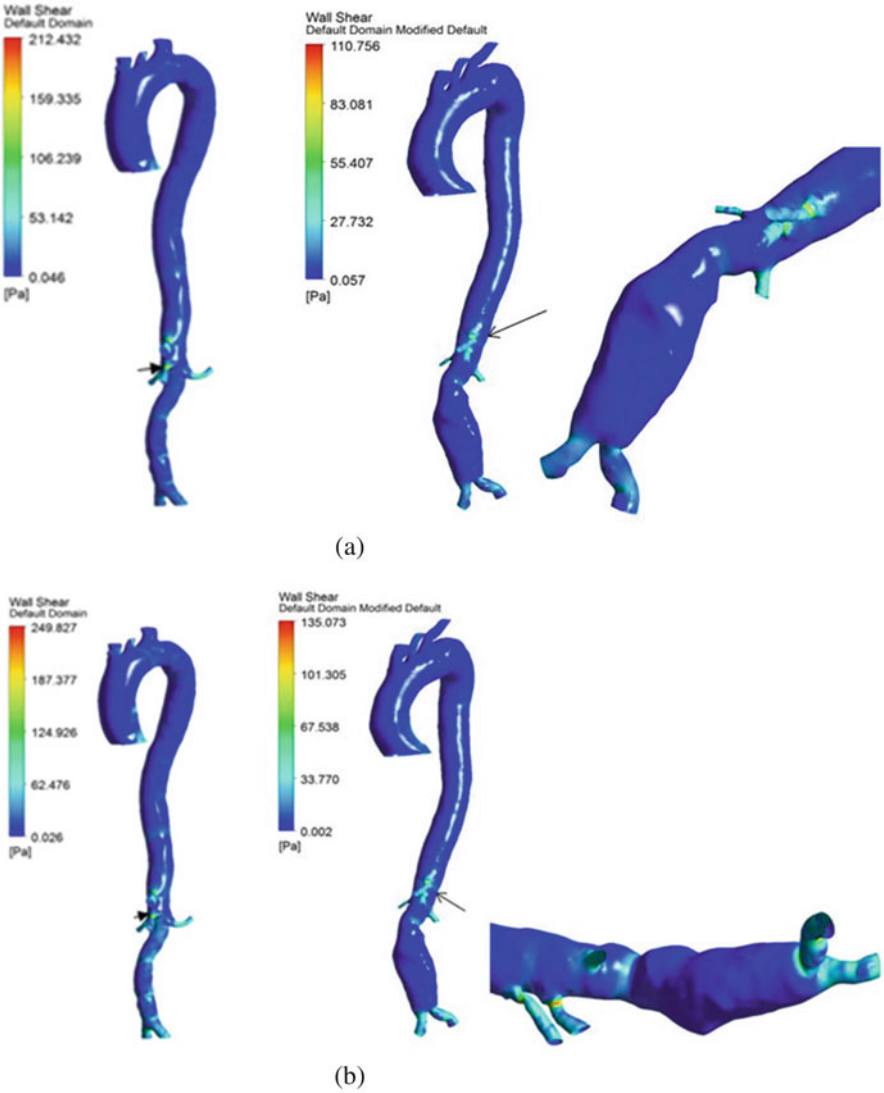

Fig. 8 Wall shear stress. (**a**) $t = 4.08$ s, (**b**) $t = 4.14$ s, (**c**) $t = 4.28$ s and (**d**) $t = 4.65$ s. Arrows indicate the peak value. Magnified image is displayed on the right side

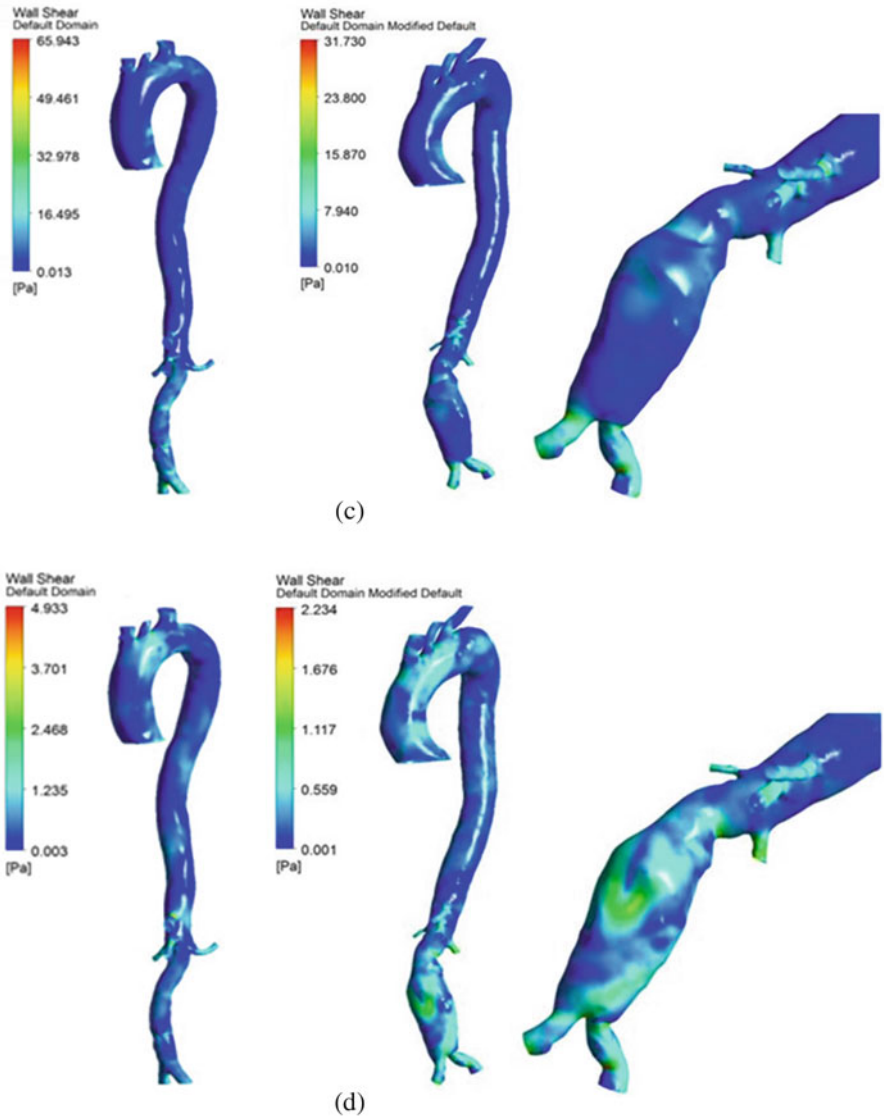

Fig. 8 (continued)

4 Conclusion

The CFD models of aorta of normal subject and patient-specific aortic aneurysm were developed. The steady and transient analyses were carried out to compare the blood flow patterns of the models. The Newtonian blood model was used for steady-state analysis, and non-Newtonian blood model was assumed for transient-state analysis. The haemodynamic parameters like wall pressure, wall shear stress and velocity distribution were estimated from the models.

It is found from the results that the flow in the patient-specific aneurysmal model was unstable. The abnormal high and low WSS occurred in the aneurysm cavity during deceleration phase of flow. It may cause rupture of aneurysm. It is observed from the results of steady-state analysis that all the measured haemodynamic parameters from aneurysmal aorta model were higher than those obtained from the aorta model of normal subject. This high magnitude of these parameters may lead to severe problem to the aneurysmal patient. These measured parameters could help the surgeons in assessing the severity of aortic aneurysms Furthermore, the usage of gold nanoparticles as a contrast agent is the emerging new sort of approach to obtain CT images of aneurysm. This may help in the prediction of rupture of aneurysm.

Acknowledgement Authors acknowledge Department of Science and Technology (DST, Govt. of India) – Nanomission Infrastructure Project #SR/NM/PG-05/2008/ for grant.

References

1. Murphy SL, Xu J, Kochanek KD (2012) Deaths: Preliminary data for 2010. National Vital Stat Syst 60(4):1–68
2. Elefteriades JA (2005) Beating a sudden killer. Sci Am 293:64–71
3. Rizzo JA, Coady MA, Elefteriades JA (1998) Procedures for estimating growth rates in thoracic aortic aneurysms. J Clin Epidemiol 51:747–754
4. Glimaker H, Holmberg L, Elvin A, Nybacka O, Almgren B, Bjorck CG, Eriksson I (1991) Natural history of patients with abdominal aortic aneurysm. Eur J Vasc Surg 5:125–130
5. Cronenwett JL, Murphy TF, Zelenock GB, Whitehouse WM Jr, Lindenauer SM, Graham LM, Quint LE, Silver TM, Stanley JC (1985) Actuarial analysis of variables associated with rupture of small abdominal aortic aneurysms. Surgery 98:472–483
6. Sonesson B, Sandgren T, Lanne T (1999) Abdominal aortic aneurysm wall mechanics and their relation to risk of rupture. Eur J Vasc Endovasc Surg 18:487–493
7. Darling RC, Messina CR, Brewster DC, Ottinger LW (1977) Autopsy study of unoperated abdominal aortic aneurysms. Circulation 56:161–164
8. Choksy SA, Wilmink AB, Quick CR (1999) Ruptured abdominal aortic aneurysm in the Huntingdon district: a 10-year experience. Ann R Coll Surg Engl 81:27–31
9. Nicholls SC, Gardner JB, Meissner MH, Johansen HK (1998) Rupture in small abdominal aortic aneurysms. J Vasc Surg 28:884–888
10. Hall AJ, Busse EFG, McCarville DJ, Burgess JJ (2000) Aortic wall tension as a predictive factor for abdominal aortic aneurysm rupture: improving the selection of patients for abdominal aortic aneurysm repair. Ann Vasc Surg 14:152–157
11. Geroulakos G, Nicolaides A (1992) Infrarenal abdominal aortic aneurysms less than five centimeters in diameter: the surgeon's dilemma. Eur J Vasc Surg 6:622–661

12. Moayeri MS, Zendehbudi GR (2003) Effects of elastic property of the wall on flow characteristics through arterial stenosis. J Biomech 36:525–535
13. Salsac AV, Sparks SR, Chomaz JM, Lasheras JC (2006) Evolution of the wall shear stresses during the progressive enlargement of symmetric abdominal aortic aneurysms. J Fluid Mech 560:19–51
14. Taylor CA, Hughes TJ, Zarins CK (1998) Finite element modeling of three-dimensional pulsatile flow in the abdominal aorta: relevance to atherosclerosis. Ann Biomed Eng 26:975–987
15. Shahcheraghi N, Dwyer HA, Cheer AY, Barakat AI, Rutaganira T (2002) Unsteady and three-dimensional simulation of blood flow in the human aortic arch. J Biomech Eng 124:378–387
16. Pedley TJ (1980) The fluid mechanics of large blood vessels. Cambridge University Press, Cambridge
17. Berger SA, Jou L (2000) Flows in stenotic vessels. Annu Rev Fluid Mech 32:347–382
18. Fung YC (1997) Biomechanics: circulation, 2nd edn. Springer, New York
19. Perktold K, Resch M, Florian H (1991) Pulsatile non-Newtonian flow characteristics in a three-dimensional human carotid bifurcation model. J Biomech Eng 113:464–475
20. Lei Y, Chen M, Xiong G, Chen J (2015) Influence of virtual intervention and blood rheology on mass transfer through thoracic aortic aneurysm. J Biomech 48(12):3312–3322
21. Rodkiewicz CM, Sinha P, Kennedy JS (1990) On the application of a constitutive equation for whole human blood. J Biomech Eng 112:198–206
22. Tu C, Deville M (1996) Pulsatile flow of non-Newtonian fluids through arterial stenosis. J Biomech 29(7):899–908
23. FJH G, Allanic E, van de Vosse FN, Janssen JD (1999) The influence of the non-Newtonian properties of blood on the flow in large arteries: unsteady flow in a 90° curved tube. J Biomech 32:705–713
24. Perktold K, Peter R, Resch M (1989) Pulsatile non-Newtonian blood flow simulation through a bifurcation with an aneurism. Biorheology 26:1011–1030
25. Ballyk PD, Steinman DA, Ethier CR (1994) Simulation of non-Newtonian blood flow in an end-to-end anastomosis. Biorheology 31(5):565–586
26. Vinoth R, Kumar D, Adhikari R, Vijay Shankar CS (2017) Non-Newtonian and Newtonian blood flow in human aorta: a transient analysis. Biomed Res 28(7):3194–3203
27. Liepsch D, Moravec S, Baumgart R (1992) Some flow visualization and laser-doppler velocity measurements in a true-to-scale elastic model of a human aortic arch- a new model technique. Biorheology 29:563–580
28. Nichols WW (1998) McDonald's blood flow in arteries: theoretical, experimental, and clinical principles, 4th edn. Oxford University Press, Arnold, London
29. Olufsen MS, Peskin C, Kim WY, Pedersen E, Nadim A, Larsen J (2000) Numerical simulation and experimental validation of blood flow in arteries with structured-tree outflow conditions. Ann Biomed Eng 28:1281–1299
30. Shipkowitz T, VGJ R, Frazin LJ, Chandran KB (2000) Numerical study on the effect of secondary flow in the human aorta on local shear stresses in abdominal aortic branches. J Biomech 33:717–728
31. Casson N (1959) A flow equation for the pigment oil sus-pensions of the printing ink type. In: Mill DC (ed) Rheology of disperse system. Pergamon Press, New York, pp 84–102
32. ANSYS CFX user guide, ANSYS, Inc. version 15
33. Charm SE, Kurland GS (1972) Chapter 15. Blood rheology. In: Bergel DH (ed) Cardiovascular fluid dynamics, vol 2. Academic, London, pp 157–203
34. Bluestein D, Niu L, Schoephoerster RT, Dewanjee MK (1996) Steady flow in an aneurysm model: correlation between fluid dynamics and blood platelet deposition. ASME Journal of Biomechanical Engineering 118(3):280–286
35. Gibbons GH, Dzau VJ (1994) The emerging concept of vascular remodeling. N Engl J Med 330:1431–1438
36. Malek AM, Alper SL, Izumo S (1999) Hemodynamic shear stress and its role in atherosclerosis. J Am Med Assoc 282:2035–2042

Blur-Specific No-Reference Image Quality Assessment: A Classification and Review of Representative Methods

Dingquan Li and Tingting Jiang

1 Introduction

Images may suffer from a variety of distortions during image acquisition, compression, transmission, display, etc. To monitor and improve the quality of images, image quality assessment (IQA) becomes a fundamental technique for modern multimedia systems. Since human is the end-user in most multimedia devices, the most accurate image quality evaluation is achieved by subjective ratings. However, subjective evaluation is difficult to carry out in real-time applications due to its drawbacks of inconvenience, high price, and inefficiency. These drawbacks lead to the need of efficient and effective objective IQA methods that can automatically predict image quality. Objective IQA can be categorized into full-reference IQA (FR-IQA, e.g., PSNR, MSSIM [27]), reduced-reference IQA (RR-IQA, e.g., FEDM [30]), and no-reference IQA (NR-IQA, e.g., BRISQUE [17]). Due to the unavailability of the reference images in most practical applications, NR-IQA is preferable but also more challenging.

In this work, we focus on blur-specific NR-IQA. Blur is one of the most common distortions and unintentional blur impairs image quality. Image blur often occurs in the following situations: (1) out of focus, (2) object motion and camera shake, (3) nonideal imaging systems, (4) atmospheric turbulence or aerosol

D. Li
LMAM, School of Mathematical Sciences & IDM, Peking University, Beijing, People's Republic of China
e-mail: dingquanli@pku.edu.cn

T. Jiang (✉)
School of Electrical Engineering and Computer Sciences & IDM, Peking University, Beijing, People's Republic of China
e-mail: ttjiang@pku.edu.cn

M. Jiang et al. (eds.), *The Proceedings of the International Conference on Sensing and Imaging*, Lecture Notes in Electrical Engineering 506,
https://doi.org/10.1007/978-3-319-91659-0_4

scattering/absorption, and (5) image compression and image denoising [6, 9, 19]. Researches on blur-specific NR-IQA can bring new perspectives for related applications, e.g., autofocusing and image deblurring [12].

Various blur-specific NR-IQA methods have been proposed over the last two decades. In 2009, Ferzli and Karam [6] summarized several traditional methods, most of which are designed for "autofocus" applications. In 2012, Vu and Chandler [25] gave an overview and classified existing methods into edge-based methods (based on measuring the edge spread), pixel-based methods (operated in the spatial domain but with no assumption on edges), and transform-based methods (operated in the spectral domain). Many novel blur-specific NR-IQA methods have been recently developed, e.g., [7, 13–15, 29]. This work aims to give an overall classification of existing methods and systematically introduces 18 representative methods, especially the recently developed ones, so as to provide an integrated and valuable reference for blur-specific NR-IQA research and help researchers keep abreast of the recent progress.

Most existing methods only test their performance on Gaussian blur images. It is thus unclear how these methods would behave in the presence of noise or in more complex realistic situations. Stability and practicability are very important for objective methods, so we conduct comparative experiments for 13 representative methods with available codes on two sorts of images, including Gaussian blur images from TID2013 [20] and realistic blur images from BID [4]. By comparing the experimental results, we can see that most existing methods have satisfactory performance on Gaussian blur images, but they fail to accurately estimate the image quality of realistic blur images. Therefore, further study is needed in this field. At last, we discuss the issues of realistic blur, on which practical blur-specific NR-IQA methods focus.

The rest of this paper is organized as follows. In Sect. 2, existing blur-specific NR-IQA methods are classified, and several representative methods are reviewed. Then experimental settings, results, analysis, and discussions are presented in Sect. 3. Finally, concluding remarks are made in Sect. 4.

2 Blur-Specific No-Reference Image Quality Assessment: Classification and Review

Blur-specific NR-IQA methods based on traditional signal/image processing technologies have been investigated over 20 years. However, traditional signal processing technologies cannot accurately express the diversity of blur process and the complexity of human visual system (HVS), so researchers have turned to machine learning technologies for estimating image quality of blur images. Though blur-specific NR-IQA methods based on machine learning technologies have only been studied in recent years, they are in a rapid growth. In terms of this natural fact, we divide the existing blur-specific NR-IQA methods into two categories: learning-free

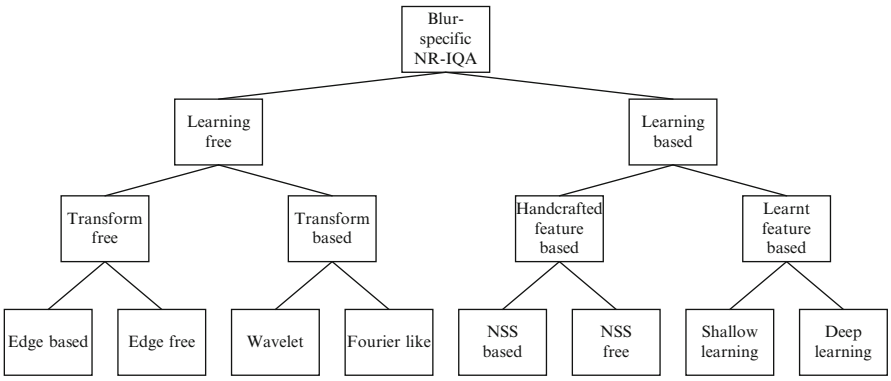

Fig. 1 An overall classification of blur-specific no-reference image quality assessment methods, including learning-free methods and learning-based methods. NSS is the abbreviation of "natural scene statistics"

methods and learning-based methods. An overall classification is shown in Fig. 1, where the representative methods in each category will be discussed in detail later. It should be noted that, for Gaussian blur images, image sharpness can be used as the synonym of image quality, while image blurriness can be used as the antonym of image quality. In previous literatures, researchers mainly considered Gaussian blur images; therefore, we not only review blur-specific NR-IQA methods but also review both sharpness and blurriness estimators. However, we should also note that the abovementioned relationships among quality, sharpness, and blurriness are not necessarily true in realistic situations.

2.1 Learning-Free Methods

Among learning-free methods, some use the characteristics of blur in the spatial domain (e.g., the spread of edges and the smoothing effects), while others further use the characteristics of blur in the transform domain (e.g., the reduction of high-frequency components and the loss of phase coherence). In this regard, learning-free methods can be classified as transform-free methods and transform-based methods.

Transform-Free Methods

Transform-free methods only make use of the spatial information. They can be further divided into edge-based methods and edge-free methods. The former makes assumptions on edges while the latter does not.

Edge-Based Methods

Given that blur affects the edge's property (e.g., blur tends to make the edge spread), a lot of blur-specific NR-IQA methods are developed based on analyzing the edges. MDWE [16], JNB [6], CPBD [19], PSI [5], and EMBM [8] are the representative edge-based methods.

A. MDWE

Marziliano et al. [16] proposed a blur-specific NR-IQA method, called MDWE, based on measuring the average edge width. The basic assumption is that blur makes the edges spread, so image blur can be directly estimated based on the edge width. The framework of MDWE is shown in Fig. 2. First, the RGB color image is transformed into the gray image. Then, the vertical Sobel filter is used as the edge detector to find vertical edges in the image. Third, for each edge point, the edge width is used as a local blur measure, where the edge width is measured by the distance between the local maximum and minimum points closest to the edge

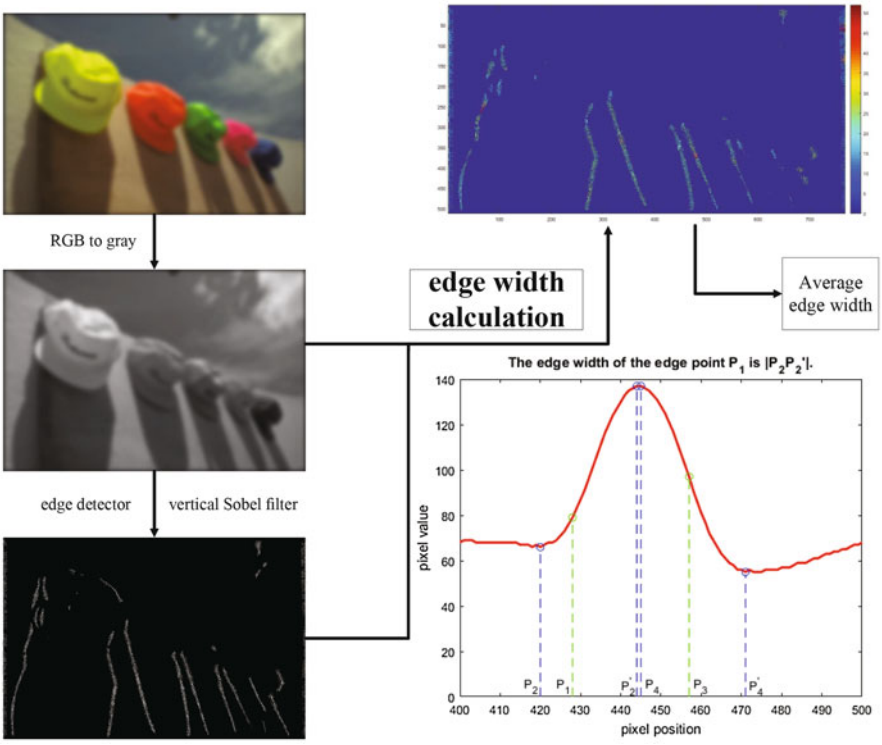

Fig. 2 The framework of MDWE, which is based on measuring the average edge width. The bottom right part is an illustration of how to compute the edge width on one row of the image

(along the horizontal direction). The bottom right part of Fig. 2 illustrates how to compute the edge width. P_2' and P_2 are the local maximum and minimum points closest to the edge point P_1, so P_1's edge width is $|P_2'P_2|$. Similarly, P_3's edge width is $|P_4'P_4|$. Finally, the global blur measure is obtained by averaging the edge width over all edge points. The smaller the global blur value is, the better image quality is.

B. JNB

Ferzli and Karam [6] estimated image quality by integrating the concept of just noticeable blur (JNB) and edge width into a probability summation model. Taking the characteristics of HVS into account, JNB is proposed to deal with the failure of estimating blur among images with different contents. It considers the minimum amount of perceived blurriness at distinct contrast levels. JNB width is the minimum edge width that people can perceive the blur, and subjective experiments were performed to obtain the JNB width. The results showed that:

$$W_{\mathrm{JNB}}(C) = \begin{cases} 5, & C \leq 50 \\ 3, & C \geq 51 \end{cases} \tag{1}$$

where W_{JNB} and C are the JNB width and the image contrast, respectively.

The probability $P(e_k)$ of detecting a blur distortion at edge e_k is determined by a psychometric function.

$$P(e_k) = 1 - \exp\left(- \left| \frac{W(e_k)}{W_{\mathrm{JNB}}(C_{e_k})} \right|^{\beta} \right) \tag{2}$$

where $W(e_k)$ is the measured edge width using MDWE [16], $W_{\mathrm{JNB}}(C_{e_k})$ is the JNB width defined in Eq. (1), and C_{e_k} is the local contrast near the edge e_k. β ranges from 3.4 to 3.8, and it is simply fixed to its median value 3.6.

Adopting a probability summation hypothesis, the localized detection probabilities over a region of interest R can be pooled as:

$$P_{\mathrm{blur}}(R) = 1 - \prod_{e_k \in R} (1 - P(e_k)) = 1 - \exp(-D_R^{\beta}) \tag{3}$$

where

$$D_R = \left(\sum_{e_k \in R} \left| \frac{W(e_k)}{W_{\mathrm{JNB}}(C_{e_k})} \right|^{\beta} \right)^{\frac{1}{\beta}}$$

Considering the size of the foveal region, the image I is divided into blocks with a block size of 64×64. The edge blocks are the blocks with more than 0.2%

edge pixels. For each edge block R_b, the probability of detecting blur in R_b can be computed by Eq. (3). Therefore, the probability of detecting blur in the image I is given by:

$$P_{\text{blur}}(I) = 1 - \prod_{R_b \in I} (1 - P_{\text{blur}}(R_b)) = 1 - \exp(-D^{\beta}) \tag{4}$$

where

$$D = \left(\sum_{R_b \in I} | D_{R_b} |^{\beta} \right)^{\frac{1}{\beta}} \tag{5}$$

Finally, the image quality score s is determined by:

$$s = \frac{L}{D} \tag{6}$$

where L is the total number of processed blocks and D is given by Eq. (5).

C. CPBD

JNB method [6] is based on the assumption that the blur impairment increases when P_{blur} increases; however, it ignores that blur is not likely to be perceived when the edge width is small enough (below the JNB width). When $W(e_k)$ equals $W_{\text{JNB}}(C_{e_k})$ in Eq. (2), the probability of blur detection $P_{\text{blur}}(e_k)$ is the just noticeable blur detection probability $P_{\text{JNB}} = 63\%$. That is, when the probability of blur detection P_{blur} at edge e_k is below $P_{\text{JNB}} = 63\%$, the blur is not likely to be detected. Based on this assumption, Narvekar and Karam [19] used the concept of JNB together with a cumulative probability of blur detection. The flowchart of CPBD is shown in Fig. 3a, which is the same as JNB method except for the last pooling step. The last pooling step in CPBD is obtained from the normalized histogram of the probability of blur detection P_{blur} in the image, and the image quality score equals to the percentage of edges whose blur cannot be detected, which can be calculated as:

$$\text{CPBD} = P(P_{\text{blur}} \leq P_{\text{JNB}}) = \sum_{P_{\text{blur}}=0}^{P_{\text{JNB}}} P(P_{\text{blur}}) \tag{7}$$

D. PSI

Feichtenhofer et al. [5] proposed a perceptual sharpness index (PSI) based on the statistical analysis of local edge gradients. First, an adaptive edge selection procedure based on a threshold and thinning process is applied to select the most

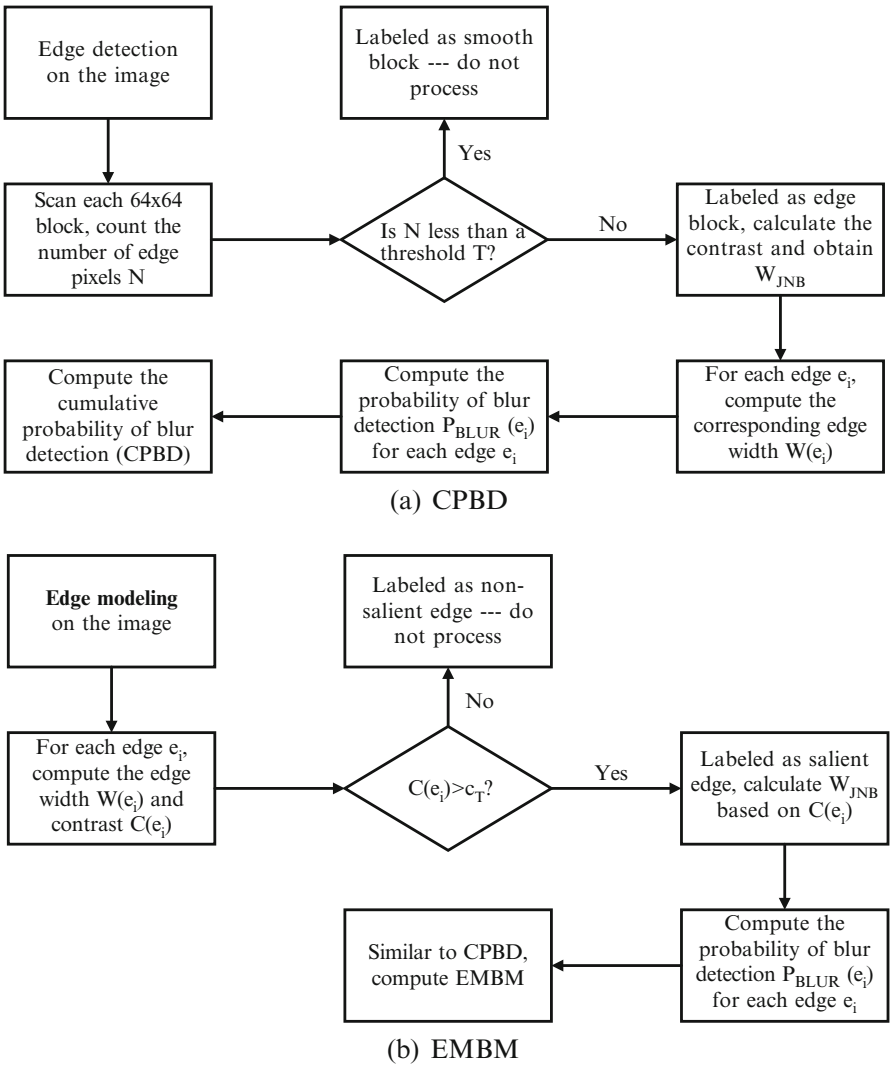

Fig. 3 The flowcharts of CPBD and EMBM

significant edges in the image. Second, the edge widths of the selected edges are computed by an improved edge width measurement based on diagonal edge gradients. Third, according to the human perception of acutance, edge widths above the JNB width are subtracted by the edge slopes. Finally, the local sharpness map is deduced by applying the above three steps in a block-wise way. Since the sharpest regions in an image are most related to human sharpness perception, the global image quality score is determined by the highest Qth percentile average of the local sharpness values.

E. EMBM

Guan et al. [8] proposed a blur-specific NR-IQA method EMBM by integrating the concept of edge modeling into JNB, where the edge is modeled as the step function convolved with a Gaussian function. The flowchart of EMBM is shown in Fig. 3b. There are some differences between EMBM and CPBD. First, unlike CPBD, the parametric edge model in EMBM is used for edge description and detection, from which the edge width and the local contrast for each edge can be computed simultaneously. Second, all edges are depicted parametrically, so EMBM needs not to be performed in a block-wise way. Third, EMBM only considers salient edges (with large contrast) that grab most attention from human visual perception.

Edge-Free Methods

Operating in the spatial domain but with no assumption on edges, edge-free methods are based on the intrinsic characteristics of the image, the comparison between an image and its re-blurred version, or the comparison between pixels and their adjacent pixels. SVC [21], BIBS [3], MLV [1], ARISMc [7], and CATV [2] are the representative edge-free methods.

A. SVC

Sang et al. [21] observed that the singular values in the singular value curve (SVC) decay exponentially, and they decay even faster with larger degree of blur. So the degree of attenuation can be used to capture the image blur. Since the shape of SVC closely resembles an inverse power function, Sang et al. fitted the singular value curve by the equation $y = x^{-q}$. After taking logarithms of the equation, the fitting process can be achieved by linear regression. Denote the kth singular value as s_k, $k = 1, 2, \cdots, r$, then the estimated q follows the formula:

$$q = \frac{\sum_{k=1}^{r} \ln k \ln \frac{1}{s_k}}{\sum_{k=1}^{r} \ln k \ln k} \tag{8}$$

Since the tails of the singular value curve are almost indistinguishable, they are not helpful for the estimation of q. Therefore, in practice, the truncated sum is considered:

$$q = \frac{\sum_{s_k > c} \ln k \ln \frac{1}{s_k}}{\sum_{s_k > c} \ln k \ln k} \tag{9}$$

where c is a threshold value and it is set to 50.

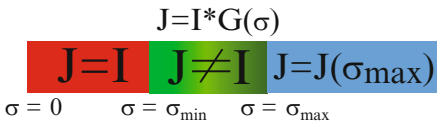

Fig. 4 The re-blurred process of image I in BIBS. $G(\sigma)$ is the 3×3 Gaussian blur kernel with standard deviation σ

B. BIBS

Image quality can be measured in a "FR-like" fashion by comparing the blurred image with its re-blurred version which is generated by applying a Gaussian filter. This is based on the observation that the blurred image changes less than the pristine image after the re-blurring process. Bong et al. [3] predicted blind image blur score (BIBS) by applying a re-blurring process (see Fig. 4), where two specific states in the re-blurring process are selected: the state ($\sigma = \sigma_{\min}$) that the re-blurred image starts to change its pixel values, and the state ($\sigma = \sigma_{\max}$) that re-blurred image never changes anymore. Then, image quality is measured based on the shape difference of local histogram between the image and its re-blurred versions.

C. MLV and CATV

Bahrami and Kot [1] proposed a novel blur-specific NR-IQA method based on the content-based weighting distribution of the maximum local variation (MLV). MLV of a pixel $I_{i,j}$ is defined as the maximum variation between the intensity of $I_{i,j}$ with respect to its 8-neighbor pixels:

$$\psi(I_{i,j}) = \max\{|\, I_{i,j} - I_{x,y} \mid |x = i-1, i, i+1; y = j-1, j, j+1.\} \tag{10}$$

And the MLV map $\Psi(I)$ of an image I is constructed by:

$$\Psi(I) = \begin{pmatrix} \psi(I_{1,1}) & \cdots & \psi(I_{1,N}) \\ \vdots & \ddots & \vdots \\ \psi(I_{M,1}) & \cdots & \psi(I_{M,N}) \end{pmatrix} \tag{11}$$

where M and N are the numbers of row and column in the image I, respectively.

Since variations in the pixel values can be an indication of image quality, the statistics of MLV distribution can be used for quality assessment. Bahrami and Kot [1] modeled the MLV distribution by the generalized Gaussian distribution (GGD), which is given by:

$$f(\Psi(I);\mu,\gamma,\sigma)=\left(\frac{\gamma}{2\sigma\Gamma(\frac{1}{\gamma})\sqrt{\frac{\Gamma(\frac{1}{\gamma})}{\Gamma(\frac{3}{\gamma})}}}\right)e^{-\left(\left(\frac{\Psi(I)-\mu}{\sigma\sqrt{\frac{\Gamma(\frac{1}{\gamma})}{\Gamma(\frac{3}{\gamma})}}}\right)\right)^{\gamma}} \tag{12}$$

where μ, σ, and γ are the mean, standard variation, and shape parameter, respectively. $\Gamma(\cdot)$ is the Γ function. The estimated standard deviation σ is an indicator of image blurriness, where σ increases by decreasing image blurriness. To take the human sharpness perception into account, high variation regions should be emphasized. This can be achieved by assigning higher weights to the larger MLV pixels, which results in a weighted MLV map $\Psi_w(I)$

$$\Psi_w(I)=\begin{pmatrix} w_{1,1}\psi(I_{1,1}) & \cdots & w_{1,N}\psi(I_{1,N}) \\ \vdots & \ddots & \vdots \\ w_{M,1}\psi(I_{M,1}) & \cdots & w_{M,N}\psi(I_{M,N}) \end{pmatrix} \tag{13}$$

where weight is defined as $w_{i,j}=e^{\eta_{i,j}}$ and $\eta_{i,j}$ is the normalized rank (ranging from 0 to 1) of $\psi(I_{i,j})$ when $\Psi(I)$ is sorted in ascending order.

Instead of considering the MLV distribution, later Bahrami and Kot [2] proposed a content aware total variation (CATV) method by parameterizing the image total variation (TV) distribution using GGD. Image quality is defined as the standard deviation σ modified by the shape parameter γ to account for the image content variation, i.e, image quality score s is given by:

$$s=\frac{\sigma}{\gamma^{\frac{1-\gamma}{2}}} \tag{14}$$

D. ARISMc

Gu et al. [7] proposed ARISMc to estimate image quality based on the analysis of the locally estimated coefficients in the autoregressive (AR) parameter space. The framework of the proposed ARISMc method is shown in Fig. 5.

To take chrominance information into account, the image is first transferred to YIQ color space. Then, for each channel, the AR parameters at each pixel are estimated based on an 8th-order AR model.

Since image blurring can increase the similarity of locally estimated AR parameters, image quality can be assessed by energy difference and contrast difference of locally estimated AR parameters. The energy difference $E_{i,j}$ and contrast difference $C_{i,j}$ of AR parameters at pixel (i, j) are given by:

$$E_{i,j}=|\max_{(x,y)\in\Omega_{i,j}}W_{x,y}-\min_{(x,y)\in\Omega_{i,j}}W_{x,y}|^2 \tag{15}$$

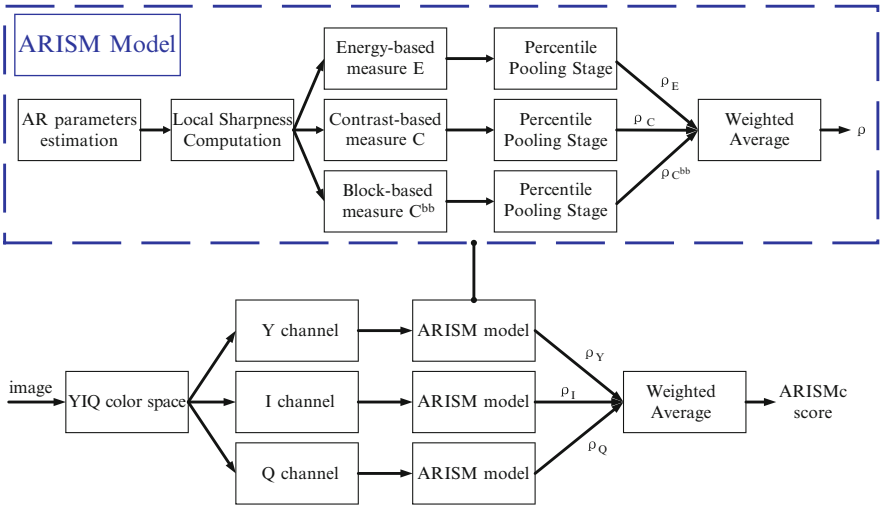

Fig. 5 The framework of ARISMc

$$C_{i,j} = \frac{|\max_{(x,y)\in\Omega_{i,j}} W_{x,y} - \min_{(x,y)\in\Omega_{i,j}} W_{x,y}|^2}{\max_{(x,y)\in\Omega_{i,j}} W_{x,y}^2 + \min_{(x,y)\in\Omega_{i,j}} W_{x,y}^2} \tag{16}$$

where $\Omega_{i,j} = \{(x, y)|x \in [i-1, i+1], y \in [j-1, j+1], (x, y) \neq (i, j)\}$ and $\{W_{x,y}, (x, y) \in \Omega_{i,j}\}$ denotes the estimated AR parameters at pixel (i, j).

The contrast difference can be further modified into block-based version:

$$C_{u,v}^{bb} = \frac{1}{B}\sqrt{\sum_{(i,j)\in\Phi u,v} C_{i,j}} \tag{17}$$

where $\Phi_{u,v} = \{(i, j)|i \in [(u-1)B, uB], j \in [(v-1)B, vB]\}, 1 \leq u \leq \lfloor M/B \rfloor, 1 \leq v \leq \lfloor N/B \rfloor$, B is the block size and M and N are the row and column of the image.

At percentile pooling stage, the largest $Q_k\%$ values in the $k(k \in \{E, C, C^{bb}\})$ are averaged to obtain ρ_k. Then, the overall score for an image channel is given by a weighted average of $\rho_k(k \in \{E, C, C^{bb}\})$. Finally, the ARISMc score for estimating the image quality is given by a weighted average of the three overall scores in YIQ channels.

Transform-Based Methods

In the transform domain, blur has some quality-relevant characteristics such as the reduction of high-frequency components and the loss of phase coherence.

Transform-based methods utilize wavelet transform or "Fourier-like" transform (e.g., Fourier transform and cosine transform), so we categorize them into wavelet-based methods and Fourier-like methods.

Wavelet Methods

A. FISHbb

Blur leads to the reduction of high-frequency components. Vu and Chandler [24] proposed a fast wavelet-based method FISHbb by analyzing the energies of the high-frequency coefficients. The image is broken into 16×16 blocks with 50% overlapping in advance.

For each block, the DWT coefficients are obtained by Cohen-Daubechies-Fauraue 9/7 filters with three levels of decomposition. The three high-frequency sub-bands are denoted as S_{LH_n}, S_{HL_n}, and S_{HH_n}, $(n = 1, 2, 3)$. Then, the overall log energy at each DWT level is computed as the weighted average log energy of the three high-frequency sub-bands, which is given by:

$$E_n = (1-\alpha)\frac{E_{LH_n} + E_{HL_n}}{2} + \alpha E_{HH_n}, \alpha = 0.8. \tag{18}$$

$$E_{XY_n} = \log_{10}\left[1 + \frac{1}{M_n N_n}\sum_{i,j} S^2_{XY_n}(i,j)\right], XY \in \{LH, HL, HH\}. \tag{19}$$

where M_n and N_n are the size of the nth sub-band.

Next, the overall sharpness score FISH of a block is given by the weighted sum of the overall log energy in the three levels, which is obtained by:

$$\text{FISH} = \sum_{n=1}^{3} 2^{3-n} E_n \tag{20}$$

Finally, a sharpness map is derived. And to consider the human sharpness perception, the single FISH_{bb} score is computed by the root mean square of the 1% largest values of the local sharpness map.

$$\text{FISH}_{\text{bb}} = \sqrt{\frac{1}{K}\sum_{k=1}^{K} \text{FISH}_k^2} \tag{21}$$

where K denotes the number of blocks which received the 1% largest FISH scores of the sharpness map and $\text{FISH}_k, k = 1, \cdots, K$ denote the FISH scores of these blocks.

B. LPC

Wang and Simoncelli [26] showed that step edges result in strong local phase coherence (LPC) structures across scales and space in the complex wavelet transform domain and blur causes the loss of such phase coherence. This gives a different perspective for understanding blur perception. Following this idea, Hassen et al. [9] proposed a blur-specific NR-IQA method based on the strength of the LPC near edges and lines. Figure 6 shows a simple flowchart of LPC. First, the image is passed through 3-scale 8-orientation log-Gabor filters, and the complex coefficient at the ath scale, the bth orientation, and the kth spatial location is denoted as c_{abk}. Then the LPC strength at bth orientation and kth spatial location is computed by:

$$S_{\mathrm{LPC}}^{\{b,k\}} = \cos\left(\sum_{a=1}^{3} w_a \Phi\{c_{abk}\}\right) = \cos\left(\Phi\left\{\prod_{a=1}^{3} c_{abk}^{w_a}\right\}\right) = \frac{\mathscr{R}\left\{\prod_{a=1}^{3} c_{abk}^{w_a}\right\}}{\left|\prod_{a=1}^{3} c_{abk}^{w_a}\right|} \quad (22)$$

where $\Phi\{\cdot\}$ and $\mathscr{R}\{\cdot\}$ are the phase function and the real part of a complex number. $[w_1, w_2, w_3] = [1, -3, 2]$ denotes the weights during LPC evaluation.

Then the LPC strength measure at all orientations and kth spatial location is pooled by a weighted average. To give higher importance for the orientations with more energy, the weights are determined by the magnitude of the first (finest) scale coefficient c_{1bk}. So the LPC strength measure at kth spatial location is given by:

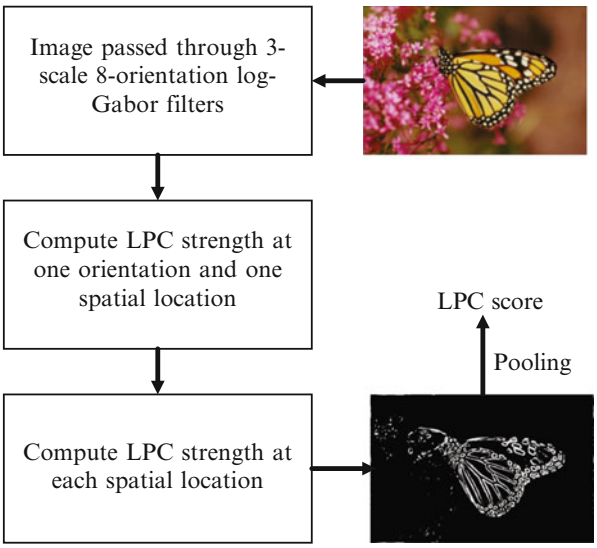

Fig. 6 A simple flowchart of LPC. It consists of three steps: computation of complex coefficients, LPC strength calculation, and LPC strength pooling

$$S_{\mathrm{LPC}}^{\{k\}} = \frac{\sum_{b=1}^{8} |c_{1bk}| S_{\mathrm{LPC}}^{\{b,k\}}}{\sum_{b=1}^{M} |c_{1bk}| + c_0} \tag{23}$$

where $c_0 = 2$ is a constant to avoid instability when $\sum_{b=1}^{M} |c_{1bk}|$ is close to zero.

Finally, a spatial LPC map is obtained. Let $S_{\mathrm{LPC}}^{\{(k)\}}, k = 1, \cdots, K$ denote the sorted LPC strength values in descending order such that $S_{\mathrm{LPC}}^{\{(1)\}} \geq S_{\mathrm{LPC}}^{\{(2)\}} \geq \cdots \geq S_{\mathrm{LPC}}^{\{(K)\}}$. To emphasize the importance of the sharpest regions in human visual perception, the overall image quality score S_{LPC} is obtained by a weighted average, where the weights are assigned based on the ranks of LPC values.

$$S_{\mathrm{LPC}} = \frac{\sum_{k=1}^{K} u_k S_{\mathrm{LPC}}^{\{(k)\}}}{\sum_{k=1}^{K} u_k} \tag{24}$$

where u_k is the weight assigned to the k-th ranked spatial LPC value and is calculated by:

$$u_k = \exp\left[-\left(\frac{k-1}{K-1} \right) / \beta_k \right], \beta_k = 1e-4. \tag{25}$$

Fourier-Like Methods

A. S3

Vu and Chandler [25] proposed a blur-specific NR-IQA method S3 based on the combination of spectral and spatial measures. The flowchart of S3 is shown in Fig. 7. According to the reduction of high-frequency components in blur images, the spectral measure $S_1(\mathbf{x})$ of a block $\mathbf{x}$ is initially defined as the slope of the local magnitude spectrum $\alpha_{\mathbf{x}}$, then rectified by a sigmoid function to account for HVS, i.e.,

$$S_1(\mathbf{x}) = 1 - \frac{1}{1 + e^{\beta_1(\alpha_{\mathbf{x}} - \beta_2)}}, \beta_1 = -3, \beta_2 = 2. \tag{26}$$

To further consider the contrast effect, the spatial measure $S_2(\mathbf{x})$ of a block $\mathbf{x}$ is calculated based on the local total variation, which is given by:

$$S_2(\mathbf{x}) = \frac{1}{4} \max_{\xi \in \mathbf{x}} \mathrm{TV}(\xi) \tag{27}$$

where ξ is a 2×2 block of $\mathbf{x}$ and $\mathrm{TV}(\xi)$ is the total variation of ξ.

Then, the overall sharpness map S_3 of the image I is obtained by a geometric mean of spectral and spatial measures in a block-wise way:

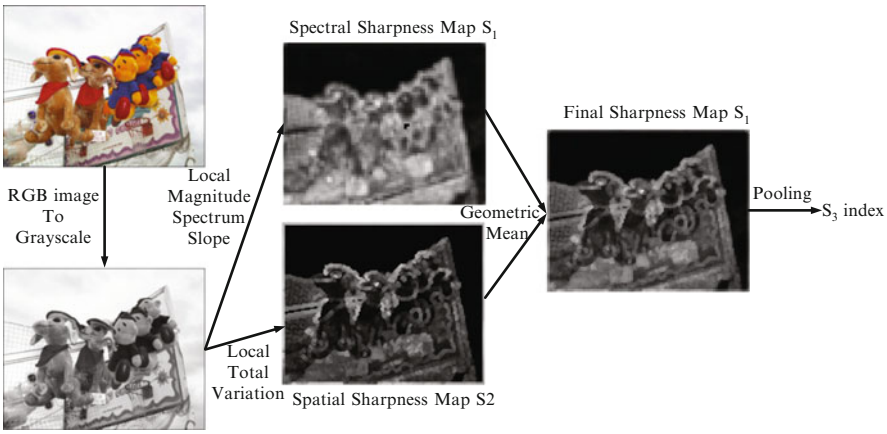

Fig. 7 The flowchart of S3

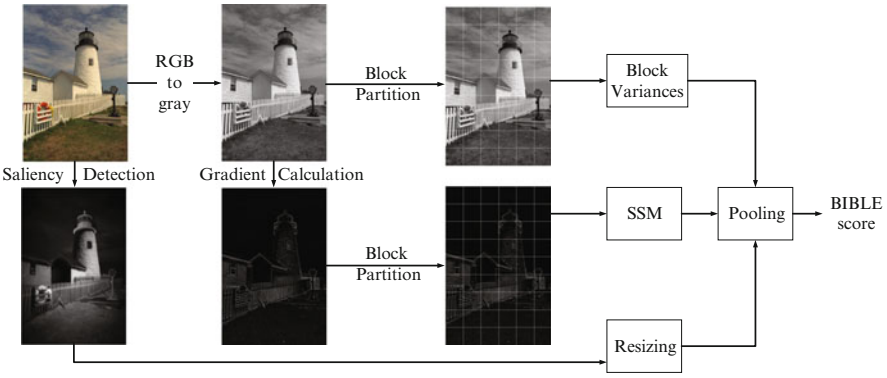

Fig. 8 The flowchart of BIBLE

$$S_3(\mathbf{x}) = \sqrt{S_1(\mathbf{x})S_2(\mathbf{x})}, \mathbf{x} \in I. \tag{28}$$

Finally, to consider the human sharpness perception, the overall sharpness score is calculated as the average of the largest 1% values of the overall sharpness map.

B. BIBLE

Having observed that blur affects the moment energy, Li et al. [13] presented a blind image blur evaluator (BIBLE) to assess image quality based on the variance-normalized moment energy. The flowchart of BIBLE is shown in Fig. 8. The gradient image is divided into equal-sized blocks, and the Tchebichef moments [18] of all blocks are computed. Then the block's energy is calculated by summing up

the squared non-DC moments. Finally, image quality is measured by the variance-normalized moment energy together with a visual saliency model to adapt to the HVS characteristics.

2.2 Learning-Based Methods

Recently, researchers turn to machine learning technologies for blur-specific NR-IQA. Learning-based methods comprise two steps: feature extraction and quality prediction. The most important thing is to extract features that can reflect image quality. Once it is done, quality prediction can be achieved by support vector regression (SVR), neural network, probabilistic prediction model, etc. To emphasize the importance of feature extraction, the learning-based methods are classified as handcrafted feature-based methods and learnt feature-based methods.

Handcrafted Feature-Based Methods

Handcrafted features are generally extracted from the nature scene statistic (NSS) models. Meanwhile, they can also be obtained by some NSS-free low-level image features (e.g., contrast, brightness, etc.) So we divide the handcrafted feature-based methods into NSS-based methods and NSS-free methods.

A Representative NSS-Based Method BIBE

It is assumed that natural scenes contain certain statistical properties that could be altered by the existence of distortions. Therefore, by modeling the statistical distributions of image coefficients, image quality can be estimated by deviations of these statistics. Wang et al. [28] proposed a blur-specific NR-IQA method BIBE based on the NSS of gradient distribution, where the flowchart of BIBE is shown in Fig. 9. First, the blurred image is passed through the horizontal and vertical Prewitt filters to get the gradient map. Then, the gradient-related distributions represented by histograms are modeled using the generalized Gaussian distribution (GGD) or asymmetric GGD. Finally, the NSS features (parameters of the models) are fed into the extreme learning machine [10] to predict the image quality.

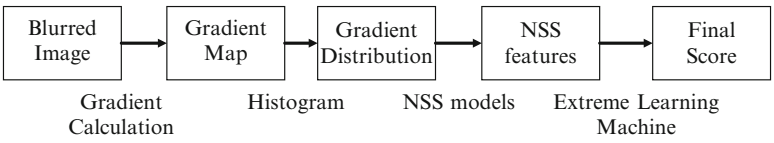

Fig. 9 The flowchart of BIBE

A Representative NSS-Free Method RISE

Inspired by the multi-scale characteristics of HVS when perceiving visual scenes, Li et al. [15] proposed a blur-specific NR-IQA method RISE based on multi-scale features extracted in both the spatial and spectral domains. The flowchart of RISE is shown in Fig. 10.

For an image $I(x, y)$, the scale space $L(x, y, \sigma)$ can be first built by convoluting it with a series of Gaussian filters $G(x, y, \sigma)$:

$$L(x, y, \sigma) = I(x, y) * G(x, y, \sigma), G(x, y, \sigma) = \frac{1}{2\pi\sigma^2} e^{-(x^2+y^2)/2\sigma^2} \tag{29}$$

where σ is the scale and $*$ denotes the convolution.

Second, multi-scale gradient similarity maps $\mathbf{GS}_k, k = 1, 2, 3, 4$ can be obtained by:

$$\mathbf{GS}_k = \frac{\mathbf{D}_k \mathbf{D}_0 + c_1}{\mathbf{D}_k^2 + \mathbf{D}_0^2 + c_1} \tag{30}$$

where $\mathbf{D}_k$ is the gradient map of the k-th scale image ($k = 1, 2, 3, 4$), $\mathbf{D}_0$ is the gradient map of the original image. c_1 is a small constant to ensure numerical stability.

The gradient similarity features are defined as:

$$f_k^G = \frac{1}{MN} \sum_{x=1}^{M} \sum_{y=1}^{N} \mathbf{GS}_k(x, y), k = 1, 2, 3, 4 \tag{31}$$

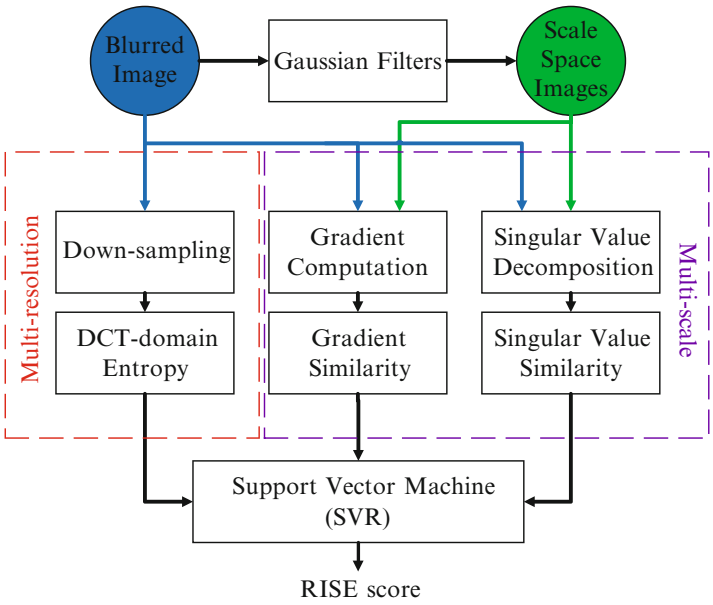

Fig. 10 The flowchart of RISE

where M and N are the number of rows and columns in the image.

Third, multi-scale singular value similarity $f_k^S, k = 1, 2, 3, 4$ is defined as:

$$f_k^S = \frac{\mathbf{s}_k^T \mathbf{s}_0 + c_2}{\mathbf{s}_k^2 + \mathbf{s}_0^2 + c_2} \tag{32}$$

where $\mathbf{s}_k$ is the singular values of the k-th scale image ($k = 1, 2, 3, 4$) and $\mathbf{s}_0$ is the singular values of the original image. c_2 is a small constant to ensure numerical stability.

To take the impact of the viewing distance into account, the blurred image is also down-sampled to get multi-resolution images, and the DCT domain entropies of all multi-resolution images are calculated as the third type of features.

Finally, all the three types of features are concatenated and fed into an SVR model with RBF kernel to get the quality score.

Learnt Feature-Based Methods

Learnt feature-based methods utilize machine learning methods to learn powerful features that can strongly reflect image quality. These methods can be divided into two categories: shallow learning methods and deep learning methods, in terms of whether features are extracted from shallow learning architectures or deep learning architectures.

A Representative Shallow Learning Method SPARISH

Having observed that over-complete dictionaries learned from natural images can capture edge patterns, Li et al. [14] proposed a blur-specific NR-IQA method SPARISH based on the sparse representation. Figure 11 shows the flowchart of SPARISH. An over-complete dictionary is learnt to construct a sparse coding model for the image gradient blocks, then the variance-normalized block energy over high-variance image blocks is used as the quality score, where the block energy is obtained from the sparse coefficients.

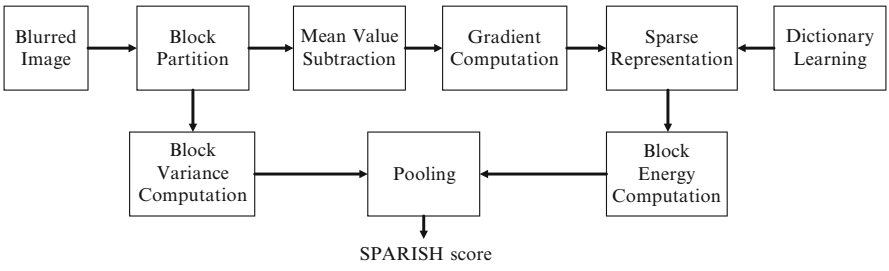

Fig. 11 The flowchart of SPARISH

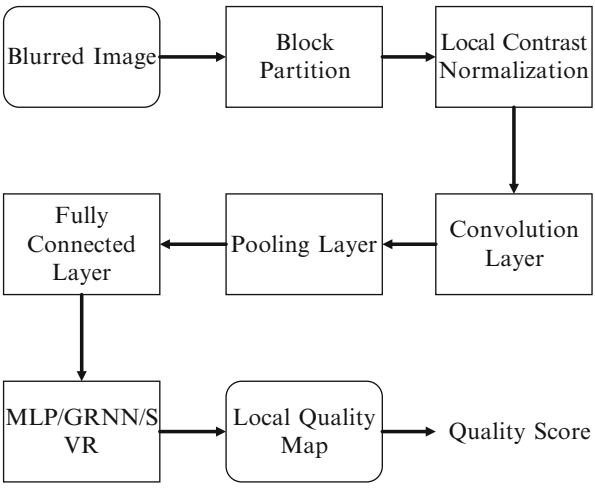

Fig. 12 The flowchart of Yu's CNN. MLP is the abbreviation of multilayer perceptron, GRNN indicates the general regression neural network and SVR means support vector regression

A Representative Deep Learning Method Yu's CNN

Human visual mechanism is very complicated and cannot be accurately expressed by shallow learning architectures. Recently, deep learning techniques have been applied for general purpose IQA [11]. Yu et al. [29] made an attempt on applying deep learning architectures to blur image quality assessment. The flowchart of Yu's CNN is shown in Fig. 12. The image patches pre-processed by the local contrast normalization are passed through a convolutional layer, a down-sampling layer and a fully connected layer to extract patch features and then the features are mapped to patch quality scores by a regression model (MLP, GRNN or SVR). Finally, the average of patch quality scores is used as the overall image quality score.

3 Experiments

3.1 Experimental Settings

Evaluated Methods

We choose the 13 representative methods with available codes for comparative experiments, i.e., 6 transform-free methods (MDWE, CPBD, PSI, EMBM, MLV, ARISMc), 4 transform-based methods (FISHbb, LPC, S3, BIBLE), 1 handcrafted feature-based method RISE, and 2 learnt feature-based methods (SPARISH and Yu's

CNN). The quality prediction models for learning-based methods are trained on the LIVE blur database [22].

Evaluation Criteria

Video Quality Experts Group (VQEG) [23] suggests to map the objective score o to the subjective score s using a four-parameter logistic function:

$$F(o) = \frac{\tau_1 - \tau_2}{1 + e^{\frac{o-\tau_3}{\tau_4}}} + \tau_2 \tag{33}$$

where τ_1, τ_2, τ_3, and τ_4 are free parameters to be determined during the nonlinear mapping process, with initial values as $\tau_1 = \max(s)$, $\tau_2 = \min(s)$, $\tau_3 = \text{mean}(o)$, and $\tau_4 = \text{std}(o)/4$.

Three evaluation criteria are chosen to evaluate the method's performance: Spearman's rank-order correlation coefficient (SRCC), Pearson's linear correlation coefficient (PLCC), and root-mean-square error (RMSE). SRCC indicates how well the relationship between subjective and objective scores can be described using a monotonic function. PLCC is a measure of the linear correlation between the subjective and objective scores after the nonlinear mapping. RMSE is used to measure the differences between the subjective and objective scores after the nonlinear mapping. For a good method, the values of SRCC and PLCC are close to 1, while the value of RMSE is close to 0.

Testing Databases

We consider blurred images from TID2013 [20] and BID [4]. **Gaussian blur images** from TID2013 are obtained using Gaussian filters, which are to approximate the out-of-focus blur. There are 125 blurred images generated from 25 reference images and 5 blur kernels. **Realistic blur images** from BID are taken from real world along with a variety of scenes, camera apertures, and exposure time. There are 586 images, most of which suffer from realistic out-of-focus blur or motion blur. The subjective scores are in the form of mean opinion score (MOS) with a range [0, 9] on TID2013 and [0, 5] in BID.

3.2 Experimental Results

The performance comparison is shown in Table 1, where the best three values are in boldface. On Gaussian blur images from TID2013, most existing methods correlate well with subject ratings in terms of SRCC and PLCC (SRCC, PLCC > 0.8). On realistic blur images from BID, FISHbb outperforms the others. However, the SRCC

Table 1 Performance comparison and average computational time (seconds/image) on TID2013 [20] and BID [4], where the best three values in each column are marked in boldface

Method	TID2013 [20]				BID [4]			
	SRCC↑	PLCC↑	RMSE↓	Time(s)↓	SRCC↑	PLCC↑	RMSE↓	Time(s)↓
MDWE [16]	0.816	0.835	0.686	0.184	0.307	0.320	1.186	3.333
CPBD [6]	0.852	0.855	0.647	**0.068**	0.018	0.004	1.252	**1.826**
PSI [5]	0.868	0.879	0.594	**0.015**	0.069	0.198	1.228	**0.210**
EMBM [8]	0.865	0.875	0.604	0.212	0.299	0.314	1.189	2.913
MLV [1]	0.879	0.883	0.587	**0.037**	0.320	0.363	1.167	**0.481**
ARISMc [7]	**0.901**	0.898	0.549	6.466	-0.013	0.155	1.237	87.966
FISHbb [24]	0.858	0.876	0.603	0.167	**0.477**	**0.473**	**1.103**	2.283
LPC [9]	0.889	0.892	0.565	0.565	0.316	**0.385**	**1.155**	8.378
S3 [25]	0.861	0.881	0.590	4.927	**0.413**	**0.423**	**1.134**	52.656
BIBLE [13]	**0.899**	**0.905**	**0.531**	0.916	**0.361**	0.370	1.163	10.982
RISE [15]	**0.932**	**0.923**	**0.481**	0.345	0.120	0.135	1.252	7.138
SPARISH [14]	0.893	**0.900**	**0.543**	1.485	0.307	0.328	1.183	25.217
Yu's CNN [29]	0.843	0.860	0.639	3.100	0.030	0.160	1.236	40.857

The negative of SRCC indicates that the prediction trend is contrary to what it is supposed to be

of FISHbb is less than 0.5 (far less than 1), which indicates that there is still a large space for designing robust and effective blur-specific NR-IQA methods for realistic blur images.

Computational time is also an important aspect for evaluating the performance of NR-IQA methods since many practical applications need to run in real time. Images in TID2013 are 512×384 pixels, while the size of images in BID is larger, ranging from 1280×960 to 2272×1704. All tests are carried out on a desktop computer with Intel Core i7 6700 K CPU at 4 GHz, 32 GB RAM, Windows 10, and Matlab R2016a (Yu'CNN is implemented using Python 2.7.6 and tested on Ubuntu 14.04 using the CPU of the same desktop computer). We used the default settings of the codes and did not optimize them. In Table 1, we also report the average computational time (seconds/image) on TID2013 and BID. We can observe that (1) the fast three methods (PSI, MLV, CPBD) are operated in the spatial domain and (2) most methods run fast on TID2013. However, as the image size increases, methods such as ARISMc, S3 get quite slow on BID, which cannot meet the requirement of time-sensitive applications.

Discussion on Realistic Blur

It is hard to model all the influence factors in the real world. Besides the Gaussian and out-of-focus blur, there are other crucial factors to be considered, e.g., motion blur, ghosting, macrophotography, and image content variation in Fig. 13.

- Motion blur: there are few NR-IQA methods for assessing the quality of motion blur images, though its related problem "motion deblurring" is a hot topic.

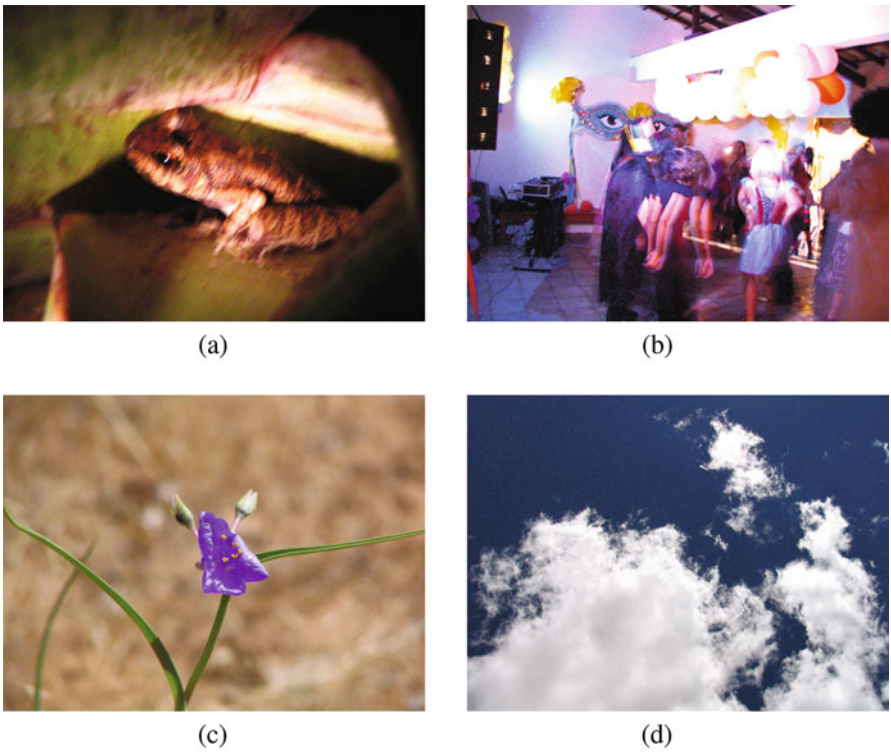

Fig. 13 Crucial factors (besides the Gaussian and out of focus blur) that influence the quality of realistic blur images. (**a**) Motion blur. (**b**) Ghosting. (**c**) Macrophotography. (**d**) Image content variation

Motion blur has directionality while Gaussian blur is isotropic. In terms of this specific characteristic of motion blur, one may further consider the directionality and the directional features for quality estimation on motion blur images. We believe that a large realistic motion blur image database with subjective ratings will facilitate the works.

- Ghosting: ghosting effect arises when the motion degree is very high, which differs from the ordinary motion blur.
- Macrophotography: the blur in Bokeh is to strengthen the photo's expressiveness. In view of this, to evaluate the quality of macrophotography images, aesthetic factors may need to be taken into account.
- Image content variation: due to the image content variation, NR-IQA methods may produce quite different objective scores for images with very similar subjective quality. At the meantime, NR-IQA methods may produce inconsistent predictions on image pairs with quite different subjective quality. To ease the impact of image content variation on blur-specific NR-IQA methods, the image content variation and blur distortion level should be jointly considered.

4 Conclusion

In this paper, we have classified previous works and have reviewed 18 representative blur-specific NR-IQA methods. Remarkable progress has been made in the past decades, evidenced by a number of state-of-the-art methods correlating well with subjective evaluations on Gaussian blur images. However, experimental results have also shown that most of the existing methods fail to estimate image quality of realistic blur images. It is the evidence that the blur-specific NR-IQA problem is far from being solved. We have also discussed on realistic blur, especially the issue on image content variation that should be considered in the development of blur-specific NR-IQA methods.

Acknowledgements This work was partially supported by National Basic Research Program of China (973 Program) under contract 2015CB351803; the National Natural Science Foundation of China under contracts 61390514, 61527804, 61572042, and 61520106004; and Sino-German Center (GZ 1025). We also acknowledge the high-performance computing platform of Peking University for providing computational resources.

References

1. Bahrami K, Kot AC (2014) A fast approach for no-reference image sharpness assessment based on maximum local variation. IEEE Sig Process Lett 21(6):751–755
2. Bahrami K, Kot AC (2016) Efficient image sharpness assessment based on content aware total variation. IEEE Trans Multimed 18(8):1568–1578
3. Bong DBL, Khoo BE (2014) Blind image blur assessment by using valid reblur range and histogram shape difference. Sig Process Image Commun 29(6):699–710
4. Ciancio A, da Costa ALNT, da Silva EAB, Said A, Samadani R, Obrador P (2011) No-reference blur assessment of digital pictures based on multifeature classifiers. IEEE Trans Image Process 20(1):64–75
5. Feichtenhofer C, Fassold H, Schallauer P (2013) A perceptual image sharpness metric based on local edge gradient analysis. IEEE Sig Process Lett 20(4):379–382
6. Ferzli R, Karam LJ (2009) A no-reference objective image sharpness metric based on the notion of just noticeable blur (JNB). IEEE Trans Image Process 18(4):717–728
7. Gu K, Zhai G, Lin W, Yang X, Zhang W (2015) No-reference image sharpness assessment in autoregressive parameter space. IEEE Trans Image Process 24(10):3218–3231
8. Guan J, Zhang W, Gu J, Ren H (2015) No-reference blur assessment based on edge modeling. J Vis Commun Image Represent 29:1–7
9. Hassen R, Wang Z, Salama MMA (2013) Image sharpness assessment based on local phase coherence. IEEE Trans Image Process 22(7):2798–2810
10. Huang GB, Zhu QY, Siew CK (2006) Extreme learning machine: theory and applications. Neurocomputing 70(1):489–501
11. Kang L, Ye P, Li Y, Doermann D (2014) Convolutional neural networks for no-reference image quality assessment. In: IEEE conference on computer vision and pattern recognition, pp 1733–1740. IEEE
12. Leclaire A, Moisan L (2015) No-reference image quality assessment and blind deblurring with sharpness metrics exploiting Fourier phase information. J Math Imaging Vis 52(1):145–172
13. Li L, Lin W, Wang X, Yang G, Bahrami K, Kot AC (2016) No-reference image blur assessment based on discrete orthogonal moments. IEEE Trans Cybern 46(1):39–50

14. Li L, Wu D, Wu J, Li H, Lin W, Kot AC (2016) Image sharpness assessment by sparse representation. IEEE Trans Multimed 18(6):1085–1097
15. Li L, Xia W, Lin W, Fang Y, Wang S (2017) No-reference and robust image sharpness evaluation based on multi-scale spatial and spectral features. IEEE Trans Multimed 19(5):1030–1040
16. Marziliano P, Dufaux F, Winkler S, Ebrahimi T (2004) Perceptual blur and ringing metrics: application to JPEG2000. Sig Process Image Commun 19(2):163–172
17. Mittal A, Moorthy AK, Bovik AC (2012) No-reference image quality assessment in the spatial domain. IEEE Trans Image Process 21(12):4695–4708
18. Mukundan R, Ong S, Lee PA (2001) Image analysis by Tchebichef moments. IEEE Trans Image Process 10(9):1357–1364
19. Narvekar ND, Karam LJ (2011) A no-reference image blur metric based on the cumulative probability of blur detection (CPBD). IEEE Trans Image Process 20(9):2678–2683
20. Ponomarenko N, Jin L, Ieremeiev O, Lukin V, Egiazarian K, Astola J, Vozel B, Chehdi K, Carli M, Battisti F, Kuo CCJ (2015) Image database TID2013: peculiarities, results and perspectives. Sig Process Image Commun 30:57–77
21. Sang Q, Qi H, Wu X, Li C, Bovik AC (2014) No-reference image blur index based on singular value curve. J Vis Commun Image Represent 25(7):1625–1630
22. Sheikh HR, Sabir MF, Bovik AC (2006) A statistical evaluation of recent full reference image quality assessment algorithms. IEEE Trans Image Process 15(11):3440–3451
23. VQEG (2000) Final report from the Video Quality Experts Group on the validation of objective models of video quality assessment. Video Quality Experts Group. http://vqeg.org/
24. Vu PV, Chandler DM (2012) A fast wavelet-based algorithm for global and local image sharpness estimation. IEEE Signal Process Lett 19(7):423–426
25. Vu CT, Phan TD, Chandler DM (2012) S_3: a spectral and spatial measure of local perceived sharpness in natural images. IEEE Trans Image Process 21(3):934–945
26. Wang Z, Simoncelli EP (2003) Local phase coherence and the perception of blur. In: Advances in neural information processing systems, pp 1435–1442
27. Wang Z, Bovik AC, Sheikh HR, Simoncelli EP (2004) Image quality assessment: from error visibility to structural similarity. IEEE Trans Image Process 13(4):600–612
28. Wang S, Deng C, Zhao B, Huang GB, Wang B (2016) Gradient-based no-reference image blur assessment using extreme learning machine. Neurocomputing 174:310–321
29. Yu S, Wu S, Wang L, Jiang F, Xie Y, Li L (2017) A shallow convolutional neural network for blind image sharpness assessment. PloS One 12(5):e0176632
30. Zhai G, Wu X, Yang X, Lin W, Zhang W (2012) A psychovisual quality metric in free-energy principle. IEEE Trans Image Process 21(1):41–52

Intensity Inhomogeneity Quantization-Based Variational Model for Segmentation of Hepatocellular Carcinoma (HCC) in Computed Tomography (CT) Images

Luying Gui and Xiaoping Yang

1 Introduction

Since the traditional method of lesion segmentation is manually finished by physicians, it is a time-consuming work for segmenting lesions from a large amount of medical images [1–3]. Besides, the accuracies of the results highly rely on the experiences of the physicians. Accurate segmentation algorithms are desired for labor saving and robustness in medical image analysis. However, the existing problems such as noise, low intensity contrast, blurred edges, and inhomogeneity cause considerable challenges for image segmentation [3–6].

To overcome these problems, some prior knowledge is used in object segmentation, including shapes [7–11], textures [12, 13], intensities [14]. With the assumption that images are piecewise smooth, extracted edges and local distribution of intensities are incorporated into an edge-based implicit active contour [15]. Besides, energy of salient edges which is derived from higher-order statistics is also incorporated into a variational level set [16].

Since the inhomogeneity is a common problem in different types of medical images, some approaches are designed to deal with this kind of artifacts [17, 18]. A piecewise constant assumption is proposed to correct the bias in magnetic resonance (MR) images [19]. In this work, bias correction and segmentation are finished at the same time by clustering based on the intensities in local regions. Additionally, local information is also described by Gaussian distributions [20]. Moreover, prior knowledge of bias fields is also utilized to tackle this problem [21].

L. Gui (✉)
Nanjing University of Science and Technology, Nanjing, China

X. Yang
Nanjing University, Nanjing, China
e-mail: yangxp@njust.edu.cn

M. Jiang et al. (eds.), *The Proceedings of the International Conference on Sensing and Imaging*, Lecture Notes in Electrical Engineering 506,
https://doi.org/10.1007/978-3-319-91659-0_5

These approaches above eliminate the effect of slowly varying intensities, which is called a kind of inhomogeneity, for segmentation on medical images.

Here we consider the problem concerning more serious uneven distribution of intensities or having heavily inhomogeneous intensities, in small regions in images. This situation may be caused by artifacts as well as the properties of the tissues and exhibit as granular appearances. For example, lesions may be constituted by various types of tissues. These tissues with different imaging characteristics will give different appearances in medical images and may cause the lesion regions with grained spots and complicated textures. Under this circumstance, segmentation curves are easily attracted by these fake edges and light or dark spots in the process of evolution and then cannot reach the real boundaries.

In order to solve this problem that segmenting lesion regions have complicated appearances, we propose a complexity measurement named complexity indicator (CI) map to evaluate the degree of uneven intensities in local regions. Embedding into a variational level set formulation, this complexity indicator map actually acts as an expansion energy for the segmentation contours. Moreover, in this paper, the real boundaries are captured by evaluating the similarities between regions. To achieve this goal, a similarity indicator (SI) map is constructed by calculating the Wasserstein distance between accumulative histograms of two regions. The SI map can drive the segmentation contours to stop at the real boundaries. This new method is applied to segment the hepatocellular carcinoma (HCC) in CT images, and most of these lesions suffer from low contrast and nonuniform textures. Experimental results and comparisons show that the proposed method is effective in dealing with these situations. The precision and Dice coefficient of the proposed method are 92.3% and 89.7%, respectively, which are higher than other two well-known methods.

2 Quantitative Analysis for Inhomogeneous Regions

Since the existence of differences between individuals and specialties in the medical field, lesion regions may have various appearances like irregular textures, intensity changes on medical images. It is hard to describe the characters of lesions by using a uniform pattern, and even these lesions are caused by the same disease. In order to deal with these regions, which are presented as inhomogeneous regions, two measurements are proposed to describe these appearances and subsequently applied in a variational segmentation method for precise separation of lesions. The two measurements are complexity measurement and similarity measurement which are presented as follows.

2.1 Complexity Measurement for Inhomogeneous Regions

In order to construct the complexity indicator map, the complexity of a region is evaluated by its intensity changes. First, we define a local region with radius r around the central pixel x:

$$R_{x,r} = \{y \in \Omega | \quad |y - x| \leq r\}. \tag{1}$$

We use I and $I_{R_{x,r}}$ to present the intensities of the whole image and intensities in the local region $R_{x,r}$, respectively. Then the differences between the intensities of the region and its Gaussian filtered result:

$$D_{R_{x,r}} = I_{R_{x,r}} - G * I_{R_{x,r}}. \tag{2}$$

In the above computation, the Gaussian filter actually implements two functions: (1) denosing and (2) assigning weights for neighbors according to their distance from the center. To highlight the different contrast between the central pixel and its surround pixels, based on the $D_{R_{x,r}}$, $CI_r(x)$ is created and computed as follows:

$$CI_r(x) = \sum^{|R_{x,r}|} D_{R_{x,r}}, \tag{3}$$

which accumulates the values of D in a local region $R_{x,r}$ (which is centered on x and has radius r), and the sum of differences are denoted as the value of CI_r in position x. $|R_{x,r}|$ represents the number of pixels in the region $R_{x,r}$.

For covering the different situation in different scales, for a center x, neighbor regions with different radii r are chosen.

The complexity indicator (CI) map is obtained by accumulating $CI_r(x)$ in different scales:

$$CI(x) = \sum_{r \in K} CI_r(x), \tag{4}$$

where K denotes the collection of all radii r. In this paper, we set $K = \{5, 7, 9\}$.

2.2 Similarity Measurement Based on the Wasserstein Distance

Besides, similarity between textures is considered as an important role in the description of the inhomogeneous regions for its talent capability of distinguishing two regions. In this paper, the similarity between regions is based on their cumulative histogram.

For a local region $R_{x,r}$, which is the region centered on x and with radius r, the histogram h is defined as:

$$h_R(y) := \frac{|z \in R_{x,r} \cap \Omega : I(z) = y|}{|R_{x,r} \cap \Omega|}, \tag{5}$$

for $0 \leq y \leq L$. And the corresponding cumulative distribution function is defined by:

$$F_R(y) := \frac{|z \in R_{x,r} \cap \Omega : I(z) \leq y|}{|R_{x,r} \cap \Omega|}, \tag{6}$$

for $0 \leq y \leq L$.

Then, the similarity between two regions R_1 and R_2 can be obtained by calculating the Wasserstein distance between their cumulative histograms:

$$W(R_1, R_2) = \int_0^L |F_{R_1} - F_{R_2}| dy. \tag{7}$$

Then, the similarity indicator (SI) map in this paper can be introduced by:

$$SI(x) = \frac{1}{W(R(x, r), R'(x, \widetilde{r}))}, \tag{8}$$

where $R'(x, \widetilde{r}) = R(x, \widetilde{r}) - R(x, r)$, $(r < \widetilde{r})$, r and $\widetilde{r}$ are two radii, respectively.

3 The Proposed Segmentation Method

3.1 The Segmentation Model Based on CI and SI

We present a new method, which combines the global and local intensity information of images, to segment images with intensity complexity. In the proposed method, the piecewise constant model [22] is implemented as the global image fitting term, and the complexity indicator map is incorporated to create the local information term. Thus, this energy functional expressed in the level set formulation is:

$$\begin{aligned} E(\phi, c_1, c_2) = \lambda_1 \int_\Omega |u_0(x, y) - c_1|^2 H(\phi(x, y)) dx dy \\ + \lambda_2 \int_\Omega |u_0(x, y) - c_2|^2 (1 - H(\phi(x, y))) dx dy \end{aligned}$$

$$+\lambda_3 \int_{\Omega} CI \cdot H(-\phi(x, y))dxdy$$
$$+\lambda_4 \int_{\Omega} SI \cdot \delta(\phi)|\nabla\phi|dxdy, \tag{9}$$

where ϕ is the level set function, H is the Heaviside function, and c_1 and c_2 are mean of intensity values in regions with $H(\phi) > 0$ and $H(\phi) \leq 0$, respectively. $\lambda_1, \lambda_2, \lambda_3, \lambda_4 > 0$. CI is the complexity indicator map, and SI is the similarity indicator map.

3.2 Implementation Details

In (9), the curve C is represented as the zero set of the level set function ϕ through using the Heaviside function H and its derivative δ_0 in the distribution sense, which are defined by:

$$H(s) = \begin{cases} 1 & if\ s \geq 0 \\ 0 & if\ s < 0, \end{cases} \quad \delta(s) = \frac{d}{ds} H(s). \tag{10}$$

In computation, H_ϵ and δ_ϵ, which are the regularized versions of the function H and its derivative, are used and expressed as follows:

$$H_\epsilon(s) = \frac{1}{2}\left(1 + \frac{2}{\pi}\arctan\left(\frac{s}{\epsilon}\right)\right),$$

and

$$\delta_\epsilon(s) = \frac{1}{\pi} \cdot \frac{\epsilon}{\epsilon^2 + s^2}.$$

Then, an artificial time $t \geq 0$ is used to parameterize the descent direction, and the equation in $\phi(t, x, y)$ is:

$$\begin{aligned} \frac{\partial\phi}{\partial t} &= \delta_\epsilon(\phi)\left[\lambda_1(u_0 - c_1)^2 + \lambda_2(u_0 - c_2)^2\right] \\ &+\lambda_3 CI\,\delta_\epsilon(\phi) \\ &+\lambda_4\delta_\epsilon(\phi)\mathrm{div}\left(SI\frac{\nabla\phi}{|\nabla\phi|}\right), \end{aligned} \tag{11}$$

which can be solved by a finite differences implicit scheme.

In this paper, we set $\lambda_1 = \lambda_2 = 1$ and $\lambda_3 = 4$, $\lambda_4 = 2$.

4 Results

4.1 Experimental Results on CT Images

In this section, we first show the efficiency of the proposed CI map and SI map. To achieve this goal, a HCC region which exhibits granular textures and similar appearances with its backgrounds is chosen for demonstration of these two quantitative measurements. The original image and its CI map, as well as its SI map, are shown in Fig. 1.

In the example shown in Fig. 1, the CI map creates a higher energy region on the position of the granular regions, including the HCC region. This high energy can encourage the segmenting contour expanding and then avoid the contour stopping at the fake edges. In Fig. 1, the CI map also presents that the high energy is decreasing when approaching to the real boundaries because the energy calculated in the CI map is influenced by the relative even regions in the background. Thus the expansion

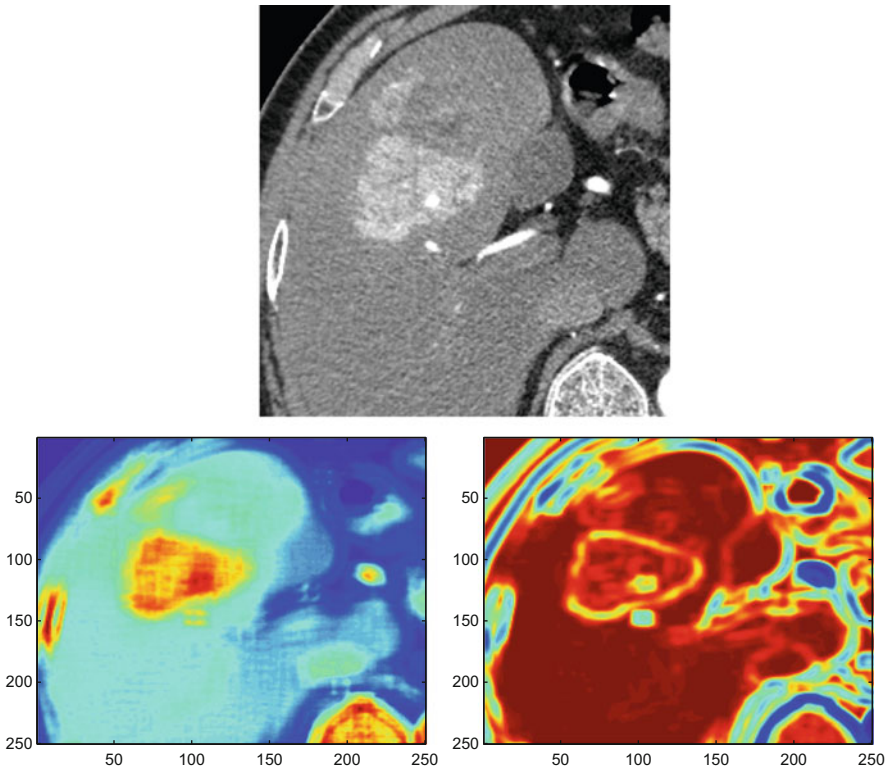

Fig. 1 First line: the original CT image with granular and low contrast HCC region; second line: left: its CI map and right: its SI map

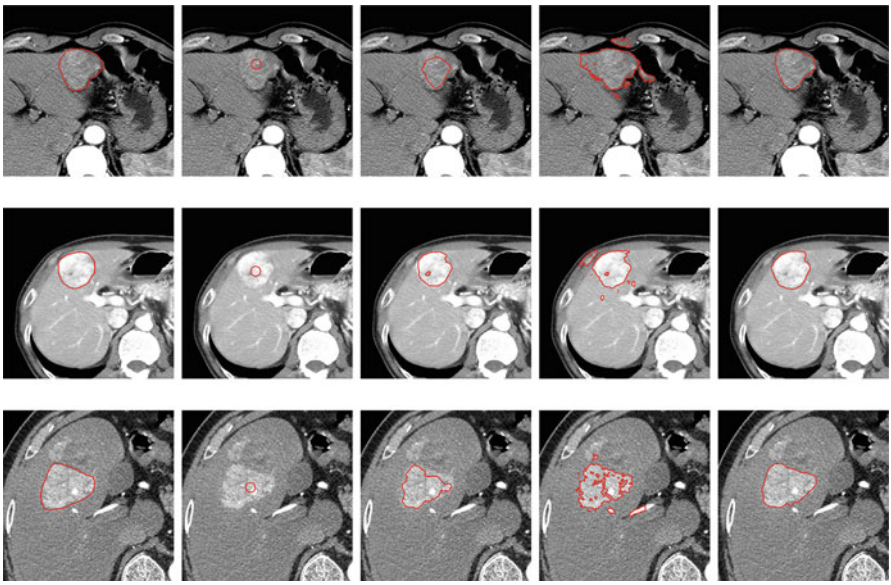

Fig. 2 Comparison results of CV model, BCS method and our method on the CT images for HCC with complicated textures. The first column, the ground truth; the second column, the initial contours; the third column, the results obtained of CV model; the fourth column, the results of BCS method; and the fifth column, the results of our proposed method

of the contour is slowing when approaching to the real boundaries. In the SI map, the real boundaries of the HCC region have low energy, which encourages the segmenting contour stopping near the positions.

To demonstrate the efficiency of the proposed method, we apply it on real medical images. In this experiment, 60 CT images with HCC are utilized. These lesion regions have various appearances, and most of them have uneven intensities and grained situations in different degrees, which present as complicated and uniform textures. Some experimental results are shown in Fig. 2.

In this section, we also compare the results of our new approach with those of two other methods: the classical CV model [22] and a segmentation method combine with bias correction [19] (hereafter termed 'BCS'). The ground truth, the initialization contours, as well as results of comparison are shown in Fig. 2.

In the first line, the HCC region exhibits similar appearances with the background; this fact causes error segmentation of the other two methods. In the second line, the HCC region has grain appearance inside the lesion, which causes some fake edges and leads to error segmentation. In the third line, the HCC lesion suffers from both blurred boundaries and granular surface, and the experimental results also show that the fake edges which are caused by the complex textures affect the accurate segmentation for other two methods in the comparison. With the CI map and SI map, which provide effective solutions for these situations, our proposed method gives precise segmentation results in this experiment.

4.2 Quantitative Measurements

In addition, comparisons of these segmentation results are also evaluated quantitatively by precision, recall [23], and Dice coefficient [24], which are expressed in (12) and (13), respectively.

$$\begin{aligned} \text{precision} &= \frac{TP}{TP + FP}, \\ \text{recall} &= \frac{TP}{TP + FN}, \end{aligned} \tag{12}$$

where TP is the number of true positive pixels, TN is the number of true negative pixels, FP is the number of false positive pixels, and FN is the number of false negative pixels.

$$\text{Dice} = \frac{2(A \bigcap G)}{A \bigcap G + A \bigcup G}, \tag{13}$$

where A is the segmenting result, and G is the ground truth.

Results of quantitative evaluation for these three methods are shown in Fig. 3. The segmentation results of the proposed method obtain average precision with

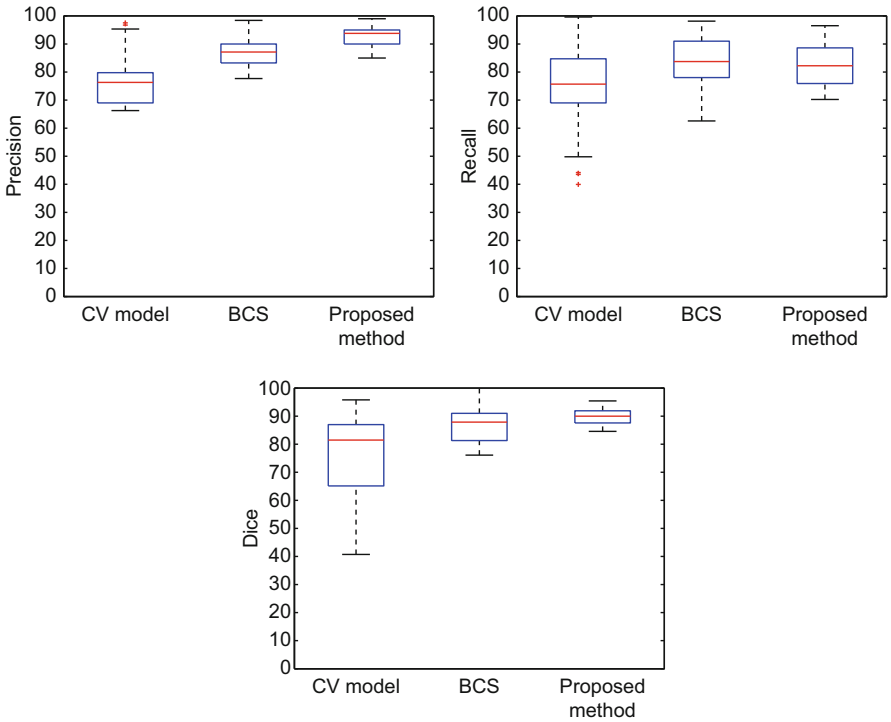

Fig. 3 Precision, recall and Dice for segmentation of HCC

92.3% and average Dice with 89.7%, which are higher than those of other two methods in the comparison.

5 Discussion and Conclusion

In this paper, a level set-based segmentation method is proposed to segment the objects with complex textures and uneven intensities.

The inhomogeneous situation imposes several difficulties for conventional segmentation algorithms. For instance, the uneven intensities may lead to fake edges, and the irregular textures may confuse the boundaries between objects and backgrounds. To deal with these problems, two quantitative measurements of complex changes of intensities are proposed in this paper, which are the complexity indicator (CI) map and the similarity indicator (SI) map.

Considering that the segmentation curves are likely to be entangled by some fake edges in inhomogeneous region, the complex indicator CI is proposed in this paper. Embedding into a level set framework, the CI map obtains higher energy in these regions which have inhomogeneous intensities and grained appearances, and this high energy will encourage the contours expanding. In addition, this power will decrease near the real boundaries, because of the changes of gray values tend to moderate.

It is worth noting that in formulation of the CI map, the Gaussian filter is adopted, which is used to realize two functions, first, acting as noise filter, and second, acting as a weight distributor. The weights assigned by the Gaussian filter actually based on their distances of pixels to their region centers, and therefore, pixels which are far away from centers have less influence on the central pixel. In a word, the distance-related weights guarantee more accurate measurement of the relationships between pixels and therefore make the CI map more efficient.

Moreover, to locate the real boundaries, the SI map is created based on the similarity evaluation between two regions by using the Wasserstein distance. Pixels in the real boundaries have more changes in their neighbor regions and then obtain higher values in distance evaluation and therefore gain smaller values in the SI map, which makes the segmenting contours stop at the suitable positions.

In this paper, different parameters are set for the CI and SI energy terms. As can be seen in Fig. 2, livers almost have relative smooth and homogeneous appearances in CT images, and on the contrary, the HCC lesion regions are complex and inhomogeneous. In this situation, a large parameter of the CI energy term will encourage the segmenting contour expand more effectively. Because of the smooth background (i.e., liver tissues), the CI energy will fade in the position that is close to the boundaries. This fact also explains that a relative small parameter is assigned for the SI energy. As an edge indicator, the function of SI energy should be strengthened when the situation becomes more complicated, like both the background and foreground have complex appearances.

The efficiency of the proposed method and the rationality of the parameter setting can be proved by the experimental results. Some typical examples are shown in Fig. 2. In the first line, a lesion with uneven intensities and blurred boundaries is shown. In the second and third lines, lesions with grained appearances, like light spots, dark lines, and dark spots, are shown. These complicated textures bring difficulties for segmentation. From these images, we can see that segmentation contours of the two well-known methods are easily stopped by the fake edges which are created by the violent intensity changes. However, these problems can be addressed by the proposed method. Experimental results in the last column also prove the effectiveness of the new approach.

Experimental results demonstrate the efficiency of the proposed method from both visual effect and quantitative evaluation. With a light spot in the dark lesion region, this spot has high contrast with the object region, so it is easy to be recognized as background and be error segmented. For the classical CV model, with a large parameter for the regularization term, i.e., the arc length, these high-contrast spots will not be segmented. However, the similar intensities for the background and foreground bring problems, and the segmentation contour stops at the fake edges which are caused by uneven intensities inside the lesion region. However, beneficial from the CI map and SI map, the proposed method has relatively low degree of dependence on initialization contours. As shown in Fig. 2, the initialization contours are only small circles in the HCC regions. Theoretically, as we have pointed out, this CI map is designed to direct the expanding of the segmenting contours, especially in the case of complex regions, and the SI map is designed to stop the movement of the contours. This idea also can be illustrated by the example in Fig. 1.

In the grained and uneven intensity cases we showed above, the proposed method has good performance, which presents segmentation contours to approach the ground truths. The efficiency of the proposed method is also confirmed by quantitative evaluations.

In conclusion, a new segmentation method for inhomogeneous regions with complex textures is proposed. Based on two measurements of complexity of regions, the active contour can expand across the fake edges which are generated by complicated textures and approach the real boundaries. Additionally, the accuracy of this method does not rely on the initialization. The efficiency of the proposed method, as well as its independency of the initializations, is proved by experimental results of segmenting HCC regions in CT images. Comparison results with other two methods also present the advantages of the novel segmentation method.

Acknowledgements This work is supported by National Nature Science Foundation of China (No. 91330101 and NO.11531005).

References

1. Yu J, Wang Y, Chen P (2008) Fetal ultrasound image segmentation system and its use in fetal weight estimation. Med Biol Eng Comput 46(12):1227–1237

2. Pham DL, Xu C, Prince JL (2000) Current methods in medical image segmentation 1. Ann Rev Biomed Eng 2(1):315–337
3. Noble JA, Boukerroui D (2006) Ultrasound image segmentation: a survey. IEEE Trans Med Imaging 25(8):987–1010
4. Gutiérrez-Becker B, Cosío FA, Huerta MEG, Benavides-Serralde JA, Camargo-Marín L, Bañuelos VM (2013) Automatic segmentation of the fetal cerebellum on ultrasound volumes, using a 3d statistical shape model. Med Biol Eng Comput 51(9):1021–1030
5. Zhang D, Liu Y, Yang Y, Xu M, Yan Y, Qin Q (2016) A region-based segmentation method for ultrasound images in hifu therapy. Med Phys 43(6):2975–2989
6. Roy S, Nag S, Maitra IK, Bandyopadhyay SK (2013) A review on automated brain tumor detection and segmentation from MRI of brain. arXiv preprint arXiv:1312.6150
7. Huang J, Yang X, Chen Y, Tang L (2013) Ultrasound kidney segmentation with a global prior shape. J Vis Commun Image Represent 24(7):937–943
8. Qiu W, Yuan J, Ukwatta E, Sun Y, Rajchl M, Fenster A (2014) Prostate segmentation: an efficient convex optimization approach with axial symmetry using 3-d trus and mr images. IEEE Trans Med Imaging 33(4):947–960
9. Gloger O, Tönnies KD, Liebscher V, Kugelmann B, Laqua R, Völzke H (2012) Prior shape level set segmentation on multistep generated probability maps of mr datasets for fully automatic kidney parenchyma volumetry. IEEE Trans Med Imaging 31(2):312–325
10. Yang F, Qin W, Xie Y, Wen T, Gu J (2012) A shape-optimized framework for kidney segmentation in ultrasound images using nltv denoising and drlse. Biomed Eng Online 11(1):82
11. Gui L, He J, Qiu Y, Yang X (2017) Integrating compact constraint and distance regularization with level set for hepatocellular carcinoma (hcc) segmentation on computed tomography (ct) images. Sens Imaging 18(1):4
12. Xie J, Jiang Y, Tsui HT (2005) Segmentation of kidney from ultrasound images based on texture and shape priors. IEEE Trans Med Imaging 24(1):45–57
13. Wu CH, Sun YN (2006) Segmentation of kidney from ultrasound b-mode images with texture-based classification. Comput Methods Prog Biomed 84(2):114–123
14. Liu B, Cheng H, Huang J, Tian J, Tang X, Liu J (2010) Probability density difference-based active contour for ultrasound image segmentation. Pattern Recogn 43(6):2028–2042
15. He L, Zheng S, Wang L (2010) Integrating local distribution information with level set for boundary extraction. J Vis Commun Image Represent 21(4):343–354
16. Vivekanantham S, Azzopardi G, Prashanth Ravindran G (2014) Active contours driven by the salient edge energy model. Br J Hosp Med (Lond: 2005) 75(4):236
17. Hou Z (2006) A review on mr image intensity inhomogeneity correction. Int J Biomed Imaging 2006
18. Li C, Gore JC, Davatzikos C (2014) Multiplicative intrinsic component optimization (MICO) for MRI bias field estimation and tissue segmentation. Magn Reson Imaging 32(7):913–923
19. Li C, Huang R, Ding Z, Gatenby J, Metaxas DN, Gore JC (2011) A level set method for image segmentation in the presence of intensity inhomogeneities with application to mri. IEEE Trans Image Process 20(7):2007–2016
20. Wang L, Chen Y, Pan X, Hong X, Xia D (2010) Level set segmentation of brain magnetic resonance images based on local Gaussian distribution fitting energy. J Neurosci Methods 188(2):316–325
21. Wang L, Pan C (2014) Image-guided regularization level set evolution for MR image segmentation and bias field correction. Magn Reson Imaging 32(1):71–83
22. Chan TF, Vese LA (2001) Active contours without edges. IEEE Trans Image Process 10(2):266–277
23. Powers DM (2011) Evaluation: from precision, recall and f-measure to roc, informedness, markedness & correlation. J Mach Learn Technol 2(1):37–63
24. Dice LR (1945) Measures of the amount of ecologic association between species. Ecology 26(3):297–302

Part II
Sensing Techonlogies

A Novel Computed Tomography Scanning Mode and Local Image Reconstruction of Impurities in Pipeline

Lingli Zhang, Li Zeng, and Dong Wu

1 Introduction

Impurities in pipeline easily cause blockage, which affects the liquid velocity and even leads to an accident. Therefore, nondestructive testing (NDT) of the pipeline in service has a great practical significance. The conventional NDT techniques in pipeline involve ultrasonic testing (UT), acoustic emission (AE), radiography testing (RT), X-ray computed tomography (CT), etc. In terms of UT's advantage of strong penetrability, accurate defection location, low cost of detection, and fast speed, it is widely used for NDT of the defect of the metal, nonmetal, and composite materials, etc., such as the defect detection of the pipeline. The correlative scanning techniques and ultrasound image processing methods were progressively developed [1]. However, UT appears more difficult in the face of complicate and irregular objects, and its detection results are commonly not intuitive. For another AE is a dynamic NDT method, and its basic principle is to utilize the sensitive instrument to receive and process the acoustic emission signal and thus infer the defect location, the change of state level, and the development of the internal structure of the material. Based on the high detection sensitivity and most of the materials possessing acoustic emission characteristics, AE has been widely used in pipeline leak detection [2]. Although AE has not too many restrictions on the shape of the

L. Zhang · L. Zeng (✉)
College of Mathematics and Statistics, Chongqing University, Chongqing, China

Engineering Research Center of Industrial Computed Tomography Nondestructive Testing of the Education Ministry of China, Chongqing University, Chongqing, China
e-mail: drlizeng@cqu.edu.cn

D. Wu
School of Computer Engineering, Jiangsu University of Technology, ChangZhou, Jiangsu, China

M. Jiang et al. (eds.), *The Proceedings of the International Conference on Sensing and Imaging*, Lecture Notes in Electrical Engineering 506,
https://doi.org/10.1007/978-3-319-91659-0_6

object and the on-site conditions, it is sensitive to the object material and merely gives the position, activity, and strength of the noise source, while it can't obtain the nature and size of the defect within the noise source. By contrast, the principle of RT is to utilize the change of the electromagnetic wave, which penetrates the detected object to obtain the images [3]. The defects can be detected with analyzing and evaluating these images.

In current years, X-ray CT has been widely used in industrial applications because of its nondestructive and effective testing technology, and it is most applicable to detection of defect, material evaluation, interior analysis of object, etc. [4–7]. CT has the ability to obtain the intuitive and clear images without overlapped and geometrical distortion compared with traditional radiate photography. Nevertheless, the conventional CT usually detects the static object such as pipeline wall. Although dual CT can detect the dynamic objects, it is mostly used in clinical diagnosis due to the high cost [8]. According to the detection of the impurities in pipeline, its scanning mode appears more difficult to be adaptive. Therefore, developing a new scanning mode for the detection of flowing fluid inclusion in pipeline is very necessary. The novel computed tomography scanning mode, which takes advantage of fluid flowing to obtain equivalent spiral cone-beam (ESCB) projection data of the fluid (including impurities), is proposed to detect impurities in pipeline in this paper, and its mechanical movement is simple and feasible, which can be easily adaptive to the live conditions of the detected pipeline in service.

In CT detection technology, spiral cone-beam scanning mode and the corresponding imaging method can solve the long object detection (such as pipeline) in view of high efficiency of the detection and good axial resolution of reconstruction image [9–14]. Meanwhile the Feldkamp-Davis-Kress (FDK) [15] algorithm is always a popular approximate cone-beam CT algorithm whose filter function is global, which is unsuitable for truncated projection data. Whereafter, an improved cone-beam image reconstruction method was developed for the circular orbit by reference [16]. However, there exist several issues about the detected object, such as the thickness of the pipeline wall, the long string part of the wall which is impenetrable by weak X-ray, the local truncation projection data in the pipeline wall, and the limited translation of detector and X-ray source. In practical, the projection data obtained is locally truncated in these situations.

In recent several years, local reconstruction methods are gradually developed aiming at improving the scanning speed and solving the projection truncation issues [17]. Since the local reconstruction methods can implement the characteristics of the reconstructed image in which X-ray only irradiates the lesion on the patient to reduce the patient's exposure dose and improve the projection reconstruction speed at the same time, it is widely applied in medical CT. Local reconstruction has also many NDT applications in industry. There were several typical local reconstruction methods such as lambda tomography algorithm [18, 19], pseudolocal tomography algorithm [20], local reconstruction algorithm based on wavelet multiresolution [21, 22], etc. The lambda tomography algorithm is a kind of strict local reconstruction algorithm which is not confined to the two-dimensional or three-dimensional field, as in the mathematical theory, it can rebuild any dimension of space information

of the image. However, the reconstructed part by lambda tomography algorithm is not the attenuation coefficient distribution of the original image but the attenuation coefficient distribution of the edge of image, which highlights the edge and leads to the large noise at the same time. The two above methods are not strict and their required data area is larger than region of interest (ROI). The reconstructed result by pseudolocal tomography algorithm is also not the attenuation coefficient distribution of the image, but a part of the Hilbert transform of the image. While local reconstruction algorithm based on wavelet multiresolution is a local reconstruction research direction in recent years, different from lambda tomography algorithm and pseudolocal tomography algorithm, its reconstructed result is the attenuation coefficient distribution of the local area, but it is very dependent on the selection of wavelet coefficients.

Furthermore the investigative interior reconstruction algorithm by Wang et al. [23] can solve local image reconstruction as well. Mao-lin Xu et al. [24] put forward a local CT image reconstruction with a new filter. Mao-lin Xu's algorithm utilizes a new filter replacing the slope filter function of filtered back-projection (FBP) method. The new filter's side lobe attenuates sooner than the probable selected filters', which has been presented in the Mao-lin Xu's paper. This algorithm realizes the local image reconstruction using new filter function, and it ignores the data far away from the calculation points. In his paper, simulated results present that the developed algorithm is convenient to reduce the Gibbs effect of reconstructed image and the reconstructed results have high spatial resolution and density resolution. Generally, reconstructed results have high spatial resolution using a filter function with high and narrow main lobe; the rapid attenuation of side lobe helps to improve the density of image resolution. The new filter obtains a good compromise between spatial resolution and density resolution, and the distant side lobe of the new filter attenuates quickly. Taking these advantages into consideration, a local spiral cone-beam FDK is presented that combines the general spiral cone-beam FDK image reconstruction algorithm and the local filter to solve the truncated projection which is obtained by the novel scanning mode in this paper.

Before introducing the novel scanning mode in this paper, the previous scanning modes such as fan-beam CT, cone-beam CT, and spiral cone-beam CT are presented in Section II. Section III introduces the proposed novel scanning mode. And then the corresponding algorithm is presented in Section IV. Finally Section V presents the results and conclusions.

2 Preparation

2.1 Fan-Beam CT Imaging

The scanning mode of CT system can be divided into two kinds: parallel-beam and fan-beam. Figure 1 shows the geometric structures of parallel-beam and fan-beam,

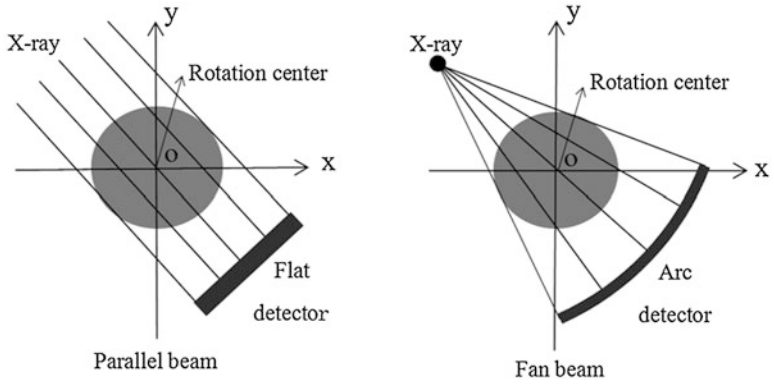

Fig. 1 The comparison between parallel-beam geometry and fan-beam geometry

Table 1 Geometrical scanning parameters for a simulated equivalent spiral cone-beam CT imaging

Parameter	Value
Distance between source and detector	354 mm
Distance between source and rotation axis	212 mm
Sampling interval between two adjacent projection views	1.406°
Diameter of ROI	60.42 mm
Pitch of each turn of spiral trajectory	10.62 mm
The number of detector array (row × column)	256 × 256
Size of each detector element	$0.196 \times 0.392\ mm^2$
Voxel size of the object	$0.354 \times 0.354 \times 0.354\ mm^3$
The number of the reconstructed object	256 × 256 × 100

respectively. The fan-beam CT scanning mode is that the X-ray source and fan-beam detector are stationary and the turntable rotates carrying the scanned object or, equivalently, X-ray source and fan-beam detector turn around the scanned object in a circular track. Since the fan-beam CT scanning has a proceeding speed, it is extensively utilized in several fields. The corresponding well-known algorithm is fan-beam FBP algorithm referring to reference [25].

Fan-beam FBP with R-L filter has a high reconstruction speed, and it can obtain a relatively good image on the premise that the projection data is complete. However, R-L filter has a Gibbs artifact which reduces the intensity resolution of image, and it will not get an ideal image when the projection data is incomplete or contains noise.

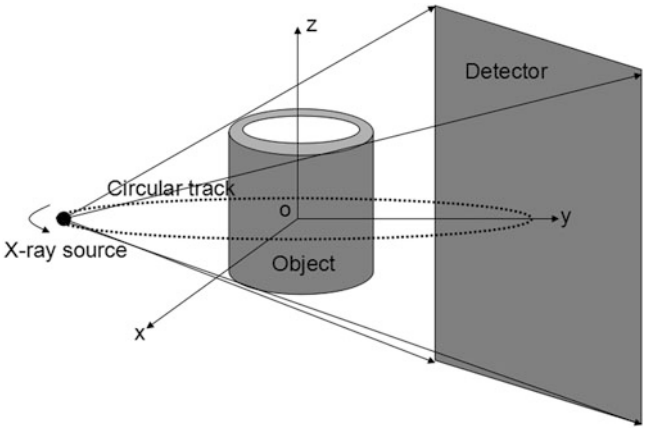

Fig. 2 The general cone-beam scanning geometry

2.2 Cone-Beam CT Imaging

A general cone-beam CT scanning mode is that the detected area should be completely covered by cone-beam X-ray. X-ray source and the flat detector turn around the object in a circular track simultaneously as shown in Fig. 2. The solution to cone-beam projection data can be divided into two kinds: one kind is analytic reconstruction method; the other is iterative reconstruction method. Since the rapid reconstruction speed is very important in applications, analytic reconstruction method is still popular. Additionally, analytic reconstruction methods can be divided into accurate reconstruction method and approximate reconstruction method. Nowadays accurate reconstruction algorithm has a good development, and approximate cone-beam reconstruction algorithm has very important value both in the application and theory. When the projection data is under the complete, noiseless, and ideal conditions, accurate reconstruction algorithm is a good choice; in the presence of measurement noise, data truncation, the movement of patients, digital processing, and the use of contrast agents, accurate reconstruction algorithm has a certain influence on image quality; by this time the approximate reconstruction algorithm or iterative reconstruction algorithm is necessary.

On consideration that cone-beam CT utilizes cone-beam X-ray and high-density flat detector, it has a great many advantages such as a fast scanning speed, a high utilization rate of X-ray, the consistent axis resolution, etc. Nevertheless, cone-beam CT is not good enough for the long rod-shaped object like a pipeline.

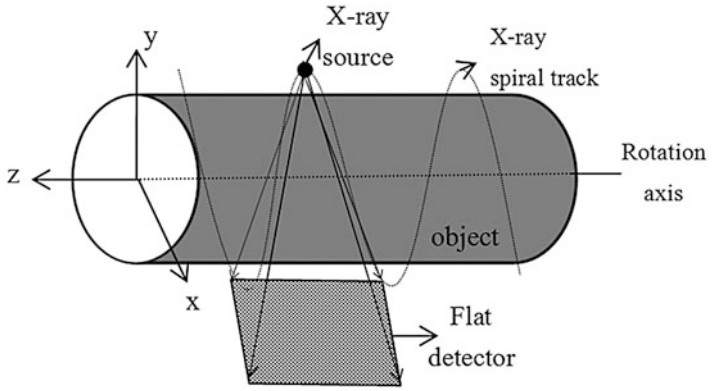

Fig. 3 Spiral cone-beam scanning geometry

2.3 Spiral Cone-Beam CT Imaging

Compared with general cone-beam CT scanning mode, spiral cone-beam CT not only has the advantages of the general cone-beam CT scanning track but also can solve the long object detection such as the pipeline and the human body, and its scanning track satisfies the condition of completeness data of the accurate reconstruction [26] as shown in Fig. 3. Spiral FDK algorithm [27] is similar to FDK algorithm. In fact, the spiral cone-beam FDK algorithm let cone-beam be treated as the accumulative fan-beam along the z-axis direction. The procedure of the spiral cone-beam FDK algorithm is presented under the corresponding to the spiral cone-beam scanning as in reference [27].

Although spiral cone-beam CT has the ability to settle the detection of a long static object, it is not suitable for the situation that the pipeline is not translated and fluid in pipeline is flowing.

3 The Proposed Novel Scanning Mode

3.1 Equivalent Spiral Cone-Beam Scanning

In order to detect flowing fluid with inclusions of the pipeline, which may lead to impact fluid speed and cause accident, the novel scanning mode is researched in this paper motivated by predecessors. Considering that X-ray source and detector cannot shift along the pipeline and big thickness of the pipeline wall may not be impenetrable, this scanning mode takes cone-beam scanning by X-ray source and detector around the fixed pipeline with circular track (as shown in Fig. 4) and uses the fluid flowing to obtain ESCB projection data of the fluid (containing inclusions),

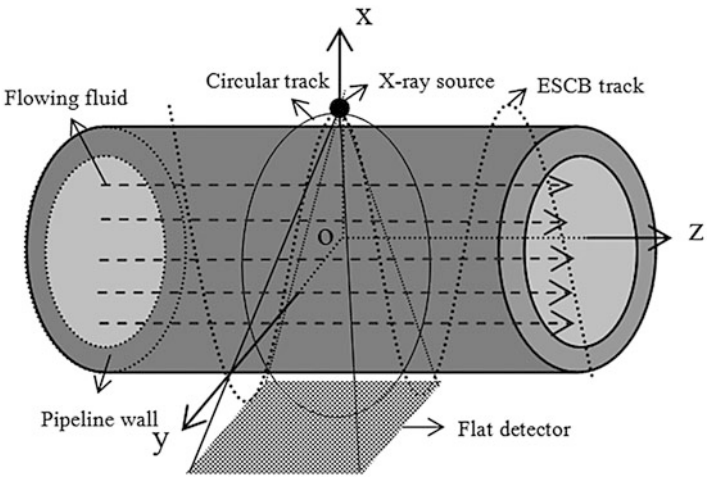

Fig. 4 The sketch map of the novel scanning mode in this paper

Fig. 5 Inclusions are following along fluid flowing (assuming that liquid flowing is uniform in a short time)

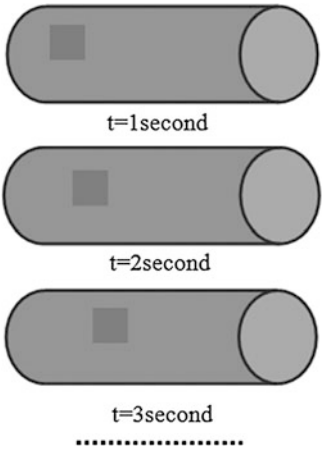

whose pitch can be estimated by tracking the change of inclusion position in one circular cone-beam scan projection image (supposing that in a short time the movement of impurities along fluid can be treated as a uniform linear motion as shown in Fig. 5). It is easy to implement the mechanical movement of this scanning mode and adapt to the inspection condition of pipeline in service. Considering that pipeline doesn't move according to the fluid flowing, this scanning mode obtains merely spiral cone-beam projection data of the internal of pipeline with impurities; therefore, its projection data in the pipeline wall is locally truncated (the projection data in pipeline wall is not involved in image reconstruction, but it has influence on the internal fluid projection data).

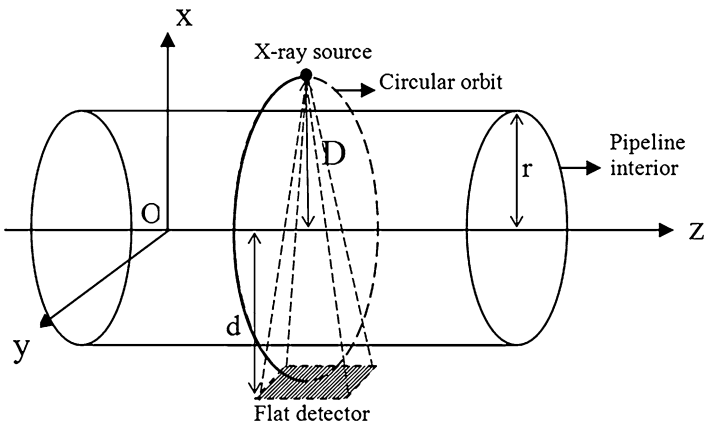

Fig. 6 Pipeline scanning coordinate system

3.2 The Equivalent Trajectory of X-Ray Source

The speed of the flowing fluid v can be determined by X-ray digital radiography for the impurities in flowing fluid of the pipeline in S seconds, where S denotes the time about X-ray source rotating along the circular orbit in one circle. And then required pitch L can be expressed as:

$$L = v^* S \tag{1}$$

Considering that the thickness of pipeline wall affects the penetrability of X-ray, this paper only utilizes the three-dimensional projection data of the pipeline internal fluid (containing impurities). It means treating the pipeline internal as ROI. As is shown in Fig. 6, r is an internal radius of the pipeline, and $z_{\min}$ and $z_{\max}$ are the starting and ending value of scanned pipeline, respectively. It can define the cylindrical ROI as follows:

$$\text{ROI} = \left\{ (x, y, z) \,\middle|\, x^2 + y^2 \le r^2, z_{\min} \le z \le z_{\max} \right\} \tag{2}$$

The equivalent trajectory of X-ray source $\Gamma(\beta)$ can be expressed as follows:

$$\Gamma(\beta) = (-D \sin\beta, D \cos\beta, \beta L/2\pi)^T \tag{3}$$

where D is the distance from X-ray source to the pipeline center, T denotes the transpose of a vector, β is a rotation angle of X-ray source, and $2\pi z_{\min}/L - \pi \le \beta \le 2\pi z_{\max}/L + \pi$.

3.3 The Estimate of the Sampling Interval ΔZ

The estimate of the sampling interval ΔZ needs to consider two aspects: one aspect is data acquisition time, and the other is the pitch L. Let D denote the distance from X-ray source to the pipeline center and d denote the distance from detector to the pipeline center. The sampling interval ΔZ can be estimated as follows.

An appropriate value of the sampling interval ΔZ can be given by the following formula:

$$\Delta Z = L * \frac{D+d}{D-r} * \frac{1}{(N-1)} \tag{4}$$

where N is the number of one-dimensional detector and ΔZ is the sampling interval. From Eq. (4), it is obvious that ΔZ can be set to a large value when L is quite large and N is relatively small. However, a too large ΔZ brings about the poor spatial resolution of the reconstruction result.

Considering spatial resolution Δz, the sampling interval can be expressed as $\Delta Z = \frac{D+d}{D+r}\Delta z$.

4 The Presented Method

4.1 A Local Filter Function [24]

A new frequency domain form of the local filter function can be expressed as the following:

$$H(w) = |w|\, W(w)$$

where the window function is:

$$W(w) = \begin{cases} \frac{er^2}{r^2-w^2} \exp\left[\frac{-r^2}{r^2-w^2}\right], |w| \le r, \\ 0, |w| > r. \end{cases} \tag{5}$$

It is easy to prove that $W(w)$ is an infinitely differential function with the support $[-r, r]$. The corresponding spatial filter function can be derived as follows:

$$h(\alpha) = -\frac{2}{(2\pi\alpha)^2} + o\left(\frac{1}{(2\pi\alpha)^5}\right)$$

Relatively, the spatial filter function of R-L filter is expressed as:

$$h(\alpha) = -\frac{2r\sin(2\pi\alpha r)}{(2\pi\alpha)^2} + \frac{2}{(2\pi\alpha)^2}(1-\cos 2\pi\alpha r).$$

From their spatial forms, it can be seen that the local filter in spatial domain decays in second order as s tends to infinite, while the R-L filter decays in first order. Generally, reconstruction image has high spatial resolution by using a filter function with the high and narrow main lobe; the rapid attenuation of side lobe helps to improve the density of the image resolution. The local filter function obtains a good compromise between spatial resolution and density resolution. And the distant side lobe of local filter attenuates quickly, which has been proved in detail in reference [24].

4.2 The Presented Approach

Aiming at reconstructing the image of the flowing fluid with impurities in pipeline, the presented approach brings the local filter into the spiral cone-beam FDK algorithm, which obtains the local spiral cone-beam FDK CT reconstruction algorithm as follows.

Let $f = \{f(x, y, z)|(x, y, z) \in \text{ROI}\}$ be the discretization data of the flowing fluid with inclusions in pipeline. The X-ray source trajectory $\Gamma(\beta)$ can be expressed as Eq. (3), and the pitch L can be defined by Eq. (1). $p(\alpha, z, \beta)$ denotes the projection data of X-ray scanning internal flowing fluid with inclusions in the pipeline. α is the angle of the current X-ray off the center X-ray (perpendicular to the center of the detector).

Step 1: weighting the projection data

$$p'(\alpha, z, \beta) = p(\alpha, z, \beta) \frac{(D + d)\cos\alpha}{\sqrt{(D + d)^2 + z^2}} \tag{6}$$

Step 2: doing one-dimensional convolution according to variable α

$$p''(\alpha, z, \beta) = \int_{-\alpha_{\max}}^{\alpha_{\max}} p'(\alpha', z, \beta) h(\alpha - \alpha') d\alpha' \tag{7}$$

where the local filter is the convolution function $h(\alpha) = D\left(\frac{\alpha}{\sin\alpha}\right)^2 \int_0^{+\infty} wW(w) \cos(w\alpha) dw$, $W(w)$ is a window function by Eq. (5) which avoids confusion error and attenuates high-frequency components, and $\alpha_{\max} = \sin^{-1}(r/D)$.

Step 3: computing three-dimensional back-projection $f(x, y, z)$ as follows:

Considering that a plane contains reconstructed point (x, y, z) and is vertical to z-axis, then the source trajectory $\alpha(\beta)$ can be computed by Eq. (3), and cross-

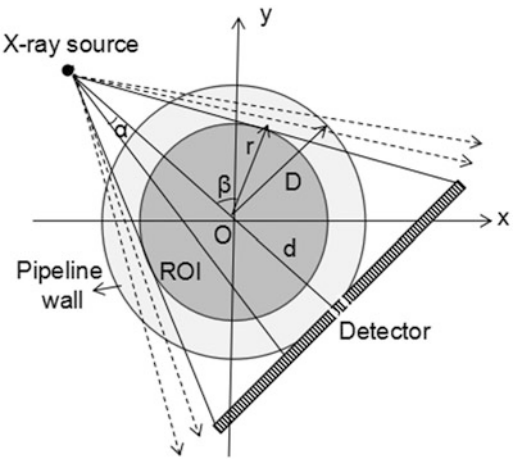

Fig. 7 It is the sectional drawing of Fig. 6

point $\alpha(\beta^{'})$ can be provided by $\beta^{'}(z) = 2\pi z/L$. Let $p''(\alpha, z, \beta)$ be back projected to the reconstructed point (x, y, z) in the range of β with $[\beta^{'}(z) - \pi, \beta^{'}(z) + \pi]$. The mathematical form can be expressed as below:

$$f(\gamma\cos\varphi, \gamma\sin\varphi, z) = \frac{1}{4\pi^2}\int_{\beta\prime(z)-\pi}^{\beta\prime(z)+\pi}\frac{1}{K^2}p''(\alpha, z, \beta)\,d\beta \tag{8}$$

where γ is the distance between the point $(0, 0, z)$ and (x, y, z) and angle φ is that the ray from the point $(0, 0, z)$ to (x, y, z) deviates from the positive direction of x-axis:

$$(\alpha, z) = \left(-\tan^{-1}\frac{\gamma\cos(\beta-\varphi)}{D+\gamma\sin(\beta-\varphi)}, \left(z - \frac{L}{2\pi}\beta\right) \times \frac{D+d}{\sqrt{D^2+d^2+2\gamma D\sin(\beta-\varphi)}}\right)$$

and $K^2 = D^2 + r^2 + 2rD\sin(\beta - \varphi)$. The physical meaning of K is the distance between two points obtained by projecting reconstructed point (x, y, z) and X-ray source location onto plane xoy, respectively. The variable geometric properties can be shown in Fig. 7.

5 Results and Conclusions

5.1 The Experimental Data Specifications and Conditions of Computer Hardware

In order to validate the scanning mode and the effectiveness of the presented reconstruction algorithm for the pipeline flow fluid with impurities in this paper, the simulation experiments are presented on personal computer with 4G

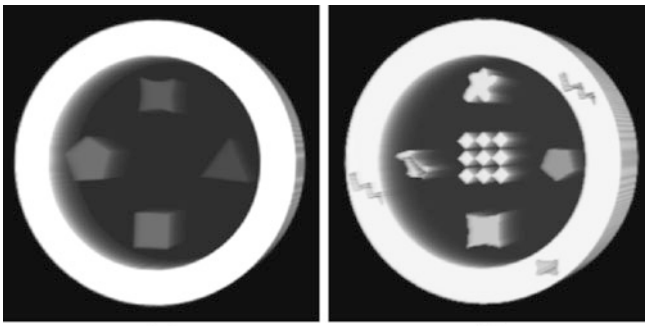

Fig. 8 It presents the simulated models: (**a**) "pipeline data1" and (**b**) "pipeline data2"

memory and 2.70GHz CPU by Microsoft Visual Studio 2010. Figure 8a shows "pipeline data1" which is composed of 256 × 256 × 100 voxels of each size 0.354 mm × 0.354 mm × 0.354 mm. Figure 8b "pipeline data2" is analogous to (a) except for a little more complicated flowing fluid impurities in pipeline. The projection data are simulated via adding Gaussian noise with zero mean and standard deviation 0%max, 0.1%max, and 0.5%max (max stands for the maximal intensity of the current projection view). The parameters of the proposed geometrical scanning mode for a simulated equivalent spiral cone-beam CT imaging are presented in Table1. In the experiment, this paper utilizes the local projection data to reconstruct using the general spiral FDK to verify our proposed scanning mode and the presented algorithm.

5.2 Performance Assessment

To quantitatively assess the performance of the presented algorithm, the following three metrics are utilized: (1) root-mean-square error (RMSE), (2) normalized root-mean-square distance (NRMSD), and (3) normalized mean absolute distance (NMAD) [28]:

$$\mathrm{RMSE} = \sqrt{\frac{1}{Q}\sum_{k=1}^{Q}\left(f(k) - f_{\mathrm{ROI}}(k)\right)^2} \tag{9}$$

$$\mathrm{NRMSD} = \sqrt{\frac{\sum_{k=1}^{Q}\left(f(k) - f_{\mathrm{ROI}}(k)\right)^2}{\sum_{k=1}^{Q}\left(\overline{f}_{ROI} - f_{\mathrm{ROI}}(k)\right)^2}} \tag{10}$$

$$\mathrm{NMAD} = \frac{\sum_{k=1}^{Q} |f(k) - f_{\mathrm{ROI}}(k)|}{\sum_{k=1}^{Q} |f_{\mathrm{ROI}}(k)|} \tag{11}$$

where f denotes the original model "pipeline data1" or "pipeline data 2," f_{ROI} denotes the reconstructed ROI of the model, $|f|$ represents the absolute value of f, and the average of the densities in ROI is $\overline{f}_{\mathrm{ROI}}$. Q is the total number of pixels in ROI. When the reconstructed results are approximately equal to the original, the values of NRMSD and NMAD will be close to 0. The NRMSD and NMAD values highlight the image quality in different aspects, respectively. The more different places in reconstructed result are, the larger the value of NRMSD is. On condition that the reconstructed result is uniformly dense with the correct average density, the value of NRMSD will be close to 1.0. Contrary to NRMSD, NMAD emphasizes the consequence of several small errors. Meanwhile, the value of NMAD is close to 1.0 in case that the reconstructed result is uniformly dense with zero density.

5.3 The Simulated Experimental Results

For the sake of verifying the superiority of our cone-beam computed tomography local image reconstruction algorithm, we made the comparison with general spiral FDK [27]. Figure 9 shows the images reconstructed by different filters from local projection data. In Fig. 9, image (a) is the 50th slice of original "pipeline data1." Images (b1), (b2), and (b3) are reconstructed by general spiral FDK with R-L filter from local projection data (short for spiral-FDK-RL-filter). Image (c1), (c2), and (c3) are reconstructed by general spiral FDK with local filter from local projection data (short for spiral-FDK-local-filter), which are processed in contrast enhancement through Adobe Photoshop CS4. Figure 10 shows the zoom-in figures according to Fig. 9. From Figs. 9 and 10, it can show that when the projection data are incomplete, the general spiral FDK algorithm with R-L filter has a certain influence on reconstructed image because of the truncated data of pipeline wall which suffers streak artifacts, meanwhile, the presented algorithm can obtain the reconstructed image which is very close to the impurities of internal pipeline. Figure 11 demonstrates the gray difference among the images which is the original image and reconstructed images using spiral FDK with R-L filter and local filter, which shows that R-L filter has relatively good contrast and local filter has good intensity resolution. It can be observed that the image using local filter is much closer to the original image in ROI compared with R-L filter. In vision, local filter is more able to mitigate streak artifacts and noise, and it makes a good trade-off between contrast and intensity resolution.

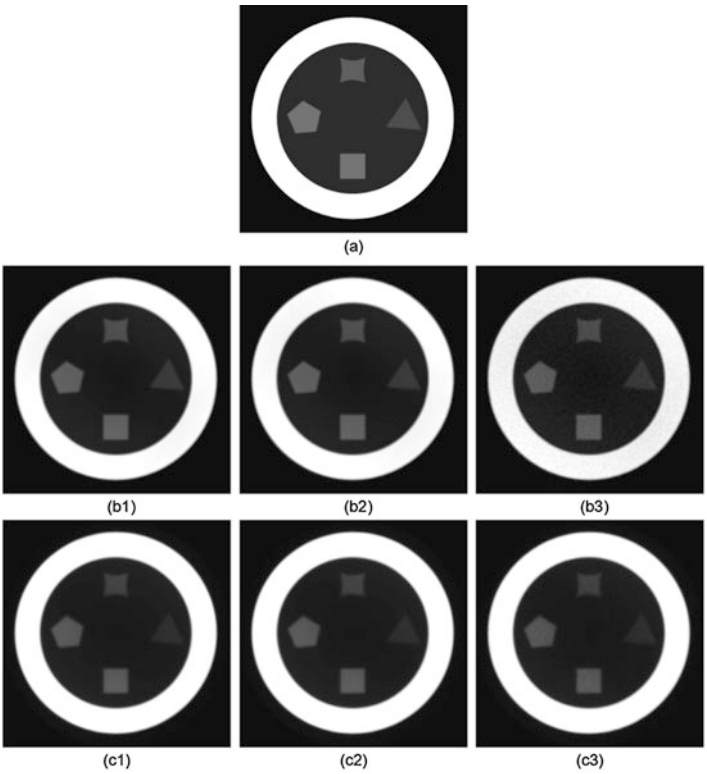

Fig. 9 It presents the 50th slice of "pipeline data1": (**a**) is the original image of the "pipeline data1"; (**b1**), (**b2**), and (**b3**) are the reconstructed results by general spiral cone-beam FDK method with R-L filter from 0%max, 0.1%max, and 0.5%max projection data; and (**c1**), (**c2**), and (**c3**) are the reconstructed results by general spiral cone-beam FDK method with local filter from 0%max, 0.1%max, and 0.5%max projection data. The grayscale window is [0.255]

To highlight the superiority of the presented algorithm, a complicated model "pipeline data2" is utilized. Figure 12 shows the reconstructed images by different filters from local projection data. Image (a) is the 50th slice of original "pipeline data2." Images (b1), (b2), and (b3) are reconstructed by general spiral FDK with R-L filter from local projection data. Images (c1), (c2), and (c3) are reconstructed by general spiral FDK with local filter from local projection data, which are processed in contrast enhancement through Adobe Photoshop CS4. Figure 13 represents the zoom-in figures corresponding to Fig. 12. Figure 14 demonstrates the gray difference among the images. It still validates the point that local filter can maintain good intensity resolution, while R-L filter can obtain high contrast. They can show that when the projection data are incomplete, the general spiral FDK algorithm also suffers streak artifact because of the truncated data of pipeline wall; however, the presented algorithm can obtain the closer image to the impurities of internal

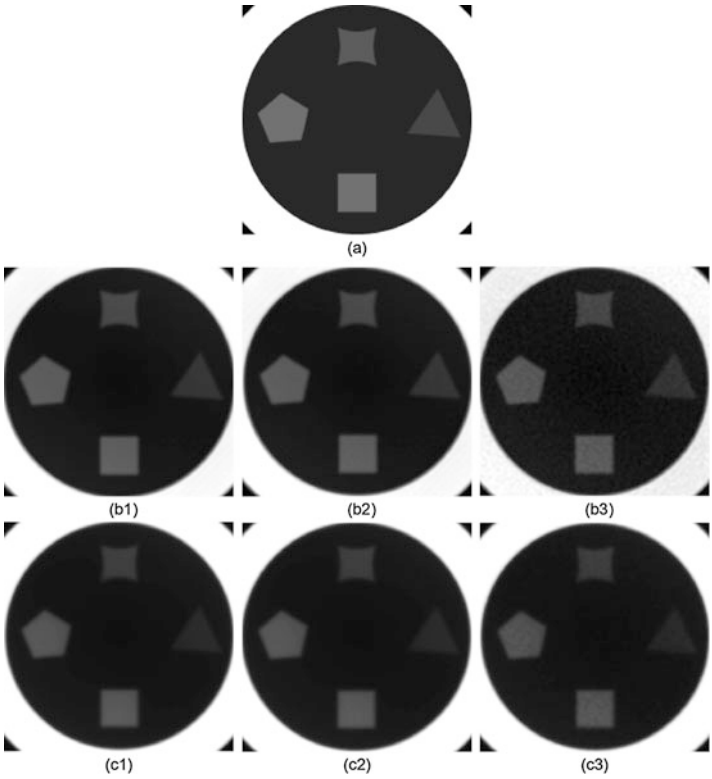

Fig. 10 It shows the zoom-in figures corresponding to Fig. 9

pipeline, compared with general spiral cone-beam FDK algorithm with R-L filter. Accordingly, it also obtains that local filter takes more advantages of suppressing streak artifacts and noise.

Furthermore, the visual inspections of the reconstructed results are necessary. Tables 2 and 3 list the RMSE, NRMSD, and NMAD assessments of the images (as shown in Figs. 9 and 12, respectively) reconstructed by general spiral FDK with R-L filter and local filter from incomplete projection data, respectively. The quantitative results using local filter exhibited better results than those from spiral-FDK-RL-filter according to the three assessments. Table 2 presents that under the incomplete projection data, for adding 0%max, 0.1%max, and 0.5%max projection data, reconstructed local ROIs using local filter outperform R-L filter with smaller RMSE, NRMSD, and NMAD assessments, respectively. Meanwhile, Table 3 also confirms the superiority of our algorithm with smaller assessments. The good valuation of the presented algorithm is attributed to the local filter with a high and narrow main lobe and the rapid attenuation of side lobe which help to improve

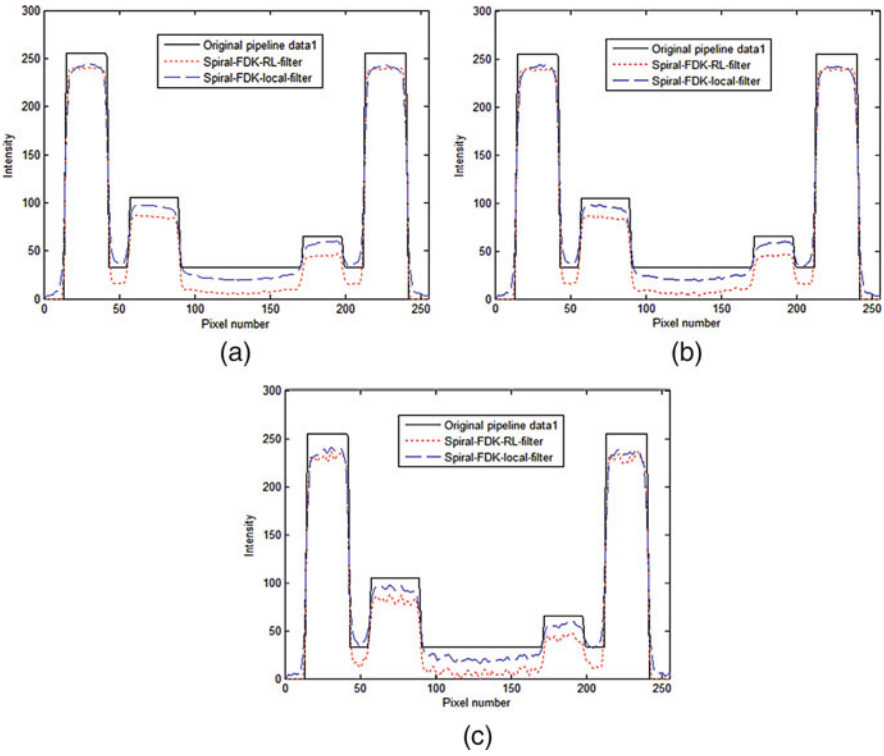

Fig. 11 (**a**–**c**) represent the gray histograms of the 128th row of Fig. 9 reconstructed from adding 0%max, 0.1%max, and 0.5%max projection data, respectively

the density of the image resolution. In addition, local filter can maintain the good properties in mitigating streak artifacts and noise. Despite increasing the noise, local filter still keeps good performance. Relatively, R-L filter does not work out this situation very well.

6 Conclusions

In order to solve the detection of impurities in pipeline in service, this paper proposed a novel scanning mode and presented a corresponding local spiral cone-beam FDK reconstruction algorithm with a local filter. On one hand, this scanning mode takes advantage of fluid flowing to obtain ESCB projection data of the liquid (including impurities), which is simple and feasible. On the other hand, the presented algorithm utilizes a novel filter as a filter function to preserve the

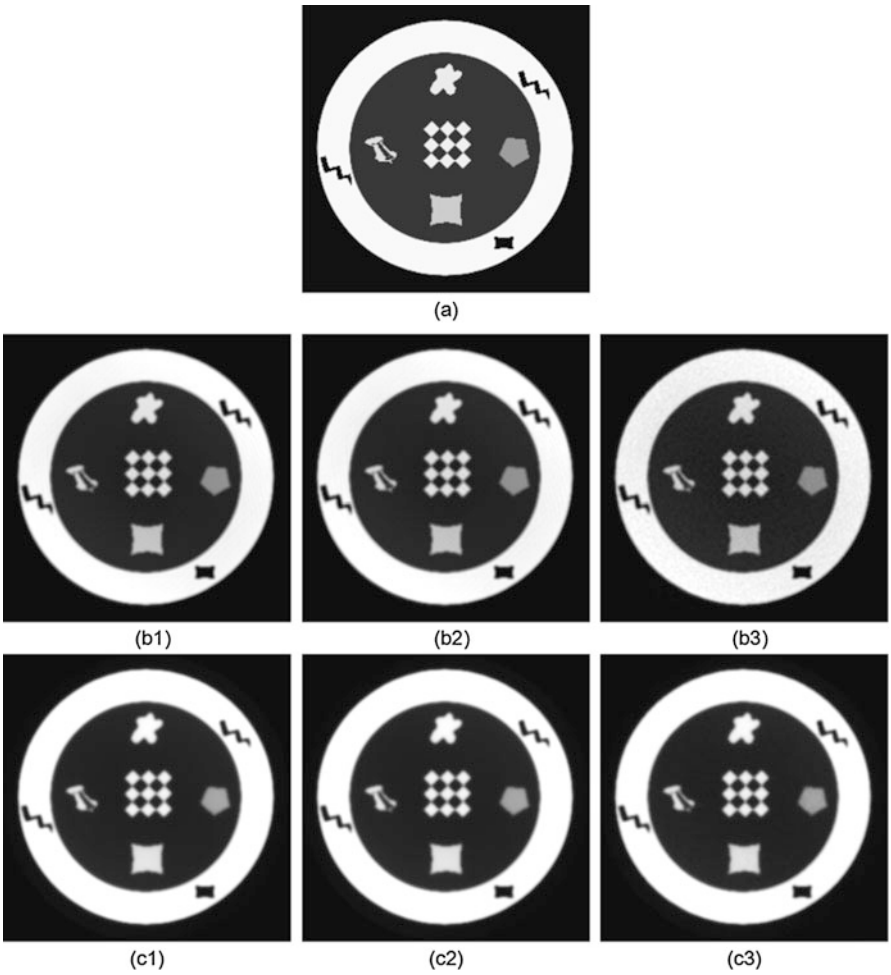

Fig. 12 It presents the 50th slice of "pipeline data2": (**a**) is the original image of the "pipeline data2"; (**b1**), (**b2**), and (**b3**) are the reconstructed results by general spiral cone-beam FDK method with R-L filter from 0%max, 0.1%max, and 0.5%max projection data; and (**c1**), (**c2**), and (**c3**) are the reconstructed results by general spiral cone-beam FDK method with local filter from 0%max, 0.1%max, and 0.5%max projection data. The grayscale window is [0.255]

resolution of the pipeline internal impurities, while the general spiral FDK with R-L filter cannot solve the incomplete projection data problem very well. It was inferred from the simulated experiments incomplete projection data that the presented algorithm showed more advantages than general spiral FDK algorithm with R-L

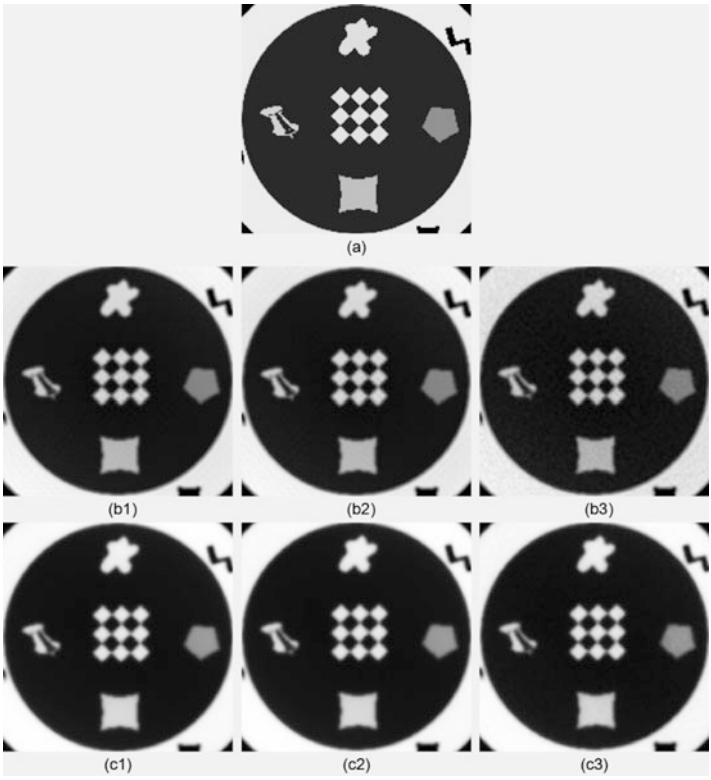

Fig. 13 It shows the zoom-in views corresponding to Fig. 12

filter according to image quality and the evaluation indexes. The streak artifacts can be better suppressed, and more accurate images can be reconstructed by the presented algorithm for the reconstruction of impurities in pipeline in service.

In the future work, we will consider the motion of the object to be reconstructed and improve the algorithm to deal with the dynamic CT for detecting the pipeline internal.

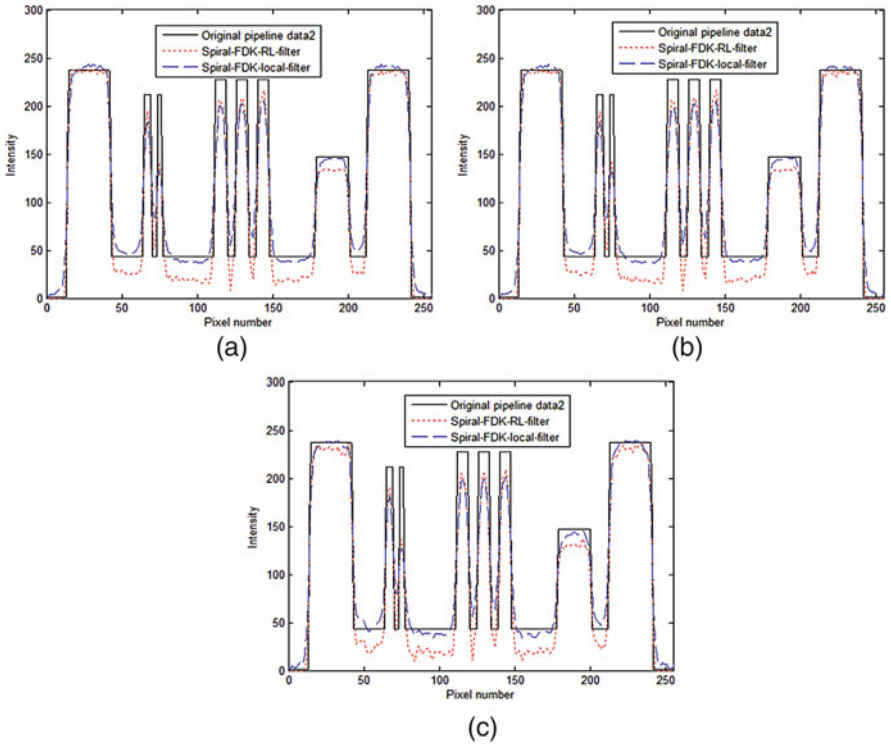

Fig. 14 (**a**–**c**) represent the gray histograms of the 128th row of Fig. 12 reconstructed from adding 0%max, 0.1%max, and 0.5%max projection data, respectively

Table 2 Evaluations of the results of 50th slice reconstructed about "pipeline data1" by different filters from local projection data with adding 0, 0.1%max, and 0.5%max

Method	Noise	ROI	RMSE	NRMSD	NMAD
Spiral-FDK-RL-filter	0%max	Global	18.1507	0.1797	0.1670
		Local	11.5026	0.7077	0.8340
	0.1%max	Global	18.3822	0.1827	0.1710
		Local	11.2209	0.7130	0.8404
	0.5%max	Global	21.2796	0.2196	0.2147
		Local	12.1180	0.7733	0.9107
Spiral-FDK-local-filter	0%max	Global	18.8058	0.1941	0.1347
		Local	6.3701	0.2902	0.1997
	0.1%max	Global	18.8937	0.1953	0.1363
		Local	6.3793	0.2911	0.2007
	0.5%max	Global	20.2487	0.2141	0.1576
		Local	6.5132	0.3039	0.2136

Table 3 Evaluations of the results of 50th slice reconstructed about "pipeline data2" by different filters from local projection data with adding 0, 0.1%max, and 0.5%max

Method	Noise	ROI	RMSE	NRMSD	NMAD
Spiral-FDK-RL-filter	0%max	Global	20.0332	0.2027	0.1478
		Local	14.3166	0.3940	0.4558
	0.1%max	Global	20.0475	0.2029	0.1480
		Local	14.3270	0.3943	0.4563
	0.5%max	Global	21.0065	0.2184	0.1643
		Local	14.9699	0.4230	0.4912
Spiral-FDK-local-filter	0%max	Global	22.1431	0.2321	0.1310
		Local	12.6541	0.3177	0.1840
	0.1%max	Global	22.1404	0.2325	0.1308
		Local	12.6606	0.3184	0.1845
	0.5%max	Global	22.2745	0.2383	0.1331
		Local	12.8027	0.3280	0.1931

Acknowledgment This work is supported by the National Natural Science Foundation of China (61271313) and National Instrumentation Program of China (2013YQ030629). Thanks to the reviewers for the valuable comments and suggestions.

References

1. Gunarathne GPP, Qureshi Y (2005) Development of a synthetic A-scan technique for ultrasonic testing of pipelines [J]. Instrum Meas IEEE Trans 54(1):192–199
2. Miller RK, Pollock AA, Watts DJ et al (1999) A reference standard for the development of acoustic emission pipeline leak detection techniques [J]. NDT E Int 32(1):1–8
3. Balaskó M, Sváb E, Kuba A, Kiss Z, Rodek L, Nagy A (2005) Pipe corrosion and deposit study using neutron-and gamma-radiation sources. Nucl Instrum Methods Phys Res, Sect A 542(1):302–308
4. Brunke O (2010) High-resolution CT-based defect analysis and dimensional measurement. Insight-Non-Destructive Test Cond Monit 52(2):91–93
5. Wang X, Tang Z, Zhu Z et al (2015) Cone-beam reconstruction of flat specimens in a super-short scan[J]. Insight-Non-Destructive Test Cond Monit 57(10):571–575
6. Ravindran VR, Sreelakshmi C, Vibinkumar S (2008) Digital radiography-based 3D-CT imaging for the NDE of solid rocket propellant systems. Insight-Non-Destructive Test Cond Monit 50(10):564–568
7. Lecomte G, Kaftandjian V, Cendre E, Babot D (2007) A robust segmentation approach based on analysis of features for defect detection in X-ray images of aluminium castings. Insight-Non-Destructive Test Cond Monit 49(10):572–577
8. Del Gaizo AJ, Silva AC, Hara AK (2014) The utility of dual-energy computed tomography in abdominal imaging. Appl Radiol 43(1):12–19
9. Wang G, Lin TH, Cheng PC, ShinozakiDM KH (1991) Scanning cone-beam reconstruction algorithms for X-ray microtomography [C]. Proc SPIE 1556:99–113
10. Wang G, Lin TH, Cheng P et al (1993) A general cone-beam reconstruction algorithm [J]. Med Imaging IEEE Trans 12(3):486–496

11. Wang G, Liu Y, Lin TH, Cheng PC (1994) Half-scan cone-beam X-ray micro-tomography formula. Scanning 16(4):216–220
12. Kudo H, Saito T (1992) Three-dimensional helical-scan computed tomography using cone-beam projections. Syst Comp Jpn 23:75–82
13. Zou X, Zeng L (2010) Half-cover scanning and reconstructing for helical cone-beam CT. Optics Precision Engineering 18(2):434–442
14. Yu W, Zeng L (2016) Iterative image reconstruction for limited-angle inverse helical cone-beam computed tomography. Scanning 38:4–13. https://doi.org/10.1002/sca.21235
15. Feldkamp LA, Davis LC, Kress JW (1984) Practical cone-beam algorithm [J]. JOSA A 1(6):612–619
16. Hu H (1996) An improved cone-beam reconstruction algorithm for the circular orbit. Scanning 18(8):572–581
17. Li L, Chen Z, Kang K, Zhang L, Xing Y (2010) Recent advance in exact ROI/VOI image reconstruction. Curr Med Imaging Rev 6(2):112–118
18. Faridani A (1992) Local tomography [J]. SIAM J Appl Math 52:549
19. Faridani A (1997) Local tomography II [J]. SIAM J Appl Math 57:1095
20. Katsevich AI (1996) Pseudolocal tomography [J]. SIAM J Appl Math 56:167
21. Byrnes JS, Hargreaves KA, Berry K (1992) Probabilistic and stochastic methods in analysis with applications [M]. Kluwer Academic Publishers, Boston, pp 187–205
22. DeStefano J, Olson T (1992) Wavelet localization of the radon transform in even dimensions [C]. Proceedings of the IEEE-SP international symposium on time-frequency and time-scale analysis. pp 137–140
23. Ye YB, Yu HY, Wang G (2007) Exact interior reconstruction with cone-beam CT [J]. Int J Biomed Imaging 3:1–5
24. XU M, QIU J, FAN H et al (2004) Local tomography with a new filter [J]. CT Theory Appl 13(1):54–58
25. You J, Liang Z, Zeng GL (1999) A unified reconstruction framework for both parallel-beam and variable focal-length fan-beam collimators by a Cormack-type inversion of exponential radon transform [J]. Med Imaging IEEE Trans 18(1):59–65
26. Smith BD (1985) Image reconstruction from cone-beam projections: necessary and sufficient conditions and reconstruction methods [J]. IEEE Trans Med Imaging MI-4(1):14–25
27. Kudo H, Saito T. (1991). Helical-scan computed tomography using cone-beam projections [C]. Nuclear science symposium and medical imaging conference, 1991. Conference record of the 1991 IEEE: 1958–1962
28. Herman G (2009) Fundamentals of computerized tomography: image reconstruction from projections. Springer

A Linearity Bootstrapped Switch with Dynamic Bulk Biasing Design for CMOS Image Sensors

Gong Chen, Weiwei Ling, Juan Zhou, Yao Yao, Li Li, Hua Wei, Yao Huang, and Jiang Du

1 Introduction

The analog-to-digital converter (ADC) is one of the essential building blocks in the CIS systems [1, 2]. High sampling accuracy of time-varying input signals is the first requirement in designing ADCs for various video applications. Therefore, improving linearity performance in ADCs, especially in front-end switch capacitor arrays, should be a prevailing concern in terms of sampling accuracy specification.

Switches produce harmonic distortion when they are sampling high-speed signals. And sampling switch nonlinearity is mainly attributed to nonlinear on equivalent on-resistance and associated parasitic capacitance. The conventional bootstrapped switches in [3] has a merit of approximate constant on-resistance because of the constant-overdrive-MOSFET approach. Although the bootstrapped switch can sample the input signal accurately, the nonlinearity of internal input-related transistors (except the booted transmission gate) and the charge rejection due to turning off some transistors slightly earlier in the overall circuit always cause a non-zero potential at the output when in holding mode. As shown in Fig. 1, the charge injection is corrected by introducing differential topology as it appears as a common-mode disturbance. Herein, a pair of cross-couple capacitors is used to eliminate unequal charges in the comparison cycles. However, the charges introduced by two switches in a differential topology do not exactly cancel each other because of two reasons. The primary error is the load capacitance mismatch in the next stage of digital-to-analog converter (DAC) arrays. The secondary factor is the two input differential signals which are not equal to each other. Hence, for the

G. Chen (✉) · W. Ling (✉) · J. Zhou · Y. Yao · L. Li · H. Wei · Y. Huang · J. Du
Chengdu University of Information Technology, Chengdu, China
e-mail: chg@cuit.edu.cn;lingweiwei@cuit.edu.cn;zhoujuan@cuit.edu.cn;174960917@qq.com;
ll550@cuit.edu.cn;weihua@cuit.edu.cn;huangyao@cuit.edu.cn;dujiang@cuit.edu.cn

M. Jiang et al. (eds.), *The Proceedings of the International Conference on Sensing and Imaging*, Lecture Notes in Electrical Engineering 506,
https://doi.org/10.1007/978-3-319-91659-0_7

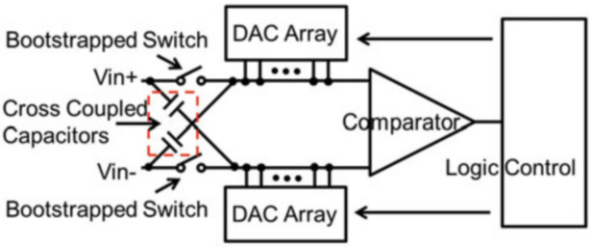

Fig. 1 SAR ADC scheme

purpose of obtaining much smaller non-zero holding biasing voltage, also achieving higher precision, an improvement for higher linearity of internal transistors is taken into consideration.

This paper presents an improved linearity bootstrapped switch architecture to be used in a successive approximation register (SAR) ADC. The full-scale input range is 1.2 V. A dynamic bulk biasing circuit for bulk compensation is implemented to improve the linearity of the input signal-related transistors. A previous work [4] has discussed a bulk-effect compensation approach within device reliability limits. A further consideration [5] has introduced a dynamically driven deep n-well (DNW) with combination of bulk-effect compensation. However, no concrete implementation of the scheme was discussed. Herein this paper goes into the particulars of circuit analysis. Actually, the bulk effect is only required in the sampling mode. Our dynamic substrate voltage compensation circuit can connect the bulk terminal to the source of the transistor while in sampling mode, like [4], without decreasing the linearity performance in the sample mode. But in holding mode, the bulk terminal is connected to the ground to reduce the charge rejection from the parasitic capacitance. Therefore, the bootstrapped switch has 2 dB second harmonic improvement in a case of single tone testing. Moreover, the errors caused by the next stage of holding potential imbalance and capacitors mismatch are decreased, to enhance the whole ADC's linearity performance.

In addition, this paper presents a reliable clock doubling circuit. Normally, simple charge pump is suggested by [6] to obtain conduction of transistors. Unfortunately, the transistors lose reliability when their gate-source voltage is approximately twice as much as the specified supply voltage. For the proposed reliable clock doubling circuit, none of the transistors have terminal voltages exceeding the specified supply voltage. Furthermore, three transistors and only one capacitor are required in comparison with the conventional charge pump which consists of at least four transistors and two capacitors.

The rest of this paper is organized as follows; Sect. 2 is an overview of the proposed bootstrapped switch architecture. The remaining sections provide simulation results and conclusions.

2 Analysis of Proposed Bootstrapped Switch

2.1 Preliminaries

Bootstrapped switch is used in CIS system. There has been a great demand in analog switches for operating with low supply voltage to analog ground difference (supply difference) since the latest generation CMOS technologies are scaled down. Another requirement is that analog switches conduct signals in the rail-to-rail range. To combine the rail-to-rail operation with the constant-overdrive-MOSFET approach leads to the conclusion that the gate potential unavoidably must exceed one of the supply rails. Hence, it is necessary to either boost the supply difference or use a signal-dependent clock booster. Figure 2 shows the conventional bootstrapped switch based on the basic principle of operation of a constant overdrive. A drawback of this switch is that NMOS transistors of M8 cannot conduct for source voltage beyond $V_{DD} - V_{\text{thM8}}$ for normal clock signals, where V_{DD} is the supply voltage and V_{th} is the threshold voltage. Thus the on-resistance is relatively nonlinear for high input voltages near $V_{DD} - V_{\text{thM8}}$. In [4], a solution to this bulk effect is proposed through the use of a separate well PMOS transistor as the main switch by controlling its bulk potential. In [7], a MOS-only implementation was presented; however, no attention has been paid to reliability problems. In [3], reliability problems have been addressed with simple circuit configurations.

In this paper, first, the bulk-effect compensation is implemented in the internal input signal-related NMOS switches of M7 and M8. Then a dynamic bulk biasing circuitry is proposed to release charge rejection of M7, M8. Finally, a revised clock doubling circuit is reported to limit the transistors' terminal voltages of the charge pump in Fig. 2 not exceeding the specified supply voltage. The circuit structure is described in the next section.

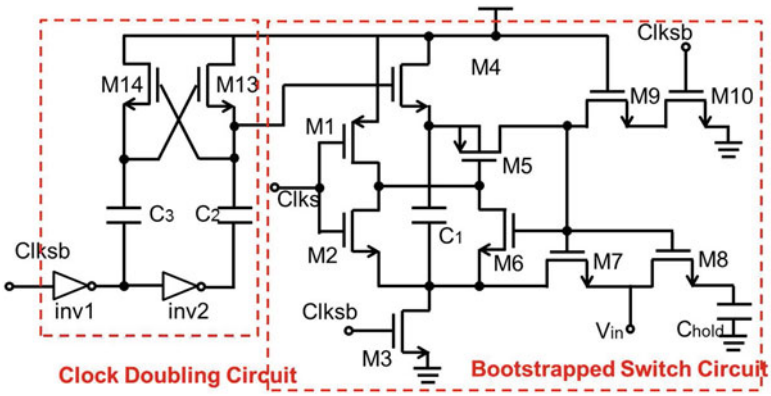

Fig. 2 The conventional bootstrapped switch in [3]

2.2 Proposed Circuit Description

Figure 3 shows the proposed circuit and clock signal. The falling edge of CLKs has a time delay compared to the rising edge of CLKsb. In the beginning of the holding mode (CLKs = 1.2 V, CLKsb = 1.2 V), the bottom plate of C1 is discharged through M3, and top plate of C1 is discharged through M5, M9, and M10 simultaneously.

The whole circuit operation is discussed in a worst case of input signal equal to V_{DD}. Transistors M3, M4, M5, M7, and M10 correspond to five ideal switches. M8 is the main sampling switch whose gate is grounded through M9 and M10 during holding mode, hence, turning it off. During the same phase, M13, M14, M15, and C2, forming a clock-boosting circuit, drive transistor M4 which unidirectionally charges capacitor C1. This solution provides clock doubling by ensuring the reliability constraint. None of the transistors in the proposed reliable clock doubling circuit have terminal voltages V_{gs}, V_{ds}, and V_{gd} exceeding the supply voltage of 1.2 V. Transistors M5 (connected to V_{DD} through M1) and M7 isolate the sampling switch M8 when the capacitor C1 is being charged to V_{DD}. The charged capacitor provides a constant voltage of V_{DD} between gate and source of M8 during sampling mode of the clock, thus also ensuring a low on-resistance independent of the input

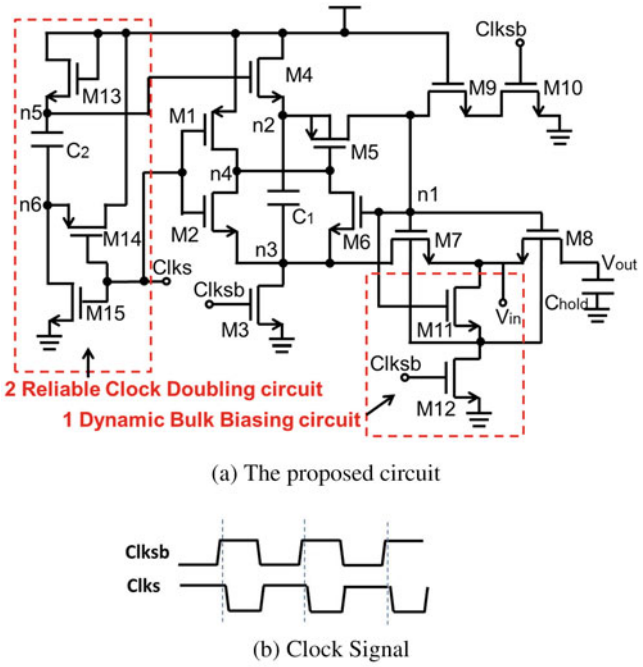

Fig. 3 The proposed circuit and clock signal

signal. During this mode, M2 pulls down the gate of M5, turning it on and allowing the charge to flow from capacitor C1 to the gate of M6, M7, and M8. This turns all three transistors on. M7 also enables node n3 to follow the input voltage shifted by V_{DD}, keeping the gate-source voltage constant regardless of the input signal. M9 reduces the V_{ds} and V_{gd} of M10 when CLKsb is off and node n1 is at $2V_{DD}$ for the worst case input of V_{DD}. Transistor M6 ensures that the gate-source voltage across MP5 does not exceed V_{DD} by allowing the input voltage to appear at node n3 during sampling mode of the clock.

The voltage at node n1 can be expressed in Eq. (1) while considering the parasitic capacitances attached to the top plate of C1. For the worst case, input voltage of M7, which is an NMOS transistor, is required to conduct. The gate of this transistor is for this reason connected to the gate of M8 for bootstrapped voltage to ensure high conductivity by maintaining V_{gs} of the transistor equal to V_{dd} during sampling mode. Yu et al. [1] report an option to use PMOS instead of M4. But it would not have been possible to turn the PMOS off during the sampling mode, and it would have been a leaky switch. In this scheme M4 is a reliable switch. During holding mode, it charges capacitor C1 to V_{dd}. During sampling mode, M4 has $V_{dd} - V_{\text{thM4}}$ at the gate and $V_{dd} + V_{\text{in}}$ at the drain. Even for the worst case, transistor M4 is off. Thus, the transistor reliability is ensured.

$$V_{n1} = V_{\text{in}} + \frac{C1}{C1 + Cp} V_{DD}, \tag{1}$$

In the proposed dynamic bulk biasing circuit, both the bulk terminals of M7 and M8 are connected to the source of M11. When in sampling mode, M12 is turned off; M11 is turned on. The potential of drain and source of M11 is the same. Thus the substrate of M8 and M7 is connected to the source of themselves. Even if V_{in} is higher than V_{DD}, the PN junction between source and bulk of M8 and M7 is not reversed. When in holding mode, M12 is turned on and M11 is turned off. This is helpful to discharge the parasitic capacitance of M7 and M8. In the reliable clock doubling circuit, during the sampling mode, capacitor C2 is pre-charged to $V_{dd} - V_{\text{thM13}}$. During the holding mode, M14 connects the bottom plate of C2. As a result the top plate of C2 rises to $2V_{dd} - V_{\text{thM13}}$. The gate potential of M4 toggles between $V_{dd} - V_{\text{thM13}}$ and $2V_{dd} - V_{\text{thM13}}$.

2.3 Charge Injection Description

Charge injection occurs due to unwanted charges injected into the circuit by turning off some transistors slightly earlier in the overall circuit. The output node V_{out} is the most sensitive from the charge injection point of view. The charge injection is concluded from two aspects. The first dominating reason is that when M8 turns off, the channel charge, source-to-bulk parasitic capacitor charge, and drain-to-bulk parasitic charge flow out to source and drain regions in a fast turning off time. The

second reason is that the gate-drain overlap capacitance introduces variation to the output voltage during the holding mode. However, the charge injection from the overlap capacitance only has marginal effects on the output voltage. Herein, only the first dominating reason is considered.

It is supposed that the channel charge, source-to-bulk parasitic capacitor charge, and drain-to-bulk parasitic charge of M8 flow equally in both directions toward source and drain. As in [8], the channel capacitance is calculated as

$$C_{\text{channel}} \cong 2/3 C_{\text{ox}} W_{\text{M8}} L_{\text{M8}}, \tag{2}$$

The parasitic capacitance can be approximated as

$$C_{\text{paraM8}} \cong C_{\text{diffusion}} W_{\text{M8}} \times \text{SA}, \tag{3}$$

Where W_{M8} and L_{M8} are the dimensions of the transistor M8. C_{ox} and $C_{\text{diffusion}}$ are the gate oxide and diffusion unit-area capacitance, respectively. SA is the diffusion length. The drain and source of M8 are assumed having the same SA. The charge flowing to the output junction V_{out} for the bootstrapped voltage of $V_{dd} - V_{\text{in}}$ at gate terminal is given by

$$\Delta Q = -\left(\frac{C_{\text{channel}}}{2} + C_{\text{paraM8}}\right)(V_{dd} - V_{\text{in}}) \tag{4}$$

The change in voltage according to $Q = CV$ at the output node because of the charge is given as

$$\Delta V = -\frac{(C_{\text{channel}}/2 + C_{\text{paraM8}})(V_{dd} - V_{\text{in}})}{C_{\text{hold}}} \tag{5}$$

Equation 5 proves that the dynamic bulk biasing circuit can decrease the charge injection effectively. Furthermore, in order to have a reduced charge injection at the output, either the size of the switch M8 should be small or the value of C_{hold} should be high. The bootstrapped switch also has an improved input voltage-dependent signal distortion by keeping $V_{gs} = V_{dd}$.

2.4 Design Strategy

The transistor size is listed in Table 1. The on-resistance of M8 is given by

$$R_{\text{on}}(t) = \frac{1}{\mu_n C_{\text{ox}} \frac{W_{\text{M8}}}{L_{\text{M8}}}(V_{\text{gsM8}}(t) - V_{\text{thM8}}(t))} \tag{6}$$

Table 1 Transistor sizes for the proposed bootstrapped switch circuit

Transistor	W[um]	L[um]	Transistor	W[um]	L[um]
M1	2	0.18	M9	2	0.3
M2	1	0.18	M10	2	0.18
M3	4	0.18	M11	1	0.18
M4	8	0.18	M12	1	0.18
M5	6	0.18	M13	2	0.18
M6	1	0.18	M14	4	0.18
M7	4	0.18	M15	2	0.18
M8	9	0.18			

The sampling switch M8 is most critical from charge injection and low R_{on} point of view. If the width of M8 is too large, then it will result in an increased charge injection at the output. On the other hand in order to have lower R_{on}, value of the width of the sampling transistor should be larger. From simulations an optimum value of 9/0.18 um was selected for these trade-offs.

The transistor M5 allows $V_{dd} + V_{\text{in}}$ to appear as gate voltage for the sampling transistor. So the propagation delay of M5 should be as small as possible. For the same reason, for charging C1 sufficiently fast, M4's width is four times that of M13. All transistors in the design have a length of 0.18 um (minimal length from design rule) except M9 whose length has been kept to 0.3 um. It is helpful to improve the punch-through voltage of M9. The rest of the transistors in the bootstrapped switch are designed to have less propagation delay and thus avoiding unnecessary leakage paths because of different turn-on times.

C1 is 120 fF and C2 is 80 fF to have low KT/C noise. The capacitance of C_{hold} is determined by the whole SAR ADC design consideration. Following [9], a unit capacitor is selected by the thermal noise, capacitor mismatch, and design rule. Herein, a unit capacitor is 17.76 fF. For 8-bit calculation, the total loading capacitance of C_{hold} is 4.2 pF.

3 Simulation Result

The simulation of the bootstrapped switch is implemented in the 65 nm triple well process. Figure 4a shows a comparison of output waveform among proposed circuit in Fig. 3 (solid line), bootstrapped switch in [1] with dynamic biasing voltage circuit (dotted line), and conventional switch in Fig. 2 with linear charge pump (mixed line). It is obvious that the proposed bootstrapped switch can obtain a best non-zero bias in the holding mode with maximum value +0.02 V/−0.07 V. Figure 4b shows the simulated gate and source voltage of M8. The discrepancy is 0.71 V.

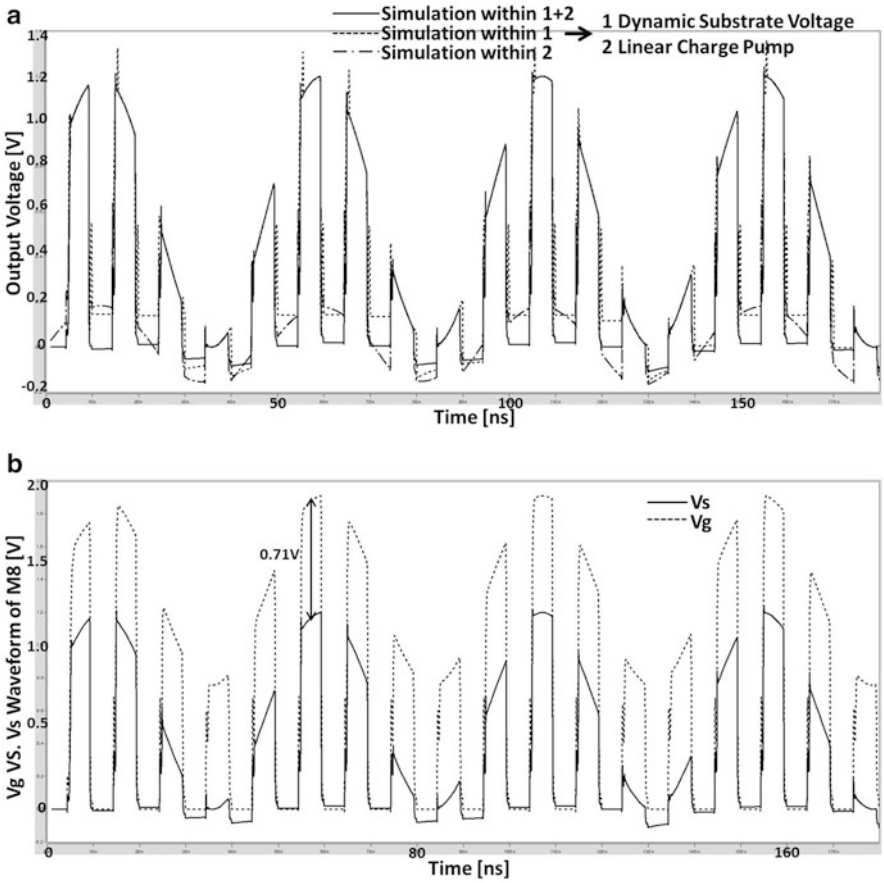

Fig. 4 Simulation of proposed bootstrapped switch terminal potential. (**a**) A comparison among proposed circuit in Fig. 3, bootstrapped switch in [1] with dynamic biasing voltage circuit and conventional switch in Fig. 2 with linear charge pump. (**b**) Simulated gate and source voltage of M8

Figure 5 varies the value of C_{hold} from 1.2 to 4.2 pF. The effect of these variations on charge injection during holding mode and on acquisition time during sampling mode verifies the discussion in Sect. 2.3.

Power spectral density simulations are demonstrated in Fig. 6. The simulation is for a single tone input sine wave of 21 MHz; the clock-controlled sampling frequency is 150 MHz. The 2nd-order harmonic is basically limiting the SNDR performance without suppression by the differential topology. The SNDR is 59.85 dBFS and SFDR is 76.02 dBFS. In comparison the power spectral density of the conventional one, for which SNDR is 57.73 dBFS and SFDR is 73.14 dBFS. This work has a 2.12 dBFS improvement in SNDR.

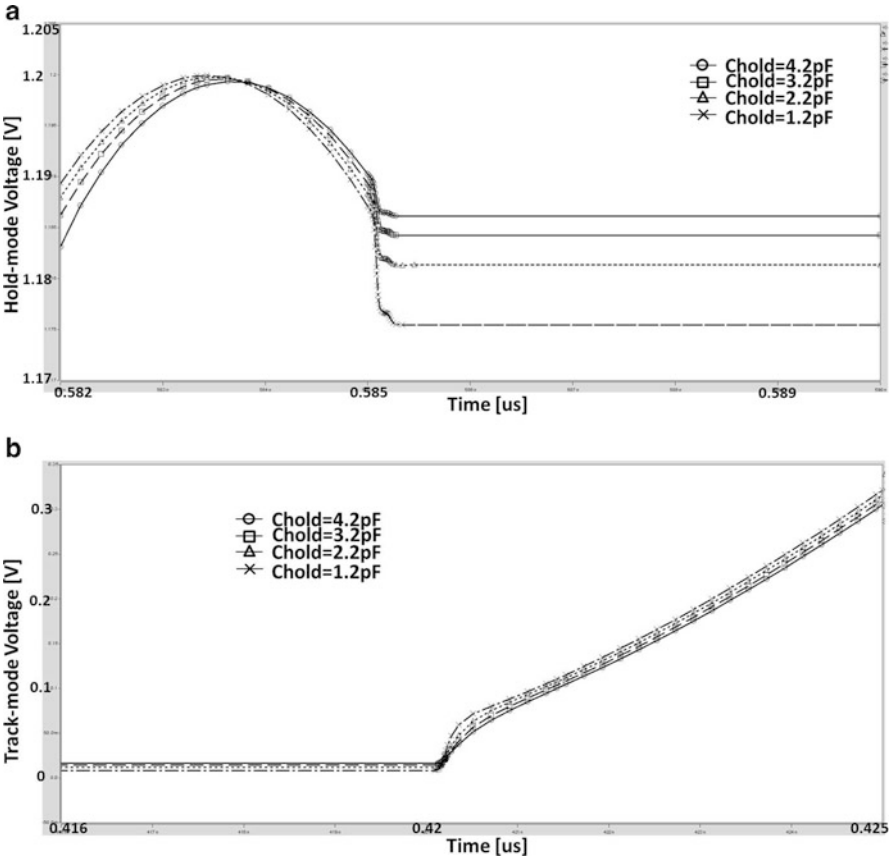

Fig. 5 Simulation of holding mode and sampling mode by sweeping different C_{hold} values. (**a**) Charge injection during holding mode by sweeping different C_{hold} values. (**b**) Acquisition time during sampling mode by sweeping different C_{hold} values

4 Conclusion

A bootstrapped switch has been simulated in 65 nm triple well process. Switch charge injection and linearity are improved due to the dynamic bulk biasing structure. A simpler clock doubling circuit is also proposed for further improvement of the linearity. Obtained results show the feasibility of the proposed bootstrapped switch.

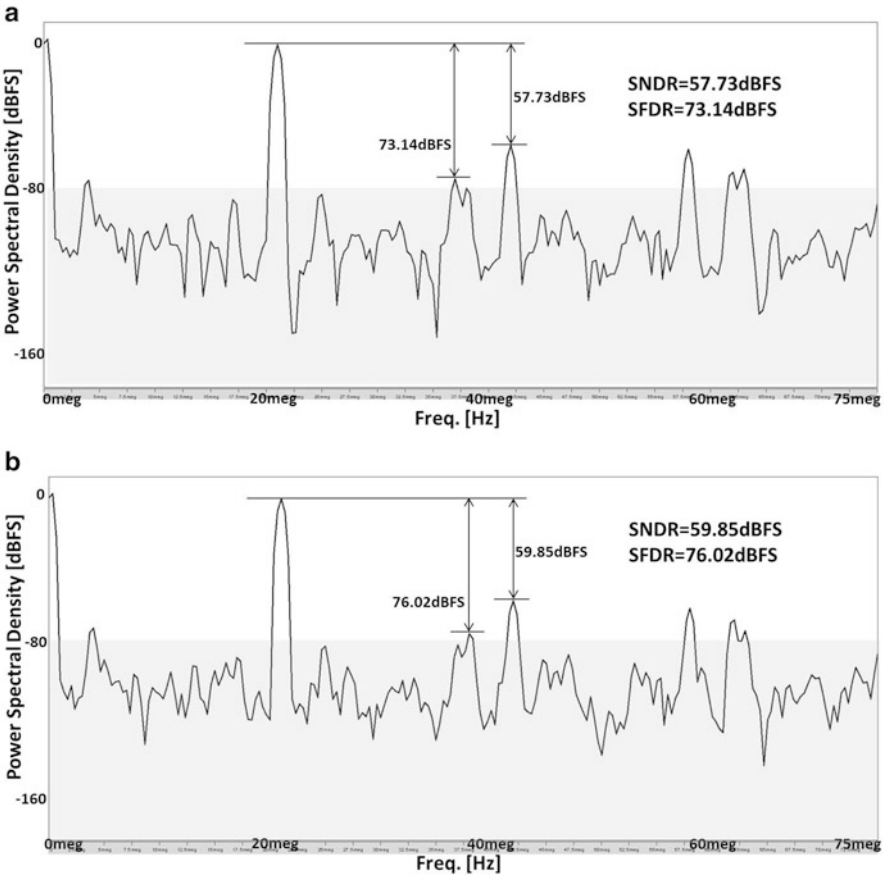

Fig. 6 Simulation of power spectrum. (**a**) Simulated power spectrum of the conventional bootstrapped switch at $f_{in} = 21$ MHz, $f_{sample} = 150$ MHz. (**b**) Simulated power spectrum of the proposed bootstrapped switch at $f_{in} = 21$ MHz, $f_{sample} = 150$ MHz

Acknowledgements This work is supported by the National Natural Science Foundation of China (No. 61601065, No. 61601064 and No. 61201094); the Supported Project of Science & Technology Department of Sichuan Province (Grant No.2016GZ0285 and No. 2015RZ0060); the key projects of Sichuan Provincial Department of Education (Grant No. 15ZA0188); the general project of Education Department of Sichuan Province under Grant No. 17ZB0081 ; the Middle-aged & Young Academic Staff Foundation of CUIT (No. J201506); the Department of Human Resources and Social Security of Sichuan, Scientific Innovation Team projects (No. 2016Z003); the Scientific Research Foundation for the Returned Overseas Chinese Scholars; and the Scientific Research Foundation of CUIT (Nos. KYTZ201701, KYTZ201415, KYTZ201501, KYTZ201502).

References

1. Yu H, Tang W, Guo M, Chen S (2017) A two-step prediction ADC architecture for integrated low power image sensors. In: IEEE transactions on circuits and systems I: regular papers, Jan 2017, vol 64, no 1, pp 50–60
2. Kobayashi M et al (2017) 4.5 A 1.8erms temporal noise over 110dB dynamic range 3.4m pixel pitch global shutter CMOS image sensor with dual-gain amplifiers, SS-ADC and multiple-accumulation shutter. In: 2017 IEEE international solid-state circuits conference (ISSCC), San Francisco, pp 74–75
3. Abo AM, Gray PR (1999) A 1.5-V, 10-bit, 14.3-MS/s CMOS pipeline analog-to-digital converter. IEEE J Solid-State Circuits 34(5):599–606
4. Waltari M, Halonen K (2002) Bootstrapped switch without bulk effect in standard CMOS technology. Electron Lett 38(12):555–557. https://doi.org/10.1049/el:20020376
5. Brunsilius J, Siragusa E, Kosic S, Murden F, Yetis E, Luu B, Bray J, Brown P, Barlow A (2011) A 16b 80MS/s 100mW 77.6dB SNR CMOS pipeline ADC. In: 2011 IEEE international on solid-state circuits conference digest of technical papers (ISSCC), 20–24 Feb 2011, pp 186–188
6. Basu S, Temes GC (1999) Simplified clock voltage doubler. Electron Lett 35(22):1901–1902. https://doi.org/10.1049/el:19991306
7. Sauer DJ (1996) Constant impedance sampling switch for an analog to digital converter, U.S. Patent 5 500 612, Mar 1996
8. Chen G, Zhang Y, Yang B, Dong Q, Nakatake S (2013) A comparator energy model considering shallow trench isolation by geometric programming. In: 2013 14th international symposium on quality electronic design (ISQED), 3–6 Mar 2013, pp 601–606
9. Zhang D, Bhide A, Alvandpour A (2012) A 53-nW 9.1-ENOB 1-kS/s SAR ADC in 0.13- m CMOS for medical implant devices. IEEE J Solid-State Circuits 47(7):1585–1593

A Low-Complexity Bound Estimation Technique for Maximum Likelihood Receivers

Li Alex Li, Hua Wei, Yao Yao, Weiwei Ling, Gong Chen, Jiang Du, and Yao Huang

1 Introduction

The union bound is usually considered as a useful analytical tool to estimate the performance of maximum likelihood (ML) receivers, because this bound only depends on the minimum Euclidean distance of received constellations and the number of nearest neighbors. The union bound closely approximates the exact probability of symbol error at high signal to noise ratio (SNR) values [2]. However the computational complexity of the union bound for the real-time application is still impractical even for multiple-input multiple-output (MIMO) systems, due to the exhaustive search in minimum Euclidean distance search (MEDS). MEDS can be applied in many works such as adaptive space-time modulation [4], dynamic pilot allocation for ML receivers in MIMO-OFDM systems [5], and optimal minimum distance-based precoding [1]. Some previous work on MEDS has been reported in [9], which employs the symmetric properties and avoids the all zero vector to reduce the complexity. However, such vectors do not have a very significant effect on computational complexity, and hence the reduction is relatively small.

L. A. Li (✉) · H. Wei · Y. Yao · W. Ling · G. Chen · J. Du · Y. Huang
Communication Engineering, Chengdu University of Information Technology, Chengdu, China
e-mail: lili1984@163.com;weihua@cuit.edu.cn;174960917@qq.com;lingweiwei@cuit.edu.cn;chg@cuit.edu.cn;dujiang@cuit.edu.cn;huangyao@cuit.edu.cn

M. Jiang et al. (eds.), *The Proceedings of the International Conference on Sensing and Imaging*, Lecture Notes in Electrical Engineering 506,
https://doi.org/10.1007/978-3-319-91659-0_8

2 System Model and Motivation

2.1 System Model

We consider the following real-valued linear model:

$$\mathbf{r} = \mathbf{H}\mathbf{t} + \mathbf{v}, \tag{1}$$

where $\mathbf{r}$, $\mathbf{v} \in \mathbb{R}^{N_r}$, $\mathbf{t} \in \mathbb{Z}^{N_t}$, $\mathbf{H} \in \mathbb{R}^{N_r \times N_t}$ has full column rank, and $\mathbb{R}$ and $\mathbb{Z}$ denote the sets of real numbers and real integers with a limited range, respectively. In wireless communications, $\mathbf{t}$, $\mathbf{r}$, and $\mathbf{v}$ are the transmitted and received vectors, and the additive white Gaussian noise (AWGN) vector, which follows the Gaussian distribution $\mathcal{N}(\mathbf{0}_{N_r \times 1}, \sigma^2 \mathbf{I}_{N_r \times 1})$. The quantity $\mathbf{H}$ is a random matrix that models the frequency-flat channel, the coefficients of which are i.i.d. (independent and identically distributed) with real Gaussian distribution. The channel state information is perfectly known to the receiver for real-time bound estimation. Here, M denotes the constellation size for each transmit antenna. $\mathscr{S}$ is the set of all possible transmit symbol vectors with the size $|\mathscr{S}| = M^{N_t}$.

2.2 Conventional Sphere Decoding Algorithms

The tree search algorithms can be categorized as depth-first search (DFS), breadth-first search (BFS), and K-best-first search (KBFS). All conventional methods or variants are based on QR decomposition and tree search algorithms.

Depth-First Search

The DFS algorithm is performed by searching down one branch with the cost within the initial radius until the first full path is obtained in this manner. The distance obtained from the first full path is used as the reference radius to replace the initial radius, and then a new search can proceed to find the minimum distance within the new radius of a sphere. If the full path cannot be achieved, the DFS will start a new search from one discarded branch in the upper level until the full path is made and repeat the search as above. Further, the complexity of DFS is the same as BFS without reference radius update.

Breadth-First Search

All branches at level i are examined by BFS first, and the survival branches within the initial radius are extended to the next level. This procedure is carried out until

BFS reaches the lowest level. The minimum distance is found based on the costs of survival branches. Then the algorithm is terminated and returns the minimum distance. Because it searches all possible branches at each level, the complexity is apparently higher than any other optimized search methods.

K-Best-First Search

The KBFS is the optimization of BFS. The only difference between KBFS and BFS is the way of keeping survival branches for level i. The KBFS sorts the survival branches according to their costs and stores the first K-best branches for the level $i + 1$. Others are eliminated simultaneously. In this case, the complexity of KBFS is largely reduced and not affected so much by the initial radius and relatively stable compared to other approaches. However, the accuracy of search cannot be guaranteed, because some discarded branches area highly likely to contain the full path corresponding to the minimum distance.

2.3 Motivation

The ML solution can be obtained by using DFS with lower complexity. From the system model above, the ML metric can be expressed as

$$\widehat{\mathbf{t}} = \text{argmin}_{\mathbf{t}\in\mathscr{S}} \|\mathbf{r} - \mathbf{H}\mathbf{t}\|^2. \tag{2}$$

The real-time symbol error rate (SER) of ML receivers can be approximated through the union bound, which can be obtained by using the square of the minimum Euclidean distance (d^2_{min}) in a Q-function. The union bound can be approximated in a looser form as [2] and [4]:

$$d^2_{\text{min}} = \text{argmin}_{\mathbf{t}_m,\mathbf{t}_n\in\mathscr{S},\mathbf{t}_m\neq\mathbf{t}_n} \frac{\|\mathbf{H}(\mathbf{t}_m - \mathbf{t}_n)\|^2}{N_t}, \tag{3}$$

$$P_e \leq N_r(M-1)\mathscr{Q}\left(\sqrt{\frac{d^2_{\text{min}}}{4\sigma^2}}\right), \tag{4}$$

where $\mathscr{Q}$ denotes the Q-function and σ^2 is the noise variance. The equation in (4) has been verified by comparing the exact error probability with the union bound in [3] and found to be a reasonable estimate of the real-time performance of the ML receiver. The exhaustive search computation in (3) is prohibitive, since in the worst case it must search $|\mathscr{S}|(|\mathscr{S}| - 1)/2$ symbol vectors.

3 The Proposed Bound Estimation Technique

In this section, we reformulate the search problem by using a QR decomposition and properties of special matrices and derive a novel sphere decoding approach for MEDS. Then we present the complexity of SDAs for this specific case in terms of the arithmetic operations. We show that it is possible to greatly simplify the procedures of MEDS with an acceptable accuracy loss. Additionally, we propose an IR based on channel statistics and a modified version of SE enumeration for SDAs.

3.1 Generalization of Sphere Decoding

The main idea behind the SDA for our case is to find the lattice point corresponding to the minimum Euclidean distance within a sphere. The tree search diagram of four levels with four child nodes for each parent node is depicted in Fig. 1. The solid line with forward arrow represents the survival branches, and the dashed line denotes the discarded branches. The red solid line which extends to the lowest level is one of full paths. One branch node corresponds to one of possible candidates as shown in Fig. 1. Once the distance for a given lattice point exceeds the radius constraint, this branch is discarded. The $\mathbf{H}$ in (3) can be decomposed into $\mathbf{Q}$ and $\mathbf{R}$ using a QR decomposition, given by

$$\mathbf{H} = \mathbf{QR} \quad \text{subject to} \quad \mathbf{QQ}^{\dagger} = \mathbf{I}_{N_t \times N_t}, \tag{5}$$

where $\mathbf{Q} \in \mathbb{R}^{N_t \times N_t}$ is an orthogonal matrix and $\mathbf{R} \in \mathbb{R}^{N_t \times N_t}$ is an upper triangular matrix. Some zeros must be added to ensure that $\mathbf{H}$ is a square matrix in the case of $N_t > N_r$. It is noted that only the first N_t columns of $\mathbf{Q}$ and the first N_t rows of $\mathbf{R}$ are used, provided $N_t < N_r$. We assume $\mathbf{e} = \mathbf{t}_m - \mathbf{t}_n, m \neq n$, so

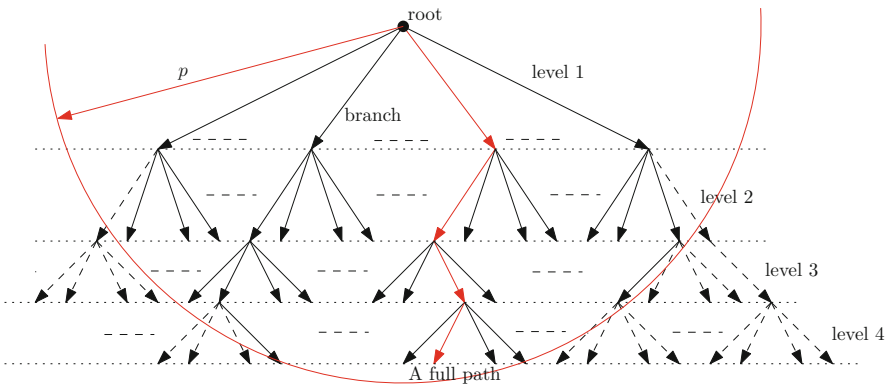

Fig. 1 Tree search diagram for sphere decoding algorithm for 4 quadrature amplitude modulation (QAM) or quadrature phase shift keying (QPSK)

$$\|\mathbf{He}\|^2 = \|\mathbf{QRe}\|^2 = \|\mathbf{Q}\|^2\|\mathbf{Re}\|^2 = \|\mathbf{Re}\|^2. \tag{6}$$

The minimum distance search problem in (3) can be converted into an equivalent form according to (6), that is,

$$d_{\min}^2 = \frac{1}{N_t}\text{argmin}_{\mathbf{e}\in\mathscr{A}}\|\mathbf{Re}\|^2. \tag{7}$$

The SDA principles are exploited to search for the minimum distance, so that (7) becomes

$$d_{\min}^2 = \frac{1}{N_t}\text{argmin}_{\mathbf{e}\in\mathscr{A}}\sum_{i=1}^{N_t}\underbrace{\left|\sum_{j=1}^{i-1} r_{i,j}e_j + r_{i,i}e_i\right|^2}_{\text{a cost at level i}} \le p, \tag{8}$$

where $\mathscr{A}$ is the set of all possible combinations of $\mathbf{e}$ and p is the radius of a sphere. The quantity $r_{i,j}$ denotes the $(N_t - i + 1, N_t - j + 1)$-th element of $\mathbf{R}$, and e_i is the $(N_t - i + 1)$-th entry of $\mathbf{e}$. Here we do not specifically discuss the complexity of SDAs, but it would be comparable to that of conventional SDAs. The number of arithmetic operations is [11]

$$\sum_{k=1}^{N_t}\frac{(2^{M-1}+1)k\pi^{k/2}}{\Gamma(k/2+1)}p^{k/2} + N_t^2, \tag{9}$$

where k is the index of transmit antennas and $\Gamma(\cdot)$ denotes the gamma function. It is obvious that the complexity of SDAs is much lower than the exhaustive search method and only grows exponentially in k not in $(2^{M-1}+1)^k$.

3.2 Channel Statistics-Based Initial Radius

The Wishart matrix $\mathbf{W}$ is a random and nonnegative definite matrix with real, nonnegative eigenvalues given by

$$\mathbf{W} = \begin{cases} \mathbf{H}^\dagger\mathbf{H} & N_t > N_r \\ \mathbf{H}\mathbf{H}^\dagger & N_t \le N_r. \end{cases} \tag{10}$$

According to (6) and [7], the Rayleigh-Ritz theorem can be applied to the Wishart matrix as below:

$$\|\mathbf{e}\|^2\lambda_{\min}\{\mathbf{W}\} \leq \frac{\|\mathbf{Re}\|^2}{\|\mathbf{e}\|^2}\|\mathbf{e}\|^2 \leq \|\mathbf{e}\|^2\lambda_{\max}\{\mathbf{W}\}, \tag{11}$$

where $\lambda_i\{\}$ denotes the ordered ith eigenvalue of the Wishart matrix, and $\|\mathbf{e}\|^2\lambda_{\min}\{\mathbf{W}\} \approx 0$ for simplicity. Here we can make an important assumption that $p \approx \lambda_{\max}\{\mathbf{W}\}$. Hence, the distribution of p can be roughly approximated by the distribution of the maximum eigenvalue of the real Wishart matrix. The CDF of the maximum eigenvalue of the real Wishart matrix can be expressed as [10]

$$\int_0^p \frac{1}{l_m}\sum_{i=1}^{l_m}\varphi_i(\lambda_1)^2\lambda_1^{l_n-l_m}e^{-\lambda_1}d\lambda_1 = 0.99, \tag{12}$$

where $\lambda_1 = \lambda_{\max}\{\mathbf{W}\}$, $l_m = \min(N_t, N_r)$, and $l_n = \max(N_t, N_r)$.

$$\varphi_{k+1}(\lambda_1) = \left(\frac{k!}{(k+l_n-l_m)}\right)^{1/2} L_k^{l_n-l_m}(\lambda_1), k = 0, \ldots, l_m - 1, \tag{13}$$

where $L_k^{l_n-l_m}(\lambda_1) = \frac{1}{k!}e^{\lambda_1}\lambda_1^{l_m-l_n}\frac{d^k}{d\lambda_1^k}\left(e^{-\lambda_1}\lambda_1^{l_n-l_m+k}\right)$ is the associated Laguerre polynomial. The IR p can be obtained by (12). For a small number of antennas, the IR p can be calculated according to

$$\int_0^{p\alpha} \frac{1}{\Gamma(N_t)}x^{t-1}e^t dt = 0.99, \tag{14}$$

where α denotes the average power of the candidate constellation. Because we assume $\mathbf{e} = [0, \ldots, e_i, \ldots, 0]^T$ is highly likely to be the vector corresponding to the minimum distance value, the distribution of p can be reduced to chi-square distribution χ^2.

3.3 Modified Schnorr-Euchner Enumeration

SDAs employing SE enumeration can further reduce the complexity, as the candidate nodes are sorted and examined according to the path metric weight[8]. The modified SE enumeration incorporated with [9] is presented in this part. The path metric weight for the ordered kth candidate in level i is

$$\begin{aligned} P_i^k &= B_i^k + P_{i-1} \\ &= \left| r_{i,i}e_i^k + \sum_{j=1}^{i-1} r_{i,j}e_j \right|^2 + P_{i-1}, \end{aligned} \tag{15}$$

where P_{i-1} denotes the path metric weight for $i-1$ levels, and $k \in [1, N_c^i]$. N_c^i is the number of candidates for level i, which is selected by the modified SE enumeration. According to (11), the corresponding range of e_i^k can be represented as (16), where $d_c^2 = \|\mathbf{e}\|^2$ is the minimum square Euclidean distance in the constellation, and $\mathbf{R}_i$ denotes the last i rows and i columns of $\mathbf{R}$. Hence e_i^k is in the range defined by (16) and is chosen as one of the candidate nodes in level i, and the sorted branch metric weights of candidate nodes can be denoted as $B_i^k > B_{i-1}^k$, which can greatly reduce the complexity of conventional SDAs. A pseudo-code of the proposed algorithm is shown in Algorithm 1, where

$$\begin{aligned} c_{\min} \leq & e_i^k \leq c_{\max} \\ \left\lfloor \frac{-(p-P_{i-1})^{1/2} - \sum_{j=1}^{i-1} r_{i,j} e_j}{r_{i,i}} \right\rfloor \leq & e_i^k \leq \left\lceil \frac{(p-P_{i-1})^{1/2} - \sum_{j=1}^{i-1} r_{i,j} e_j}{r_{i,i}} \right\rceil. \end{aligned} \tag{16}$$

Algorithm 1 Proposed algorithm for MEDS

Require: p, $\mathbf{R}$, $\mathscr{S}$
Ensure: $d_{\min}^2$
1: Set $i = 1$, $P_0 = 0$
2: Compute the bounds $(c_{\min}, c_{\max})$ of e_i^k by (16) and sort them according to the distance from $\lambda_i = -\sum_{j=1}^{i-1} r_{i,j} e_j / r_{i,i}$, $k \in [1, N_c^i]$. Set $k = 0$.
3: $k = k + 1$.
4: **if** $k > N_c^i$ **then**
5: go to 15.
6: **else**
7: **If** $e_j = 0$, $j = 1, \ldots, i-1$ **or** $i = 1$ **then** $k = k + 1$. go to 9.
8: **end if**
9: Calculate the path metric for kth candidate node at ith level, $P_i^k = B_i^k + P_{i-1}$.
10: **if** $i = N_t$ **then**
11: go to 21.
12: **else**
13: **If** $P_i^k < p$, $i = i + 1$, $P_{i-1} = P_{i-1}^k$, **then** go to 2.**end if**
14: **end if**
15: $i = i - 1$.
16: **if** $i = 0$ **then**
17: Output $d_{\min}^2 = p$ and terminate.
18: **else**
19: go to 3.
20: **end if**
21: **if** $P_i^k < p$ **then**
22: $p = P_i^k$, go to 15.
23: **end if**

4 Applications in Dynamic Pilot Allocation

As stated in the previous section, the proposed methods can be naturally exploited in the other algorithms, which use the union bound as a performance indicator. In this section, we apply the union bound to the dynamic pilot allocation [6] to validate the effectiveness of the proposed method. In other words, the dynamic pilot allocation does place the pilots in the same positions with the method as the conventional union bound estimation.

4.1 Application Examples

The dynamic pilot allocation algorithm is an optimized pilot placement strategy, which can improve the SER performance of the receiver at the expense of the channel estimation mean square error (MSE) performance degradation. Hence, it is very important to evaluate the real-time performance of the receiver. In this case, we use the ML detection in the receiver side and use the proposed method to estimate the performance with different pilot placements. In the next, one particular pilot placement with the minimum SER estimate will be found and used in the transmitter side to improve the detection performance of the ML receivers. In this part, we will compare the optimized pilot patterns using the conventional union bound estimates in [2] and the proposed method, respectively. According to our observations, the pilots will be allocated the deep faded subcarriers. The length of channel impulse response is 8, the number of subcarrier is 32, and the number of pilots is 8. The signal to noise ratio (SNR) is set to 20 dB to avoid the effects of the noise. The transmitter and receiver are equipped with two antennas. In Fig. 2, the pilot placement for the channel impulse response of the first transmit antenna is shown, and the pilot placement for the second transmit antenna is shown in Fig. 2. The result is similar to the first antenna example. The pilot placement with the proposed method as selection metric is almost identical to the conventional union bound. It implies that the proposed method can accurately obtain the real-time SER and can be used in some other algorithms which require the real-time SER performance (Fig. 3).

5 Simulation Results

For comparison purposes, the conventional DFS [9] and K-best-first search (KBFS) SDAs are introduced. The complexity of the proposed and other algorithms is compared via Monte Carlo simulations in terms of floating-point operations (FLOPS). Note that the zeros in matrices or vectors do not count in FLOPS. The union bound and real-time performance of the ML receiver are measured in terms

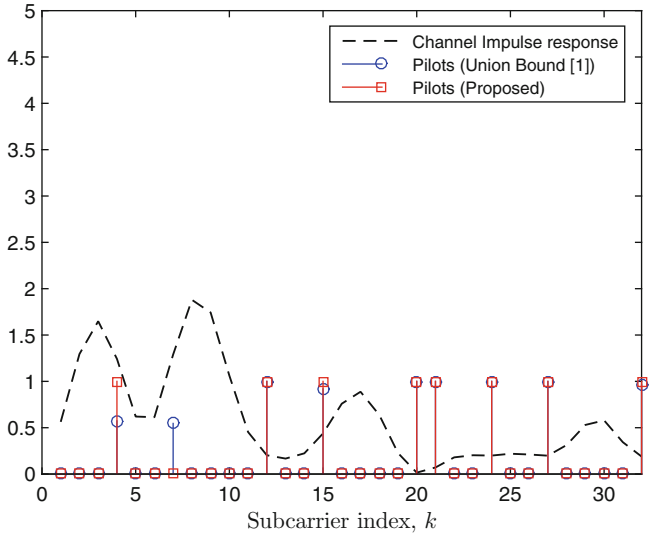

Fig. 2 Comparison of pilot placement between proposed method and union bound for the first transmit antenna with 4QAM

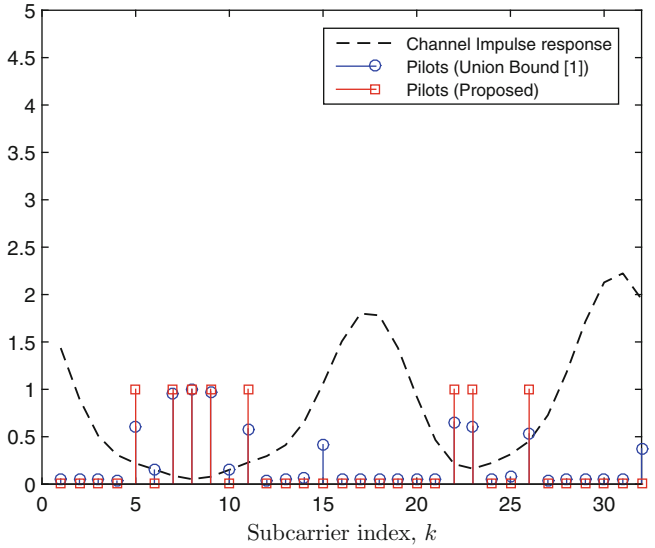

Fig. 3 Comparison of pilot placement between proposed method and union bound for the second transmit antenna with 4QAM

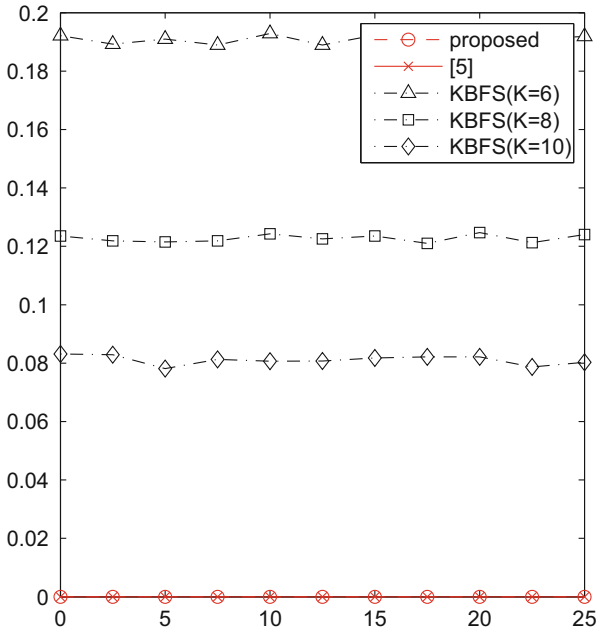

Fig. 4 Comparison of RMSE between the proposed and KBFS for $N_t = N_r = 8$ with $L = [-2, 0, 2]$ (4QAM case)

of symbol error rate (SER). The power of the transmit antennas is normalized to unity. The signal to noise ratio (SNR) is defined as $\mathrm{SNR(dB)} = 10\log_{10}\left(\frac{E_s N_r}{\sigma^2}\right)$. The IR obtained in (12) is applied to the proposed and conventional DFS, and $p = \infty$ in KBFS. The complexity of MEDS is greatly reduced by employing SDAs. From Figs. 4 and 5, further complexity reduction is achieved by the proposed algorithm with negligible RMSE performance loss. Additionally, the root-mean-square error (RMSE) is defined as $\mathrm{RMSE} = \sqrt{E[|\hat{d}^2_{\min} - d^2_{\min}|^2]}$. The curves for the union bound and the exact performance (simulation result) approximately agree as shown in Fig. 6, so the proposed bound estimation technique is shown to be tight and requires lower complexity and hence is suited to real-time applications.

6 Discussion

From the simulation results above, the proposed algorithm has achieved the same performance with a lower complexity compared to the conventional algorithm. From the conventional point of view, the SDAs based on SE enumeration have reached a very low complexity in the sense that there is no much room to be improved in terms of complexity. However, the proposed algorithm performs better for the

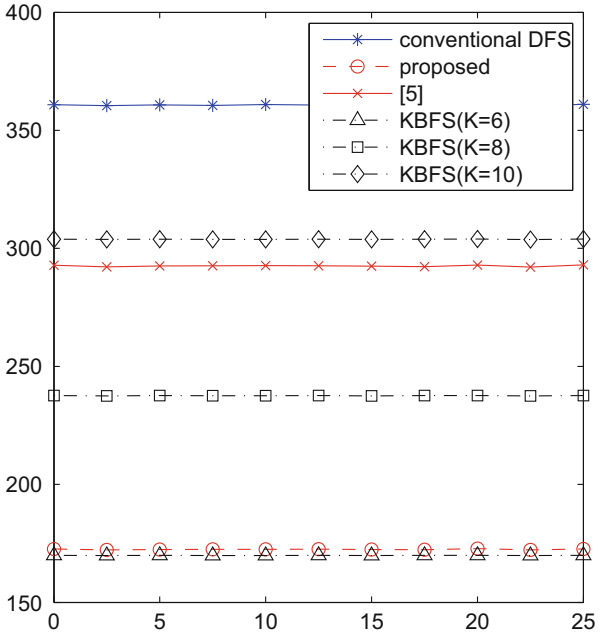

Fig. 5 Comparison of FLOPS between the proposed and KBFS for $N_t = N_r = 8$ with $L = [-2, 0, 2]$ (4QAM case). The FLOPS of exhaustive search is more than 10^6

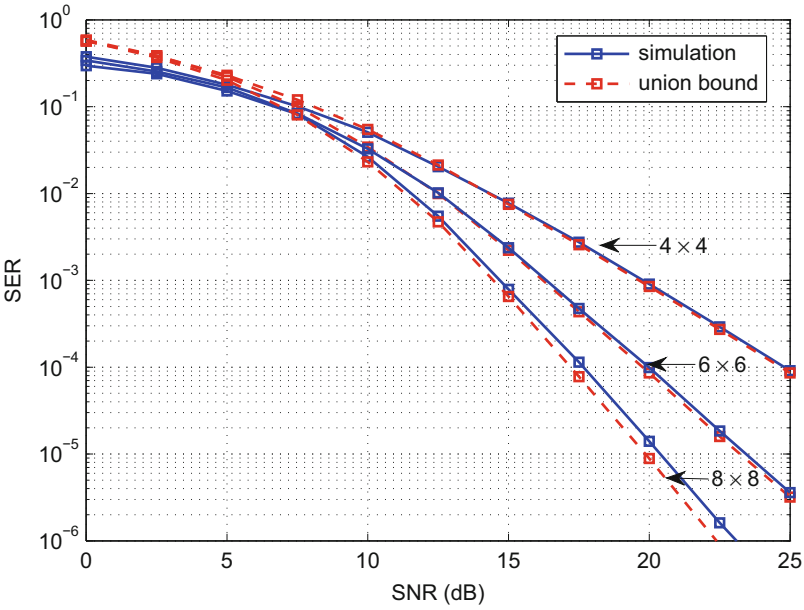

Fig. 6 Comparison of SER performance between union bound (proposed) and simulation results for $N_t = N_r = [4, 6, 8]$ with $L = [-2, 0, 2]$ (4QAM case)

performance estimates of MIMO systems using ML receivers. There are three reasons:

1. The proposed algorithm does not transverse the tree span in the first place, but proceeds down one particular branch that has high probability to be the desired solution. Because with the good channel conditions, the nulling canceling results are identical to the results of maximum likelihood criterion. In other cases, the first search result is very close to the final ML result.
2. The additional constrain of the radius has been set initially, and the first search radius is also available. Although the SDAs are unlikely to fail in most cases, they cannot reach the optimum solutions in some extreme cases. In other words, the SDAs cannot reach the correct solutions even with every node checked. This is because the maximum likelihood criterion fails, and the SDAs are not needed to search the correct solution with intensive efforts. After the first search, the proposed algorithm ensures that there is one of solutions available. Thus, the tight radius will not lead to the failure of the SDAs.
3. In each search layer, the accessed nodes are bounded by the lower and upper bound, which results in a more efficient search in each layer. Although some desired nodes may be eliminated accidentally, the SDAs are constrained by the initial radius and the first search radius to keep the unvisited nodes that belong to the possible solutions to ML.

7 Conclusion

This paper provides a novel low-complexity algorithm for real-time union bound applications. The union bound is still tight at low and high SNR values. Hence, this approach can be applied to a range of applications that require real-time estimates of SER.

Acknowledgements This work is supported by the Scientific Research Foundation of CUIT (KYTZ201501, KYTZ201502, KYTZ201701), Sichuan Provincial Department of Science and Technology Innovation and R&D projects in Science and Technology Support Program (2015RZ0060,2016GZ0285), Department of Human Resources and Social Security of Sichuan, Scientific Innovation Team projects (2016Z003) and Regular and key projects of Department of Education of Sichuan (15ZA0188,16ZB0210), Middle-aged & Young Academic Staff Foundation of CUIT (No. J201506), the Scientific Research Foundation for the Returned Overseas Chinese Scholars, State Education Ministry, and the National Natural Science Foundation of China (61201094,61601065).

References

1. Collin L, Berder O, Rostaing P, Burel G (2004) Optimal minimum distance-based precoder for MIMO spatial multiplexing systems. IEEE Trans Signal Processs 52:617–627
2. Goldsmith A (2005) Wireless communications. Cambridge University Press, Cambridge/New York
3. Heath RW Jr, Paulraj AJ (2001) Space-time signaling in multiantenna systems. Standford University, Standford
4. Heath RW Jr, Paulraj AJ (2005) Switching between diversity and multiplexing in MIMO systems. IEEE Trans Commun 169:963–968
5. Li L, de Lamare RC, Burr AG (2010) Dynamic pilot allocation with channel estimation in closed-loop MIMO-OFDM systems. IET Commun 8:2017–2025
6. Li L, de Lamare RC, Burr AG (2014) Dynamic pilot allocation with channel estimation in closed-loop MIMO-OFDM systems. IET Commun 8:2017–2025
7. Lütkepohl H (1996) Handbook of matrices. Wiley, New York
8. Schnorr CP, Euchner M (1994) Lattice basis reduction: improved practical algorithms and solving subset sum problems. Math Program 66:181–191
9. Shin M, Kang J, Yoo B, Lee C (2004) An efficient searching algorithm for receive minimum distance in MIMO systems with ML receiver. IEICE Trans Commun E92-B:330–333
10. Telatar E (1999) Capacity of multi-antenna Gaussian channels. Eur Trans Telecommun 10:585–595
11. Vikalo H, Hassibi BJ (2005) On the sphere-decoding algorithm I. Expected complexity. IEEE Trans Signal Processs 53:2806–2818

Analysis of RF Channel Isolation Impact in Wireless Co-Time Co-Frequency Full Duplex

Juan Zhou, Ying Shen, Gong Chen, Yajuan Xue, and Kun Mao

1 Introduction

Co-time co-frequency full duplex (CCFD) operation has emerged as an attractive solution for increasing the spectrum efficiency of wireless communication systems. With CCFD, a wireless terminal is allowed to transmit and receive simultaneously in the same frequency band [1–4]. For example, the terminal can do the signal detection work while transmitting signals at the same frequency at the same time. However, one of the biggest practical impediments to CCFD operation is the presence of self-interference, i.e., the interference that the modem's transmitter causes to its own receiver. To suppress the self-interference in a better way, the RF feedback chain is employed to provide the reference self-interference signal in the CCFD framework [5, 6]. The problem is that this architecture is analyzed with the perfect RF chain isolation, which is impossible in practical projects.

Experimental results have shown that the self-interference cancelation (SIC) performance is impacted by RF chain isolation, because of the RF signal leak due to imperfect RF chain isolation. In this paper, we analyze the impact of RF chain

J. Zhou (✉) · G. Chen · K. Mao
College of Communication Engineering, Chengdu University of Information Technology, Chengdu, China
e-mail: zhoujuan@cuit.edu.cn.

Y. Shen
National Key Laboratory of Science and Technology on Communications, University of Electronic Science and Technology of China, Chengdu, China
e-mail: shenying@uestc.edu.cn

Y. Xue
SINOPEC Key Laboratory of Geophysics, Nanjing, China
e-mail: xueyj0869@163.com

M. Jiang et al. (eds.), *The Proceedings of the International Conference on Sensing and Imaging*, Lecture Notes in Electrical Engineering 506,
https://doi.org/10.1007/978-3-319-91659-0_9

isolation on the SIC mathematically. We first give a brief description of the system model, and then the RF leakage signal is described, and then the self-interference signal is estimated with the RF leakage signal. Since the estimated self-interference signal is not correct due to the RF chain isolation, the SIC performance is degraded.

The system model is shown in Sect. 2. In Sect. 3, the impact on SIC of the RF chain isolation is explained. The simulation results and experimental results are presented in Sect. 4, and Sect. 5 concludes the paper.

2 System Model

The multiple-antenna CCFD architecture with RF feedback chain is shown in Fig. 1, which is shown to be better in SIC performance in wireless CCFD. On the transmitter side, the digital signal to be transmitted is mapped into the analog signal by digital-analog converter (DAC) and is further up-converted and amplified to the radio-frequency (RF) signal x_1 by Tx chain. On the receiver side, the wireless self-interference signal is received at the Rx antenna and down-converted to the analogy signal Rx chain, and then the analogy signal is mapped into the digital signal by analog-digital converter (ADC). In addition, the RF signal is not only used for transmitting at the Tx antenna but also coupled for digital self-interference cancelation. Correspondingly, a feedback path is added to process the coupled signal, where the coupled signal is down-converted by the feedback chain, and is further mapped into the digital signal by ADC.

In this paper, we focus on the architecture with two transmit antennas and two receive antennas; correspondingly, two feedback chains are employed for better SIC performance. Of course, similar analysis can be applied to more antennas.

3 Analysis of Imperfect RF Chain Isolation Impact

As shown in Fig. 1, the expected transmit signals and feedback signals are x_1 and x_2. However, due to the RF signal leakage, the signals to be transmitted are $x_1 + \gamma_1 x_2$ and $x_2 + \gamma_2 x_1$, and then the corresponding feedback signals are

$$z_1 = x_1 + \beta_1 x_2 \tag{1}$$

and

$$z_2 = x_2 + \beta_2 x_1 \tag{2}$$

Suppose the transmit pilot signals $x_{1,p}$ and $x_{2,p}$ are FDD (frequency division duplex), though TDD (time division duplex) could be similarly analyzed. With $h_{ij}(i = \{1, 2\} \quad \text{and} \quad j = \{1, 2\})$ denoting the channel condition from $Tx_i(i =$

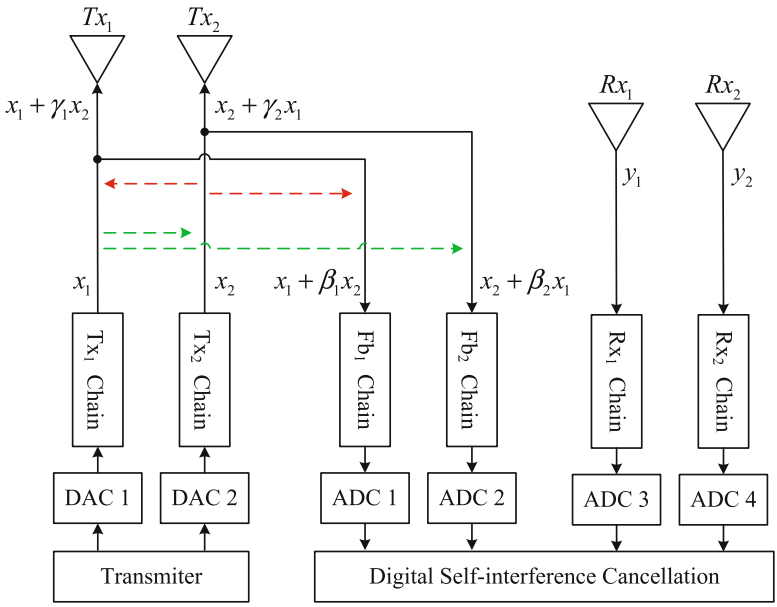

Fig. 1 CCFD architecture with feedback chains. Tx, Fb, and Rx represent transmit, feedback, and receive, respectively

$\{1, 2\}$) antenna to $Rx_j (j = \{1, 2\})$ antenna, the signals at the receive antennas can be represented as

$$y_1 = h_{11}(x_{1,p} + \gamma_1 x_{2,p}) + h_{21}(x_{2,p} + \gamma_2 x_{1,p}) \tag{3}$$

and

$$y_2 = h_{12}(x_{1,p} + \gamma_1 x_{2,p}) + h_{22}(x_{2,p} + \gamma_2 x_{1,p}) \tag{4}$$

For the SIC in the CCFD, the channel condition is necessary. The estimation of channel condition is usually executed as follows.

At time t_1, the pilot signals $x_{1,p}$ is transmitting at Tx_1, while Tx_2 is silent. The corresponding feedback signal is

$$z_{1,p} = x_{1,p} \tag{5}$$

The received signals at Rx_1 and Rx_2 are, respectively, described as

$$y_{1,p} = h_{11}x_{1,p} + h_{21}\gamma_2 x_{1,p} \tag{6}$$

and

$$y_{2,p} = h_{12}x_{1,p} + h_{22}\gamma_2 x_{1,p} \tag{7}$$

Then the estimated channel conditions $\hat{h}_{11}$ and $\hat{h}_{12}$ can be expressed as

$$\hat{h}_{11} = E(y_{1,p}/z_{1,p}) = h_{11} + h_{21}\gamma_2 \tag{8}$$

and

$$\hat{h}_{12} = E(y_{2,p}/z_{1,p}) = h_{12} + h_{22}\gamma_2 \tag{9}$$

At time t_2, the pilot signals $x_{2,p}$ is transmitting at Tx_2 while Tx_1 is silent. Here, the corresponding feedback signal is

$$z_{2,p} = x_{2,p} \tag{10}$$

The received signals at Rx_1 and Rx_2 are respectively described as

$$y_{1,p} = h_{11}\gamma_1 x_{2,p} + h_{21}x_{2,p} \tag{11}$$

and

$$y_{2,p} = h_{12}\gamma_1 x_{2,p} + h_{22}x_{2,p} \tag{12}$$

The estimated channel condition $\hat{h}_{21}$ and $\hat{h}_{22}$ can be similarly analyzed as

$$\hat{h}_{21} = E(y_{1,p}/z_{2,p}) = h_{21} + h_{11}\gamma_1 \tag{13}$$

and

$$\hat{h}_{22} = E(y_{2,p}/z_{2,p}) = h_{22} + h_{12}\gamma_1 \tag{14}$$

With $\hat{h}_{11}$ and $\hat{h}_{21}$, the estimated self-interference signal $\hat{s}_1$ at the RX_1 chain can be obtained by

$$\hat{s}_1 = \hat{h}_{11}z_1 + \hat{h}_{21}z_2 \tag{15}$$

Since the signals to be transmitted are $x_1 + \gamma_1 x_2$ and $x_2 + \gamma_2 x_1$ due to the RF imperfect isolation, the practical self-interference signal is

$$s_1 = h_{11}(x_1 + \gamma_1 x_2) + h_{21}(x_2 + \gamma_2 x_1) + \eta_1 \tag{16}$$

where η denotes the receiver white noise with the noise power σ^2. The residual self-interference after SIC at RX_1 chain can be calculated as

$$\hat{e}_1 = s_1 - \hat{s}_1 \tag{17}$$

Depending on (1), (2), (8), and (13), (17) can be further expressed as

$$\hat{e}_1 = h_{11}(\beta_1 x_2 + \gamma_1 \beta_2 x_1) + h_{21}(\beta_2 x_1 + \gamma_2 \beta_1 x_2) + \eta_1 \tag{18}$$

The expected residual power of self-interference signal at the RX_1 chain is $\|\hat{e}_1\|^2 = \sigma^2$, which is true only under the conditions $\beta_1 = 0$ and $\beta_2 = 0$. In addition, it is found that γ_1 and γ_2 will not impact the SIC performance under the perfect conditions.

The signal at the RX_2 chain is similarly analyzed as follows. With $\hat{h}_{22}$ and $\hat{h}_{12}$, the estimated self-interference signal $\hat{s}_2$ at the RX_2 chain can be obtained by

$$\hat{s}_2 = \hat{h}_{12} z_1 + \hat{h}_{22} z_2 \tag{19}$$

Since the practical self-interference signal is

$$s_2 = h_{12}(x_1 + \gamma_1 x_2) + h_{22}(x_2 + \gamma_2 x_1) + \eta_2, \tag{20}$$

the residual self-interference after SIC at RX_1 chain can be calculated as

$$\hat{e}_2 = s_2 - \hat{s}_2 \tag{21}$$

Depending on (1), (2), (9), and (14), (21) can be further expressed as

$$\hat{e}_2 = h_{12}(\beta_1 x_2 + \gamma_1 \beta_2 x_1) + h_{22}(\beta_2 x_1 + \gamma_2 \beta_1 x_2) + \eta_2 \tag{22}$$

The expected residual power of self-interference signal at the RX_2 chain is also $\|\hat{e}_2\|^2 = \sigma^2$, which is true only under the conditions $\beta_1 = 0$ and $\beta_2 = 0$. It is also found that γ_1 and γ_2 will not impact the SIC performance under perfect conditions.

From the analysis above, we can find the impact on SIC in CCFD is inevitable due to imperfect RF isolation, because the perfect conditions are too critical to realize. Besides it is shown that the SIC in RX_1 chain is similarly for that in RX_2 chain. Hence, for convenience of analysis, we only focus on the SIC performance in RX_1 chain in the following analysis.

Based on (18), the residual power of self-interference signal at the RX_1 chain can be defined by

$$\|\hat{e}_1\|^2 = \|h_{11}\gamma_1\beta_2 + h_{21}\beta_2\|^2 \|x_1\|^2 + \|h_{11}\beta_1 + h_{21}\gamma_2\beta_1\|^2 \|x_2\|^2 + \sigma^2 \tag{23}$$

For convenience of analysis, it is assumed that the power of the signal to be transmitted is unity, meaning that $\|x_1\|^2 = 1$ and $\|x_2\|^2 = 1$. Then (23) can be rewritten as

$$\|\hat{e}_1\|^2 = \|h_{11}\gamma_1 + h_{21}\|^2\beta_2^2 + \|h_{11} + h_{21}\gamma_2\|^2\beta_1^2 + \sigma^2 \tag{24}$$

Since h_{11} and h_{21} are the wireless channel conditions of self-interference signal with almost the same circumstance, it is reasonable to assume that the order of magnitude of h_{11} is the same as that of h_{21}, approximated as h_0. Similarly, since the γ_1, γ_2, β_1, and β_2 are leakage coefficients of the same node, we can assume that γ_1, γ_2, β_1, and β_2 have the same order of magnitude, approximated as γ_0 and β_0.

Therefore, the imperfect RF isolation impact on SIC performance in CCFD can be analyzed in three cases as follows.

1. If the magnitude of channel condition is much larger than the magnitude of leakage coefficient, the residual power of self-interference signal can be approximated as

$$\|\hat{e}_1\|^2 \approx \|h_{21}\|^2\beta_2^2 + \|h_{11}\|^2\beta_1^2 + \sigma^2 \tag{25}$$

which can be further simplified as

$$\|\hat{e}_1\|^2 \approx 2\|h_0\|^2\beta_0^2 + \sigma^2 \tag{26}$$

It is found that the residual power of self-interference signal is obtained by the receiver noise and the multiplex of the magnitude of wireless self-interference channel condition and that of the RF leakage coefficient. Here, we note that if $2\|h_0\|^2\beta_0^2$ is much smaller than the receiver noise, then the SIC performance is determined by the receiver noise, and the impact from the RF chain isolation can be neglected. In practice, the receiver noise is always much smaller; hence, for the convenience of analysis, we assume that σ^2 is small enough to be canceled in the following analysis.

With s_1 in (16), the power of the received self-interference signal is

$$\|s_1\|^2 = \|h_{11}(x_1 + \gamma_1 x_2)\|^2 + \|h_{21}(x_2 + \gamma_2 x_1)\|^2 + \sigma^2 \tag{27}$$

Since γ_1 and γ_2 are much smaller than 1 in practice, and $\|x_1\|^2$ and $\|x_2\|^2$ are assumed to be unite one, the self-interference signal power can be approximated as

$$\|s_1\|^2 \approx 2\|h_0|^2 \tag{28}$$

The SIC performance in CCFD can be calculated as

$$\begin{aligned}\Theta_{dB} &= 10\log 10(\|s_1\|^2/\|\hat{e}_1\|^2) \\ &= 10\log 10(1/(\beta_0^2+\sigma^2))\end{aligned} \tag{29}$$

2. If the magnitude of channel condition is much smaller than the magnitude of leakage coefficient, the residual power of self-interference signal can be approximated as

$$\|\hat{e}_1\|^2 \approx \|h_{11}\|^2\beta_1^2(1+\gamma_1)^2 \tag{30}$$

Since the leakage coefficient is usually much smaller than 1, (25) can be further simplified as

$$\|\hat{e}_1\|^2 \approx 2\|h_0\|^2\beta_0^2 \tag{31}$$

Then the SIC result is the same as that of case (1), which is $\Theta_{dB} = 10\log 10(1/\beta_0^2)$.

3. If the magnitude of channel condition has the same order as that of leakage coefficient, the residual power of self-interference signal can be approximated as

$$\|\hat{e}_1\|^2 \approx \|h_0\|^2\beta_0^2(1+\gamma_0)^2 \tag{32}$$

Similar SIC result can be obtained, which is $\Theta_{dB} = 10\log 10(1/\beta_0^2)$.

From the analysis above, we can find that the RF isolation impact on SIC performance is determined by the leakage coefficient β_1 and β_2, and the leakage coefficient γ_1 and γ_2 can be neglected. The residual power of self-interference signal can be obtained by (29).

4 Experimental Results and Simulation Results

We first give the experimental results. The transmitted signal power is 30 dBm with 20 MHz bandwidth, and the leakage signal in the feedback 2 chain is measured as −37 dBm. The signal power is measured in the practical project by a spectrum analyzer, which is shown in Fig. 2. From this figure, we can find that the RF leakage signal damages the SIC performance apparently.

To confirm the theoretical analysis, a simulation platform is developed as follows: 3GPP LTE protocol with 20 MHz bandwidth is applied in the CCFD system, and the RLS (recursive least square) algorithm is employed as the digital self-interference cancelation method. For clear insight of the RF isolation impact, the receiver noise is set as −95 dBm. The RF chain leakage coefficient β is set as {0.0001, 0.0004, 0.0016, 0.0064, 0.0256, 0.1024}. From Fig. 3, the theoretical SIC

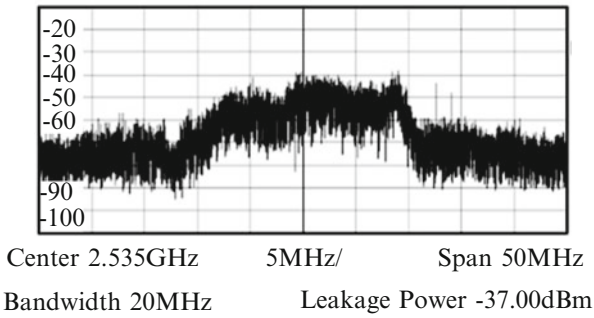

Fig. 2 The experimental SIC performance in CCFD with the imperfect RF chain isolation

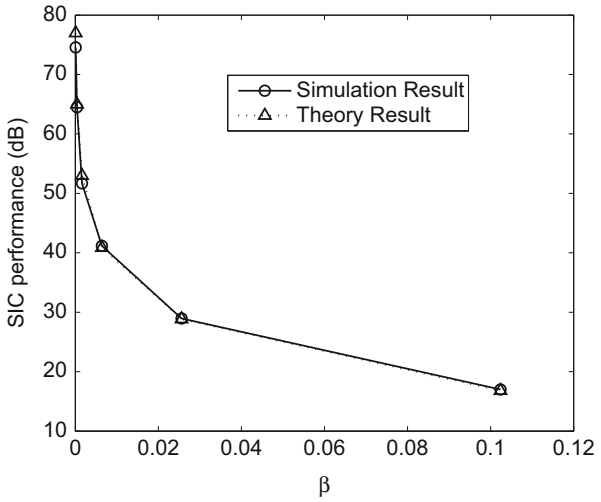

Fig. 3 Theoretical SIC performance and simulation SIC performance are compared in CCFD, where β denotes the RF chain leakage coefficient

performance is calculated by (29), which matches well with the simulation SIC performance.

5 Conclusion

In this paper, it is first described that the RF leakage signal, due to the imperfect RF chain isolation, damages the self-interference cancelation performance in CCFD wireless communication system. Through mathematical analysis, we find that RF chain isolation impact is determined by the RF leakage coefficient. The residual power of self-interference signal is inversely proportional to the magnitude of RF

leakage coefficient; the smaller the RF leakage coefficient, the larger SIC capability in CCFD. Since RF isolation is always imperfect, the method of the analysis can also be applied to other fields, such as signal detection and signal processing.

Acknowledgements This work was supported by the National Natural Science Foundation of China (No.61601064, No.61471108, No.61601065, No.41404102), Sichuan Youth Science and Technology Foundation (No. 2016JQ0012), and Key Project of Sichuan Provincial Education Department (No. 16ZA0218).

References

1. Duarte M, Sabharwal A (2010) Full-Duplex wireless communications using off-the-shelf radios: feasibility and first results. In: Proceedings of the Asilomar conference on signals, systems and computers (ASILOMAR), pp 1558–1562
2. Nguyen D, Tran L-N, Pirinen P, Latva-Aho M (2014) On the spectral efficiency of full-Duplex small cell wireless systems. IEEE Trans Wirel Commun 13:4896–4910
3. Jang Y, Min K, Park S, Choi S (2015) Spatial resource utilization to maximize uplink spectral efficiency in full-Duplex massive MIMO. In: Proceedings of the IEEE ICC, pp 1583–1588
4. Soury H, ElSawy H, Alouini M-S (2017) Downlink error rates of half-Duplex users in full-Duplex networks over a Laplacian inter-user interference limited and EGK fading. IEEE Trans Wirel Commun 16:2693–2707
5. Shen Y, Juan Z, Tang Y (2015) Digital self-interference cancellation in wireless co-time and co-frequency full-Duplex system. Wirel Pers Commun 82:2557–2565
6. Ahmed E, Eltawil AM (2015) All-digital self-interference cancellation technique for full-Duplex systems. IEEE Trans Wirel Commun 14:3519–3532

Application of a Dual Motor Synchronous Servo Control System to the Photoelectronic Detection System

Ai Xiong, Meng-Yun Lin, and Xin Li

1 Introduction

Single motor direct drive is widely used in the servo control system of the photoelectronic detection system [1, 2]. The telescope as one kind of the photoelectronic detection system uses the single motor to drive the elevation axis; with the increment of telescope diameter, the single motor hasn't met the system requirements because of its limitations [3]: when the single motor drives the mass balanced load, the output toque is unbalanced which will make the drive force different and is not suitable for the demand of the big power device. The single motor can make the temperature change rapidly, can make the rigid strut deformation, and will degrade the tracking performance of the photoelectronic detection system.

The servo control of the photoelectronic tracking system normally consists of position loop, velocity loop, and current loop [4]. However, because of the limitation of the actuators, the servo control may become nonlinear and degrade the photoelectronic tracking system performance which cannot meet the performance demand. The real-time and synchronization of the communication in multi-motor control system is put out. EtherCAT [5], which was proposed by Beckhoff Company in

This work was supported by the Introduction of Talent Research Funding of Chengdu University of Information Technology of China (No. 376133).

A. Xiong (✉)
Control Engineering College, Chengdu University of Information Technology, Chengdu, People's Republic of China
e-mail: xiongai@cuit.edu.cn

M.-Y. Lin · X. Li
Institute of Optics and Electronics, CAS, Chengdu, People's Republic of China

M. Jiang et al. (eds.), *The Proceedings of the International Conference on Sensing and Imaging*, Lecture Notes in Electrical Engineering 506,
https://doi.org/10.1007/978-3-319-91659-0_10

Germany, has been widely used and developed rapidly for its superior performance. By comparing and analyzing a variety of real-time industrial Ethernet, it is clear that EtherCAT can be effectively applied to multi-motor synchronous control system. KINGSTAR Motion software to achieve PC-based EtherCAT master function, with the configuration of AxN servo driver EtherCAT slave of Phase Motion Ltd., is given [6, 7]. The EtherCAT master and slave communication program design is described in details. A single motor closed-loop test was carried out to verify the feasibility of the system.

The rest of the paper is organized as follows. In Sect. 2, an overview of the PI control scheme, the current loop, and the EtherCAT bus technique is given. In Sect. 3, we present a structure of a dual motor synchronous servo control system which combines the cross-coupling law with the EtherCAT bus, and the comparison of dual motor synchronous servo control system to the single motor system is also given. Section 4 introduces the experimental platform of the proposed dual motor synchronous servo control system. Also, results of the presented algorithm implemented on the experimental platform are given. Finally, Sect. 5 concludes with further discussion on the results and the servo control system presented.

2 PI Control, Current Loop, and EtherCAT

2.1 PI Control

The popularity of PI (proportional plus integral) controllers can be attributed partly to their robust performance in a wide range of operating conditions and partly to their functional simplicity, which allow engineers to operate them in a simple, straightforward manner. To implement such a controller, two parameters must be determined for the given process: proportional gain (providing an overall control action proportional to the error signal through the all-pass gain factor) and integral gain (reducing steady-state errors through low-frequency compensation by an integrator).

A standard PI written in the "parallel form" is given in (1):

$$G_{\mathrm{PI}}(s) = \frac{U(s)}{E(s)} = K_{\mathrm{p}} + \frac{K_{\mathrm{i}}}{s} \tag{1}$$

where $U(s)$ is the control signal acting on the error signal $E(s)$, K_{p} is the proportional gain, and K_{i} is the integral gain. In the time domain, (1) can be rewritten as follows:

$$u(t) = K_{\mathrm{p}} + K_{\mathrm{i}} \int_0^t e(\tau)\, d\tau \tag{2}$$

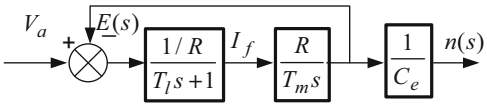

Fig. 1 Block diagram of the current open-loop

2.2 Current Loop

Nowadays, the demand for high precision of the servo control system of photoelectronic detection system is increasing. In the past designs of servo control system, the structure of speed loop and position loop is normally employed. However, the low-frequency gain of the speed loop is influenced by the system phase gain and is hard to increase. Through adding a current loop in the speed loop, the speed loop characteristics of the system can be altered which will improve the tracking precision of the servo control system. In Fig. 1, the current open-loop of the servo control system of the photoelectronic detection system is shown.

Where V_a the armature voltage, L the armature inductance, R the armature resistance, I_f the armature current, T_m the torque constant, J the moment of inertia, T_l the constant of counter electromotive force, and n the electromotor speed.

Firstly, we consider the current open-loop, as shown in Fig. 1. The transfer function relating the output E to the input V_a is

$$G_c(s) = E(s)/V_a(s) = (T_m/R)\, s/\left(T_m T_l s^2 + T_m s + 1\right) \tag{3}$$

In most servo control applications, T_l and T_m are constants if the electromotor is selected and the two transition frequencies of the system are also constants. This can be shown by changing (3) to

$$G_c(s) = (R/T_l)\, s/\,(s - T_1)\,(s - T_2) \tag{4}$$

where $T_{1,2} = \left(-1 \pm \sqrt{1 - 4T_l/T_m}\right)/2T_l$ and $T_{1,2} < 0$ ($T_l/T_m < 0.1$ is normally the case in the real applications).

It is shown from (4) that the two poles of $G_c(s)$ are on the left plane of the complex plane and the system is stable. However, the system bandwidth seldom can meet the design need. To expand the system bandwidth of the current open-loop, a PI controller with the transfer function

$$G_{acr}(s) = K\,(T_e s + 1)\,/\,T_e s \tag{5}$$

is designed as shown in Fig. 2.

Therefore, the transfer function relating I_f to I_{ref} is

$$\begin{aligned} &I_f(s)/I_{ref}(s) = (KT_m T_e s + KT_m) \\ &/\left(RT_m T_l T_e s^2 + (T_e T_m R + T_e T_m R)\, s + (RT_e + KT_m)\right) \end{aligned} \tag{6}$$

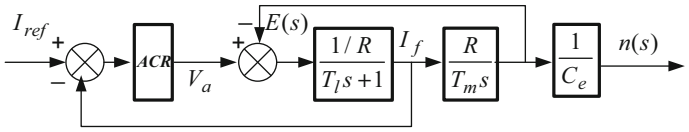

Fig. 2 Block diagram of the current closed-loop using a PI controller

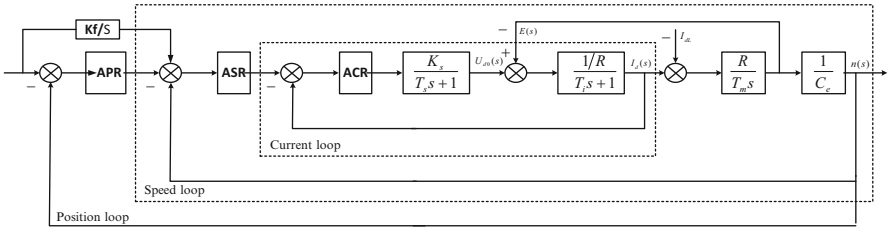

Fig. 3 Block diagram of the three closed-loop of the servo control system

If the PI controller and electromotor parameters are selected to satisfy $KT_{\mathrm{m}} \gg R\mathrm{T_e}$ and $T_{\mathrm{e}} < T_{\mathrm{l}}$, (6) is simplified as following:

$$I_{\mathrm{f}}(s)/I_{\mathrm{ref}}(s) \approx (KT_{\mathrm{e}}s + K) / \left(RT_{\mathrm{l}}T_{\mathrm{e}}s^2 + (T_{\mathrm{e}}R + T_{\mathrm{e}}R)\, s + KT_{\mathrm{m}}\right) \tag{7}$$

It is shown from (7) that the system is not influenced by the electromechanical load and the performance (mainly the system bandwidth) of the system will not change if the control system doesn't saturate. Now, the transfer function relating the output $n(s)$ and the input I_{ref}(s) is

$$\begin{aligned} &n(s)/I_{\mathrm{ref}}(s) = (KRT_{\mathrm{e}}s + KR) \\ &/ \left(T_{\mathrm{m}}T_{\mathrm{l}}T_{\mathrm{e}}C_{\mathrm{e}}Rs^3 + C_{\mathrm{e}}T_{\mathrm{e}}T_{\mathrm{m}}\,(R+K)\, s^2 + C_{\mathrm{e}}\,(RT_{\mathrm{e}} + KT_{\mathrm{m}})\, s\right) \end{aligned} \tag{8}$$

To simplify (8), we use the following assumptions

$$\begin{cases} T_{\mathrm{m}}T_{\mathrm{l}}T_{\mathrm{e}}C_{\mathrm{e}} \ll R1 \\ K \gg R \\ KT_{\mathrm{m}} \gg RT_{\mathrm{e}} \end{cases} \tag{9}$$

and get the equation

$$n(s)/I_{\mathrm{ref}}(s) \approx R\,(T_{\mathrm{e}}s + 1)\,/C_{\mathrm{e}}T_{\mathrm{m}}\,(T_{\mathrm{e}}s + 1)\, s \approx (R/C_{\mathrm{e}}T_{\mathrm{m}})\,(1/s) \tag{10}$$

The motor driver of the servo control system uses three closed-loop, as shown in Fig. 3.

2.3 EtherCAT

EtherCAT is by and large the fastest industrial Ethernet technology, but it also synchronizes with nanosecond accuracy. This is a huge benefit for all applications in which the target system is controlled or measured via the bus system. The rapid reaction times work to reduce the wait times during the transitions between process steps, which significantly improves application efficiency. Lastly, the EtherCAT system architecture typically reduces the load on the CPU by 25–30% in comparison to other bus systems (given the same cycle time). When optimally applied, EtherCAT's performance leads to improved accuracy, greater throughput, and thus to lowered costs.

The EtherCAT master sends a telegram that passes through each node. Each EtherCAT slave device reads the data addressed to it "on the fly" and inserts its data in the frame as the frame is moving downstream. The frame is delayed only by hardware propagation delay times. The last node in a segment (or branch) detects an open port and sends the message back to the master using Ethernet technology's full duplex feature.

The telegram's maximum effective data rate increases to over 90%, and due to the utilization of the full duplex feature, the theoretical effective data rate is even higher than 100 Mbit/s (>90% of two times 100 Mbit/s).

The EtherCAT master is the only node within a segment allowed to actively send an EtherCAT frame; all other nodes merely forward frames downstream. This concept prevents unpredictable delays and guarantees real-time capabilities.

The master uses a standard Ethernet Media Access Controller (MAC) without an additional communication processor. This allows a master to be implemented on any hardware platform with an available Ethernet port, regardless of which real-time operating system or application software is used. EtherCAT slave devices use an EtherCAT slave controller (ESC) to process frames on the fly and entirely in hardware, making network performance predictable and independent of the individual slave device implementation.

3 Dual Motor Cross-Coupling Control

3.1 Dual Motor Drive Model

The structure of the elevation axis frame of the gimbal is shown in Fig. 4, and it includes the U-type gimbal, load, motor one, motor two, and so on.

The control model of Fig. 4 is shown in Fig. 5 [3].

Where J_L the moment of inertia of the load, J_{m1} the moment of inertia of the motor one, J_{m2} the moment of inertia of the motor two, T_{m1} and T_{m2} are the torque of motor one and motor two, θ_L and θ_{m1} and θ_{m2} are the rotary angles of the load and motor one and motor two, K_1 and K_2 are the stiffness of the axis.

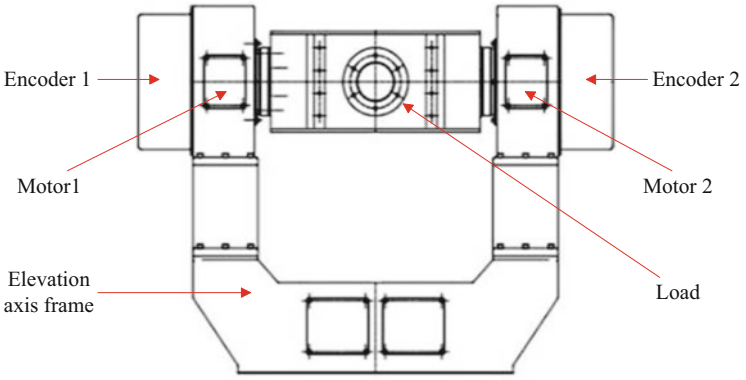

Fig. 4 Block diagram of the elevation axis frame of the gimbal

Fig. 5 Block diagram of the dual motor drive model

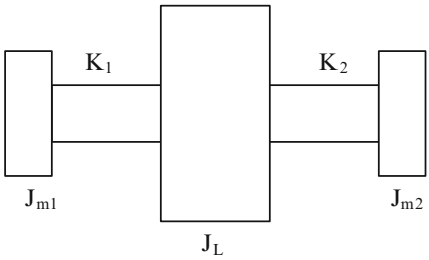

The dynamics equation of the dual motor drive model is [8, 9, 10]:

$$J_{\mathrm{m1}}\ddot{\theta}_{\mathrm{m1}} + K_1\left(\theta_{\mathrm{m1}} - \theta_{\mathrm{L}}\right) = T_{\mathrm{m1}} \tag{11}$$

$$\mathrm{J_L}\ddot{\theta}_{\mathrm{L}} + K_2\left(\theta_{\mathrm{L}} - \theta_{\mathrm{m2}}\right) + K_1\left(\theta_{\mathrm{L}} - \theta_{\mathrm{m1}}\right) = 0 \tag{12}$$

$$J_{\mathrm{m2}}\ddot{\theta}_{m2} + K_2\left(\theta_{\mathrm{m2}} - \theta_{\mathrm{L}}\right) = T_{\mathrm{m2}} \tag{13}$$

The equation of the torque output is:

$$J_{\mathrm{m1}}\ddot{\theta}_{\mathrm{m1}} + J_{\mathrm{m2}}\ddot{\theta}_{\mathrm{m2}} + J_{\mathrm{L}}\ddot{\theta}_{\mathrm{L}} = T_{\mathrm{m2}}T_{\mathrm{m1}} \tag{14}$$

3.2 Dual Motor Cross-Coupling Drive Control

Dual motor cross-coupling is based on the dual motor equal control [11, 12]. The method of dual motor cross-coupling position drive control is shown in Fig. 6.

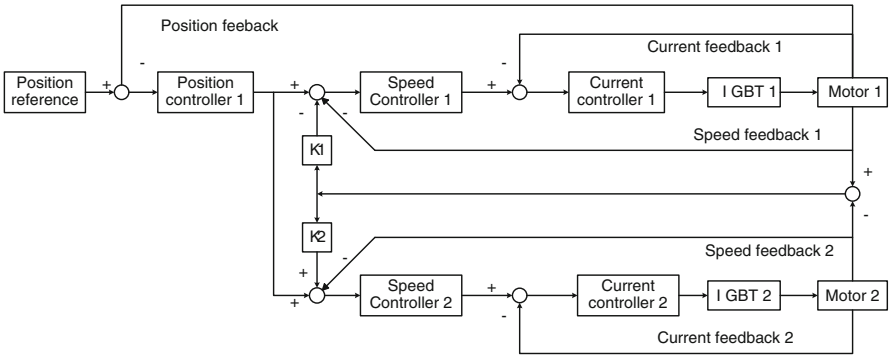

Fig. 6 Block diagram of the structure of the dual motor cross-coupling drive control

Fig. 7 Block diagram of the experimental platform

In the dual motor cross-coupling position drive control system, every motor will respond to the other motor disturbance and finally decrease the synchronous error with high precision. The encoder 1 feedback will be used as the position feedback because of the installation errors of the two encoders.

4 Experiments

4.1 Experimental Platform

The experimental platform of the dual motor cross-coupling position drive control system is shown in Fig. 7.

KINGSTAR is a complete "plug-and-play" PC-based platform for industrial motion control, machine vision, and programmable logic controllers (PLC). Built on the EtherCAT standard and supported by a real-time 64-bit Windows operating

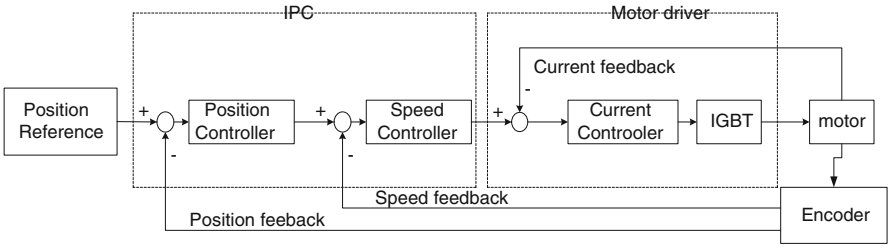

Fig. 8 Block diagram of the three closed-loop of the motor driver

system (RTOS), KINGSTAR empowers engineers to design, develop, and integrate applications with KINGSTAR's soft motion, machine vision, and PLC or third-party software. Using a single industrial PC, you can replace all hardware with software-only motion controllers and machine vision positioning systems, quickly and cost effectively.

The IPC of Beckhoff with Windows 7 and KINGSTAR is configured as the EtherCAT master and receives the position, speed value, and so on, from the EtherCAT slaves. After the calculation of position loop and speed loop, the reference torque is sent to the EtherCAT slaves. The AxN motor drivers of the Phase Motion Ltd. are configured as the EtherCAT slaves, sample the encoder data, run the torque loop, return the data to the master, and receive the commands from the master. The three closed-loop tasks allocation is shown in Fig. 8.

The 100BASE-TX Ethernet wire is the media which connect the master and the slaves. The Encoder is the ECA4000 of 27 bits resolution, with Endat 2.2 interface, from the Heidenhain Ltd. The motor is PMSM motor manufactured by the Phase Motion Ltd., and the rated torque is 35 Nm, the max speed is 1150°/s.

4.2 Experimental Results

1. Bandwidth Comparison

The sweep sine signal is used to drive the speed open-loop and speed closed-loop, and the signals of responds are processed by MATLAB's system identification toolbox. The Bode plots of the single motor and dual motor speed closed-loop are shown in Fig. 9.

From the figures above, the speed closed-loop bandwidth of the single motor drive is 18 Hz, while the speed closed-loop bandwidth of the single motor drive is 29 Hz. The bandwidth comparison shows that the stiffness of dual motor drive is better than that of the single motor drive.

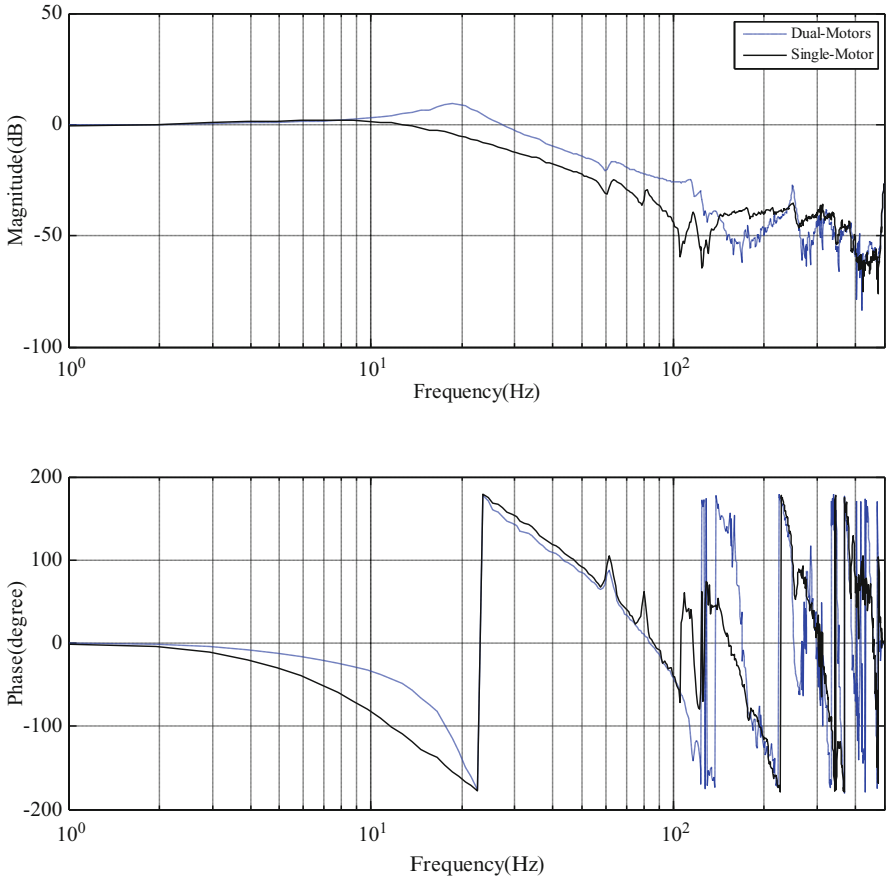

Fig. 9 Block diagram of the Bode plots of single motor drive and dual motor drive

2. Tracking Error

Given the sine signal of 20° sin (0.1t), the speed and position loop use the PI controller, and the position tracking errors (PosTrackErr) of single and dual motor drive are shown in Figs. 10 and 11, respectively.

Because the platform of the elevation axis is small and the stiffness of the axis is big, the error of the dual motor drive is a little better than that of the single motor drive.

3. Tracking Error with Disturbance

Given the sine signal of 20° sin (0.1t) and the sine disturbance of 9.72 Nm, the position tracking errors of single and dual motor drive are shown in Figs. 12 and 13, respectively.

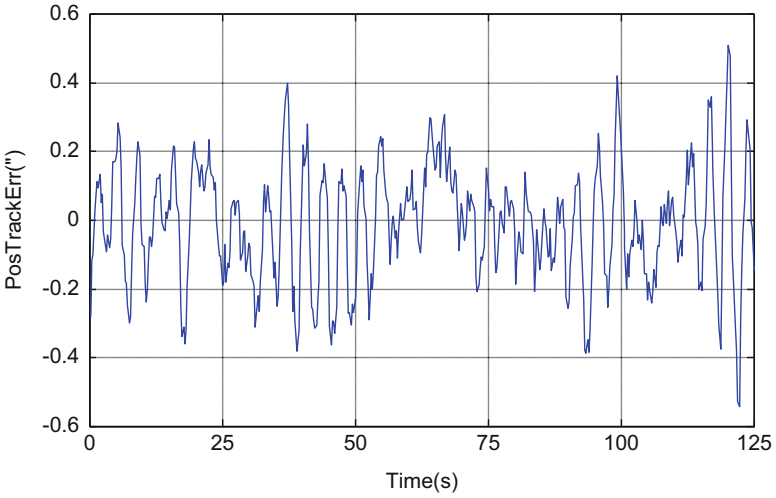

Fig. 10 Block diagram of the position error of single motor drive

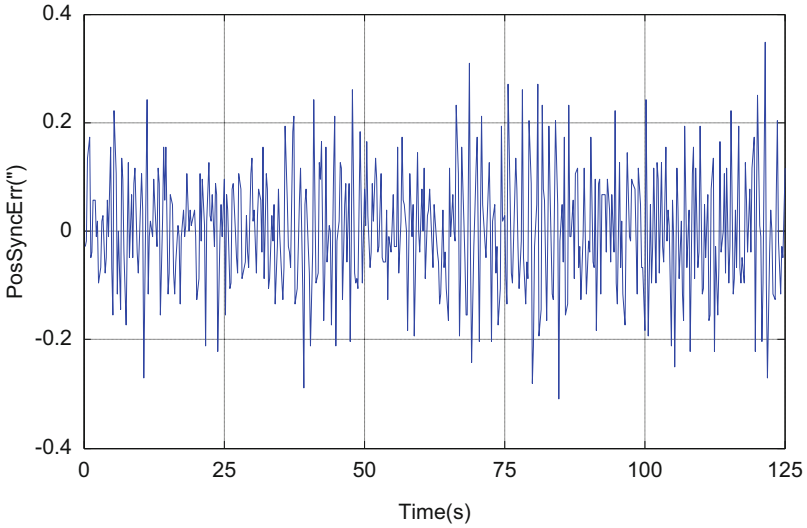

Fig. 11 Block diagram of the position error of dual motor drive

The figures above show that the error of the dual motor drive with the tracking error 4.66″ is better than that of the dual motor drive with the tracking error 8.96″.

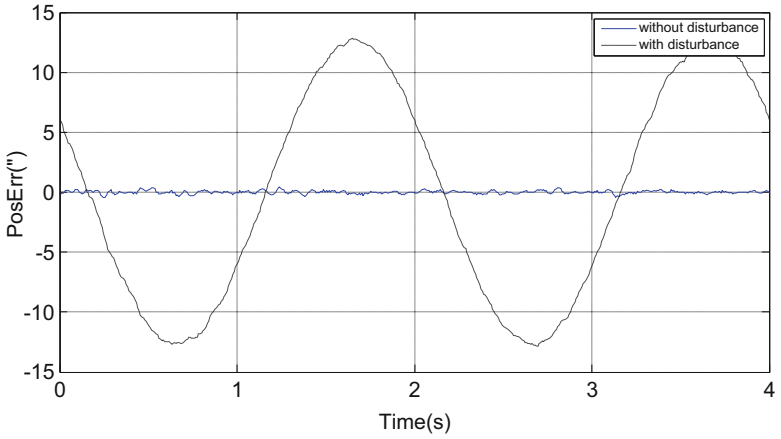

Fig. 12 Block diagram of the position error of single motor drive under the disturbance noise

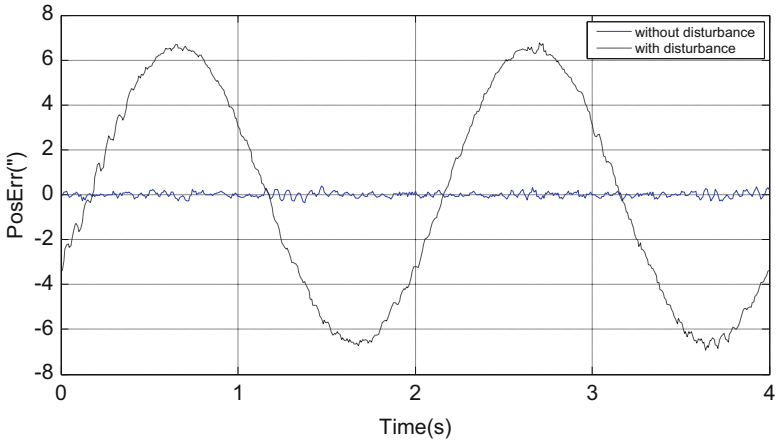

Fig. 13 Block diagram of the position error of dual motor drive under the disturbance noise

5 Conclusions

The dual motor cross-coupling drive control system based on EtherCAT is implemented on the basis of single motor drive control. The experimental analysis of single motor drive control and dual motor drive control is carried out, which clarifies the advantages of dual motor drive control.

The resulting performance could be improved in the big telescope as the stiffness of the elevation axis of the big telescope is worse. Furthermore, PI controller gains and relevant command signal selected empirically should be decided with some techniques.

References

1. Gawronski W (2007) Control and pointing challenges of large antennas and telescopes. IEEE Trans Control Syst Technol 15(2):276–289
2. Ai X, Yongkun F, Qinzhang W (2010) Design of a variable structure PI controller and its application in photoelectronic tracking system. Optics Precision Eng 18(8):1855–1861. (in Chinese)
3. Tao T, Tong Z, Junfeng D et al (2014) Two motors synchronization control for photoelectric theodolite. Opto-Electronic Eng 41(1):1–5. (in Chinese)
4. Ang KH, Chong G, Li Y (2005) PID control system analysis, design, and technology. IEEE Trans Control Syst Technol 13(4):559–576
5. ETG. *EtherCAT_Communication_EN*, [Online], Available: http://www.ethercat.org. March, 2011
6. KingStar. *KingStarProductBriefSimpleChinese*, [Online], Available: http://www.kingstar.com, January, 2014
7. Phase. *10460–0-D-M-ENG.AxM-II.RefMan*, [Online], Available: http://www.phase.com.cn, July, 2014
8. Koren Y (1980) Cross-coupled biaxial computer control for manufacturing systems. J Dyn Syst Meas Control 102(4):265–272
9. Shih Y, Chen C, Lee A (2002) A novel cross-coupling control design for bi-axis motion. Int J Mach Tool Manu 42(14):1539–1548
10. Su Y, Xu G (2010) Research of multi-motor synchronous driving system based on fuzzy smith control. In: 2010 international conference on electrical and control engineering, IEEE, Wuhan, China, pp. 5466–5469
11. Tomizuka M, Hu J, Chiu Kmanao T (1992) Synchronization of two motion control axes under adaptive feedforward control ASME. J Dyn Syst Measurement Control 114(2):196–203
12. Francisco J, Ciro N, Ricardo A et al. (2004) Comparison of multi-motor synchronization techniques. In: 30th annual conference of the IEEE industrial electronics society, IEEE, Busan, Korea, pp 1670–1675

Calibrating TOF Sensor by Fusing Normal Maps

Hanyu Ni, Yiguang Liu, Zhenyu Xu, Jianyu Heng, and Ling Jin

1 Introduction

The TOF sensor has been introduced for many years, which based on reconstruction methods provides the real distance of scene. However, depth images obtained by the TOF camera suffer from the problems of low resolution, noises, and radial distortion. For example, compared with the images of conventional color camera with 1280*960 or 1920*1080, *The Swiss Ranger 3000* [1] based on 3D-TOF can only produce 176*144 depth images, which are rather low resolution. Since the problem of low resolution has not been effectively solved, the TOF sensor remains in the experimental phase.

There are many works attempting to improve the resolution of depth images; in general, methods of calibration are roughly categorized into two classes. The first-class methods based on time redundancy use image super-resolution means. However, the second-class methods based on spatial redundancy realize sensor fusion; our method based on the second-class methods fuses the Kinect [2] sensor with the TOF sensor. We will simply discuss now works in both classes. 3D shape scanning [3] based on image super-resolution means is commonly aligned several scans taken from multiple viewpoints. The scanning data based on accurate calibration techniques, such as iterative closest points (ICP) [4], is used to iterate each other. But because the TOF sensor is sensitive to movement, it is difficult to obtain depth images of high resolution from different viewpoints. Cui et al. [5] use some low-resolution depth images captured from slightly mobile views of the TOF sensor, the improvement task based on a convex optimization framework to maintain

H. Ni (✉) · Y. Liu · Z. Xu · J. Heng · L. Jin
Vision and Image Processing Lab (VIPL), College of Computer Science, SiChuan University, Chengdu, Peoples Republic of China
e-mail: Hanyu2943@outlook.com;liuyg@scu.edu.cn;lygpapers@aliyun.com

M. Jiang et al. (eds.), *The Proceedings of the International Conference on Sensing and Imaging*, Lecture Notes in Electrical Engineering 506,
https://doi.org/10.1007/978-3-319-91659-0_11

the original measurement and suppress noises. Depth fusion methods solve the problem that multiple frames are obtained by merging the other devices to provide data captured simultaneously. This technique is applied to many calibration works, for example, [6] build a calibration system that is consist of a TOF sensor and of a stereoscopic sensor, which allows depth fusion to address the weaknesses of both individual sensors, and they propose a novel method based on the calibration system that uses the TOF data projected onto the stereo image to finish fusion. To obtain more reliable and accurate depth images produced by the TOF sensor, [7] and [8] fuse the TOF sensor with other stereo sensors. Schwarz et al. [9] present a sensor fusion approach to TOF, based on the combination of depth and texture sources; this method is appropriate for depth scenery capture. Yu et al. [10] propose a solution of low computation cost to fuse depth images from TOF with high-resolution color images to improve the resolution of depth images. Besides, other works [11–13] based on the second-class methods improve the resolution of TOF.

The innovations of this paper include (1) a novel method combined depth images with normal maps is proposed to improve the resolution of those depth images produced by TOF; and (2) compared with classic photometric stereo, the normal maps based on photometric stereo are captured by adding an extra light source around the Kinect sensor, which are sufficiently illuminated to achieve better effects of fusion.

In the other sections, we introduce our system overview in Sect 2, introduce experimental principles of the TOF and photometric stereo in Sect 3, show and discuss the results of our experiment in Sect 4, and, finally, give conclusions and future outlooks in Sect 5.

2 Process of Fusing TOF with Normal Maps

Our system follows three steps. First, original static depth images are obtained by the TOF sensor; after that, we use the bilateral filtering [14] techniques to smooth original depth images. Second, as shown in Fig. 1, the Kinect sensor based on photometric stereo obtains normal maps. In order to solve the problems that some areas cannot be illuminated adequately, one extra light source is added around the Kinect sensor. In addition, two triggers are used for two LED light sources to turn on them conveniently. To obtain smooth normal maps, original normal maps are optimized by joint bilateral filtering [15]. Finally, depth images are fused with normal maps by our algorithm. Figure 2 shows our framework of experiments.

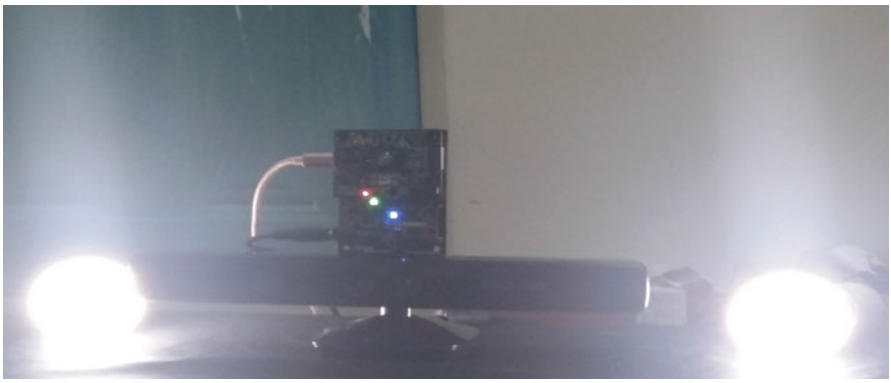

Fig. 1 Obtaining normal maps

Fig. 2 Overview of our experiments

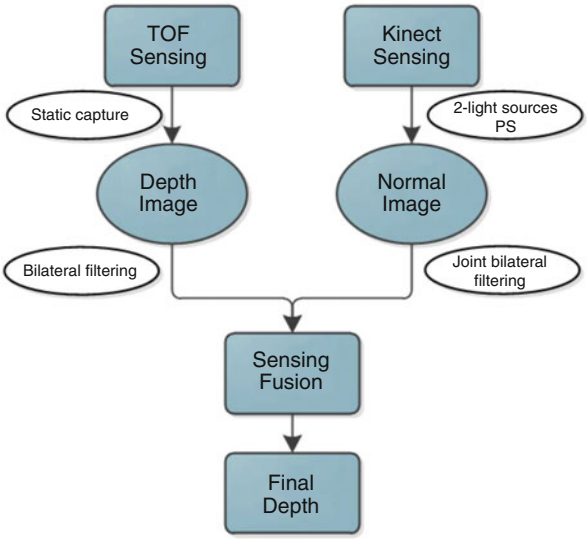

3 Photometric Stereo with One Extra Light Source

3.1 Classic Photometric Stereo

The fundamental principles of photometric stereo are described in the pioneering works of Woodham in the 1980s [16]. Light source is calibrated by estimating the light direction, so we use a ball where the brightest spot is used to identify the direction of light, as shown in Fig. 3. The direction of light is computed as:

Fig. 3 A sphere determines the direction of the light

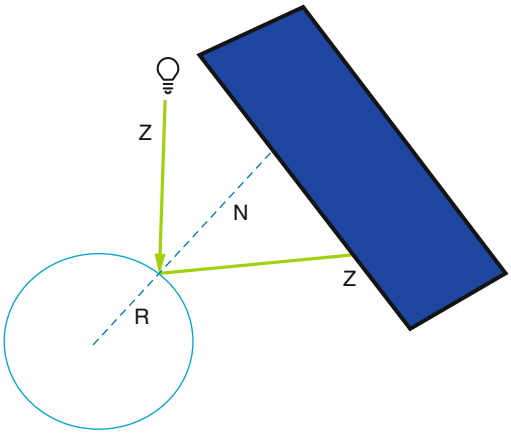

Fig. 4 Classic model of photometric stereo

$$\begin{aligned} Z &= (2N \cdot R)N - R, N_x = Q_x - H_x \\ N_y &= Q_y - H_y, N_z = \sqrt{R^2 - N_x^2 - N_y^2} \end{aligned} \tag{1}$$

where $[Q_x, Q_y]$ denotes the location of the brightest point and $[H_x, H_y]$ denotes central position of the ball. R (as shown in Fig. 4) denotes the direction of reflection taken as [0, 0, 1]. According to Lambertian surfaces, intensity at any point on the surfaces is able to be computed as:

$$I = k_d N \cdot Z \tag{2}$$

where N is the normal of point and Z is the reflected light direction. As for different light sources, $I_i (i = 1, 2, 3 \ldots n)$ is also different; therefore, we can obtain I_i as:

$$I_i = k_d (N_x Z_{ix} + N_y Z_{iy} + N_z Z_{iz}) \tag{3}$$

for determining N, according to Eq. 3, we need at least three light sources that these light sources are not in the same location. Then Eq. 3 is written as:

$$[M] = k_d[N] \tag{4}$$

Only when $Z > 3$, the N can be computed as:

$$\begin{aligned} &[Z]M = [I], Z^T ZM = Z^T I \\ &M = \left(Z^T Z\right)^{-1} Z^T I, k_d = \|M\|, N = G/k_d \end{aligned} \tag{5}$$

3.2 Obtaining Normal Images with Two Light Sources

After the sphere is illuminated by two different horizontal LED lights, according to Fig. 5, respectively, we can obtain two spatial planes I and II, then the two planes intersect in 3D space. As for Eq. 2, we know that $N_1 \cdot Z_1 = I_1$ and $N_2 \cdot Z_2 = I_2$. In addition, assuming that we use the surfaces of a hemisphere, if Z and N were 90 degrees, the intensity $I = 0$ (see also Eq. 2), which is impossible, so we ignore the data of this situation. Using the following formula, we find the normal N_2, which closets to the true value:

$$N_2 = N_1 - (I_2 Z_1 - I_1 Z_2) \frac{N_1 \cdot (I_2 Z_1 - I_1 Z_2)}{\|I_2 Z_1 - I_1 Z_2\|^2} \tag{6}$$

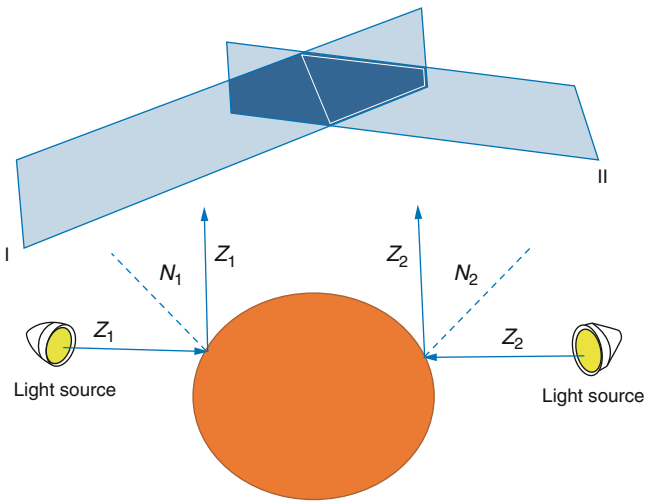

Fig. 5 Two different horizontal LED lights illuminate the areas

3.3 TOF Based on Phase Shift

TOF is based on phase shift, so we give the phase shift σ for the correlation function $z(\sigma)$.

$$z(\sigma) = \lim_{t\to\infty} \int \cos(\zeta t) \times \theta \cos(\zeta(t+\sigma)+\varphi)dt \tag{7}$$

where θ is the amplitude of incident light, ζ is the frequency, and φ is the phase angle. Its light source is pulsed or modulated by continuous wave (CW). According to pulsed modulation, we use square wave modulation to detect phase shifts between the illumination and the reflection. There are four phase images $P_i(i = 1, 2, 3, 4)$ with the same period (Δt). So, distance d is computed as:

$$d = \frac{1}{2} c\Delta t \left(\frac{P_2}{P_4 + P_2}\right) \tag{8}$$

Besides, the second way is CW that takes multiple samples per measurement. Our system is based on this method. So the φ and the offset (H) can be computed as:

$$\varphi = \arctan\left(\frac{P_3 - P_1}{P_4 - P_2}\right), H = \frac{P_1 + P_2 + P_3 + P_4}{4} \tag{9}$$

Besides, we can also get the amplitude θ and the distance d as:

$$d = \frac{r}{4\pi f}\varphi, \theta = \frac{\sqrt{(P_3 - P_1)^2 + (P_4 - P_2)^2}}{2} \tag{10}$$

where γ is the speed-of-light constant. By computing the phase delay φ and the incident light x, we can get the light positions $L_i(i = 1, 2, 3, 4)$ as:

$$Li = \left[\left(\frac{\varphi\gamma \times (x-1)}{4\pi f}\right) - \frac{\gamma\theta_i}{2\pi f}\right] \tag{11}$$

After multiple iterations and refinements, L_i is computed by Eq. 9 through Eq. 11. According to the light source positions, the phase delay φ is computed by many refinements. Finally, we obtain depth images.

3.4 Combining Normal Maps with Depth Images

The position information from the surfaces normal and depth images is obtained by minimizing:

$$\begin{aligned} E = {} & \gamma_1 \sum_{n,m} \|v_{nm}\|^2 (H_{ij} - H^0_{ij})^2 + \gamma_n \sum_{n,m} [(N^0_{nm} \cdot v_{ij}) \tfrac{\partial H}{\partial v}|_{nm}) + \tfrac{N^0_{xij}}{f_x} Z_{ij})]^2 \\ & + \gamma_n \sum_{n,m} [(N^0_{nm} \cdot v_{ij}) \tfrac{\partial H}{\partial v}|_{nm}) + \tfrac{N^0_{ynm}}{f_y} Z_{nm})]^2 \end{aligned} \tag{12}$$

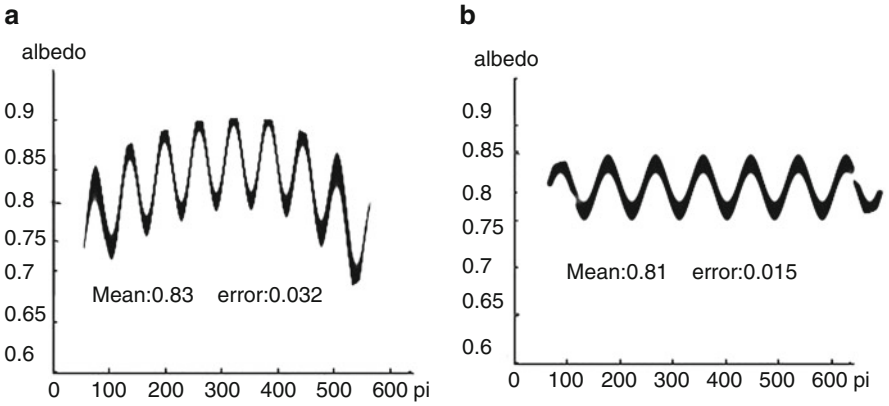

Fig. 6 (**a**) Albedo of classic method, (**b**) albedo of our method

$\gamma_1+\gamma_n = 1$ and $\gamma_1, \gamma_n \geqslant 0$, H_{ij}^0 denotes the original depth images, and N_{ij}^0 denotes normal that are computed by Sects. 3.2 and 3.3, and v_{ij} is the weight of pixel. Then we compute and amend the normal N^0 to update normal images. After several iterations and optimizations, the depth images are obtained.

4 Experimental Results

4.1 Results of Photometric Stereo

In order to prove that our method is more suitable than the classic photometric stereo in obtaining normal maps, we launch an experiment that examines the albedo of "captain" handwritten on white paper. Experiment (as shown in Fig. 6) shows that the albedo ratio is more stable and the relative error of albedo produced by our method is smaller than traditional method with the increase of pixel. Because some areas are insufficient illumination, which will have an influence on fusion effect, our method strengthens illumination intensity, and the result of fusion is smoother.

4.2 Results of Fusion

As shown in Fig. 7ii, mesh from the depth image of TOF is almost impossible to recognize before being fused, and only the contour is visible. But we perform our fusion algorithm that fuses the depth image of TOF with normal maps in Fig. 7iii and iv, respectively; effects of mesh are obviously improved in Fig. 7v and vi. However, compared with the normal map from our method in Fig. 7iv, the normal map based

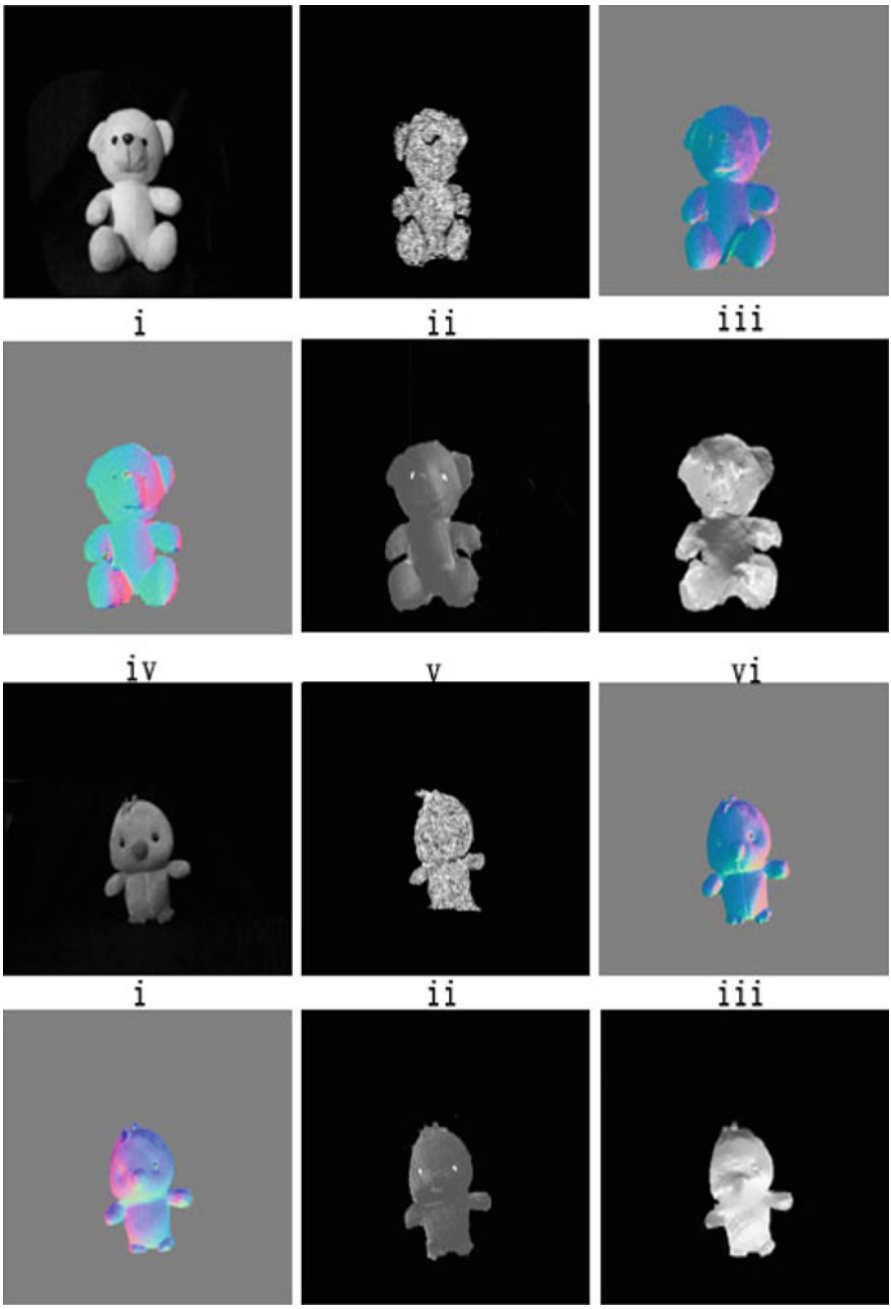

Fig. 7 From left to right: (i) intensity image; (ii) mesh from TOF; (iii) normal map from classic photometric stereo; (iv) normal map from our method; (v) mesh from fusion of the normal map iii and the depth image of TOF; (vi) mesh from fusion of the normal map iv and the depth image of TOF

on classic photometric stereo is very dim in Fig. 7iii. Besides, the effects of mesh in Fig. 7vi are better than mesh in Fig. 7v. Finally, there are still some holes on the mesh; this is the research of next step.

5 Conclusion

In this paper, we have proposed a novel fusion framework to improve the low resolution of TOF depth images. Besides, to obtain applicable normal maps, we equip two source lights to the Kinect sensor and successfully overcame the problem of lack of sufficient illumination faced by traditional photometric stereo. By using the two sensors as a combination, the resolution of TOF is improved. We hope that our method could be applied to many other fields and provide insights about the next generation of TOF production. In future works, we will put more effort to address the problem of sensitivity to movement of the TOF sensor, making it able to be used in dynamic scene.

Acknowledgements Thanks to the editor and reviewers for time and effort spent handling this paper. This work was supported by the Science and Technology Innovation seedling project of Sichuan (2016–2017).

References

1. Oggier T, Buttgen B, Lustenberger F, Becker G, Ruegg B, Hodac A (2005) Swissranger sr3000 and first experiences based on miniaturized 3D-ToF cameras. In: Proceedings of the first range imaging research day at ETH Zurich
2. Microsoft (2010) Kinect camera. http://www.xbox.com/enUS/kinect/default.htm
3. Furukawa Y, Ponce J (2007) Accurate, dense, and robust multi-view stereopsis. In: CVPR 07
4. Besl PJ, Mckay ND (1992) A method for registration of 3-D shapes. In: Sensor fusion IV: control paradigms and data structures, pp 239–256
5. Cui Y, Schuon S, Chan D et al (2010) 3D shape scanning with a time-of-flight camera. In: Computer vision and pattern recognition, IEEE, pp 1173–1180
6. Liu JL, Su-Mei LI, Yong-Da LI et al (2016) High-resolution depth maps based on TOF-stereo fusion. Inform Technol
7. Marin G, Zanuttigh P, Mattoccia S (2016) Reliable fusion of ToF and stereo depth drivenby confidence measures. In: Computer vision C ECCV 2016. Springer International Publishing
8. Nair R, Lenzen F, Meister S et al (2012) High accuracy TOF and stereo sensor fusion at interactive rates. In: International conference on computer vision. Springer, pp 1–11
9. Schwarz S, Sjostrom M, Olsson R (2013) A weighted optimization approach to time-of-flight sensor fusion. IEEE Trans Image Process Publ IEEE Signal Process Soc 23(1):214
10. Yu H, Zhao K, Wang Y et al (2013) Registration and fusion for ToF camera and 2D camera reading. In: Chinese automation congress, pp 679–684
11. Zhang Y, Xiong Z, Wu F (2015) Fusion of time-of-flight and phase shifting for high-resolution and low-latency depth sensing. In: IEEE international conference on multimedia and expo. IEEE, pp 1–6

12. Gandhi V, Cech J, Horaud R (2012) High-resolution depth maps based on TOF-stereo fusion. In: IEEE international conference on robotics and automation. IEEE, pp 4742–4749
13. Salinas C, Fernndez R, Montes H et al (2015) A new approach for combining time-of-flight and RGB cameras based on depth-dependent planar projective transformations. Sensors 15(9):24615–24643
14. Paris S, Kornprobst P, Tumblin J (2009) Bilateral filtering. Int J Numer Methods Eng 63(13):1911–1938
15. Kopf J, Cohen MF, Lischinski D et al (2007) Joint bilateral upsampling. In: ACM siggraph. ACM, p 96
16. Woodham RJ (1980) Photometric method for determining surface orientation from multiple images. Opt Eng 19:139–144

Flame Temperature Sensor Based on a Silicon Nitride Hot Surface Igniter

Rikesh Shakya and Nathan Ida

1 Introduction

Combustion is a chemical reaction that occurs when fuel and air burn together at very high temperature producing heat and combustion products. One of the primary concerns during combustion is to make efficient use of the fuel. The amount of fuel and air required for the combustion process is referred in comparison with a stoichiometric air-fuel ratio. The stoichiometric air-fuel ratio is the ratio of the amount of air necessary to burn a particular fuel completely. Fuel-air equivalence ratio (ϕ) for a combustion process is the ratio of the mass of fuel to air compared to the stoichiometric ratio of fuel and air. Fuel-air equivalence ratio in the combustion process defines the temperature profile at different points in the flame. The maximum theoretically achievable flame temperature in the combustion process is called adiabatic flame temperature, which is specified in either constant volume or constant pressure with no heat transfer to the surroundings. Adiabatic flame temperature is a function of fuel composition, stoichiometry of fuel and air, and temperature and pressure of the reactants. In a constant pressure and constant reactant temperature combustion process, knowledge of the fuel-air ratio gives the temperature of the flame and vice versa. Flame temperature is one of the parameters, which can be used to determine the efficiency of a combustion.

R. Shakya (✉) · N. Ida
Department of ECE, The University of Akron, Akron, OH, USA
e-mail: rs156@zips.uakron.edu; ida@uakron.edu

M. Jiang et al. (eds.), *The Proceedings of the International Conference on Sensing and Imaging*, Lecture Notes in Electrical Engineering 506,
https://doi.org/10.1007/978-3-319-91659-0_12

There are various temperature measurement devices that are used for different applications. In general, temperature measurement methods can be broadly categorized by the principle of measurements into mechanical, electrical, acoustic, and optical methods. Each of these methods has their own strengths and weaknesses. The choice of the temperature sensor depends upon application, temperature range, and accuracy requirement. Early temperature sensors were mechanical, and these include devices such as in-glass thermometer [1, 2], bimetallic strip thermometer [1], and fluid expansion thermometer [1]. These are based on the change in mechanical dimensions of fluids with changes in temperature. Another class of temperature measurement methods uses optical techniques, which includes the sodium spectrum line reversal method [3, 4]; brightness and emissivity methods [3]; two-color pyrometry [6]; Schlieren [5, 7], shadowgraph [5], and interferometric methods [5, 8]; Rayleigh scattering, Raman scattering, or resonant fluorescent scattering [1, 5], [9]; LIF [10, 11]; etc. Acoustic thermography method is a relatively inexpensive method for noninvasive temperature measurement. The method is based on the principle of variation in speed of sound with changes in temperature [5, 12–14]. Another category of temperature measurement devices involves electrical methods. These methods possess the advantage of easy detection and also permit various signal processing techniques unlike other methods. Thermocouples [1, 15, 16], thermistors [17], and platinum resistance thermometers (PRT) [18–20] are some popular electrical temperature sensors.

This paper presents the use of hot surface igniters (HSI) that are made up of silicon nitride (SN), for temperature measurements in a premixed combustion system. The use of SN HSI has the distinct advantage of being a dual-purpose device serving as an igniter and as a temperature sensor, and since most combustion system already employs hot surface igniters, their dual use contributes to lowering costs. The resistance of the SN HSI varies with the change in temperature, and this property is utilized for temperature measurements. Silicon carbide (SiC) HSI was prevalent before the introduction of silicon nitride HSI. The SN HSI has low density, corrosion resistance, and high mechanical strength at high temperatures and possesses great hardness in comparison with SiC HSIs. Additionally, SN HSIs are very good insulators helping in preventing electric shocks.

Flame temperature is an important parameter of combustion systems. It provides a way to estimate the fuel-air equivalence ratio (ϕ) for air-fuel mixtures. Knowledge of equivalence ratio permits adjustment of fuel and airflow rates to maximize the efficiency of premixed combustion systems. Since the equivalence ratio is applicable only for premixed combustion systems, the flame temperature sensor discussed is only useful to control the efficiency of premixed combustion systems. Extra interfacing circuits are required for dual functioning of the sensor, which increases the cost of the burner control system. However, the HSI sensor as a dual-purpose sensor saves the cost of fuel by increasing the efficiency of the combustion system.

2 Theory of Operation

Flames are categorized into diffusion and premixed flames based on mixing of fuel and air during combustion as shown in Fig. 1. Diffusion flames have fuel and air coming to the interface only in the region of combustion. The rate of combustion is dependent on the rate of diffusion and mixing. There is no true final flame temperature in the case of diffusion flames, although some points of flame reach nearly the theoretical maximum for stoichiometric premixed mixtures, unless the air supply as well as the fuel supply is restricted. Premixed flames are produced by the combustion of the mixture of fuel and air, which are mixed prior to reaching the combustion chamber. Premixed flame has flammability limits with the ratio of fuel and air to be within certain lower and upper limits of lean and rich air. Premixed flames are generally employed for small-scale burners as large-scale premixed flames require large mixer that adds the risk of fire and explosion. The fuel-air equivalence ratio varies between 0 and 1 for lean mixtures and from 1 to infinity for rich mixtures. Combustion stoichiometry plays a major role in the combustion process as it is directly related to stack losses, unburnt fuel, auxiliary power consumption, and different environmental pollutant formation.

Theoretically, there should be stoichiometric ratio of fuel and air for complete combustion. This raises the flame temperature to adiabatic flame temperature; however, a small amount of excess air is necessary in practice to reduce the risk of production of harmful flue gases. A method to estimate the adiabatic flame temperature is to use the average specific heat (C_p) method. In the constant pressure combustion process, flame temperatures are calculated as follows [21]:

For $\phi \leq 1$,

$$T_P = T_R + \frac{\phi f_s LHV}{(1 + \phi f_s)\,\overline{C}_{p,p}} \tag{1}$$

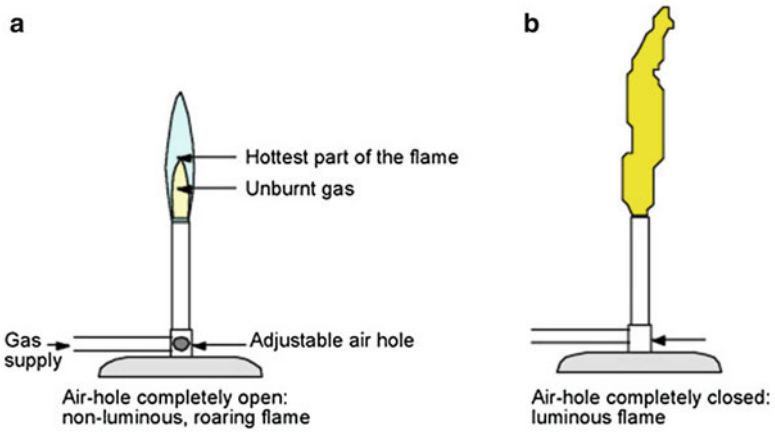

Fig. 1 Example of premixed flame (**a**) and diffusion flame (**b**)

For $\phi \geq 1$,

$$T_{\mathrm{P}} = T_{\mathrm{R}} + \frac{f_{\mathrm{s}}\mathrm{LHV}}{(1 + \phi f_{\mathrm{s}})\,\overline{C}_{\mathrm{p,p}}} \tag{2}$$

where f_{s} is the fuel-air ratio, LHV the lower heating value of water vapor, and $\overline{C}_{\mathrm{p,p}}$ the average specific heat at constant pressure per unit mass of mixture at temperatures $T_0 = 25\ ^{\circ}\mathrm{C}$ and reactant temperature T_{R}.

These expressions show that the flame temperature is directly related to the equivalence ratio of fuel and air. Theoretically, the maximum adiabatic flame temperature should occur at the equivalence ratio of 1. However, in practice, it could differ for different fuels. The maximum value of adiabatic flame temperature (T_{ad}) of mixtures of hydrocarbon and air occurs slightly on the rich side of the fuel equivalence ratio as shown in Fig. 2. This is due to reduced heat release due to product dissociation, although specific heat increases with an increase in the equivalence ratio. However, the direction of shifting is determined by the peak heat release. Furthermore, in case of fuels like N_mH_n/F_2 mixtures, the shift is toward the lean side of the mixture. This is because the variation of specific heat with equivalence ratio dominates the reduced heat due to product disassociation for these fuels.

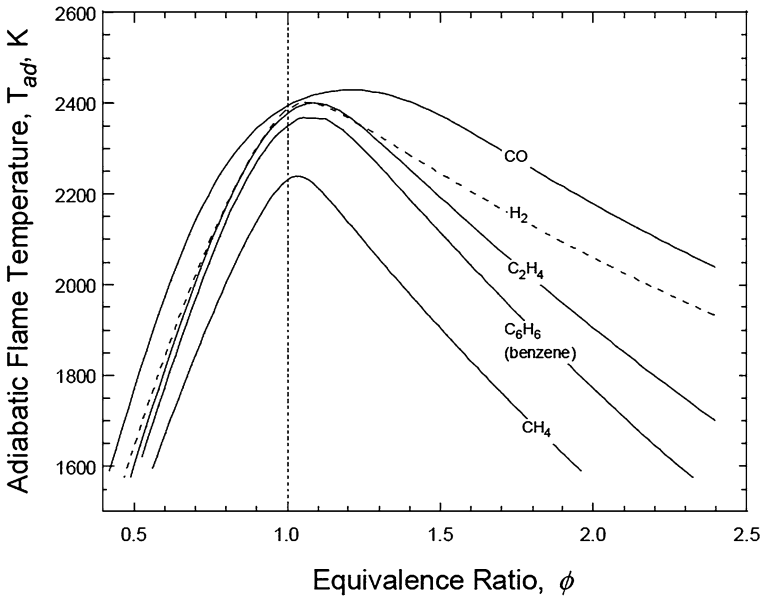

Fig. 2 Variation of adiabatic flame temperature vs equivalence ratio for various hydrocarbon fuels at STM [23]

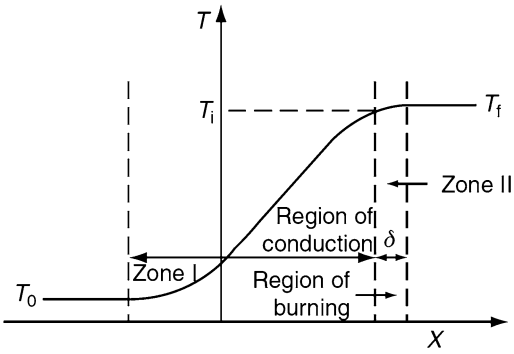

Fig. 3 Mallard and Le Chatelier's flame zones in laminar premixed flames [24]

One of the early theories of flame propagation (by Mallard and Le Chatelier [24]) that discusses the flame propagation mechanism in a combustion process was based on heat transfer between layers of gas. According to Mallard and Le Chatelier, there are two zones in combustion of laminar, premixed flame. Figure 3 shows these two zones which were termed as the preheat zone (Zone I) and the burning region (Zone II). The temperature of flame varies at different points of the flame as there shown in the figure.

3 Methodology

A test combustion chamber was set up for performing experiments to analyze different properties of the HSI igniter sensor. There were different aspects of the HSI sensor, which needed to be tested for flame temperature measurements.

- The variation of resistance of the sensor with variations in the equivalence ratio.
- The positioning of the sensor at various locations of the combustion chamber to find out the location of a sensor that gives optimum results.
- The testing of several types of sensors having different dimensions. Three different types of sensors from Kyocera and CoorsTek were tested to find out the appropriate dimensions of the sensor and to evaluate its performance.

All the tests were performed to minimize the error and increase accuracy of the HSI sensors. The results obtained were verified by employing multiple samples of different varieties of the sensor. Figure 4 shows the test combustion chamber setup used for the experiment. A Bosch Greenstar Wall Hung boiler model ZBR21-3 was used as the test combustion chamber. The boiler was customized for the measurement of airflow intake and gas flow intake to the combustion chamber. Tap water without any recirculation was used for the boiler. There were three different types of HSI sensors used to test the feasibility of dual-purpose sensor. Beckett 7590 control board was employed to control the operation of gas flow valves and blower

Fig. 4 Experimental setup for flame temperature sensor

motor. An electronic control board was also designed to control the fuel and airflow rate intake into the boiler system and to control the operation of sensor for both ignition and temperature measurements.

Silicon nitride HSI sensors were used as test dual-purpose igniter/flame temperature sensor. Figure shows different sensors used during the experiment. Figure 5a – Kyocera (a) and Fig. 5b – Kyocera (b) are two HSI sensors from Kyocera. The Kyocera sensor shown in Fig. 5a (Kyocera SN220) has short sensor stem and sensor length compared to the one shown in Fig. 5b, which is a modified version of Kyocera SN220. The body of sensor in Fig. 5a did not reach into the flame; therefore the sensor in Fig. 5b was custom designed with a longer stem and sensor length such that the whole body of sensor element lies within the flame. The maximum temperature range of the sensor is 1200 °C. Figure 5c shows a CoorsTek sensor, which has hairpin-like sensor element. These SN igniters have rapid heat increase, higher chemical resistance, high electrical efficiency, and long life due to oxidation proof design. The resistance ratio with respect to resistance at 23 °C (R/R_{23}) vs temperature variations for these devices is linear in the working range of the combustion chamber up to 1200 °C.

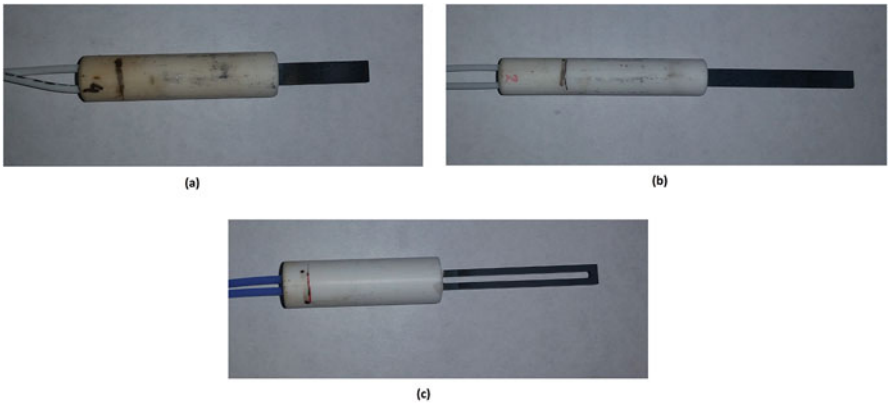

Fig. 5 Three commercial SN igniters

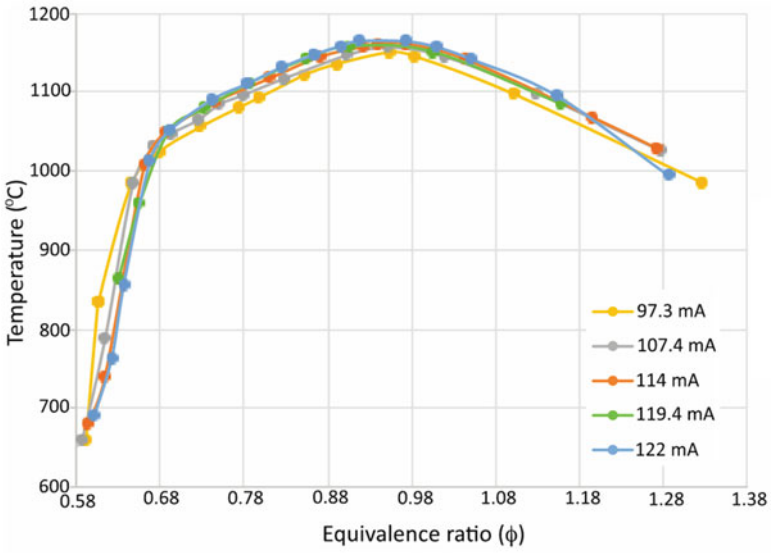

Fig. 6 Corrected flame temperature vs equivalence ratio at different gas flow rates for a sample of the Kyocera (a) sensor

4 Results

The resistance ratio was correlated to the equivalence ratio of the combustion system as shown in Fig. 6. Figure 6 shows that the flame temperatures varied not only with the variations in equivalence ratio but also with the variations in mass airflow rates and gas flow rates for the same value of equivalence ratio. These results were found to be in agreement with the study conducted by S. Prucker [22] for combustion of

premixed H_2/air flames. For the same value of ϕ, the flame temperature increased with the increase in fuel and gas flow rates. Higher gas flow rate resulted in an increase in heat generation as the combustion was not adiabatic and additional heat generation resulted in an increase in flame temperature. This was the reason for the increase in flame temperature at a specific value of equivalence ratio with increase in gas flow.

The mass airflow rate computed using a commercial MAF sensor was used to compensate the effect of increased fuel flow rate in the flame temperature for different equivalence ratios. Figure 6 shows the MAF rate compensated flame temperatures for different values of equivalence ratio. It can be observed that there is a reduction in the flame temperature variation at an equivalence ratio with different mass airflow rate and fuel flow rate. Higher errors were noticed for $\phi < 0.7$, and very low errors were noticed for ϕ between 0.7 and 1. Equivalence ratio between 0.7 and 1 is the working range for most of the combustion systems. Mathematical relationships can be derived for corrected flame temperature and equivalence ratio for two different regions of the stoichiometry using the plots 7 (Fig. 7).

The corrected flame temperature for different samples of the same sensor did not converge to a single curve. Rather they were separated from each other by some constant offsets. The temperature tolerance for Kyocera sensors was specified as $\pm 20\%$. And the difference in corrected curves for different sensors was found to be due to temperature tolerance of different sensors. However, the temperature difference between the corrected temperature curves for different sensors remained constant for ϕ between 0.7 and 1. These temperature variations for different samples of same sensor at a specific value of equivalence ratio are corrected by using the offset of resistance ratio at a temperature (Fig. 8).

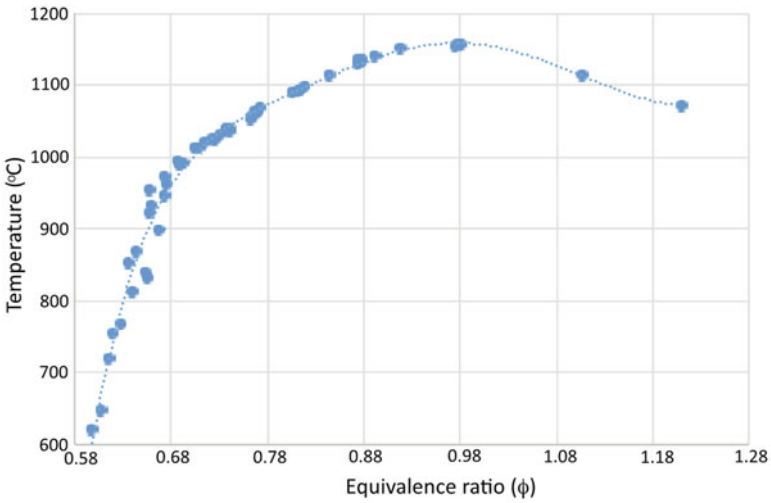

Fig. 7 Corrected flame temperature vs equivalence ratio for a sample of the Kyocera (a) sensor

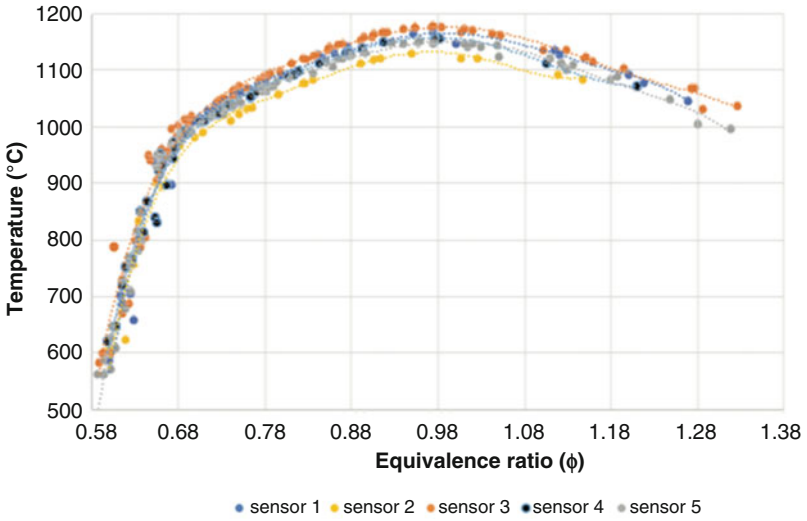

Fig. 8 Corrected flame temperature vs equivalence ratio for multiple samples of Kyocera (a) sensors

Steps in calibration of a reference flame temperature sensor:

1. Plot the flame temperature (T_f) vs equivalence ratio (ϕ) curves by keeping gas regulator current constant and varying the airflow of the system. Obtain multiple curves for different values of the gas regulator current.
2. Obtain the relationship for corrected flame temperature (T_c) by compensating flame temperature based on the mass airflow rate ($\dot{m}_a$) of the system.
3. Plot the corrected flame temperature vs equivalence ratio for the sensor, and obtain a calibration curve for the calculation of equivalence ratio based on corrected flame temperature for the leaner side of stoichiometry ($\phi = f_2(T_c)$; $\phi < 1$).

The calibration curve for the Kyocera (a) sensor is shown in Fig. 9. Figures 10, 11, and 12 show the comparison in the errors of the calculated equivalence ratio using the sensors and actual equivalence ratio for Kyocera (a) and (b) and CoorsTek sensor, respectively.

5 Performance Characteristics

The characteristics of the flame temperature sensor were analyzed considering the maximum allowable temperature tolerance of the sensor being 1200 °C for both the Kyocera and CoorsTek sensors. The average nominal resistance of the Kyocera sensor at 23 °C was taken as 50 Ω and that for the CoorsTek sensor was taken as 45 Ω. Also, all the results were verified within the range of ϕ between 0.6 and 1. Similarly, test range for the fuel flow rate was between 0.29 to 0.53 g/s, and the airflow rate was varied between the range 3.7 and 14.75 g/s.

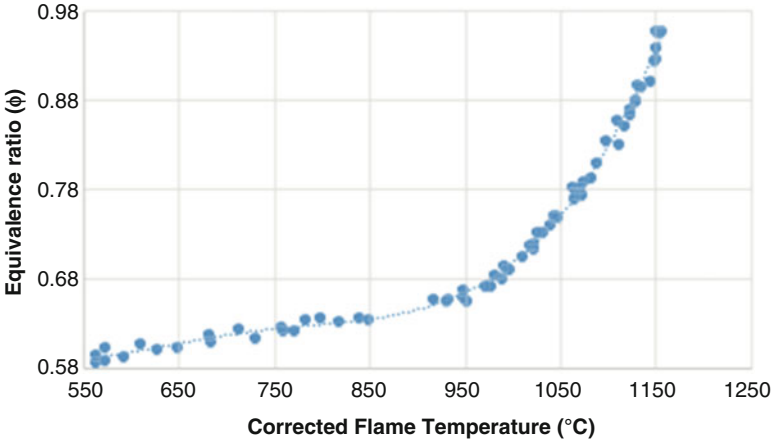

Fig. 9 Calibration curve for flame temperature sensor Kyocera (a) sensor

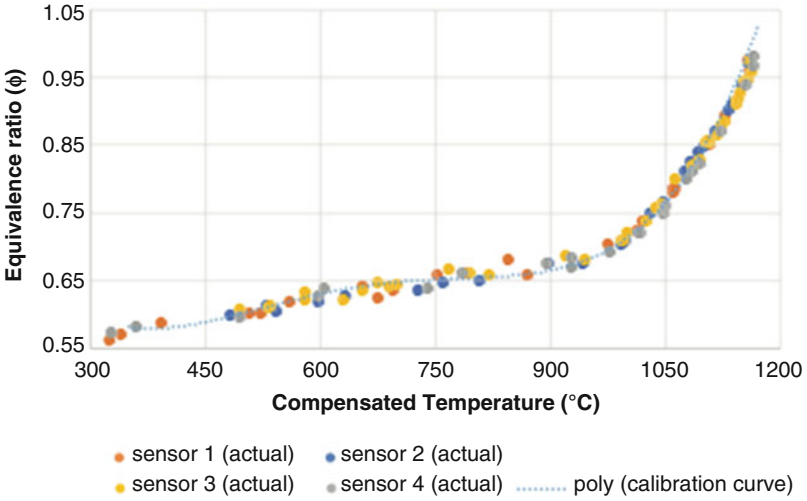

Fig. 10 Comparison of calculated ϕ with actual values for Kyocera (a) sensor

Range

Each type of sensors has been calibrated, and the results were verified using a multiple number of the same type of sensor over the range of ϕ between 0.6 and 1.

Resolution

The resolution of the sensor is related to resolution in the measurement of resistance value. Considering the resolution of ADC as 12 bits, the resolution of different sensors is tabulated in Table 1.

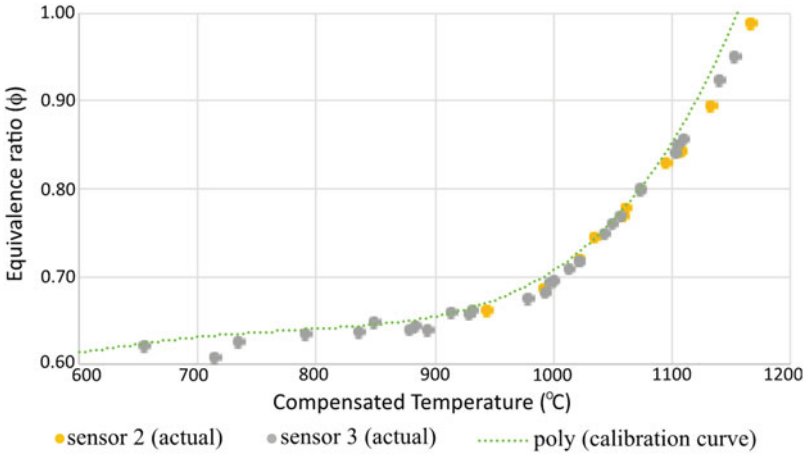

Fig. 11 Comparison of calculated ϕ with actual values for Kyocera (b) sensor

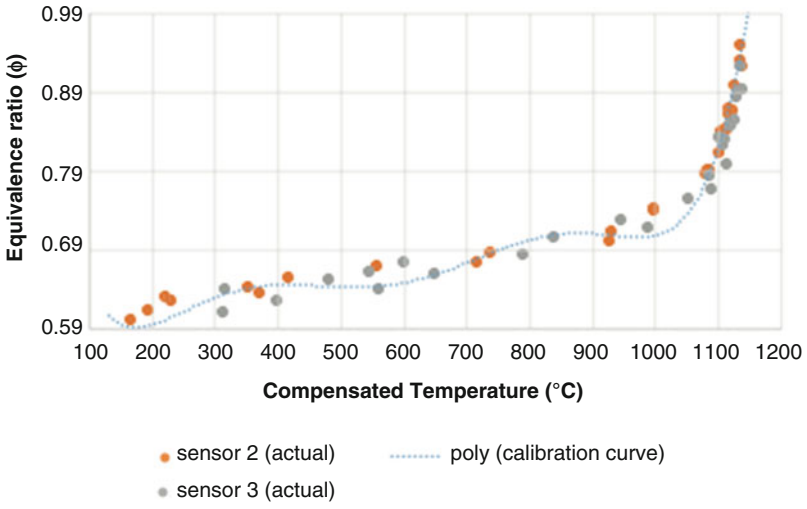

Fig. 12 Comparison of calculated ϕ with actual values for CoorsTek sensors

Table 1 Resolution of different sensors

Sensor	Resistance resolution	Resolution in ϕ ($\Delta\phi$)
Kyocera's long sensor	0.23 Ω	±0.00659
Kyocera's short sensor	0.23 Ω	±0.00748
CoorsTek sensor	0.15 Ω	±0.0106

Table 2 Sensitivity of different sensors

Sensor	Sensitivity (°C/$\phi = 1$)
Kyocera (b)	615
Kyocera (a)	652
CoorsTek	437

Table 3 Errors in different sensors

Sensor	Error in ϕ ($\pm\phi$)
Kyocera (b)	0.045
Kyocera (a)	0.04
CoorsTek	0.057

Table 4 Response time of different HSI sensors

Sensor	Rise time (s)	Settling time (s)
Kyocera (b)	22	25
Kyocera (a)	33	35
CoorsTek	25	28

Table 5 Percentage nonlinearity for different sensors

Sensor	Nonlinearity (%)
Kyocera (a)	25
Kyocera (b)	25
CoorsTek	30

Sensitivity

The calibration curve for the sensor was nonlinear, and the sensitivity varied along the working range of the sensor. The average sensitivity was calculated over this linear range of calibration curve. The average sensitivity is tabulated for each type of sensors in Table 2.

Accuracy and Precision

All three types of sensors were calibrated and tested for accuracy and precision for different values of air and gas flow rates. The maximum errors for different sensors are tabulated in Table 3.

Response Time

The response time of the sensor is presented based on rise time and settling time. Average rise time was calculated as the time required for flame temperature to reach from 10% to 90% of changes in temperature. Similarly, setting time was calculated as time required for flame temperature to reach within 5% of the steady-state error in temperature. The average response time for the three sensors for changes in ϕ, ($\Delta\phi = \pm 0.0$) was obtained experimentally and is shown in Table 4.

Linearity

The relationship between the corrected flame temperature and changes in equivalence ratio is highly nonlinear. The percentage nonlinearity for different sensors calculated using a best-fit straight-line method is shown in Table 5.

6 Conclusion

The flame temperature sensor discussed was designed to make use of existing hot surface igniters for dual functioning as an igniter and equivalence ratio calculation. The flame temperature sensor was calibrated to measure the equivalence ratio of the premixed air combustion system, along with the knowledge of mass airflow intake of the combustion system. The flame temperature sensor was also found to be dependent upon the combustion chamber setup. The variations in airflow and gas flow patterns of the combustion chamber required recalibration of the sensor. Therefore, any variations in gas air mixing pattern affects the output of the sensor, which makes the sensor output dependent upon the combustion chamber setup. The flame temperature sensor can be used as either a standalone sensor or can be easily integrated with other combustion control systems.

References

1. Holman JP (1994) Experimental methods for engineers. McGraw-Hill, New York, pp 1–616 Series in mechanical engineering
2. David R, Hunter IW (2005) A liquid-in-glass thermometer read by an interferometer. Sensors Actuators A Phys 121(1):31–34
3. Gaydon AG, Wolfhard HG (1979) Flames, their structure, radiation, and temperature. Halsted Press, Chapman and Hall Ltd., London
4. Strong HM, Bundy FP, Larson DA (1948) Temperature measurement on complex flames by sodium line reversal and sodium d line intensity contour studies. In: Symposium on combustion and flame, and explosion phenomena, vol 3, pp 641–647
5. Peter R, Childs N (2001) Practical temperature measurement. Butterworth-Heinemann, Oxford
6. Zhou Y, Zheng D (2006) Study on measurement of flame temperature using a linear CCD. In: Technology and Innovation Conference, ITIC 2006. International, Hangzhou, China
7. Alvarez-Herrera C, Moreno-Hernandez D, Barrientos-Garcia B (2008) Temperature measurement of an axisymmetric flame by using a Schlieren system. J Opt A Pure Appl Opt 10(10):104014
8. Donnelly VM, McCaulley JA (1990) Infrared-laser interferometric thermometry: a nonintrusive technique for measuring semiconductor wafer temperatures. J Vac Sci Technol A 8(1):84–92
9. Fristrom RM (1995) Flame structure and processes. Oxford University Press, New York
10. Copeland C, Friedman J, Renksizbulut M (2007) Planar temperature imaging using thermally assisted laser induced fluorescence of oh in a methane air flame. Exp Thermal Fluid Sci 31(6):221–236
11. Alaruri SD, Brewington AJ, Thomas M, Miller J et al (1993) High-temperature remote thermometry using laser-induced fluorescence decay lifetime measurements of y 2 o 3: Eu and yag: Tb thermographic phosphors. IEEE Trans Instrum Meas 42(3):735–739
12. Stones RB, Webb PJ (1993) The application of acoustic pyrometry to gas temperature measurement and mapping. In: IEEE Colloquium on ultrasound in the process industry, IET. pp 9–14
13. Kleppe J, Maskaly J, Beam G et al (1996) The application of image processing to acoustic pyrometry. Proc Int Conf on Image Processing 1:657–659
14. Moss B, Leen G, Lewis E, Bremer K, Niven A (2009) Temperature measurement of gases using acoustic means. In: 6th international multi-EEE conference on systems, signals and devices, SSD'09. pp 1–6

15. Marr MA, Wallace JS, Chandra S, Pershin L, Mostaghimi J (2010) A fast response thermocouple for internal combustion engine surface temperature measurements. Exp Therm Fluid Sci 34(2):183–189
16. Tagawa M, Ohta Y (1997) Two-thermocouple probe for fluctuating temperature measurement in combustion rational estimation of mean and fluctuating time constants. Combust Flame 109(4):549–560
17. Prudenziati M, Majni G (1973) Boron thermistors for high temperature measurements. IEEE Trans Ind Electron Control Instrum 30(1):33–39
18. Carvell RP (2000) Robust instrumentation for high accuracy temperature measurement. In: IEE seminar on advanced sensors and instrumentation systems for combustion processes (Ref. No. 2000/080). pp 10/1–10/4
19. Arai M, Kawata A (2001) Stability of high-temperature platinum resistance thermometers above 962 c up to 1200 c. Proc 41st SICE Annu Conf 1:507–509
20. Arai M, Yamazawa K (2004) High-temperature furnace controlled by a platinum resistance thermometer. Proc SICE Annu Conf 2:1172–1175
21. McAllister S, Chen JY, Fernandez-Pello AC (2011) Fundamentals of combustion processes. Springer, New York
22. Prucker S, Meier W, Stricker W (1994) A flat flame burner as calibration source for combustion research: Temperatures and species concentrations of premixed H2/air flames. Rev Sci Instrum 65(9):2908–2911
23. Law CK, Makino A, Lu TF (2006) On the off-stoichiometric peaking of adiabatic flame temperature. Combust Flame 145(4):808–819
24. Glassman I, Yetter RA, Glumac NG (2014) Combustion. Academic Press, Cambridge

Analytical Calculation of Induced Voltages of Uniform Eddy Current Probes Above a Moving Conductor

Siquan Zhang and Nathan Ida

1 Introduction

Eddy-current testing (ECT) techniques are widely used with advantages such as sensitivity to surface flaws in conductive structures. Depending on the method of inspection, an ECT probe can consist of a single coil serving as both exciting and receiving coil or one or more excitation coils with one or more pick-up coils. In conventional ECT testing, a cylindrical coil carrying AC current is placed in proximity to the conductive specimen, and the alternating current in the coil produces a changing magnetic field that interacts with the test specimen and generates eddy currents inside the conductor [1–3]. The change in eddy currents is monitored by observing the impedance variation of the coil affected by the eddy currents associated with the magnetic field [4–7].

A probe consisting of one or more exciting coils and one or more pick-up coils is also called a send-receive probe. The exciting coils are driven with a sinusoidal current, and the change in eddy currents inside the conductor is monitored by measuring the voltage induced in the pick-up coil. This makes the exciting magnetic flux independent of the exciting coil resistance. The induced magnetic flux can also be measured directly but to do so requires additional magnetic field sensors [8–10].

A uniform ECT probe consists of a wide rectangular exciting coil and a small pick-up coil. The wide rectangular exciting coil induces uniform eddy currents in the conductor, and the pick-up coil detects only the perpendicular component of the eddy currents. The probe has the advantage of being self-differential, self-nulling,

S. Zhang (✉)
Department of Electrical and Automation, Shanghai Maritime University, Shanghai, China

N. Ida
Department of Electrical and Computer Engineering, The University of Akron, Akron, OH, USA
e-mail: ida@uakron.edu

M. Jiang et al. (eds.), *The Proceedings of the International Conference on Sensing and Imaging*, Lecture Notes in Electrical Engineering 506,
https://doi.org/10.1007/978-3-319-91659-0_13

and lift-off noise free. By positioning the pick-up coil right under the exciting coil center, the probe can eliminate the influence of disrupting objects perpendicular to the uniform eddy current due to its self-differential feature, so it can be used to detect flaws in weld zones and material edges [11].

In this paper, a uniform ECT probe is placed above multilayer conductive plates, and the double Fourier transform method is introduced to evaluate and compare the voltages induced in the rectangular and cylindrical pick-up coils by calculating the incident and reflected magnetic field. The remainder of the paper is organized as follows. In Sect. 2, an AC-excited single-turn rectangular coil located above and perpendicular to the conductive plates is analyzed, and the z component of the magnetic flux density is derived by computing the incident and reflected magnetic fields. In Sect. 3, the expressions of the voltage induced in the cylindrical and rectangular pick-up coils are derived, by calculating the magnetic flux penetrating through the pick-up coils. In Sect. 4, the voltages induced in the coils at different exciting frequencies and moving speeds of the conductor are calculated and compared. The analytical calculated results are verified with experiments. The probes are also used to test the flaws in conductor. Finally, the conclusion is drawn in Sect. 5.

2 Theoretical Analysis

2.1 Analytical Model

Figure 1a shows a rectangular exciting filamentary coil located above a conductive plate. The coil is perpendicular to the plate with the center of the coil at (0, y_0, z_0). The surface of the conductor coincides with the $z = 0$ plane. The coil dimensions are $2a_1$ and $2b_1$. The conductive medium is assumed to be linear, isotropic, and homogeneous. The thickness, conductivity, and permeability of the plate are assumed to be d_1, σ_1, and μ_1, respectively. The plate is moving along the y direction at a speed v. The material below the plate is assumed to be half infinite; its conductivity and permeability are assumed to be σ_2 and μ_2. The exciting current in the coil is sinusoidal.

For analysis convenience, the entire space in Fig. 1 is divided into three regions:

1. Region 0 ($z > 0$): In this region, the incident magnetic flux density B_i generated by the exciting current and the reflecting magnetic flux density B_r generated by induced eddy currents exist simultaneously. The incident magnetic flux density B_i can be expressed by the vector potential A_i as follows:

$$\nabla \times \nabla \times A_\mathrm{i} = \mu_0 J \tag{1}$$

$$B_\mathrm{i} = \nabla \times A_\mathrm{i} \tag{2}$$

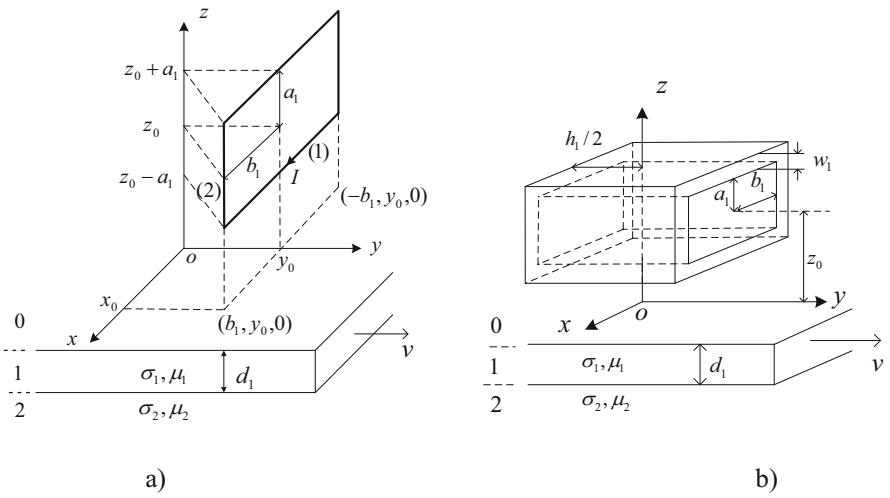

Fig. 1 (**a**) Single-turn and (**b**) multi-turn rectangular exciting coil located above conductive plates

The reflected magnetic flux density B_r satisfies the following:

$$\nabla \times B_r = 0 \tag{3}$$

$$\nabla^2 \times B_r = 0 \tag{4}$$

2. Region 1 ($-d_1 < z < 0$): The magnetic flux density B_1 in this region satisfies the following:

$$\nabla^2 B_1 - \sigma_1 \mu_1 v \frac{\partial B_1}{\partial y} - j\omega\sigma_1\mu_1 B_1 = 0 \tag{5}$$

$$\nabla \cdot B_1 = 0 \tag{6}$$

3. Region 2 ($z < -d_1$): The magnetic flux density B_2 in this region satisfies the following:

$$\nabla^2 B_2 - j\omega\sigma_2\mu_2 B_2 = 0 \tag{7}$$

$$\nabla \cdot B_2 = 0 \tag{8}$$

The double Fourier transform and inverse transform methods are introduced to solve the above equations:

$$b(\xi, \eta, z) = \int_{-\infty}^{\infty}\int_{-\infty}^{\infty} B(x, y, z) \cdot e^{j(x\xi + y\eta)} dx dy \tag{9}$$

$$B(x, y, z) = \frac{1}{4\pi^2}\int_{-\infty}^{\infty}\int_{-\infty}^{\infty} b(\xi, \eta, z) \cdot e^{-j(x\xi+y\eta)} d\xi d\eta \tag{10}$$

Where ξ and η are the integration variables used in the double Fourier transform.

2.2 Incident Magnetic Flux Density

As shown in Fig. 1a, the single filamentary rectangular coil consists of four finite length wires; it is analyzed as follows:

Solving (1), the vector potential for an arbitrary point $p(x,y,z)$ in region 0 generated by the source point (x',y',z') in the coil can be written as:

$$A(x, y, z) = \frac{\mu_0}{4\pi}\int_v \frac{J\left(x', y', z'\right) du'}{R} \tag{11}$$

where J is the current density, u is the exciting coil, and R is the distance from $p(x,y,z)$ to the point source (x',y',z'):

$$R = \sqrt{(x - x')^2 + (y - y')^2 + (z - z')^2} \tag{12}$$

The vector potential in the region $z < z_0$ can be obtained by applying the Fourier transform to (11):

$$\begin{aligned} a(\xi, \eta, z) &= \frac{\mu_0}{4\pi}\int_v J\left(x', y', z'\right)\left\{\int_{-\infty}^{\infty}\int_{-\infty}^{\infty}\frac{1}{R}e^{j(x\xi+y\eta)}dxdy\right\}du' \\ &= \frac{\mu_0}{2}\int_v J\left(x', y', z'\right)e^{j(\xi x'+\eta y')}\frac{1}{\sqrt{\xi^2+\eta^2}}e^{-|z-z_0|\sqrt{\xi^2+\eta^2}}du' \end{aligned} \tag{13}$$

The components of the incident magnetic flux density can be obtained by applying the Fourier transform to (2):

$$b_x = -j\eta a_z - \frac{\partial a_y}{\partial z}, \quad b_y = \frac{\partial a_x}{\partial z} + j\xi a_z, \quad b_z = -j\xi \cdot a_y + j\eta \cdot a_x \tag{14}$$

As shown in Fig. 1a, the wire (1) of the rectangular coil, parallel to the x axis, satisfies $J(x', y', z') = I$, $y' = y_0$, and $z - z_0 < 0$. Substituting these into (13), the x component of the vector potential is obtained:

$$\begin{aligned} a_x &= \frac{\mu_0}{2}\int_v J\left(x', y', z'\right)e^{j(\xi x'+\eta y')}\frac{1}{\sqrt{\xi^2+\eta^2}}e^{-|z-z_0|\sqrt{\xi^2+\eta^2}}du' \\ &= \frac{\mu_0 I}{2}\frac{e^{(z-z_0)\sqrt{\xi^2+\eta^2}}}{\sqrt{\xi^2+\eta^2}}e^{j\eta y_0}\int_{-x_0}^{x_0}e^{j\xi x'}dx' = \frac{\mu_0 I\sin(\xi x_0)e^{j\eta y_0}e^{(z-z_0)\sqrt{\xi^2+\eta^2}}}{\xi\sqrt{\xi^2+\eta^2}} \end{aligned} \tag{15}$$

The single-turn rectangular coil shown in Fig. 1a is perpendicular to the y axis and hence only has x component a_x and z component of the vector potential. Therefore, the z component of the magnetic flux density in (14) can be written directly:

$$b_z = j\eta a_x \tag{16}$$

Substituting (15) into (16), the z component of the incident magnetic flux density in region 0 becomes:

$$\begin{aligned} b_{iz} &= j\eta \left\{ a_x \left(b_1, y_0, z_0 + a_1 \right) - a_x \left(b_1, y_0, z_0 - a_1 \right) \right\} \\ &= -\frac{j\mu_0 I \eta \sin(b_1\xi) e^{jy_0\eta} \left(e^{a_1\sqrt{\xi^2+\eta^2}} - e^{-a_1\sqrt{\xi^2+\eta^2}} \right) e^{(z-z_0)\sqrt{\xi^2+\eta^2}}}{\xi\sqrt{\xi^2+\eta^2}} \end{aligned} \tag{17}$$

We have the general solution expression for the z component of the incident magnetic flux density as:

$$b_{iz} = C_{iz} e^{z\sqrt{\xi^2+\eta^2}} \tag{18}$$

Where the coefficient of the incident magnetic flux density is:

$$C_{iz} = -\frac{j\mu_0 I \eta \sin\left(b_1\xi\right) e^{jy_0\eta} \left(e^{a_1\sqrt{\xi^2+\eta^2}} - e^{-a_1\sqrt{\xi^2+\eta^2}} \right) e^{-z_0\sqrt{\xi^2+\eta^2}}}{\xi\sqrt{\xi^2+\eta^2}} \tag{19}$$

2.3 *Reflected Magnetic Flux Density*

Applying the Fourier transform to (4), the reflected magnetic flux density in region 0 can be written as:

$$\frac{\partial^2 b_r}{\partial z^2} - \left(\xi^2 + \eta^2 \right) b_r = 0 \tag{20}$$

Similarly, applying the Fourier transform to (5) and (7), the magnetic flux density in regions 1 and 2 can be obtained as:

$$\frac{\partial^2 b_1}{\partial z^2} - \left(\xi^2 + \eta^2 - j\sigma_1\mu_1 v\eta + j\omega\sigma_1\mu_1 \right) b_1 = 0 \tag{21}$$

$$\frac{\partial^2 b_2}{\partial z^2} - \left(\xi^2 + \eta^2 + j\omega\sigma_2\mu_2 \right) b_2 = 0 \tag{22}$$

The normal component of B and the tangential component of H must be continuous at the $z = 0$ and $z = -d_1$ planes.

Continuity of B_z:

$$b_{iz} + b_{rz} = b_{1z} \quad (z = 0) \tag{23}$$

$$b_{1z} = b_{2z} \quad (z = -d) \tag{24}$$

Continuity of H_x:

$$\frac{(b_{ix} + b_{rx})}{\mu_0} = \frac{b_{1x}}{\mu_1} \quad (z = 0) \tag{25}$$

$$\frac{b_{1x}}{\mu_1} = \frac{b_{2x}}{\mu_2} \quad (z = -d) \tag{26}$$

Continuity of H_y:

$$\frac{\left(b_{iy} + b_{ry}\right)}{\mu_0} = \frac{b_{1y}}{\mu_1} \quad (z = 0) \tag{27}$$

Due to the fact that $\nabla \cdot J = 0$ inside the conductor, no z component of current density J_z is present in regions 1 and 2:

$$\xi b_{1y} = \eta b_{1x} \tag{28}$$

$$\xi b_{2y} = \eta b_{2x} \tag{29}$$

According to (3):

$$-j\eta b_{rz} = \frac{\partial b_{ry}}{\partial z} \tag{30}$$

$$-j\xi b_{rz} = \frac{\partial b_{rx}}{\partial z} \tag{31}$$

According to (6) and (8):

$$-j\xi b_{1x} - j\eta b_{1y} + \frac{\partial b_{1z}}{\partial z} = 0 \tag{32}$$

$$-j\xi b_{2x} - j\eta b_{2y} + \frac{\partial b_{2z}}{\partial z} = 0 \tag{33}$$

Let:

$$\xi = \varsigma\cos\phi,\quad \eta = \varsigma\sin\phi,\quad \varsigma = \sqrt{\xi^2+\eta^2},\quad \frac{\mu_1\varsigma}{\mu_2\gamma_1} = m,\quad \frac{1+m}{1-m} = P,$$
$$\frac{\mu_0\gamma_1}{\mu_1\varsigma} = n,\quad \frac{(n+1)+(1-n)Pe^{2\gamma_1 d}}{1-n+(1+n)Pe^{2\gamma_1 d}} = \kappa,\quad \gamma_1 = \sqrt{\xi^2+\eta^2-j\sigma_1\mu_1 v\eta+j\omega\sigma_1\mu_1} \tag{34}$$

Solving the above equations, the coefficient of the reflected magnetic flux density is obtained as:

$$D_{rz} = \kappa\cdot C_{iz} = -\frac{j\mu_0 I\eta\kappa\sin(b_1\xi)\,e^{jy_0\eta}\left(e^{a_1\sqrt{\xi^2+\eta^2}}-e^{-a_1\sqrt{\xi^2+\eta^2}}\right)e^{-z_0\sqrt{\xi^2+\eta^2}}}{\xi\sqrt{\xi^2+\eta^2}} \tag{35}$$

The reflected magnetic flux density can be obtained as:

$$b_{rz} = D_{rz}e^{-z\sqrt{\xi^2+\eta^2}} = -\frac{j\mu_0 I\eta\kappa\sin(b_1\xi)e^{jy_0\eta}\left(e^{a_1\sqrt{\xi^2+\eta^2}}-e^{-a_1\sqrt{\xi^2+\eta^2}}\right)e^{-(z+z_0)\sqrt{\xi^2+\eta^2}}}{\xi\sqrt{\xi^2+\eta^2}} \tag{36}$$

Applying the Fourier inverse transform to (36), the z component of the reflected magnetic flux density of the single-turn rectangular coil in region 0 becomes:

$$B_{rz} = -\frac{j\mu_0 I}{4\pi^2}\int_{-\infty}^{\infty}\int_{-\infty}^{\infty}\frac{\kappa\eta}{\xi\varsigma}\sin(b_1\xi)\left(e^{a_1\varsigma}-e^{-a_1\varsigma}\right)e^{jy_0\eta}e^{-(z+z_0)\varsigma}e^{-j(\xi x+\eta y)}d\xi d\eta \tag{37}$$

2.4 Magnetic Flux Density of Multi-turn Rectangular Exciting Coil

Figure 1b shows the arrangement of a multi-turn rectangular exciting coil located above the conductive plates. The coil contains N_1 turns.

By integrating (37) on the width and length of the multi-turn rectangular coil shown in Fig. 2, where y_0 shown in Fig. 1a coincides with the origin of the system of coordinates, the reflected magnetic flux density generated from the multi-turn exciting coil can be obtained as:

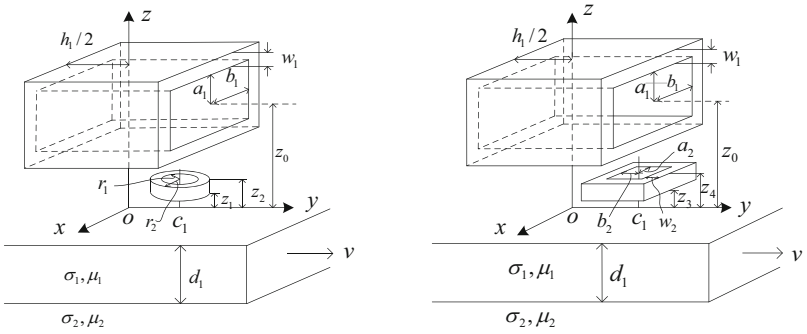

Fig. 2 Configuration of multi-turn rectangular coil. (**a**) Cylindrical and (**b**) rectangular pick-up coil

$$B_{rz}^{\text{total}} = -\frac{j\mu_0 I N_1}{4\pi^2 w_1 h_1} \int_{-\infty}^{\infty}\int_{-\infty}^{\infty} \frac{\kappa\eta}{\xi\varsigma} \left\{ \int_0^{w_1} \sin\left[(b_1+p)\,\xi\right] \left[e^{(a_1+p)\varsigma} - e^{-(a_1+p)\varsigma}\right] dp \right\}$$
$$\cdot \left\{ \int_{-h_1/2}^{h_1/2} e^{j\eta y_0} dy_0 \right\} e^{-(z+z_0)\varsigma} e^{-j(\xi x+\eta y)} d\xi\, d\eta = -\frac{j\mu_0 I N_1}{2\pi^2 w_1 h_1} \int_{-\infty}^{\infty}\int_{-\infty}^{\infty} \frac{\kappa k_1}{\xi\varsigma} \sin\left(\frac{\eta h_1}{2}\right)$$
$$\cdot\, e^{-(z+z_0)\varsigma} e^{-j(\xi x+\eta y)} d\xi\, d\eta \tag{38}$$

where:

$$\int_{-h_1/2}^{h_1/2} e^{j\eta y_0} dy_0 = \frac{2}{\eta} \sin\left(\frac{\eta h_1}{2}\right) \tag{39}$$

$$k_1 = \int_0^{w_1} \sin\left[(b_1+p)\,\xi\right] \cdot \left[e^{(a_1+p)\varsigma} - e^{-(a_1+p)\varsigma}\right] dp = -\int_0^{w_1} \sin\left[(b_1+p)\,\xi\right]$$
$$e^{-(a_1+p)\varsigma} dp$$
$$= \left[\frac{\varsigma \sin\xi(b_1+w_1) - \xi\cos\xi(b_1+w_1)}{\xi^2+\varsigma^2}\right] e^{\varsigma(a_1+w_1)} - \left[\frac{\varsigma\sin\xi b_1 - \xi\cos\xi b_1}{\xi^2+\varsigma^2}\right] e^{\varsigma a_1}$$
$$+ \left[\frac{\varsigma \sin\xi(b_1+w_1) + \xi\cos\xi(b_1+w_1)}{\xi^2+\varsigma^2}\right] e^{-\varsigma(a_1+w_1)} - \left[\frac{\varsigma\sin\xi b_1 + \xi\cos\xi b_1}{\xi^2+\varsigma^2}\right] e^{-\varsigma a_1} \tag{40}$$

3 Variation of Induced Voltage in the Pick-Up Coils

3.1 Magnetic Flux Penetrating Through the Cylindrical Coil

Figure 2a, b show the arrangement of a multi-turn rectangular exciting coil and one cylindrical and one rectangular pick-up coil located above the conductive plates. The axis of the pick coils is located at $(0, c_1)$. The turns of the exciting coil and cylindrical and rectangular pick-up coils are N_1, N_2, and N_3, respectively.

The reflected magnetic flux penetrating through the multi-turn cylindrical pick-up coil shown in Fig. 2a can be obtained by first assuming a single-turn circular pick-up coil with radius r_0 located at $(0, c_1, z')$ and then performing the coordinate transformation $x = r_0 cos\theta$ and $y = r_0 sin\theta + c_1$. The reflected magnetic flux penetrating through a single-turn circular pick-up coil is obtained by integrating (38) on its circular area as follows:

$$\varphi_{rzc} = \int_0^{r_0} r dr \int_0^{2\pi} B_{rz}^{\text{total}}\big|_{z=z'} d\theta = -\frac{j\mu_0 I N_1}{\pi w_1 h_1} \int_{-\infty}^{\infty}\int_{-\infty}^{\infty} \frac{\kappa k_1}{\xi \varsigma^2} \sin\left(\frac{\eta h_1}{2}\right) e^{-j\eta c_1} r_0 J_1(r_0\varsigma) e^{-(z'+z_0)\varsigma} d\xi d\eta \tag{41}$$

The reflected magnetic flux penetrating through the multi-turn cylindrical pick-up coil shown in Fig. 2a is obtained by integrating (41) on its radial direction $(r_1 \to r_2)$ and axial direction $(z_1 \to z_2)$ as follows:

$$\begin{aligned} \varphi_{rzc}^{\text{total}} &= \frac{N_2}{(z_2-z_1)(r_2-r_1)} \int_{r_1}^{r_2} dr_0 \int_{z_1}^{z_2} \varphi_{rzc} dz_1 \\ &= \frac{-j\mu_0 I N_1 N_2}{\pi w_1 h_1 (r_2-r_1)(z_2-z_1)} \int_{-\infty}^{\infty}\int_{-\infty}^{\infty} \frac{\kappa k_1}{\xi \varsigma^5} \sin\left(\frac{\eta h_1}{2}\right) e^{-j\eta c_1} \cdot Int(r_1\varsigma, r_2\varsigma) \\ &\quad \left[e^{-\varsigma(z_0+z_1)} - e^{-\varsigma(z_0+z_2)}\right] d\xi d\eta \end{aligned} \tag{42}$$

where:

$$Int(x_1, x_2) = \int_{x_1}^{x_2} x J_1(x) dx \tag{43}$$

$$\int_{z_1}^{z_2} e^{-z'\varsigma} dz' = \frac{e^{-\varsigma z_1} - e^{-\varsigma z_2}}{\varsigma} \tag{44}$$

3.2 Magnetic Flux Penetrating Through the Rectangular Coil

Figure 2b shows a multi-turn rectangular pick-up coil located below the exciting coil and its central axis perpendicular at (0, c_1); the number of turns is N_3. First, we obtain the reflected magnetic flux penetrating through a single-turn rectangular pick-up coil with dimensions $2a_2$ and $2b_2$ and located at (0, c_1, z') by integrating (38) on its rectangular area:

$$\begin{aligned}\varphi_{rzr} &= \int_{-a_2}^{a_2} dx \int_{c_1-b_2}^{c_1+b_2} B_{rz}^{\text{total}}\big|_{z=z'} dy = -\frac{j\mu_0 I N_1}{2\pi^2 w_1 h_1} \int_{-\infty}^{\infty}\int_{-\infty}^{\infty} \frac{\kappa k_1}{\xi\varsigma} \sin\left(\frac{\eta h_1}{2}\right) \cdot e^{-(z'+z_0)\varsigma} \\ &\quad \cdot \left\{\int_{-a_2}^{a_2} e^{-j\xi x} dx\right\} \\ &\left\{\int_{c_1-b_2}^{c_1+b_2} e^{-j\eta y} dy\right\} d\xi d\eta = -\frac{2j\mu_0 I N_1}{\pi^2 w_1 h_1} \int_{-\infty}^{\infty}\int_{-\infty}^{\infty} \frac{\kappa k_1}{\xi^2\eta\varsigma} \sin\left(\frac{\eta h_1}{2}\right) e^{-j\eta c_1} \cdot e^{-(z'+z_0)\varsigma} \\ &\quad \cdot \sin(\xi a_2) \sin(\eta b_2)\, d\xi d\eta\end{aligned} \tag{45}$$

Then the reflected magnetic flux penetrating through the multi-turn rectangular pick-up coil is obtained by integrating (45) on the coil width and length as:

$$\begin{aligned}\varphi_{rzr}^{\text{total}} &= \frac{N_3}{w_2(z_4-z_3)} \int_{z_3}^{z_4} dz' \int_0^{w_2} \varphi_{rzr}\, dp \\ &= \frac{-j2\mu_0 I N_1 N_3}{\pi^2 w_1 h_1 w_2 (z_4-z_3)} \int_{-\infty}^{\infty}\int_{-\infty}^{\infty} \frac{\kappa k_1}{\xi^2\eta\varsigma} \sin\left(\frac{\eta h_1}{2}\right) e^{-j\eta c_1} e^{-z_0\varsigma} \left\{\int_{z_3}^{z_4} e^{-\varsigma z'} dz'\right\} \\ &\quad \cdot \left\{\int_0^{w_2} \sin[\xi(a_2+p)] \sin[\eta(b_2+p)]\, dp\right\} d\xi d\eta \\ &= \frac{-j2\mu_0 I N_1 N_3}{\pi^2 w_1 h_1 w_2 (z_4-z_3)} \int_{-\infty}^{\infty}\int_{-\infty}^{\infty} \frac{\kappa k_1 k_2}{\xi^2\eta\varsigma^2} \sin\left(\frac{\eta h_1}{2}\right) e^{-j\eta c_1} e^{-z_0\varsigma} \cdot \left(e^{-\varsigma z_3} - e^{-\varsigma z_4}\right) d\xi d\eta\end{aligned} \tag{46}$$

where:

$$\int_{z_4}^{z_4} e^{-z'\varsigma} dz' = \frac{e^{-\varsigma z_3} - e^{-\varsigma z_4}}{\varsigma} \tag{47}$$

$$\begin{aligned}k_2 &= \int_0^{w_2} \sin[\xi(a_2+p))] \sin[\eta(b_2+p)]\, dp \\ &= \frac{\sin[a_2\xi - b_2\eta + (\xi-\eta)w_2] - \sin(a_2\xi - b_2\eta)}{2(\xi-\eta)} + \frac{\sin(a_2\xi + b_2\eta) - \sin[a_2\xi + b_2\eta + (\xi+\eta)w_2]}{2(\xi+\eta)}\end{aligned} \tag{48}$$

3.3 Variation of Induced Voltage in the Pick-up Coil

The relationship between the magnetic flux ϕ penetrating through the pick-up coil and the voltage V induced in the coil is:

$$V = -\frac{d\varphi}{dt} = -j\omega\varphi \tag{49}$$

The voltage induced in the cylindrical pick-up coil can be obtained as:

$$V_c = \frac{-\omega\mu_0 I N_1 N_2}{\pi w_1 h_1 (r_2 - r_1)(z_2 - z_1)} \int_{-\infty}^{\infty}\int_{-\infty}^{\infty} \frac{\kappa k_1}{\xi\varsigma^5} \sin\left(\frac{\eta h_1}{2}\right) e^{-j\eta c_1} \cdot Int\,(r_1\varsigma, r_2\varsigma) \cdot \left[e^{-\varsigma(z_0+z_1)} - e^{-\varsigma(z_0+z_2)}\right] d\xi\, d\eta \tag{50}$$

Similarly, the voltage induced in the rectangular pick-up coil can be obtained as:

$$V_r = \frac{-2\omega\mu_0 I N_1 N_3}{\pi^2 w_1 h_1 w_2 (z_4 - z_3)} \int_{-\infty}^{\infty}\int_{-\infty}^{\infty} \frac{\kappa k_1 k_2}{\xi^2\eta\varsigma^2} \sin\left(\frac{\eta h_1}{2}\right) e^{-j\eta c_1} \cdot \left[e^{-\varsigma(z_0+z_3)} - e^{-\varsigma(z_0+z_4)}\right] d\xi\, d\eta \tag{51}$$

Because we only consider the reflected magnetic flux in deriving the induced voltage expressions (50) and (51), the calculated results are variations of voltage induced in pick-up coil due to eddy currents generated in the conductor.

4 Results

The analytical results of the induced voltage in the cylindrical and rectangular pick-up coils can be calculated using Wolfram Mathematica according to (50) and (51). The parameters of the coils and conductive plates are given in Tables 1 and 2, respectively.

Table 1 Parameters of the coils

		Pick-up coil			
Excitation coil		Cylindrical		Rectangular	
a_1 (mm)	5	r_2 (mm)	9	a_2 (mm)	6
b_1 (mm)	12	r_1 (mm)	7.9	b_2 (mm)	6
z_0 (mm)	11.9	z_1 (mm)	1.2	z_3 (mm)	1.2
w_1 (mm)	0.5	z_2 (mm)	5.2	z_4 (mm)	5.2
h_1 (mm)	24	c_1 (mm)	5	w_2 (mm)	1.5
c_1 (mm)	5	N_2	100	N_3	100
N_1	420				
Current (mA)	100				

Table 2 Parameters of the conductive plates

d_1 (mm)	1
σ_1 (S/m)	3.6×10^7
σ_2 (S/m)	0
μ_{r1}, μ_{r2}	1

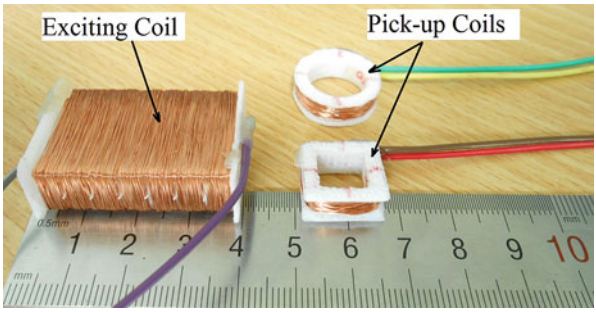

Fig. 3 The fabricated exciting and pick-up coils

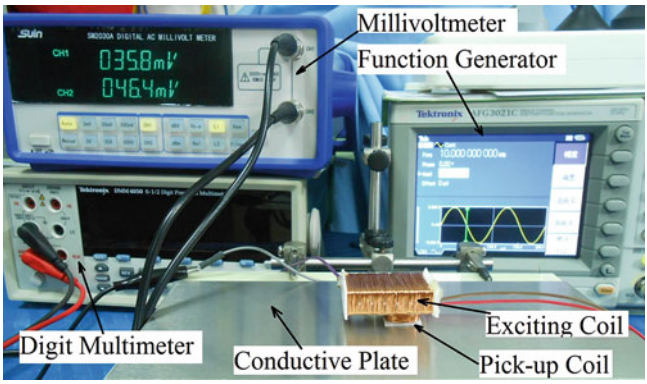

Fig. 4 Experimental setup

The cylindrical and rectangular pick-up coils are given same number of turns and are given dimensions to let them have the same upper and lower surface area, so we can compare the voltages induced in them under the same conditions. The upper plate is assumed to be made of aluminum, 1 mm in thickness. The fabricated coils are shown in Fig. 3, and the experimental setup is shown in Fig. 4. The exciting sinusoidal signal is generated by a function generator and then amplified with a power amplifier. The voltage induced in the pick-up coils is measured with a millivoltmeter.

Here we consider the condition of a single-layer conductor. In Fig. 2, if the axis of the pick-up coil coincides with the z axis and the conductive plate is without defect, the uniform eddy currents induced in the plate will generate a net zero magnetic flux penetrating through the pick-up coil, so the induce voltage in pick-up coil is zero. Here we set the distance between the axis of the pick-up coil and z axis as 5 mm. Figure 5 shows results of the induced voltage calculated and measured

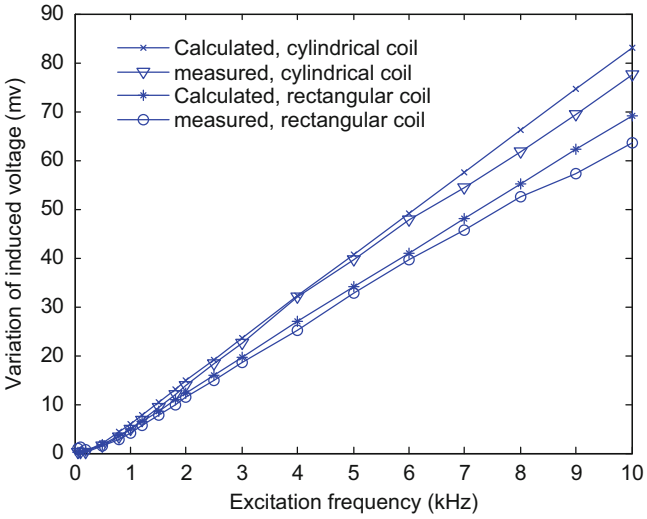

Fig. 5 The variation of induced voltage in the cylindrical coil and rectangular coil calculated and measured at different exciting frequencies

from the cylindrical and rectangular pick-up coils, respectively, at different exciting frequencies. The analytical results are obtained as the square root of the sum of squares of the calculated real and imaginary parts using (50) and (51).

In experiments, the thickness of the single-layer conductive plate is also 1 mm. The central axes of the pick-up coils are perpendicular at (0, 5). The exciting current is 100 mA. The measured quantities in the experiments are the effective values of voltage induced in the pick-up coils. The variation of the induced voltage in the pick-up coils is obtained by subtracting the measured value when the probe is above the plate from the measured value when the probe is in air. It can be seen from Fig. 5 that the variations of induced voltage in the two pick-up coils increase with frequency, but the cylindrical coil has a larger variation than the rectangular coil at the same frequency.

The relationship between the induced voltage variation and the moving speed of the conductor was also evaluated analytically and experimentally. The induced voltage variations are calculated and measured at speeds from $v = 0$ to $v = 25$ m/s. The effective value of the exciting current is 200 mA, the excitation frequency is fixed at 2 kHz, and the thickness of the aluminum plate is 2 mm. The experimental setup is shown in Fig. 6, where the conductive plate is rotated by a speed adjustable motor, so we can control the rotation rate to adjust the linear speed of the conductor and obtain an approximate moving speed of the conductor. To avoid rubbing between the coils and the conductive plate, the distances of z_1, z_2, and z_0 in Table 1 are increased to 4.2, 8.2, and 14.9 mm, respectively, and they are used in both the analytical calculations and experiments.

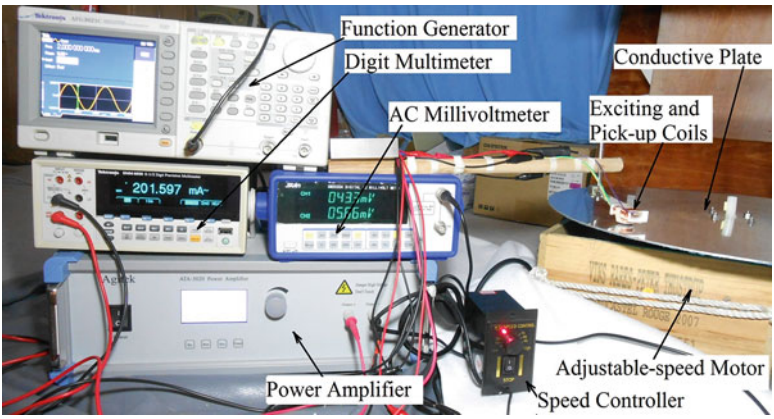

Fig. 6 Experimental setup for speed characterization of the moving conductor

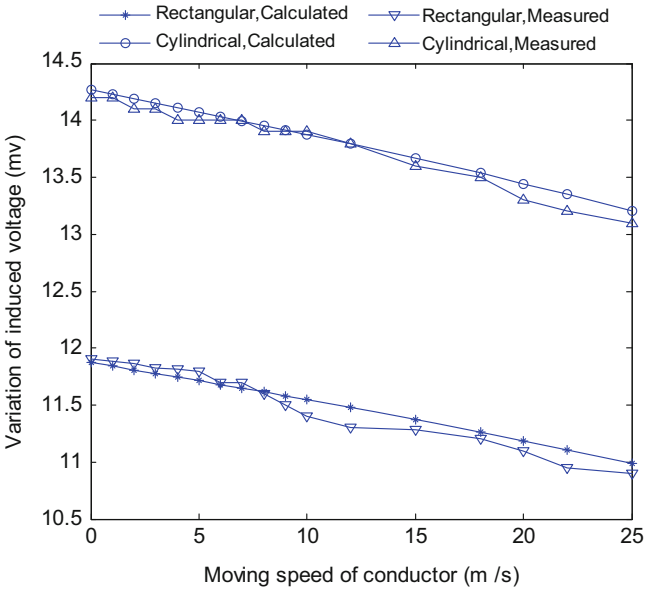

Fig. 7 Variation of induced voltage in the pick-up coils at different moving speed of conductor

The results are shown in Fig. 7. The voltages induced in the two coils both decrease as the speed of the conductor increases. At the same moving speed of the conductor, a larger variation in the induced voltage is observed in the cylindrical coil compared to the rectangular coil.

The designed coils are also used to test electro-discharge machined (EDM) slit flaws in the aluminum plate. The slit flaws shown in Fig. 8 are 0.5 mm wide and 0.2, 0.5, 0.8, 1, 1.2, 1.5, 1.8, 2, 2.2, 2.5, 2.8, and 3 mm deep from left to right. The

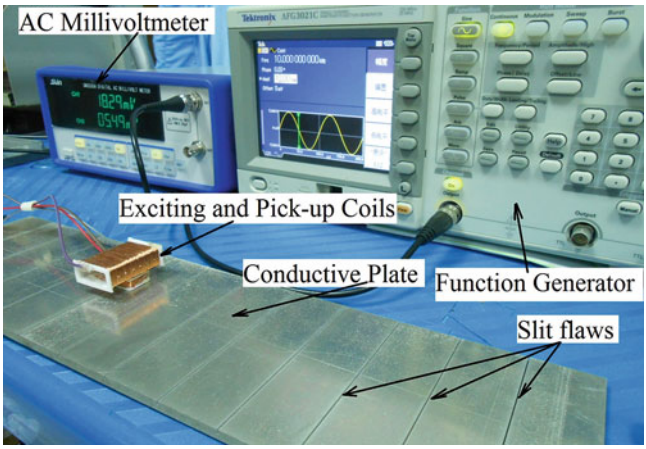

Fig. 8 The experimental setup for testing slit flaws of different depths

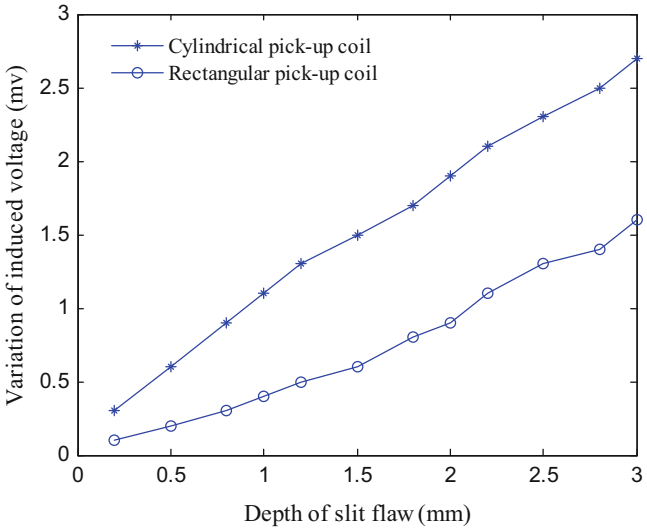

Fig. 9 Variation of induced voltages in cylindrical and rectangular pick-up coils for different depths of slit flaws

induced voltages are measured with a millivoltmeter when the coil is located above the slit flaws of different depths. The excitation frequency and voltage are fixed at 10 kHz and 10 V, respectively. The distance from the center of the pick-up coil to the center of the exciting coil (z axis) is 5 mm. The results shown in Fig. 9 were obtained by subtracting the measured voltages when coil is above the slit flaw from the measured value when the coil is above the conductor without flaws. It can be

seen from Fig. 9 that the variations of induced voltage in the pick-up coils both increase with the depth of slits, but larger variations are obtained in the cylindrical coil than in the rectangular coil for slit flaws of the same depth.

5 Conclusions

In this article, we start from Maxwell equation to obtain governing equations for an analytical model of the uniform send-receive ECT probe. The double Fourier transform method and the magnetic vector potential are introduced to solve the problem, and the components of the magnetic flux density in the region above the conductive plate are derived by computing the incident and reflected magnetic flux density. The induced voltages in the cylindrical and rectangular pick-up coils are calculated when the probes are used at different exciting frequencies and moving speeds of the conductor. The analytical calculated results agree well with experimental results.

The calculated and measured results demonstrate that the uniform ECT probes are sensitive to the variation of excitation and conductive parameters; the cylindrical pick-up coil is more sensitive to the changing magnetic field and induces larger voltages than the rectangular pick-up coil when they are applied under identical conditions. The uniform probes and analytical model can be used as a forward model in conductive material characterization and defect quantitative inversion.

Acknowledgment The authors would like to acknowledge the financial support by the National Natural Science Foundation of China (51175321) and the Shanghai Maritime University (20130463).

References

1. Dodd CV, Deeds WE (1968) Analytical solutions to eddy current probe coil problems. J Appl Phys 39(6):2829–2838
2. Theodoulidis T, Poulakis N, Dragogias A (2010) Rapid computation of eddy current signals from narrow cracks. NDT E Int 43(1):13–19
3. Li G, Huang P, Chen P, Hou D, Zhang G, Zhou Z (2010) Quantitative nondestructive estimation of deep defects in conductive structures. Int J Appl Electromagnetics Mech 33(3):1273–1278
4. Theodoulidis T, Kriezis E (2005) Series expansions in eddy current nondestructive evaluation models. J Mater Process Technol 161(1–2):343–347
5. Luquire JW, Deeds WE, Dodd CV (1970) Alternating current distribution between planar conductors. J Appl Phys 41(10):3983–3991
6. Burke SK, Theodoulidis TP (2004) Impedance of a horizontal coil in a borehole: a model for eddy-current bolthole probes. J Phys D Appl Phys 37(3):485–494
7. Zhang D, Yu Y, Chao L, Tian G (2015) Thickness measurement of multi-layer conductive coatings using multifrequency eddy current techniques. Nondestructive Test Eval:1–18
8. Laurinavičius L (2011) Helicon resonator based strong magnetic field sensor. Meas Sci Rev 11(11):149–153

9. Hesse O, Pankratyev S (2005) Usage of magnetic field sensors for low frequency eddy current testing. Meas Sci Rev 5(3):86–93
10. Matkova V, Strapacova T (2012) Detection sensors for electromagnetic nondestructive evaluation. *IEEE ELEKTRO*:435–438
11. Hoshikawa H, Koyama K (1998) Uniform Eddy current probe with little disrupting noise. Rev Prog Quant Nondestructive Eval 17:1059–1066

Part III
Imaging and Image processing

An Enhanced Unscented Kalman Filter Method Based on the Covariance Intersection Algorithm

Yao Huang, Wei Hua, Li Li, Weiwei Ling, Yao Yao, Gong Cheng, Jiang Du, and Haijun Zhang

1 Introduction

For linear systems, the Kalman filter is recursively performed with the promising performance. However, for nonlinear systems, the performance of Kalman filter will be significantly degraded and possibly diverged [1]. The extended Kalman filter (EKF) is a kind of nonlinear optimal algorithm with its robustness in the nonlinear systems, but the EKF requires the computation of the Jacobian matrix, which greatly increases the complexity of the filter [2].

Later, it is found that the Gaussian approximation is simpler, compared to the nonlinear function approximation. Motivated by the Gaussian approximation, the unscented Kalman filter (UKF) is proposed. On the basis of no trace transform, the deterministic sampling and the linear Kalman filtering framework are adopted in the UKF. It has the following characteristics [3, 4]: (1) compared to the EKF, its accuracy is raised to the third-order accuracy for Gauss data and the second-order accuracy for the nonlinear non-Gaussian data; (2) the computation of the Jacobian matrix is not required; (3) the discrete system and the additive noise can be handled by the UKF; (4) the computational complexity is the same order with that of the EKF; and (5) the deterministic sampling strategy is adopted to avoid the problem of particle recession and dilution.

But for a practical system, the UKF performance will be greatly reduced due to the uncertainty model used and unknown signal statistical properties. In addition, because of the bit precision of the hardware and filtering errors, the calculations in

Y. Huang · W. Hua (✉) · L. Li · W. Ling · Y. Yao · G. Cheng · J. Du
Chengdu University of Information Technology, Chengdu, China
e-mail: weihua@cuit.edu.cn

H. Zhang
University Of Science and Technology Beijing, Beijing, China

M. Jiang et al. (eds.), *The Proceedings of the International Conference on Sensing and Imaging*, Lecture Notes in Electrical Engineering 506,
https://doi.org/10.1007/978-3-319-91659-0_14

every step yield the uncompensated errors. In the UKF, the calculation is iteratively performed. Therefore, the accuracy of UFK will be significantly reduced by error accumulation in hundreds of iterations. Hence, some improved filter methods are proposed.

Particle filter is presented in [5]. In this method, a large number of particles will be produced, and its computation will be more intensive. Based on MIT an adaptive UKF with the robustness to interference [6] is proposed, but there are also a large number of partial differential calculations required. In [7], a confidence interval is proposed to overcome the accuracy of UKF prediction degradation. Meanwhile, the numerical stability in the UKF is considered [8]. Minimum entropy criterion [9], confidence interval [10], and singular value decomposition [11] are used in the UKF to improve the accuracy.

Motivated by the covariance intersection algorithm (CIA) [12], we propose an improved UKF. The improved value can be derived via the actual value and the estimate value, given the unknown correlation between these two values. In this method, there is correlation between the true value for the present moment and the estimate value for the next moment. But the numerical value of correlation is unknown in actual situation. Through the CIA, the improved value is gotten without the correlation.

2 The Covariance Intersection Algorithm

A and B are relevant information. When information A and information B need fusion, the correlation information between A and B is very helpful for information fusion. But in most instances, the correlation information is unknown.

How to solve this problem? The CIA is provided. $\{\mathbf{a}, \mathbf{P}_{aa}\}$ and $\{\mathbf{b}, \mathbf{P}_{bb}\}$ represent information A and its covariance and information B and its covariance, respectively. Meanwhile, $\tilde{a} = a - \overline{a}$, $\tilde{b} = b - \overline{b}$, and $\tilde{\mathbf{c}} = c - \overline{c}$. $\tilde{a}$, $\tilde{b}$, and $\tilde{\mathbf{c}}$ are error values. a, b, and c are actual values. $\overline{a}$, $\overline{b}$, and $\overline{c}$ are mean values.

The mean squared error $\overline{\mathbf{P}}_{aa}$ and $\overline{\mathbf{P}}_{bb}$ and the covariance $\overline{\mathbf{P}}_{ab}$ are computed as follows:

$$\overline{\mathbf{P}}_{aa} = \mathrm{E}\left[\tilde{\mathbf{a}}\tilde{\mathbf{a}}^T\right], \overline{\mathbf{P}}_{bb} = \mathrm{E}\left[\tilde{b}\tilde{b}^T\right], \overline{\mathbf{P}}_{ab} = \mathrm{E}\left[\tilde{\mathbf{a}}\tilde{b}^T\right]$$

$\overline{a}$ and $\overline{b}$ are actually not known. Hence, $\overline{\mathbf{P}}_{aa}$ and $\overline{\mathbf{P}}_{bb}$ are also unknown.

In the CIA, $\overline{\mathbf{P}}_{aa}$ and $\overline{\mathbf{P}}_{bb}$ are approximated by the values $\mathbf{P}_{aa}$ and $\mathbf{P}_{bb}$. Based on $\{\mathbf{a}, \mathbf{P}_{aa}\}$ and $\{\mathbf{b}, \mathbf{P}_{bb}\}$, the improved estimated value of $\{\mathbf{c}, \mathbf{P}_{cc}\}$ is obtained by the CIA without correlation $\mathbf{P}_{ab}$.

In Fig. 1, the solid line ellipses are $\mathbf{P}_{aa}$ and $\mathbf{P}_{bb}$, and the dotted lines ellipses are $\mathbf{P}_{cc}$. Based on $\mathbf{P}_{aa}$ and $\mathbf{P}_{bb}$, different $\mathbf{P}_{cc}$ is derived from different $\mathbf{P}_{ab}$. $\mathbf{P}_{ab}$ is the correlation information between information A and information B.

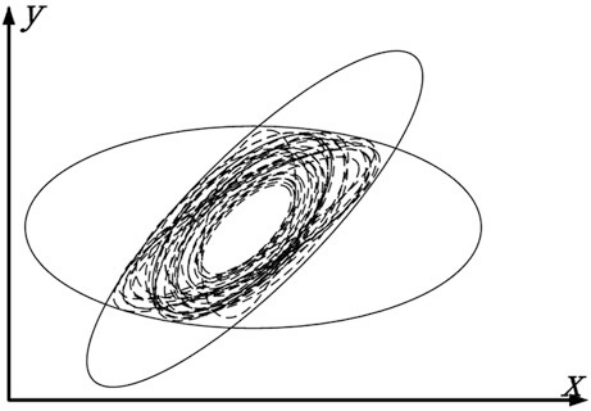

Fig. 1 Improved covariance elliptical shape

As shown in Fig. 1, $\mathbf{P}_{cc}$ is always located in the intersection of $\mathbf{P}_{aa}$ and $\mathbf{P}_{bb}$ for any value of $\mathbf{P}_{ab}$. Hence, according to the CIA, $\mathbf{P}_{cc}$ is obtained even if $\mathbf{P}_{ab}$ is unknown, and the more information $\mathbf{P}_{cc}$ can be recovered with the better $\mathbf{P}_{ab}$. The CIA process is expressed by:

$$\mathbf{P}_{cc}^{-1} = w\mathbf{P}_{aa}^{-1} + (1-w)\,\mathbf{P}_{bb}^{-1} \tag{1}$$

$$\mathbf{P}_{cc}^{-1}\mathbf{c} = w\mathbf{P}_{aa}^{-1}\mathbf{a} + (1-w)\,\mathbf{P}_{bb}^{-1}\mathbf{b} \tag{2}$$

where w is the weighting factor assigned to $\mathbf{a}$ and $\mathbf{b}$. w is adopted different value in $0 \leq w \leq 1$ under different optimization method, for example, the Newton-Raphson method, positive semi-definite method, and convex optimization method. If the optimization method is improved, $\{\mathbf{c}, \mathbf{P}_{cc}\}$ will be more accurate. Therefore the optimal values $\{\mathbf{c}, \mathbf{P}_{cc}\}$ are unique and relative to the optimization method.

In the CIA, $\{\mathbf{c}, \mathbf{P}_{cc}\}$ are computed based on $\{\mathbf{a}, \mathbf{P}_{aa}\}$ and $\{\mathbf{b}, \mathbf{P}_{bb}\}$. The only constraint is consistent, which is $\mathbf{P}_{aa} - \overline{\mathbf{P}}_{aa} \geq 0$ and $\mathbf{P}_{bb} - \overline{\mathbf{P}}_{bb} \geq 0$, to satisfy the consistency constraint $\mathbf{P}_{cc} - \overline{\mathbf{P}}_{cc} \geq 0$ [12]. $\overline{\mathbf{P}}_{cc}$ is the error variance and $\overline{\mathbf{P}}_{cc} = \mathrm{E}\left[\tilde{c}\tilde{c}^T\right]$.

3 The Improved UKF

3.1 UKF

It is assumed that the nonlinear system is:

$$\mathbf{X}(k) = f\ (\mathbf{X}(k-1)) + \mathbf{W}(k-1) \tag{3}$$

$$\mathbf{Y}(k) = h\left(\mathbf{X}(k)\right) + \mathbf{V}(k) \tag{4}$$

where $f(\cdot)$ and $h(\cdot)$ are nonlinear functions, k is the kth time, $\mathbf{X}(k)$ is the system state vector, $\mathbf{Y}(k)$ is the system measurement vector, and $\mathbf{V}(k)$ and $\mathbf{W}(k)$ are process noise and measurement noise. Their statistical properties are:

$$\begin{cases} E\left[\mathbf{W}(k)\right] = \mathbf{0}, E\left[\mathbf{V}(k)\right] = \mathbf{0} \\ E\left[\mathbf{W}(i)\mathbf{W}(j)\right] = \mathbf{R}\delta_{ij}, \forall i, j \\ E\left[\mathbf{V}(i)\mathbf{V}(j)\right] = \mathbf{Q}\delta_{ij}, \forall i, j \\ E\left[\mathbf{W}(i)\mathbf{V}(j)^T\right] = \mathbf{0} \end{cases} \tag{5}$$

$\mathbf{R}(k)$ and $\mathbf{Q}(k)$ are their mean squared error.

1. Initialization

$$\widehat{\mathbf{X}}^a\left(0\,|0\right) = \left[\widehat{\mathbf{X}}(0\,|0)^T 00\right]^T \tag{6}$$

$$\mathbf{P}_{\mathbf{XX}}^a\left(0\,|0\right) = \begin{bmatrix} \mathbf{P}_{\mathbf{XX}}\left(0\,|0\right) & 0 & 0 \\ 0 & \mathbf{Q}\left(0\,|0\right) & 0 \\ 0 & 0 & \mathbf{R}\left(0\,|0\right) \end{bmatrix} \tag{7}$$

2. Proportion symmetry sampling

$$\boldsymbol{\chi}\left(k-1\,|k-1\right) = \begin{bmatrix} \widehat{\mathbf{X}}\left(k-1\,|k-1\right) \\ \widehat{\mathbf{X}}\left(k-1\,|k-1\right) + \sqrt{(n+\lambda)\,\mathbf{P}_{\mathbf{XX}i}\left(k-1\,|k-1\right)} \\ \widehat{\mathbf{X}}\left(k-1\,|k-1\right) - \sqrt{(n+\lambda)\,\mathbf{P}_{\mathbf{XX}i}\left(k-1\,|k-1\right)} \end{bmatrix}^T \tag{8}$$

$$\mathbf{P}_{\mathbf{XX}}\left(k\,|k\right) = \begin{bmatrix} \mathbf{P}_{\mathbf{XX}}\left(k\,|k\right) & 0 & 0 \\ 0 & \mathbf{Q}\left(k\,|k\right) & 0 \\ 0 & 0 & \mathbf{R}\left(k\,|k\right) \end{bmatrix} \tag{9}$$

$\widehat{\mathbf{X}}\left(k-1\,|k-1\right)$ is the filter value at the $k-1$th time. $\mathbf{P}_{\mathbf{XX}}(k-1|k-1)$ is the mean squared error of $\widehat{\mathbf{X}}\left(k-1\,|k-1\right)$. $\mathbf{P}_{\mathbf{XX}i}(k-1|k-1)$ is the ith column of $\mathbf{P}_{\mathbf{XX}}(k-1|k-1)$ and $i = 1, 2, \cdots, n.\lambda = \alpha^2(n+\kappa) - n$, where α and κ are impact factors and they generally take small values.

3. Time update equations

$$\boldsymbol{\chi}\left(k\left|k-1\right.\right)=f\left(\boldsymbol{\chi}\left(k-1\left|k-1\right.\right),k-1\right) \tag{10}$$

$$\boldsymbol{\chi}\left(k\left|k-1\right.\right)=f\left(\boldsymbol{\chi}\left(k-1\left|k-1\right.\right),k-1\right) \tag{11}$$

$$\boldsymbol{\mu}\left(k\left|k-1\right.\right)=h\left(\boldsymbol{\chi}\left(k\left|k-1\right.\right),k-1\right) \tag{12}$$

$$\widehat{\mathbf{Y}}\left(k\left|k-1\right.\right)=\sum_{i=0}^{2n}\mathbf{W}_{m}^{(i)}\boldsymbol{\mu}_{i}\left(k\left|k-1\right.\right) \tag{13}$$

In Eq.(13), $\boldsymbol{\mu}_i(k|k-1)$ is the ith column of $\boldsymbol{\mu}(k|k-1)$ and $i=1,2,\cdots,2n$. $\mathbf{W}_m^{(i)}$ is the weighted value. $\mathbf{W}_m^{(0)}=\lambda/\left(n+\lambda\right)$, $\mathbf{W}_m^{(0)}=\lambda/\left(n+\lambda\right)$, and $i=1,2,\cdots,2n$:

$$\begin{aligned}\mathbf{P}_{\mathbf{XX}}\left(k\left|k-1\right.\right)=\sum_{i=0}^{2n}\mathbf{W}_{c}^{(i)}&\left[\left(\boldsymbol{\chi}_{i}\left(k\left|k-1\right.\right)-\widehat{\mathbf{X}}\left(k\left|k-1\right.\right)\right)\right.\\&\left.\times\left(\boldsymbol{\chi}_{i}\left(k\left|k-1\right.\right)-\widehat{\mathbf{X}}\left(k\left|k-1\right.\right)\right)^{T}\right]\end{aligned} \tag{14}$$

$\boldsymbol{\chi}_i(k|\,k-1)$ is the ith column of $\boldsymbol{\chi}(k|\,k-1)$ and $i=0,1,\cdots,2n$, and $\mathbf{W}_c^{(i)}$ is the weighted covariance matrix.

$\mathbf{W}_c^{(0)}=\lambda/\left(n+\lambda\right)+\left(1\text{-}\alpha^2+\beta\right)$ and $\mathbf{W}_c^{(i)}=1/2\left(n+\lambda\right),i=1,2,\cdots,2n$. β is the prior distribution factor (it is usually set to 2 for Gaussian distribution).

4. Measurement update equations

$$\begin{aligned}\mathbf{P}_{\mathbf{XY}}\left(k\left|k-1\right.\right)=\sum_{i=0}^{2n}\mathbf{W}_{c}^{(i)}&\left[\left(\boldsymbol{\chi}_{i}\left(k\left|k-1\right.\right)-\widehat{\mathbf{X}}\left(k\left|k-1\right.\right)\right)\right.\\&\left.\times\left(\boldsymbol{\mu}_{i}\left(k\left|k-1\right.\right)-\widehat{\mathbf{Y}}\left(k\left|k-1\right.\right)\right)^{T}\right]\end{aligned} \tag{15}$$

$$\begin{aligned}\mathbf{P}_{\mathbf{YY}}\left(k\left|k-1\right.\right)=\sum_{i=0}^{2n}\mathbf{W}_{c}^{(i)}&\left[\left(\boldsymbol{\mu}_{i}\left(k\left|k-1\right.\right)-\widehat{\mathbf{Y}}\left(k\left|k-1\right.\right)\right)\right.\\&\left.\times\left(\boldsymbol{\mu}_{i}\left(k\left|k-1\right.\right)-\widehat{\mathbf{Y}}\left(k\left|k-1\right.\right)\right)^{T}\right]\end{aligned} \tag{16}$$

$$\mathbf{K}(k)=\mathbf{P}_{\mathbf{XY}}\left(k\left|k-1\right.\right)\mathbf{P}_{\mathbf{YY}}^{-1}\left(k\left|k-1\right.\right) \tag{17}$$

$$\widehat{\mathbf{X}}\left(k\left|k\right.\right)=\widehat{\mathbf{X}}\left(k\left|k-1\right.\right)+\mathbf{K}(k)\left(\mathbf{Y}(k)-\widehat{\mathbf{Y}}\left(k\left|k-1\right.\right)\right) \tag{18}$$

$$\mathbf{P}_{\mathbf{XX}}\left(k\left|k\right.\right)=\mathbf{P}_{\mathbf{XX}}\left(k\left|k-1\right.\right)-\mathbf{K}(k)\mathbf{P}_{\mathbf{YY}}\left(k\left|k-1\right.\right)\mathbf{K}^{T}(k) \tag{19}$$

where $\mathbf{P_{XX}}$, $\mathbf{P_{XY}}$, $\mathbf{P_{YY}}$ represent covariance matrix between $\mathbf{X}$ and $\mathbf{X}$, $\mathbf{X}$ and $\mathbf{Y}$, and $\mathbf{Y}$ and $\mathbf{Y}$, respectively. $\mathbf{K}$ is filter gain; $\widehat{\mathbf{X}}(k\,|k)$ is the filter value at the kth time.

3.2 The Improved UKF

The UKF, incorporating the CIA, can obtain the better estimated value $\widehat{\mathbf{X}}_{\text{improved}}(k\,|k)$ without the covariance information between the real value $\mathbf{X}(k-1)$ and the estimated value $\widehat{\mathbf{X}}(k\,|k)$. Meanwhile, the UKF accuracy is improved in the proposed method. Equations are expressed as follows:

$$\mathbf{P}^{-1} = w\mathbf{P}_{\mathbf{XX}}^{-1}(k\,|k) + (1-w)\,\mathbf{P}_{\mathbf{XX}}^{-1}(k-1\,|k-1) \tag{20}$$

$$\mathbf{P}^{-1}\widehat{\mathbf{X}}_{\text{improved}}(k\,|k) = w\mathbf{P}_{\mathbf{XX}}^{-1}(k\,|k)\,\widehat{\mathbf{X}}(k\,|k) + (1-w)\,\mathbf{P}_{\mathbf{XX}}^{-1}(k-1|k-1)\,\mathbf{X}(k-1) \tag{21}$$

$\widehat{\mathbf{X}}_{\text{improved}}(k\,|k)$ is the improved filter value and its covariance matrix is $\mathbf{P}^{-1}$. w is the weighting factor assigned to $\widehat{\mathbf{X}}(k\,|k)$ and $\mathbf{X}(k-1)$.

At the kth time, the real value $\mathbf{X}(k-1)$ is known. Through the UKF, the filter value $\widehat{\mathbf{X}}(k\,|k)$ is computed. Due to the mismatched system model, noises, and interferences existing in the UKF process, the accuracy of $\widehat{\mathbf{X}}(k\,|k)$ is reduced.

But the relevancy between the real value $\mathbf{X}(k-1)$ and the filter value $\widehat{\mathbf{X}}(k\,|k)$ is existing in the practice and unknown in the actual situation. Through the proposed method, the relevancy computation about covariance matrix between $\widehat{\mathbf{X}}(k\,|k)$ and $\mathbf{X}(k-1)$ is avoided, and the accuracy of $\widehat{\mathbf{X}}(k\,|k)$ is improved. $\widehat{\mathbf{X}}_{\text{improved}}(k\,|k)$ is obtain by (20) and (21) without the covariance matrix. The algorithm procedure of improved UKF is in Fig. 2.

It is the algorithm flow chart in Fig. 2. $\widehat{\mathbf{X}}(k\,|k)$ and $\mathbf{P_{XX}}(k|\,k)$ are computed through UKF. And then $\widehat{\mathbf{X}}_{\text{improved}}(k\,|k)$ is got by the CIA.

In fact, some methods [9–11] are adopted to keep filter result stability in the UKF algorithms, for example, $\mathbf{U}-\mathbf{D}$ decomposition filter and singular value decomposition filter. In the $\mathbf{U}-\mathbf{D}$ decomposition filter, covariance matrix $\mathbf{P}$ is decomposed as $\mathbf{UDU}^T$, where $\mathbf{U}$ is an upper triangular matrix and $\mathbf{D}$ is diagonal matrix. Hence, $\mathbf{UD}^{1/2}$ is equivalent to $\mathbf{P}^{1/2}$. In the singular value decomposition filter, $\mathbf{V}$ is the eigenvector matrix of $\mathbf{P}$, and $\mathbf{D}$ is diagonal matrix, where the diagonal element is the singular value of $\mathbf{P}$. Therefore, $\mathbf{VD}^{1/2}$ is also equivalent to $\mathbf{P}^{1/2}$. These two algorithms keep positive definite of $\mathbf{P}$ and make better robustness of the UKF algorithms.

In these two algorithms, there will be few changes in the process of UKF. $\mathbf{P}_{\mathbf{XX}}^{a}(k-1\,|k-1)$ is decomposed. In $\mathbf{U}-\mathbf{D}$ decomposition filter, Eqs. (8) and (9) transform into Eqs. (22) and (23).

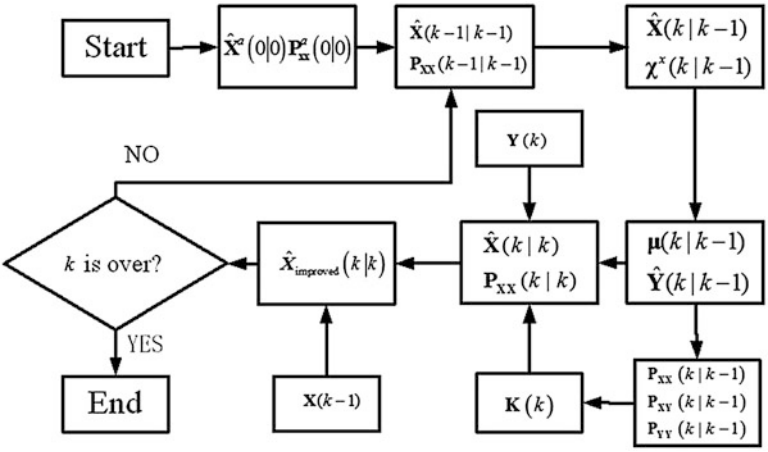

Fig. 2 Algorithm flow chart

$$\mathbf{P_{XX}}(k-1|k-1) = \mathbf{U}(k-1|k-1)\,\mathbf{D}(k-1|k-1)\,\mathbf{U}(k-1|k-1)^T \quad (22)$$

$$\begin{aligned}&\boldsymbol{\chi}(k-1|k-1)\\ &= \begin{bmatrix} \widehat{\mathbf{X}}(k-1|k-1) \\ \widehat{\mathbf{X}}(k-1|k-1) + \mathbf{U}_i(k-1|k-1)\sqrt{(n+\lambda)\,\mathbf{D}_i(k-1|k-1)} \\ \widehat{\mathbf{X}}(k-1|k-1) - \mathbf{U}_i(k-1|k-1)\sqrt{(n+\lambda)\,\mathbf{D}_i(k-1|k-1)} \end{bmatrix}^T\end{aligned} \quad (23)$$

In the singular value decomposition filter, change equations are:

$$\mathbf{P_{XX}}(k-1|k-1) = \mathbf{V}(k-1|k-1)\,\mathbf{D}(k-1|k-1)\,\mathbf{V}(k-1|k-1)^T \quad (24)$$

$$\begin{aligned}&\boldsymbol{\chi}(k-1|k-1)\\ &= \begin{bmatrix} \widehat{\mathbf{X}}(k-1|k-1) \\ \widehat{\mathbf{X}}(k-1|k-1) + \mathbf{V}_i(k-1|k-1)\sqrt{(n+\lambda)\,\mathbf{D}_i(k-1|k-1)} \\ \widehat{\mathbf{X}}(k-1|k-1) - \mathbf{V}_i(k-1|k-1)\sqrt{(n+\lambda)\,\mathbf{D}_i(k-1|k-1)} \end{bmatrix}^T\end{aligned} \quad (25)$$

$\mathbf{V}_i(k-1|k-1)$, $\mathbf{U}_i(k-1|k-1)$, and $\mathbf{D}_i(k-1|k-1)$ are the ith column of $\mathbf{V}(k-1|k-1)$, $\mathbf{U}(k-1|k-1)$, and $\mathbf{D}(k-1|k-1)$. $i = 1, 2, \cdots, n$. Hence, $\widehat{\mathbf{X}}(k|k)$, $\mathbf{P_{XX}}(k|k)$, and $\mathbf{X}(k-1)$ can be obtained. And then the CIA is also used to improve accuracy.

4 The Improved Kalman Filter (KF)

The linear system model is:

$$\begin{cases} \mathbf{X}(\mathbf{k}+\mathbf{1}) = \mathbf{\Phi}(\mathbf{k})\,\mathbf{X}(\mathbf{k}) + \mathbf{\Gamma}(\mathbf{k})\,\mathbf{W}(\mathbf{k}) \\ \mathbf{Y}(k) = \mathbf{H}(k)\mathbf{X}(k) + \mathbf{V}(k) \end{cases} \tag{26}$$

$\mathbf{X}(k+1)$ represents the system state vector, and $\mathbf{Y}(k)$ is the system measurement vector. $\mathbf{V}(k)$ and $\mathbf{W}(k)$ are process noise and measurement noise. Their statistical properties are in (5). $\mathbf{\Phi}(\mathbf{k})$, $\mathbf{\Gamma}(\mathbf{k})$, and $\mathbf{H}(k)$ are computation models according to the object.

1. Time update equations

$$\begin{cases} \widehat{\mathbf{X}}(k) = \mathbf{\Phi}(k)\widehat{\mathbf{X}}(k-1) \\ \mathbf{P}(k\,|k-1) = \mathbf{\Phi}(k)\mathbf{P}(k)\mathbf{\Phi}(k)^T + \mathbf{\Gamma}(k)\mathbf{Q}(k)\mathbf{\Gamma}(k)^T \end{cases} \tag{27}$$

$\mathbf{P}$ is the covariance matrix of $\widehat{\mathbf{X}}$.

2. Measurement update equations

$$\begin{cases} \mathbf{K}(k) = \mathbf{P}(k\,|k-1)\,\mathbf{H}(k)^T\left(\mathbf{H}(k)\mathbf{P}(k\,|k-1)\,\mathbf{H}(k)^T + \mathbf{R}(k)\right)^{-1} \\ \widehat{\mathbf{X}}(k\,|k) = \widehat{\mathbf{X}}(k\,|k-1) + \mathbf{K}(k)\left(\mathbf{Y}(k) - \mathbf{H}(k)\widehat{\mathbf{X}}(k\,|k-1)\right) \\ \mathbf{P}(k\,|k) = (\mathbf{I} - \mathbf{K}(k)\mathbf{H}(k))\,\mathbf{P}(k\,|k-1) \end{cases} \tag{28}$$

At time k, $\mathbf{K}$ is filtering gain and $\widehat{\mathbf{X}}(k\,|k)$ is the filter value.

From the model in (26), (27), and (28), there are also noises and interferences existing in the KF process. Hence, the accuracy of KF is also improved by the presented method.

According to the KF, $\widehat{\mathbf{X}}(k\,|k)$, $\mathbf{P}(k|k)$, and $\mathbf{X}(k-1)$ are obtained. The presented method is also used in the KF.

$$\mathbf{P}_{KF}^{-1} = w\mathbf{P}^{-1}(k\,|k) + (1-w)\,\mathbf{P}^{-1}(k-1\,|k-1) \tag{29}$$

$$\mathbf{P}_{KF}^{-1}\widehat{\mathbf{X}}_{\text{improved}}(k\,|k) = w\mathbf{P}^{-1}(k\,|k)\,\widehat{\mathbf{X}}(k\,|k) + (1-w)\,\mathbf{P}^{-1}(k-1\,|k-1)\,\mathbf{X}(k-1) \tag{30}$$

$\mathbf{P}_{KF}^{-1}$ is the fused covariance matrix; $\widehat{\mathbf{X}}_{\text{improved}}(k\,|k)$ is the improved filter value.

5 Simulation

In this model, the position, velocity, and acceleration (PVA) motion model is usually adopted. Two sensors are used to track one target. This model is in (31) and (32).

$$\mathbf{X}(k) = \begin{pmatrix} 1 & 0 & \Delta t & 0 \\ 0 & 1 & 0 & \Delta t \\ 0 & 0 & 1 & 0 \\ 0 & 0 & 0 & 1 \end{pmatrix} \mathbf{X}(k-1) + \mathbf{W}(k-1) \tag{31}$$

$$\theta(k)^i = \arctan\left(\frac{y_k - s_y^i}{x_k - s_x^i}\right) + V(k)^i \tag{32}$$

$\mathbf{X}(k)$ is a state variable vector, $\mathbf{X}(k) = \begin{pmatrix} x_k & y_k & \dot{x}_k & \dot{y}_k \end{pmatrix}^T$. The initial value of $\mathbf{X}$ is $\begin{pmatrix} 0 & 0 & 1 & 0 \end{pmatrix}^T$. x_k, y_k are horizontal and vertical position, and $\dot{x}_k$, $\dot{y}_k$ are the corresponding horizontal and longitudinal velocity. $\mathbf{W}(k-1)$ and $V(k)^i$ represent Gaussian noise, $\mathbf{W}(k-1)$ mathematical expectation is zero, and the covariance is $\begin{bmatrix} \frac{1}{30}\Delta t^3 & 0 & \frac{1}{20}\Delta t^2 & 0 \\ 0 & \frac{1}{30}\Delta t^3 & 0 & \frac{1}{20}\Delta t^2 \\ \frac{1}{20}\Delta t^2 & 0 & \frac{1}{10}\Delta t & 0 \\ 0 & \frac{1}{20}\Delta t^2 & 0 & \frac{1}{10}\Delta t \end{bmatrix}$. V_k^i $N(0, 0.05^2)$. s_x^i and s_y^i are the ith sensor measurement value. The location of them are represented by $\left(s_x^1, s_y^1\right) = (1, 1)$ and $\left(s_x^2, s_y^2\right) = (-1, -2)$, respectively. The time interval Δt is 0.01 s; the simulation time is 5 s. And [11] is the compared method.

In Fig. 3, two black triangles are the sensors' location. Black line is the real trajectory. Red line is the compared method estimation trajectory. Blue line represents the trajectory obtained by the presented method. As shown in Fig. 3, the presented method is closer to the real trajectory, compared to the compared method.

In Fig. 4, the vertical axis represents MSE on the x-axis, and the horizontal axis represents time. In Fig. 5, the vertical axis represents MSE on the y-axis, and the horizontal axis represents time. Red line is the presented method MSE, and blue line is the UKF MSE in both of these two figures. From Figs. 4 and 5, the precision is improved by more than half at some time, for example, time 120, 230, and 400 on the x-axis and time 100, 190, and 380 on the y-axis. Generally speaking, the accuracy of proposed method is overall higher than the accuracy of the compared method. Especially,

In Fig. 6, the MSE and Monte Carlo methods are adopted to compare these two methods' performance, and the number of Monte Carlo simulations is 500. The expression is as follows:

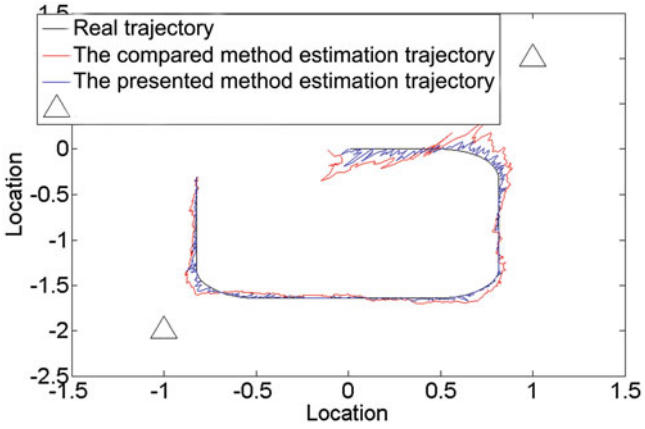

Fig. 3 Tracking trajectory between the UKF and the presented method

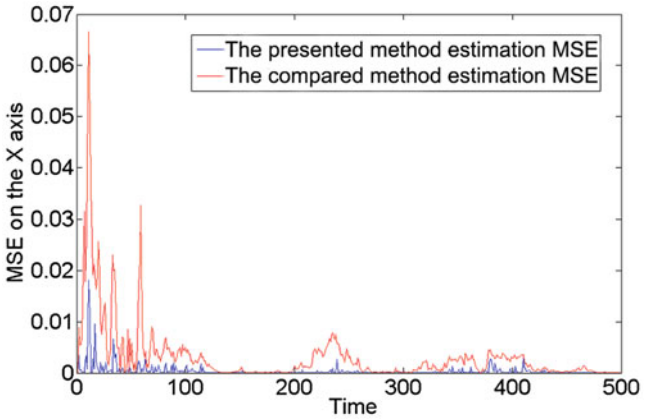

Fig. 4 MSE on the x-axis

$$\mathrm{MSE} = \sqrt{\frac{1}{M}\sum_{n=1}^{M}\left((x\,(k\,|k\,) - x(k))^2 + (y\,(k\,|k\,) - y(k))^2\right)} \tag{33}$$

$M = 500$, the value of k is from 1to 500.

In Fig. 6, the presented method MSE is lower than the compared MSE. It is expressed that the accuracy of the proposed method is better than one of the compared method.

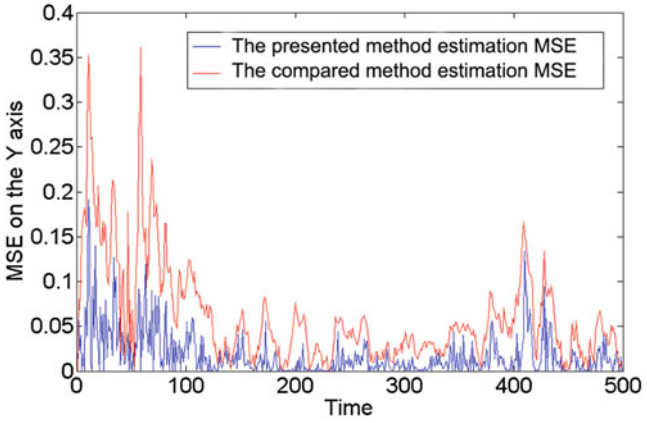

Fig. 5 MSE on the y-axis

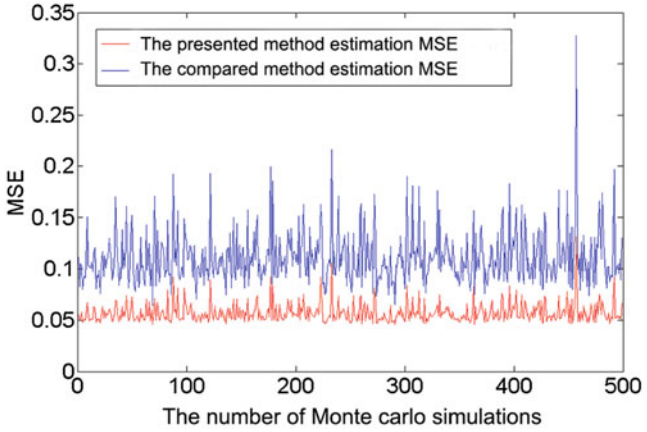

Fig. 6 MSE

5.1 The Second Model

$$\mathbf{X}(k+1) = \begin{bmatrix} 1 & 1 \\ -1 & -1 \end{bmatrix} \mathbf{X}(k) + \begin{bmatrix} 1 \\ 1 \end{bmatrix} W(k) \tag{34}$$

$$\mathbf{Y}(k) = \begin{bmatrix} 1 & 1 \end{bmatrix} \mathbf{X}(k) + V(k) \tag{35}$$

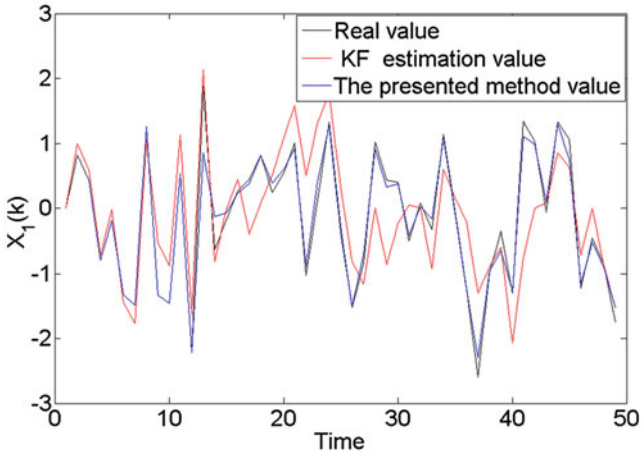

Fig. 7 $X_1(k)$

$\mathbf{X}(k) = \left[X_1(k)\ X_2(k) \right]^T$, the initial value is $\left[0\ 0\right]^T$; $W(k)$, $V(k)$ are zero-mean independent white noise with different variance$Q$ and R. $Q = 0.7$, $R = 0.9$. Other element values are as follows:

$$\mathbf{\Phi}(k) = \begin{bmatrix} 1 & 1 \\ -1 & -1 \end{bmatrix}, \quad \mathbf{\Gamma}(k) = \begin{bmatrix} 1 \\ 1 \end{bmatrix}, \quad \mathbf{H}(k) = \begin{bmatrix} 1\ 1 \end{bmatrix}$$

Because the second model is a linear system, KF is used.

In Figs. 7 and 8, red line is the KF estimation value, and blue line is the presented method value. As is shown in Figs. 7 and 8, the accuracy of KF is obviously higher than the one of the proposed method. It is also instruction that the proposed method is effective.

6 Conclusion

In this paper, an enhanced UKF method based on CIA is proposed. According to the real value at time $k - 1$ and the filter value at time k, the accuracy is effectively improved by this method. And more importantly, the correlation information between the real value and the filter value is not involved.

Acknowledgments This work is supported by the Science and Technology Support Plan of Department of Science and Technology of Sichuan province under Grant No. 2014RZ0017, the general project of the Education Department of Sichuan province under Grant No. 17ZB0081, the Scientific Research Foundation of CUIT (No.KYTZ201501, No.KYTZ201502), and the Meteorological information and Signal Processing Key Laboratory of Sichuan Higher Education Institutes. The authors declare that there is no conflict of interest regarding the publication of this article.

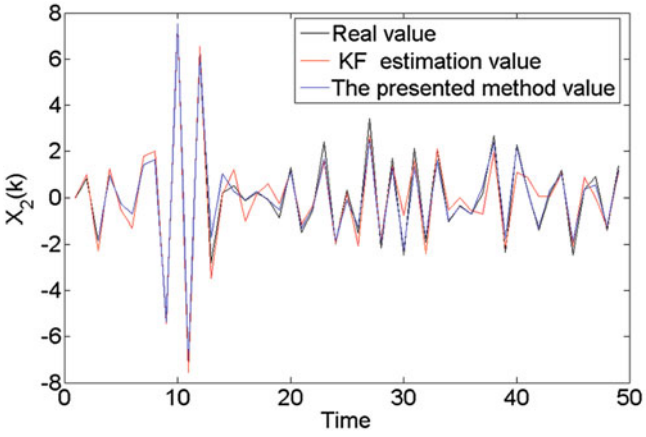

Fig. 8 $X_2(k)$

References

1. Vullings R, de Vries B, Bergmans JWM (2011) An adaptive Kalman filter for ECG signal enhancement. IEEE Trans Biomed Eng 58(4):1094–1103
2. Yang XJ, Zou HX, Zhou ZJ (2010) An iterated fuzzy extended Kalman filter for nonlinear systems. Int J Syst Sci 41(6):717–726
3. Pan Q, Yang F, Liang Y (2005) Survey of a kind of nonlinear filters-UKF [J]. Control Decis 20(5):483–494
4. JSimon D (2010) Kalman filtering with state constraints: a survey of linear and nonlinear algorithms. Control Theory Appli IET 4(8):1303–1318
5. Gustafasson F (2010) Particle filter theory and practice with positioning applications. IEEE Trans Aerosp Electron Syst Mag 25(7):53–82
6. Qi J, Jianda H (2009) Adaptive UKF and its application in fault tolerant control of rotorcraft unmanned aerial vehicle. J Mech Eng 45(4):115–124
7. Luo Z, Fang H (2013) Modified state prediction algorithm based on UKF. J Syst Eng Electron 24(1):135–140
8. Vartiainen P, Bragge T, Arokoski JP, Karjalainen PA (2014) Nonlinear state-space modeling of human motion using 2-D marker observations. IEEE Trans Biomed Eng 61(7):2167–2178
9. Liu Y, Wang H, Hou C (2013) UKF based nonlinear filtering using minimum entropy criterion. IEEE Trans Signal Process 61(20):4988–4999
10. Luo Z, Fang H (2013) Modified state prediction algorithm based on UKF. J Syst Eng Electron 24(1):135–140
11. Cilden D, Hajiyev C, Soken HE (2015) Attitude and attitude rate estimation for a nanosatellite using SVD and UKF. 7th Int Conf Recent Adv Space Technol (RAST) 2015:695–700
12. Julier SJ, Uhlmann JK (1997) A non-divergent estimation algorithm in the presence of unknown correlation. Am Control Conf Albuquerque, NM 4:2369–2373

Application in Image Denoising Using Fractional Total Variation Theory

Guo Huang, Qing-li Chen, Tao Men, Xiu-Qiong Zhang, Hong-Ying Qin, and Li Xu

1 Introduction

Image processing based on partial differential equations is a brand new interdisciplinary branch with the integration of the theories of various fields [1, 2]. This method has a powerful mathematical theory foundation and many advantages which other image denoising methods do not have, but during in-depth studies, many scholars at home and abroad still find many inadequacies in image denoising models based on partial differential equations. For example, though PM model [3] and ROF model [4] can effectively remove noise from the smooth region of image, the denoised image will produce a "ladder effect" and piecewise smooth phenomenon; the LLT model [5] takes advantage of the higher-order partial differential equation modeling, even though it can eliminate the "ladder" effect, the resulting denoised image presents bad visual effects; and the MCM model [6] can protect edge information of the image, but the denoised image will produce many of the artifacts.

In recent years, many scholars applied fractional calculus theory to low-layer image processing and obtained better simulation results [7, 8]. Fractional differential can improve high-frequency component of the signal and retain very low-frequency signal nonlinearly at the same time. Therefore applying this theory to image processing can make the edges of the image more prominent, while retaining the texture information of the smooth region of the image [9, 10]. Zhang et al. introduced the classical fractional calculus Grümwald-Letnikov definition into the

G. Huang (✉) · Q.-l. Chen · T. Men · X.-Q. Zhang · H.-Y. Qin
School of Computer Science, Leshan Normal University, Leshan, China

L. Xu
School of Physics and Electronics, Leshan Normal University, Leshan, China

M. Jiang et al. (eds.), *The Proceedings of the International Conference on Sensing and Imaging*, Lecture Notes in Electrical Engineering 506,
https://doi.org/10.1007/978-3-319-91659-0_15

building of the energy functional and derived another type of image denoising model based on fractional partial differential equations [11]. The image denoising model based on fractional partial differential equations is actually based on spatial partial differential equations, that is, in spatial domain they use the memory of fractional calculus and non-locality for image denoising. This can obtain better denoising effects while effectively suppressing "ladder phenomenon" to some extent. However, some shortcomings exist in the fractional order partial differential equation-based image denoising model: (1) Zhang's denoising model does not introduce edge stop function, so detailed information such as edge and texture in the denoised image is not ideal. (2) Numerical implementation of the Zhang's denoising model only considers the fractional differential of the X-axis and Y-axis direction and this method overlooks the role of pixel points in several other directions, thus resulting in the imprecision of the numerical calculation of the fractional differential.

To solve the problems of Zhang's image denoising model, this paper attempts to introduce edge-stop function with fractional gradient amplitude as the parameter and implement the numerical calculation of spatial partial differential equations by building fractional differential mask in eight directions, this method could obtain the solution of the denoising model by transforming the image denoise model based on what is proposed in this paper to correlation and convolution operations between fractional differential mask operator and noise image.

2 Analysis of Definitions and Theorems

Digital images are usually described by two-dimensional functions. Thus the key of image-processing models based on PDE is to seek some appropriate function space to model the digital image. In general, most of the images possess rather complicated characteristics such as non-regular boundary, highly sophisticated texture, and random noise. In order to describe as completely as possible the complicated characteristics of the images, many researchers tried to find the "characteristic function space" that can describe the complicated characteristics of the images and modeled the complicated characteristic information of the images using this "characteristic function space."

In the ROF model [12], because all the functions in the "BV space" are allowed to have leaping discontinuity, it provides important theoretical basis for maintaining noncontinuous features and structures such as image boundary and texture in the denoising process. The "BV space" is thus deemed appropriate function space to describe non-texture images. This section extends "Total variation" and "Bounded variation function space" with the basic definitions in the theory of fractional calculus to derive "Fractional total variation" and "Fractional bounded variation function space" which can more precisely describe the detailed characteristics of the images such as boundary and texture.

2.1 Total Variation and Bounded Variation Function Space

Let Ω be a bounded subset on the real plane, function $\mu \in L^1(\Omega)$, if the distribution derivative or general derivative can be represented by some limited vector value Radon measurement (when $\forall\phi = (\phi_1, \phi_2) \in C_0^1(\Omega)^2$, and $\left|\phi_{L^\infty(\Omega)}\right| \leq 1$, it is satisfied that $\int_\Omega \mu div\phi d\Omega = -\int_\Omega D\mu \cdot \phi d\Omega$, in which $D\mu = (D_x\mu, D_y\mu)$ is the limited vector value measurement on Ω, and it becomes the distributed gradient or general gradient of μ). Thus function μ can be called the limited variation function on Ω and define the total variation of μ as:

$$\int_\Omega |D\mu| = \sup\left\{\int_\Omega \mu div\phi d\Omega : \phi = (\phi_1, \phi_2) \in C_0^1(\Omega)^2, \left|\phi_{L^\infty(\Omega)}\right| \leq 1\right\} \tag{1}$$

Thus, according to the definition of fractional order total variation [13], we could obtain the definition of bounded variation function space as:

$$BV(\Omega) = \left\{\mu \in L^1(\Omega), \int_\Omega |Du| d\Omega < \infty\right\} \tag{2}$$

in which, when $\forall\mu \in C^1(\Omega)$, μ is a first-order continuous differentiable function defined on Ω, it can be derived by Green formula that $\int_\Omega \mu div\phi d\Omega = -\int_\Omega D\mu \cdot \phi d\Omega$, and thus $\int_\Omega |D\mu| d\Omega = \int_\Omega |\nabla\mu| d\Omega$.

2.2 Fractional Total Variation and Bounded Variation Function Space

Suppose there is function $\mu(x, y) \in R^{N\times N}$, $\phi(x, y) \in R^{N\times N} \times R^{N\times N}$ it can be discretized with distance $h = 1$ in the $N \times N$ plane $\mu = \left(\mu_{i,j}\right)_{i.j=1}^N$, $\phi = \left(\phi_{i,j}\right)_{i.j=1}^N$, thus it can be obtained that the fractional gradient of function $\mu(x, y)$ and fractional divergence of function $\phi(x, y)$ are:

$$\nabla^v\mu = \left(\nabla^v\mu_{i,j}\right)_{i,j=1}^N = \left(D_x^v\mu_{i,j}, D_y^v\mu_{i,j}\right)_{i,j=1}^N \tag{3}$$

$$\mathrm{div}^v\phi = \left(\overline{(-1)^v}\left(D_x^v\phi_{i,j} + D_y^v\phi_{i,j}\right)\right)_{i,j=1}^N \tag{4}$$

Thus, the fractional Green formula is as:

$$\int_\Omega \mu \mathrm{div}^v\phi d\Omega = \overline{-}\int_\Omega \overline{(-1)^v} D^v\mu \cdot \phi d\Omega \tag{5}$$

So, according to the fractional Green formula, we could get the fractional total variation and bounded variation function space as follows:

Suppose Ω is a real subset on real plane, fun value is Radon measurement on Ω, when $\forall\phi = (\phi_1, \phi_2) \in C_0^1(\Omega)^2$, and $\left|\phi_{L^\infty(\Omega)}\right| \leq 1$, it satisfies the Green function $\mu \in L^1(\Omega)$. Suppose the distributed derivative or general derivative of μ can be represented by the limited vector formula $\int_\Omega \mu \mathrm{div}^v \phi d\Omega = \overline{-}\int_\Omega \overline{(-1)^v} D^v \mu \cdot \phi d\Omega$, in which $D^v\mu = (D_x{}^v\mu, D_y{}^v\mu)$ is the limited vector value measurement on Ω, that is, the fractional gradient of μ; thus, it can be called that μ is the fractional limited variation function on Ω and can define the fractional total variation of μ as:

$$\int_\Omega \left|D^v\mu\right| d\Omega = \sup\left\{\int_\Omega \mu \mathrm{div}^v \phi d\Omega : \phi = (\phi_1, \phi_2) \in C_0^1(\Omega)^2, \left|\phi_{L^\infty(\Omega)}\right| \leq 1\right\} \tag{6}$$

The fractional limited variation function space is as:

$$BV^v(\Omega) = \left\{\mu \in L^1(\Omega), \int_\Omega \left|D^v u\right| d\Omega < \infty\right\} \tag{7}$$

in which, when $\forall\mu \in C^1(\Omega)$, that is, μ is the first-order continuous differentiable function defined on Ω, from the fractional Green formula, it can be derived that $\int_\Omega \mu \mathrm{div}^v \phi d\Omega = \overline{-}\int_\Omega \overline{(-1)^v} D^v \mu \cdot \phi d\Omega$ and thus $D^v\mu = \nabla^v\mu = \left(\frac{\partial^v \mu}{\partial x_1{}^v}, \frac{\partial^v \mu}{\partial x_2{}^v}\right)$.

3 Construction of the Image Denoising Model Based on Fractional Total Variation

It is already known the noisy image $I(x, y)$, $x, y \in \Omega$, and let the noisy image $I(x, y)$ be independent on X axis and Y axis. Thus, it is only needed to calculate the fractional gradient modulus of the image signal on the X axis. The same is for the Y axis. From the Grümwald-Letnikov definition of the fractional gradient modulus [14], it is known that the fractional derivative of image signal $I(x, \cdot)$ is:

$${}_a^G D_t^v I(x, \cdot) = \left(\frac{1}{h}\right)^n \sum_{j=0}^{N-1} (-1)^j \frac{\Gamma(v+1)}{\Gamma(j+1)\Gamma(v-j+1)} I(x - jh, \cdot) \tag{8}$$

When step size is $h = 1$, the following can be derived:

$${}_a^G D_t^v I(x) = \sum_{j=0}^{N-1} (-1)^j \binom{v}{j} I(x - j) \tag{9}$$

Let function $c^v(x)$ satisfies the below:

$$c^v(x) = \begin{cases} (-1)^x \binom{v}{x} & x \geq 0 \\ 0 & x < 0 \end{cases} \tag{10}$$

Thus, the fractional derivative of the signal $I(x, \cdot)$ can be rewritten as the convolution of signal $I(x, \cdot)$ and function $c^v(x)$ is below:

$$\overset{G}{a} D_t^v I(x, \cdot) = c^v(x) * I(x, \cdot) \tag{11}$$

Further, put formula (11) into the energy functional based on fractional $BV^v(\Omega)$ space, and the fractional variation model based on convolution integral can be obtained as in formula (12).

$$E(I) = \int_{\Omega} \left| c^v * I \right| dxdy + \frac{\lambda}{2} \| f - I \|_{L_2}^2 \tag{12}$$

The image denoising model based on Grümwald-Letnikov definition of fractional partial derivative equations can be derived by combining the basic property of function and gradient descent flow as in formula (13).

$$\frac{\partial I}{\partial t} = -\left(\int_{\Omega} c^v(z) \frac{(c^v * I)_x}{|c^v * I|} (x + z, y)\, dz + \int_{\Omega} c^v(z) \frac{(c^v * I)_y}{|c^v * I|} (x, y + z)\, dz \right) + \lambda (I_0 - I) \tag{13}$$

4 Experiments and Theoretical Analysis

In solving the denoising model to get the numeric value of the fractional derivative, we still use the fractional derivative mask operator W_j in reference [11] that fractional derivative operator is rotation invariant [15], that is, it includes mask W_x^+ along the positive direction of X axis, mask W_x^- along the negative direction of X axis, mask W_y^+ along the positive direction of X axis, mask W_y^- along the negative direction of X axis, mask W_x^{45} along the 45° direction counterclockwise to the positive X axis, mask W_x^{135} along the 135° direction counterclockwise to the positive X axis, mask W_x^{225} along the 225° direction counterclockwise to the positive X axis, and mask W_x^{315} along the 315° direction counterclockwise to the positive X axis.

This paper mainly studies the image denoising model based on fractional partial derivative equations with fractional gradient as the measurement, assuming the denoising effect mainly relates with the regularization term in the denoising model, that is, without considering compensation for the information loss in the noisy image. Thus the experiments about image denoising model in this paper all ignore the effect of fidelity term, that is, all assuming fidelity coefficient $\lambda = 0$. Consequently the denoising performance of different denoising models can be compared in the same condition. And replacing the function c^v with fractional derivative modulus W_i^j, we can obtain the improved denoising model based on spatial fractional partial derivative equations as shown in (14).

$$\frac{\partial I}{\partial t} = -\begin{pmatrix} \left(W_{x^+} \circ \frac{(W_{x+} * I)}{|c^v * I|}\right) + \left(W_{x^-} \circ \frac{(W_{x-} * I)}{|c^v * I|}\right) + \left(W_{y^+} \circ \frac{\left(W_{y+} * I\right)}{|c^v * I|}\right) + \left(W_{y^-} \circ \frac{\left(W_{y-} * I\right)}{|c^v * I|}\right) + \ldots \\ \left(W_{x^{45}} \circ \frac{(W_{x45} * I)}{|c^v * I|}\right) + \left(W_{x^{135}} \circ \frac{(W_{x135} * I)}{|c^v * I|}\right) + \left(W_{x^{225}} \circ \frac{(W_{x225} * I)}{|c^v * I|}\right) + \left(W_{x^{315}} \circ \frac{(W_{x315} * I)}{|c^v * I|}\right) \end{pmatrix} \tag{14}$$

As shown in Figs. 1, 2, and 3, subgraphs (c), (d), (e), and (f) in graph, respectively, represent the resulting images and their residual image after denoising the camera man image, lena image, and barbara image which have Gaussian white noise (mean $\mu = 0$ and variance $\sigma^2 = 0.15$), using the model in reference [11] and the model proposed in this paper, correspondingly (the order of the fractional derivative in the model proposed in this paper is the same as that in reference [11], that is, $v = 1.2$). Observing directly, compared with the traditional FPDE model, the proposed model in this paper is able to preserve the detailed information such as image boundary and texture because of the use of the boundary stop function with fractional gradient modulus as the parameter.

As shown in Figs. 4, 5, and 6, compare the denoising performance curves of both the traditional model and the improved model. It can be observed that the signal-to-noise ratios (SNR) both increase to some peak level and then decrease with the number of iteration increasing in the denoising process. The denoising model proposed in this paper is able to obtain higher SNR than that of the traditional FPDE model (camera man images experiment, SNR by the model proposed in this paper is 19.09 db, while SNR by FPDE is 18.5 db; lena images experiment, SNR by the model proposed in this paper is 16.24 db, while SNR by FPDE is 15.5 db; barbara images experiment, SNR by the model proposed in this paper is 17.31 db, while SNR by FPDE is 16.67 db).

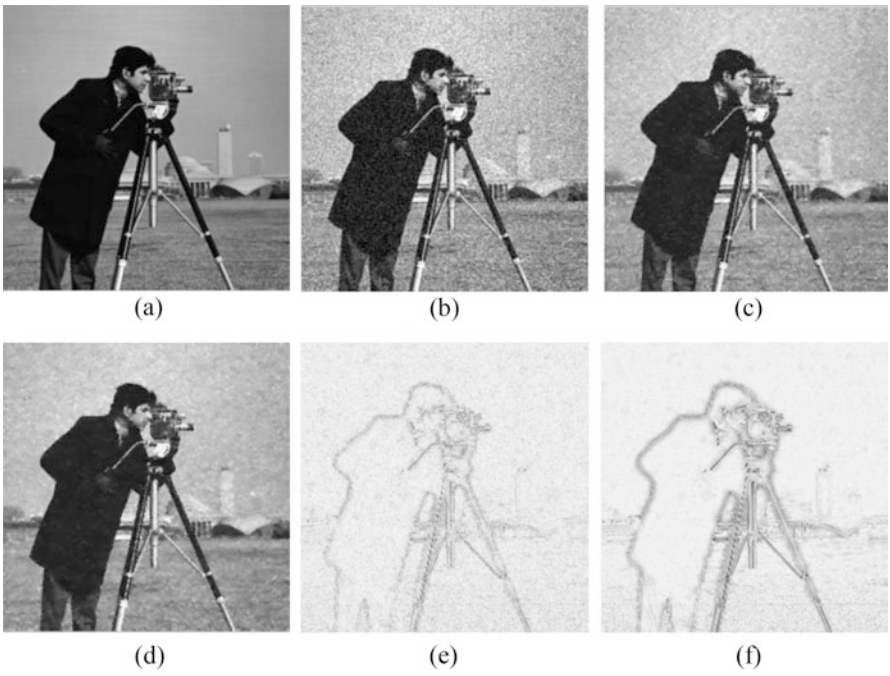

Fig. 1 The camera man images and their corresponding level lines after implementing denoising by traditional model and improved model. (**a**) Original, (**b**) noise image, (**c**) FPD, (**d**) improved model, (**e**) residual image by FPDE, (**f**) residual image by improved model

5 Conclusion

To solve the problems existing in the various image denoising models based on integer-order partial differential equations, researchers introduced fractional calculus theory into the image denoising models based on partial derivative equations and constructed image denoising models based on fractional partial differential equations [16]. These models build the energy functional of the denoising model by replacing integer-order gradient operator with fractional-order gradient operator and solved issues such as "staircase effect" in image denoising modes based on integer-order partial differential equations. On this basis, targeting the issues in the existing image denoising models based on space-fractional partial differential equations, this paper tries to introduce the boundary stop function with fractional gradient modulus as the parameter and implement the numeric computation of the space-fractional partial differential equations by constructing the fractional differential mask operators along eight directions. Thus the proposed denoising model not only has the same advantage or preserving boundary information of the image as that of the models based on integer-order partial differential equations, but also in some degree preserves the texture information of the image.

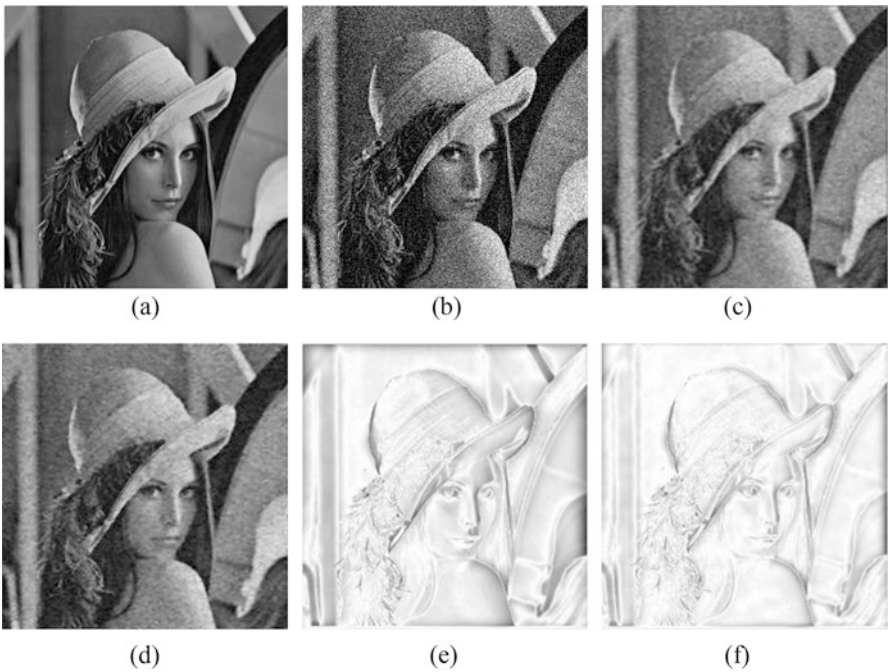

Fig. 2 The lena images and their corresponding level lines after implementing denoising by traditional model and improved model. (**a**) Original, (**b**) noise image, (**c**) FPD, (**d**) improved model, (**e**) residual image by FPDE, (**f**) residual image by improved model

Experimental results show that the proposed model is more capable of noise suppressing and boundary preserving, compared with traditional denoising models. Especially, this model will not greatly attenuate the detailed texture information in the smooth regions of the image where there is little change in gray levels. On the contrary, it nicely preserves more detailed texture information of the image. On the other hand, the image denoising model proposed in this paper, which is based on space-fractional partial differential equations, is only some initial attempts and promotion of the fractional differential theory applying to image enhancement.

The algorithm is not flawless, and the future improvements need to solve the following issues: how to design the numeric computation methods for the space-fractional partial differential equations to obtain more accurate numeric solution, how to construct more reasonable boundary stop function to better preserve the detailed information such as edges and textures in the image during the denoising process, and how to establish the complex relations between the order of the space-fractional differential equations and the effect of the denoised image so that the model can make the denoising process more self-adaptively based on the local noise and texture characteristics of the image.

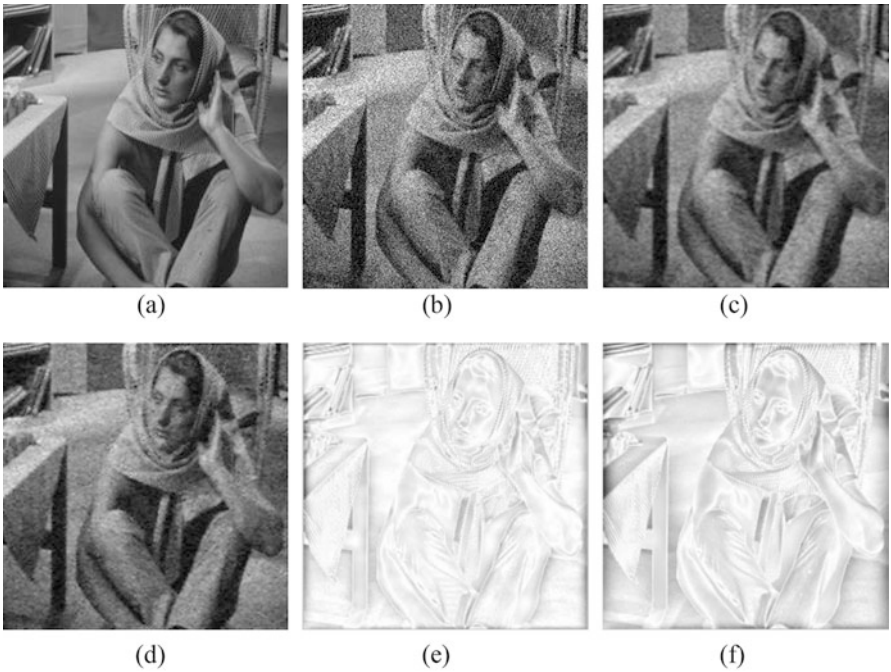

Fig. 3 The barbara images and their corresponding level lines after implementing denoising by traditional model and improved model. (**a**) Original, (**b**) noise image, (**c**) FPD, (**d**) improved model, (**e**) residual image by FPDE, (**f**) residual image by improved model

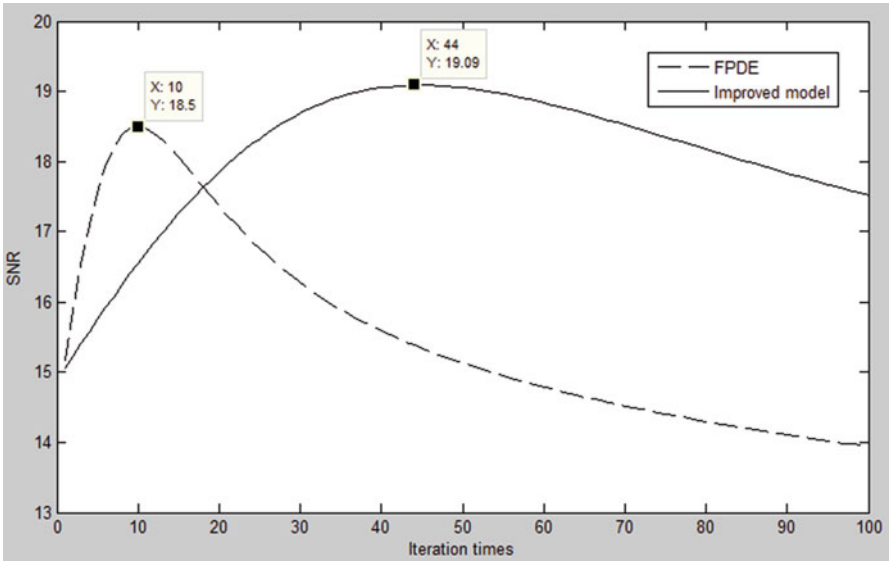

Fig. 4 The contrast of denoising performance curves about camera man image implementing by traditional FPDE model and improved model

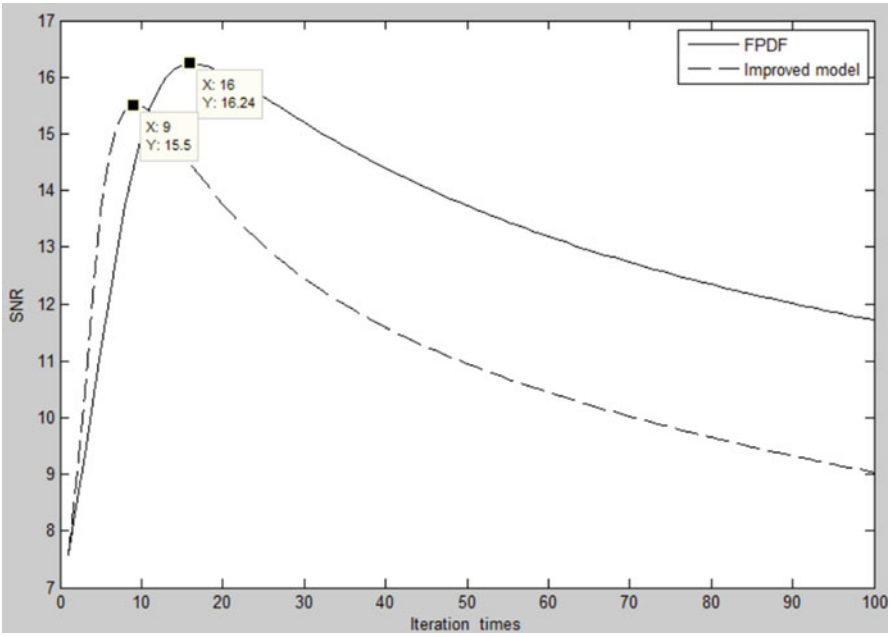

Fig. 5 The contrast of denoising performance curves about lena image implementing by traditional FPDE model and improved model

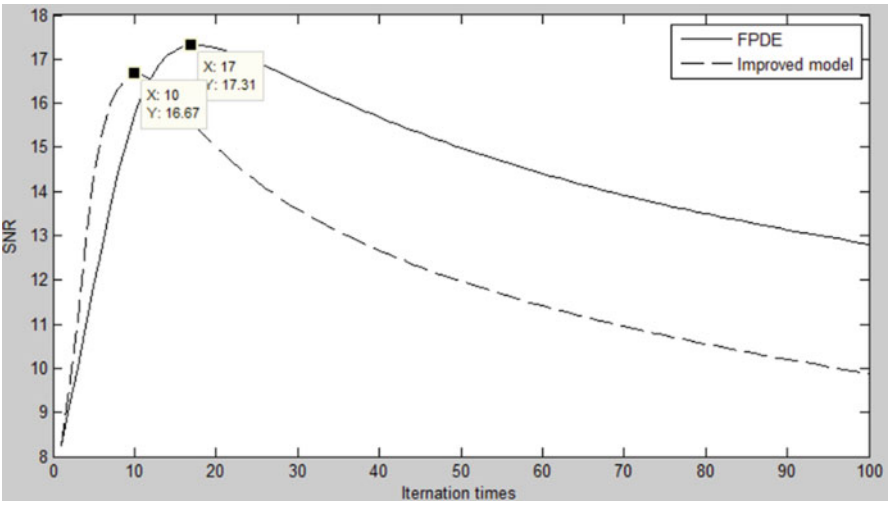

Fig. 6 The contrast of denoising performance curves about barbara image implementing by traditional FPDE model and improved model

Acknowledgment This work is supported by Sichuan province science and technology department application foundation project (2016JY0238) and Scientific Research Fund of Sichuan Province Education Department(18ZA0363,18ZB0374, 18ZB0376) and Key Research Base for Social Science in Sichuan Province-Sichuan Tourism Development Research Center Project (LYC15-09).

References

1. Tschumperle D, Deriche R (2005) Vector-valued image regularization with PDEs: a common framework for different applications [J]. IEEE Trans Pattern Anal Mach Intell 27(4):506–517
2. Gilboa G, Sochen N, Zeevi YY (2006) Variational denoising of partly textured images by spatially varying constraints [J]. IEEE Trans Image Process 15(8):2281–2289
3. Perona P, Malik J (1990) Scale-space and edge detection using anisotropic diffusion [J]. IEEE Trans Pattern Anal Machine Intell 12(7):629–639
4. Ruding L, Osher S, Fatemi E (1992) Nonlinear total variation based noise removal algorithms [J]. Physical D 60(1–4):259–268
5. Osher S, Rudin LI, Fatemi E (1992) Nonlinear total variation based noise removal algorithms [J]. Physica D Nonlinear Phenomena 60(3):259–268
6. Kass M, Witkin A, Terzopoulos D (1988) Snakes: active contour models [J]. Int J Comput Vis 1(4):321–331
7. Pu Y-F, Zhou J-L, Siarry P (2013) Fractional extreme value adaptive training method: fractional steepest descent approach. IEEE Trans Neural Netw Learn Syst 26(4):653–663
8. Pu YF, Siarry P, Zhou JL (2014) Fractional partial differential equation denoising models for texture image [J]. Science China Inf Sci 57(7):1–19
9. Bai J, Feng X-C (2007) Fractional-order anisotropic diffusion for image Denoising [J]. IEEE Trans Image Process 16:2492–2502
10. Zhang J, Wei Z (2011) A class of fractional-order multi-scale variational models and alternating projection algorithm for image denoising [J]. Appl Math Model 35(5):2516–2528
11. Zhang J, Wei Z (2010) Fractional-order multi-scale variation PDE model and adaptive algorithm for SAR image denoising [J]. J Electron Inf Technol 32(7):1654–1659
12. Wu C, Tai XC (2010) Augmented Lagrangian method, dual methods, and split Bregman iteration for ROF, vectorial TV, and high order models [J]. Siam J Imaging Sci 3(3):300–339
13. Ren Z, He C, Zhang Q (2013) Fractional order total variation regularization for image super-resolution [J]. Signal Process 93(9):2408–2421
14. Ortigueira MD, Rodríguez-Germá L, Trujillo JJ (2011) Complex Grünwald–Letnikov, Liouville, Riemann–Liouville, and Caputo derivatives for analytic functions [J]. Commun Nonlinear Sci Numerical Simulation 16(11):4174–4182
15. Tomovski Ž (2012) Generalized Cauchy type problems for nonlinear fractional differential equations with composite fractional derivative operator [J]. Nonlinear Anal 75(7):3364–3384
16. Jiang W, Wang ZX (2012) Image denoising new method based on fractional partial differential equation [J]. Adv Mater Res 532-533:797–802

Total Variation with Overlapping Group Sparsity for Removing Mixed Noise

Jin-Jin Mei and Ting-Zhu Huang

1 Introduction

In imaging applications, the observed images are unavoidably corrupted by the noise during the process of acquisition, transmission, or storage. Therefore, the image denoising is always an essential task in image processing. Researchers have proposed many methods to remove the noise; see [1–12] and references therein. But in the synthetic aperture radar (SAR) imaging system, the observed images are usually contaminated with the multiplicative noise due to the image formation under coherent radiation while the additive noise due to the thermal vibrations of image capture radiation [13, 14]. Assume that $\Omega \subset \mathbb{R}^2$ is a connected bounded domain with the compacted Lipschitz boundary; we consider a degradation model under the mixed additive and multiplicative noise,

$$f = u + k_0\eta + k_1 u\eta \tag{1}$$

where $f \in L^2(\Omega)$ is the noisy image, u is the unknown original image, η denotes the Gaussian white noise with mean zero and variance one, and $k_0, k_1 > 0$ represent the noise level.

As far as we know, there are a few mathematical techniques for removing the mixed additive and multiplicative noise. In [14], the authors assume that a patch from the original image is a linear combination of patches from the noisy image. They considered the total least square (TLS) sense to obtain the true image. In [15],

J.-J. Mei (✉) · T.-Z. Huang
School of Mathematical Sciences, University of Electronic Science and Technology of China, Chengdu, Sichuan, China

School of Mathematics and Statistics, Fuyang Normal University, Fuyang, Anhui, China
e-mail: meijinjin666@126.com;tingzhuhuang@126.com

M. Jiang et al. (eds.), *The Proceedings of the International Conference on Sensing and Imaging*, Lecture Notes in Electrical Engineering 506,
https://doi.org/10.1007/978-3-319-91659-0_16

since the TV regularization preserves the image edges effectively, Chumchob et al. proposed a convex variational model (called TV-EXP for short) for removing the mixed noise,

$$\min_{u\in BV(\Omega)} \int_{\Omega} |\nabla u| dx + \frac{\alpha_1}{2} \int_{\Omega} (u-f)^2 dx + \alpha_2 \int_{\Omega} (u + fe^{-u}) dx \tag{2}$$

where α_1 and α_2 are the positive regularization parameters, which control the trade-off between the TV regularization term and the data-fitting terms. $BV(\Omega)$ is the space of functions $u \in L^1(\Omega)$ such that

$$\int_{\Omega} |\nabla u| dx := \sup \left\{ \int_{\Omega} u \ \mathrm{div}\varphi \ dx : \varphi \in (C_0^{\infty}(\Omega))^2, \|\varphi\|_{\infty} \leq 1 \right\}$$

is finite. With the norm $\|u\|_{BV(\Omega)} = \|u\|_{L^1(\Omega)} + \int_{\Omega} |\nabla u| dx$, $BV(\Omega)$ is a Banach space. For more details, see [16, 17] and references therein. In order to obtain the solution of (2), they applied a nonlinear multigrid method based on the fixed-point smoother. But this mathematical method is comparatively complicated and time-consuming. Moreover, there exist some staircase artifacts in the restored images.

Recently, researchers have studied a new TV regularization method based on the overlapping group sparsity [10, 18, 19]. The numerical experiments showed that this regularization can suppress the staircase artifacts effectively. Therefore, inspired by the advantage of the TV with overlapping group sparsity, we propose two convex models for removing the mixed additive and multiplicative noise. In this paper, we develop the ADMM algorithm to solve the proposed models, and the convergence of the algorithm is guaranteed under certain conditions. Furthermore, according to the peak signal-to-noise ratio (PSNR) and the structural similarity index (SSIM) [20], experimental results show that our proposed methods are effective.

This paper is summarized as follows. In the next section, we review the TV with overlapping group sparsity and the framework of ADMM. In Sect. 3, we propose two variational models based on the TV with overlapping group sparsity and develop the ADMM algorithm for solving the proposed models. The experiments show the superior performance in Sect. 4. Finally, we conclude the paper in Sect. 5.

2 Preliminaries

2.1 TV with Overlapping Group Sparsity

For completeness, we briefly review the TV with overlapping group sparsity. Firstly, we assume that the original image $u \in \mathbb{R}^{n^2}$ which is rearranged in the lexicographically order. In other words, the $((j-1)n+i)$th element of the vector u is equal to the (i, j)th element of the corresponding square matrix. According to [10], a K-square-point group of a two-dimensional image is defined as follows:

$$\tilde{u}_{i,j,K} = \begin{pmatrix} u_{i-K_1,j-K_1} & u_{i-K_1,j-K_1+1} & \cdots & u_{i-K_1,j+K_2} \\ u_{i-K_1+1,j-K_1} & u_{i-K_1+1,j-K_1+1} & \cdots & u_{i-K_1+1,j+K_2} \\ \vdots & \vdots & \ddots & \vdots \\ u_{i+K_2,j-K_1} & u_{i+K_2,j-K_1+1} & \cdots & u_{i+K_2,j+K_2} \end{pmatrix} \in \mathbb{R}^{K\times K},$$

where $K_1 = \left[\frac{K-1}{2}\right]$, $K_2 = \left[\frac{K}{2}\right]$, and $[x]$ represents the largest integer no more than x. Similarly, by stacking all the columns of $\tilde{u}_{i,j,K}$, we obtain a vector $u_{i,j,K} \in \mathbb{R}^{K^2}$. Then an overlapping group sparsity functional is defined as

$$\phi(u) = \sum_{i,j=1}^{n} \|u_{i,j,K}\|_2.$$

According to [10, 18, 19], the anisotropic TV functional with overlapping group sparsity is given by

$$\Phi(Du) = \phi(D_1 u) + \phi(D_2 u),$$

where the operator $D : \mathbb{R}^{n^2} \to \mathbb{R}^{2n^2}$ is the discrete gradient operator satisfied $(Du)_{i,j} = ((D_1u)_{i,j}, (D_2u)_{i,j})$. Here, D_1 and D_2 are the first-order finite difference operators in the horizontal and vertical directions under the periodic boundary condition.

2.2 Classic ADMM

The ADMM technique is widely applied for solving the constrained separable optimization problem

$$\min_{x\in X, y\in Y} f(x) + g(y) \quad \text{s.t.} Ax + By = b \tag{3}$$

where $f(x)$ and $g(y)$ are closed convex and lower semicontinuous functions, $X \subset \mathbb{R}^m$ and $Y \subset \mathbb{R}^n$ are closed convex sets, and $A \in \mathbb{R}^{l\times m}$ and $B \in \mathbb{R}^{l\times n}$ are linear operators [21–23]. By introducing a multiplier $\lambda \in \mathbb{R}^l$, the corresponding augmented Lagrangian function is given by

$$\mathcal{L}(x, y; \lambda) = f(x) + g(y) + \lambda^\top (Ax + By - b) + \frac{\beta}{2}\|Ax + By - b\|_2^2 \tag{4}$$

where β is a positive penalty parameter. According to the framework of ADMM, the solution (x^{k+1}, y^{k+1}) is obtained by

$$\begin{cases} x^{k+1} = \arg\min_x f(x) + \frac{\beta}{2}\|Ax + By^k - b + \frac{\lambda^k}{\beta}\|_2^2, \\ y^{k+1} = \arg\min_y g(y) + \frac{\beta}{2}\|Ax^{k+1} + By - b + \frac{\lambda^k}{\beta}\|_2^2, \\ \lambda^{k+1} = \lambda^k + \gamma\beta(Ax^{k+1} + By^{k+1} - b) \end{cases} \tag{5}$$

where $\gamma > 0$ represents a relax parameter. Based on the work [22], if $\gamma \in \left(0, \frac{\sqrt{5}+1}{2}\right)$, the convergence of ADMM is guaranteed.

3 The Proposed Model

Inspired by the works [1, 6, 10], we propose an exponential variational model (just referred to as OGSTV-EXP) for removing the mixed additive and multiplicative noise

$$\min_{u>0} \phi(D_1 u) + \phi(D_2 u) + \frac{\alpha_1}{2}\|u - f\|_2^2 + \alpha_2\langle u + fe^{-u}, \mathbf{1}\rangle \tag{6}$$

where $\mathbf{1}$ denotes a vector which all components are equal to one and the multiplication between two vectors is performed in componentwise. The fourth data-fitting term of the model (6) is obtained by the logarithmic transformation. But the logarithmic transformation is nonlinear. For overcoming the disadvantage, we also present an I-divergence variational model by combining the TV with overlapping group sparsity,

$$\min_{u>0} \phi(D_1 u) + \phi(D_2 u) + \frac{\alpha_1}{2}\|u - f\|_2^2 + \alpha_2\langle u - f\log u, \mathbf{1}\rangle. \tag{7}$$

We refer to the above model as OGSTV-Idiv. According to [7], due to the invariant property of TV, the solutions of the exponential model and the I-divergence model for removing the mixed additive and multiplicative noise are equal. Then for dealing with the models (6) and (7), we rewrite these two models as the following synthetical model:

$$\min_{u>0} \phi(D_1 u) + \phi(D_2 u) + \frac{\alpha_1}{2}\|u - f\|_2^2 + \alpha_2 F(u), \tag{8}$$

where $F(u)$ is equal to $\langle u + fe^{-u}, \mathbf{1}\rangle$ for (6) and $\langle u - f\log u, \mathbf{1}\rangle$ for (7). In the following, we apply the ADMM technique mentioned above to solve the minimization model (8).

By introducing three auxiliary variables v_1, v_2, and $w \in \mathbb{R}^{n^2}$, we transform the model (8) into the equivalent constrained minimization,

$$\min_{u>0,v_1,v_2,w} \phi(v_1) + \phi(v_2) + \frac{\alpha_1}{2}\|u - f\|_2^2 + \alpha_2 F(w). \tag{9}$$
$$\text{s.t.} v_1 = D_1 u, v_2 = D_2 u, w = u$$

Then, the corresponding augmented Lagrangian function is given as

$$\begin{aligned}\mathcal{L}(u, v_1, v_2, w; \lambda_1, \lambda_2, \lambda_3) = \phi(v_1) + \langle \lambda_1, v_1 - D_1 u\rangle + \frac{\beta_1}{2}\|v_1 - D_1 u\|_2^2 + \phi(v_2) \\ + \langle \lambda_2, v_2 - D_2 u\rangle + \frac{\beta_1}{2}\|v_2 - D_2 u\|_2^2 + \frac{\alpha_1}{2}\|u - f\|_2^2 \\ + \alpha_2 F(w) + \langle \lambda_3, w - u\rangle + \frac{\beta_2}{2}\|w - u\|_2^2,\end{aligned}$$

where $\beta_1, \beta_2 > 0$ are the penalty parameters. By the framework of ADMM, the whole algorithm for removing the mixed additive and multiplicative noise is given as follows.

Algorithm 1 ADMM algorithm for solving (8)

1: Initialize u^0, v_1^0, v_2^0, w^0, λ_1^0, λ_2^0 and λ_3^0; set $\alpha_1, \alpha_2, \beta_1, \beta_2, \gamma$.
2: For $k = 1, 2, \ldots$, calculate u^{k+1}, v_1^{k+1}, v_2^{k+1}, w^{k+1}, λ_1^{k+1}, λ_2^{k+1}, λ_3^{k+1} by

$$v_l^{k+1} = \arg\min_{v_l} \phi(v_l) + \frac{\beta_1}{2}\|v_l - D_l u^k + \frac{\lambda_l^k}{\beta_1}\|_2^2, \quad l = 1, 2 \tag{10}$$

$$w^{k+1} = \arg\min_{w} \alpha_2 F(w) + \frac{\beta_2}{2}\|w - u^k + \frac{\lambda_3^k}{\beta_2}\|_2^2 \tag{11}$$

$$u^{k+1} = \arg\min_{w} \mathcal{L}(u, v_1^{k+1}, v_2^{k+1}, w^{k+1}; \lambda_1^k, \lambda_2^k, \lambda_3^k) \tag{12}$$

$$\lambda_l^{k+1} = \lambda_l^k + \gamma\beta_1(v_l^{k+1} - D_l u^{k+1}), \quad l = 1, 2$$

$$\lambda_3^{k+1} = \lambda_3^k + \gamma\beta_2(w^{k+1} - u^{k+1})$$

3: If u^{k+1} satisfies the stopping criteria $\|u^{k+1} - u^k\|_2/\|u^k\|_2 \le 1 \times 10^{-4}$, return u^{k+1} and stop.

1. For obtaining v_1^{k+1} and v_2^{k+1}, we utilize the classical majorization-minimization (MM) method to deal with (10). The MM method is a good way to address the difficult optimization problem. Specifically, let $Q(t, t')$ be a majorizor[1] of the

[1] A function $Q(t, t')$ is a majorizor of the function $P(t)$, if $Q(t, t') \ge P(t)$ for all t, t' and $Q(t, t) = P(t)$.

function $P(t)$. Then instead of directly solving the minimizer of $P(t)$, the MM iterative method is formulated as an easier optimization minimization problem

$$t^{k+1} = \arg\min_{t} Q(t, t^k). \tag{13}$$

Note that when $P(t)$ is convex, the iterative sequence t^{k+1} obtained by (13) converges to the minimizer of $P(t)$. Therefore, in order to solve (10), we first need to find a majorizor of $\phi(v_l)$. Based on the fact that $\frac{1}{2}\left(\frac{1}{\|t\|_2}\|s\|_2^2 + \|t\|_2\right) \geq \|s\|_2$ for all $t, s \in \mathbb{R}^{n^2}$ and $t \neq 0$, we have a majorizor of $\phi(v_l)$,

$$\begin{aligned} S(t, v_l) &= \frac{1}{2}\sum_{i,j=1}^{n}\left(\frac{1}{\|t_{i,j,K}\|_2}\|(v_l)_{i,j,K}\|_2^2 + \|t_{i,j,K}\|_2\right) \\ &= \frac{1}{2}\|\Lambda(t)v_l\|_2^2 + C(t), \quad l = 1, 2 \end{aligned}$$

where $t_{i,j,K} \neq 0$, $C(t)$ is independent of v_l and $\Lambda(t)$ is a diagonal matrix with each diagonal element $\sqrt{\sum_{m_1,m_2=-K_1}^{K_2}\left(\sum_{n_1,n_2=-K_1}^{K_2}|t_{i-m_1+n_1,j-m_2+n_2}|^2\right)^{-1/2}}$. As a result, we solve the minimization

$$v_l^{k+1} = \arg\min_{v_l} \frac{1}{2}\|\Lambda(v_l^k)v_l\|_2^2 + \frac{\beta_1}{2}\|v_l - D_l u^k + \frac{\lambda_l^k}{\beta_1}\|_2^2, \quad l = 1, 2.$$

The solutions of (10) are obtained by

$$v_l^{k+1} = \left(I + \frac{1}{\beta_1}\Lambda^2(v_l^k)\right)^{-1}\left(D_l u^k - \frac{\lambda_l^k}{\beta_1}\right), \quad l = 1, 2 \tag{14}$$

where I represents the identity matrix.

2. For the w-subproblem, if $F(w) = \langle w + fe^{-w}, \mathbf{1}\rangle$, we apply the Newton iterative method to solve (11). But if $F(w) = \langle w - f\log w, \mathbf{1}\rangle$, by the first-order condition with respect to w, we deduce the following equation:

$$w^2 + \left(\frac{\alpha_2}{\beta_2}I + \frac{\lambda_3^k}{\beta_2} - u^k\right)w - \frac{\alpha_2}{\beta_2}f = 0.$$

The solution is given by

$$w^{k+1} = \frac{u^k - \frac{\alpha_2}{\beta_2}I - \frac{\lambda_3^k}{\beta_2} + \sqrt{(u^k - \frac{\alpha_2}{\beta_2}I - \frac{\lambda_3^k}{\beta_2})^2 + 4\frac{\alpha_2}{\beta_2}f}}{2}. \tag{15}$$

3. With respect to the u-subproblem, we obtain the corresponding normal equation

$$\left(\beta_1 D^\top D + (\alpha_1 + \beta_2) I\right) u = \sum_{l=1}^{2} D_l^\top (\lambda_l^k + \beta_1 v_l^{k+1}) + \alpha_1 f + \lambda_3^k + \beta_2 w^{k+1}.$$

Under the periodic boundary condition, the Hessian matrix on the left-hand side can be diagonalized by the discrete fast Fourier transform $\mathcal{F}$. Consequently, we get the solution

$$u = \mathcal{F}^{-1}\left(\frac{\mathcal{F}(\sum_{l=1}^{2} D_l^\top (\lambda_l^k + \beta_1 v_l^{k+1}) + \alpha_1 f + \lambda_3^k + \beta_2 w^{k+1})}{\mathcal{F}\left(\beta_1 D^\top D + (\alpha_1 + \beta_2) I\right)}\right) \tag{16}$$

where $\mathcal{F}^{-1}$ represents the inverse fast Fourier transform.

Algorithm 1 is a direct application of the classic ADMM. Motivated by [22], we give the convergence analysis of Algorithm 1.

Theorem 1 *For fixed $\beta_1, \beta_2 > 0$ and $\gamma \in (0, \frac{\sqrt{5}+1}{2})$, the ADMM algorithm for the model (8) converges.*

Proof For illustrating the convergence of Algorithm 1, we first transform (8) into the general constrained convex problem (3). Therefore, we let

$$x = (v_1, v_2, w)^\top, \qquad f(x) = \phi(v_1) + \phi(v_2) + \alpha_2 F(w)$$
$$y = u, \qquad g(y) = \frac{\alpha_1}{2}\|u - f\|_2^2.$$

The constrained conditions in (9) are rewritten as the following form:

$$Ax + By = b$$

where

$$A = \begin{pmatrix} I & 0 & 0 \\ 0 & I & 0 \\ 0 & 0 & I \end{pmatrix}, \qquad B = \begin{pmatrix} -D_1 \\ -D_2 \\ -I \end{pmatrix}, \qquad b = \mathbf{0}.$$

According to [22, 24], we deduce that for fixed $\beta_1, \beta_2 > 0$, and $\gamma \in (0, \frac{\sqrt{5}+1}{2})$, Algorithm 1 is convergent.

Note that the v_1, v_2 and u-subproblems have the closed solutions in Algorithm 1. Although the w-subproblem is approximatively solved by the Newton iterative method, Algorithm 1 is empirically convergent. Furthermore, Fig. 1 shows the curve of the energy functional values is decreasing along the iteration number increasing.

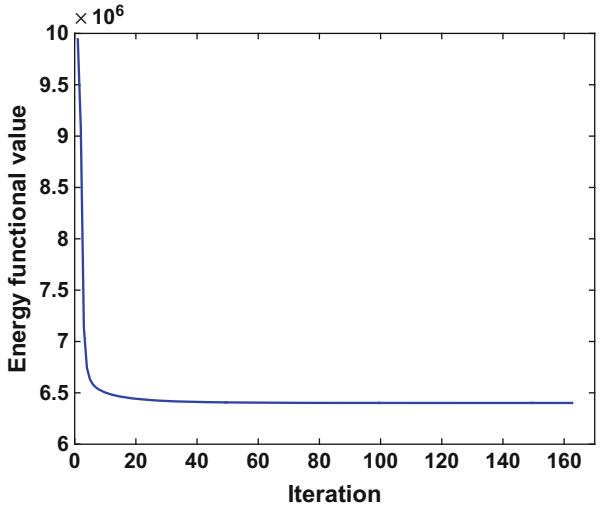

Fig. 1 Plot of the energy functional values in (8) for the image "test," where the level of the mixed noise is (10, 0.3)

Fig. 2 Original images. (**a**) Test (256 × 256); (**b**) house (256 × 256); (**c**) peppers (512 × 512); (**d**) SAR (256 × 256)

4 Numerical Experiments

In this section, we demonstrate the performance of the proposed methods for removing the mixed additive and multiplicative noise. Figure 2 shows four 8-bit grayscale test images including three natural images and one real SAR image. We compare the proposed methods with TV-EXP [15]. All numerical experiments are performed under Windows 10 and MATLAB R2015b running on a Lenovo desktop with 3.4 GHz Intel Core CPU and 4GB RAM. We apply PSNR and SSIM to measure the quality of the restored images, which are, respectively, defined as

$$\mathrm{PSNR} = 20\log 10\left(\frac{255n}{\|u^* - u\|_2}\right), \quad \mathrm{SSIM} = \frac{2\mu_{u^*}\mu_u(2\sigma + c_2)}{(\mu_{u^*}^2 + \mu_u^2 + c_1)(\sigma_{u^*}^2 + \sigma_u^2 + c_2)},$$

Table 1 The values of PSNR and SSIM for the restored images by applying different methods

Image	Noisy	TV-EXP		OGSTV-EXP		OGSTV-Idiv	
Test	(10,0.1)	35.83	0.9451	36.26	0.9664	**36.35**	0.9680
	(20,0.1)	33.83	0.9335	**34.40**	0.9623	34.33	0.9570
	(10,0.3)	30.31	0.9160	**31.15**	0.9460	31.10	0.9450
	(20,0.3)	29.68	0.9014	30.27	0.9424	**30.31**	0.9270
House	(10,0.1)	30.18	0.8142	30.68	0.8231	**30.72**	0.8240
	(20,0.1)	28.77	0.7917	29.26	0.8023	**29.32**	0.8040
	(10,0.3)	26.47	0.7421	27.02	0.7564	**27.06**	0.7570
	(20,0.3)	25.72	0.7188	26.35	0.7421	**26.38**	0.7350
Peppers	(10,0.1)	30.55	0.9205	31.11	0.9265	**31.13**	0.9270
	(20,0.1)	28.97	0.8890	29.66	0.9041	**29.67**	0.9050
	(10,0.3)	27.09	0.8521	**27.65**	0.8626	27.65	0.8620
	(20,0.3)	26.48	0.8292	**26.96**	0.8482	26.96	0.8470
SAR	(10,0.1)	27.42	0.7542	27.71	0.7670	**27.77**	0.7701
	(20,0.1)	26.00	0.7119	26.25	0.7164	**26.30**	0.7203
	(10,0.3)	24.10	0.6297	24.32	0.6353	**24.35**	0.6395
	(20,0.3)	23.56	0.6021	23.77	0.6103	**23.81**	0.6180

where u^* is the restored image, μ_{u^*} is the mean of u^*, μ_u is the mean of the original image u, $\sigma^2_{u^*}$ and σ^2_u are their respective variances, σ is the covariance of u^* and u, and $c_1, c_2 > 0$ are constants.

For the parameters $\alpha_1, \alpha_2, \beta_1$ and β_2 in Algorithm 1, we manually tune for obtaining the highest PSNR values. Since the value of γ affects the convergent speed, we set $\gamma = 1.618$ which makes the ADMM algorithm converge faster than $\gamma = 1$. In addition, we set the iteration number of the Newton method for solving (6) as 5. The iteration number of the MM method equals 10 for solving (6) and (7). For the TV regularization with overlapping group sparsity, we set the group size $K = 3$.

In the experiments, the original images are corrupted by the mixed additive and multiplicative noise with the noisy levels $(10, 0.1)$, $(20, 0.1)$, $(10, 0.3)$, and $(20, 0.3)$. In order to show the superior performance, we compare the three methods for the mixed additive and multiplicative noise removal. Table 1 lists the values of PSNR and SSIM of the restored images. Obviously, comparing with OGSTV-EXP and OGSTV-Idiv, the TV-EXP model provides the worst values of PSNR and SSIM. Especially, the values of PSNR by the proposed methods are about 0.6dB higher than the TV-EXP model. Furthermore, the OGSTV-EXP and OGSTV-Idiv models obtain the competitive results in terms of PSNR and SSIM.

Figure 3 shows the comparison of different methods for removing the mixed noise. By using the different methods, the restored images of the TV-EXP model obviously bring in the staircase effect. However, our proposed methods preserve the image details and remove the mixed additive and multiplicative noise. Due to the TV with overlapping group sparsity, it is obvious that two variational methods outperform TV-EXP, and the staircase artifacts are effectively eliminated. To further

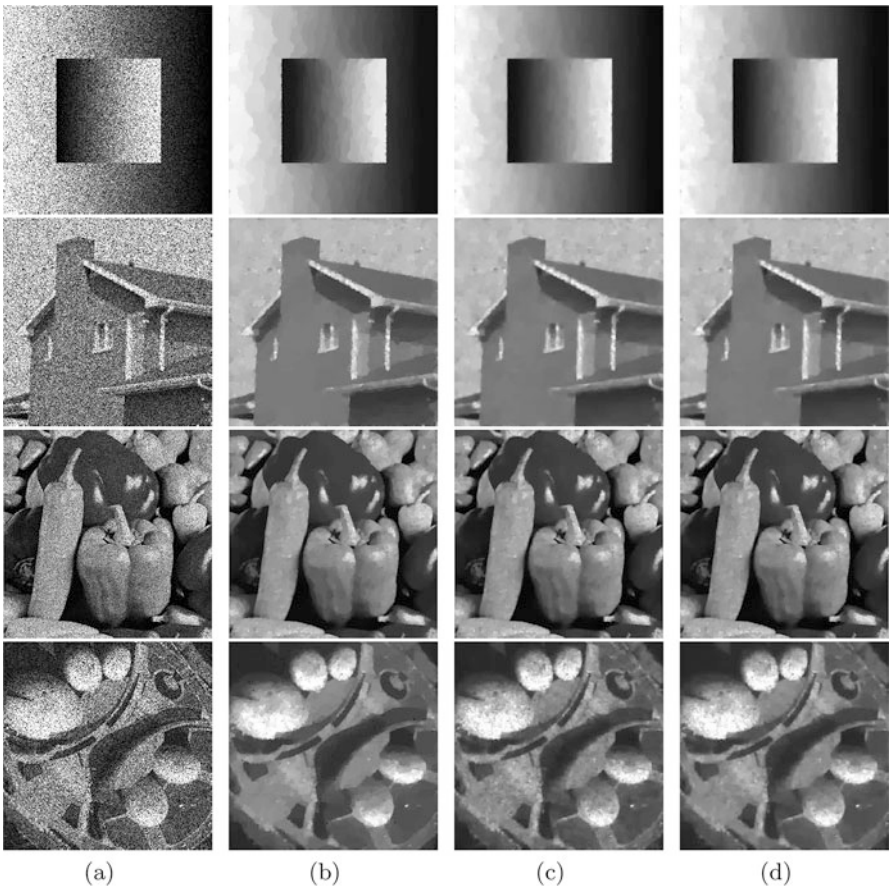

Fig. 3 Comparison of different methods for removing the mixed additive and multiplicative noise with the noise level $(10, 0.3)$. (**a**) Noisy images; (**b**) TV-EXP; (**c**) OGSTVEXP; (**d**) OGSTVIdiv

illustrate the performance of the proposed methods, we give the zoomed version of the original images and restored images shown in Fig. 4. Obviously, we find that the staircase artifacts are reduced in the homogeneous region by using the proposed methods, especially in the restored images "test," "peppers," and "SAR."

5 Conclusion

In this paper, we review the TV regularization with overlapping group sparsity and the classic ADMM. Based on the exponential model [6] and the I-divergence model [7], we present two convex variational models for removing the mixed additive and

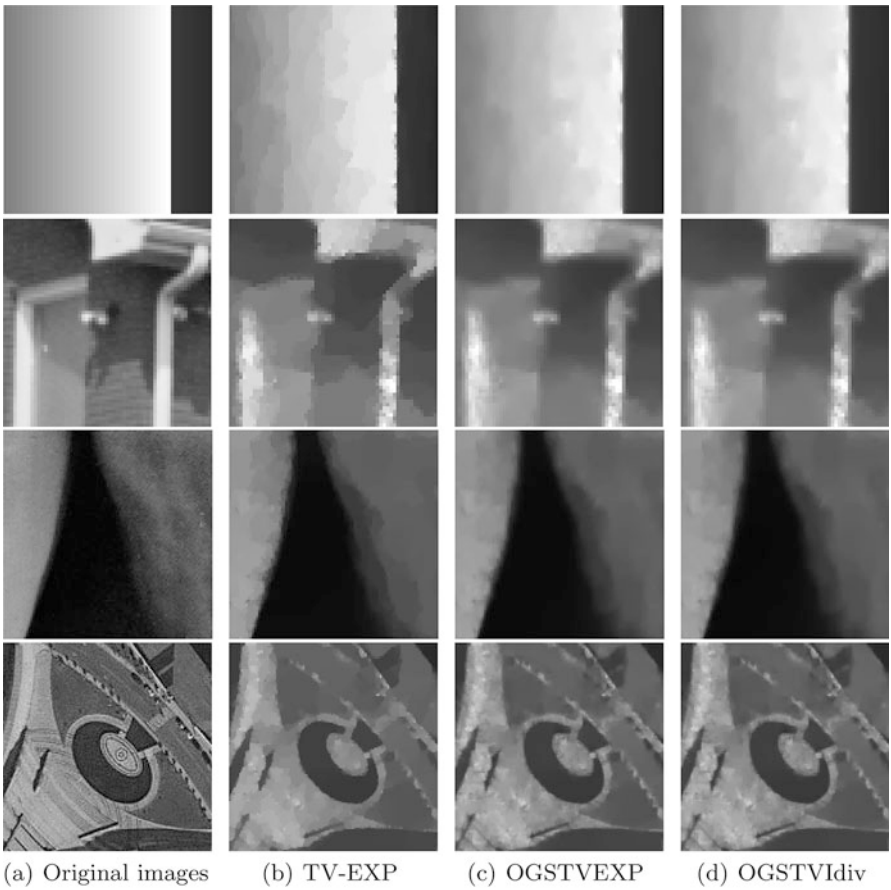

Fig. 4 Zoomed version of the images in Fig. 3. (**a**) Original images; (**b**) TV-EXP; (**c**) OGSTVEXP; (**d**) OGSTVIdiv

multiplicative noise. Due to the convergent property, ADMM is applied to solve the proposed variational problems. Numerical experiments show that the proposed methods outperform the TV-EXP model in qualitative and quantitative comparisons.

Acknowledgements This research is supported by NSFC (61772003, 61402082, 11401081) and the Fundamental Research Funds for the Central Universities (ZYGX2016J129).

References

1. Rudin LI, Osher S, Fatemi E (1992) Nonlinear total variation based noise removal algorithms. Phys D Nonlinear Phenom 60:259–268. https://doi.org/10.1016/0167-2789(92)90242-F

2. Chambolle A (2004) An algorithm for total variation minimization and applications. J Math Imaging Vis 20:89–97. https://doi.org/10.1023/B:JMIV.0000011325.36760.1e
3. Chan RH, Tao M, Yuan XM (2013) Constrained total variation deblurring models and fast algorithms based on alternating direction method of multipliers. SIAM J Imaging Sci 6:680–697. https://doi.org/10.1137/110860185
4. Aubert G, Aujo JF (2008) A variational approach to removing multiplicative noise. SIAM J Appl Math 28:925–946. https://doi.org/10.1137/060671814
5. Beck A, Teboulle M (2009) Fast gradient-based algorithms for constrained total variation image denoising and deblurring problems. IEEE Trans Image Process 18:2419–2434. https://doi.org/10.1109/TIP.2009.2028250
6. Bioucas-Dias JM, Figueiredo MAT (2010) Multiplicative noise removal using variable splitting and constrained optimization. IEEE Trans Image Process 19:1720–1730. https://doi.org/10.1109/TIP.2010.2045029
7. Steidl G, Teuber T (2010) Removing multiplicative noise by Douglas-Rachford splitting methods. J Math Imaging Vis 36:168–184. https://doi.org/10.1007/s10851-009-0179-5
8. Zhao XL, Wang F, Ng MK (2014) A new convex optimization model for multiplicative noise and blur removal. SIAM J Imaging Sci 7:456–475. https://doi.org/10.1137/13092472X
9. Dong YQ, Zeng TY (2013) A convex variational model for restoring blurred images with multiplicative noise. SIAM J Imaging Sci 6:1598–1625. https://doi.org/10.1137/120870621
10. Liu J, Huang TZ, Selesnick IW, Lv XG, Chen PY (2015) Image restoration using total variation with overlapping group sparsity. Inform Sci 295:232–246. https://doi.org/10.1016/j.ins.2014.10.041
11. Mei JJ, Huang TZ (2016) Primal-dual splitting method for high-order model with application to image restoration. Appl Math Model 40:2322–2332. https://doi.org/10.1016/j.apm.2015.09.068
12. Mei JJ, Dong YQ, Huang TZ, Yin WT (2017) Cauchy noise removal by nonconvex ADMM with convergence guarantees. J Sci Comput 1–24. https://doi.org/10.1007/s10915-017-0460-5
13. Lukin VV, Fevralev DV, Ponomarenko NN, Abramov SK, Pogrebnyak O, Egiazarian KO, Astola JT (2010) Discrete cosine transform-based local adaptive filtering of images corrupted by nonstationary noise. J Electron Imaging 19:023007–023007. https://doi.org/10.1117/1.3421973
14. Hirakawa K, Parks TW (2006) Image denoising using total least squares. IEEE Trans Image Process 15:2730–2742. https://doi.org/10.1109/TIP.2006.877352
15. Chumchob N, Chen K, Brito-Loeza C (2013) A new variational model for removal of combined additive and multiplicative noise and a fast algorithm for its numerical approximation. Int J Comput Math 90:140–161. https://doi.org/10.1080/00207160.2012.709625
16. Almgren F (1987) Review: Enrico Giusti, minimal surfaces and functions of bounded variation. Bull Am Math Soc (NS) 16:167–171
17. Ambrosio L, Fusco N, Pallara D (2000) Functions of bounded variation and free discontinuity problems. Oxford mathematical monographs. The Clarendon Press/Oxford University Press, New York
18. Selesnick IW, Chen PY (2013) Total variation denoising with overlapping group sparsity. In: 2013 IEEE international conference on acoustics, speech and signal processing (ICASSP), pp 5696–5700. https://doi.org/10.1109/ICASSP.2013.6638755
19. Liu G, Huang TZ, Liu J, Lv XG (2015) Total variation with overlapping group sparsity for image deblurring under impulse noise. PLOS ONE 10:1–23. https://doi.org/10.1371/journal.pone.0122562
20. Wang Z, Bovik AC, Sheikh HR, Simoncelli EP (2004) Image quality assessment: from error visibility to structural similarity. IEEE Trans Image Process 13:600–612. https://doi.org/10.1109/TIP.2003.819861
21. Yang JF, Zhang Y, Yin WT (2010) A fast alternating direction method for TVL1-L2 signal reconstruction from partial Fourier data. IEEE J Sel Top Signal Process 4:288–297. https://doi.org/10.1109/JSTSP.2010.2042333

22. He BS, Yang H (1998) Some convergence properties of a method of multipliers for linearly constrained monotone variational inequalities. Oper Res Lett 23:151–161. https://doi.org/10.1016/S0167-6377(98)00044-3
23. Chen C, Ng MK, Zhao XL (2015) Alternating direction method of multipliers for nonlinear image restoration problems. IEEE Trans Image Process 24:33–43. https://doi.org/10.1109/TIP.2014.2369953
24. Glowinski R (1984) Numerical methods for nonlinear variational problems. Springer, Berlin/Heidelberg. https://doi.org/10.1007/978-3-662-12613-4

Image Restoration for Target Behind Inhomogeneous Turbid Medium via Longitudinal Laser Tomography

Wenjun Yi, Xiaofeng Wang, Zhengzheng Shao, Meicheng Fu, Lei Wang, and Xiujian Li

1 Introduction

Imaging through optically inhomogeneous turbid medium is an essential observing and detecting tool in many fields such as underwater observation, astronomical observation, medical imaging, and security surveillance [1–5]. Generally, it is difficult to perfectly remove the influence of inhomogeneous turbid medium embedded into the target image through blind image restoration algorithms such as the filtering algorithms [6–10] and the total variation methods [11–15]. In order to improve the imaging performance, great progress has been made recently with methods such as ghost imaging [16, 17], wavefront shaping [18–20], and speckle correlations [21, 22]. However, most of the methods presented above, if not all, are generally designed for short-range imaging or imaging through opaque solid scattering layer in stable environments while are unable to effectively eliminate the inhomogeneous degradations induced by the fast-changing turbid medium.

Range-gated laser imaging [23–27] can effectively improve the signal-to-noise ratio (SNR) of target images by removing the backscattering noises; however, the range-gated target images will still suffer from the degradation of inhomogeneous turbid medium over the long laser transmission path, especially when the targets are partially obscured by the medium layer. In fact, the photons backscattered from the turbid medium clusters usually carry plentiful physical information of the turbid medium and the light beams, thus the inhomogeneous degradations. Therefore, rather than being ignored, the backscattering images of the turbid medium should be captured and analyzed for the target image restorations.

W. Yi · X. Wang · Z. Shao · M. Fu · L. Wang · X. Li (✉)
College of Science, National University of Defense Technology, Changsha, Hunan, China
e-mail: xjli@nudt.edu.cn

M. Jiang et al. (eds.), *The Proceedings of the International Conference on Sensing and Imaging*, Lecture Notes in Electrical Engineering 506,
https://doi.org/10.1007/978-3-319-91659-0_17

Here, based on longitudinal laser tomography (LLT) [28, 30], which can capture both the target images and the backscattering images of turbid medium to form an image sequence, we describe an optical approach to estimate the degradation caused by the turbid medium with the help of some prior system parameters and the backscattering images and further to retrieve the true target images by a proper variational model.

2 Principles of Image Restoration

The LLT system consists of a nanosecond pulsed laser and an intensified charge-coupled device (ICCD) camera, as shown in Fig. 1. By changing the gate delay of the ICCD camera through the signal timings shown in Fig. 1, the echo signals from various ranges will be captured by the camera to generate an image sequence [28]. In this paper, both the target image and the backscattering image of the turbid medium will be captured by the LLT system, and then the degradations of the target image will be estimated for further image restoration, assisted by the backscattering images together with some prior system parameters.

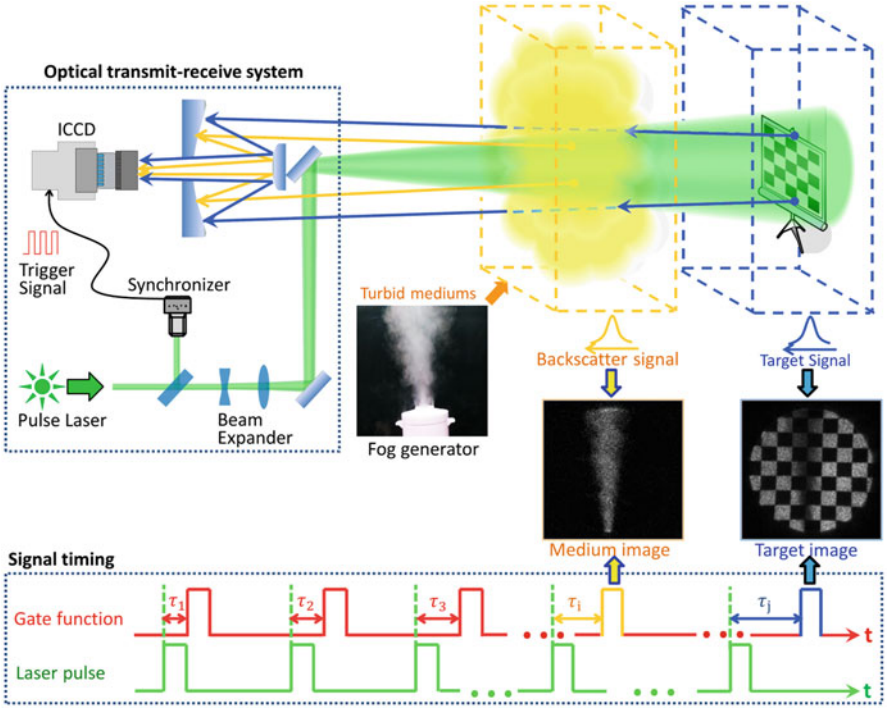

Fig. 1 Schematic diagram of the LLT system

The degradation model of the observed target image can be simplified as:

$$U_0 = V \cdot U + N, \tag{1}$$

Here, U_0 represents the observed target image, U represents the ideal image without degeneration, V is the degradation matrix determined by the turbid medium along the laser transmission path, and N is the additive noise of the system [28]. Based on the degradation model, the restoration of the target image can be divided into two steps: first, estimate the degradation matrix, and second, solve the degradation model in Eq. (1).

2.1 Degradation Matrix Establishment

According to light detection and ranging (LIDAR) [31–34] theories, the energy reflected from the target with reflectivity of ρ_t will be captured by a pixel (i,j) of the ICCD camera [28]:

$$I_{\text{tar}}(i,j) = \frac{E_t D^2 d_{\text{pix}}^2 \rho_t (X_t, Y_t, Z_t)}{\alpha^2 f^2 {Z_t}^2} \cdot \exp\left[-2\int_0^{Z_t} K_{\text{e}}(x,y,z)\,dz\right], \tag{2}$$

Here, Z_t is the distance between the ICCD and the target, E_t is the single pulse energy in the measurement, α is the divergence angle of the laser beam, d_{pix} is the pixel size, D is the camera aperture, f is the focal length of the optical receiving system, and K_{e} is the extinction coefficient of the atmospheric turbid medium, respectively; moreover, as shown in Fig. 2, the reflection point positions (X_t, Y_t, Z_t) and the pixel coordinates (i,j) satisfy the projective transformation, i.e., $\begin{cases} id_{\text{pix}} = -fX_t/Z_t \\ jd_{\text{pix}} = -fY_t/Z_t \end{cases}$.

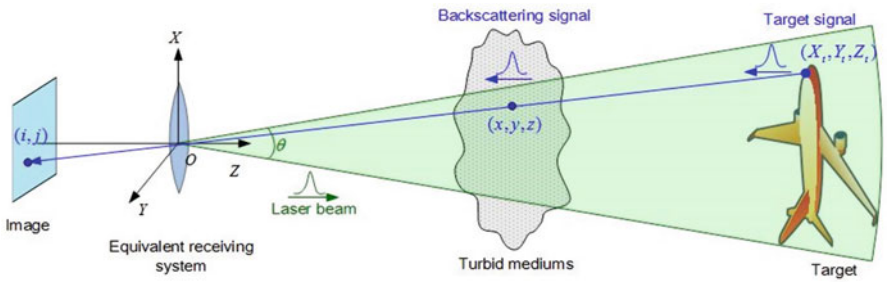

Fig. 2 Coordinate system of LLT setup

Obviously, on the right-hand side of Eq. (2), the last factor, which depends on the atmospheric parameters rather than the parameters of the transceiver system and the target, can be defined as the degradation matrix caused by the turbid medium:

$$V(i, j) \equiv \exp\left[-2\int_0^{Z_t} K_{\mathrm{e}}(x, y, z)\, dz\right] \tag{3}$$

Introducing the LIDAR ratio [34], i.e., the extinction-to-backscattering ratio $S = K_{\mathrm{e}}/\beta$, the degradation matrix can be rewritten by:

$$V(i, j) = \exp\left[-2\int_0^{Z_t} S\beta(x, y, z)\, dz\right] \tag{4}$$

where β is the backscattering coefficient of the turbid medium. The LIDAR ratio S can be assumed to be constant, which depends on the complex refractive index and the size distribution of the medium particles but is independent with the number density of the particles [34]. When the gate range is set to cover the whole layer of the turbid medium as shown in Fig. 1, the exponential term turns out to be approximately the total reflectivity ρ_S of the medium layer, i.e., $\int_0^{Z_t} \beta(x, y, z)\, dz \approx \rho_S(x, y)$. Therefore, the degradation matrix can be simplified as:

$$V(i, j) = \exp\left[-2S\rho_S(x, y)\right]. \tag{5}$$

Certainly, the reflectivity ρ_S of the turbid medium can be calibrated by a reference target with uniform reflectivity $\overline{\rho_0}$ which can be premeasured. Basically, the gray value of the medium image is proportional to the reflectivity of the turbid medium; therefore the medium reflectivity ρ_S is supposed to be obtained by the pre-calibration of the transceiver system as follows: the turbid-medium-free LLT experiments can be performed by using a reference target plate with uniform perpendicular-incidence reflectivity $\overline{\rho_0}$, which needs to be measured in advance. The average gray value of the target in the reference target image I_0 can be represented as:

$$\overline{I_0} = CE_0\overline{\rho_0}/{Z_0}^2, \tag{6}$$

Here, E_0 is the single pulse energy in the pre-calibration, C is a constant determined by the system parameters, and Z_0 is the distance between the reference target and the camera. In the LLT system, the distance of the target is easy to calculate as $Z_0 = c\tau_0/2$, in which c denotes the light speed and τ_0 denotes the target signal delay.

After that, LLT can be performed with the same experimental system under the existence of turbid medium to capture the gated images of the new targets and the turbid medium; in this measurement, the transceiver system parameters except the pulse energy of the laser are supposed to remain unchanged. The gate range for the backscattering image of the turbid medium needs to cover the whole medium layer, and its image intensity can be represented as:

$$I_S(i, j) = C E_S \rho_S(x, y) / {Z_s}^2, \tag{7}$$

where E_S is the single pulse energy in this measurement and Z_S is the distance of the medium layer. Then, the medium reflectivity ρ_S can be obtained by:

$$\rho_S(x, y) = \frac{E_0 {Z_S}^2 \overline{\rho_0}}{E_S {Z_0}^2 \overline{I_0}} I_S(i, j) \tag{8}$$

Moreover, in Eq. (5) there is still an unknown value, i.e., the LIDAR ratio S, which is supposed to be obtained by the premeasurement or by the estimation through the prior information of the turbid medium. After that, by substituting the S value and the calibrated ρ_S into Eq. (5), the estimated degradation matrix can be achieved as:

$$\tilde{V}(i, j) = \exp\left[-2S \frac{E_0 {Z_S}^2 \overline{\rho_0}}{E_S {Z_0}^2 \overline{I_0}} I_S(i, j)\right]. \tag{9}$$

2.2 Image Restoration Algorithm

In order to eliminate the influence of the degradation matrix, we still use the following variational model proposed in Ref. [28] to solve the degradation model in Eq. (1):

$$\min_U \int_\Sigma \left[|\nabla U| + \gamma |U_0 - \tilde{V} \cdot U|\right], \tag{10}$$

Here, γ denotes the regularization parameter, U_0 represents the observed target image, U represents the restored target image, and $\tilde{V}$ represents the estimated degradation matrix, respectively. The flowchart of the image restoration process is presented in Fig. 3.

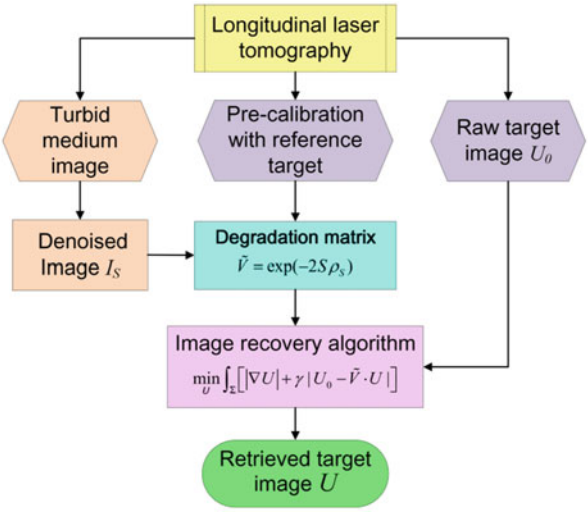

Fig. 3 Flowchart of the restoration method

3 Image Restoration Experiments

In this section, the validity and feasibility of the proposed method will be verified through experiments. The LLT experimental system and the signal timing were set up as Fig. 1. A synchronization beam, detected by a Si photodetector, was sampled from the main laser beam to provide external triggering for the ICCD camera. A layer of turbid medium was produced and controlled by a fog generator, which could atomize water and spray out the columnar fogs as shown in Fig. 1.

In the experiments, the wavelength, the pulse width, the divergence angle, the laser repetition frequency, and the pulse energy of the laser beam fed by a Quanta-Ray PRO Series pulsed Nd:YAG laser was 532 nm, 20 ns, 10 mrad, 10 Hz, and 2 mJ, respectively. The image resolution, gate time, and frame frequency of the Andor iStar ICCD camera were set to be 340 × 340 pixels, 20 ns, and 10 fps, respectively. The targets, some plastic plates with various patterns including the aircraft model in the simulations, were placed 30 m away from the ICCD camera. In the experiments, the backscattering image of the artificial fogs and the target image were captured in one single longitudinal scan to reduce the temporal variation of the fogs. According to the laser repetition frequency and the camera frame frequency, the time interval of the backscattering image and the target image is about 100 ms.

3.1 Pre-calibration Measurements

Before LLT experiment, the pre-calibration was first performed based on the pre-calibration method proposed in Sect. 2.1. A reference target plate with uniform

reflectivity $\overline{\rho_0}$ was used to calibrate the medium reflectivity ρ_S. The perpendicular-incidence reflectivity $\overline{\rho_0}$ of the reference target plate was premeasured by an optical power meter at various ranges, according to the following Eq. (11):

$$E_{\mathrm{r}} = \overline{\rho_0} \frac{A_{\mathrm{r}}}{Z_{\mathrm{r}}^2} E_{\mathrm{i}} \tag{11}$$

Here, E_{i} is the incident energy, E_{r} is the received energy, the incident direction and the receiving direction are both normal to the surface of the reference target, A_{r} is the receiving area of the optical power meter, and Z_{r} is the distance between the reference target and the optical power meter. The average reflectivity was obtained as $\overline{\rho_0} = 0.4643\mathrm{sr}^{-1}$ by linear fitting of $E_{\mathrm{r}}/E_{\mathrm{i}}$ versus $A_{\mathrm{r}}/Z_{\mathrm{r}}^2$, as shown in Fig. 4.

Then, by using this plate as the reference target, the turbid-medium-free LLT experiments were performed; the reference target I_0 is shown in Fig. 4, and the average gray value of the reference target plate is denoted by $\overline{I_0}$. In the pre-calibration experiment, the single pulse energy E_0 and the target distance Z_0 together with $\overline{\rho_0}$ and $\overline{I_0}$ served as the prior parameters for the following image restoration process.

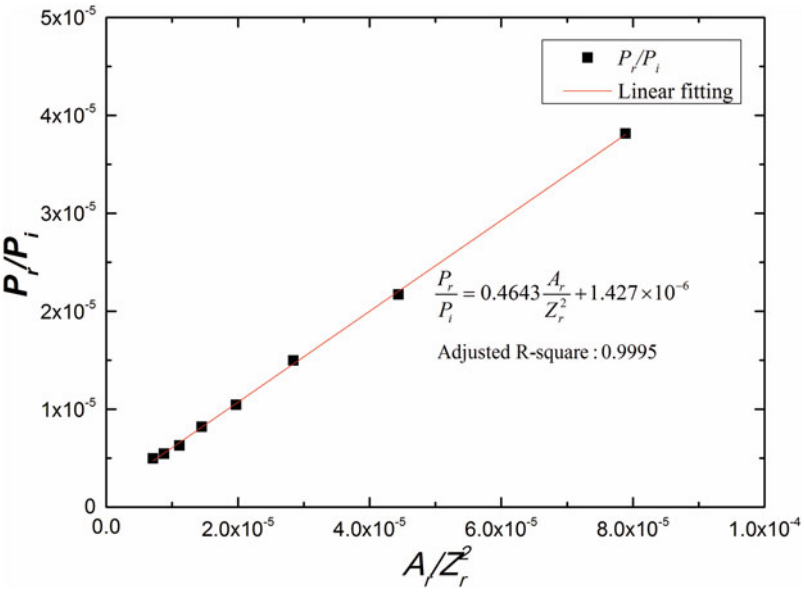

Fig. 4 Linear fitting of $E_{\mathrm{r}}/E_{\mathrm{i}}$ versus $A_{\mathrm{r}}/Z_{\mathrm{r}}^2$

3.2 Restoration Results

The observed raw target image and the backscattering image of the medium layer were captured by the LLT system, as shown in Fig. 5. The LIDAR ratio S can be estimated according to the prior information of the turbid medium. In these experiments, the turbid media were water droplets sprayed by the fog generator, and the complex refractive index of water is $m = 1.334 - 1.32 \times 10^{-9} i$ at the wavelength of 532 nm [35]. For water clouds, the LIDAR ratio has a near-constant value close to 19 sr at 532 nm [36, 37]. Considering the good robustness of the LIDAR ratio S [29], the average of the three values, i.e., $S = 19sr$, is chosen as the estimate of the LIDAR ratio for image recovery.

According to Eq. (9), the degradation matrix $\tilde{V}$ can be approximately estimated by the backscattering image I_S together with the prior parameters such as E_0, Z_0, $\overline{\rho_0}$, $\overline{I_0}$, and S; through the proposed variational model in Eq. (10), the retrieved target images U can be solved with the estimated degradation matrix $\tilde{V}$ and the observed target image U_0 as shown in Fig. 5.

The structural similarity (SSIM) index, which is a decimal value between 0 and 1, is used for the image quality assessment [38]. By considering the captured fog-free target images in Fig. 5 as the ideal target image I_{ideal} approximately, the SSIM indexes are listed in the corresponding images. Obviously, the proposed method can improve the SSIM indexes remarkably and achieve a higher degree of structural similarity with the ideal images, which indicates that the retrieved image is more

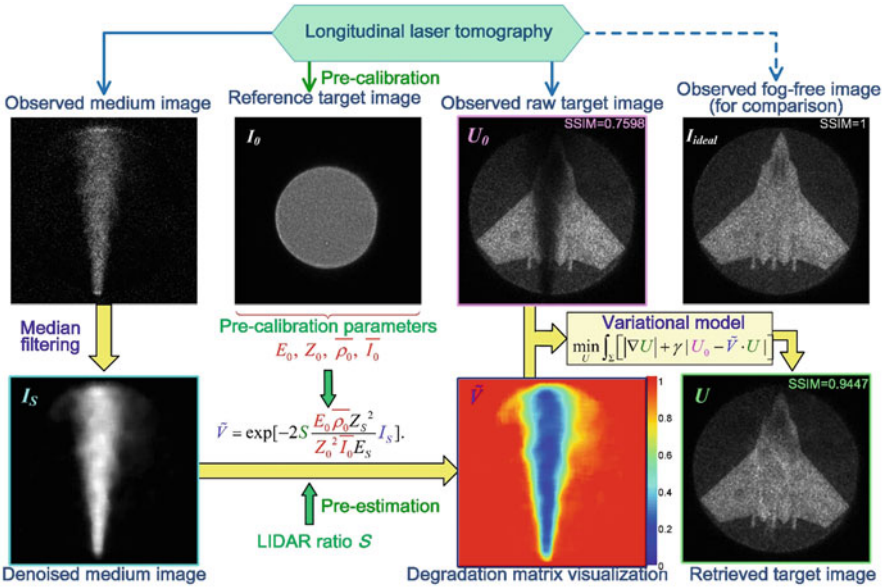

Fig. 5 Recovery process of the first experimental image group

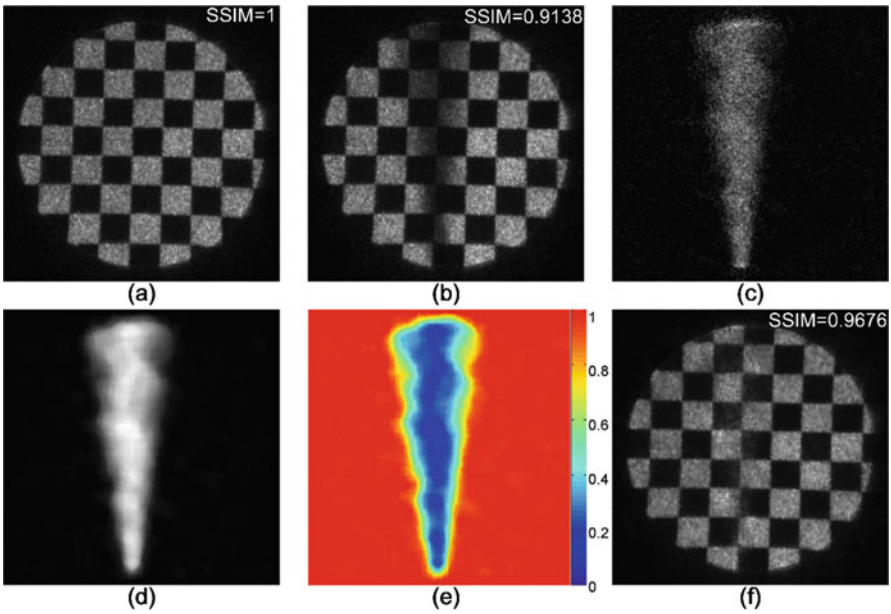

Fig. 6 Recovery results of the second experimental image group. (**a**) Observed fog-free image, (**b**) observed raw target image, (**c**) observed medium image, (**d**) denoised medium image, (**e**) degradation matrix visualization, (**f**) retrieved target image

similar to the ideal image and that the proposed method is effective in eliminating the inhomogeneous degradations caused by the turbid medium. The same procedure can be performed for the restorations of another group of results, as shown in Fig. 6, which comes to the same conclusions.

3.3 Homomorphic Filtering Recovery for Comparison

As we have known, homomorphic filtering [8] is a common technique to extract high-frequency information by logarithmic transformation and frequency domain filtering. Taking homomorphic filtering as an example, we compare the proposed method with the blind digital image restoration algorithms. The Butterworth filter functions [39] for homomorphic filtering algorithm and their corresponding results for the single degraded target image (Fig. 6b) are shown in Figs. 7 and 8, respectively. The results indicate that homomorphic filtering can visually weaken the influence of the turbid medium to some extent. However, at the same time, homomorphic filtering changes the relative gray value, i.e., the relative reflectivity of the target image. By considering the captured fog-free target images in Fig. 6a as the ideal target image, the SSIM indexes are listed in the corresponding images in Fig. 8;

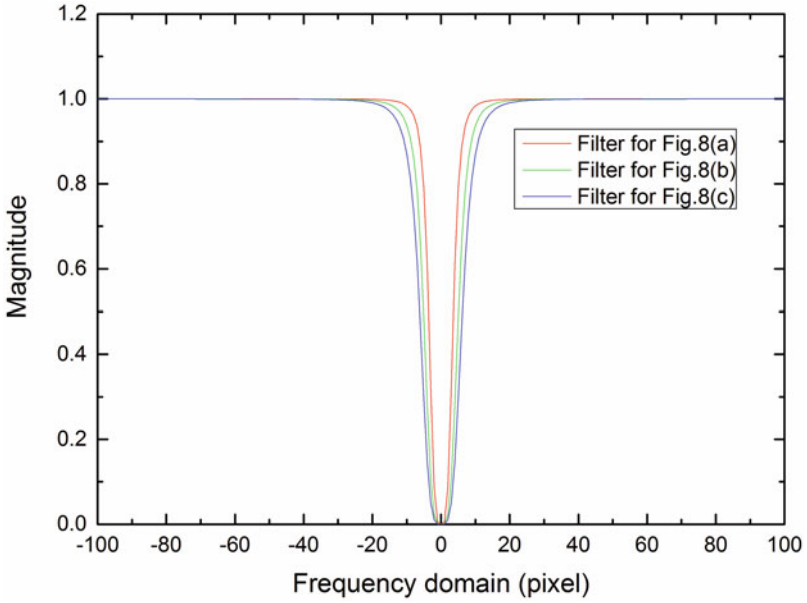

Fig. 7 Butterworth filter functions of homomorphic filtering

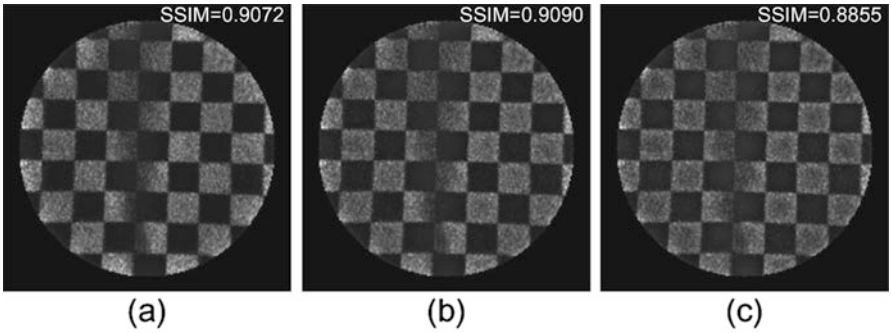

Fig. 8 Recovery results of homomorphic filtering. (**a**–**c**) show homomorphic filtering results of various Butterworth filter functions as shown in Fig. 7

obviously, homomorphic filtering cannot improve the SSIM indexes remarkably. Unlike homomorphic filtering, the proposed method can reveal the degradation area of the target without changing the relative reflectivity of the rest parts.

4 Conclusion

Based on LLT, a novel and feasible image restoration method is developed to estimate the degradation caused by the inhomogeneous turbid medium, assisted by the backscattering images and some prior system parameters, and further to restore the target images with the estimated degradation matrix through a proper total variation model.

The proposed restoration method is based on the physical signal relevance between the target layer and the turbid medium layer, instead of a blind image restoration algorithm. Experimental results indicate that the proposed method can effectively eliminate the interferences of the inhomogeneous turbid medium to achieve real target images.

As the proposed method can reveal the true target behind inhomogeneous turbid medium, it can reduce the false recognition rate for target recognition and identification. The proposed approach is aimed at target imaging through rapidly changing turbid medium such as moving cloud/mist in the air and flowing muddy masses under the water. The proposed method potentially will be applied in target acquisition for the astronomical observation, the military reconnaissance, the underwater imaging, and the fire rescue.

References

1. Ishimaru A (1978) Wave propagation and scattering in random media. Academic, New York
2. McLean EA, Burris HR, Strand MP (1995) Short-pulse range-gated optical imaging in turbid water. Appl Opt 34:4343–4351
3. Kang S, Jeong S, Choi W, Ko H, Yang TD, Joo JH, Lee JS, Lim YS, Park QH, Choi W (2015) Imaging deep within a scattering medium using collective accumulation of single-scattered waves. Nat Photon 9:253–258
4. Gibson A, Hebden J, Arridge S (2005) Recent advances in diffuse optical imaging. Phys Med Biol 50:R1–R43
5. Wu KD, Cheng QL, Shi YL, Wang H, Wang PG (2015) Hiding scattering layers for noninvasive imaging of hidden objects. Sci Rep 5:8375
6. Gonzalez RC, Woods RE (2007) Digital image processing, 3rd edn. Prentice Hall, Upper Saddle River
7. Tomasi C, Manduchi R (1998) Bilateral filtering for gray and color images. In Proceedings of IEEE International Conference on Computer Vision (IEEE, 1998). pp 839–846
8. Oppenheim AV, Schafer RW, Stockham TG (1968) Nonlinear filtering of multiplied and convolved signals. Proc IEEE Trans Audio Electroacoustics (IEEE, 1968) 56(8):1264–1291
9. Martin FM, Munoz ME, Alberola LC (2006) A speckle removal filter based on anisotropic Wiener filtering and the Rice distribution. Proc IEEE Ultrasonics Symp (IEEE, 2006) 7(3):1694–1697
10. Lainiotis DG, Papaparaskeva P, Plataniotis K (1996) Nonlinear filtering for LIDAR signal processing. Math Probl Eng 2(5):367–392

11. Rudin L, Osher S, Fatemi E (1992) Nonlinear total variation based noise removal algorithms. Phys D 60:259–268
12. Chambolle A (2004) An algorithm for total variation minimization and applications. J Math Imaging Vis 20:89–97
13. Chan TF, Esedoglu S (2005) Aspects of total variation regularized L1 function approximation. SIAM J Appl Math 65:1817–1837
14. Yang JF, Zhang Y, Yin WT (2009) An efficient TVL1 algorithm for deblurring multichannel images corrupted by impulsive noise. SIAM J Sci Comput 31(4):2842–2865
15. Jin ZM, Yang XP (2011) A variational model to remove the multiplicative noise in ultrasound images. J Math Imaging Vis 39:62–74
16. Strekalov DV, Sergienko AV, Klyshko DN, Shih YH (1995) Observation of two photon 'ghost' interference and diffraction. Phys Rev Lett 74:3600–3603
17. Bennink RS, Bentley SJ, Boyd RW (2002) Two-photon' coincidence imaging with a classical source. Phys Rev Lett 89:113601
18. Freund I (1990) Looking through walls and around corners. Phys A 168:49–65
19. Mosk AP, Lagendijk A, Lerosey G, Fink M (2006) Controlling waves in space and time for imaging and focusing in complex media. Nat Photon 6:283–292
20. Katz O, Small E, Silberberg Y (2011) Focusing and compression of ultrashort pulses through scattering media. Nat Photon 5:372–377
21. Bertolotti J, Puttenb EG, Blumc C, Lagendijkb A, Vos WL, Mosk AP (2012) Non-invasive imaging through opaque scattering layers. Nature 491:232–234
22. Katz O, Heidmann P, Fink M, Gigan S (2014) Non-invasive single-shot imaging through scattering layers and around corners via speckle correlations. Nat Photon 8:784–790
23. Gillespie LF (1966) Apparent illumination as a function of range in gated, laser night-viewing systems. J Opt Soc Am 56:883–887
24. Fournier GR, Bonnier D, Forand JL, Pace PW (1993) Range-gated underwater laser imaging system. Opt Eng 32:2185–2190
25. Digger RG, Vollmerhausen RH, Devitt N, Halfort C, Barnard KJ (2003) Impact of speckle on laser range-gated shortwave infrared imaging system target identification performance. Opt Eng 42(3):738–746
26. Andersson P (2006) Long-range three dimensional imaging using range-gated laser radar images. Opt Eng 45:034301
27. Laurenzis M, Christnacher F, Monnin D (2007) Long-range three-dimensional active imaging with superresolution depth mapping. Opt Lett 32(21):3146–3148
28. Yi WJ, Hu WH, Wang P, Li XJ (2016) Image restoration method for longitudinal laser tomography based on degradation matrix estimation. Appl Opt 55(20):5432–5438
29. Yi WJ, Liu HB, Wang P, Fu MC, Tan JC, Li XJ (2017) Reconstruction of target image from inhomogeneous degradations through backscattering medium images using self-calibration. Opt Express 25(7):7392–7401
30. Yi WJ, Wang P, Fu MC, Tan JC, Zhu JB, Li XJ (2017) Restoration of longitudinal laser tomography target image from inhomogeneous medium degradation under common conditions. Opt Express 25(14):15687–15698
31. Richmond RD, Cain SC (2010) Direct-detection LADAR systems. SPIE Press, Bellingham
32. Andrews LC, Phillips RL (2005) Laser beam propagation through random media. SPIE Press, Bellingham
33. McManamon PF (2012) Review of ladar: a historic, yet emerging, sensor technology with rich phenomenology. Opt Eng 51(6):060901
34. Fernald FG (1984) Analysis of atmospheric lidar observations: some comments. Appl Opt 23(5):652–653

35. George MH, Marvin RQ (1973) Optical constants of water in the 200-nm to 200-μm wavelength region. Appl Opt 12(3):555–563
36. Pinnick RG, Jennings SG, Chylek P, Ham C, Grandy WT Jr (1983) Backscatter and extinction in water clouds. J Geophys Res 88(C11):6787–6796
37. O'Connor EJ, Illingworth AJ, Hogan RJ (2004) A technique for autocalibration of cloud lidar. J Atmos Ocean Technol 21(5):777–786
38. Wang Z, Bovik AC, Sheikh HR, Simoncelli EP (2004) Image quality assessment: from error visibility to structural similarity. Proc IEEE TransImage Processing (IEEE, 2004) 13(4):600–612
39. Adelmann HG (1998) Butterworth equations for homomorphic filtering of images. Comput Biol Med 28(2):169–181

A Hybrid Approach for Object Proposal Generation

Muhammd Aamir, Yi-Fei Pu, Waheed Ahmed Abro, Hamad Naeem, and Ziaur Rahman

1 Introduction

Recent years have witnessed a rapid evolution in computer vision and machine learning, with much effort being invested to enable machines to "see." Major road blocks have been solved, such as detecting edges in an image, segmenting images in more accurate ways, and learning different image features. The first step toward enabling machines to "see" is to enable a computer to recognize objects – which is the foundation of the visual world.

Object class detection is one of the key problems present in computer vision. While a human can easily recognize and detect objects, machines and computers still struggle due to diverse viewpoint variations like size, angle, perspective, occlusion, and illumination. In recent years, several approaches to object detection have been proposed to overcome these variations. A traditional approach for object detection is the sliding window approach, where the classifier is applied at every object location and scale. However, Girshick et al. [3] revolutionized this approach when he demonstrated a two-phase process method. In Girshick's process, a set of object proposals is first generated using a FAST algorithm, and then post-classification deep convolutional network classifier is applied on each of the proposals. This approach provides dramatic improvements in object detection accuracy as compared to the sliding window approach. Since Girshick's revolutionary demonstration, most current state-of-the-art object detectors have followed Girshick's lead and use object proposals as a first preprocessing step.

M. Aamir (✉) · Y.-F. Pu · H. Naeem · Z. Rahman
College of Computer Science Sichuan University, Chengdu, Sichuan, China

W. A. Abro
School of Computer Science and Engineering, Southeast University, Nanjing, China

M. Jiang et al. (eds.), *The Proceedings of the International Conference on Sensing and Imaging*, Lecture Notes in Electrical Engineering 506,
https://doi.org/10.1007/978-3-319-91659-0_18

Object detection performance depends upon both the object proposal algorithms and the post-classification detection networks. Merely improving post-classification, while beneficial, is not sufficient on its own. It is necessary for any post-classification improvements to be combined with a reduction in the number of image locations in order to be significant. Reducing image proposal not only speeds up object detection but also reduces the false positives in the post-classification stage. The goal is to reduce the number of proposals at the generation time in order to be used in real-time applications more efficiently and to automatically generate a small number of diverse regions that may contain objects in an image. Each object of an image must be well represented in at least one region.

In this paper, we propose a new hybrid object proposal method which significantly reduces the number of proposals generated and the number of false positives in the post-classification phase. We first get initial proposals from hierarchical segmentations [1] and then rank the proposals as per score criteria. Scoring regions is done using contours enclosed in the region, and then top of object proposals passes for post-classification.

2 Related Works

In this section, we concisely review previous approaches to object detection, most of which use object classifiers and object proposal algorithms. These methods are broadly divided into two categories: groping methods and window scoring methods. Grouping methods generate multiple segments of an image which are likely to contain objects. The most common approach to grouping methods is to do hierarchical image segmentation and merge segments according to the similarities between those segments. Most grouping algorithm performance relies on initial segmentation algorithms. Felzenszwalb [4] algorithm is well suited for this purpose, as his algorithm is both efficient and timely. Algorithms generate set of small initial regions at a rapid speed, which, in turn, define segmentation as graph problems where each vertex is an element to be segmented, and edges are between two neighboring regions. Algorithms then make region comparisons, each segment corresponding to a connected component of the graph.

Carreira and Sminchisescu [5], CMPC, and Endres and Hoiem [6] methods solve multiple graph cuts with different seeds and parameters to generate class-independent proposals. Both of these methods generate binary foreground/background segments, with each obtained foreground segment as an object hypothesis, and both of these methods learn to predict the segments that cover complete objects and rank proposals accordingly. However, both algorithms are slow due to their reliance on the gPb edge detector but generate high-quality segmentation masks. Selective search [1] method is the most widely used method in object recognition and object detection and is based on multiple hierarchical segmentation using superpixels. For covering a diverse set of regions, different kinds of grouping strategies and color spaces are used which produces high recall at fast speeds – a few seconds per image. However, there is no scoring mechanism on the proposals; therefore, proposals cannot be ranked.

Table 1 The performance comparisons of both approaches are given in the chart below

Methods	Approach	Output segments	Output score	Time (s)
Selective search [1]	Grouping	Yes	No	10
CPMC [5]	Grouping	Yes	Yes	250
Endres and Hoiem [6]	Grouping	Yes	Yes	100
Rantalankila [7]	Grouping	Yes	No	10
Objectness [8]	Window scoring	No	Yes	3
Rahtu [9]	Window scoring	No	Yes	3
EdgeBox [2]	Window scoring	No	YES	0.3
Bing [10]	Window scoring	No	YES	0.2

On the other hand, window scoring methods is very different, with each window score being calculated according to how likely it is to contain an object. This approach generates a bounding box much faster than the grouping methods. However, this approach has low localization accuracy. Objectness [8] is a window-based approach in which each candidate window score is calculated on different image cues. Objectness stands as one of one of the earliest object proposal methods and is capable of measuring the likelihood that objects are present in the image. This method uses saliency, color contrast, edge density, and superpixel straddling cues to obtain characteristics of images and adopts Bayesian's framework to combine several cues. This has shown that the new combined cues outperform the state-of-the-art saliency measure. The last advantage of objectness is its slow emergence of drawback, which appears at a snail's speed. This method has low localization accuracy, but the first few proposals it obtains are of high quality.

EdgeBox [2] is another window-based approach and is among the fastest object proposal generation methods. EdgeBox generates object proposals directly from the edges of an image. Initial edge maps are computed from edge detectors [11] and then are combined into eight connecting edges to form an edge group. This method uses sliding window search over a scale to generate a candidate box and then scores each box, selecting the top few thousand proposals. Rahtu et al. [9] begins with a large number of randomly sampled boxes from an objectness and multiplies them with proposal regions generated from single, pair, and triplet superpixel segmentations. And their score function is similar to that of objectness, where they have made some improvements by adding low-level features (Table 1).

Girshick et al. [3] introduced their R-CNN method which defines object detection in a two-step process. This method generates a set of category-independent proposals using bottom-up grouping (i.e., selective search). Girshick et al. then used a deep convolutional neural network on those generated proposals. This method dramatically improves the performance proposal generation, proposal classification, and overall object detection by replacing the traditional sliding window approach with object proposals, thus achieving a state-of-the-art object detection performance. Fast R-CNN [8] is an improvement of Girshick et al.'s previous work and allows for faster object detection.

This paper presents a hybrid approach which combines both grouping and window scoring methods to increase the detection performance. This hybrid method results in excellent object detection task completion at relatively fast speeds compared to selective search methods and greatly reduces the false-positive rate.

3 Proposed Work

In this paper, we have proposed a new hybrid object proposal approach which combines hierarchical segmentations [1] and window scoring method [2]. First, we generate object proposals through the agglomerative clustering grouping method. We then score the boxes according to the sums of the magnitude of the all the edges in each edge group minus the edge groups of the contours that straddle the bounding box. Finally, we rank the object proposals according to score of the boxes. The top-ranked proposals can then be chosen for the classification task. However, there is still a great deal of importance in reducing object proposal generation time, as it also reduces the false-positive rate.

We observed that R-CNN achieves object detection at a faster rate due to reducing object location – from all locations to proposed location – while the object proposal generated by selective search [1] was still very high (around 8–10 thousand). Furthermore, we have reduced object proposals by ranking object proposal according to box score and only have select top few thousand proposals for object detection.

3.1 Algorithm Overview

The major steps of our algorithm are as follows:

1. Segmentation: Our proposal begins by generating a set of initial regions on which we apply hierarchical clustering.
2. Hierarchical Clustering: We group initial segments obtained from the above step according by the similarity measure between neighboring regions.
3. Edge detection and edge groups: We generate image edge maps with the structured edge detector. And, from edge map, we form edge groups by grouping neighboring edges according to orientation similarity.
4. Score regions: Regions obtained from clustering are forwarded for scoring. We score regions according to the strength of the edges in the edge groups within the region and then subtract the strength of edges in the edge groups that straddle the region.
5. Ranking: We rank the proposal according to score of the region.

Segmentation

As most of the grouping methods generate object proposals using segmentation, we also use segmentation to obtain a small set of starting regions for hierarchical clustering. We use Felzenszwalb and Huttenlocher's graph-based algorithm, which is an efficient method for obtaining regions. This method is well suited for our purpose because of its speed and accuracy. It converts images into a graph – pixels are the vertices and neighboring pixels are connected with the edges. We then manipulate the graph to segment the image.

Hierarchical Clustering

Regions obtained from step 1 serve as starting points for hierarchical clustering. Agglomerative (bottom-up) clustering method is then used, where initially each region is a cluster. We repeatedly combine two similar neighboring regions – after each combination new similarities are calculated. This process continues until the whole image becomes one cluster/region. We then use color, texture, size, and gap similarity measures. Hierarchical clustering is applied on different color spaces to cover a more diverse set of regions. Regions from each hierarchy are then combined, while duplicate regions are removed at the end. Clusters obtained from hierarchical clustering are the object proposals; we repeat the clustering algorithm in different color spaces.

Edge Detection and Edge Group

For edge detection, we use structured edge detection. Structure forest extract image patches from the image, convert each image patch into vectors, extract the image features for each patch, and then predict scores of the patches at the edge. The edges obtained from detector are then combined into eight connected neighboring edges with similar orientation until the orientation differences above pi/2 form the edge groups. This method shows good accuracy and speed as compared to traditional edge detectors.

Score Regions

Given set object proposals obtained from hierarchical clustering, we calculate the score of each object proposal. This is accomplished by summing the magnitude of every wholly enclosed edge in the group in a given region and subtracting the magnitude of every edge in the group which straddles the object region. The value of $w_b(s_i)$ is calculated for each edge group to check if the group is wholly enclosed

in the region. When an edge group is not wholly closed in the box, then $w_b(s_i) = 0$. If an edge group is wholly enclosed in the box $w_b(s_i)$ is calculated as below:

$$w_b\left(\mathrm{s}_i\right) = 1 - \max_t \prod_j^{|\mathrm{T}|-1} a\left(t_j - t_{j+1}\right) \tag{1}$$

where "a" is the affinity and "t" is the order path, so the above equation finds the order path with the max affinity between the groups. We then compute the score using the formula:

$$h(b) = \frac{\sum_i w_b\left(s_i\right) m_i}{2(b_w + b_h)^k} \tag{2}$$

where b_w and b_n are the box width and height and k is the bias value for larger boxes.

Ranking

We rank objects proposed according to score obtained from Eq. 2, where a few thousands of object proposals passed for classification task (Figs. 1 and 2).

4 Evaluations and Results

Most of our experiments were performed on a PASCAL VOC 2007 dataset [12], which contains 9963 images, with a training set containing 2501 images, validation set containing 2510 images, and test set containing 4952 images. The dataset has 20 object classes in four broad categories – person, animal, vehicle, and indoor.

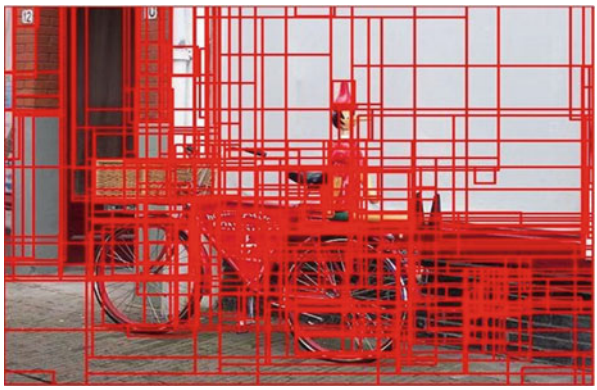

Fig. 1 Proposal evaluation on VOC

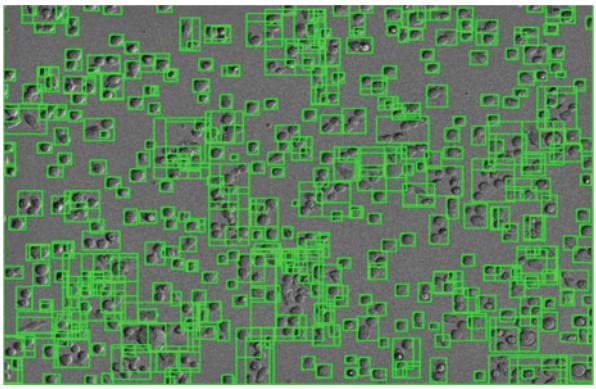

Fig. 2 Proposal evaluation on migrating cancer dataset

Training images are labeled with ground truth from 20 object classes. Every image has an annotation that contains the bounding box information and difficulty level of the object.

PASCAL VOC provides standardized images, which contain a large number of objects and a cornucopia of categories, scales, illuminations, viewpoints, and positions – making this database ideal for object reorganization. PASCAL 20 visual object classes are airplane, bicycle, bird, boat, bottle, bus, car, cat, chair, cow, dining table, dog, horse, motorbike, person, potted plant, sheep, sofa, train and TV monitor. We have performed all our experiments on a CPU with 4GB RAM. For evaluating the quality of our object proposals, we use two measures: ABO (average best overlap) and MABO (mean average best overlap).

4.1 Average Best Overlap (ABO)

Average best overlap, for any class, is achieved by calculating best overlap on ground truth of class and proposed object region of said class and then taking its average. Overlap is the intersection of proposed region with ground truth over area of their union.

$$\text{IoU}\ \ (\text{box}, \text{gtruth}) = \frac{\text{area}\ (\text{box}) \cap \text{area}\ \ (\text{gtruth})}{\text{area}\ (\text{box}) \cup \text{area}\ \ (\text{gtruth})}$$

4.2 Mean Average Best Overlap (MABO)

Mean average best overlap, is the mean ABO over all classes. We have evaluated our proposal on PASCAL VOC 2007 test set and compare with selective search and edge box proposal generation methods (Tables 2 and 3).

Table 2 Mean average best overlap on VOC dataset

Methods	Test images	Proposals	MABO (mean average best overlap)
Edge box	4952	1500	0.799
Selective search	4952	1500	0.820
Our proposal	4952	1500	0.833

Table 3 Average best overlap for 20 classes of VOC on top 1500 proposals

VOC classes	Edge box ABO	Selective search ABO	Our proposal ABO
Plane	0.771	0.796	0.807
Bicycle	0.824	0.844	0.861
Bird	0.796	0.812	0.812
Boat	0.779	0.768	0.784
Bottle	0.692	0.660	0.673
Bus	0.841	0.864	0.868
Car	0.788	0.783	0.808
Cat	0.827	0.906	0.909
Chair	0.783	0.798	0.808
Cow	0.827	0.829	0.854
Table	0.817	0.891	0.894
Dog	0.837	0.895	0.900
Horse	0.815	0.828	0.841
Bike	0.815	0.829	0.846
Person	0.755	0.754	0.766
Potted plant	0.746	0.740	0.758
Sheep	0.814	0.797	0.828
Sofa	0.828	0.904	0.907
Train	0.801	0.856	0.863
TV monitor	0.821	0.842	0.868

5 Conclusions and Future Work

In summary, our efficient, new hybrid method for generating object proposals uses selective search proposal and scores them according to edges present in the proposed regions. This method results in adequate detection rates for object detection task – compared to object detection solely utilizing selective search – and significantly decreases the false-positive rate. Throughout this paper, we demonstrate that our purposed hybrid method matches the accuracy of selective search, with only 25% the number of proposal after ranking said proposals. Our method results in high-quality class-independent object locations, with mean average best overlap of 0.833 at 1500 locations.

In the future, the score function can be further optimized by penalizing the portion of edge groups that overlap the region boundary, instead of subtracting strength of edges present in edge group. The edge box generates redundant object

proposals in each scale; therefore, by reducing redundant object proposals, edge box performance can also be further improved. Furthermore, we can use a strong post-classification, deep convolutional features and strong appearance models for object detection with reduced object proposals.

Acknowledgments This work was supported by the National Natural Science Foundation of China under grants 61571312, Academic and Technical Leaders Support Foundation of Sichuan province under grants (2016)183-5, and National Key Research and Development Program Foundation of China under grants 2017YFB0802300. The authors would like to thank Ms. Siobhan Kathryn He for the constructive criticism of the manuscript.

References

1. Uijlings JRR, van de Sande KEA, Gevers T, Smeulders AWM (2013) Selective search for object recognition. Inter J Comp Vision 104(2):154–171
2. Zitnick CL, Dollár P (2014) Edge boxes: locating object proposals from edges. In: Fleet D, Pajdla T, Schiele B, Tuytelaars T (eds) Computer vision – ECCV 2014. Lecture notes in computer science, vol 8693. Springer, Cham
3. Girshick RB, Donahue J, Darrell T, Malik J (2014) Rich feature hierarchies for accurate object detection and semantic segmentation. In: 2014 IEEE conference on computer vision and pattern recognition, pp 580–587
4. Felzenszwalb PF, Huttenlocher DP (2004) Efficient graph-based image segmentation. Inter J Comp Vision 59(2):167–181
5. Carreira J, Sminchisescu C (2012) Cpmc: automatic object segmentation using constrained parametric min-cuts. PAMI 34(7):1312
6. Endres I, Hoiem D (2014) Category-independent object proposals with diverse ranking. PAMI 36:222
7. Rantalankila P, Kannala J, Rahtu E (2014) Generating object segmentation proposals using global and local search. In: Computer vision and pattern recognition (CVPR), 2014 IEEE conference on. IEEE, pp 2417–2424
8. Alexe B, Deselaers T, Ferrari V (2012) Measuring the objectness of image windows. PAMI 34(11):2189
9. Rahtu E, Kannala J, Blaschko M (2011) Learning a category independent object detection cascade. In: Computer vision (ICCV), 2011 IEEE international conference on. IEEE, pp 1052–1059
10. Cheng M-M, Zhang Z, Lin W-Y, Torr P (2014) BING: Binarized normed gradients for objectness estimation at 300fps. In: Proceedings of the IEEE conference on computer vision and pattern recognition, pp 3286–3293
11. Dollar P, Zitnick CL (2014) Fast edge detection using structured forests. CoRR abs/1406.5549
12. Everingham M, Ali Eslami SM, Van Gool L, Williams CKI, Winn J, Zisserman A (2015) The pascal visual object classes challenge: a retrospective. Inter J Comp Vision 111(1):98–136

Adaptive-Order Regression-Based MR Image Super-Resolution

Jing Hu

1 Introduction

Magnetic resonance (MR) imaging is widely used to assess brain diseases, spinal disorders, cardiac function, as well as musculoskeletal injuries. Several factors can affect the resolution of MR images, including the acquisition time, short physiological characteristics, and organ motion. Compared with computed tomography, a longer acquisition time is required in MR imaging, making it more prone to several image artifacts caused by involuntary patient motion [1]. To minimize the likelihood of such motion artifacts, scan time is often shortened in MR imaging, as such fewer slices are obtained in an image set and the spacing between those slices becomes larger. In this way, MR images are usually highly anisotropic (e.g., $1 \times 1 \times 6\ \text{mm}^3$) with a lower resolution in the slice-selection direction compared to the in-plane directions [2]. However, in many medical applications, an isotropic MR image is required for visualization purposes [3]. Besides the demand for an isotropic resolution, a higher resolution is also essential for a comprehensive understanding of human anatomy, which facilitates early detection of abnormalities and improving clinical assessment accuracy.

Traditional interpolation methods such as spline interpolation are the simplest solution to improve MR image resolution. However, they often produce images with blurred edges and stair-casing artifacts that result in a loss of fine-detail information. In recent years, some sophisticated interpolation-based super-resolution (SR) methods are proposed. To some extent, they all belong to a family of adaptive 3D interpolation filters. Using the pattern-redundancy property that has been widely used in natural image processing [4], Manjón et al. [5] calculated the interpolation

J. Hu (✉)
Department of Computer Science, Chengdu University of Information Technology, Chengdu, Sichuan, People's Republic of China

M. Jiang et al. (eds.), *The Proceedings of the International Conference on Sensing and Imaging*, Lecture Notes in Electrical Engineering 506,
https://doi.org/10.1007/978-3-319-91659-0_19

coefficients as the similarity of the intensities between 3D image patches around the unknown voxel and its neighboring voxels. Afterward, the unknown voxel in the super-resolved MR images was estimated by weighted averaging. Under a same framework, Plenge et al. [6] used 3D patch similarity in in-plane directions to estimate the high-resolution (HR) voxel for the voxel in slice-selection. Later, several researchers [7–11] acclaimed that using an HR image of the same subject in other modalities to refine interpolation weights can effectively improve the quality of reconstructed images.

Whether using a different imaging modality or not, these advanced interpolation-based SR algorithms all focus on the refinement of interpolation weights. In our previous work [12], we have pointed out these interpolation-based SR algorithms actually fall into the framework of zero-order regression estimation, hence cannot faithfully reconstruct high-frequency details for low-resolution (LR) images. To this end, a regression-inspired SR method using second-order polynomials was proposed in our pilot study. Though this high-order method was successful in providing a better fine-detail reconstruction capability compared to conventional interpolation-based methods, its computational burden is much heavier, due to the fact that an exhaustive search for suitable patches is needed to estimate the second-order polynomials for each HR voxel. What is worse, the high dimensionality of MR image further increases computational cost.

To speed up this high-order regression-based SR method together with competitive image reconstruction quality, an adaptive-order strategy is proposed in this paper. Specifically, a voxel classification scheme is devised to discriminate voxels in structure regions from voxels in flat regions. Afterward, the specific order of regression is determined according to the classification result.

The reminder of this paper is organized as follows. Firstly, the second-order regression-based SR framework is briefly introduced in the next section, and then the proposed adaptive-order strategy is clarified. Experimental results and comparisons are demonstrated in Sect. 3. Finally, Sect. 4 concludes this paper.

2 Method

Let $\mathbf{Z}$ and $\mathbf{I}$ denote HR (output) and LR (input) images and $\mathbf{Z}_s$ and $\mathbf{I}_s$ denote their corresponding low-frequency images. That is, $\mathbf{Z}_s$ is lack of the high-frequency details in $\mathbf{Z}$ and likewise for $\mathbf{I}_s$ and $\mathbf{I}$. Let $\mathbf{p}$ and $\mathbf{q}$ denote the column vectors of two $s \times s$ image patches which are extracted from $\mathbf{I}$ and $\mathbf{Z}$, respectively; $\mathbf{p}_s$ and $\mathbf{q}_s$ are the corresponding column vectors of two $s \times s$ image patches taken from $\mathbf{I}_s$ and $\mathbf{Z}_s$, respectively.

2.1 Regression-Based SR Method

In regression-based SR method, the mapping function f between HR and LR patches relates these two kinds of patches as $\mathbf{q} = f(\mathbf{q}_s)$. Considering that singular structures are scale invariant, $\mathbf{q}_s$ in image $\mathbf{Z}_s$ is able to find its similar patch $\mathbf{p}_s$ in image $\mathbf{I}_s$. In this way, the mapping function of patch $\mathbf{q}_s$ to its high-resolution counterpart $\mathbf{q}$ can be regarded as the same mapping function of patch $\mathbf{p}_s$ to patch $\mathbf{p}$. More specifically, to estimate the function f for patch $\mathbf{q}_s$, a local expansion of f could be developed by utilizing an Nth order Taylor series, if patches $\mathbf{q}_s$ and $\mathbf{p}_s$ are similar:

$$\begin{aligned}\mathbf{q} &= f(\mathbf{q}_s) = f(\mathbf{p}_s + \mathbf{q}_s - \mathbf{p}_s) \\ &= f(\mathbf{p}_s) + f'(\mathbf{p}_s) \circ (\mathbf{q}_s - \mathbf{p}_s) + \tfrac{1}{2} f''(\mathbf{p}_s) \circ (\mathbf{q}_s - \mathbf{p}_s) \circ (\mathbf{q}_s - \mathbf{p}_s) + \cdots \\ &\approx \mathbf{p} + f'(\mathbf{p}_s) \circ (\mathbf{q}_s - \mathbf{p}_s) + \tfrac{1}{2} f''(\mathbf{p}_s) \circ (\mathbf{q}_s - \mathbf{p}_s) \circ (\mathbf{q}_s - \mathbf{p}_s)\end{aligned} \quad (1)$$

where $\circ$ denotes the element-wise product of two matrices and $f'(\cdot)$ and $f''(\cdot)$ denote the first and second derivatives of the mapping function f.

From Eq. (1), we can see that in order to reconstruct the HR version of path $\mathbf{q}_s$, the multi-order derivative of the mapping function should be estimated first. However, derivative estimation is an ill-posed problem [12, 13], and a proper image regularization is required. In our previous work [12], we have proposed to exploit the self-similarity property [5] in the three-dimensional image data so as to obtain a reliable second-order derivative estimation. That is, inside image $\mathbf{I}_s$, patches with a similar layout to the patch $\mathbf{p}_s$ can also be explored (see green box $\mathbf{p}_{1,s}$ in Fig. 1). Therefore, the mapping function of the patch $\mathbf{q}_s$ to its high-resolution counterpart $\mathbf{q}$ can also be regarded as the same mapping function of patch $\mathbf{p}_{1,s}$ to patch $\mathbf{p}_1$, where $\mathbf{p}_1$ is $\mathbf{p}_{1,s}$'s high-resolution counterpart in image $\mathbf{I}$. Like Eq. (1), the mapping function on patch $\mathbf{p}_{1,s}$ could also be locally expanded as:

$$\begin{aligned}\mathbf{p}_1 &= f(\mathbf{p}_{1,s}) = f(\mathbf{p}_s + \mathbf{p}_{1,s} - \mathbf{p}_s) \\ &= f(\mathbf{p}_s) + f'(\mathbf{p}_s) \circ (\mathbf{p}_{1,s} - \mathbf{p}_s) + \tfrac{1}{2} f''(\mathbf{p}_s) \circ (\mathbf{p}_{1,s} - \mathbf{p}_s) \circ (\mathbf{p}_{1,s} - \mathbf{p}_s) + \cdots \\ &\approx \mathbf{p} + f'(\mathbf{p}_s) \circ (\mathbf{p}_{1,s} - \mathbf{p}_s) + \tfrac{1}{2} f''(\mathbf{p}_s) \circ (\mathbf{p}_{1,s} - \mathbf{p}_s) \circ (\mathbf{p}_{1,s} - \mathbf{p}_s)\end{aligned} \quad (2)$$

Besides $\mathbf{p}_{1,s}$, more patches similar to $\mathbf{p}_s$ could also be found in $\mathbf{I}_s$, and each of them derives the formulation of $f'(\cdot)$ and $f''(\cdot)$ like Eq. (2). By incorporating the J-most similar patches $\{\mathbf{p}_{i,s}\} J\ i = 1$ and their paired HR patches $\{\mathbf{p}_i\}\ J\ i = 1$, we can learn the function f in a weighted least-square formulation:

$$\begin{aligned}\min_{f'(\mathbf{p}_s), f''(\mathbf{p}_s)} \sum_{i=1}^{J} \Big\| \mathbf{p}_i - \mathbf{p} - f'(\mathbf{p}_s) \circ (\mathbf{p}_{i,s} - \mathbf{p}_s) - \tfrac{1}{2} f''(\mathbf{p}_s) \circ (\mathbf{p}_{i,s} - \mathbf{p}_s) \\ \circ (\mathbf{p}_{i,s} - \mathbf{p}_s) \Big\|_2^2 w(\mathbf{p}_{i,s} - \mathbf{p}_s)\end{aligned} \quad (3)$$

where $w(\mathbf{p}_{i,s} - \mathbf{p}_s)$ measures the similarity between patches $\mathbf{p}_{i,s}$ and $\mathbf{p}_s$, and its specific formation could be found in our previous work [12]. Denote

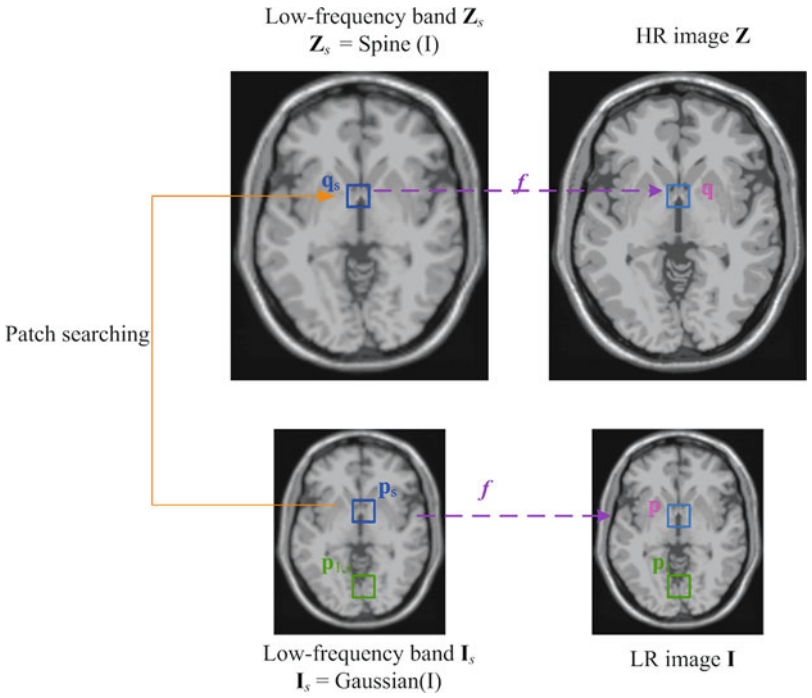

Fig. 1 The patch relations of the proposed method

$\mathbf{b} = [f'(\mathbf{m}), f''(\mathbf{m})]^T$, and convert the linear equations in Eq. (3) to matrix form. A closed form of Eq. (3) is obtained by using weighted square estimation method:

$$\begin{aligned} &\widehat{\mathbf{b}} = \left(\mathbf{X}^T\mathbf{W}\mathbf{X}\right)^{-1}\mathbf{X}^T\mathbf{W}\mathbf{y} \text{ with} \\ &\mathbf{y} = \left[\mathbf{p}_{1,s} - \mathbf{p}_s \;\; \mathbf{p}_{2,s} - \mathbf{p}_s \;\; \cdots \;\; \mathbf{p}_{J,s} - \mathbf{p}_s\right]^T \end{aligned} \tag{4}$$

$$\mathbf{W} = \begin{bmatrix} \text{diag}\left(w\left(\mathbf{p}_{1,s} - \mathbf{p}_s\right) \times \mathbf{1}\right) & & \\ & \text{diag}\left(w\left(\mathbf{p}_{2,s} - \mathbf{p}_s\right) \times \mathbf{1}\right) & \\ & & \vdots \\ & & \text{diag}\left(w\left(\mathbf{p}_{J,s} - \mathbf{p}_s\right) \times \mathbf{1}\right) \end{bmatrix} \text{ and}$$

$$\mathbf{X} = \begin{bmatrix} \text{diag}\left(\mathbf{p}_{1,s} - \mathbf{p}_s\right) & \text{diag}\left(\left(\mathbf{p}_{1,s} - \mathbf{p}_s\right) \circ \left(\mathbf{p}_{1,s} - \mathbf{p}_s\right)\right) \\ \text{diag}\left(\mathbf{p}_{2,s} - \mathbf{p}_s\right) & \text{diag}\left(\left(\mathbf{p}_{2,s} - \mathbf{p}_s\right) \circ \left(\mathbf{p}_{2,s} - \mathbf{p}_s\right)\right) \\ \vdots & \vdots \\ \text{diag}\left(\mathbf{p}_{J,s} - \mathbf{p}_s\right) & \text{diag}\left(\left(\mathbf{p}_{J,s} - \mathbf{p}_s\right) \circ \left(\mathbf{p}_{J,s} - \mathbf{p}_s\right)\right) \end{bmatrix}$$

with $\mathbf{1}$ denoting a unit vector and *diag*(■) defining a diagonal matrix.

2.2 Regression-Based SR Method

Although using a high-order regression is beneficial to high-frequency detail reconstruction, it is very time-consuming. Intuitively, it is not necessary to use high-order regression for smooth regions since their intensity values are nearly constant. In light of this, to estimate the HR patch $\mathbf{q}$ in Eq. (1), an adaptive regression-order strategy is proposed in this paper: for highly detailed regions, a second-order regression is used to recover complex structures; for medium-detailed regions, a first-order derivative estimation is sufficient; for smooth regions, we simply paste the results from $\mathbf{q}_s$ to $\mathbf{q}$.

To discriminate textured areas from flat areas, image structure tensor is adopted in this paper. It has been alleged that the relative discrepancy between image structure tensor's eigenvalues is able to reflect how strongly the distribution of gradients in an image patch is biased toward a particular direction [14]. That is, for a voxel in the smooth region, there is a small eigenvalue difference; for a voxel in a texture region, there is a large eigenvalue difference. Therefore, voxel classification can be achieved by examining the eigenvalue difference for each voxel. More specifically, for each voxel (i, j) in every MR image slice, its structure tensor matrix is defined as:

$$S = \begin{bmatrix} s_{11} & s_{12} \\ s_{21} & s_{22} \end{bmatrix} = \begin{bmatrix} (g_x(i,j))^2 & g_x(i,j)\, g_y(i,j) \\ g_x(i,j)\, g_y(i,j) & \left(g_y(i,j)\right)^2 \end{bmatrix} \tag{5}$$

where g_x and g_y denote gradient information in the x and y directions. The eigenvalues of S are calculated as:

$$\lambda_1 = \frac{1}{2}\left(s_{11} + s_{22} + \sqrt{(s_{11} - s_{22})^2 + 4s_{12}^2}\right) \text{ and } \lambda_2 = \frac{1}{2}\left(s_{11} + s_{22} - \sqrt{(s_{11} - s_{22})^2 + 4s_{12}^2}\right) \tag{6}$$

$T = \lambda_1 - \lambda_2$ is used to reflect the texture degree for every voxel, and voxels with different texture magnitudes are classified by analyzing the cumulative histogram of T value in that image slice:

$$(i, j) \in \begin{cases} c_1 & T(i,j) > t_1 \\ c_2 & t_2 < T(i,j) \le t_1 \\ c_3 & TM(i,j) \le t_2 \end{cases} \tag{7}$$

where $T(i,j)$ is the T value of the voxel at location (i,j); t_1 and t_2 are the bin values that correspond, respectively, to 50% and 20% in the cumulative T histogram; c_1, c_2, and c_3, respectively, represent the hard- and medium-detailed regions and smooth regions. Figure 2 presents the voxel classification result for a T1 image using Eq. (7). We see that by using this criterion, more than one third of the voxels are regarded as

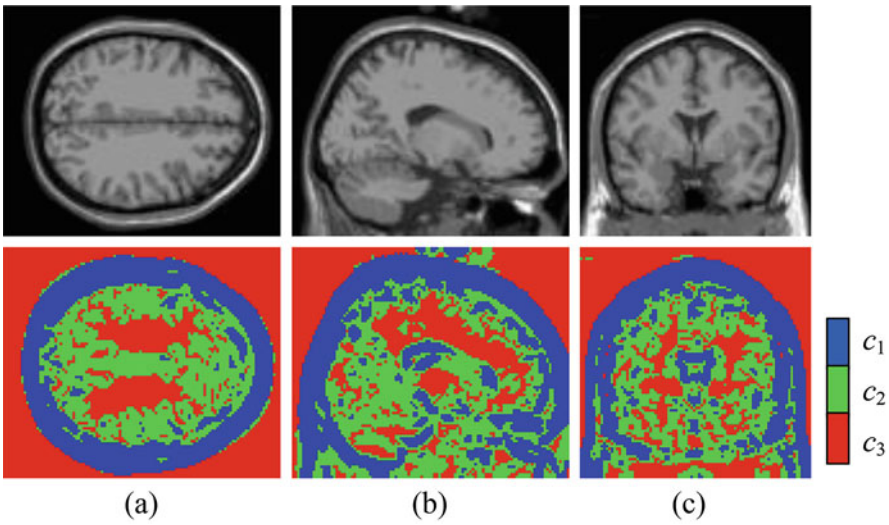

Fig. 2 Voxel classification results of a T1 volume. The first row: a typical slice is shown at (**a**) axial, (**b**) sagittal, and (**c**) coronal views. The second row: corresponding voxel classification results

located in smooth regions. Intuitively, avoiding a second-order regression estimation on these voxels helps to speed up the algorithm.

3 Experiments

In this section, the proposed method is evaluated on an open-access dataset provided by BrainWeb MRI (http://brainweb.bic.mni.mcgill.ca/brainweb/). A fixed set of parameters is used for the proposed method in all experiments. In detail, the patch size is 5×5, the 3D searching area for finding similar patches is a $13 \times 13 \times 3$ window. The state-of-the-art algorithms NLM [10] and our previous work [12] are selected as a comparison baselines. Peak signal-to-noise ratio (PSNR) and structural similarity (SSIM) index [15] are adopted to evaluate the objective performance.

The HR T1W volume in BrainWeb dataset has $181 \times 217 \times 181$ voxels with a resolution of 1 mm^3. To generate LR volume, blurring and down-sampling steps are involved. That is, the blurred image is generated by convolving the HR images with a 3D Gaussian kernel with a standard deviation of 0.8 (in voxel space) along dimensions. Next, the blurred images were down-sampled to lower voxel resolutions, such as $2 \times 2 \times 2$ mm^3 and $3 \times 3 \times 3$ mm^3.

These simulated LR data are upsampled by T1W image to 1 mm isotropic resolution using the proposed method and other compared methods. Figure 3 compares the reconstruction results using different methods, in which the local regions of interest (ROIs) in blue boxes are presented at the lower corner for providing a better comparison. Table 1 summarizes the quantitative comparisons

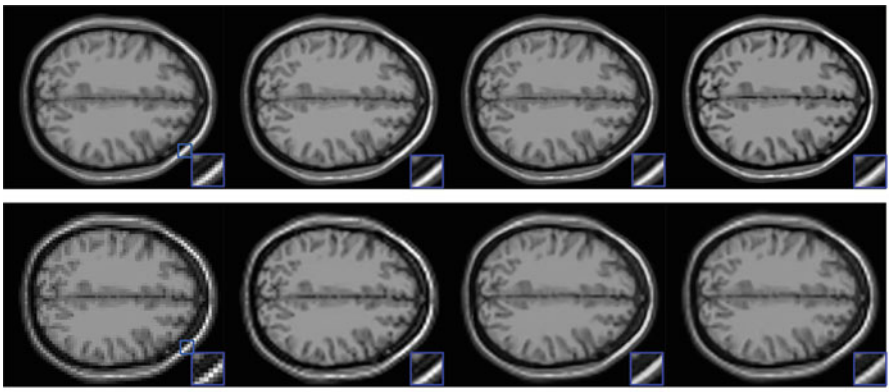

Fig. 3 Super-resolution results ($1 \times 1 \times 1$ mm^3) for simulated data (first row, $2 \times 2 \times 2$ mm^3; second row, $3 \times 3 \times 3$ mm^3) on BrainWeb using different methods. (**a**) NN, (**b**) NLM, (**c**) second-order regression method, and (**d**) the proposed method

Table 1 PSNR, SSIM, and time cost for different methods on different slice thickness (PSNR [dB] /SSIM/time [s])

Slice thickness (mm^3)	NN	NLM	Second-order regression method
$2 \times 2 \times 2$	26.6297	28.5482	29.2822
	0.8932	0.9387	0.9472
	0.05	3.21[a]	246.11
$3 \times 3 \times 3$	22.2134	25.1146	27.0874
	0.7562	0.8586	0.9094
	0.05	3.62[a]	241.66

[a]Note that NLM uses MATLAB/C++ (.Mex) to speed up, while the other three methods use MATLAB only

and the computational time. We can clearly observe that the proposed method can produce comparable HR results as compared with the second-order regression-based method but with improved computational efficiency. Compared with NLM method, which is a zero-order regression-based, the proposed method produces smoother contours.

4 Conclusions

In this paper, we devise a new adaptive-order strategy in a regression-based MR image super-resolution framework. Leveraging image structure tensor to measure the texture degree, image voxels are classified into different groups. The regression order is then adaptively selected voxel-wisely according to the classification results. Experimental results demonstrate that the proposed method is more time efficient

than second-order regression-based method and produces a comparative performance than some state-of-the-art SR approaches, both visually and quantitatively.

Acknowledgments This work was supported in part by the National Natural Science Foundation of China under Grant 61602065, Sichuan province Key Technology Research and Development project under Grant 2017RZ0013, Scientific Research Foundation of the Education Department of Sichuan Province under Grant No.17ZA0062, J201608 supported by Chengdu University of Information and Technology (CUIT) Foundation for Leaders of Disciplines in Science, project 762001009 supported by Open Fund of CUIT, and project KYTZ201610 supported by the Scientific Research Foundation of CUIT.

References

1. Reeth EV, Tham IW, Tan CH, Poh CL (2012) Super-resolution in magnetic resonance imaging: a review. Concep Magn Reson Part A 40((6):306–325
2. Jog A, Carass A, Prince JL (2016) Self super-resolution for magnetic resonance images. In: Proc. MICCAI, pp 553–560
3. Greenspan H (2009) Super-resolution in medical imaging. Comput J 52(1):43–63
4. Buades A, Coll B, Morel JM (2005) A non local algorithm for image denoising. IEEE Comput Soc Conf Comput Vis Pattern Recognit 2:60–65
5. Manjón JV, Coupé P, Buades A et al (2010) Non-local MRI upsampling. Med Image Anal 14:784–792
6. Plenge E, Poot DH, Niessen WJ et al (2013) Super-resolution reconstruction using cross-scale self-similarity in multi-slice MRI. In: Proc. MICCAI, pp 123–130
7. Rousseau F (2010) A non-local approach for image super-resolution using intermodality priors. Med Image Anal 14(4):594–605
8. Manjón JV, Coupé P, Buades A et al (2010) MRI superresolution using self-similarity and image priors. Int J Biomed Imaging:Article ID 425891
9. Coupé P, Manjón JV, Chamberland M et al (2013) Collaborative patch-based super-resolution for diffusion-weighted images. NeuroImage 83:245–261
10. Jafari-Khouzani K (2014) MRI upsampling using feature-based nonlocal means approach. IEEE Trans Med Imag 33(10):1969–1985
11. Jafari-Khouzani K, Gerstner E, Rosen B et al (2015) Upsampling dynamic contrast enhanced MRI. IEEE Int Symp Biomed Imaging:1032–1035
12. Hu J, Wu X, Zhou J (2017) Second-order regression-based MR image upsampling. Comput Math Methods Med:Article ID 6462832
13. Hu J, Luo Y (2014) Single-image superresolution based on local regression and nonlocal self-similarity. J Elect Imaging 23(3):033014–033014–14
14. Choi B, Kim SD, Ra JB (2008) Region-based super-resolution using adaptive diffusion regularization. Opt Eng 47(2):027006-11–027006-11
15. Wang Z, Bovik AC, Sheikh HR, Simoncelli EP (2004) Image quality assessment: from error visibility to structural similarity. IEEE Trans Image Process 13(4):600–612

A Cone-Beam CT Reconstruction Algorithm Constrained by Non-local Prior from Sparse-View Data

Zhichao Zhang, Yining Hu, and Limin Luo

1 Introduction

The problem of potential effects of X-ray radiation on human genetic diseases and cancer has gained concerns in many computed tomography applications. Sparse-view scan is an effective way to reduce the total radiation dose received by patients. But the reconstruction from sparse sampling is a serious ill-posed problem [1]. In this situation, the conventional analytical methods based on projection geometry can introduce many strip artifacts. And by the common iterative algorithms, such as MLEM or OSEM, we also cannot gain satisfactory reconstruction results. The model of maximum a posteriori (MAP) tends to prevent the solution fall into local minimum in the iterative process by introducing prior information [2].

With excellent filtering performance, non-local method is applied to image denoising [3], initially. This paper introduces non-local MRF idea to the MAP reconstruction of CBCT from sparse-view data. Using large-scale search window and block similarity, the non-local prior can keep boundary sharp while suppressing strip artifacts effectively caused by sparse sampling. Experiments show that, compared with local MRF prior, the non-local model can obtain better reconstruction images.

Z. Zhang
Laboratory of Image Science and Technology, Southeast University, Nanjing, China

The 28th Research Institute of China Electronics Technology Group Corporation, Nanjing, China

Y. Hu (✉) · L. Luo
Laboratory of Image Science and Technology, Southeast University, Nanjing, China

Key Laboratory of Computer Network and Information Integration (Southeast University), Ministry of Education, Nanjing, China
e-mail: hyn.list@seu.edu.cn

M. Jiang et al. (eds.), *The Proceedings of the International Conference on Sensing and Imaging*, Lecture Notes in Electrical Engineering 506,
https://doi.org/10.1007/978-3-319-91659-0_20

Although excellent reconstruction results can be gained by MAP-NL method, the computationally expensive feature of non-local idea is the most obvious barrier to its application. And the CPU does not have enough capacity to support the iterative optimization process of MAP algorithm constrained by non-local prior in three-dimensional image space. In recent years, the optimization strategy of objective function using GPU, with strong parallel computing power, has become an effective solution. In this paper, we use technology of CUDA to solve this problem.

1.1 Maximum A Posteriori (MAP)

According to Bayesian theory:

$$P\left(X|\,Y\right) = P\left(Y|\,X\right)P(X)/P(Y) \tag{1}$$

where $X = \{x_j\}$, $j = 1\cdots J$ represents the image to be reconstructed, $Y = \{y_i\}$, $i = 1\cdots I$ is the projection data. According to MAP reconstruction model, given the measure data Y, optimize the image X to maximize the posterior probability $P(X|Y)$. Considering the non-negativity of probability and the monotonicity of natural logarithmic function, the optimization of the above equation is equivalent to optimizing the logarithmic relation. Then we have objective function:

$$f(X) = \arg\min_{X}\left(-L\left(Y\,|X\right) + \beta U(X)\right) \tag{2}$$

where $L(Y|X) = \ \ln\left(P(Y|X)\right)$, $\beta U(X) = \ \ln\left(P(X)\right)$, and β is the balance parameter and controls the degree of constraint on the reconstruction image; $U(X)$ is the regularization function. Minimizing the above formula, the reconstruction result of MAP model is obtained. Based on the Poisson statistical model, the multiplicative iterative formula of the observed data X is:

$$x_j^{k+1} = \frac{x_j^k}{\sum\limits_i a_{ij} + \beta\frac{\partial U\left(X^k\right)}{\partial x_j^k}}\sum_i a_{ij}\frac{y_i}{\sum\limits_l a_{il}x_l^k} \tag{3}$$

where $A = \{a_{ij}\} \in \mathbb{R}^{I\times J}$ is the system matrix and a_{ij} is the contribution of pixel x_j to the attenuation of ith X-ray. And the ideal observation model can be simply expressed as $Y = AX$.

1.2 Non-local Method

The commonly used MRF l_p-norm prior can be defined with the following form:

$$U(X) = \sum_i \sum_{j\in W_i} w_{ij}\left\|x_i - x_j\right\|_p \tag{4}$$

where W_i represents the MRF window of pixel x_i, x_j is the pixel in W_i, and w_{ij} is the weight between x_i- and x_j-based Euclidean distance. The l_2-norm is widely used in many researches in the field of iterative imaging. But considering the l_1-norm is better than l_2-norm in removing artifacts and preserving edges [4, 5], the former is used in this paper. The conventional MRF prior models are calculated in small neighborhood region, normally. It is difficult to distinguish whether the abrupt change of gray level is artifact or boundary.

Non-local prior can provide constraint according to patch similarity. It has been applied to two-dimensional CT reconstruction [6–8]. And in this paper, with the help of CUDA, this prior model is introduced into CBCT reconstruction. Filtering in a relatively wide neighborhood (search window) and considering similarity between patches named similarity patch-window, it makes full use of the similarity structure in image space and has better performance in suppressing artifacts and edge-preserving. And the similarity patch-window is a small window about the central pixel (voxel).

The weight w_{ij} of non-local model can be calculated by [6]:

$$w_{ij} = \frac{1}{Z(i)} e^{\frac{-\left\| v(N_i) - v\left(N_j\right) \right\|_2^2}{h^2}} \tag{5}$$

where N_i and N_j are cubic neighbor centered by voxel x_i and voxel x_j, respectively; $v(N_i)$ and $v(N_j)$ are vectors about N_i and N_j, respectively; $\| \|_2^2$ represents the sum of distance between two patch-windows; h is a parameter controlling the decay of exponential function; and $Z(i)$ is the normalization factor.

$$Z(i) = \sum_j e^{\frac{-\left\| v(N_i) - v\left(N_j\right) \right\|_2^2}{h^2}} \tag{6}$$

On the CUDA programming platform, we can apply a thread for each voxel to compute the non-local prior of this voxel. Because of the parallel execution of threads, the computation speed of non-local method could be greatly improved. The parallel kernel function of non-local prior calculation is given as follows:

```
__global__ void NonlocalPriorKernel(float *prior, float *object)
{
    //get the index of thread
    int tid = threadIdx.x+(blockIdx.x+blockIdx.y*gridDim.x)
    *blockDim.x;
    calculate value: the non-local prior of voxel x_tid
    prior[tid] = value;
}
```

Containing information of thread, gridDim, blockDim, blockIdx, and threadIdx are built-in variables of CUDA. And in order to faster iterative optimization speed further, we use parallelized projection and back-projection methods according to our previous work [9].

2 Experimentation and Discussion

In this paper, the performance of non-local is evaluated with both three-dimensional Shepp-Logan phantom data and clinical data. We compare non-local method with conventional MRF prior model in experiments.

2.1 Simulated Data

In the three-dimensional Shepp-Logan digital phantom experiment, the distance from X-ray source to object center (DSO) is 2000 mm; the distance from X-ray source to the center of detector plate (DSD) is 2200 mm; the plate size is 200×400; the detector size is 0.75 mm^2; the size of this phantom is $256 \times 256 \times 100$; and the voxel size is 1 mm^3. The size of search window is $9 \times 9 \times 9$. The size of similarity patch-window is $3 \times 3 \times 3$. The reconstruction experiments form 60 projection images and 40 projection images are carried out to test the performances of different algorithms. Although the noise distribution in real scan are often characterized in the Gaussian model due to the correction and calibration process in acquisition, the Poisson model is still available because in sparse-view scan, the tube current and tube voltage are not reduced; therefore the expectation of projection is relatively high, and in this case, the Poisson distribution is similar to Gaussian.

Figure 1 shows the reconstruction images of different methods from projection data of 60 angles, and Fig. 2 gives those from 40 projection images. The result of traditional local MRF prior has many artifacts.

Figure 3 shows the reconstruction values of the 128th line of the middle slice of reconstruction images. Compared to the local MRF prior, the non-local idea has better performance, and its results are closer to the original image.

Table 1 shows the PSNR and SSIM of reconstruction images gained by different algorithms. We can know that the result of local MRF model is relatively poor.

The above results show that, on Shepp-Logan phantom data, non-local prior improves greatly the image quality of sparse-view reconstruction. And in the aspects

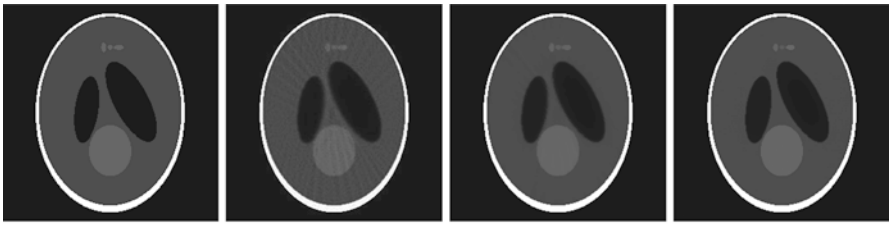

Fig. 1 Reconstruction images using 60 projection views data. (**a**) Original image, (**b**) no prior, (**c**) local MRF prior, (**d**) non-local prior

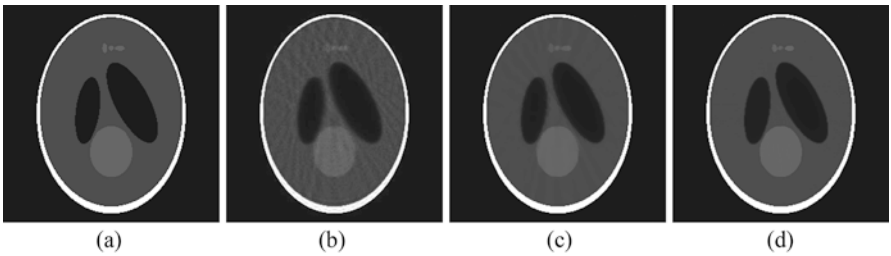

Fig. 2 Reconstruction images using 40 projection views data. (**a**) Original image, (**b**) no prior, (**c**) local MRF prior, (**d**) non-local prior

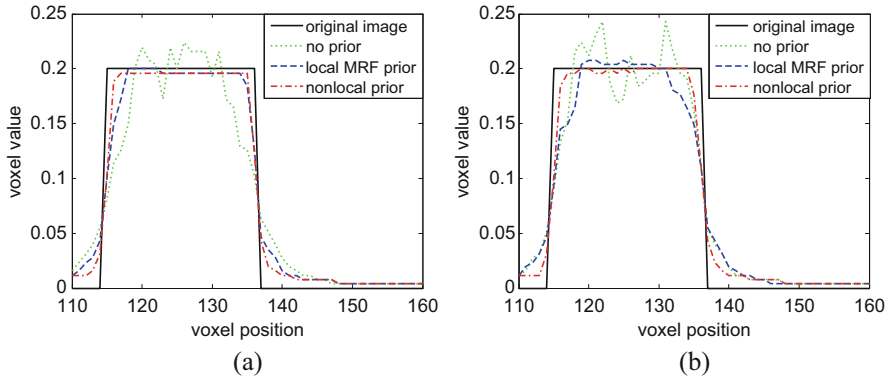

Fig. 3 The voxel values of the 128th line of the middle slice of object data. (**a**) 60 projection images, (**b**) 40 projection images

Table 1 PSNR and SSIM of results using different methods

Algorithm	60 projection angles		40 projection angles	
	PSNR	SSIM	PSNR	SSIM
No prior	31.3451	0.8997	30.2750	0.8798
Local MRF prior	35.0551	0.9633	34.9139	0.9608
Non-local prior	35.5360	0.9671	35.2953	0.9672

of structural artifact removal and boundary preserving, non-local method has better capability than local MRF model. In order to verify the performance of our method on real CBCT data, further experiments are executed.

2.2 Clinical Acquisitions

The CBCT projection images of human head are collected from 650 angles, and the size of those images is 768 × 1024. In this CBCT system, the DSO is 1000 mm; the

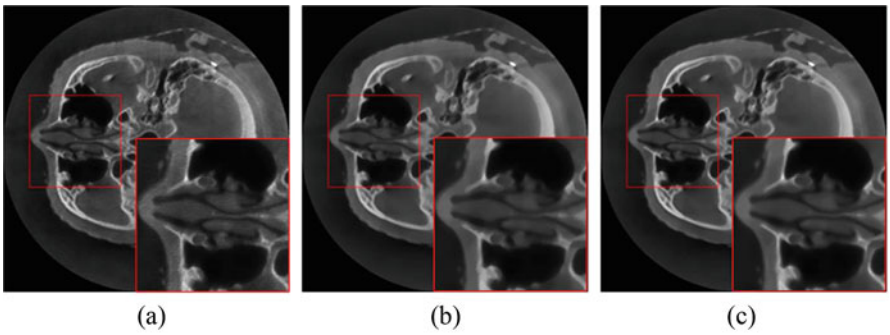

Fig. 4 Reconstruction images using 650 projection views data. (**a**) No prior, (**b**) local MRF prior, (**c**) non-local prior

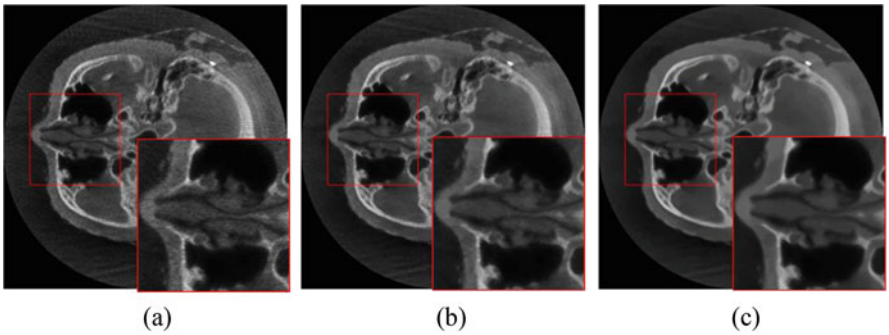

Fig. 5 Reconstruction images using 216 projection views data. (**a**) No prior, (**b**) local MRF prior, (**c**) non-local prior

DSD is 1500 mm; and the pixel size is 0.388 mm^2. The size of the reconstruction object is $450 \times 450 \times 450$, and the voxel size is 0.5 mm^3.

In this paper, reconstruction experiments with 650 projection images, 216 projection images, and 130 projection images were carried out. In those experiments, the size of search window is $15 \times 15 \times 15$, and the size of similarity patch-window is $5 \times 5 \times 5$.

Figure 4 gives the reconstruction results using 650 projection images. Non-local method is slightly better than the local MRF prior in the visual effect of reconstruction results, but the difference is not obvious. The SSIM value of images constructed by them is 0.9888. Then one of the two images can be selected as a reference image for evaluating sparse scan reconstruction results. In this paper, we chose the reconstruction image of non-local model.

Figure 5 shows the reconstruction images of different methods from projection data of 216 angles, and Fig. 6 gives those from 130 projection images. In visual effect, the reconstruction images of constrained by non-local model are better than traditional MRF prior in the same number of iterations.

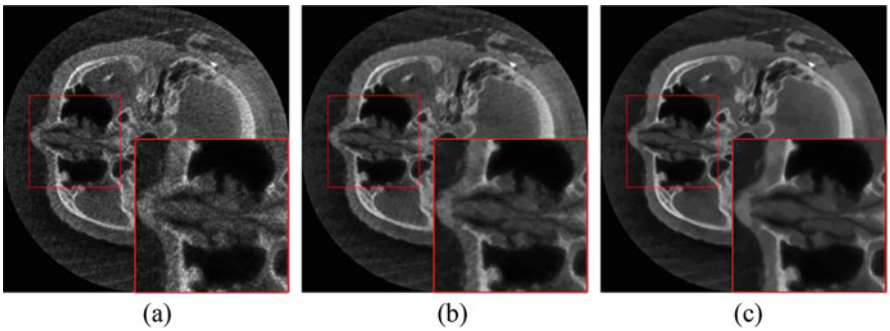

Fig. 6 Reconstruction images using 130 projection views data. (**a**) No prior, (**b**) local MRF prior, (**c**) non-local prior

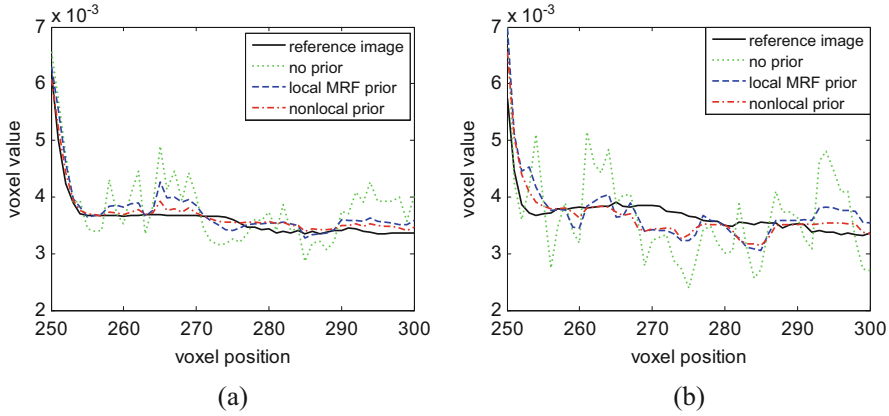

Fig. 7 The voxel values of the 225th line of the middle slice of object data. (**a**) 216 projection images, (**b**) 130 projection images

Table 2 PSNR and SSIM of results using different methods

	216 projection angles		130 projection angles	
Algorithm	PSNR	SSIM	PSNR	SSIM
No prior	32.3900	0.8071	28.2371	0.6779
Local MRF prior	39.2123	0.9656	33.3851	0.8922
Non-local prior	40.7190	0.9743	35.4098	0.9479

Figure 7 shows the reconstruction line profile of the 225th line of the middle slice of object data reconstructed by different algorithms, and the line profile of non-local method is closer to that of reference image. Table 2 shows the PSNR and SSIM of reconstruction images gained by different algorithms, and the reference image is Fig. 4c. We can know that the non-local methods can gain higher PSNR and SSIM and has better ability to remove artifacts.

All above results show that the non-local prior can produce satisfactory reconstruction results in sparse scan reconstruction of CBCT.

3 Conclusion

This paper introduces non-local prior into CBCT reconstruction from sparse-view data in the platform of CUDA. We use non-local filter function to constrain the objective function in the iterative method, so that noise and artifacts are suppressed better and details are kept as much as possible. Experiments show that compared with local MRF idea, the prior model of non-local has better performance in suppressing noise and artifacts caused by sparse sampling.

References

1. Hu Y, Xie L, Chen Y, et al. (2013) Adaptive L0 norm constrained reconstructions for sparse-view scan in cone-beam CT[C]. Nucl Sci Symp Med Imag Conf (NSS/MIC), 2013 IEEEIEEE. 1–4
2. Geman S, Geman D (1984) Stochastic relaxation, Gibbs distributions, and the Bayesian restoration of images[J]. Pattern Anal Mach Intel, IEEE Transactions on, 1984 (6): 721-741
3. Buades A, Coll B (2005) Morel J M. A non-local algorithm for image denoising[C]. IEEE Comp Soc Conf Comp Vision Pattern Recog (CVPR'05) IEEE 2005(2):60–65
4. Zhang H, Wang J, Ma J et al (2014) Statistical models and regularization strategies in statistical image reconstruction of low-dose X-ray CT: a survey[J]. arXiv preprint arXiv 1412:1732
5. Zeng GL (2010) Medical image reconstruction[M]. Springer, Heidelberg
6. Chen Y, Ma J, Feng Q et al (2008) Nonlocal prior Bayesian tomographic reconstruction[J]. J Math Imag Vision 30(2):133–146
7. Zhang Q, Liu Y, Shu H et al (2013) Application of regularized maximum likelihood algorithm in PET image reconstruction combined with nonlocal fuzzy anisotropic diffusion[J]. Optik-Int J Light Elect Opt 124(20):4561–4565
8. Chan C, Fulton R, Feng D D, et al. (2010) Median non-local means filtering for low SNR image denoising: application to PET with anatomical knowledge[C]. IEEE Nucl Sci Symp Med Imag Conf. IEEE, 2010: 3613–3618
9. Xie L, Hu Y, Yan B et al (2015) An effective CUDA parallelization of projection in iterative tomography reconstruction[J]. PLoS One 10(11):1–17

Robust Binary Keypoint Descriptor Based on Local Hierarchical Octagon Pattern

Ling Jin, Yiguang Liu, Zhenyu Xu, Yunan Zheng, and Shuangli Du

1 Introduction

In recent years, keypoint descriptors have been popularized in computer vision and pattern recognition application tasks such as object matching, object recognition, and texture analysis [1]. Moreover, with the recent progress in research on application of keypoint descriptors, object recognition based on matching becomes more practical and attractive in the field of machine vision [2]. To create a descriptor with strong robustness, high discriminative power as well as high efficiency in computation is the goal of this paper. Existing keypoint descriptors can be categorized into two classes according to their composition: floating-point values and binary string. The former (e.g., SIFT [3], SURF [4]) are widely used in CV applications since they are highly discriminative and robust to general image deformations such as image rotation and scale; however they are inefficient to compute, store, and match; thus their extensions to real-time applications are hindered. The latter (e.g., BRIEF [5], ORB [6], BRISK [7], or FREAK [8]) is a binary string realized by comparing the intensities of selected pixels to each other, and the binary string is memory saving and can be matched efficiently; nevertheless, they face the problem of being less robust and discriminative and may result in lots of mismatching. Moreover, before building the latter descriptors, the image should be filtered with specified Gaussian kernels to suppress the noise, which is also time-consuming. Although SIFT descriptor and binary descriptor have been

L. Jin (✉) · Y. Liu · Z. Xu · Y. Zheng · S. Du
College of Computer Science, Sichuan University, Chengdu, Sichuan Province, People's Republic of China
e-mail: lygpapers@aliyun.com

M. Jiang et al. (eds.), *The Proceedings of the International Conference on Sensing and Imaging*, Lecture Notes in Electrical Engineering 506,
https://doi.org/10.1007/978-3-319-91659-0_21

widely studied in recent years (e.g., [9–11]), most of the research focuses only on improving matching rate and existing keypoint descriptors do not handle the problems they face explicitly. To address the problems the above descriptors face, we propose a new descriptor called LHOP.

2 LHOP Descriptor

Compared to the aforementioned descriptors, the main features of LHOP descriptor can be highlighted as follows: (1) It is robust. Binary tests are performed between average intensities from different image patches instead of individual pixel intensities, which makes it more robust to local image distortions and noise. (2) It is efficient to compute. Integral image is employed to guarantee the computing speed, and Gaussian smoothing is not used in our method since the average intensity of a patch is not sensitive to image noise. (3) It is highly discriminative. The average intensities are sampled from multi-scale patches on hierarchical layers, which contain more distinct information than individual pixel intensities sampled on single layer. (4) It is memory saving and compact. The LHOP descriptor consists of 256 independent bits which are obtained from 256 independent binary tests.

Before building the descriptor, each keypoint is assigned an orientation estimated by the *intensity centroid measure* [6] to make the LHOP descriptor invariant in the plane rotation. Let K denotes a keypoint. For a given patch P with a radius of 5σ (where σ is the keypoint's scale), we set O as the centroid of it and K as the center. Vector $\overrightarrow{KO}$ is the orientation of the keypoint K. Then, for any image patch P, its moment, denoted by M_{pq}, is defined as follows:

$$M_{pq} = \sum_{(x,y)\in P} x^p y^q I(x, y) \tag{1}$$

where $I(x, y)$ denotes the intensity of the pixel at point (x, y) and the keypoint K also is the origin of this coordinate system. By using these moments, the centroid and the orientation can be computed as follows:

$$O = \left(\frac{M_{10}}{M_{00}}, \frac{M_{01}}{M_{00}}\right), \theta = atan2(M_{01}, M_{10}) \tag{2}$$

In order to compute the moment M_{01} quickly, we divide the patch P into n subpatches $P_1, P_2, \ldots, P_n$ (12 in our implementation), as shown in Fig. 1a, and then the M_{01} can be written as:

$$\begin{aligned} M_{01} &= \sum_{(x,y)\in P} yI(x, y) \\ &= \sum_i \sum_{(x,y)\in P_i} yI(x, y) \approx \sum_i \left(Y_i \sum_{(x,y)\in P_i} I(x, y) \right) \end{aligned} \tag{3}$$

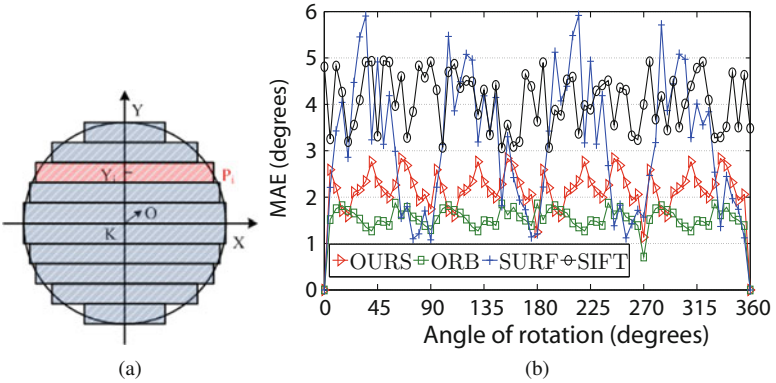

(a) (b)

Fig. 1 Fast orientation estimation, the method, and its mean absolute error. (**a**) The method. (**b**) MAE (mean absolute error)

Table 1 Average times of computing orientations for 10,000 keypoints resulted by several methods

Methods	SIFT	SURF	ORB	OURS
Time[ms]	452	368	98	7

where Y_i is the Y-coordinate of the center point of P_i and $\sum_{(x,y)\in P_i} I(x, y)$ can be fast computed by integral image (Fig. 1a). The M_{10} can be computed in a similar way. The parameter n is determined by the keypoint scale and the size of the region for keypoint orientation computation. In our method, the diameter of the region is chosen as 12 $\sum$, and the parameter n is also set as 12; thus the width of each subpatch is 1 sigma, making our method resistant to noise and also efficient to compute.

Reference [6] has shown that centroid-based orientation has higher rotation estimation accuracy and better noise resistance ability compared to gradient-based orientation. It is proposed in this paper that centroid is approximately computed by using the integral image, which increases the computation speed by more than one order of magnitude. In Table 1, we can observe that the average time of computing orientations for 10,000 keypoints resulted by our method is less than other methods. We tested the accuracy of several methods on the 1000 image patches randomly selected from 100 different images, with each image patch being artificially rotated by a series of given angles. As shown in Fig. 1b, for the orientation produced by our method, the mean absolute error of its angle is less than 3°, which is more stable and accurate than the methods used in SIFT and SURF.

The LHOP descriptor is built on a single structure – the octagon filter – which is firstly invented as a keypoint detector in [12]. We find this shape of filter can also be used efficiently to build a binary descriptor, since it possesses both of the following valuable properties: (1) It's very fast to compute by using of slanted integral image, which needs only 11 additions to calculate the sum of pixel intensities within an octagon area. (2) It is almost rotational invariant, as shown in Table 2.

Table 2 Overlap ratios resulted by filters of different shapes with random rotations around their centers

Shapes	Circle	Box	Octagon
Overlap ratios	100%	>84%	>96%

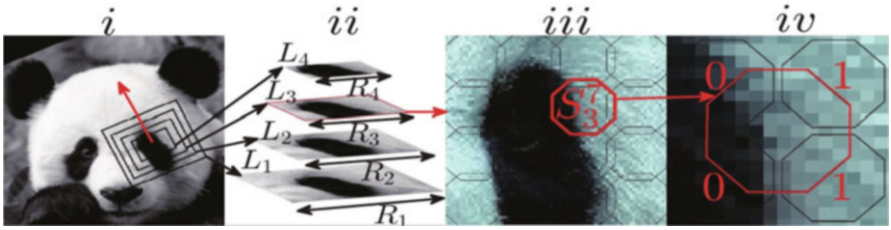

Fig. 2 The process to construct the binary string (i) Four oriented square patches are selected (ii) The description pyramid (iii) The third layer of pyramid L_3 is partitioned into 16 octagonal subpatches (iv) The sub-path S_3^7 contributes 4 bits to the final descriptor

The binary string of LHOP descriptor is constructed by starting with selecting several orientated patches (Fig. 2(i)) with the keypoint as their center to create a *description pyramid* (Fig. 2(ii)). The pyramid has n layers L_i $(i = 1, \cdots, n)$ (4 in our implementation), and an upper layer gives more detailed information of a smaller region surrounding the keypoint to LHOP descriptor as opposed to a lower layer. Each L_i is equally partitioned into 16 octagonal subpatches S_i^j $(j = 1, 2, \ldots, 16)$, as shown in Fig. 2(iii). Let R_i be the side length of L_i, $R_i = k^i \times R_1$ $(0 < k < 1.0)$. When the factor k is close to 1.0, the layers become quite similar to each other, which will introduce redundant information to LHOP descriptor; when k is close to 0, the layers become quite different to each other, but the patch S_i^j is no longer resistant to local image distortions. So, in order to get better performance, it is very important that we should know how to choose the value of the factor k. Tentative experiments show that with $R_1 = 10\sigma$ and $k = 0.4^{\frac{1}{3}}$, the descriptor performs well in most cases. Let $F(X)$ be the average intensity of patch X, and let $F_c(X)$ $(c = 1, 2, 3, 4)$ be the average intensity of the four corner octagonal patches around X. Each bit b in LHOP descriptor is corresponding to:

$$b = \begin{cases} 0, & if \quad F\left(S_i^j\right) \leq F_c\left(S_i^j\right) \\ 1, & \text{otherwise} \end{cases} \tag{4}$$

Each S_i^j contributes 4 bits to LHOP descriptor (Fig. 2(iv)), and LHOP descriptor consists of 256 bits in total. Figure 2 gives an overview of the process to construct the binary string.

By computing the Hamming distance, LHOP descriptors can be matched extremely fast on modern CPUs which often provide a specific instruction to perform a XOR or bit count operation.

Table 3 The average times of constructing 10,000 keypoint descriptors resulted by several methods

Methods	SIFT	SURF	ORB	LHOP
Time[ms]	9971	2812	250	91

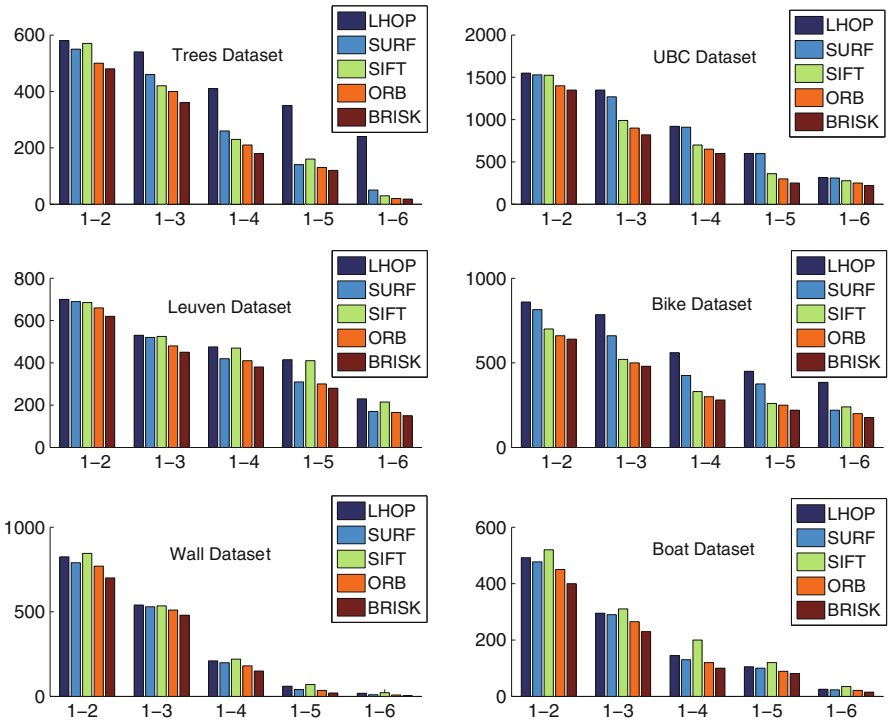

Fig. 3 Performance evaluation on the datasets introduced by Mikolajczyk and Schmid. The abscissa represents the image pair, e.g., "1–4" is the image pair consisting of the first and the fourth images in a dataset, and the ordinate represents the number of correct matches

3 Experiments and Results

Experiments have been done on a laptop with a 2.6 GHz CPU, 2GB memory and without using multi-threading. The datasets for experiments were proposed by Mikolajczyk and Schmid [13] with transformations covering zoom and rotation (Boat), viewpoint change (Wall), brightness changes (Leuven), blur (Trees and Bikes), as well as JPEG compression (UBC). Each dataset has six images; we match the first image against the other five images. SURF keypoint is extracted in each image for matching, and the descriptor's performance is evaluated by the number of correct matches. As shown in Table 3, LHOP descriptor is about two orders of magnitude faster than SIFT descriptor and 2 times faster than ORB descriptor in construction. For the matching performance as shown in Fig. 3, LHOP descriptor performs better than SURF descriptor, ORB descriptor, and BRISK descriptor in all

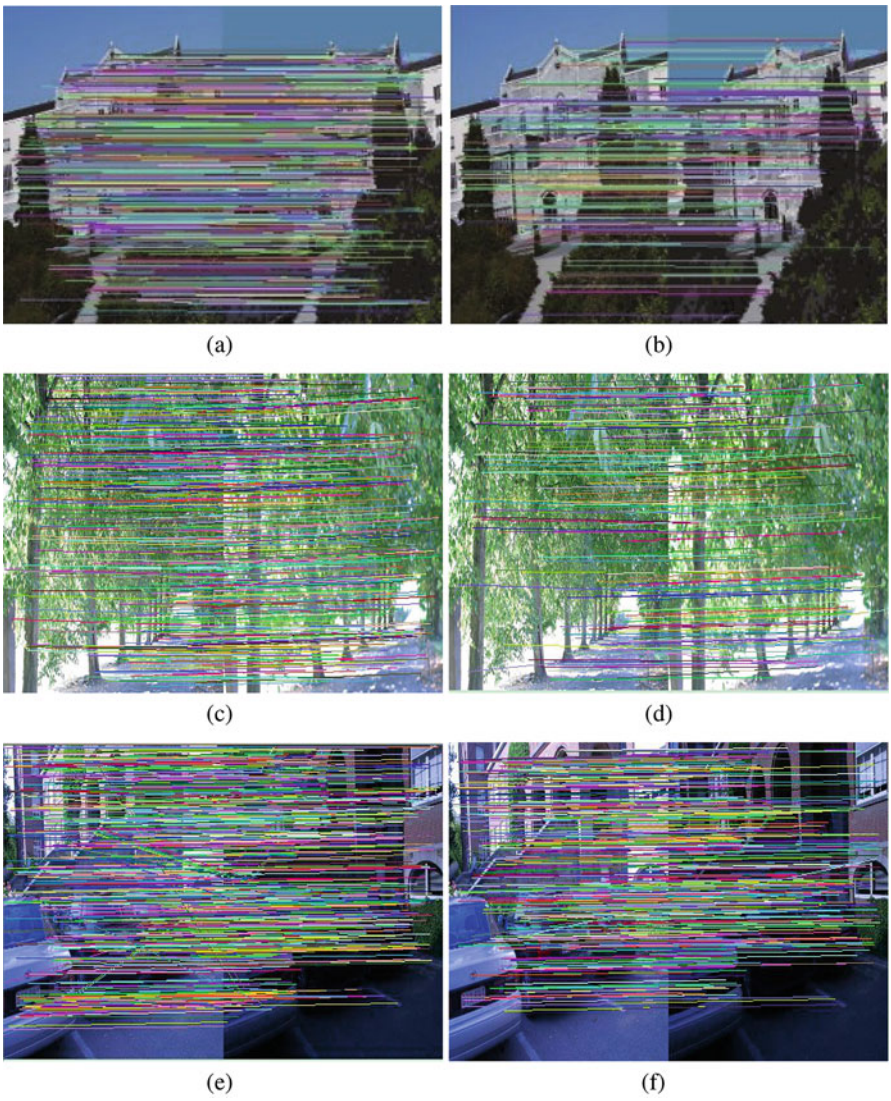

Fig. 4 The comparison of the matching performance between LHOP and SIFT and the comparison between LHOP and SURF (**a**) LHOP, 810 correct matches, (**b**) SIFT, 212 correct matches, (**c**) LHOP, 325 correct matches, (**d**) SIFT, 146 correct matches, (**e**) LHOP, 601 correct matches, (**f**) SURF, 407 correct matches

of the 6 datasets and performs better than SIFT descriptor in 4 datasets (Trees, Bikes, Leuven, and UBC). We compare the proposed descriptor with a number of state-of-the-art keypoint descriptors including SIFT and SURF. And the comparison results of the matching performance on an image pair with one image under high JPEG compression are shown in Fig. 4. We can observe from these comparison results

that our LHOP descriptor offers the better matching performance compared to other descriptors. And it is clear that our proposed descriptor is more stable and accurate than other descriptors including SIFT descriptor and SURF descriptor through these experiments.

4 Conclusion

In this paper a new effective descriptor, LHOP, with low computational complexity has been proposed. Experimental results show that LHOP descriptor runs at a speed much higher than the state-of-the-art keypoint descriptors under almost the same or better matching performance, making LHOP a compelling choice for real-time tasks.

Acknowledgements Thanks to all the persons who have actively contributed to the progress of this paper with their advice and efforts. In addition, thanks to the associate editors and the reviewers for the time and effort spent handling this paper. This work was supported by the Science and Technology Innovation seedling project of Sichuan (2016–2017).

References

1. St-Charles PL, Bilodeau GA, Bergevin R (2016) Fast image gradients using binary feature convolutions. In: Proceedings of the IEEE conference on computer vision and pattern recognition workshops, pp 1–9
2. Loncomilla P, Ruiz-del-Solar J, Martnez L (2016) Object recognition using local invariant features for robotic applications: a survey. Pattern Recogn 60:499–514
3. Lowe DG (2004) Distinctive image features from scale-invariant keypoints. Int J Comput Vis 60(2):91–110
4. Bay H, Ess A, Tuytelaars T et al (2008) Speeded-up robust features (SURF). Comput Vis Image Underst 110(3):346–359
5. Calonder M, Lepetit V, Strecha C et al (2010) Brief: binary robust independent elementary features. In: Proceedings of the European conference on computer vision, Springer, Berlin/Heidelberg, pp 778–792
6. Rublee E, Rabaud V, Konolige K et al (2011) ORB: an efficient alternative to SIFT or SURF. In: Proceedings of the 2011 IEEE international conference on computer vision (ICCV). IEEE, pp 2564–2571
7. Leutenegger S, Chli M, Siegwart RY (2011) BRISK: binary robust invariant scalable keypoints. In: Proceedings of the 2011 IEEE international conference on computer vision (ICCV). IEEE, pp 2548–2555
8. Alahi A, Ortiz R, Vandergheynst P (2012) Freak: fast retina keypoint. In: Proceedings of the 2012 IEEE conference on computer vision and pattern recognition (CVPR). IEEE, pp 510–517
9. Ma W, Wen Z, Wu Y et al (2017) Remote sensing image registration with modified SIFT and enhanced feature matching. IEEE Geosci Remote Sens Lett 14(1):3–7
10. Yang C, Wanyu L, Yanli Z et al (2016) The research of video tracking based on improved SIFT algorithm. In: Proceedings of the 2016 IEEE international conference on mechatronics and automation (ICMA). IEEE, pp 1703–1707

11. Stcharles PL, Bilodeau GA, Bergevin R (2016) Fast image gradients using binary feature convolutions. In: Proceedings of the IEEE computer society conference on computer vision and pattern recognition workshops. IEEE, pp 1074–1082
12. Agrawal M, Konolige K, Blas MR (2008) Censure: center surround extremas for realtime feature detection and matching. In: Proceedings of the European conference on computer vision. Springer, Berlin/Heidelberg, pp 102–115
13. Mikolajczyk K, Schmid C (2005) A performance evaluation of local descriptors. IEEE Trans Pattern Anal Mach Intell 27(10):1615–1630

Seamless Mosaicking of Multi-strip Airborne Hyperspectral Images Based on Hapke Model

Junchuan Yu, Bokun Yan, Wenliang Liu, Yichuan Li, and Peng He

1 Introduction

As one of the hottest topics in remote sensing (RS) society, hyperspectral technology plays a significant role in earth observation. With the continuous improvement of resolution and dimensionality, the development of hyperspectral RS application gradually inclines toward more quantitative field. However, due to the impact of view angle, irradiance, and bidirectional reflectance distribution function, the image intensity has been varying in both single image and in-between images, which can cause problems in generating mosaics of multi-strip images [1]. This issue has drawn enough attention in satellite RS data processing for some large-scale applications [2], such as land-cover classifications, but is still insufficient in terms of airborne hyperspectral image processing. Different from multispectral images, the seamless mosaicking of airborne hyperspectral images can improve the visual continuity and help remove line-to-line radiometric inconsistencies for subsequent analyses, which is critical to the quality of quantitative applications [3]. Traditionally, the statistical model and semiempirical model are two mainstream methods for correcting the illumination gradient (IG) of hyperspectral images. The statistical model is suitable for massive RS data processing because of its simple principle and efficient calculation [4]. In contrast, the semiempirical model describes the mechanism between light and surface objects, so the physical meaning of its parameters is more straightforward [5]. Consequently, the semiempirical model is more suitable to airborne hyperspectral images, although the inversion of model parameters is complex.

J. Yu (✉) · B. Yan · W. Liu · Y. Li · P. He
China Aero Geophysical Survey and Remote Sensing, Center for Land and Resources, Beijing, China

M. Jiang et al. (eds.), *The Proceedings of the International Conference on Sensing and Imaging*, Lecture Notes in Electrical Engineering 506,
https://doi.org/10.1007/978-3-319-91659-0_22

Table 1 The spectral configuration of HyMap (C) sensor

Module	Spectral range (nm)	Bandwidth (nm)	Sampling interval (nm)	Bands
VIS	400∼905	15∼16	15	36
NIR	880∼1410	18∼20	18	36
SWIR1	1400∼1960	18∼20	18	36
SWIR2	1950∼2500	18∼20	18	36

In this paper, a new method for seamless mosaicking of multi-strip airborne hyperspectral images is introduced based on Hapke model, which quantitatively describes physical properties of electromagnetic radiation interacting with semi-infinite particle medium and has been widely used in photometric correction of lunar images, such as IIM [6] and M3 data [7]. As an example, the HyMap images in Lop Nor area of Hami province are selected to illustrate the implementation method and evaluate the results of the application.

2 Materials and Methods

2.1 The HyMap Images

The HyMap (C) is a mainstream aircraft-mounted commercial hyperspectral sensor developed by Integrated Spectronics, Sydney, Australia, and operated by HyVista Corporation [8]. With the bandwidths between 15 nm ∼ 20 nm, the HyMap (C) provides 144 spectral channels covering the 0.45 μm ∼ 2.5 μm range over a 668 pixel swath. The spectral configuration of HyMap (C) sensor is shown in Table 1. The HyMap (C) provides signal-to-noise ratios of 600 ∼ 1000 or better, which offers a reliable validation dataset for this study.

Eight strips of HyMap images were obtained in Lop Nor area of Hami province on June 28, 2016, between 13:00 and 16:30. The spatial resolution of HyMap images is 2.5 m by 2.5 m, with the flight height of 1.5 km. All the data were converted to radiance and geometrically corrected by picking ground control points. The atmosphere correction and EFFORT correction of the radioactive data were performed by a plug-in routine for ENVI software supplied by HyVista Corporation.

2.2 The Hapke Model

Our work is mainly based on Hapke's bidirectional reflectance model. In this study, both the model prediction and measurement are presented in terms of bidirectional reflectance factor (REF), which is defined as

$$\mathrm{REF} = \frac{I}{F} \tag{1}$$

where I is the scattered radiance and F is the incident irradiance. According to the Hapke model [9], the reflectance factor can be described as below:

$$\mathrm{REF} = \frac{I}{F} = \frac{\mu_i}{\mu_i + \mu_e} \frac{w}{4} \left[(1 + B(g))\, p(g) + H\left(\mu_i\right) H\left(\mu_e\right) - 1 \right] \tag{2}$$

where $\mu_i = \cos(\theta_i)$ and $\mu_e = \cos(\theta_e)$ are the cosine of incidence angle (θ_i) and emittance angle (θ_e), respectively, g is the phase angle, $p(g)$ is the function of phase angle and wavelength regardless of the condition of particle surface, $B(g)$ is the backward scattering function used to explain shadow-hiding opposition effect, and $H(\mu_i)$ and $H(\mu_e)$ are the Chandrasekhar's H-functions, which describe multiple scattering contributions. To further simplify the formula, we use $f(g)$ as a phase function, which is separated from the incidence and emission angles. Then, Eq. (2) can be simplified as

$$\mathrm{REF} = \frac{I}{F} = \frac{\mu_i}{\mu_i + \mu_e} f(g) \tag{3}$$

Previous studies have shown that the surface phase function describes changes in the intensity on the surface due to phase angle and contains the physical attributes of the surface [10]. Consequently, the $f(g)$ can be expressed as a multi-order fitting of phase angle. In this study, the $f(g)$ is fit with a four-order polynomial

$$f(g) = \mathrm{a}_0 + \mathrm{a}_1 g + \mathrm{a}_2 g^2 + \mathrm{a}_3 g^3 + \mathrm{a}_4 g^4 \tag{4}$$

where the phase angle g is expressed in degrees. The parameters $\mathrm{a}_0 \sim \mathrm{a}_4$ are adjusted to make the phase function fit the data.

3 Seamless Mosaicking of HyMap Images

The imaging angle including incidence angle (θ_i), emittance angle (θ_e), and phase angle g can be calculated by pixel, based on the GPS and POS information acquired with the hyperspectral data. In order to reduce the computing, a resampling of images is first required. The resampled points need to cover the whole surface of the images. A simple regular grid in object space was suggested in this study. According to Eq. (3), a group of $f(g)$ can be solved by pixel through the known incidence and emittance angle. The parameters $\mathrm{a}_0 \sim \mathrm{a}_4$ of each band were determined by fitting each $f(g)$ and g with Eq. (4).

As mentioned above, the systematic variation in intensity from one image region to another is associated with the varying of view and incident angles. A normalization of imaging angle is needed to remove the illumination gradient of images. Usually, the normalized emittance angle is set to 0°, and the normalized incidence angle is set to 25°, which is the average sun zenith of all eight strips.

According to Eq. (5), which is a transformation formula of Eq. (3), the radiance of each image can be corrected to normalized sensor angle.

$$I_{(25)} = \frac{\mu_{i=25}\,(\mu_i + \mu_e)}{\mu_i\,(\mu_{i=25} + \mu_{e=0})} \frac{f_{(g=25)}}{f_{(g)}} \frac{F_{(25)}}{F} I \tag{5}$$

where the $I_{(25)}$ is the corrected radiance, the $f_{(g=25)}$ is the phase function with $g = 25°$, and the $F_{(25)}$ is the incident irradiance with $g = 25°$. It is noted that the $F_{(25)}/F$ can be approximated as equal to $\mu_{i=25}/\mu_i$.

The radiative correction of HyMap images removed the systematic illumination gradient from one image edge to another, resulting in smooth mosaicking of two adjacent images.

4 Experimental Results

The visual change of the images is the most reliable evidence to assess if the radiative correction is complicated. As shown in Fig. 1a, we can see a scene of HyMap image without radiative correction displayed in true color, which clearly presents an IG along the vertical direction of sensor travel. In contrast, the corrected image (Fig. 1b) shows that the illumination of each ground object smoothly transits from one edge to the other without obvious distortion. The radiative differences of the corrected and uncorrected image shown in Fig. 1c illustrate the value differences between both sides of the image and further reveal the essential problems of producing "seamless" mosaic for the multi-strip images (Fig. 2a).

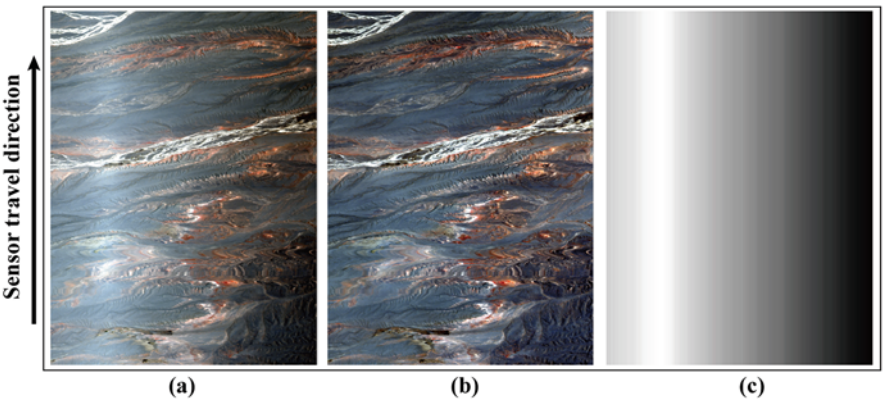

Fig. 1 (**a**) Uncorrected HyMap image, (**b**) corrected HyMap image using Hapke model presented in this paper, and (**c**) the radiative difference of the HyMap image before and after correction. All in true color

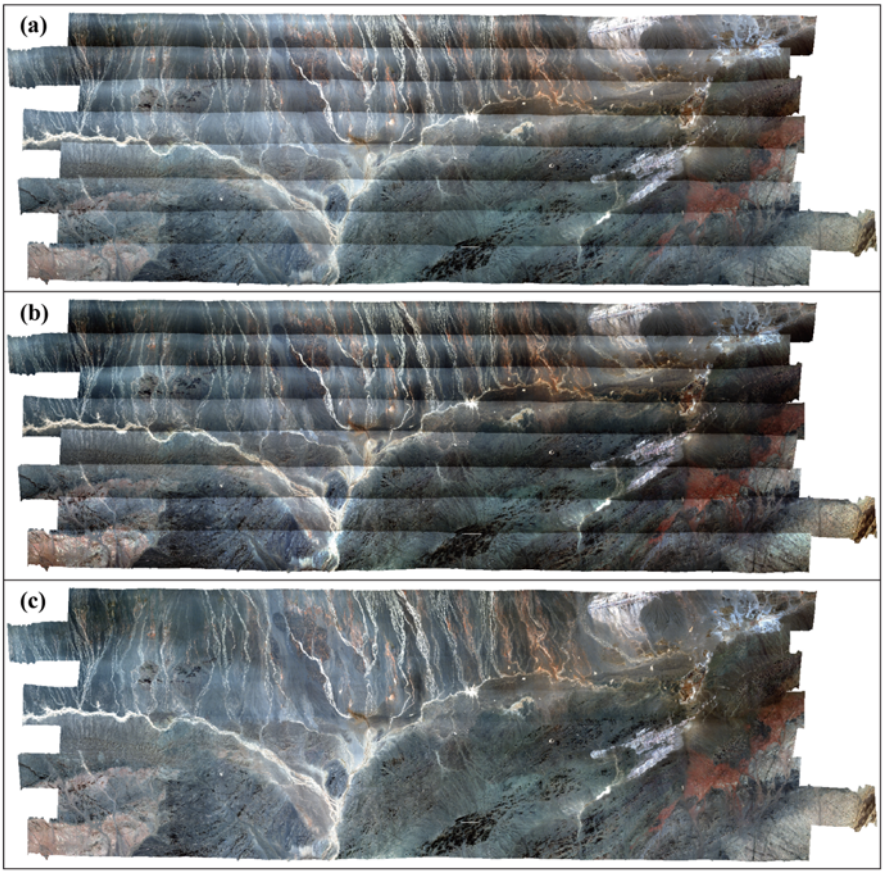

Fig. 2 (**a**) A mosaicking of original images, (**b**) a mosaicking of corrected images (using statistical method), and (**c**) a mosaicking of corrected images (using techniques presented in this paper). All in true color

For multispectral images, the IG between multi-scene images is mainly caused by different acquisition time and probably can be removed by RS processing software, such as ENVI. However, these tools are ineffective for aerial hyperspectral images (Fig. 2b), because the IG exists with each single image and cannot be removed by statistical-based method, such as histogram match. As shown in Fig. 2c, all eight strips corrected using techniques presented in this paper could stitch together generating a "seamless" mosaic.

In order to further illustrate the contribution of IG correction for hyperspectral data, we transfer the hyperspectral data by the minimum noise fraction (MNF) as an alternative method of principal components analysis. As shown in Fig. 3a, the radiative difference between adjacent images becomes even larger. This is because the main valid information of hyperspectral data concentrated in the first few bands after MNF transformation, which further highlights the existing differences. The

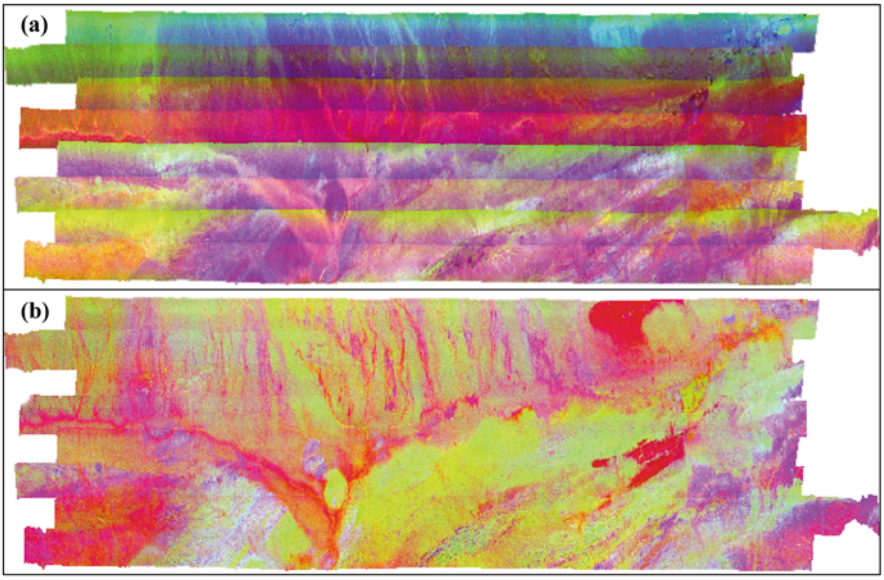

Fig. 3 (**a**) A mosaicking of eight-strip MNF-transformed image, (**b**) a seamless mosaicking of eight-strip MNF-transformed image. All in false color

seamless mosaicking of MNF-transformed data shown in Fig. 3b proves that the radiative correction is valid for all band.

Generally, hyperspectral data approximate the true spectral response of an object. Thus, it is a common method to quantify the extent of the change in spectrum by comparing the spectral characteristics before and after correction. Figure 4 shows the original and corrected spectrum of a selected pixel on overlap between two adjacent images. As shown in Fig. 4a, the original spectrum of target from strip1 to strip2 shows poor agreement on overlapping regions, revealing the cause of IG between adjacents. In contrast, the corrected spectrum of two images strip showed good consistency (Fig. 4b), without changing the spectral curve shape, indicating that this method can effectively improve the airborne hyperspectral mosaicking effect.

Radiometric inconsistencies between adjacents can seriously affect the subsequent analyses of hyperspectral data, such as ground cover-type classification and mineral information extraction. The traditional image mosaic methods mainly built based on statistical model were generally achieved by adjusting the mean and variance between images. Although the statistical method can solve the problem of color continuity, it is still difficult to correct the radiometric inconsistencies within the image. The new method presented in this paper was built based on the imaging principle of the sensor and was achieved by correcting the radiance to normalized imaging angle, which can largely preserve the true information of the data. Furthermore, the implementation of seamless mosaicking technology also

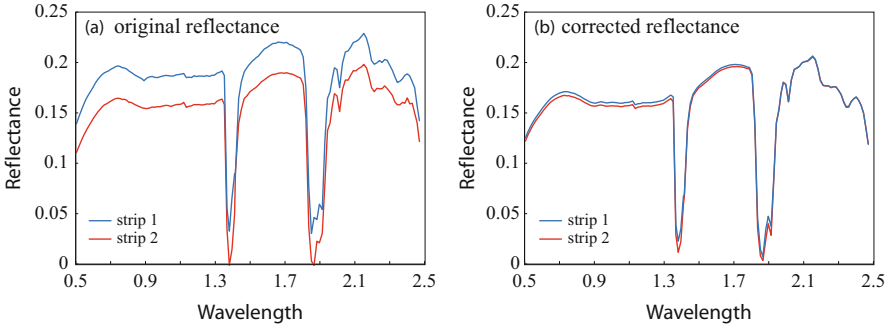

Fig. 4 Selected spectrum from overlap of adjacent images (blue and red trace). (**a**) Uncorrected spectrum, (**b**) corrected spectrum

improves the efficiency of hyperspectral data processing by treating the mosaic data simultaneously instead of treating each image separately.

5 Conclusion

In this study, we present a semiempirical method based on the Hapke model to remove the varying brightness gradient of airborne hyperspectral images, which severely affect the radiometric consistencies for subsequent analysis. The multi-strip and MNF-transformed HyMap images were chosen to assess the model. The experimental results show that the method given in this paper can efficiently remove the illumination gradient in both single image and between multi-scene images. In comparison with the statistical method, the new method preserves the true spectral information of the data to a large extent and can be used in both qualitative and quantitative analyses, which can considerably benefit the subsequent applications.

Acknowledgment This work was supported in partly by the Major Projects of High-resolution Earth Observation System (04-Y20A35-9001-15/17) and jointly by the China Geological Survey Program (121201003000150008).

References

1. Collings S, Caccetta P, Campbell N, Wu X (2010) Techniques for brdf correction of hyperspectral mosaics. Geoscience & Remote Sensing IEEE Transactions on 48(10):3733–3746
2. Wu A, Li Z, Cihlar J (1995) Effects of land cover type and greenness on advanced very high resolution radiometer bidirectional reflectances: analysis and removal. J Geophys Res Atmos 100(D5):9179–9192

3. Rogge D, Bachmann M, Rivard B, Feng J (2012) Hyperspectral flight-line leveling and scattering correction for image mosaics. In: Geoscience and remote sensing symposium, IEEE, vol 22, pp 4094–4097
4. Schiefer S, Hostert P, Damm A (2006) Correcting brightness gradients in hyperspectral data from urban areas. Remote Sens Environ 101(1):25–37
5. Roberts G (2001) A review of the application of brdf models to infer land cover parameters at regional and global scales. Prog Phys Geogr 25(4):483–511
6. Wu Y, Besse S, Li JY, Combe JP, Wang Z, Zhou X et al (2013) Photometric correction and in-flight calibration of Chang' e-1 interference imaging spectrometer (iim) data. Icarus 222(1):283–295
7. Besse S, Sunshine J, Staid M, Boardman J, Pieters C, Guasqui P et al (2013) A visible and near-infrared photometric correction for moon mineralogy mapper (m3). Icarus 222(1):229–242
8. Kruse FA, Boardman JW, Lefkoff AB, Young JM, et al. (1985) HyMap: an Australian hyperspectral sensor solving global problems-results from USA HyMap data acquisitions
9. Hapke B (1993) Theory of reflectance and emittance spectroscopy. Cambridge University Press, Cambridge, UK
10. Hicks MD, Buratti BJ, Nettles J, Staid M, Sunshine J, Pieters CM et al (2011) A photometric function for analysis of lunar images in the visual and infrared based on moon mineralogy mapper observations. Journal of Geophysical Research Planets 116(E6):1281–1292

Computational Calibration and Correction for Gigapixel Imaging System

Jiazhi Zhang, Jie He, Haiwen Li, Yuanchao Bai, Huizhu Jia, Louis Tao, and Heng Mao

1 Introduction

Remote sensing system is broadly used in many fields. In most cases, users require both a large field of view (FOV) for monitoring a large area and high spatial resolution for capturing more details. However, these two requirements are in intrinsic conflict. The larger area an image covers, the more details it omits. Gigapixel cameras are built to solving these problems. A practical approach to build a gigapixel camera is to align multiple sensors into an array [1]. But the packs of the sensors will bring in blind gaps between sensors and thus may omit important details. To overcome this problem, another approach is to adopt optical path mosaic methods in the imaging system, including external optical mosaic and internal optical mosaic. For the external optical mosaic method, several identical imaging

J. Zhang
Center for Bioinformatics, National Laboratory of Protein Engineering and Plant Genetic Engineering, School of Life Sciences, Peking University, Beijing, China
e-mail: zhangjz@mail.cbi.pku.edu.cn

J. He · H. Li · H. Mao (✉)
LMAM, School of Mathematical Sciences, Peking University, Beijing, China
e-mail: haiwen.li@pku.edu.cn; heng.mao@pku.edu.cn

Y. Bai · H. Jia
School of Electronics Engineering and Computer Science, Peking University, Beijing, China
e-mail: yuanchao.bai@pku.edu.cn; hzjia@pku.edu.cn

L. Tao (✉)
Center for Bioinformatics, National Laboratory of Protein Engineering and Plant Genetic Engineering, School of Life Sciences, Peking University, Beijing, China

Center for Quantitative Biology, Peking University, Beijing, China
e-mail: taolt@mail.cbi.pku.edu.cn

M. Jiang et al. (eds.), *The Proceedings of the International Conference on Sensing and Imaging*, Lecture Notes in Electrical Engineering 506,
https://doi.org/10.1007/978-3-319-91659-0_23

systems are built up to image the same FOV, so that multiple detectors/chips have enough space to distribute on the detection plane and finally mosaic the entire FOV from such sub-images [2]. This kind of methods often involves complex structures to make duplicated light ways. Hence the system will be heavy, complex, and hard to assemble and adjust. For the internal optical mosaic method, several relay imaging systems stand behind the customized object lens to, respectively, image sub-FOV at the first image plane or surface and finally mosaic the entire FOV from such sub-images, even doing the non-planar mosaic [3–7]. These systems usually utilize second-imaging methods to collect lights. Therefore, the volume of the system will be huge. The second-imaging subsystems are more sensible to errors, which means these subsystems need to be calibrated carefully. Furthermore, the lens for first-imaging can be huge to produce enough FOV. Heavy loads, huge volumes, and hardness of assembling and adjustment always mean high cost, both for producing and carrying.

Our system is an implementation of external optical mosaic method. We simplified the structure of the optical system by utilizing four duplicated subsystems. We use commercial lens and sensors to lower the producing cost. The simplified system contains no complex mechanical structures; this lowers the load and the volume. As a sacrifice, we have more volatile errors that make the system more vulnerable to the changes of conditions. To compensate this defect, we developed a set of methods for calibrating and correcting errors. These help the system achieve a precision on single-pixel level and can be used to observe very small details.

The system involves tens of errors and parameters which must be corrected to make the output image visible for human. In this paper, a series of calibrating methods based on carefully designed templates are adopted to calibrate and correct the parameters. The paper is organized as follows. The system is described in Sect. 2. The detailed calibrating and correcting methods are exposed in Sect. 3. And the correcting results are shown in Sect. 4.

2 System Overview

The system layout is shown in Fig. 1a, b. And the optical pathway is shown in Fig. 1c. Four @Zeiss Apo Sonnar F2/135 mm lenses are arranged in a 2×2 array. This major lens images the same object plane, and their images are the same to each other. Each lens covers $4(2 \times 2)$ to $16(4 \times 4)$ @Sony IMX135 sensors, which are installed on one PCB. Gaps between sensors are 80% of the sensor size. So the gaps in one group of sensors can be compensated by other groups. And there can be overlapping area between the images of the sensors. According to these overlaps, the images can be mosaiced to form the final large FOV image. Each sensor has 13 million pixels. The total pixel number of the large image can be calculated with Eq. (1)

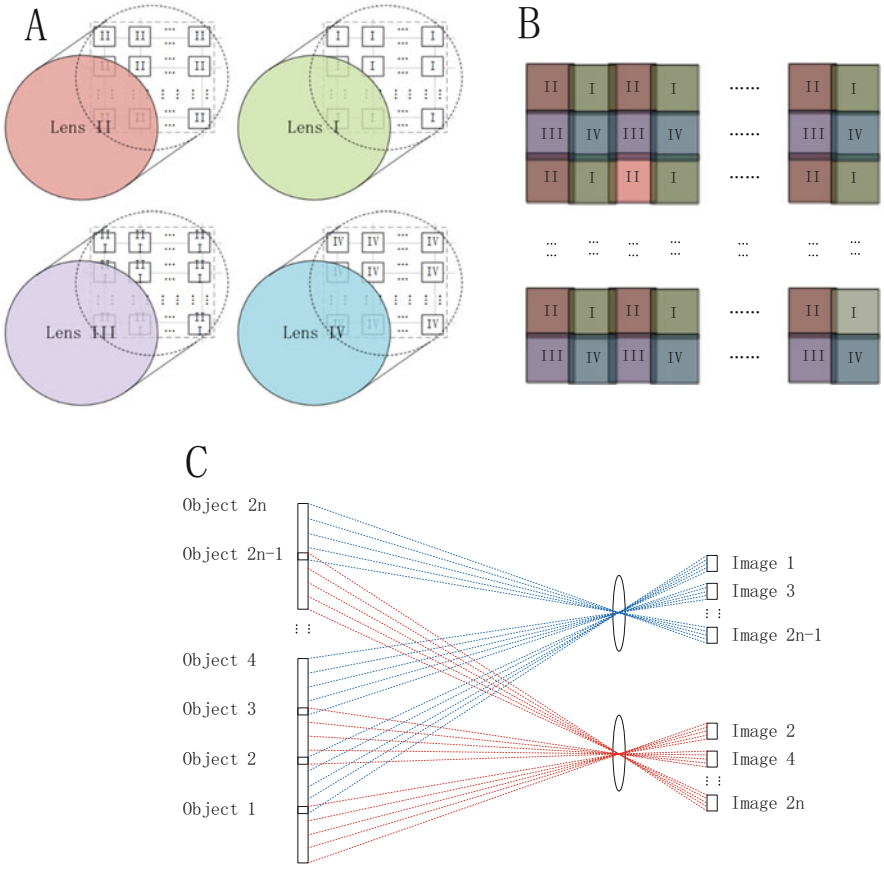

Fig. 1 Layout of our gigapixel camera. (**a**) Perspective layout of major lens and sensors. (**b**) Layout of the sensors. Sensors with the same Roman numbers are covered by the same major lens. (**c**) Optical pathway of our gigapixel camera. Paths in the same color go through the same major lens

$$r = 0.9^2 \times r_S \times S \times L \tag{1}$$

in which r_S is the pixel number of a single sensor, S is the number of sensors covered by each lens, and L is the number of major lenses. The final image can have a pixel number of 0.16 gigapixels to 0.67 gigapixels.

The computation part is implemented on a workstation with @Intel i7 CPU, @NVidia GTX970 GPU, and @RedHat CentOS 5. A self-developed software is used to process the captured images and to mosaic them to form the final large FOV image.

According to our analysis, when the object distance changes, the distances between each group must change to make the images of the four major lens the same. To achieve this, each PCB is installed on a two-axis motion stage. The stage moves when the object distance changes.

3 Parameter Calibrating and Correcting

3.1 Parameters in the System

Sensing a large area with multiple sensors can induce many errors caused by sensor alignment. In our system, sensors that are covered by the same lens are packed on one PCB. Inaccurate manufacture will cause position errors, rotation errors, and scaling errors between their images. Meanwhile, the four PCBs are, respectively, installed on four motion stages. The stages are then installed on one motherboard. This will also bring installation errors, including position errors, rotation errors, and scaling errors. Furthermore, the sensors are not absolutely parallel with the PCBs, and the latter are not parallel with the motherboard plane. This can bring perspective errors. The position errors can be corrected by stage motion and overlap-based mosaic, and the installation errors are actually coupled. Thus, there are three groups of errors left to be calibrated: rotation errors of each sensor, scaling errors of each sensor, and perspective errors of each sensor. These errors are called the geometric parameters.

Vignetting is another part of errors to be calibrated in our system. The IMX135 sensors we adopt have a micro lens before the CMOS chip. The lens induces a vignetting distribution for the image. Besides, each major lens induces a vignetting distribution into the system, and this distribution influences all the images of the sensors covered by the lens. Calibrating and correcting the vignetting distribution is called de-vignetting.

To calibrate the above parameters, we first calibrate the vignetting parameters firstly because vignetting is not related to the position relationships between sensors. Then we calibrate the geometric parameters.

3.2 De-vignetting

In common cases, the vignetting distribution is complex. It can be caused by off-axis illumination induced by the lens, the spatial relationship between the image plane and the object plane, and the deformation of the image plane and the object plane [8]. But here we consider the vignetting distribution of our system as a curved surface which can be described by a low-frequency distribution. To fit the surface, a white printing paper is imaged by the camera as a template. The paper is pasted on a flat

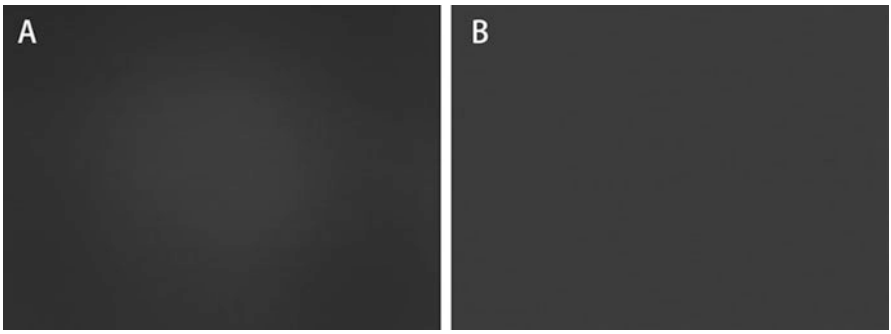

Fig. 2 De-vignetting using white template. (**a**) Before de-vignetting. (**b**) After de-vignetting

wall so there is no deformation on the object plane. White paper means there is no interferential distributions for observing the vignetting distribution. Based on these conditions, we consider the images as the pure vignetting distribution of each sensor. A discrete low-frequency surface is fitted according to the response of the white plane for each image. This fitted surface can represent the vignetting distribution.

To correct the vignetting distribution, the image processing software should calculate the vignetting distribution level for each pixel and divide the raw image pixel value with the vignetting distribution value. To accelerate the calculation on GPU, we calculate the vignetting distribution value for each pixel offline and use a hyper-parameter λ to normalize it [9].

$$K\,(x,\,y) = \frac{\lambda}{P\,(x,\,y)} \tag{2}$$

In Eq. (2), $P(x, y)$ is the vignetting distribution value of each pixel calculated from the fitted polynomial. And the matrix K is calculated and stored in the GPU memory. When image I comes in, the dot product of I and K is calculated and output as the de-vignetted image. See Fig. 2 for the de-vignetting result.

3.3 Rotation and Scaling Calibrating and Correcting

Rotation and scaling errors are actually space transformations. To calibrate these parameters, we need to find some points whose coordinates are known. And calculate the rotation degree and the scale rate from the original coordinates and the transformed coordinates. As we calibrate these parameters for mosaic, we just concern about the relative rotation and scaling between the images from different sensors. For the system with $4(2 \times 2)$ sensors covered by each lens, we designed a dot array pattern and print it in a suitable size as a template. The pattern is shown in Fig. 4a. There are $16(4 \times 4)$ duplicated dot arrays in the image. Each sensor will

image one of the arrays so that each image is an image of the same pattern. In this way, we can observe how do the images transform from each other.

Rotation and scaling transformation can be expressed as affine transformation in Eq. 3:

$$\begin{bmatrix} x_i \\ y_i \end{bmatrix} = \begin{bmatrix} m\cos\theta & -m\sin\theta \\ m\sin\theta & m\cos\theta \end{bmatrix} \begin{bmatrix} x_0 \\ y_0 \end{bmatrix} + \begin{bmatrix} \Delta x \\ \Delta y \end{bmatrix} \tag{3}$$

A sensor 0 is chosen as the benchmark sensor, which means it is considered to have no rotation and scaling. Images of other sensors are transformations of this sensor's image. The transformation involves two parameters, the rotation degree θ_i and the scaling ratio m_i. This equation induces another two unknown parameters Δx and Δy, which represent the translation errors and are not concerned. To calibrate the four parameters, at least 2 points are required to find out the solution of the linear equation. One of the points is the reference center point. Our pattern contains 19 dots, and their centers of mass can be calculated as 19 points. The best approximate parameters can be found out by least square fitting.

To correct the images, a coordinate transformation is calculated firstly, according to Eq. 3 and the fitted parameters. Then the pixel is recalculated with bilinear interpolation algorithm [10] described in Eq. 4.

$$\begin{aligned} I\left(x_f, y_f\right) = & \left(\lceil x_f \rceil - x_f\right)\left(\lceil y_f \rceil - y_f\right) I\left(\lfloor x_f \rfloor, \lfloor y_f \rfloor\right) \\ & + \left(x_f - \lfloor x_f \rfloor\right)\left(\lceil y_f \rceil - y_f\right) I\left(\lceil x_f \rceil, \lfloor y_f \rfloor\right) \\ & + \left(\lceil x_f \rceil - x_f\right)\left(y_f - \lfloor y_f \rfloor\right) I\left(\lfloor x_f \rfloor, \lceil y_f \rceil\right) \\ & + \left(x_f - \lfloor x_f \rfloor\right)\left(y_f - \lfloor y_f \rfloor\right) I\left(\lceil x_f \rceil, \lceil y_f \rceil\right) \end{aligned} \tag{4}$$

3.4 Perspective Error Calibrating and Correcting

We assume that our sensor plane is flat and with no deformation. Then the field distortion can be considered as simple perspective transformation, or perspective transformation. Perspective transformation is a more general affine transformation [11]. If perspective error is calibrated, rotation and scaling are calibrated at the same. The perspective transformation can be described with Eq. 5.

$$\begin{cases} x_i^{,} = k_1 x_i + k_2 y_i + k_3 x_i y_i + \Delta x \\ y_i = k_4 x_i + k_5 y_i + k_6 x_i y_i + \Delta y \end{cases} \tag{5}$$

To calibrate perspective error, at least 4 points are required as there are eight unknown parameters including two translation errors. Similar to Sect. 3.3, least square fitting is used to solve the parameter values, and bilinear interpolation is used to calculate the pixel values of the transformed image.

Table 1 Rotation (θ) and scaling (m) errors

	$D = 875$ cm		$D = 622$ cm		$D = 415$ cm	
Sensor #	$\theta(^\circ)$	m	$\theta(^\circ)$	m	$\theta(^\circ)$	m
1	0.0000	1.0000	0.0000	1.0000	0.0000	1.0000
2	0.8833	1.0009	0.9539	1.0024	0.8491	1.0017
3	−0.0501	0.9998	0.0491	1.0008	−0.0681	1.0002
4	0.1657	0.9995	0.2842	1.0019	0.1524	1.0016
5	0.4340	1.0013	0.5137	1.0026	0.4323	1.0007
6	0.4153	0.9988	0.5492	1.0005	0.3952	0.9980
7	0.4152	1.0023	0.5561	1.0038	0.3637	1.0012
8	0.6116	0.9988	0.8008	1.0011	0.5938	0.9990
9	0.0594	0.9992	0.1812	0.9987	0.0663	0.9992
10	0.4029	1.0010	0.5930	1.0027	0.4234	1.0011
11	0.0696	0.9998	0.2124	1.0012	0.0256	1.0000
12	0.0580	1.0004	0.2713	1.0026	0.0460	1.0013
13	0.3909	1.0009	0.5650	1.0026	0.4284	1.0000
14	0.3303	0.9989	0.5551	1.0009	0.3803	0.9982
15	0.4304	1.0018	0.5685	1.0038	0.3894	1.0015
16	0.6569	0.9988	0.8864	1.0019	0.7030	0.9994

Three working distances ($D = 875$ cm, $D = 622$ cm, and $D = 415$ cm) and 16 sensors are involved in the experiments. All the errors are relative to sensor 1

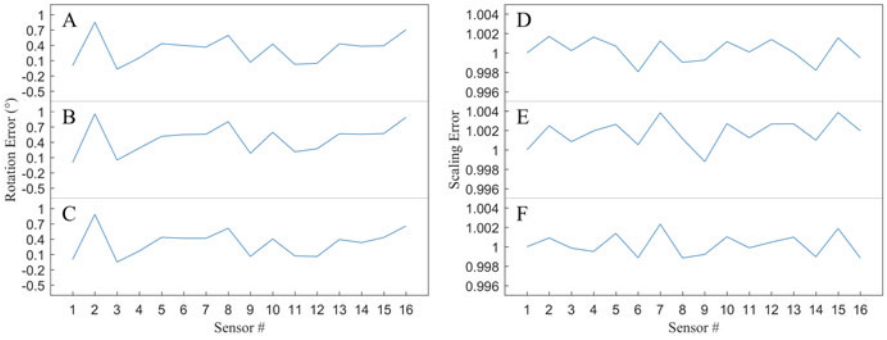

Fig. 3 Affine errors of 16 sensors, with different working distances. (**a**–**c**) Rotation errors ($^\circ$) of different working distances (**a**, 875 cm; **b**, 622 cm; **c**, 415 cm); (**d**–**f**) scaling errors of different working distances (**d**, 875 cm; **e**, 622 cm; **f**, 415 cm)

4 Correcting Results

We have calibrated the rotation and scaling errors and the vignetting patterns of 16 sensors in laboratory conditions. The de-vignetting result is shown in Fig. 6b. The calibrated rotation and scaling errors are shown in Table 1 and Fig. 3.

To evaluate our correcting results intuitively, we designed another template, shown in Fig. 4b. The template contains various shapes that are randomly arranged.

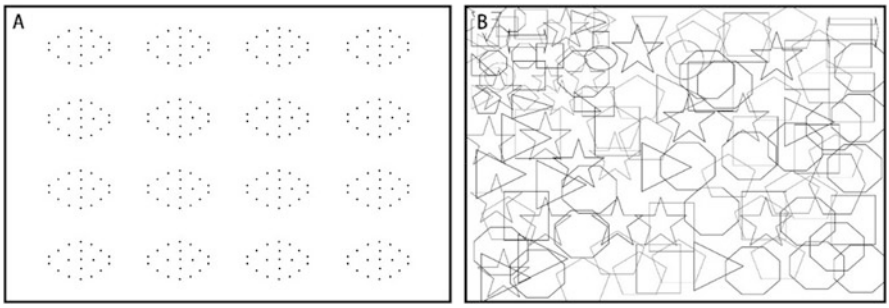

Fig. 4 Calibrating templates. (**a**) Dot array template. (**b**) Geometric shapes template

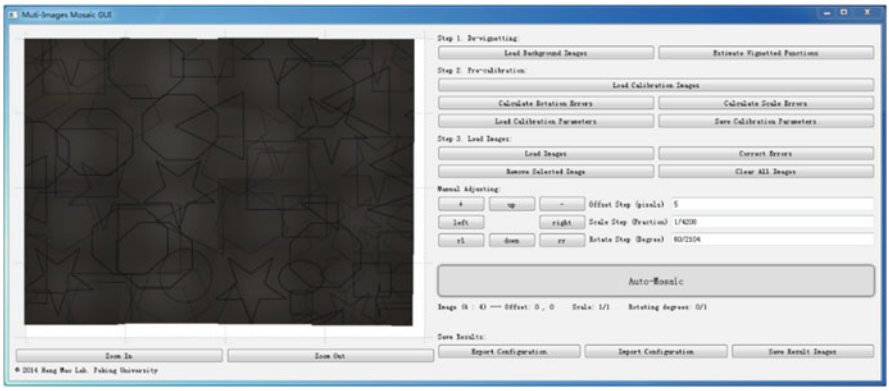

Fig. 5 Mosaic GUI software

The pattern well reconstructed with the corrected images implies the correcting effectiveness of correcting.

To check the output images of correcting, we developed an experimental software to mosaic the images by hand. The software allows user to move, rotate, and scale each image and shows the result of mosaicking the images. See Fig. 5.

Considering that the sensors are in the central area of the effective FOV of the four lenses, we have only corrected the vignetting caused by the micro lens in single sensor. Our correcting result shows that the vignetting is corrected very well. Besides, with only rotation and scaling errors corrected, the images can be mosaicked well. Most joint edges are accurate on single-pixel level. Our laboratory experiment images can be completely mosaiced with no error larger than 1 pixel (Fig. 6). For outdoor experiments, we can mosaic the images with errors no larger than 5 pixels. The errors mainly come from rapid motions of the natural objects, such as swinging trees and moving cars.

Fig. 6 Correcting results. (**a**) Before correcting. (**b**) After correcting and mosaic. (**c–f**) Zoom-in view of details in the joint area of two neighboring images. Red lines indicate the boundary of the images

5 Discussion

Gigapixel imaging is a strong and increasing requirement for remote sensing and other related fields. Users demand large FOV as well as many small details. In this paper, we develop a novel gigapixel imaging system and propose a series of calibrating and correcting methods to correct the errors and parameters in our system. The methods utilize carefully designed templates to calibrate the various errors in the system. The correcting results improve the precision of the system to single-pixel level and prove the effectiveness and efficiency of the methods.

For calibrating and correcting vignetting, a white template is used to reflect the vignetting distribution. The vignetting correcting matrix is calculated offline and used for accelerating the online correcting process. However, the vignetting caused by the four major lenses are not taken into consideration. A problem is that the influence of these vignetting distributions on single sensor changes as the object distance changes and the carrier PCBs move. This means the online correcting matrix must be recalculated on object distance changes.

For geometric errors, we only calibrated the rotation and scaling errors between images. By using the carefully designed dot array template, the parameters are calibrated well. However, the perspective errors are not calibrated. Correcting perspective errors are more complex than correcting the rotation and scaling errors and may bring performance problems. Since the perspective errors are not obvious, they are ignored to improve the system performance.

Finally, to check our correcting results, we developed a mosaic GUI software which allows us to move and mosaic the images by hand. With the software, we have successfully validated our gigapixel imaging system in the laboratory and outdoor conditions. The mosaic result proves our calibrating methods powerful.

References

1. Onaka P, Tonry JL (2008) The pan-starrs gigapixel camera #1 and stargrasp controller results and performance. Proceedings of SPIE - The International Society for Optical Engineering 7014:70140D-70140D-12
2. Leininger B, Antoniades J, Stevens M, Targove JD (2008) Autonomous real-time ground ubiquitous surveillance-imaging system (argus-is). Proceedings of SPIE - The International Society for Optical Engineering 6981:69810H-69810H-11
3. Brady DJ, Gehm ME, Stack RA, Marks DL, Kittle DS, Golish DR et al (2012) Multiscale gigapixel photography. Nature 486(7403):386
4. Marks DL, Kim J, Brady DJ (2012) Engineering a gigapixel monocentric multiscale camera. Opt Eng 51(8):3202
5. Golish DR, Vera EM, Kelly KJ, Gong Q, Jansen PA, Hughes JM et al (2012) Development of a scalable image formation pipeline for multiscale gigapixel photography. Opt Express 20(20):22048
6. Son HS, Johnson A, Stack RA, Shaw JM, Mclaughlin P, Marks DL et al (2013) Optomechanical design of multiscale gigapixel digital camera. Appl Opt 52(8):1541
7. Marks DL, Llull PR, Phillips Z, Anderson JG, Feller SD, Vera EM et al (2014) Characterization of the aware 10 two-gigapixel wide-field-of-view visible imager. Appl Opt 53(13):54–63
8. Zheng Y, Yu J, Kang SB, Lin S (2008) Single-image vignetting correction using radial gradient symmetry. Computer vision and pattern recognition, 2008. CVPR 2008. IEEE Conf IEEE 31:1–8
9. Zhang Z, Zou S, Zuo Z (2011) An improved algorithm of mask image dodging for aerial image. MIPPR 2011: remote sensing image processing. Geogr Inform Syst Other Appl 8006:420–430
10. Gribbon KT, Bailey DG (2004). A novel approach to real-time bilinear interpolation. IEEE international workshop on electronic design, test and applications. IEEE Computer Society. pp 126
11. Weng J, Cohen P, Herniou M (1992) Camera calibration with distortion models and accuracy evaluation. Pattern Analysis & Machine Intelligence IEEE Transactions on 14(10):965–980

Expected Value Correction-Based Computed Tomography for Airplane Engine

Wang Bo, Xiao Yongshun, Han Fangda, Yu Daiwei, and Chen Zhiqiang

1 Introduction

Airplane engine is the key part of the plane. However, the rotating parts in the airplane engine are vulnerable to high pressure, high temperature, high speed, and possible exotic objects like birds and ice. As a result, it is essential to conduct regular test on these parts [1, 2].

Industrial CT is a nondestructive test method that has been widely used in product quality control in many fields for its high precision and efficiency [3]. It has also been used in aerospace industries such as turbine blades detection and blades wall thickness measurement of airplane engines. Compared with other nondestructive test methods, industrial CT can provide qualitative and quantitative analysis of defects as well as high-resolution images of the inner structure of the objects, and it has a high tolerance for dimension and different shapes. However, when it comes to some special conditions, such as the in situ nondestructive test of airplane engine, the relatively higher cost and lower efficiency block its further development [4–6] since it is impossible to conduct CT process on the entire aircraft.

In this paper, we mainly concentrate on monitoring the deformations and defects of airplane engine. The detection often needs to be conducted in situ due to the inconvenience and inefficiency to disassemble the engines from planes for tests. Meanwhile, there are deformations that can only be detected during operation. As a result, the detection is often needed to be conducted in an in situ form.

W. Bo · X. Yongshun · H. Fangda · Y. Daiwei · C. Zhiqiang (✉)
Department of Engineering Physics, Tsinghua University, Beijing, China

Key Laboratory of Particle & Radiation Imaging (Tsinghua University), Ministry of Education, Beijing, China
e-mail: czq@mail.tsinghua.edu.cn

M. Jiang et al. (eds.), *The Proceedings of the International Conference on Sensing and Imaging*, Lecture Notes in Electrical Engineering 506,
https://doi.org/10.1007/978-3-319-91659-0_24

The rotating parts of the engine are surrounded by all kinds of blocks, which calls for more powerful X-ray sources and more sensitive detectors, resulting in high test cost. So testing the engine with a dynamic tomographic imaging system is an approach to solve the problem. Based on researches on the in situ nondestructive testing methods for airplane engine, we put forward a system using CT technique to detect the rotating parts of the airplane engine, taking advantage of the objects' self-rotation [7, 8].

The dynamic tomography system makes use of the rotation of the engine to acquire projection data. A sensor is set to track the status of the rotating parts and trigger the accelerator to emit X-ray. More details about the system will be introduced in the next part.

However, some components like the casing, pipelines, and fuel tanks always remain static when the engine is in operation. These static parts will appear as strip artifacts in the projection data and result in the ring artifacts in the reconstruction image [8]. The MVC (minimum value correction) method and the PIC (prior image correction) method have been proposed to solve the problem. The first one is fast but cannot reconstruct the image with high clearness due to the existence of artifacts, while the second one is more accurate but time-consuming to get prior image using iterative method with additional projection data from conventional CT [9, 10].

In this paper, the features and causes of the blocking artifacts are analyzed, and expected value correction (EVC) is proposed to eliminate the blocking artifacts, and both numerical and physical experiments are carried out to verify its effectiveness.

1.1 System Design

Compared with conventional CT systems, the dynamic CT system doesn't have a turntable, and the projection from different angles is acquired using the rotation of the rotating parts. As shown in Fig. 1, STS (synchronous triggering system) is deployed over the engine to monitor the rotation of the rotating parts and trigger the accelerator to flash. The sensor detects the specific marker on the rotor and sends signal to STS, then STS delays the signal with different values to trigger the accelerator. In this way the projection data can be obtained to reconstruct the structure of the airplane engine.

The sequence diagram of STS system is shown in Fig. 2. Once the delay time t_{d} is set, the kth trigger signal t_k is $t_{\Delta k}$ after the kth sensor signal, while the $(k+1)$th trigger signal t_{k+1} is $t_{\Delta k} + t_d$ after the $(k+1)$th sensor signal.

1.2 Data Processing and Artifacts

The projection process in conventional industrial CT system can be expressed as

$$Hf = p \tag{1}$$

where H is the projection operator, f is the object, and p is the projection.

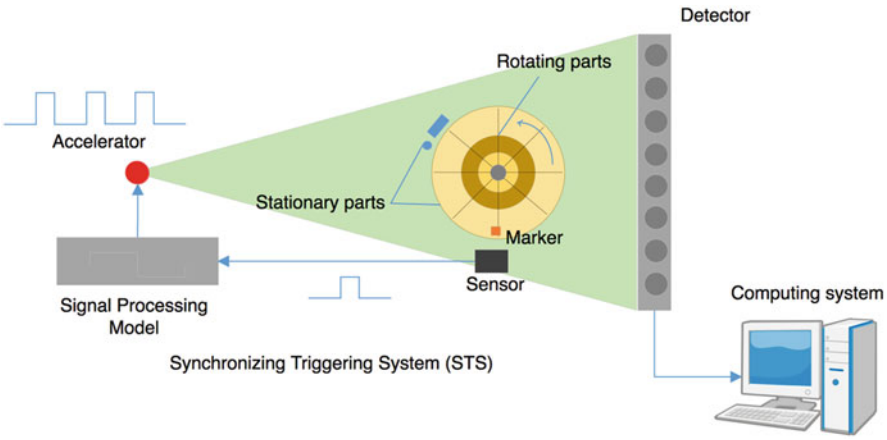

Fig. 1 The schematic diagram of the dynamic CT system

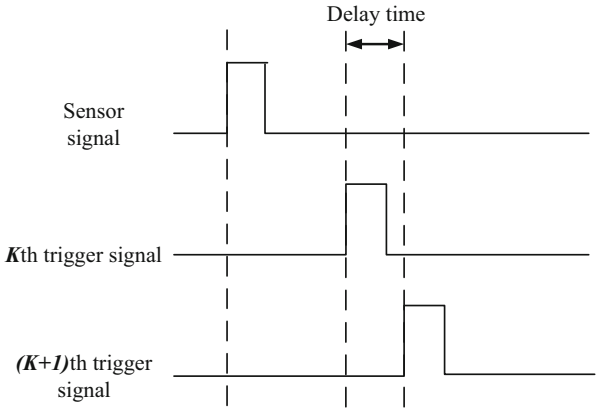

Fig. 2 STS trigger signal sequence diagram

Thus to reconstruct the object from the projection, a reverse process is needed as

$$f = H^{-1}p \tag{2}$$

But, as mentioned above, several parts stay static during the dynamic CT process. So in our dynamic CT system, the projection operator cannot be shared by the static parts, which always have the same projection value in all views. Thus, the projection process in our case can be expressed as

$$Hf + b = p \tag{3}$$

where b is the projection of the static parts remaining as a constant value.

The projection process is separated into two parts, the static one and the rotating one. In the projection data, the static one appears as strips and will turn into ring artifacts in the reconstruction image without artifact correction. But if the constant static projection value can be obtained, the reconstruction process can be simplified as

$$f = H^{-1}(p - b) \tag{4}$$

where *p–b* represents the corrected projection data of the rotating parts. Therefore, once the exact projection of static parts is determined, the object can be reconstructed accurately.

According to the above, the key point to reconstruct the object with dynamic CT system is to find out the constant static projection value, which remains unknown in our test process and will be discussed in the next part.

2 Methodology

A novel method based on expected value correction has been proposed to eliminate the blocking artifacts.

The rotational symmetry parts of the measured object contribute to strip projection data. In our dynamic CT system, the static blocks share the same feature with the rotational symmetry parts in conventional CT. Thus if the projection data is reconstructed directly, those strip projection data would turn into ring artifacts.

The image to be reconstructed from the projection data from our dynamic CT system is actually made up of the rotating parts and the static parts and expressed as

$$\mathrm{img}(x, y) = \mathrm{img}_{\mathrm{rot}}(x, y) + \mathrm{img}_{\mathrm{sta}}(x, y) \tag{5}$$

And the projection data of the object can be divided into two parts at the mean time:

$$\mathrm{prj}(\theta, t) = \mathrm{prj}_{\mathrm{rot}}(\theta, t) + \mathrm{prj}_{\mathrm{sta}}(\theta_0, t) \tag{6}$$

where prj represents the projection data, θ is the projection angle, *t*is the detector position, and θ_0 represents the stable projection angle of the static parts. After getting the projection data $\mathrm{prj}(\theta, t)$ from dynamic CT system, the next step is to restore the projection data of rotating parts $\mathrm{prj}_{\mathrm{rot}}(\theta, t)$ from $\mathrm{prj}(\theta, t)$. There are several approaches to reconstruct the rotating parts from the mixed projection data. One possible way is to estimate the contribution of the static parts and remove it from the projection data. The MVC method estimates the contribution by using the minimum value of projection data, while the PIC method uses the prior image, which needs additional projection data as mentioned before.

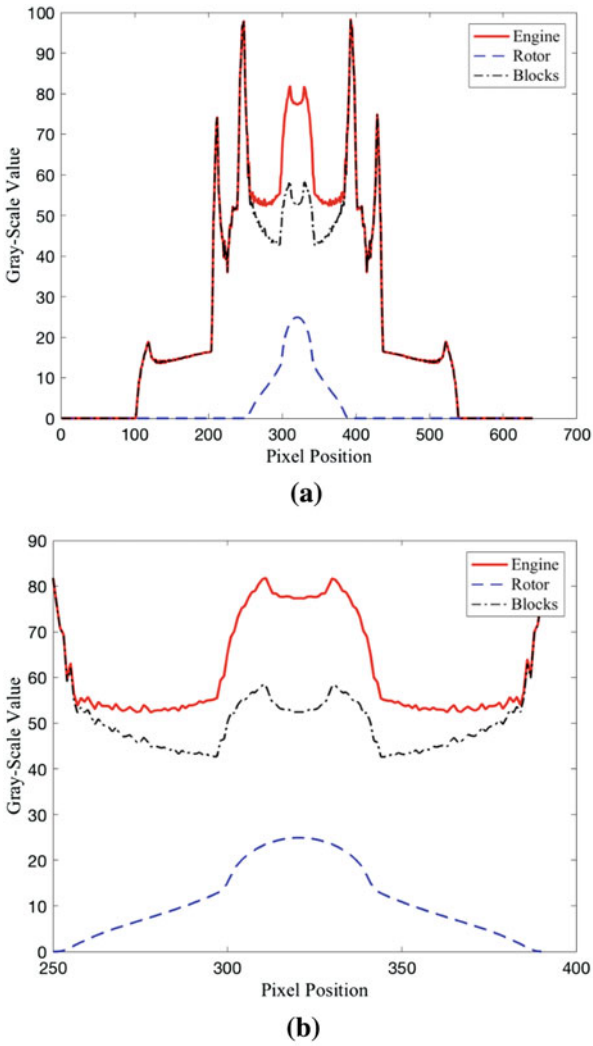

Fig. 3 The comparison of expected value of different projection data. (**a**) Gray value of the projection data of engine, rotor, and blocks. (**b**) Gray value of the projection data of engine, rotor, and blocks in [250, 390]

Inspirited by the MVC method, we attempt to use the expected value to estimate the blocking projection data. Before we start to introduce our method, a brief graph is provided to explain why we use expected value instead of the minimum value.

As shown in Fig. 3, we compare the expected value of different projection data. The blocking data is shown as the black dotted line, which is continuous and smooth in most parts. The rotating data is shown as the blue dashed line and the projection of engine is the red one.

As shown in Fig. 4, the distributions of the expected value, minimum value, and maximum value are almost the same when the pixel is away from the rotation center. When it comes to the data near the rotation center, the minimum and maximum

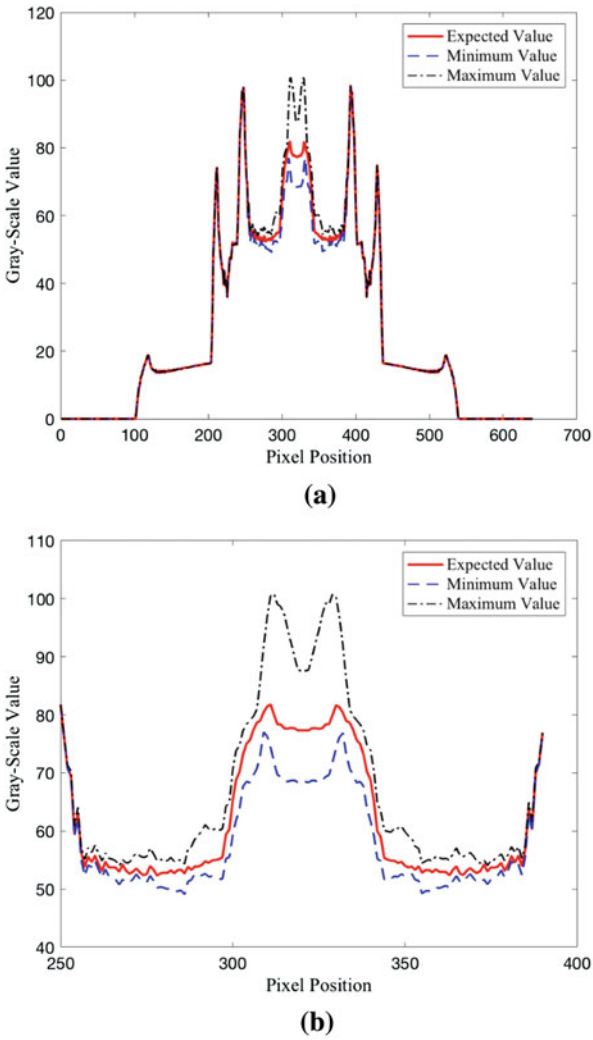

Fig. 4 The comparison of the expected value, minimum and maximum. (**a**) Gray value of the projection data of expected value, minimum value, and maximum value. (**b**) Gray value of the projection data of expected value, minimum value and maximum value in [250, 390]

value has the same trend of distribution, in spite of the different values. Because of the existence of the rotating parts, the minimum value of the projection data has some intense fluctuations in some specific position. But the expected value of the projection data is continuous and much smoother. Thus it is better to use the expected value to estimate the blocking projection. And more details of the difference between the minimum value and expected value will be shown in the next part as well as the comparison of the two methods.

Table 1 Parameters In numerical simulation

Distance between source and object	2542.3 mm
Distance between object and detector	859.7 mm
Detector length	832 mm
Detector bins	640
Image size	256×256
Total views in 360°	512

3 Experiments and Results

In this section, we use numerical experiments to verify the feasibility of the proposed method. Our numerical experiments are based on MATLAB, and parameters used in simulation are listed in Table 1.

3.1 Phantom

The phantom used in our numerical experiments is a simplified model of airplane engine (Fig. 5a). The phantom is made up of two main parts, the rotating part and the static part. The rotating part in Fig. 5c is a rotor with nine blades. As shown in Fig. 5e, the shell of engine, fuel tank, and pipeline which remain still during working make up the blocks. To make the phantom more suitable to the actual in situ engine, an ellipse is added to represent the wing of the aircraft, the two concentric annuluses are on behalf of the shell of engine, and the other small parts are designed to be fuel tank and pipelines. All these phantoms are of uniform pixel grid as 256×256.

As shown in Fig. 5b, the projection data of the engine consists of two parts. The first part is the projection data of the rotor obtained from the conventional CT processing on the phantom of it (Fig. 4d). The other one is the projection data of the blocks which can be obtained from one specific angle since it's static (Fig. 5f).

3.2 Results

To verify our method, we compare our result with the directly reconstructed image (Fig. 6). Figure 6b is the reconstructed image using FBP directly, and Fig. 6c is the projection data after expected value correction. Figure 6d is the reconstructed image obtained from Fig. 6c. Compared with the original rotor, our method can reconstruct the blade pretty well, but the rotational shaft is missing because its projection data has the same feature with the blocks and is removed during the correction process.

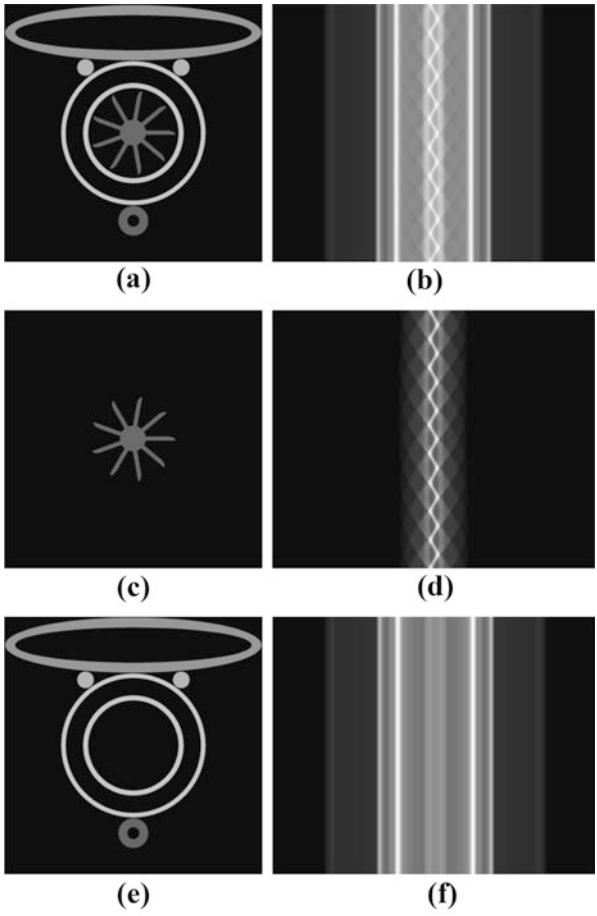

Fig. 5 Numerical simulation. (**a**) Phantom of engine. (**b**) Projection data of engine. (**c**) Phantom of rotor. (**d**) Projection data of rotor. (**e**) Phantom of blocks. (**f**) Projection data of blocks. The gray scale of phantoms is [0, 1]

As shown in Fig. 7, the blocks projection estimation using minimum value is conducted. From the reconstructed image Fig. 7b, though the shape of the rotor can be reconstructed correctly and the blocks can also be removed, there are several obvious ring artifacts in the image, which will result in the misjudgment of the defects of the rotor.

More tests are taken to test our method. As shown in Fig. 8a, a broken model with distorted and cracked blades is designed. The reconstructed image is shown in Fig. 8c. A more badly broken model is designed to testify that our method can work well under nonperiodic symmetry condition (Fig. 9).

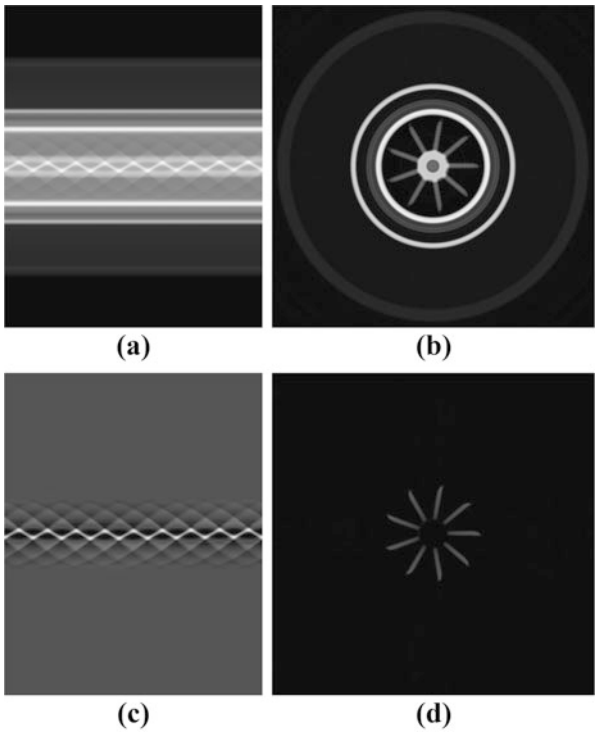

Fig. 6 Reconstruction results. (**a**) Projection data. (**b**) Directly reconstructed image. (**c**) Expected value corrected projection data. (**d**) Reconstructed image with our method. The gray scale of phantom and images is [0, 1]

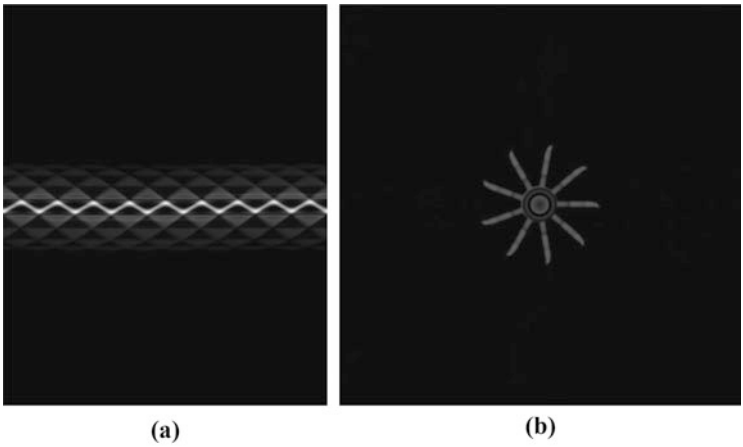

Fig. 7 The result of minimum value correction method. (**a**) The corrected projection data of minimum value correction method. (**b**) The reconstructed image using the corrected projection data

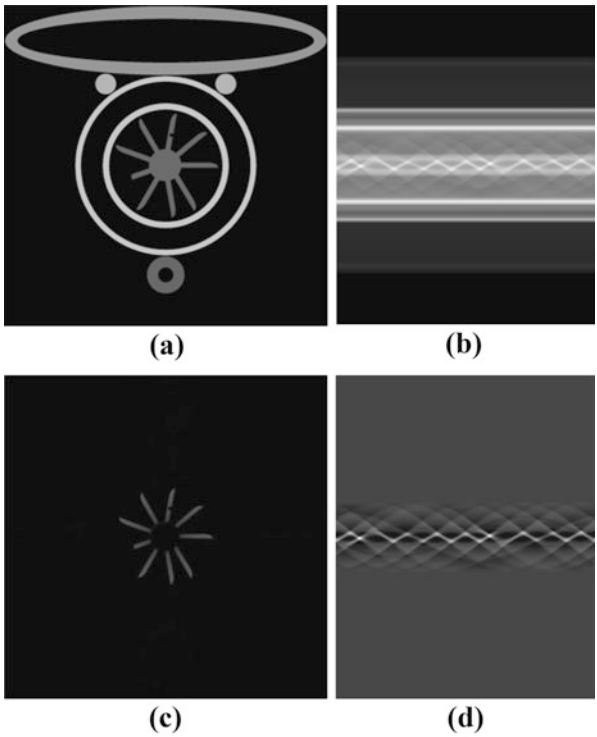

Fig. 8 Reconstruction results. (**a**) Phantom of broken rotor. (**b**) Projection data. (**c**) Reconstructed image with our method. (**d**) Expected value corrected projection data. The gray scale of phantom and reconstructed image is [0, 1]

3.3 Noise Condition

To verify the feasibility of our method under conditions with noises, more numerical experiments are done to compare with the conventional CT progress. Projection data is obtained with noise during projection process; both dynamic and conventional CT processes are used for comparison.

As shown in Fig. 10a, c, the projection data with noise from dynamic CT and conventional CT is prepared. Our method is used for reconstruction of the dynamic CT projection data, while FBP method is used for the conventional CT projection data.

The reconstructed images of the two processes are shown in Fig. 10b, d. Considering the image quality, the reconstructed image from conventional CT is clearer than the dynamic one. Signal-to-noise ratio of dynamic one is 2.080 and the conventional one is 2.727. Though the image quality is lower comparing with conventional method, the structural integrity of the rotor can be identified from the reconstructed image (Fig. 10b).

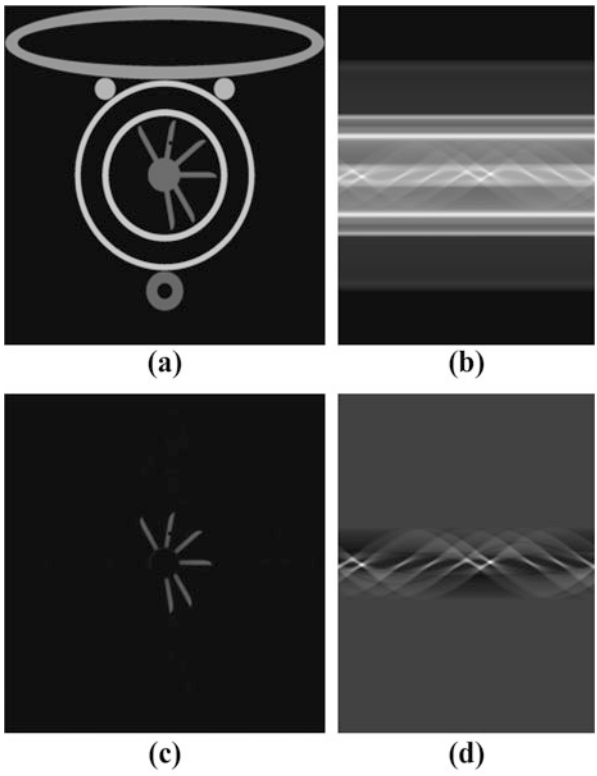

Fig. 9 Reconstruction results. (**a**) Phantom of broken rotor. (**b**) Projection data. (**c**) Reconstructed image with our method. (**d**) Expected value corrected projection data. The gray scale of phantom and reconstructed image is [0, 1]

Further discussions on the practicability of our method are taken, which concentrate on the ability of deformation identification of reconstructed images. Additional numerical experiments are done using the broken rotor phantom and the badly broken rotor phantom (Fig. 11). The reconstructed images from conventional CT process with FBP method are also provided for comparison. From the results, the deformations and defects of the rotor can be identified from the reconstructed images, though the image quality of our method is a little bit lower comparing with the results of conventional CT.

4 Conclusion

In this paper, a block-eliminating method based on expected value correction is proposed, which attempts to eliminate the ring artifacts caused by static blocks in dynamic CT system. Our method works well to reconstruct the rotating part such

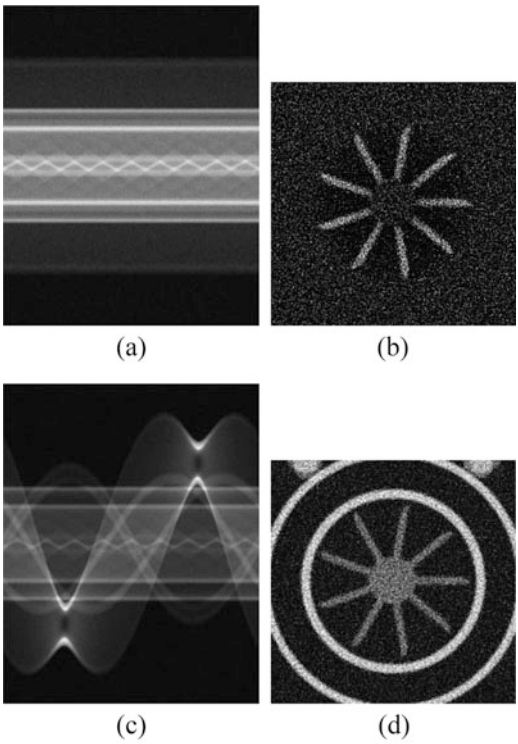

Fig. 10 Reconstruction results. (**a**) Dynamic CT projection data with noise. (**b**) Reconstructed image with our method. (**c**) Conventional CT projection data with noise. (**d**) Reconstructed image with FBP method. The gray scale of reconstructed images is [0, 1]

as blades, though the parts that have the same features with the blocks are removed. Numerical experiments of non-noise and noise condition are carried out to verify the practicability of our method, which verify that our method works well on both non-noise and noise conditions. In the future, more works will be done focusing on the effects caused by vibration of rotor during operation.

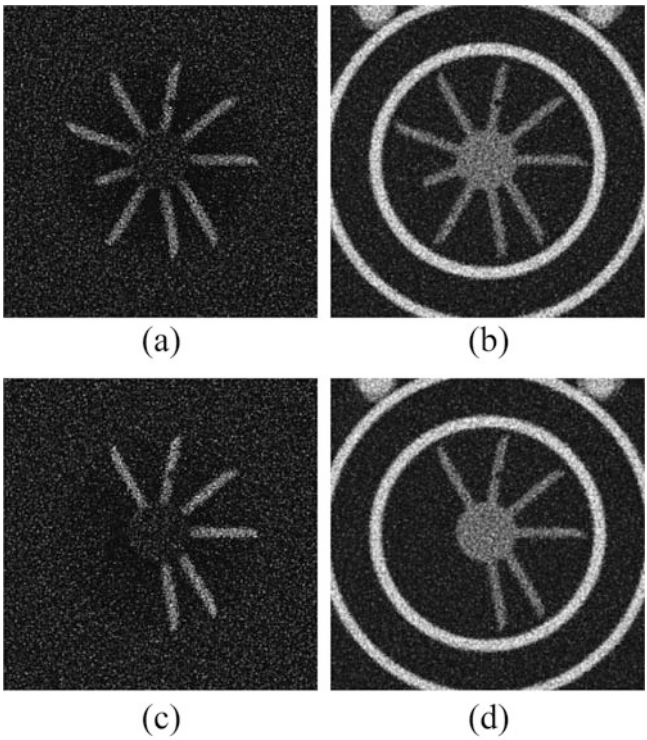

Fig. 11 Reconstruction results. (**a**) Reconstructed image from dynamic CT with our method. (**b**) Reconstructed image from conventional CT with FBP method. (**c**) Reconstructed image from dynamic CT with our method. (**d**) Reconstructed image from conventional CT with FBP method. The gray scale of reconstructed images is [0, 1]

Acknowledgments The work is supported by Tsinghua University Initiative Scientific Research Program No. 2014Z05092.

References

1. Zenzinger G, Bamberg J, Aero MTU (2005) Crack detection using EddyTherm. no APRIL 2016
2. Wugang T (2011) Research on technology of Borescope and Eddy current integrative in-situ nondestructive testing for key components of aeroengine. National University of Defense Technology
3. Mccormick P (2003) Visualizing industrial CT volume data for nondestructive testing applications driving application. In: Proceedings of the 14th IEEE visualization conference, vol D, pp 547–554
4. Jin Y (2007) Research of turbine blade defects detection based on 3D ICT images. Northwestern Polytechnical University
5. Ross J B MK (1990) Computed tomographic imaging of turbine blades. Mater Eval 10:48

6. Zhang X, Zhang L, Wang J (2015) The application of industrial CT technology in the airplane engine single crystal blades for wall thickness measurement. Nondestruct Test 37(2)
7. Chang M, Xiao Y, Chen Z (2013) Study of dynamic data acquisition and processing in a novel x-ray process tomography system for rapid rotating airplane engine, pp 1–4
8. Xiao Y, Chang M, Chen Z (2013) A novel X-ray process tomography system design for monitoring the running airplane engine. In: 7th world Congr. Ind. Process Tomogr., no. September, pp 605–614
9. Chang M, Xiao Y, Chen Z (2012) An interaction based CT reconstruction algorithm for blocked projection data in a dynamic ICT system. In: Proc. of SPIE, vol 8506
10. Han F, Xiao Y, Chang M (2015) A block-eliminating method by limited-view scan in a dynamic CT system for running airplane engine. In: Proceedings of the IEEE NSS/MIC

Low-Dose CT Post-processing Based on 2D Residual Network

Huijuan Zhang, Yunbo Gu, Wei Yang, Jiasong Wu, Xiangrui Yin, Yang Chen, Huazhong Shu, Limin Luo, Gouenou Coatrieux, and Qianjin Feng

1 Introduction

X-ray computed tomography (CT) provides major anatomical and pathological information of the human body for medical diagnosis and treatment. However, repetitive clinical CT examinations require reducing the radiation dose. The easier access to filtered back projection (FBP) reconstructed CT images and to the projection data obtained from the manufacturers opens the way for post-processing methods which offer good implementability and expansibility to existing CT scanner equipment in hospitals [1]. Chen et al. proposed a large-scale nonlocal mean algorithm to remove the low-dose CT (LDCT) artifacts via a nonlinear large-scale filter correction [2]. In [3], the authors reported an effective processing of abdomen LDCT images based on a sparse representation using a pretrained dictionary. Deep learning techniques have recently been considered to tackle this

H. Zhang · Y. Gu · J. Wu · X. Yin · Y. Chen (✉) · H. Shu · L. Luo
Laboratory of Image Science and Technology, Southeast University, Nanjing, China

Centre de Recherche en Information Biomedicale Sino-Francais (LIA CRIBs), Rennes, France

Key Laboratory of Computer Network and Information Integration (Southeast University), Ministry of Education, Nanjing, China
e-mail: chenyang.list@seu.edu.cn

W. Yang · Q. Feng
Department of Biomedical Engineering, Southern Medical University, Guangzhou, China
e-mail: fengqj99@fimmu.com

G. Coatrieux
Institut Mines-Telecom, Telecom Bretagne, Brest, France

INSERM U1101 LaTIM, Brest, France
e-mail: gouenou.coatrieux@telecom-bretagne.edu

M. Jiang et al. (eds.), *The Proceedings of the International Conference on Sensing and Imaging*, Lecture Notes in Electrical Engineering 506,
https://doi.org/10.1007/978-3-319-91659-0_25

problem. A multilayer perceptron (MLP) machine-based method was introduced to learn the mapping from the noisy images to the corresponding noise-free images and has shown an impressive performance in image restoration [4–6]. In [7], a residual convolutional network architecture was designed to build the relationship between the wavelet coefficients of low-dose and high-dose CT images. Han et al. [8] proposed a U-net structured architecture with residual learning to predict the artifacts in sparse-angle reconstructed CT image.

This paper explores the application of 2D residual network in LDCT image processing. The proposed residual network (ResNet) performs noise-artifact removal by predicting the residual component (mainly composed of noise-artifact component) between the LDCT images and the corresponding standard-dose CT (SDCT) images included in the training data set. The experiment results validate the good performance of the 2D ResNet method in improving LDCT image quality.

2 Residual Network Architecture

Commonly used network architectures include plain network, with connections only between adjacent layers, and multi-branch network structured as directed acyclic graph. Deep network layers (i.e., deep CNN) provide an improved representation accuracy of image features. Some examples of plain networks are AlexNet [9] to VGGNet [10]. However, a gradient diffusion tends to occur when the depth is increased, which might result in training failure. This gradient diffusion problem can be solved by ReLU and batch normalization (BN) [11] to some extent. Indeed, as the network depth continues to increase, both the training error and the testing error surprisingly increase. ResNet [12] is introduced to solve this difficulty by learning the local and global features via skip connections combining different levels.

2.1 Residual Network

Compared to the plain network, a residual network [12] consists of an ensemble of basic residual unit, containing two stacked convolution layers. Here x_l and x_{l+1} are the input and output of the l-th residual unit, respectively, and $F(x)$ denotes the residue mapping of the stacked convolution layers. W_l represents the convolution weight of the l - th layer. If the dimensions of the input x_l and the mapping $F(x_l)$ match in the element-wise addition, their relation can be expressed by

$$x_{l+1} = x_l + F\left(x_l, \{W_l\}\right) \tag{1}$$

Otherwise, a dimension mapping convolution layer is needed in the skip connection, whose convolution kernel is represented as W_s; thus

$$x_{l+1} = F(x_l, \{W_l\}) + W_s x_l \tag{2}$$

Recursively, from the *0-th* layer to the *L-th* layer, Eq. (2) can be expressed as $x_L = x_0 + \sum_{i=0}^{L-1} F(x, \{W_i\})$. Such residual network appears as a straight addition operation between layers except for the activation and BN layers.

In [13], He et al. suggest that the form of residue should be as simple as possible, with a shortcut connection minimum train error and test error. But provided that the residue is $0.5x$, convolution or dropout will block the forward and backward propagation, leading to an increased error [13]. So we adopt the shortcut connection, and the convolution layer, which aims at realizing the dimension mapping, is added only when the dimensions do not match.

Using ResNet with the skip connection, a simple identity mapping directly connects the input and output layers. It has the same computational complexity as the plain network with the same depth because no extra parameters need to be learned and the only computation required is the gradient of loss with respect to the input.

2.2 Batch Normalization

Batch normalization [11] can be used to solve the internal covariate shift, which is caused by the change of distribution of each layer's input after the convolution and activation layers during training. With the batch normalization, the input of each layer is normalized to zero mean and unit variance and is then scaled and shifted to restore the distribution. It was pointed out in [11] that the dependence on dropout can be reduced due to the regularization role of BN. Another merit of BN is that it can significantly accelerate the CNN training because the inputs of each layer have a similar distribution.

2.3 Loss Function

The strategy of residual learning [8, 14] is adopted to learn the residue in the ResNet processing. The benefit of learning residue is that it can avoid building complicated regression model for mapping LDCT images to HDCT images due to the inherently rich details in CT images. To measure the similarity between the predicted residue N' and the real residue N, which can be obtained by subtracting HDCT image Q from LDCT image P in the training data set, we can build the loss function $J(W, b)$ as follows:

$$J(W,b) = \left[\frac{1}{m}\sum_{i=1}^{m} J\left(W,b;x^{(i)},y^{(i)}\right)\right] + \frac{\lambda}{2}\sum_{l=1}^{n_l-1}\sum_{i=1}^{s_l}\sum_{j=1}^{s_{l+1}}\left(W_{ji}^{(l)}\right)^2 \quad (3)$$

where m is the sample number in current batch and $J(W,b)$ is the loss of these samples. (x^i, y^i) is the i-th sample. $J(W,b;x^{(i)},y^{(i)})$ is the mean square error (MSE) of the i-th sample, which is defined as $J\left(W,b;x^{(i)},y^{(i)}\right) = \frac{1}{RC}\sum_{j=0}^{C-1}\sum_{k=0}^{R-1}\left\|N'(j,k) - N(j,k)\right\|^2$, where $N = P - Q$. R and C are, respectively, the width and height of the sample. The second term in Eq. (3) is the regularization term called weight decay. n_l is the number of convolution layers. s_l is the number of nodes in the *l-th* layer, and s_{l+1} is the number of nodes in the *l + 1-th* layer. The weight can be constrained by setting different weight decay parameter λ. A smaller λ will lead to a wider weight range.

The Adam optimization method in [15] is applied to update the learning rate of parameters using the unbiased estimation of the gradient's first moment m and the second moment v during backward propagation.

3 Low-Dose CT Image Post-processing

The randomly sampled and cropped 128 × 128 size low-dose CT and the corresponding noise patches, obtained by subtracting high-dose CT images from the corresponding low-dose CT images, are used as the training set. Here the Adam method is used to minimize the MSE between the output of the last convolution layer and the actual residual images (low-dose noise). Zero padding strategy is used here in order to ensure that the size of the output image is equal to the original input size. For each layer, the numbers of convolution kernels are set to 64 and the convolution stride to 1. Then, the CT slides are input into the trained model to estimate the residual data contained in the LDCT images, since our model is independent of the input size by the fact that a fully convolution layer is used instead of a fully connection layer.

Experiments were conducted to explore the factors that might influence the model performance, e.g., model width, depth, and dropout options. We analyzed three different depths by setting (n is the number of basic units for plain network or residual network), leading to a total of 12, 16, and 24 convolution layers (the layer number is $2n + 6$), in the plain network and the residual network.

In order to study the influence of the convolution kernel number in each network layer, we compared the 2D-Resnet-9 network with a broader network, whose parameters are listed in Table 1. The cell across multiple step lines of the table represents the skip connection in the residual network. Here, the suffix of layer name "conv" represents the convolution; besides, "bn" is the BN; and "relu" represents the ReLU activation function. The suffix "sum" presents the element-wise sum. The

Table 1 2D residual network with increased width

Layer	Kernel size	Channel number
C1_conv, C1_bn, C1_relu	3×3	32
C2_conv, C2_bn, C2_relu	3×3	64
C3_conv, C3_bn, C3_relu	3×3	96
C4_conv	3×3	96
resBlock1_bn, resBlock1_reluresBlock1_conv	$\begin{bmatrix} 3 \times 3 \\ 3 \times 3 \end{bmatrix} \times 3$	128
resBlock2_bn, resBlock2_reluresBlock2_conv	128	
res_sum		
res_bn, res_relu		
C10_convC10_bn, C10_relu	3×3	64
C11_conv	3×3	1

prefix "Ci" denotes the i-th convolution layer. "res" indicates the layer related to the residual blocks. "resBlocki" denotes the i-th convolution layer in the residual network. 3×3 denotes the convolution kernel size, and the channel number is the number of kernels in the current convolution layer.

4 Results and Evaluation

The data set for evaluation was provided by AAPM Low-Dose CT Grand Challenge, thanks to the Mayo Clinic [16] which consists of low-dose and high-dose CT images from ten patients, with 512×512 resolution. The utilization of the real projection data is permitted with signed agreement authorized by the Mayo Clinic. The high-dose scanning voltage is 100 or 120 V, and the X-ray tube current varies from 200 to 500 mA. The slice thickness is 1 mm. Poisson noise was inserted into the full-dose projection data to simulate the corresponding 25% of the full-dose data. The reconstruction CT images using both the full-dose and the quarter-dose projection data are provided in the challenge data set. We use nine patient CT images as the training data set (5080 CT slices in total). The remaining patient data set is used as the test data to validate the algorithm performance. We randomly sample small patches over the whole training set to allow more images to be included in the training process in single batch. The patch size for training the 2D model is 128×128. Mean value subtraction and variance normalization were carried out on each patch to obtain training samples with an approximate Gaussian distribution.

The computer platform was configured as follows: CPU is Intel(R) Core(TM) i7-4790 K 4.00GHz; GPU is NVIDIA gtx1080 with 8G memory. We used the MatConvNet deep learning framework [17], the MATLAB version R2015b, and the MSRA method to initialize the weights of convolution layers. The learning rate is set to 0.001 (halved every 40 epochs) and the weight decay to $1e^{-5}$. The moments

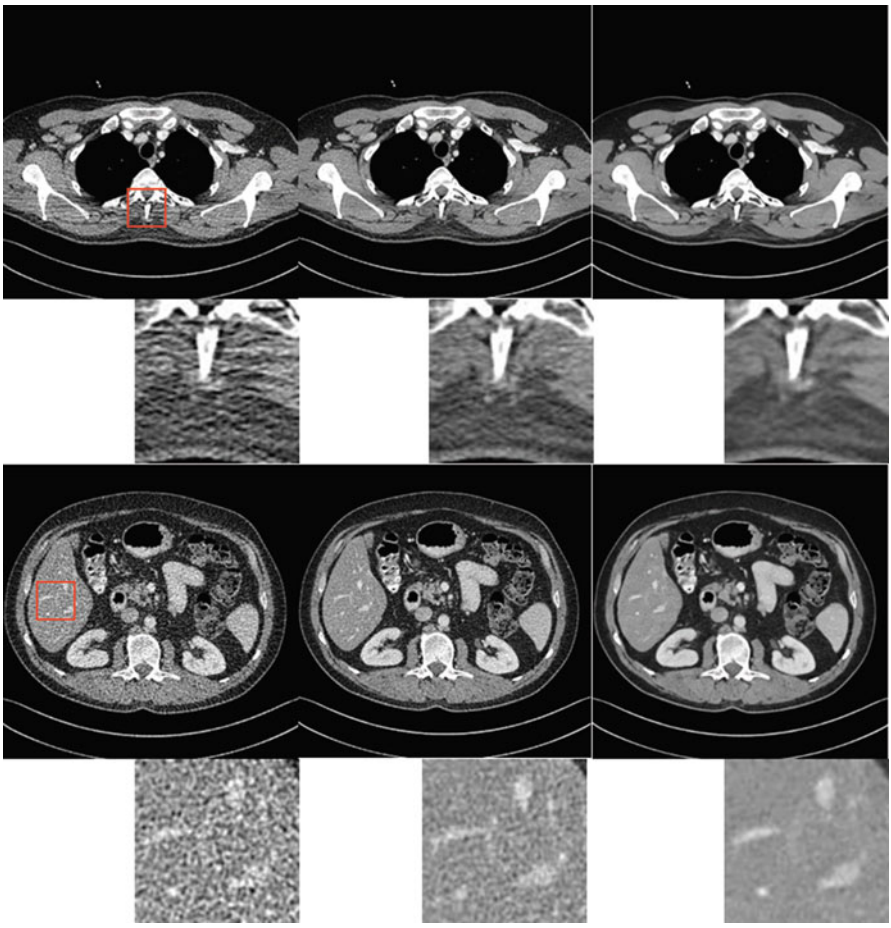

Fig. 1 Selected axial views of the 2D post-processing results. From left to right, illustration of the original LDCT images, the reference SDCT images are the processed LDCT images are given

for the Adam algorithm were, respectively, set as default values 0.9 and 0.999. The batch size was set to 64 and 2 for 2D networks to fully exploiting GPU memory. Following the principle that stacked small convolution kernels can achieve the same receptive field size as the large kernels, whereas saving memory, we adopted the small convolution kernel size 3×3 for all networks. The model training has t 150 epochs.

The final results are obtained by subtracting the LDCT images to the residue components estimated using the trained residual network. It can be clearly seen in Fig. 1 that the 2D ResNet model works well in preserving the original image details without causing significant over-smoothing. The computation time on a single GPU for each CT image using the 2D model is 0.3 s. Figure 2 shows that the training

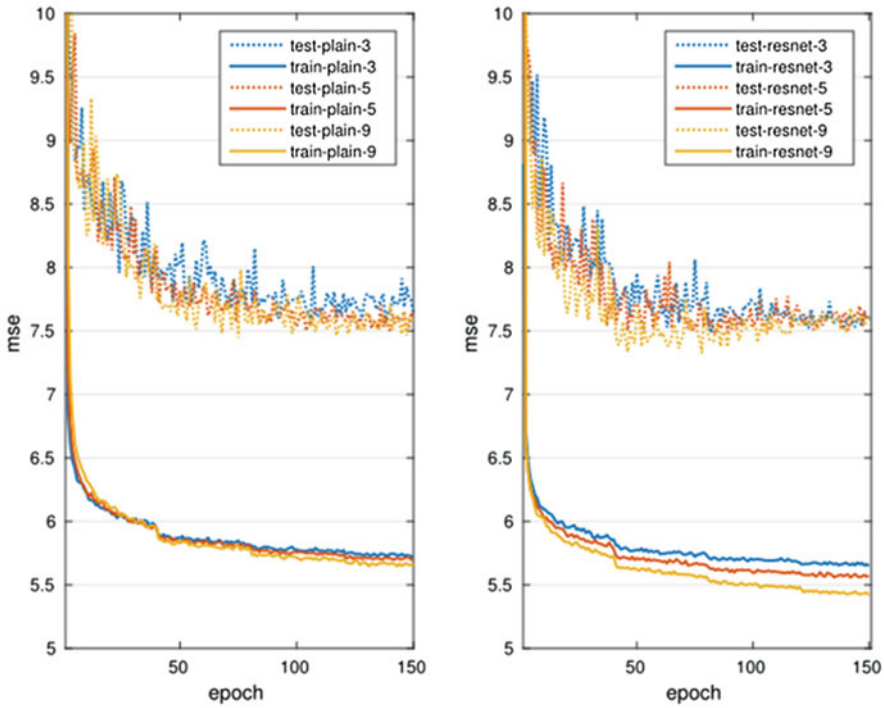

Fig. 2 Solid lines denote training loss, and dashed lines are testing loss. Left: plain networks. Right: residual networks (The legend is formatted "A-B-n"; "A" denotes the training and testing phase; "B" is the network type; "plain" means the plain networks; "resnet" is the residual networks; "n" represents the number of basic element blocks; here n is selected from the values in {3, 5, 9})

error and testing error decrease in both plain networks and residual networks when the depth increases. The deep 2D-resnet_deep-20 model ($n = 20$, 46 layers in total) performs also very well.

5 Conclusion

Experimental results have shown that the proposed 2D residual-based networks have good performance on preserving image details and removing noise-artifact structure as well. The 2D model is thus suggested for LDCT scans with sick thickness. Our work in progress will focus on methodological issues (such as compensating the contrast loss after processing) and extended clinical assessment. Algorithm acceleration will also be considered in order to better fulfill clinical requirements.

Acknowledgments The authors would like to thank Dr. Cynthia McCollough (the Mayo Clinic, USA) for providing clinical projection data of Somatom Definition AS+ CT.

References

1. Zhu Y, Zhao M, Zhao Y, Li H, Zhang P (2012) Noise reduction with low dose CT data based on a modified ROF model. Opt Express 20(16):17987–18004
2. Chen Y et al (2012) Thoracic low-dose CT image processing using an artifact suppressed large-scale nonlocal means. Phys Med Biol 57(9):2667
3. Chen Y et al (2013) Improving abdomen tumor low-dose CT images using a fast dictionary learning based processing. Phys Med Biol 58(16):5803
4. Burger HC, Schuler CJ, Harmeling S (2012) Image denoising with multi-layer perceptrons, part 1: comparison with existing algorithms and with bounds. arXiv preprint arXiv 1211:1544
5. Burger HC, Schuler CJ, Harmeling S (2012) Image denoising with multi-layer perceptrons, part 2: training trade-offs and analysis of their mechanisms. arXiv preprint arXiv 1211:1552
6. Burger HC, Schuler CJ, Harmeling S (2012) Image denoising: can plain neural networks compete with BM3D? In: Computer vision and pattern recognition (CVPR), 2012 IEEE conference on, pp 2392–2399
7. Kang E, Min J, Ye JC (2016) A deep convolutional neural network using directional wavelets for low-dose X-ray CT reconstruction. arXiv preprint arXiv 1610:09736
8. Han Y, Yoo J, Ye JC (2016) Deep residual learning for compressed sensing CT reconstruction via persistent homology analysis. arXiv preprint arXiv 1611:06391
9. Krizhevsky A, Sutskever I, Hinton GE (2012) Imagenet classification with deep convolutional neural networks. Adv Neural Inf Proces Syst:1097–1105
10. K. Simonyan and A. Zisserman, "Very deep convolutional networks for large-scale image recognition," 2015
11. Ioffe S, Szegedy C (2015) Batch normalization: accelerating deep network training by reducing internal covariate shift. arXiv preprint arXiv 1502:03167
12. He K, Zhang X, Ren S, Sun J (2016) Deep residual learning for image recognition. In: Proceedings of the IEEE conference on computer vision and pattern recognition, pp 770–778
13. He K, Zhang X, Ren S, Sun J (2016) Identity mappings in deep residual networks. In: European conference on computer vision, pp 630–645
14. Zhang K, Zuo W, Chen Y, Meng D, Zhang L (2017) Beyond a Gaussian denoiser: residual learning of deep CNN for image denoising. In: IEEE transactions on image processing
15. Kingma D, Ba J (2014) Adam: a method for stochastic optimization. arXiv preprint arXiv 1412:6980
16. Low Dose CT Grand Challenge. [Online]. Available: http://www.aapm.org/GrandChallenge/LowDoseCT/. Accessed 06 Apr 2017
17. Vedaldi A, Lenc K (2015) Matconvnet: convolutional neural networks for matlab. In: Proceedings of the 23rd ACM international conference on multimedia, pp 689–692

Phase Congruency and Its Application to Tubular Structure Extraction

Xiaojuan Deng and Hongwei Li

1 Introduction

A number of tubular structure extraction algorithms have been developed in the literature. Thresholding [1] is the fastest one among all of them. For images from the industry, however, the varied contrast of the tubular structures makes it difficult to determine an appropriate threshold. To tackle this issue, noise suppression and tubular structure enhancement are usually applied before thresholding. Popular enhancement methods are based on filtering with filters constructed from an analysis of multi-scale space or local Hessian matrix, such as the Frangi operator [2] and Krissian operator [3]. The response of the Hessian matrix-based operators is considerably sensitive to the local image contrast. In order to overcome the shortcomings of Frangi and Krissian operators, Bauer [4] proposed an approach based on gradient vector flow (GVF) fields. By providing a new external force for active contours and snakes, the GVF method has a strong ability to suppress noise. However, it will lose some of fragile tubular structures. The recently proposed method [5, 6] defines a nonlinear and nonlocal path operators, which can be used to filter out tubular structures. However, its low efficiency prevents its further application to real CT images which are often big volume datasets.

In this paper, we propose an efficient tubular and tabular structure extraction approach based on the idea of phase congruency [7–10]. Phase congruency is a dimensionless quantity and much less sensitive to local image contrast, which makes it very suitable for extracting edges with various contrast.

X. Deng · H. Li (✉)
School of Mathematics, Capital Normal University, Beijing, China
Beijing Advanced Innovation Center for Imaging Technology, Capital Normal University, Beijing, China
e-mail: hongwei.li91@cnu.edu.cn

M. Jiang et al. (eds.), *The Proceedings of the International Conference on Sensing and Imaging*, Lecture Notes in Electrical Engineering 506,
https://doi.org/10.1007/978-3-319-91659-0_26

The remainder of this paper is organized as follows. The idea of phase congruency and phase symmetry are introduced in Sect. 2. The proposed approach is described in Sect. 3. Experiments to verify and validate the proposed approach are provided in Sects. 4, and 5 goes for remarks and conclusions.

2 Related Work

To address the extraction problems with real CT images outlined above, two-dimensionless quantities, i.e., phase congruency (PC) and phase symmetry, are employed in our tubular structure detection method, which provide information invariant to image contrast.

Phase Congruency: The definition of PC has been given in [11], and Morrone and Owens et al. have also proposed a method to compute the PC values. The computation can be illustrated geometrically as shown in Fig. 1. The local, complex valued, Fourier components at a location x in the signal will each have an amplitude $A_n(x)$ and a phase angle $\phi_n(x)$. The magnitude of the vector from the origin to the end point defines the local energy $E(x)$, and the phase angle of $E(x)$ is $\overline{\phi}(x)$. Phase congruency is measured as the ratio of $E(x)$ to the overall path length taken by the local Fourier components in reaching the end point as shown in the following formula:

$$PC(x) = \frac{|E(x)|}{\sum_n A_n(x)}, \quad 0 \leq PC(x) \leq 1 \tag{1}$$

where $F(x)$ measures the response of the even-symmetric filter, while $H(x)$ measures the response of the odd-symmetric filter. If all the Fourier frequency

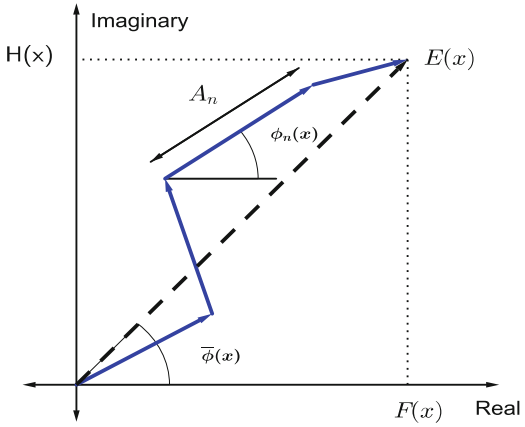

Fig. 1 Local energy model at point x

components at point x are in phase, then all the complex vectors would be aligned, and the ratio $|E(x)|/\sum_n A_n(x)$ would be 1 (i.e., $PC(x) = 1$). Another extreme case is that there is no coherence of phase, and then the ratio drops to 0. A phase congruency of value one means that there is an edge, while a phase congruency of value zero means that there is no structure.

The local energy model $E(x)$ can be expressed by the cosine function, and the phase congruency, i.e., PC, has the following form:

$$PC(x) = \frac{\sum_n W(x)\left\lfloor A_n\left(\cos\left(\phi_n(x) - \overline{\phi}(x)\right) - \left|\sin\left(\phi_n(x) - \overline{\phi}(x)\right)\right|\right) - T\right\rfloor}{\sum_n A_n(x) + \varepsilon}. \tag{2}$$

$W(x)$ is a weight factor to reduce the responses (PC values) where the frequency spread is very narrow. If the frequency spread is sparse, e.g., there is only one (or nearly one) frequency component presented in the signal, the PC will be nearly constant one everywhere, losing its role as edge indicator. In this case, $W(x)$ could help to avoid false detection of edge points. The parameter ε intends to prevent the denominator of formula (1) becoming zero. The symbols $\lfloor\rfloor$ denote a thresholding operator such that the enclosed quantity is equal to itself when its value is positive and zero otherwise. The parameter T is used to control the effect of noise, see [8, 9] for details.

Phase Symmetry: In 1997, Peter Kovesi published a paper [12] emphasizing the importance of local symmetry information on feature detection. It is pointed out that the absolute response values of the even-symmetric filter through the local symmetry points will be very large and the absolute response values of the odd symmetric filter through the local symmetry points will be very small. The measurement of the degree of symmetry was given in the following formula:

$$\mathrm{Sym}(x) = \frac{\sum_n \lfloor A_n[|\cos(\phi_n(x))| - |\sin(\phi_n(x))|] - T\rfloor}{\sum_n A_n(x) + \varepsilon}. \tag{3}$$

At a point of symmetry, the Fourier components are at a maxima or minima (at the symmetric points of their cycle). At a point of asymmetry, the Fourier components are at the asymmetric points of their cycle. Phase symmetry can be combined into the phase congruency to suppress noisy false detected structures.

3 Algorithm

Noise and other structural artifacts are usually seen in real CT images, and the cracks might demonstrate quite various contrast levels. So to successfully extract the cracks, preprocessing to reduce noises (as well as other unrelated artifacts) and tubular structure enhancement techniques are indispensable.

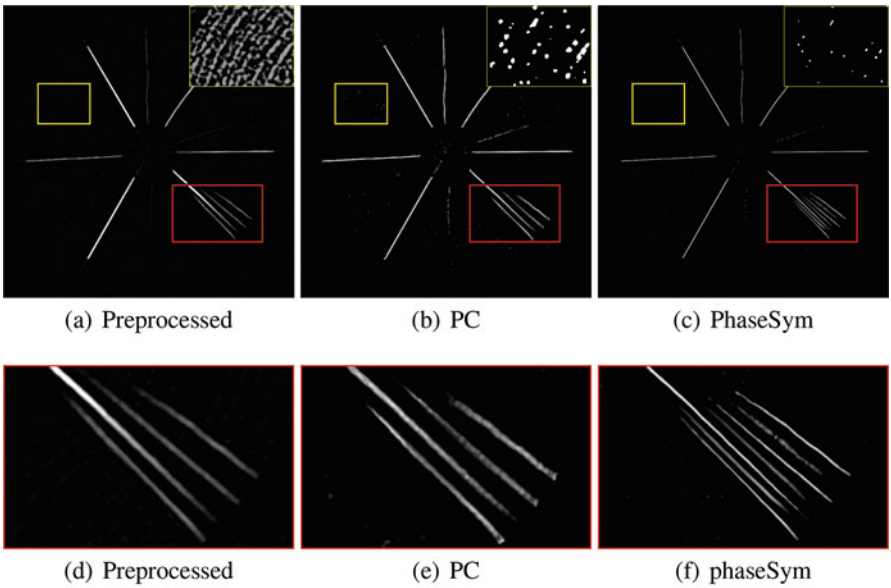

Fig. 2 (**a**) The preprocessed image; (**b**) the phase congruency of image (**a**); (**c**) the phase symmetry of (**a**). The red ROIs of (**a**), (**b**), and (**c**) are zoomed in and shown in (**d**), (**e**), and (**f**), respectively

So our algorithm includes a preprocessing procedure to remove noise, bottom-hat transformation to remove background, and the phase congruency and symmetry congruency for further tubular structure enhancement. For the denoising algorithm, we chose the nonlocal means algorithm [13], since it works well in most situations.

Calculating Phase Congruency and Phase Symmetry: The calculation of the phase congruency and phase symmetry for the preprocessed CT images is demonstrated in Fig. 2. By checking the box-framed area, i.e., region of interest, one can tell that both phase congruency and phase symmetry produce noisy structures. However, usually their false structures appear at different locations. This observation motivates the idea of combining the phase congruency and phase symmetry to reduce false detections by helping each other.

Thresholding: After computing and combining the phase congruency and phase symmetry, thresholding segmentation shall be easy, i.e., a proper threshold is easy to be determined. The results are demonstrated in Fig. 3. Figure 3a shows an image patch, Fig. 3b shows the mixed phase congruency and phase symmetry, and (c) and (d) shows the densities of the yellow line segments in (a) and (b), respectively.

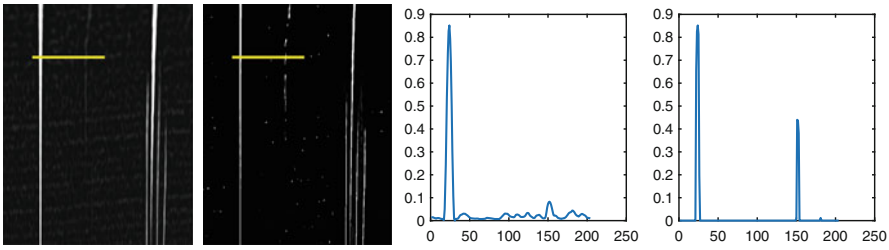

(a) Preprocessed (b) mixed (c) Profile of (a) (d) Profile of (b)

Fig. 3 Combining the phase congruency and phase symmetry. (**a**) Original image; (**b**) phase congruency + phase symmetry; (**c**) zoomed in of the yellow line segment in (**a**); (**d**) zoomed in of the yellow line segment in (**b**)

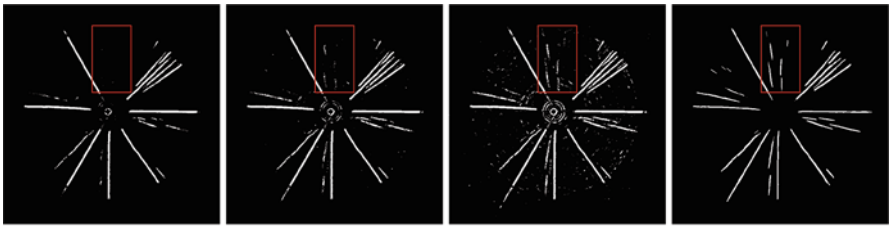

(a) Frangi th=0.02 (b) Frangi th=0.01 (c) Frangi th=0.005 (d) Ours

Fig. 4 Comparison with Frangi's approach: (**a**)–(**c**) resulting image from Frangi's approach with threshold values 0.02, 0.01 and 0.005, respectively; (**d**) the result by our approach

4 Experiments

Two experiments are performed. One is to compare the proposed approach with the popular Frangi's approach, and the other one demonstrates the result from applying the proposed approach to a 3D image. Note that just as in Eq. (2), the parameter of ε in Eq. (3) is empirically set to $1e-4$ in our experiments, while the noise threshold T is estimated automatically by the algorithm, which is based on a statistical modeling of the noise distribution for the image. Assume that the noise is Gaussian, and the response of the filters to noise will form Rayleigh distribution. Then the filter responses at the smallest scale can be utilized as a guide to the estimation of the underlying noise level. Because the smallest scale filters spend most of their time responding to noises. See [8] for more details. In our implementations, the threshold T are set to 0.2, which seems appropriate for all the tests.

Experiment 1: Comparison with Frangi's Approach

The results are shown in Fig. 4. It's clear that the Frangi's approach is sensitive to the threshold parameters. A large threshold leads to incomplete extraction, and weak cracks get lost, while small thresholds introduce more noise and noisy false structure. On the contrary, our approach gives clean and complete result.

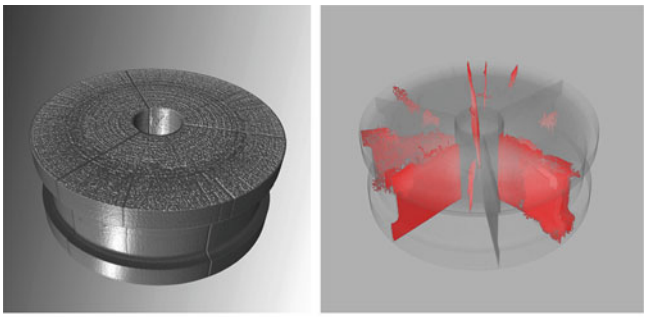

Fig. 5 3D result by our approach. (**a**) the 3D image to be processed; (**b**) the extracted tabular structures by our approach

Experiment 2: 3D Result with the Proposed Approach

In this experiment, we apply our approach to a 3D image that reconstructed from scanning an industrial object. Figure 5a shows the 3D image, while Fig. 5b shows the segmentation result. By checking the resulting 3D image slice by slice, it turns out that almost all favorite cracks are effectively detected.

5 Conclusion and Remark

Phase congruency as well as phase symmetry provides a contrast invariant way of identifying features within images. Combining phase congruency and phase symmetry to extract the cracks in a certain kind of 3D objects from the industry is an efficient approach, which is validated by experiments on real CT images.

Acknowledgements Thanks for the support of the Natural National Science Foundation of China (NSFC) (61371195). And the authors are grateful to Beijing Higher Institution Engineering Research Center of Testing and Imaging as well as Beijing Advanced Innovation Center for Imaging Technology for funding this research work.

References

1. Adams R, Bischof L (1994) Seeded region growing. IEEE Trans Pattern Anal Mach Intell 16(6):641–647
2. Frangi AF, Niessen WJ, Vincken KL et al (1998) Multiscale vessel enhancement filtering. In: International conference on medical image computing and computer-assisted intervention. Springer, Berlin/Heidelberg, pp 130–137
3. Krissian K, Malandain G, Ayache N et al (2000) Model-based detection of tubular structures in 3D images. Comput Vis Image Underst 80(2):130–171

4. Bauer C, Simpson H (2010) Segmentation of 3D tubular tree structures in medical images.
5. Talbot H, Najman L, Passat N (2014) Tubular structure filtering by ranking the orientation responses of path operators. Lect Notes Comput Sci 8690:203–218
6. Merveille O, Talbot H, Najman L et al (2016) Tubular structure analysis by ranking the orientation responses of path operators
7. Kovesi P (1996) Invariant measures of image features from phase information. University of Western Australia
8. Kovesi P (1999) Image features from phase congruency. Videre J Comput Vis Res 1(3):1–26
9. Kovesi P (2000) Phase congruency: a low-level image invariant. Psychol Res 64(2):136–148
10. Kovesi P (2004) Matlab functions for computer vision and image analysis. School of Computer Science & Software Engineering, The University of Western Australia. http://www.csse.uwa.edu.au/pk/research/matlabfns
11. Morrone MC, Owens RA (1987) Feature detection from local energy. Pattern Recogn Lett 6(5):303–313
12. Kovesi P (1997) Symmetry and asymmetry from local phase. In: Tenth Australian joint conference on artificial intelligence, Citeseer, vol 190, pp 2–4
13. Buades A, Coll B, Morel JM (2005) A review of image denoising algorithms, with a new one. Multiscale Model Simul 4(2):490–530

Non-rigid 3D CT/MR Liver Registration with Discontinuous Transforms Using Total Variation Regularization

Min Ding, Xueying Du, Hanqiu Liu, Cheng Zhang, Ming Li, Zhonghua Shen, and Lun Gong

1 Introduction

Research to improve the registration accuracy of computed tomography (CT)/magnetic resonance (MR) images of the abdomen plays an important role in clinical diagnosis; to, these imaging modalities can allow observation of nodule growth, monitoring of emphysema progression, analysis of respiratory movement, and so on. Conventional registration methods with L_2-regularization expect smooth and continuous displacement fields throughout an image. This constraint is unsuitable when discontinuous motion fields exist, for example, when organs such as the liver slide against the abdominal wall during respiration. In this case, the adjacent structures undergo a different motion pattern and move relatively independently. To solve this problem, some effective registration methods were proposed in a previous study.

M. Ding · Z. Shen
School of Science, Nanjing University of Science and Technology, Nanjing, China

X. Du · L. Gong (✉)
Suzhou Institute of Biomedical Engineering and Technology, Chinese Academy of Sciences, Suzhou, China

University of Chinese Academy of Sciences, Beijing, China
e-mail: gonglun@hotmail.com

H. Liu
Department of Radiology, Huashan Hospital, Fudan University, Shanghai, People's Republic of China

C. Zhang · M. Li
Suzhou Institute of Biomedical Engineering and Technology, Chinese Academy of Sciences, Suzhou, China

M. Jiang et al. (eds.), *The Proceedings of the International Conference on Sensing and Imaging*, Lecture Notes in Electrical Engineering 506,
https://doi.org/10.1007/978-3-319-91659-0_27

Using motion masks [1] is a popular way to accommodate for discontinuities near sliding interfaces. But this can dismiss discontinuities on the mask border and require initial segmentation. Some diffusion-based methods were introduced to accommodate for discontinuities near sliding interfaces. Direction-dependent regularizations [2] were used to decompose the deformation field into two directions at the discontinuity interface, and smoothing was only applied in tangential components, not across the boundary. A locally adaptive regularization [3] was proposed in the commonly used demonstration to recover motion discontinuities, but it involved an implicit regularization term and lacked a formal cost definition for a proper optimization scheme. In summary, some of the methods mentioned above need segmentation and others do not have an explicit regularization term. By contrast, total variation (TV) [4, 5] can be defined as an explicit penalty that allows for a well-defined optimization framework and does not need any segmentation; also, discontinuations can be well preserved at sliding boundaries.

Only a few articles [6, 7] currently focus on the complicated sliding motion of the liver during breathing. Moreover, most studies are limited to mono-modal registration. Yet in our work, we use TV as the regularization term in the cost function, which can constrain its spatial incoherence without restricting it to be smooth. To deal with multi-modal registration, we adopt our previous work and use correlation ratio–based mutual information (CRMI) [8] as the similarity metric; CRMI has been proven to have excellent performance in multi-model registration. Furthermore, the parametric transformation model known as free-form deformation (FFD) was used by B-splines; this offers a more physically plausible motion field with a large displacement capture range.

2 Registration Method

2.1 Image Registration

Let $\Omega = \{\mathbf{X} = (x, y, z) | \, 0 \leq x < X, 0 \leq y < Y, 0 \leq z < Z\} \subseteq R^3$ denote the image domain and $\mathbf{u}$ represent the displacement field between $F(\mathbf{x})$ and $M(\mathbf{x})$. $F(\mathbf{x})$ represents the fixed image and $M(\mathbf{x})$ represents the moving image. The registration problem can be seen as selecting the best transformation to minimize the cost function:

$$C = D\left(F\left(\mathbf{X}\right), M\left(\mathbf{u}\left(\mathbf{X}\right)\right)\right) + \lambda R\left(\mathbf{u}\right) \tag{1}$$

where D represents the similarity metric of the registration and R is the regularization term; λ controls the weight of the regularization term. The popular L_2 regularization is global smoothing that cannot accurately model the discontinuities created by the lung or liver; therefore, TV was chosen as our penalty to recover discontinuous motion.

2.2 TV Regularization

The formulation of TV regularization can be written as the L_1-norm:

$$R^{\mathrm{TV}}(\mathrm{u}) = \sum_{l=1}^{3} \sum_{\mathbf{x}\in\Omega} \left\| \nabla \mathbf{u} \right\|_1 \tag{2}$$

where

$$\mathrm{TV}(\mathbf{u}) = \sum_{\mathbf{x}\in\Omega} \left\| \nabla \mathbf{u} \right\|_1 = \sum_{\mathbf{x}\in\Omega} \sqrt{\left(\frac{\partial \mathbf{u}}{\partial x}\right)^2 + \left(\frac{\partial \mathbf{u}}{\partial y}\right)^2 + \left(\frac{\partial \mathbf{u}}{\partial z}\right)^2} \tag{3}$$

Herein, ∇ is a linear operator for gradient. $\partial\mathbf{u}/\partial x$, $\partial\mathbf{u}/\partial y$, and $\partial\mathbf{u}/\partial z$ are derivatives of the deformation field of pixel $\mathbf{x}$. However, the function of the regularization term is non-differentiable at zero, so we use a smooth semi-norm approximation to TV [9], which is defined as $\mathrm{TV}(u_l) = \int_\Omega \sqrt{|\nabla u_l| + \beta} d\mathrm{x}$, in order to prevent dividing by zero.

2.3 Cubic B-Spline Transformation

To form an explicit optimization scheme, we choose FFDs based on the cubic B-spline as our deformation model. To define the cubic B-spline equation for 3-dimensional images of the lung, given an $n_x \times n_y \times n_z$ mesh (denoted by Φ) with uniform spacing (δ mm), let $\phi_{i,j,k}$ be the control points in the image plane. So, the deformation of pixels at coordinate (x, y, z) can be written as:

$$\mathbf{u}(x, y, z; \phi) = \sum_{l=0}^{3} \sum_{m=0}^{3} \sum_{n=0}^{3} B_l(u) B_m(v) B_n(w) \phi_{p_x+l, p_y+m, p_z+n} \tag{4}$$

where $p_x = \lfloor x/\delta \rfloor - 1$, $p_y = \lfloor y/\delta \rfloor - 1$, $p_z = \lfloor z/\delta \rfloor - 1$, $u = x/\delta - \lfloor x/\delta \rfloor$, $v = y/\delta - \lfloor y/\delta \rfloor$, and $w = z/\delta - \lfloor z/\delta \rfloor$. $\lfloor . \rfloor$ is the floor function and B is the basis function of the cubic B-spline [10].

2.4 Similarity Measurement

Because the experiment evaluates mono-model images and multi-modal images, mutual information (MI) [11] is the most widely used similarity metric that can satisfy both conditions. MI is, however, sensitive to intensity distortion and noise,

and it falls into the local extreme under the condition of small sampling points. To improve the accuracy of restoration of lung images, we choose the recently developed CRMI algorithm as our similarity measure. The correlation ratio can make up for the shortcomings of MI, which corrects only the deformation of location and ignores the function mapping of intensity values. The similarity metric was defined as [8]

$$\mathrm{CRMI}\,(M, F; \phi) = (2 - \mathrm{NMI}\,(M, F; \phi)) \cdot (1 - \mathrm{CR}\,(M, F; \phi)) \tag{5}$$

2.5 Optimization

Transformation minimizes CRMI by iterating to find the best alignment position. In our method, we choose as the optimizer the algorithm of limited memory Broyden-Fletcher-Goldfarb-Shanno, which is known for its high performance in handling high-dimensional problems [12]. Here we compute the analytical gradients of the cost function to find the minimum value with respect to grid displacement:

$$C = \frac{\partial \mathrm{CRMI}\,(M, F; \phi)}{\partial \phi_{i,j,k}} + \lambda \frac{\partial R(u)}{\partial \phi_{i,j,k}} \tag{6}$$

Lun et al. [8] show the derivation of the similarity metric. Considering equation (3), we determine the gradient of TV as follows:

$$\frac{\partial \mathrm{TV}\,(\mathbf{u})}{\partial \phi_{i,j,k}} = \int_{\Omega} \left(\frac{\partial \mathbf{u}}{\partial x} \frac{\partial\,(\partial \mathbf{u}/\partial x)}{\partial \phi_{i,j,k}} + \frac{\partial \mathbf{u}}{\partial y} \frac{\partial\,(\partial \mathbf{u}/\partial y)}{\partial \phi_{i,j,k}} + \frac{\partial \mathbf{u}}{\partial z} \partial \frac{(\partial \mathbf{u}/\partial z)}{\partial \phi_{i,j,k}} \right) / \sqrt{\left(\frac{\partial \mathbf{u}}{\partial x}\right)^2 + \left(\frac{\partial \mathbf{u}}{\partial y}\right)^2 + \left(\frac{\partial \mathbf{u}}{\partial z}\right)^2 + \beta} d\mathbf{x} \tag{7}$$

The first-order derivative of the deformation field with respect to $\mathbf{x}$ is as follows; Lun et al. [8] show the calculation process:

$$\frac{\partial \mathbf{u}}{\partial x} = \frac{1}{\delta} \sum_{l=0}^{3} \sum_{m=0}^{3} \sum_{n=0}^{3} \frac{\partial B_l(u)}{\partial u} B_m(v) B_n(w) \phi_{p_x+l, p_y+m, p_z+n} \tag{8}$$

$$\frac{\partial \mathbf{u}}{\partial y} = \frac{1}{\delta} \sum_{l=0}^{3} \sum_{m=0}^{3} \sum_{n=0}^{3} B_l(u) \frac{\partial B_m(v)}{\partial v} B_n(w) \phi_{p_x+l, p_y+m, p_z+n} \tag{9}$$

$$\frac{\partial \mathbf{u}}{\partial z} = \frac{1}{\delta} \sum_{l=0}^{3} \sum_{m=0}^{3} \sum_{n=0}^{3} B_l(u) B_m(v) \frac{\partial B_n(w)}{\partial w} \phi_{i_x+l, j_y+m, k_z+n} \tag{10}$$

An arbitrary control point $\phi_{i,j,k}$ influences the pixels in a local neighborhood, which is defined as $\{\mathbf{x} \subset \Omega || \mathbf{x} - \phi_{i,j,k}| \leq 2\delta\}$. Therefore, the derivative of the aforementioned derivative with respect to $\phi_{i,j,k}$ is:

$$\frac{\partial\left(\partial \mathbf{u}/\partial x\right)}{\partial \phi_{i,j,k}} = \begin{cases} \frac{1}{\delta}\frac{\partial B_{i-p_x}(u)}{\partial u} B_{j-p_y}(v) B_{k-p_z}(w) & \left|\mathbf{x} - \phi_{i,j,k}\right| \leq 2\delta \\ 0 & \text{others} \end{cases} \tag{11}$$

$$\frac{\partial\left(\partial \mathbf{u}/\partial y\right)}{\partial \phi_{i,j,k}} = \begin{cases} \frac{1}{\delta} B_{i-p_x}(u)\frac{\partial B_{j-p_y}(v)}{\partial v} B_{k-p_z}(w) & \left|\mathbf{x} - \phi_{i,j,k}\right| \leq 2\delta \\ 0 & \text{others} \end{cases} \tag{12}$$

$$\frac{\partial\left(\partial \mathbf{u}/\partial z\right)}{\partial \phi_{i,j,k}} = \begin{cases} \frac{1}{\delta} B_{i-p_x}(u) B_{j-p_y}(v)\frac{\partial B_{k-p_z}(w)}{\partial w} & \left|\mathbf{x} - \phi_{i,j,k}\right| \leq 2\delta \\ 0 & \text{others} \end{cases} \tag{13}$$

3 Results and Discussion

3.1 4-Dimensional CT Deformable Image Registration Database Registration

To verify the validity of the proposed method, we tested it in the public 4-dimensional Deformable Image Registration Laboratory (DIR-Lab) data sets on the basis of quantitative and qualitative criteria. To highlight the characteristics of TV in preserving boundary discontinuities, we compared TV regularization with L_2 regularization while selecting the same metric and deformation model.

The public data set contains 10 CT sequences from patients treated for esophageal and lung cancers. Each sequence of the data set has an average spatial resolution of $1 \times 1 \times 2.5$ mm^3 and a size ranging from $256 \times 256 \times 94$ to $512 \times 512 \times 136$. The average target registration error (TRE) is used to access registration accuracy calculated for 300 anatomical landmarks in phases of extreme inhalation and exhalation. The displacement field was used as the qualitative metric and the TRE, as the quantitative metric. Because of computer performance limitations, we selected the first five cases in our experiment because they were relatively small and had a consistent size.

Figure 1 shows the qualitative results of two approaches tested on the 4-dimensional CT image of patient 4. From Fig. 1c we can clearly see that the motion vectors are smoothed and continuous between the lung and rib cage. A displacement field like this is unreal and increases errors at this boundary. By contrast, Fig. 1f shows lung sliding against the pleura; the motion of the lung is large, while the rib cage moves only a little. TV spreads slowly along edges, and it can preserve discontinuation at sliding boundaries, which allows more plausible displacement fields and correspondences to be obtained when registering sliding organs.

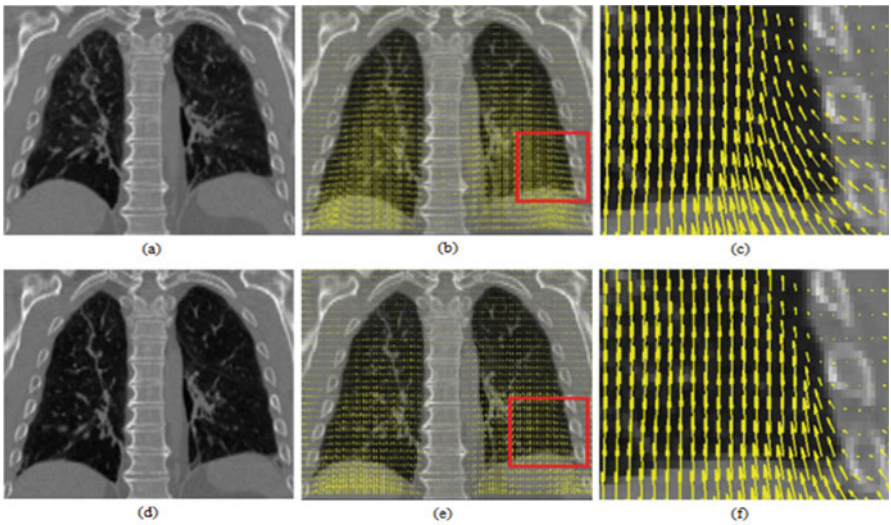

Fig. 1 Coronal view of the 170th slice in 4-dimensional computed tomography. (**a**) Fixed image. (**b**) Displacement field overlaid with L_2 regularization. (**c**) Enlarged view of the displacement vector field of the highlighted region in (**b**. **d**) A moving image. (**e**) Displacement field overlaid with total variation regularization. (**f**) Enlarged view of the displacement vector field of the highlighted region in (**e**)

Table 1 Mean Target Registration Error (millimeters) from the DIR-Lab data set compared among methods

Case	TRE (mm)				
	Before registration	Method of Vandemeule-broucke [1]	Method of Pace et al. [2]	Method of Papież et al. [3]	Our method
1	3.89	1.52	1.06	1.05	1.02
2	4.34	1.30	1.45	1.08	0.98
3	6.94	1.69	1.88	1.49	1.24
4	9.83	1.82	2.04	1.90	1.38
5	7.48	2.75	2.73	1.99	1.75
Mean	6.50	1.82	1.83	1.50	1.27

Table 1 compares the quantitative results of TRE obtained by our methods with results from some popular methods used in the DIR-Lab. The smaller the TRE value, the better the registration result. The table shows the value of TRE before registration, with a mean of 6.50 mm for the first five cases. The TRE with our method is 1.27 mm—lower than that for all the other methods listed in Table 1. In particular, our method achieved the best results for all cases, which proves the feasibility and superiority of our algorithm.

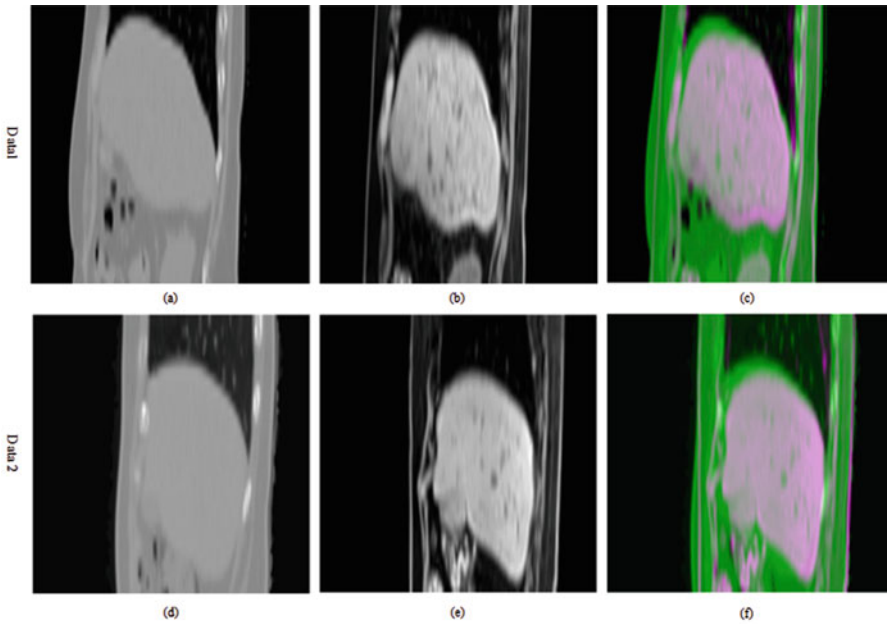

Fig. 2 The clinical computed tomography/magnetic resonance image pairs and a fusion image after rigid registration of the 65th slice in sagittal view from data 1 and the 52nd slice from data 2. The top row shows data 1 and the bottom row shows data 2. (**a**) and (**d**) represent fixed images, (**b**) and (**e**) represent moving images, and (**c**) and (**f**) represent the fusion image. The fusion image before non-rigid registration is color-coded

3.2 Clinic CT/MR Data set

We verified the capability of our algorithm in two clinical CT/MR liver data sets, which were obtained from Shanghai Huashan Hospital. To improve registration accuracy, the clinic data were resampled to an isotropic $1.47 \times 1.47 \times 3$ mm^3 resolution with a size of $256 \times 256 \times 48$. We use the CT image as the fixing image and the MR image as the moving image. Rigid registration was used to roughly aligned the two images. Then non-rigid registration was performed using CRMI, with TV regularization compared with L_2 regularization. Here we take the fusion image and the displacement field as the qualitative measure. In addition, the Hausdorff distance (HD) and M-Hausdorff distance (MHD) [13] were used as the quantitative metrics in clinical data sets. These metrics objectively measure the algorithm registration accuracy through a set of points extracted by the edge detector at the boundaries.

Figure 2a–f shows the original image pairs and fusion image from data 1 and data 2. Figures 3a, d and 4a, d show that the images were well aligned after non-rigid registration, although the difference between the fusion images is small in both methods. The difference in the displacement field is visible. Figures 3c and

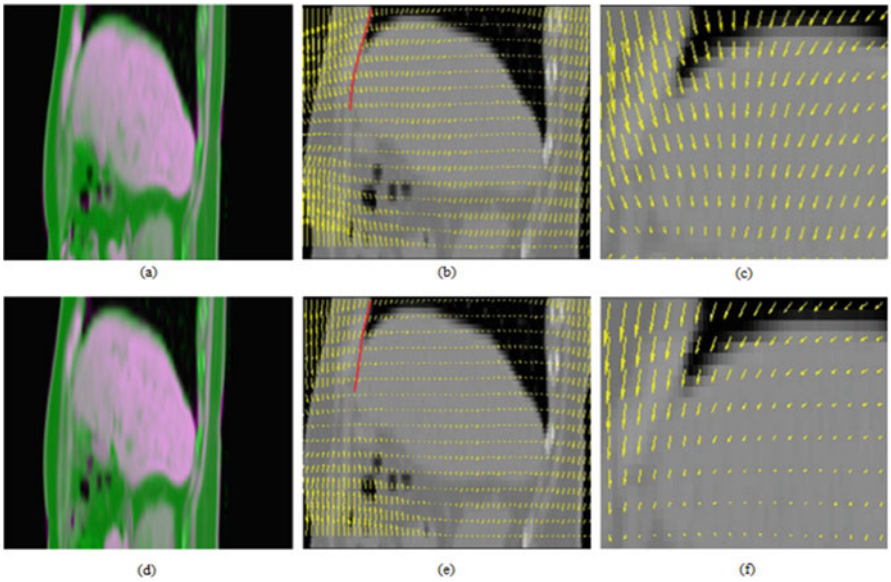

Fig. 3 Sagittal view of 3-dimensional deformable computed tomography/magnetic resonance liver registration results for data 1. The top row represents the results using L_2-regularization, and the bottom row represents results obtained with our methods. (**a**) and (**d**) are fusion images, (**b**) and (**e**) show displacement vector fields, and (**c**) and (**f**) provide enlarged views at the abdominal wall

4c show a continuous displacement field at the boundaries between the liver and abdominal wall, and the motion vector moves across the boundary, which shows implausible displacement fields. By contrast, Figs. 3f and 4f show the liver sliding against the abdominal wall; the motion of the abdominal wall beside the lower liver is large because of the small limitation applied by the rib cage. Although the results of data 2 are not as good as those of data 1, we can also see the improvement at the boundary. Therefore, TV regularization can make a correction in the displacement field between the liver and abdominal wall and can reduce the registration error between such boundaries.

Table 2 exhibits the HD and MHD as the quantitative metrics of data 1 and data 2; their small values indicates that the method achieves a better registration result at the boundary of the liver. In each case, the HD obtained by TV regularization is obviously less than the L_2-norm. As for the MHD, it is easy to see that TV regularization provides better results. Both results verify that TV regularization can preserve discontinuous movement well and can improve registration accuracy.

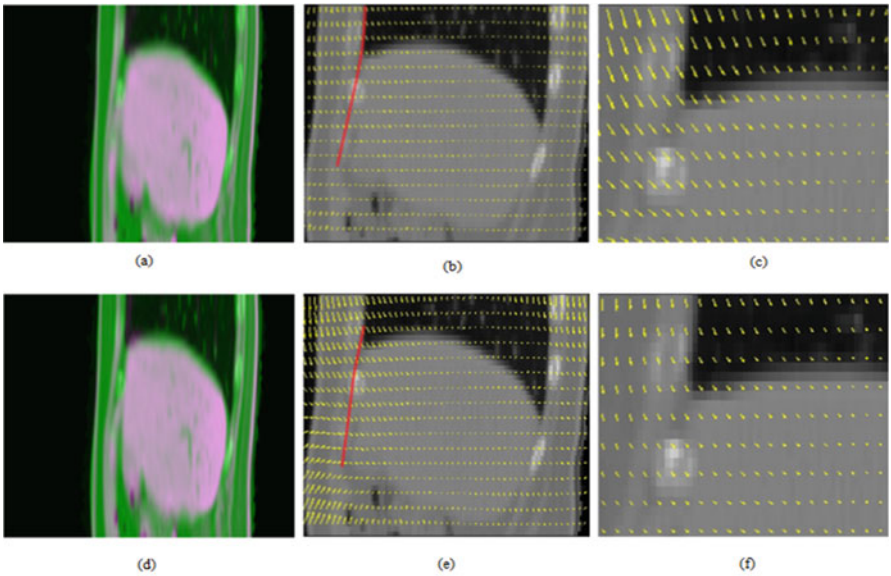

Fig. 4 Sagittal view of 3-dimensional deformable computed tomography/magnetic resonance liver registration results for data 2. The top row represents the results using L_2-regularization, and the bottom row represents results obtained with our methods. (**a**) and (**d**) are fusion images, (**b**) and (**e**) show displacement vector fields, and (**c**) and (**f**) provide enlarged views at the abdominal wall

Table 2 Hausdorff distances (millimeters) and M-Hausdorff distances (millimeters) with different methods applied to data 1 and data 2

Data	Metric	Before registration	L_2-norm	TV
1	HD	37.87	23.12	14.40
	MHD	10.61	2.98	2.12
2	HD	32.98	25.19	20.22
	MHD	5.87	2.35	1.83

HD Hausdorff distance, *MHD* M-Hausdorff distance, *TV* total variation

4 Conclusion

In this chapter we presented a 3-dimensional multi-modal registration strategy for CT/MR images of the liver, with the aim of preserving physiologically plausible deformation at discontinuous borders. TV was used as the regularization term in place of traditional L_2-regularization. We have demonstrated the robustness of the algorithm by experimenting with a 4-dimensional CT data set and clinical data. In the 4-dimensional CT data set, the TRE showed improved registration accuracy compared with some other state-of-the-art methods. The displacement field we obtained shows that TV can preserved discontinuation well at borders. In the clinical data, although we found little difference in the fusion image obtained with the two methods, the difference in the displacement field is obvious. In addition, better

results were achieved for both HD and MHD with TV regularization than with L_2 regularization. All these results show that TV can preserved well real motion in the liver. The proposed method will be further improved in our subsequent work and be used in clinical applications.

Acknowledgements This work was supported in part by the National Program on Key Research and Development Project (grant nos. 2016YFC0103500, 2016YFC0103502, 2016YFC0104500, and 2016YFC0104505), the National Natural Science Foundation of China (grant no. 61201117), the Natural Science Foundation of Jiangsu Province (grant no. BK20151232), and the Youth Innovation Promotion Association CAS (grant no. 2014281).

References

1. Vandemeulebroucke J, Bernard O, Rit S et al (2012) Automated segmentation of a motion mask to preserve sliding motion in deformable registration of thoracic CT. Med Phys 39(2):1006–1015
2. Pace DF, Aylward SR, Niethammer M (2013) A locally adaptive regularization based on anisotropic diffusion for deformable image registration of sliding organs. IEEE Trans Med Imaging 32(11):2114
3. Papież BW, Heinrich MP, Fehrenbach J et al (2014) An implicit sliding-motion preserving regularisation via bilateral filtering for deformable image registration. Med Image Anal 18(8):1299
4. Vishnevskiy V, Gass T, Székely G (2014) Total variation regularization of displacements in parametric image registration. Abdominal imaging. Computational and clinical applications. Springer International Publishing
5. Vishnevskiy V, Gass T, Szekely G et al (2016) Isotropic Total variation regularization of displacements in parametric image registration. IEEE Trans Med Imaging PP(99):1–1
6. Papież BW, Franklin J, Heinrich MP et al (2015) Liver motion estimation via locally adaptive over-segmentation regularization. Medical image computing and computer-assisted intervention – MICCAI 2015. In: Springer International Publishing
7. Goksel O, Vishnevsky V, Carrillo AG et al (2016) Imaging of sliding visceral interfaces during breathing. IEEE Int Symp Biomed Imaging IEEE 2016:298–301
8. Lun G, Wang H, Peng C et al (2017) Non-rigid MR-TRUS image registration for image-guided prostate biopsy using correlation ratio-based mutual information. Biomed Eng Online 16(1):8
9. Chumchob N (2013) Vectorial total variation-based regularization for variational image registration. IEEE Trans Image Process 22(11):4551
10. Rueckert D, Sonoda L, Hayes C et al (1999) Nonrigid registration using free-form deformations: application to breast MR images. IEEE Trans Med Imaging 18(8):712
11. Viola P, Wells WMI (1997) Alignment by maximization of mutual information. IEEE Comp Soc
12. Zhu C, Byrd RH, Lu P (1999) L-BFGS-B-Fortran subroutines for large-scale bound constrained optimization. ACM Trans Math Softw 23(4):550–560
13. Jung WS, Ohkyu K, Albert JS, Gary WC (2012) CT-PET weighted image fusion for separately scanned whole body rat. Med Phys 39(1):533

Directional Diffusion Filter Bank and Texture Quality Measurement for Robust Orientation Estimation and Enhancement of Fingerprint Images

Hong Liu, Chao Yang, and Zengmei Lan

1 Introduction

Fingerprint recognition systems are becoming more and more widely used as effective authentication tools in personal identification applications [1]. The robustness of their performance, however, is still a critical constraint in practice, especially in situations where fingerprint images are of low quality. There are many causes leading to low-quality fingerprint images, such as finger scars or small foreign interferences causing ruptures of fingerprint ridge lines, noises caused by perspiration, information lost from dry fingers, etc. In addition, excessive pressing pressure by fingers can often cause fingerprint deformation and artifacts. There are a variety of complications that can produce different forms of interferences to fingerprints. This is exactly the reason why estimating orientation fields and enhancing images for low-quality fingerprints are difficult. An effective algorithm that can adapt to all low-quality cases is yet to be reported.

In order to improve the robustness of recognition and matching capabilities for low-quality fingerprint images, it is necessary to effectively enhance the images and obtain accurate corresponding orientation fields. Classic fingerprint enhancement algorithms are based on prior orientation field estimations. They usually first complete a fast estimation of the orientation field and then construct a filtering algorithm with the estimated orientation field to enhance the image [2, 3]. These methods usually perform well but with an obvious limitation: an effective enhancement of the image depends on an accurate estimation of the orientation field, and an accurate estimation of the orientation field in turn often depends on a well-enhanced image. For low-quality fingerprint images, errors in orientation

H. Liu · C. Yang (✉) · Z. Lan
School of Computer Science and Communication Engineering, Guangxi University of Science and Technology, LiuZhou, Guangxi Province, People's Republic of China

M. Jiang et al. (eds.), *The Proceedings of the International Conference on Sensing and Imaging*, Lecture Notes in Electrical Engineering 506,
https://doi.org/10.1007/978-3-319-91659-0_28

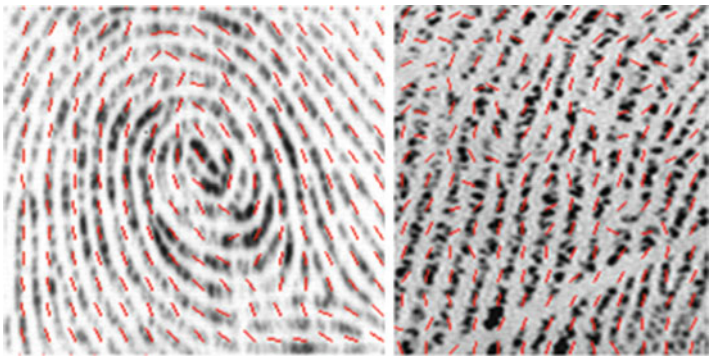

Fig. 1 Examples of orientation field estimation by [6] in low-quality regions

estimation can often cause the subsequent enhancement to magnify the existing artifacts, resulting in low recognition rate. In addition, an orientation field is not only a starting point for image enhancement but also provides important information for fingerprint matching [4]. At present, algorithms of orientation field estimation are mainly based on the following computations: local gradient information [5], fingerprint "ridge" and "valley" line extractions [6], structural tensor [7], Fourier analysis [8], and so on. These methods can synthesize the local information of the image to realize fast calculations of local texture directions and have certain interference-resistant performance. However, it is easy for them to produce incorrect orientation estimations in the cases where either texture information is missing or noises or scratches are strong. To illustrate this, examples created by the method described in [6] are shown in Fig. 1.

In general, orientation field estimation of a fingerprint image can be easily affected by interferences such as noises and scars. In order to mitigate this problem, some scholars have proposed to use a directional filter bank to enhance fingerprint images and then locally analyze each of the enhanced images. Finally a final enhanced fingerprint image is synthesized. The computational complexity of these approaches increases as the number of filters increases, and the accuracy of the synthesized enhancement image depends on proper parameter selections of the directional filter bank as well as on the local analysis method used for each enhanced image. For example, Oh SK et al. [9] proposed to first use a directional filter bank (DFB) to process the fingerprint image and use the sum of the local grayscales as a measure of local energy of the enhanced image and, finally, based on this energy measurement, to obtain an orientation field estimation and a synthesis of the final enhanced image. In their paper, there is no clear description of the construction of the directional filter bank, and the definition of local energy also ignores the frequency information of fingerprints. The robustness of their algorithm is not high. Khan MAU and Khan TM [10] proposed the use of a three-level filter structure to obtain enhanced images in different directions and then used the principal component analysis (PAC) to enhance the sub-band directional images. However,

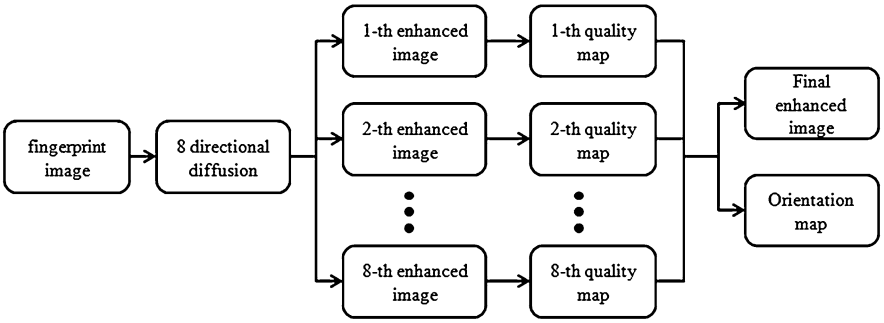

Fig. 2 Flow diagram of our proposed process

their paper did not give details on sub-band energy calculation, and there was no discussion of orientation field estimation.

In this paper, we first use a bank of eight directional diffusion filters to process fingerprint images. We then analyze the localized spectral information of the eight filtered images in the specific directions and get a quantitative measure of the fingerprint texture clarity, that is, a measure of the fingerprint quality. Finally, we obtain a robust estimation of local ridge/valley orientation and a final enhanced image based on the quality measurement. The process is shown in Fig. 2.

2 Method

2.1 Directional Diffusion Filter

Nonlinear diffusion filtering is widely used in image denoising, edge extraction, smoothing, and texture pattern analysis [11]. The filter is capable of preserving edge information and at the same time connecting broken texture patterns [12]. It is defined as follows:

$$\frac{\partial u}{\partial t} = div\left(\mathbf{D}\nabla u\right) \tag{1}$$

where *div* is the divergence operator, u is the image, and $\mathbf{D} = \begin{bmatrix} a & b \\ b & c \end{bmatrix}$ is the diffusion coefficient matrix which controls the behavior of diffusion. This equation can be rewritten as:

$$\begin{aligned} \partial_t u &= \partial_x\left(a\partial_x u + b\partial_y u\right) + \partial_y\left(b\partial_x u + c\partial_y u\right) \\ &= a\partial_x^2 u + 2b\partial_x u\partial_y u + c\partial_y^2 u \end{aligned} \tag{2}$$

where $\partial_x u$, $\partial_x^2 u$ represents the first- and second-order partial differential operations for the x direction of the image, respectively, and the same for the y direction.

The coefficient matrix **D** is generally a symmetric, positive semi-definite matrix with two eigenvalues, λ_1, λ_2 and $\lambda_1 > \lambda_2$, and two corresponding eigenvectors, u_1, u_2. The direction of the diffusion or smoothing is along u_2.

Reversely, in order to make the direction of the diffusion in a specified direction, one can construct a specific diffusion coefficient matrix **D** with the following steps:

1. Specify the direction of the diffusion as θ, and construct two vectors that are perpendicular to each other:

$$u_1 = \begin{bmatrix} \cos(\theta) \\ \sin(\theta) \end{bmatrix}, u_2 = \begin{bmatrix} \sin(\theta) \\ -\cos(\theta) \end{bmatrix} \tag{3}$$

2. Specify two values as $\lambda_1 = s$, $\lambda_2 = 1 - s$, where s is set to be 0.99 in our experiment.
3. A matrix **D** can be constructed to have u_1, u_2 as its eigenvectors and λ_1, λ_2 as their corresponding eigenvalues.

We can then use Formula (2) to realize a diffusion filtering of an image in any arbitrary direction by creating a proper diffusion coefficient matrix **D**. In order to effectively denoise and connect broken texture patterns, it is usually necessary to have many iterations in a numerical scheme of the Formula (2). The number of iterations in this paper is set to be $n = 40$.

Selecting $\theta = [-90, -67.5, -45, -22.5, 0, 22.5, 45, 67.5]$ as the eight directions for the diffusion filtering processing, we show an example of the filtering effect in Fig. 3.

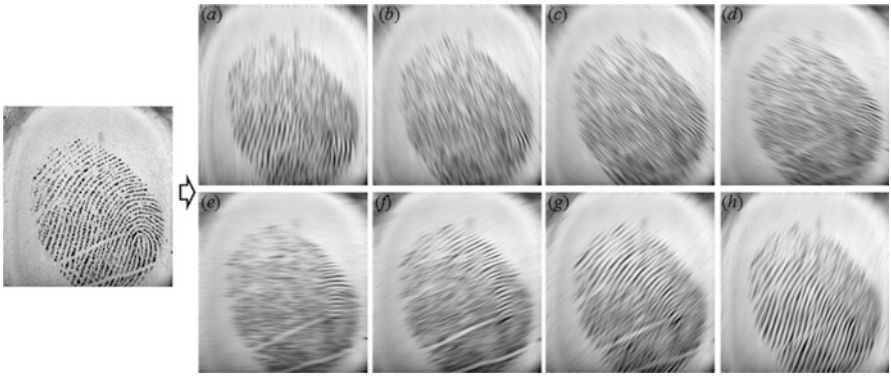

Fig. 3 Directional diffusion filtering. (**a**–**h**) are the diffusion-filtered image in the directions $\theta = [-90, -67.5, -45, -22.5, 0, 22.5, 45, 67.5]$, respectively

It can be observed that for each of the filtered images, local texture information is effectively enhanced for some regions while the rest has been destroyed or blurred. To be more specific, regions with texture orientations consistent with the diffusion filter direction is effectively enhanced while regions with texture orientations significantly different from it are blurred. Notice that effectively enhanced regions in all eight images are complementary. We argue that the number of and spacing between the directions of the filter bank seems reasonable, which provides a basis for the subsequent synthesis of a completely enhanced image.

2.2 Quality Measurement Based on Spectrum Analysis

For a diffusion filter of a given direction, if the actual texture direction of a region is in a close proximity with the filter direction, the region will be effectively enhanced, broken texture patterns will be connected to a certain extent, and noises will be effectively suppressed.

Assuming that a local region of a fingerprint can be effectively enhanced by the diffusion filter in the direction of θ, an intensity profile in the direction perpendicular to the diffusion direction is similar to a sinusoidal curve because of the alternating ridge/valley pattern. When the resolution of the images is fixed, the frequency of the intensity profile will also be stabilized within a certain range. For example, fingerprint images obtained at 500dpi are considered to have a ridge/valley alternating period of approximately 10 (pixels/cycles), and therefore the period of the intensity profile is also about 10 (pixels/cycles). In order to reduce noise interference, we use an oriented sampling rectangle instead of an oriented sampling line and calculate the mean intensity in the direction of the filter to obtain a one-dimensional intensity profile as illustrated in Fig. 4.

Figure 4 shows that the intensity profile of a clearly enhanced region is similar to a sinusoidal curve, and the fluctuation amplitude is large. In poor quality regions, intensity profiles are irregular, and the fluctuation amplitudes are small. We apply fast Fourier transform (FFT) to the profiles and observe the spectrums as shown in Fig. 5.

Figure 5a shows a very concentrated spectrum which has a peak at about the sixth frequency component (about 1/13 (cycles/pixels)) which is close to the statistically common value of the fingerprint ridge/valley frequency (1/10 (cycles/pixels)). Figure 5b depicts a relatively dispersed spectrum, and the energy near the 1/10 (cycles/pixels) frequency component is not dominant. Therefore, the quality of a fingerprint image can be measured in the frequency domain using these characteristics. We propose the following algorithm:

1. A rectangular window of length 64 is sampled in the direction of the filter centered at each pixel as shown in Fig. 6, and the directional intensity profile is created as shown in Fig. 7.
2. A 64-point fast Fourier transform (FFT) is performed on the profile, and the module of the transform is computed.

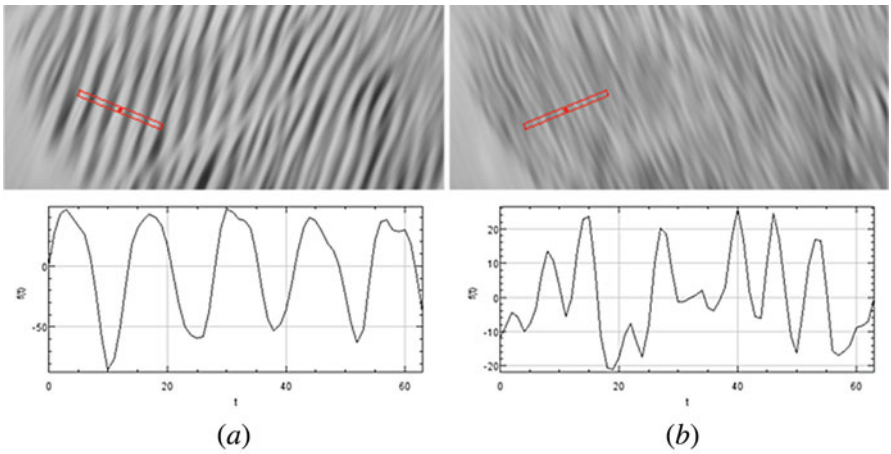

Fig. 4 Rectangular sampling regions and corresponding intensity profiles. (**a**) Directional diffusion-filtered image corresponding to $\theta = 67.5$, (**b**) filtered image corresponding to $\theta = -67.5$

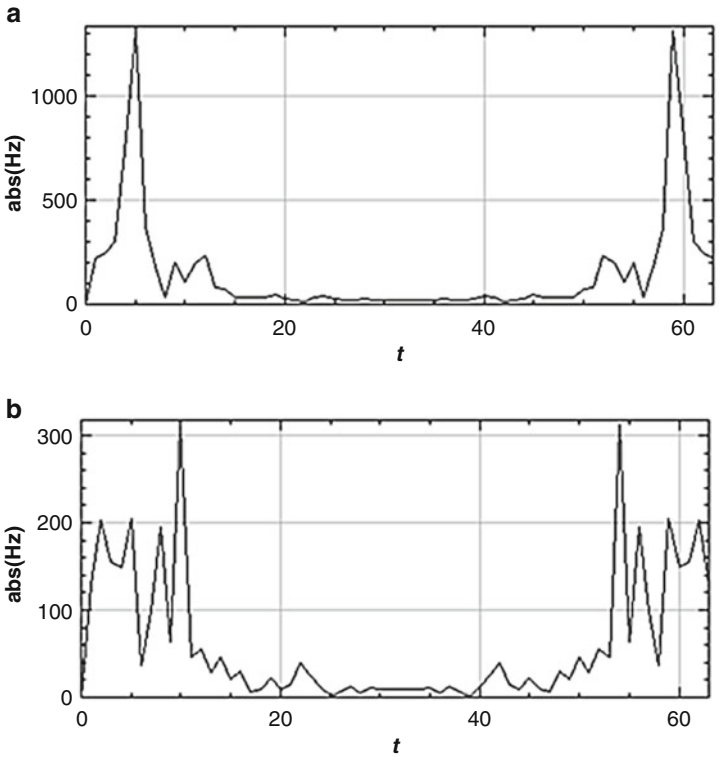

Fig. 5 Spectral analysis of intensity profiles. (**a**, **b**) correspond to the cases of (**a**, **b**) in Fig. 4

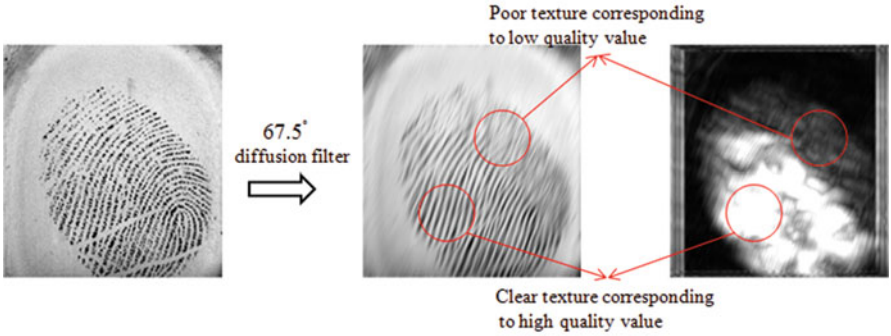

Fig. 6 Directional diffusion-enhanced image with its quality image based on spectrum analysis

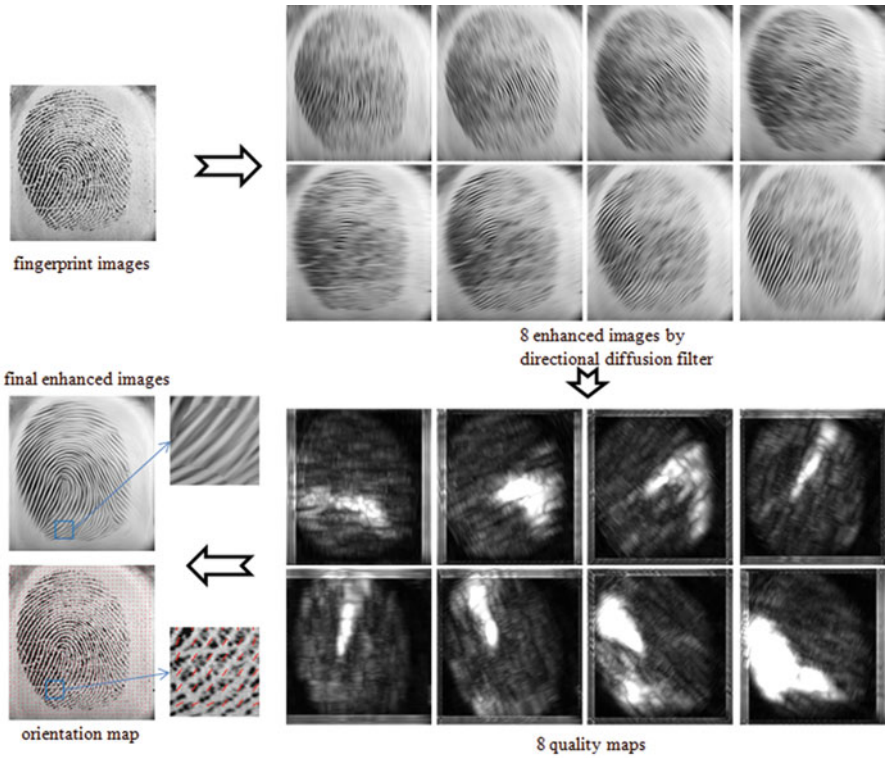

Fig. 7 Fingerprint image enhancement and direction field estimation framework and renderings

3. Since the ridge/valley alternating period of 500DPI fingerprint images is typically about 10 (pixels/cycles), in good quality areas, the spectrum is expected to have a peak near frequency 10 (pixels/cycles). Taking into account the spectral leakage of the FFT, the fence effect, and variations among fingerprint images, we measure the maximum energy, that is, the maximum amplitude, between 1/16 and 1/7 (cycles/pixels) or between the fifth and the tenth frequency components, to reflect the quality of the fingerprint. Figure 6 shows the effectiveness of the quality image corresponding to the filtering result in a specific direction.

Calculated quality image based on the spectrum analysis contains the frequency information, the energy information, and the directional information of the local regions of a fingerprint image, which makes it a very reasonable and effective fingerprint quality measurement.

2.3 Final Synthesis of Image Enhancement and Estimation of Orientation Field

According to the quality image of each diffusion filtered image, the final enhanced image can be obtained by selecting the best from the filtered images pixel by pixel. At the same time, the direction of the selected diffusion filter for each pixel gives the best estimation of the orientation for that pixel.

Figure 7 shows the entire process. The quality measurement based on spectrum analysis given in this paper can efficiently quantify the local quality of the fingerprint image. Based on these quality images, the filtered image pixels with the maximum quality values for each pixel are taken to form the final enhanced image, and at the same time, the orientation field is obtained by using the corresponding diffusion filter directions.

Figure 7 also shows the effectiveness of the algorithm at the places where excessive noises and significant scars exist. Any low-quality region in the image can always be effectively enhanced by one diffusion filter in the right direction. Our algorithm avoids the problem of directly estimating the orientation field of the image because any direct estimation will be unstable in the presence of strong noise and other significant interferences. The proposed method has excellent robustness for images with low quality and is superior to the existing methods.

3 Results

As a comparison with the proposed algorithm, we present here a classical method for orientation field estimation proposed by Kass and Witkin [5]. The main idea of the method is to extract local gradient information. The specific steps are the following:

1. Divide the image into small blocks of size $w \times w$.
2. Calculate a horizontal gradient $\partial_x(i,j)$ and a vertical gradient $\partial_y(i,j)$ at the pixel (i,j).
3. Calculate the direction at (i,j) by the following equations:

$$\begin{bmatrix} V_x(i,j) \\ V_y(i,j) \end{bmatrix} = \begin{bmatrix} \sum_{u=i-w/2}^{i+w/2} \sum_{v=j-w/2}^{j+w/2} \left(\partial_x^2(u,v) - \partial_y^2(u,v)\right) \\ \sum_{u=i-w/2}^{i+w/2} \sum_{v=j-w/2}^{j+w/2} 2\partial_x(u,v)\,\partial_y(u,v) \end{bmatrix} \tag{4}$$

$$\theta(i,j) = \frac{1}{2}\tan^{-1}\left(\frac{V_y(i,j)}{V_x(i,j)}\right) + \frac{\pi}{2} \tag{5}$$

where $\theta(i,j)$ is the estimated direction and $\theta(i,j) \in [0,\pi)$. The value of w is important to the algorithm. In general, a smaller block size tends to produce large error in areas where noise and interference are strong, while a larger block size can get a relatively accurate direction estimation. But in the region where there is a sharp change in the directions of the texture, for example, near a core, a larger block size will result in poor estimation.

Our algorithm does not exhibit such a problem. Although the iteration number as a parameter replaces the block size, we can choose one iteration number to handle all types of local areas of the fingerprint (Fig. 8).

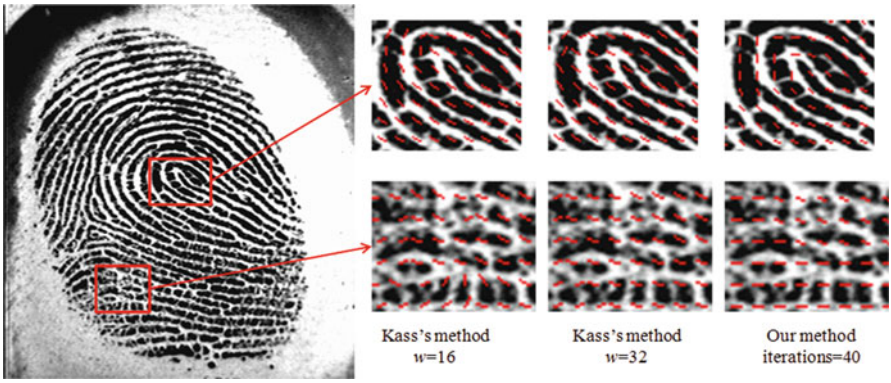

Fig. 8 Compared with a classical algorithm

4 Conclusion

In this paper, we observed risks in direct orientation field estimation for low-quality fingerprint images and proposed a robust fingerprint image enhancement and orientation field estimation method. Our work includes two main points. First, we introduce the directional diffusion filtering method to form a filter bank, which makes the design of the filter simple and effective. Second, we define a quality measurement of filtered images based on spectrum analysis. This quality measurement affords more robustness due to the consideration of both energy and frequency information.

The experimental examples are taken from the FVC2004 database. The results show that the algorithm is robust for low-quality images with strong noise and significant interferences and is superior to the existing methods. In this paper, the fingerprint images are used as examples, but obviously the algorithm is well-suited for processing any type of images with directional textures.

Acknowledgments 牋This work is partially supported by the Doctoral Fund of Guangxi University of Science and Technology (14Z12); Scientific Fund of Guangxi University of Science and Technology (174522); Scientific Fund of Guangxi University of Science and Technology (20161309); the Basic Ability Improvement Project of Young and Middle-aged Teachers in Guangxi Colleges and Universities (2017KY0359); the Basic Ability Improvement Project of Young and Middle-aged Teachers in Guangxi Colleges and Universities (2017KY036);

References

1. Zhu E, Yin JP, Zhang GM (2005) Fingerprint matching based on global alignment of multiple reference minutiae. Pattern Recogn 38(10):1685–1694
2. Hong L, Wan Y, Jain A (1998) Fingerprint image enhancement: algorithm and performance evaluation[J]. IEEE Transact Pattern Anal Machine Intel 20(8):777–789
3. Turroni F, Maltoni D, Cappelli R et al (2011) Improving fingerprint orientation extraction[J]. IEEE Transact Inform Forens Secur 6(3):1002–1013
4. Medinapérez MA, Gutiérrezrodríguez A, Garcíaborroto M (2009) Improving fingerprint matching using an orientation-based minutia descriptor[J]. Lect Notes Comput Sci 5856(5856):121–128
5. Kass M, Witkin A (1987) Analyzing oriented patterns[J]. Comp Vision Graph Image Process 37(3):362–385
6. Gottschlich C, Mihailescu P, Munk A (2009) Robust orientation field estimation and extrapolation using semilocal line sensors[J]. IEEE Transact Inform Forens Secur 4(4):802–811
7. Brox T, Weickert J, Burgeth B et al (2006) Nonlinear structure tensors[J]. Image Vision Comput 24(1):41–55
8. Yoon S, Feng J, Jain AK (2011) Latent fingerprint enhancement via robust orientation field estimation[C]. In: International joint conference on biometrics. IEEE, pp 1–8
9. Oh SK, Lee JJ, Park CH et al (2003) New fingerprint image enhancement using directional filter Bank.[J]. Union Agency – Science Press
10. Khan MAU, Khan TM (2013) Fingerprint image enhancement using data driven directional filter Bank[J]. Optik - Int J Light Elect Opt 124(23):6063–6068

11. Gilboa G, Sochen N, Zeevi YY (2002) Forward-and-backward diffusion processes for adaptive image enhancement and denoising[J]. IEEE Trans Image Process 11(7):689–703
12. JianGang C, Jie T, Yu Liang HE et al (2004) Fingerprint enhancement algorithm based on nonlinear diffusion filter [J]. Acta Automat Sin 30(6):854–862

Part IV
Sensing and Imaging Applications

Optimization of Event Processing in RFID-Enabled Healthcare

Shanglian Peng and Jia He

1 Introduction and Motivation Example

With increasing smart devices introduced in healthcare monitoring applications, it becomes possible to manage people and objects in real time in the Internet of Things (IoT) era. Radio-frequency identification (RFID) is one of the most popular techniques used in healthcare monitoring scenarios which can be used to identify and monitor elderly people and patients, track hospital assets and medical instruments, validate patients' drug compliance, check status of operations, etc. [1] In RFID-enabled healthcare applications, streams of data are collected in real time and need to be processed within second response time in order to reduce risk of decisions.

To ensure error-free decision-making in life-critical RFID-enabled monitoring applications, a careful and fast responsive computing model is needed. Complex event processing (CEP) [2], as a stream-based computing paradigm, has been widely used in time-critical stream processing systems. Over RFID streams, queries of interest are considered as complex patterns (or complex events) which can be defined using SQL-style declarative [3] or rule-based languages [4]. To evaluate these patterns (queries), a non-deterministic or tree-based model is needed which could be running over the real-time RFID event streams [5]. However, existing event detection engines are limited in optimization algorithms over RFID-enabled healthcare applications [6, 7]. This paper is motivated by the need to efficiently

S. Peng (✉) · J. He
College of Computer Science and Technology, Chengdu University of Information Technology, Chengdu, China
e-mail: psl@cuit.edu.cn; hejia@cuit.edu.cn

M. Jiang et al. (eds.), *The Proceedings of the International Conference on Sensing and Imaging*, Lecture Notes in Electrical Engineering 506,
https://doi.org/10.1007/978-3-319-91659-0_29

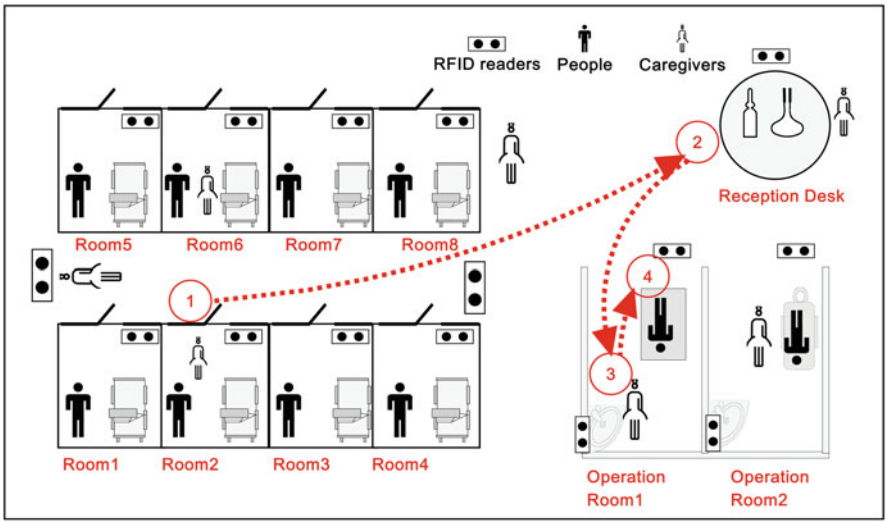

Fig. 1 Motivation example of RFID-enabled healthcare monitoring

run event detection queries in a healthcare RFID application with specialized optimization algorithms supported.

Motivation Example As shown in Fig. 1, in a RFID-enabled healthcare application, suppose we want to monitor people and caregiver's activity and movement in order to make error-free decisions. Monitored people are attached with RFID tags, the objects such as medicine, dosages, and instruments are also tracked by RFID tags. Due to cost consideration, we assume to use passive tags. RFID tags are read at fixed points and mobile readers. The readings of RFID tags, which we call simple events (records), will be pushed to a local server. Event patterns (queries) can be defined over these event streams. In a healthcare application, many activities need to be monitored with specific workflow. For example, in Fig. 1, to track whether a person in Room2 gets the right caring process, we can define an event detection pattern query over the RFID streams with a declarative pattern definition language proposed in [8, 9]:

Query 1:
PATTERN SEQ(Room r, ReceptionDesk rd,
! SEQ(SPD spd, Decontamination d, Packing p, Sterilization s, StoragePatch sp, spd.id = d.id = p.id = s.id = sp.id),
Washing w, Operating o, rd.id=w.id=o.id)

Here, the control flow of RFID-based sterile processing [10] is shown in Fig. 2 which can be formulated as a subpattern in Query1 SEQ(SPD spd, Decontamination d, Packing p, Sterilization s, StoragePatch sp, spd.id = d.id = p.id = s.id = sp.id).

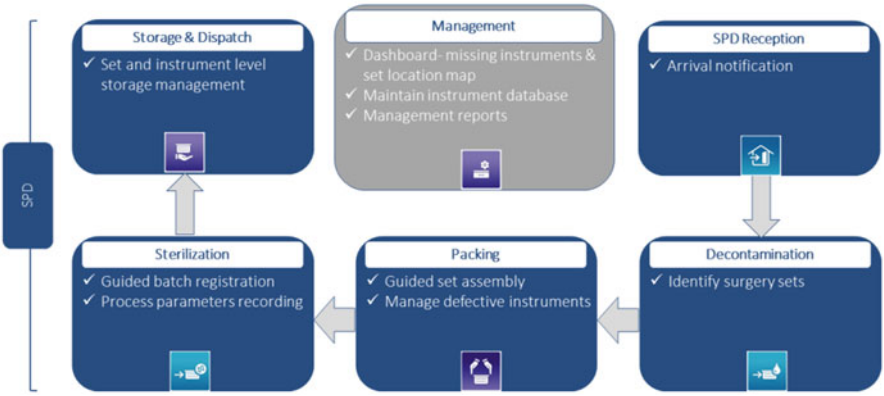

Fig. 2 The life cycle and workflow of surgical items in healthcare and hospital [10]

Query1 is a long sequence pattern query with a negated nested SEQ pattern imbedded. Semantic meaning of Query1 is that a person moving from the room area to the operation room should be followed by a reception desk reading and a washing reading, and if the tools used for the operation are not (!) disinfected by the flow in Fig. 2, then a complex event is triggered. The state-of-art complex event processing (CEP) works [1, 2, 6] do not support such nested pattern evaluation. In the Cayuga system [11], authors define composable queries with negation operator which is only applied to a single atomic event type of SEQ pattern. NEEL [8, 9] aims to solve nested pattern queries with query rewrite and some data structures, and their works are the closest to the work in this paper. In this paper, we address the problem of evaluate negation nested sequence queries in a healthcare context. The rest of the paper is organized as follows: Section 2 introduces the event model. Section 3 presents the NFA-based evaluation model. In Sections 4, we present optimization method of the evaluation model. Section 5 discusses experimental analysis of the evaluation model, while in Section 8, we draw a conclusion of the paper.

2 Event Model

Event type is a specification or class label of objects that have the same semantic meaning. Primitive event/atom event is an event which cannot be divided into smaller events. Each primitive event has an event type. A complex event is an event which is a combination of primitive events and/or complex events connected by event operators. Event operators used in our event model include SEQ, Negation (!), AND, and OR. An event instance denotes occurrence of a primitive or composite event. Primitive event instance is denoted by lowercase letters, for instance, in Query1 “s”. Event instance has temporal information denoted with start time and end time. For a primitive event instance, start time equals to end time.

Event type is denoted as E_i which includes attributes of the event instances of this type. Primitive event types are predefined in the application domain. For example, event type of decontamination event in Query 1 is denoted as "D," while $d_i \in D_i$ denotes d_i is an event instance of event type D_i. Each event type has attributes which is denoted as $e_i.\ attr_j$ meaning the *jth* attribute of event instance e_i [3, 8].

3 Evaluation Model

To evaluate a pattern query as described in Query, there are some models such as tree-based model [12], petri-net-based model [13], rule-based model [14], and NFA-based model [3]. We use the NFA-based model to evaluate pattern queries because NFA is suitable for fast stream processing and is easy to be implemented.

For an event query defined with SASE language, the query is first transformed into a query plan, and the query plan is then transformed into a NFA model. The transformation of Query 1 is shown in Fig. 3.

In Fig. 3, the event pattern is first compiled into a query plan tree, event operators are round nodes in the tree (SEQ in in Fig. 3.), and event types are transformed into rectangular square nodes. Attribute constraints of different operators are attached to corresponding nodes.

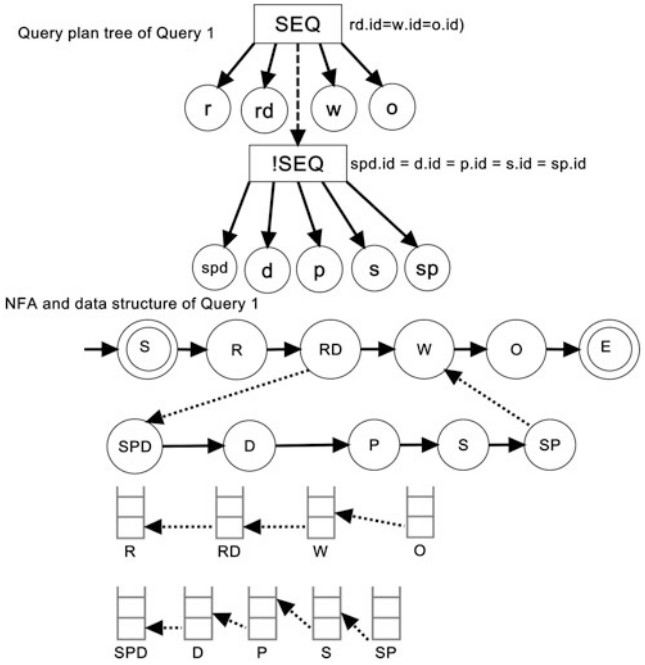

Fig. 3 Query plan and NFA of Query1

Table 1 Running example of Query1 over a stream snapshot of a healthcare application

Timestamp	Location	TagID	Timestamp	Location	TagID
8:00:24 13-04	**R1**	**0001**	9:05:28 13-04	RD	0007
8:05:33 13-04	**W**	**0006**	9:05:33 13-04	R1	0003
8:08:55 13-04	R2	0002	9:11:55 13-04	R2	0004
8:12:21 13-04	**RD**	**0001**	**9:22:21 13-04**	**W**	**0001**
8:24:35 13-04	RD	0003	**9:30:35 13-04**	**O**	**0001**
9:00:01 13-04	RD	0002	9:32:01 13-04	O	0002

The query plan tree is then transformed into a NFA model. A start and end node is constructed for a query as shown in Fig. 3. As there exists a Negation SEQ pattern in Query, we construct a sub-NFA embedded into the overall NFA. A stack-based data structure is used to store event instances of different event types. Events of the same tag ID in different event types are connected with forwarded arrows.

Running Example For a given event stream snapshot as shown in Table 1, the evaluation works as follows: For event types of R (R1-R8 in Fig. 1), each primitive event should be stored in stack of type R in Fig. 3. In Table 1, caregivers with TagID 0001, 0002, 0003, and 0004 are stored into a stack first, and then according to the NFA model in Fig. 3, we should check whether there exist subsequent events that fulfill the attribute constraint described in Query 1. This operation is checked by traversing the corresponding stacks of RD, W, and O of the NFA and checks the TagID attribute constraint over each stack. So we need to keep all the events of types R, RD, W, and O in the evaluation process which would result in great memory consumption and search operations. As shown in Table 1, the event with TagID 0001 in red color would satisfy partial matches of Query 1; we need to check whether the caregiver with TagID 0001 took the disinfected tools to people in the operation room with sequence pattern SEQ(SPD spd, Decontamination d, Packing p, Sterilization s, StoragePatch sp, spd.id = d.id = p.id = s.id = sp.id). This pattern should be detected over workflow streams in Fig. 2; in this running example, we omit the stream processing of this pattern.

4 Optimization Algorithm

In the evaluation process of the NAF of an event query, we need to keep all the partial matches of the subpattern until we slide forward to the next processing window. With this mechanism, we need to keep partial matches in the stack and delete related events which would not contribute to future matches. As stack operations are hard to apply to batch deletions over the event streams, we propose to use an ordered B-tree-based data structure to optimize the deletion operation of partial matches. The ordered B-tree structure is shown in Fig. 4.

In Fig. 4, we only store a pointer in the stack data structure of NFA, and the event data is stored in leaf nodes of a time-ordered B-tree data structure. Each TagID is stored only once. Batch deletion of events from the memory works as the following steps:

1. At the end of the sliding window, compute the time range which indicates the start and end time of the window in the ordered B-tree.
2. For each TagID in the ordered B-tree, search for related stack, and search for the subsequent events from the pointers between different types of stacks; output the patterns that satisfy the query.
3. Delete the partial matches that do not generate matches in the time window, and re-initialize the stack, and readjust the ordered window.

The event detection processing will move to the next sliding window after the deletion process.

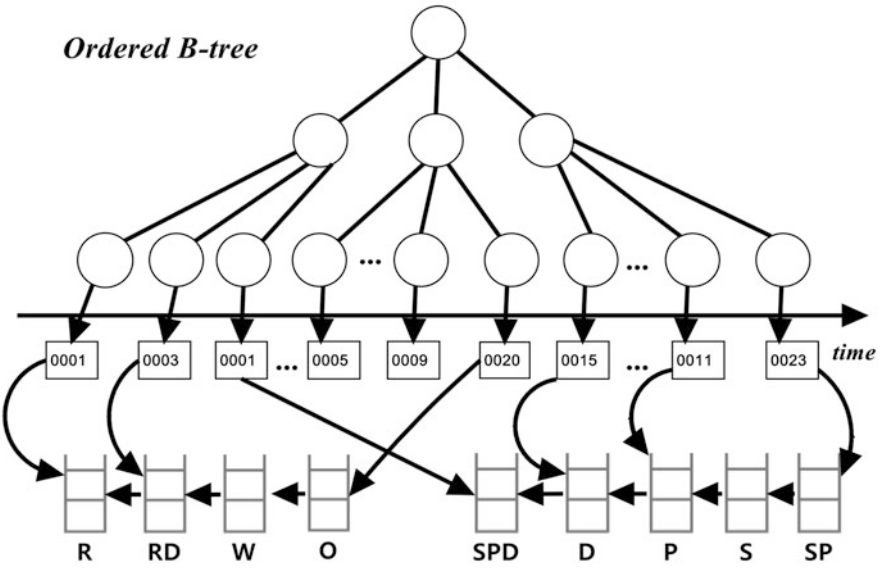

Fig. 4 Illustration of the ordered B-tree of Query1

5 Experimental Analysis

In this section, we present experimental study of the event detection model with a simulated RFID-enabled healthcare application. In the application, RFID read interval is set to seconds that means we generate RFID data stream from different RFID readers in seconds. We generate events in Fig. 1 with multithread styles to simulate a practical scenario. The streams vary in hours long with different volumes. Events of different event types fulfills a predefined normal probability distribution.

The simulation system is implemented in Visual Studio with C ++; data generator is implemented with C#. The computer used in the experiment is with i5 core processor and 4G memory. To compare the model and algorithm, we use NEEL [9] as the benchmark.

We have tested response time and memory consumption of the algorithms over different volume of streams with sliding window set 30 min. The results are shown in Figs. 5 and 6.

From Fig. 5, we can see NEEL outperforms the NFA implementation of the straightforward algorithm in this paper due to their optimization over a nested pattern match, while with optimization method, our algorithm outperforms NEEL as we delete partial matches in a batch manner.

Figure 6 is the memory comparison of different methods. As we can see, the straightforward implementation algorithm of this paper uses less memory than other methods. NFA + B-tree utilizes the most memory because it needs a B-tree to store all events and the stack data structure to store relationship between different event types. But considering time is critical in monitoring applications, we think it is acceptable to use more memory to get a quick response.

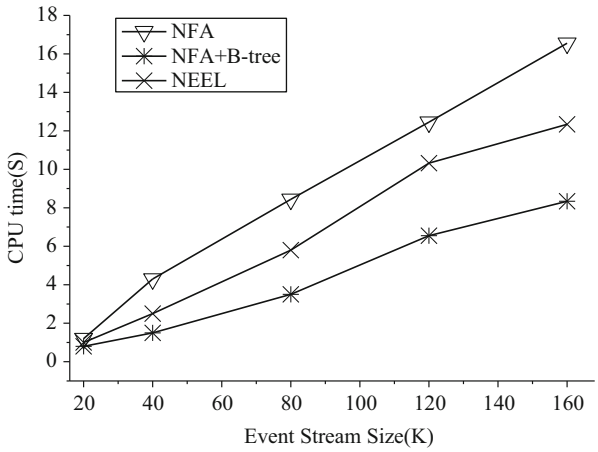

Fig. 5 CPU time consumption of three algorithms of Query1 (Window 30 mins, SEQ query length 4, imbedded SEQ length 4)

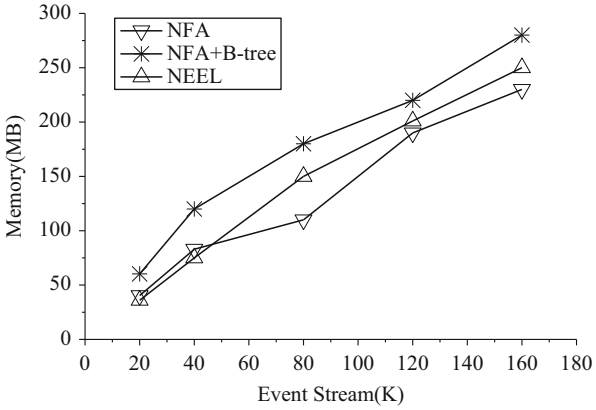

Fig. 6 Memory consumption of three algorithms of Query1 (Window 30 mins, SEQ query length 4, imbedded SEQ length 4)

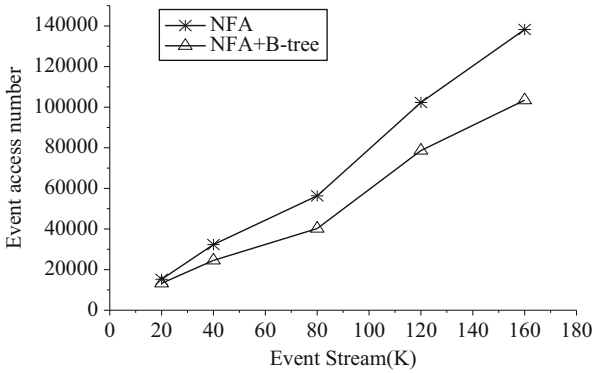

Fig. 7 Event access number of two algorithms of Query1 (Window 30 mins, SEQ query length 4, imbedded SEQ length 4)

We test the event access number of the NFA-based methods to see the efficiency of searching different data structures. The result is shown in Fig. 7.

From Fig. 7, we can see that B-tree-based method utilizes few searches than the straight method because the batch operation reduces some event access in the memory which would also reduce partial match management cost in a way.

6 Conclusion

In this paper, we present event detection method over RFID-enabled healthcare data streams with NFA-based model. To enhance fast partial matches deletion and reduce event access numbers, we utilize ordered B-tree to store the events. Experimental

results show that while our optimization method consumes more memory, it can provide fast response and utilizes few searches over streams. In the future, we would like to optimize the query execution plan over multiple queries.

Acknowledgments This work has been supported by funds from Chengdu University of Information Technology, China (J201410), the Applied Basic Research Key Project of Sichuan Province (2017JY0011), and the China Scholarship Council.

References

1. Yao W, Chu C-H, Li Z (2011) Leveraging complex event processing for smart hospitals using RFID. J Netw Comput Appl 34(3):799–810
2. Luckham D (2002) The power of events, vol 204. Addison-Wesley, Reading
3. Wu E, Diao Y, Rizvi S (2006) High-performance complex event processing over streams. In: Proceedings of the 2006 ACM SIGMOD international conference on management of data. ACM
4. Cugola G, Margara A (2010) TESLA: a formally defined event specification language. In: Proceedings of the fourth ACM international conference on distributed event-based systems. ACM
5. Gyllstrom D et al (2008) On supporting kleene closure over event streams. In: Data engineering, 2008. ICDE 2008. IEEE 24th international conference on. IEEE
6. Wamba SF (2012) RFID-enabled healthcare applications, issues and benefits: an archival analysis (1997–2011). J Med Syst 36(6):3393–3398
7. Tu Y-J, Zhou W, Piramuthu S (2009) Identifying RFID-embedded objects in pervasive healthcare applications. Decis Support Syst 46(2):586–593
8. Liu M et al (2011) High-performance nested CEP query processing over event streams. In: Data engineering (ICDE), 2011 IEEE 27th international conference on. IEEE
9. Liu M et al (2010) NEEL: the nested complex event language for real-time event analytics. In: International workshop on business intelligence for the real-time Enterprise. Springer, Berlin/Heidelberg
10. The ORLocate Solution. http://www.haldor-tech.com/products/the-orlocate-solution/
11. Demers AJ et al (2007) Cayuga: a general purpose event monitoring system. CIDR 7:412–422
12. Mei Y, Madden S (2009) Zstream: a cost-based query processor for adaptively detecting composite events. In: Proceedings of the 2009 ACM SIGMOD international conference on management of data. ACM
13. Gatziu S, Dittrich KR (1994) Detecting composite events in active database systems using petri nets. In: Research issues in data engineering, 1994. Active database systems. Proceedings fourth international workshop on. IEEE
14. Teymourian K, Paschke A (2009) Semantic rule-based complex event processing. In: International workshop on rules and rule markup languages for the semantic web. Springer, Berlin/Heidelberg

Measurement of the Gas-Solid Flow in a Wurster Tube Using 3D Electrical Capacitance Tomography Sensor

H. Q. Che, J. M. Ye, W. Q. Yang, and H. G. Wang

1 Introduction

The bottom spray fluidized bed with a Wurster tube is widely applied for the pellets coating due to its good performance on coating uniformity and efficiency [1]. The Wurster tube is a vertical tube placed above the air distributor in the bed; the air distributor was designed to control the airflow with a higher speed in the center and a lower in the annulus zone. During coating, the pellets in the annulus zone are pneumatically transported to the Wurster tube through the bottom gap between the Wurster tube and air distributor. In the Wurster tube, the pellets interact with the coating solvent from a bottom spray nozzle. The pellets are dried as they move upward into a fountain zone; after that, the pellets fall back into the annulus zone [2]. This circulation of solid particles is repeated until the desired coating film on the surface of particles was achieved. The gas-solid flow characteristic is one of the most important parameters which affects the coating quality.

Electrical capacitance tomography (ECT) gives an option to visualize the gas-solid flow inside the Wurster-type fluidized bed. It has several advantages including non-intrusive and simple structure, low cost, and fast imaging speed [3]. It has been reported to be used in the monitoring of the fluidized bed with Wurster tube

H. Q. Che · H. G. Wang (✉)
Institute of Engineering Thermophysics, Chinese Academy of Sciences, Beijing, China

University of Chinese Academy of Sciences, Beijing, China
e-mail: wanghaigang@iet.cn

J. M. Ye
Institute of Engineering Thermophysics, Chinese Academy of Sciences, Beijing, China

W. Q. Yang
School of Electrical and Electronic Engineering, University of Manchester, Manchester, UK

M. Jiang et al. (eds.), *The Proceedings of the International Conference on Sensing and Imaging*, Lecture Notes in Electrical Engineering 506,
https://doi.org/10.1007/978-3-319-91659-0_30

[4, 5]. However, only 2D images are used to investigate the flow characteristics and limited information are given for the process control. Recently, 3D ECT has been successfully applied in the measurement of gas-solid flow in fluidized beds. Wang et al. [6] investigated the instantaneous properties of the shape of the jets in a 0.3 m bubbling gas-solid fluidized bed using the 3D electrical capacitance volume tomography (EVCT). Mao et al. [7] investigated the gas-solid flow in the bottom region of a circulating fluidized bed by four types of 3D ECT sensor. 3D ECT gives more details on the flow characteristics than the traditional 2D images.

In this paper, a 3D ECT sensor with 16 electrodes is designed and installed in the Wurster tube in a lab-scale fluidized bed. The 3D sensitivity maps are calculated based on the structure of electrodes. Several sets of experiments are carried out with different operational conditions. The objectives of this research are (1) to reconstruct the 3D solid distributions inside the Wurster tube using a unique ECT sensor, (2) to analyze the effect of operational parameters on the flow hydrodynamic behaviors, and (3) to explore the factors which might affect the image quality from the 3D ECT sensor.

2 Experiment

2.1 Experimental Setup

The lab-scale fluidized bed with Wurster tube is depicted in Fig. 1. The main frame of the fluidized bed consists of a plenum in the bottom, a conical chamber with a height of 350 mm, an expansion chamber with a height of 500 mm, and a filter on the top. The Wurster tube is made of stainless steel, and the diameter and the length of the Wurster tube are 65 and 150 mm, respectively. The fluidization air was supplied by a root blower, and the airflow rate ranged from 0.89 to 3.50 m/s. 3 kg sugar pellets with the mean diameter of 800 μm and density of 900 kg/m^3 was used as the bed material. All the experiments were conducted without solution spraying, and the bottom nozzle was removed.

2.2 ECT Sensor Design and Image Reconstruction

The 3D ECT sensor totally has 16 electrodes, and the electrodes are placed in dual planes in the inner wall of Wurster tube as shown in Fig. 2. The Wurster tube is made of stainless steel to act as a shielding layer. The dual planes are located 1.5∼6.5 cm and 8.5∼13.5 cm above the bottom of the Wurster tube, respectively. The measured volume is the region surrounded by the electrodes, and it has a height of 12 cm. An AC-ECT system with 16 channels from ECT Instruments Ltd., UK, is connected to the ECT electrodes. During the measurement, the electrodes are excited one after the other and the capacitance between the excited electrode and the remaining

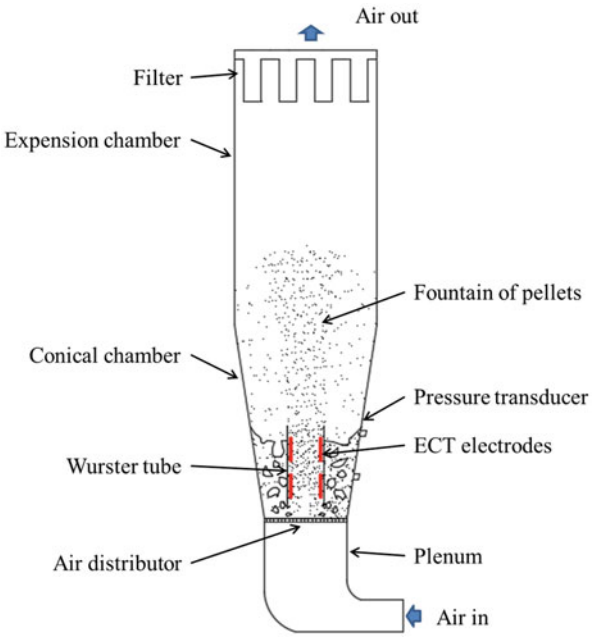

Fig. 1 A lab-scale fluidized bed with Wurster tube

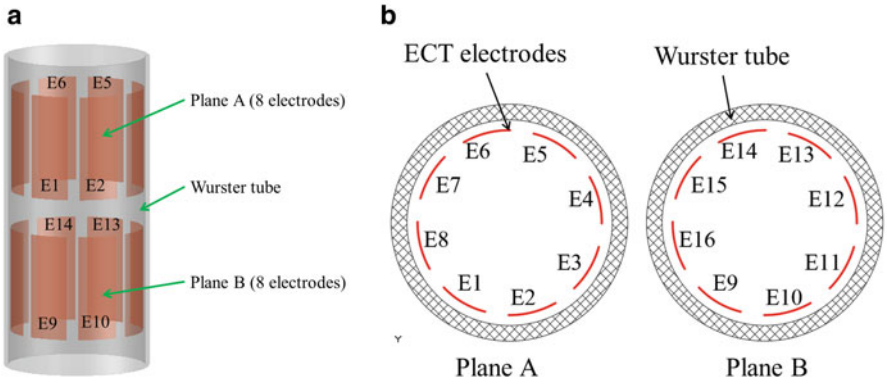

Fig. 2 Structure of the 3D ECT sensor. (**a**) Overall view. (**b**) Cross sections

ones is measured. The total number of independent measured capacitances is 120 in one frame.

There are two major computational problems in ECT: the forward problem and the inverse problem. The forward problem is to determine the capacitances from the permittivity distribution, and the inverse problem is to determine the permittivity distribution from capacitance measurements [8]. For forward problem, the capacitance between electrode pairs can be considered as a function of permittivity distribution.

$$C = \xi(\varepsilon) \tag{1}$$

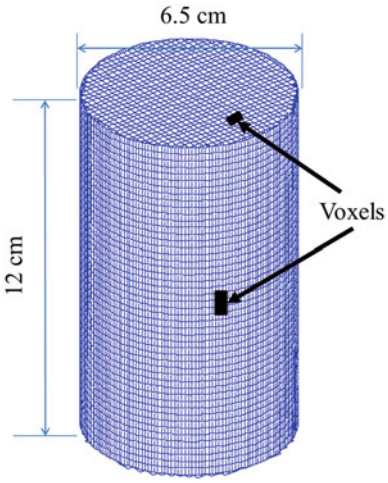

Fig. 3 Voxels in the sensing region (952 × 50 voxels)

where C is the capacitance between electrodes and ε is the permittivity of object.

The change in capacitance with the perturbation of the permittivity distribution is

$$\Delta C = \frac{d\xi}{d\varepsilon}(\Delta\varepsilon) + o(\Delta\varepsilon) \tag{2}$$

where $o(\Delta\varepsilon)$ represent higher-order terms of $\Delta\varepsilon$, and they are usually small. By neglecting $o(\Delta\varepsilon)$, Eq. (2) is simplified by

$$\Delta C = s\ \Delta\varepsilon \tag{3}$$

where $s = \frac{d\xi}{d\varepsilon}$ is the sensitivity of the capacitance to the changes in permittivity.

In order to visualize the permittivity distribution, the measured volume is discretized into voxels as shown in Fig. 3. Based on Eq. (3), the discrete form of the forward problem is

$$\underset{M\times 1}{\boldsymbol{\lambda}} = \underset{M\times N}{\mathbf{S}}\ \underset{N\times 1}{\mathbf{G}} \tag{4}$$

where $\boldsymbol{\lambda}$ is the normalized capacitance vector; $\boldsymbol{S}$ is the sensitivity distribution matrix, giving a sensitivity map for each electrode pair; $\boldsymbol{G}$ is the normalized permittivity distribution, i.e., the gray level of voxels for visualization; and M and N are the number of independent electrode measurements and the number of voxels in the sensing area, respectively.

The sensitivity maps were calculated by COMSOL Multiphysics™ software based on the finite element methods (FEM). The sensitivity maps are calculated as [9]

$$S_{ij}(P) = -\iiint_P \frac{E_i(x,y,z)}{V_i} \cdot \frac{E_j(x,y,z)}{V_j} dxdydz \tag{5}$$

where $S_{ij}(P)$ is the sensitivity value between the ith and jth electrodes over the voxel P and $\boldsymbol{E}_i(x,y,z)$ is the electric field vector when the ith electrode is excited with a voltage of V_i.

The normalized capacitance vector in Eq. (4) is defined as

$$\boldsymbol{\lambda} = \frac{\mathbf{C} - \mathbf{C_L}}{\mathbf{C} - \mathbf{C_H}} \tag{6}$$

where $\boldsymbol{C}$ is the measured capacitance vector and $\boldsymbol{C_L}$ and $\boldsymbol{C_H}$ are the low- and high-calibration capacitance vectors, respectively.

If the inverse of S existed in Eq. (4), the inverse problem, i.e., 3D image reconstruction, could be solved by

$$\boldsymbol{G} = \boldsymbol{S}^{-1}\boldsymbol{\lambda} \tag{7}$$

However, the inverse of $\boldsymbol{S}$ does not exist, and Eq. (7) is not applicable. The liner back projection (LBP) algorithm [9] is one of the solutions of the inverse problem; it gives the fastest imaging speed. LBP algorithm is written as

$$\boldsymbol{G} = \mathbf{S}^{\mathrm{T}}\boldsymbol{\lambda} \tag{8}$$

Another commonly used algorithm is Landweber iteration [10]; it is slower but may give better image quality. It is written as

$$\boldsymbol{G}^{n+1} = \boldsymbol{G}^n + \boldsymbol{\alpha} \cdot \boldsymbol{S}^T \cdot \left(\boldsymbol{\lambda} - \boldsymbol{S} \cdot \boldsymbol{G}^n\right) \tag{9}$$

where α is the step length, and it is decided by the method in [11]. Normally, the initial value of $\boldsymbol{G}$, i.e., $\boldsymbol{G}^0$, is obtained by Eq. (8).

3 Results and Discussion

3.1 3D Sensitivity Map Analysis

Figure 4 shows the iso-surfaces of sensitivity maps between different electrode pairs. As can be seen, the map has high sensitivity between adjacent electrodes, such as electrode pairs E1–E2 and E1–E9 (in the order of 2.5×10^{-4}), and low sensitivity between opposing electrodes, such as E1–E5 and E1–E13 (in the order of 1.0×10^{-4}). Also, the symmetric feature can be seen clearly in Fig. 4 for the opposite electrodes among different planes.

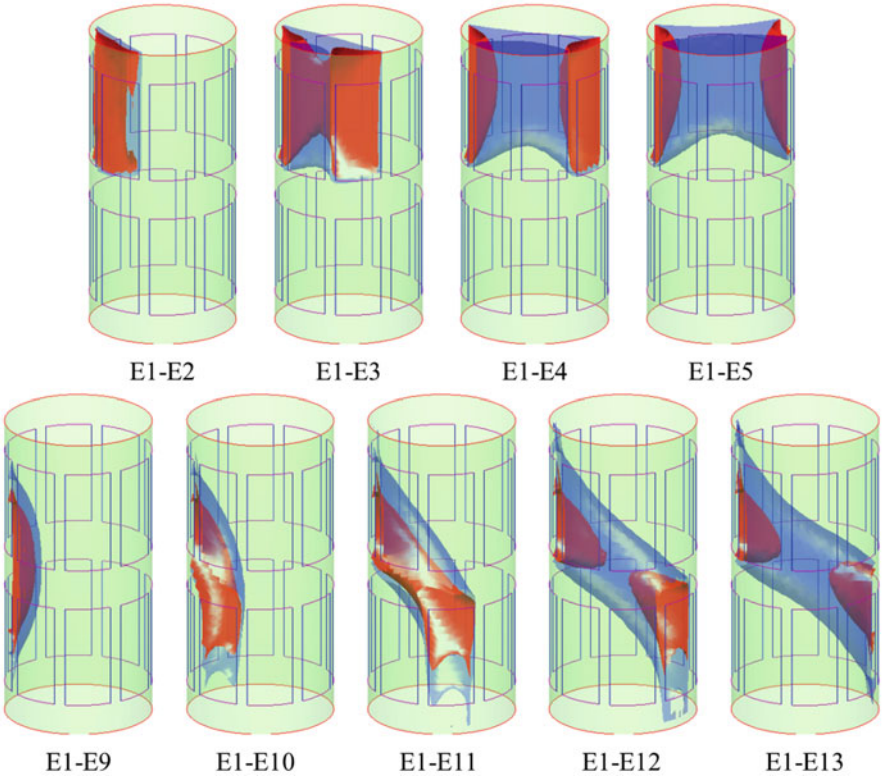

Fig. 4 Iso-surfaces of normalized sensitivity distributions between typical electrodes pairs (the sensitivity value of the iso-surfaces is 2.5×10^{-4} for red color and 1.0×10^{-4} for blue color)

3.2 Different 3D Visualization Methods

Figure 5 gives the 3D iso-surfaces and 3D slices of two typical of flow structures inside a Wurster tube. The value of iso-surfaces is 0.3 for these figures. The 3D slices are stacked up by several 2D images at different cross sections. Comparing the iso-surfaces and slices, it can be found that the flow behaviors can be more clearly recognized by the slices, especially for the dispersed flow case. The following discussion will be based on the slices.

3.3 Static Tests of ECT Sensor

To validate the measurement of 3D ECT sensor, static tests were carried out before the dynamic tests. Two parameters are introduced to assess the measurement accuracy of ECT sensor and compare the different imaging algorithms: (1) correlation coefficient (C_{coef}) and (2) signal-to-noise ratio (*SNR*). They are defined as follows:

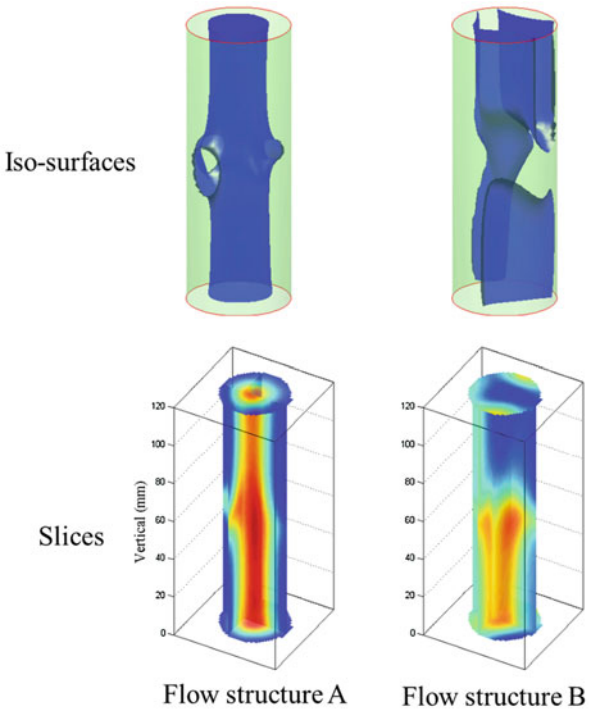

Fig. 5 Different 3D visualization methods (iso-surface value = 0.3)

Correlation coefficient:

$$C_{\text{coef}} = \frac{\sum_{i=1}^{N} \left(\widehat{G}_i - \overline{\widehat{\boldsymbol{G}}}\right)\left(G_i - \overline{\boldsymbol{G}}\right)}{\sqrt{\sum_{i=1}^{N} \left(\widehat{G}_i - \overline{\widehat{\boldsymbol{G}}}\right)^2 \sum_{i=1}^{N} \left(G_i - \overline{\boldsymbol{G}}\right)^2}} \tag{10}$$

Signal-to-noise ratio:

$$\text{SNR} = 20\lg\left(\frac{\text{Signal}}{\text{Noise}}\right) = 20\lg\sqrt{\frac{\sum_{i=1}^{F} C_i^2}{\sum_{i=1}^{F} \left(C_i - \overline{C}\right)^2}} \tag{11}$$

where $\boldsymbol{G}$ is the measured permittivity distribution, $\widehat{\mathbf{G}}$ is the true permittivity distribution of the sensing area, C_i is the mean value of measured capacitances of the ith frame, and F is the total frames of measurement.

Figure 6 shows the true solid distributions and the reconstructed images of static tests, and totally four typical solid distributions are chosen for validation. Table 1 summarizes the C_{coef} and *SNR* for different distributions. As can be seen from both the figure and the table, the Landweber iteration gives higher C_{coef} values and better

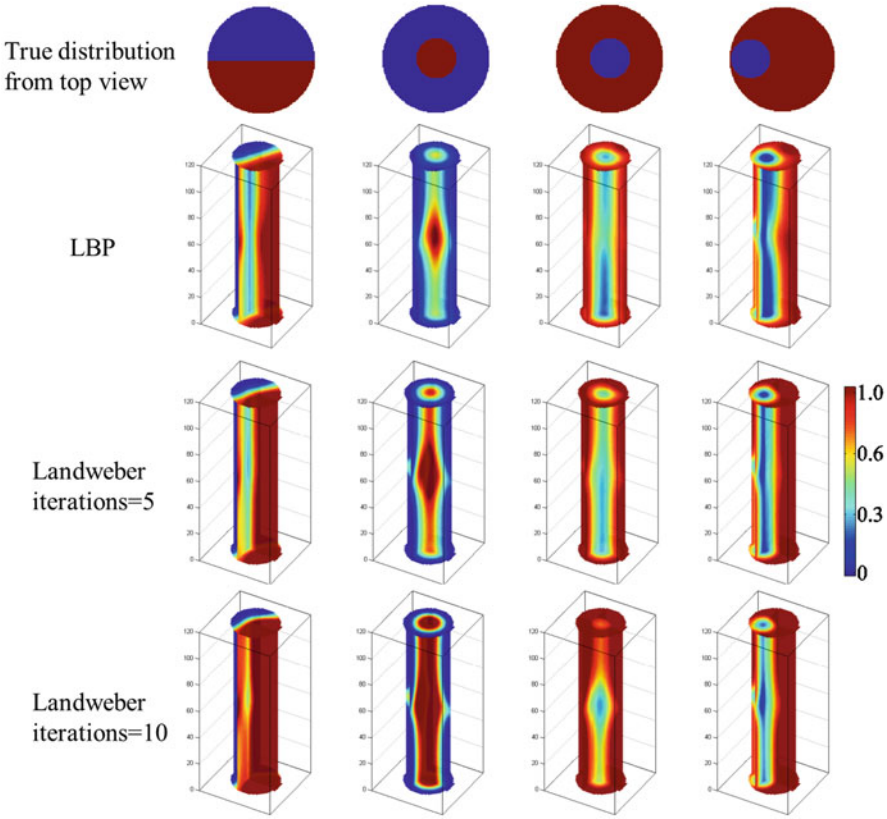

Fig. 6 Image reconstruction for static measurements

image reconstruction performance than LBP method. From the results of Landweber iteration, the image quality of "half" and "core" types are better than "annular" and "near-wall" types. In addition, the image quality turns worse with the iteration number increases from 5 to 10; this is due to the semi-convergence characteristics of Landweber iteration [12]. The *SNR* values in Table 1 show that the noise in present research is very low compared with the ECT sensor in reference [13]. The main source of the noise in ECT measurements is the parasitic capacitance between the shielding (Wurster tube) and electrodes; the static electricity of pellets generated by flow may also affect the capacitance values. Hence, proper grounding and shielding are crucial for the measurement.

It can be concluded that Landweber method with five iterations is the proper option for 3D image reconstruction in this research, and the following dynamic measurements are based on that. More information about the static validation of 3D ECT sensor can be found in reference [9].

Table 1 C_{coef} and *SNR* for static tests

Distribution		Half	Core	Annular	Near wall
C_{coef}	LBP	0.96	0.63	0.68	0.77
	Iterations = 5	0.90	0.86	0.72	0.85
	Iterations = 10	0.73	0.76	0.45	0.56
SNR		50.01	67.56	61.12	59.31

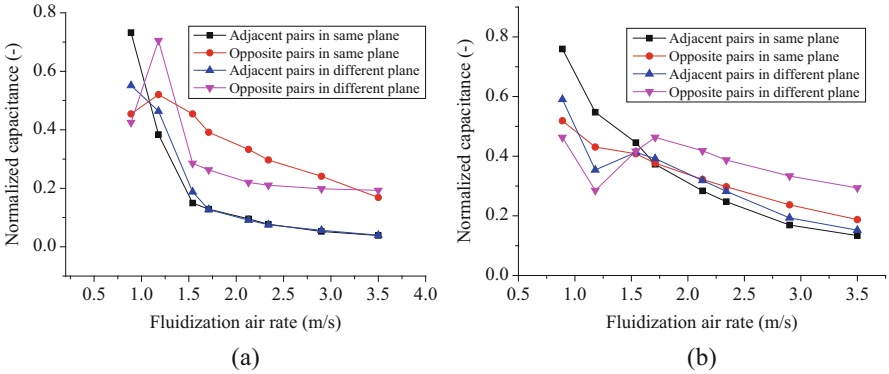

Fig. 7 Normalized capacitances with the air rate. (**a**) $h_{gap} = 10$ mm. (**b**) $h_{gap} = 20$ mm

3.4 Capacitance Analysis in Dynamic Tests

To analyze the measured capacitances of dynamic tests, the capacitances between four types of electrode pairs are selected for comparison, i.e., adjacent electrode pairs in the same plane, opposite electrode pairs in the same plane, adjacent electrode pairs in different planes, and opposite electrode pairs in different planes. For example, the four types of electrodes can be E1–E2, E1–E5, E1–E9, and E1–E13, respectively.

Figure 7 shows the change in normalized capacitances with the airflow rate; the capacitances are the averaged values of the same type. The capacitances decrease with the increase in airflow rate, which is induced by the decrease in the solid concentration inside the sensing region. It should be noted that for the case of $h_{gap} = 10$ mm, the capacitance value from adjacent electrode pairs is obviously lower than the opposite ones, which indicates the near-wall solid concentration decreases more dramatically. This phenomenon is related to the gas-solid flow regime inside the Wurster tube, which will be discussed in the following parts.

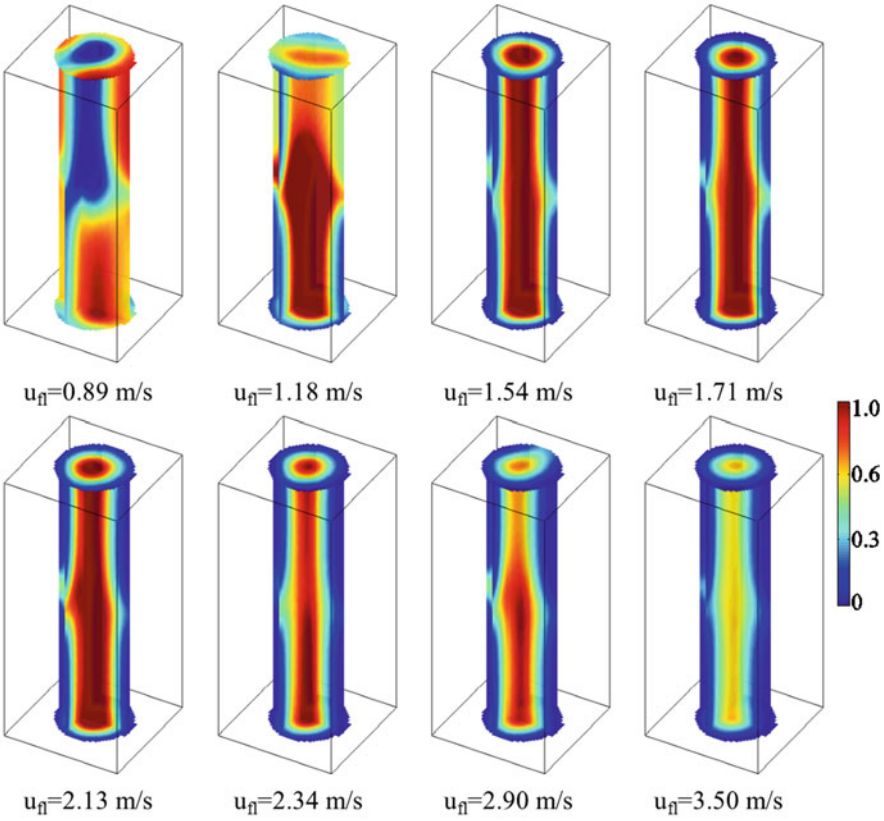

Fig. 8 3D slices of solid distribution with different air rates ($h_{gap} = 10$ mm)

3.5 3D Solid Distribution with Different Operating Conditions

In the bottom of the bed chamber, the particles flow from the annulus zone to the coating zone though the gap between the Wurster tube and air distributor, and thus the height of that gap (h_{gap}) plays an important role for the gas-solid flow inside the Wurster tube. The 3D slices of the solid distribution with the case of $h_{gap} = 10$ mm are given in Fig. 8. As can be seen, for the flow rate of 0.89 and 1.18 m/s, the flow structures are unsteady and difficult to qualify. With the flow rate increased up to 1.71 m/s, the solids are mainly concentrated in the central region of the tube as "core" flow regime. With further increasing the flow rate, the solid concentration decreased gradually, but the flow is still in "core" regime.

Figure 9 shows the 3D slices for the case of $h_{gap} = 20$ mm. Compared with the case of $h_{gap} = 10$ mm, the solid flow is more complex. It can be observed that the flow includes two typical regimes, i.e., the "core" flow regime in the bottom and dispersed flow regimes in the upper.

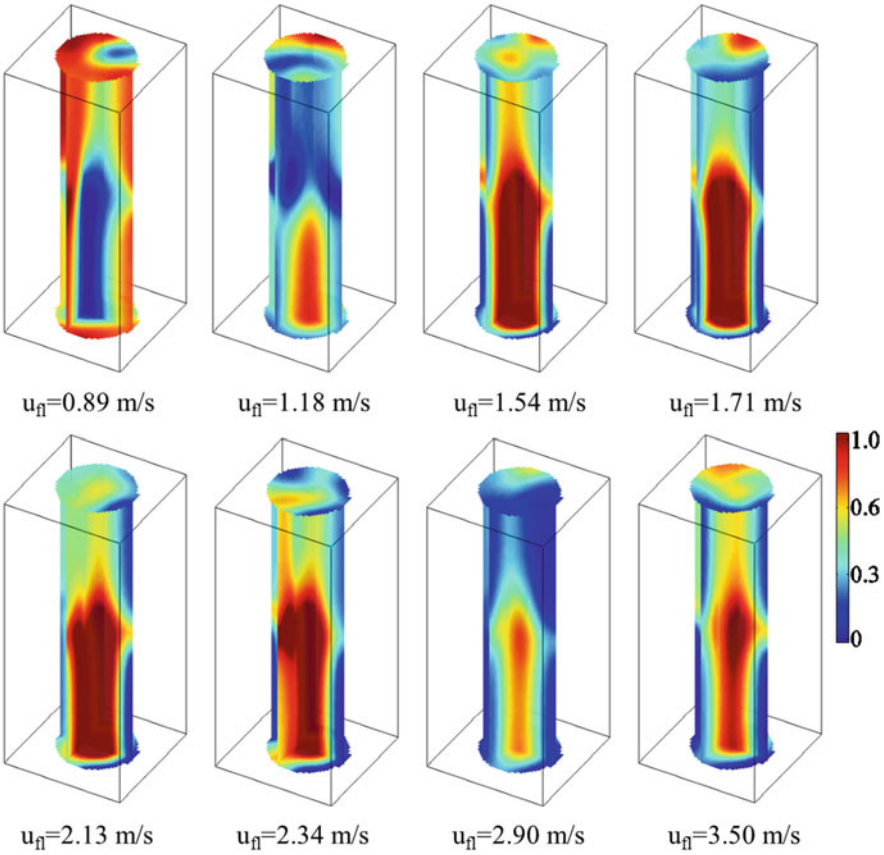

Fig. 9 3D slices of solid distribution with different air rates ($h_{gap} = 20$ mm)

Figure 10 gives the cross-sectional slices in different heights of the Wurster tube. From these slices, it can be clearly seen that the gas-solid flows in the Wurster tube are all initially "core" flow. However, the profile of the "core" of the case of $h_{gap} = 20$ mm is irregular; it is actually in an unsteady state and turns dispersed with further moving upward. In contrast, for the case of $h_{gap} = 10$ mm, the "core" profile is uniform and keeps all through the tube. It should be noted from Fig. 10 that the slices in the middle position of tube are obviously distorted, and the gray level is larger than other slices. It is likely that this feature is image artifacts and not a true representation of the distribution of the solids. One of the possible reasons is the unequal distribution of sensitivity strength in that region [14]. As can be seen from Fig. 4, the sensitivity in that region is induced by the electrodes from different planes, and iso-surfaces are highly distorted.

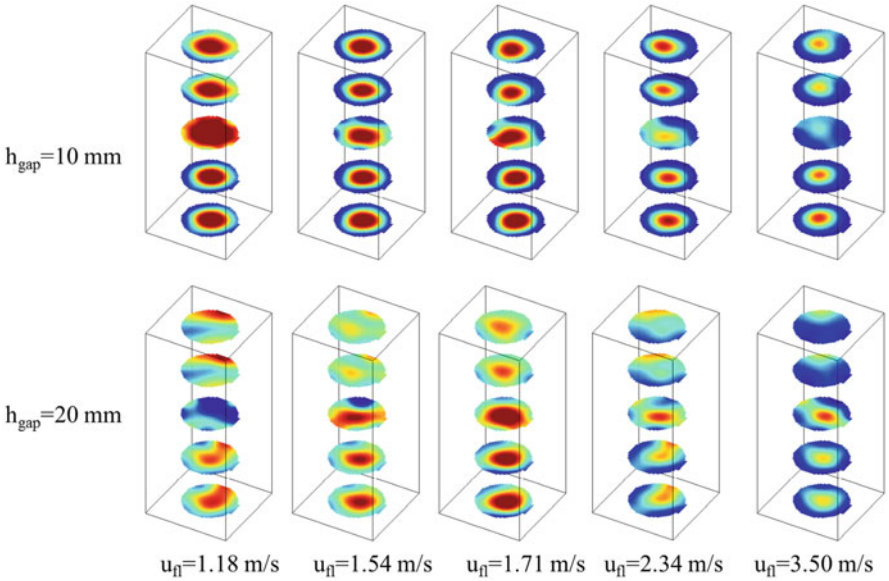

Fig. 10 Cross-sectional slices along the vertical direction of the Wurster tube

3.6 Averaged Solid Concentration

The average solid concentration of β in the measuring region can be calculated based on the reconstructed image from ECT by

$$\beta = \vartheta \cdot \frac{\sum_{i=1}^{N} G_i\,(x, y, z) \cdot \mathrm{vol}_i\,(x, y, z)}{\sum_{i=1}^{N} \mathrm{vol}_i\,(x, y, z)} \tag{12}$$

where vol(*x,y,z*) is the volume of the voxel, N is the total number of voxels in the sensing region, and ϑ is the loosely packed voidage of the solid, and it is estimated to be 0.62.

Figure 11 shows the variation in the average solid concentration with fluidization flow rate. The solid concentration decreases with the increase in the air rate. In addition, the solid concentration for the case of $h_{\mathrm{gap}} = 10$ mm is lower than for the case of $h_{\mathrm{gap}} = 20$ mm. One possible reason is that the smaller gap height blocks the solid flow into the Wurster tube.

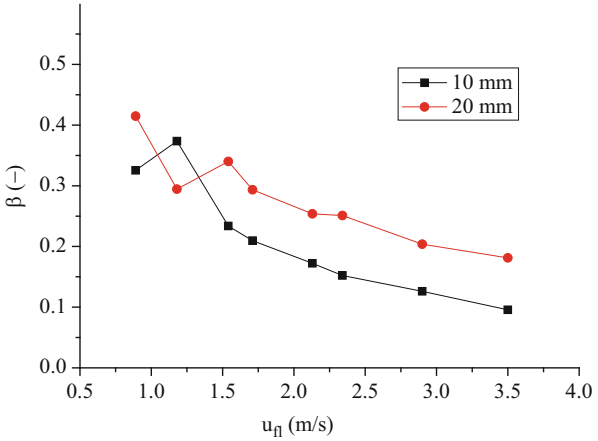

Fig. 11 Averaged solid concentration with different air rates

3.7 Time-Series Properties of Gas-Solid Flow

Figure 12 gives several 3D slice sequences in a continuous period with different operational parameters; the time interval between adjacent images is 1 s. As can be seen from these figures, the gas-solid flow tends to be unstable with the increase of flow rate, i.e., from 1.71 to 3.50 m/s, and the process is easy to control in terms of solid homogeneous distributions.

To quantify the intensity of solid flow fluctuation, the coefficient of variation (CV) of solid concentration of the sensing region is used. The definition of CV is written as

$$\mathrm{CV} = \sqrt{\frac{1}{L-1}\sum_{n=1}^{L}(x(n)-\overline{x})^2/\overline{x}}, \quad \overline{x} = \frac{1}{L}\sum_{n=1}^{L}x(n) \tag{13}$$

where $x(n)$ is the measured time-series concentration signal and L is the length of the signal. Generally, a low CV value would indicate that the flow is steady.

Figure 13 gives the time-series curves of the averaged solid concentration of all experiments. Figure 14 compares the CV value of these cases. The CV increases with the increase of air rate, and the CV for the case of $h_{\mathrm{gap}} = 10$ mm is lower than that for the case of $h_{\mathrm{gap}} = 20$ mm. It can be concluded that the gas-solid fluctuation inside the Wurster tub is enhanced with the h_{gap} changes from 10 mm to 20 mm.

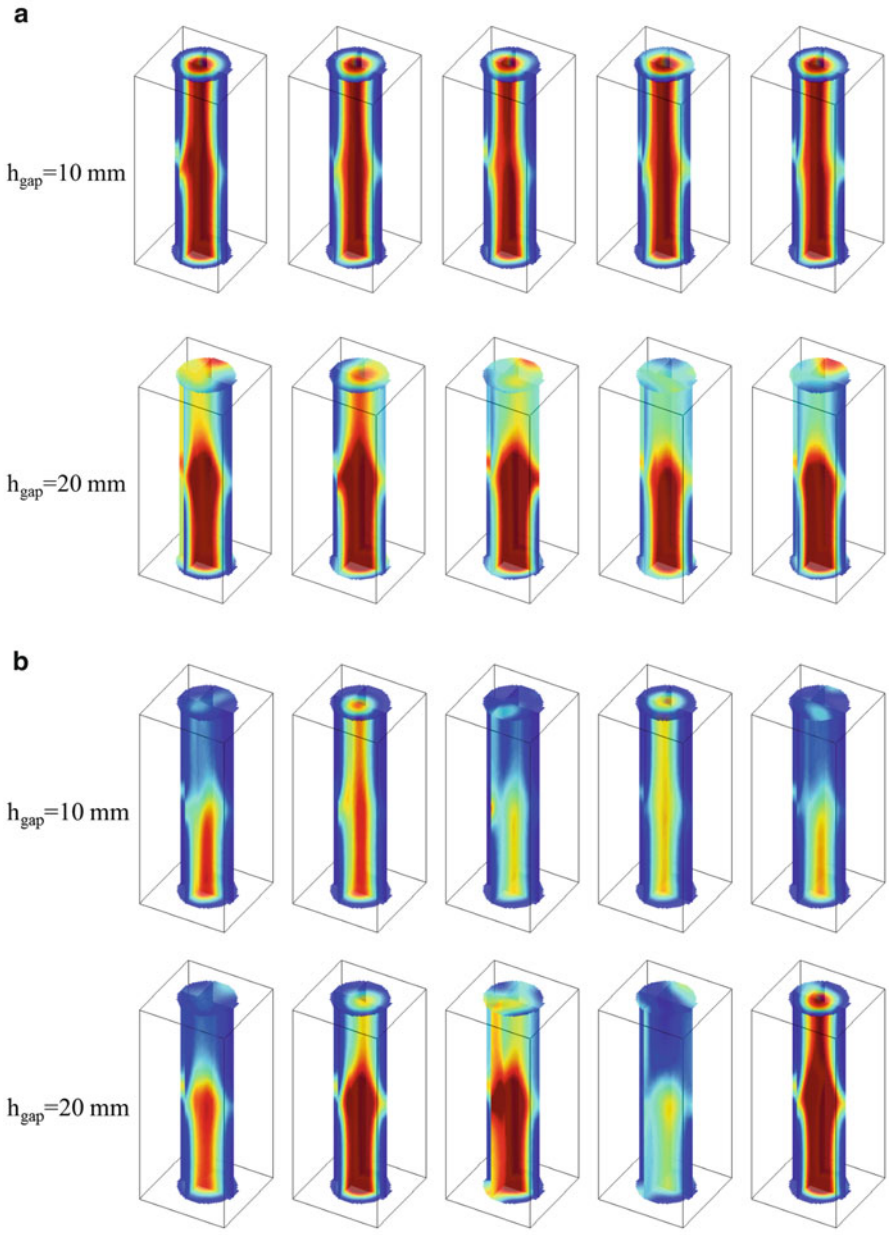

Fig. 12 3D slices of image sequences in a continuous period (the time interval between adjacent images is 1 s). (**a**) $u_{\mathrm{fl}} = 1.71$ m/s. (**b**) $u_{\mathrm{fl}} = 3.5$ m/s

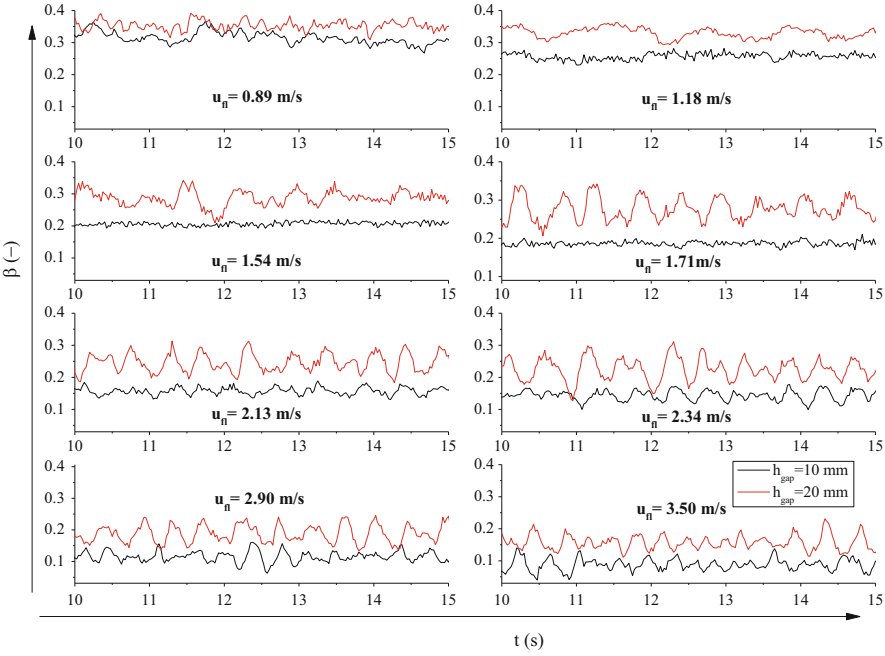

Fig. 13 Variation in the averaged solid concentration with time

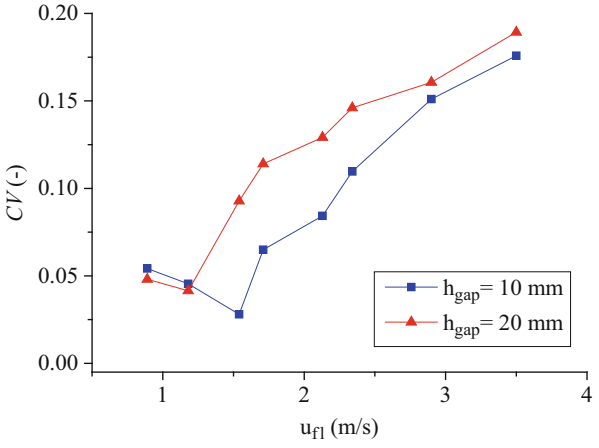

Fig. 14 Comparison of the *CV* values of solid concentration with different cases

4 Conclusion

This paper presents an approach to visualize the 3D gas-solid flow structure inside a Wurster-type fluidized bed using electrical capacitance tomography. The main conclusions are given as follows:

1. The 3D ECT sensor with 16 electrodes in a dual plane is suitable for the visualization of gas-solid flow in a Wurster-type fluidized bed, and the Landweber algorithm is the proper option for 3D image reconstruction.
2. For the case of $h_{\text{gap}} = 10$ mm, the solids are mainly concentrated in the center of the tube, and the distribution keeps all through the tube. For the case of $h_{\text{gap}} = 20$ mm, the gas-solid flow turn dispersed with increase in height.
3. With h_{gap} changes from 10 to 20 mm, the solid concentration in the Wurster tube increases; meanwhile, the gas-solid fluctuation is enhanced.
4. The image quality in the region among electrode planes is low, and it is possibly induced by the unequal distribution of sensitivity strength in that region.

Acknowledgments The authors are grateful for the support from the National Natural Science Foundation of China (Nos. 61320106004 and 61374018) and the CAS Interdisciplinary Innovation Team.

References

1. da Silva CAM, Butzge JJ, Nitz M, Taranto OP (2014) Monitoring and control of coating and granulation processes in fluidized beds–a review. Adv Powder Technol 25(1):195–210
2. Shelukar S, Ho J, Zega J, Roland E, Yeh N, Quiram D, Nole A, Katdare A, Reynolds S (2000) Identification and characterization of factors controlling tablet coating uniformity in a Wurster coating process. Powder Technol 110(1):29–36
3. Yang W (2010) Design of electrical capacitance tomography sensors. Measure Sci Technol 21(4):447–453
4. Ge R, Ye J, Wang H, Yang W (2014) Measurement of particle concentration in a Wurster fluidized bed by electrical capacitance tomography sensors. AICHE J 60(12):4051–4064. https://doi.org/10.1002/aic.14595
5. Wang H, Qiu G, Ye J, Yang W (2016) Experimental study and modelling on gas–solid flow in a lab-scale fluidised bed with Wurster tube. Powder Technol 300. https://doi.org/10.1016/j.powtec.2016.01.025
6. Wang F, Yu Z, Marashdeh Q, Fan L-S (2010) Horizontal gas and gas/solid jet penetration in a gas–solid fluidized bed. Chem Eng Sci 65(11):3394–3408
7. Mao M, Ye J, Wang H, Yang W (2016) Investigation of gas–solids flow in a circulating fluidized bed using 3D electrical capacitance tomography. Meas Sci Technol 27(9):095401
8. Xie C, Huang S, Hoyle B, Thorn R, Lenn C, Snowden D, Beck M (1992) Electrical capacitance tomography for flow imaging: system model for development of image reconstruction algorithms and design of primary sensors. IEE Proceed G-Circuits Dev Syst 139(1):89–98
9. Mao M, Ye J, Wang H, Zhang J, Yang W (2015) Excitation strategy for three-dimensional electrical capacitance tomography sensor. In: 2015 IEEE international conference on imaging systems and techniques (IST). IEEE, pp 1–6
10. Yang WQ, Spink DM, York TA, McCann H (1999) An image-reconstruction algorithm based on Landweber's iteration method for electrical-capacitance tomography. Meas Sci Technol 10(11):1065
11. Liu S, Fu L, Yang WQ (1999) Optimization of an iterative image reconstruction algorithm for electrical capacitance tomography. Measure Technol 10(7):1970–1980
12. Peng L, Merkus H, Scarlett B (2000) Using regularization methods for image reconstruction of electrical capacitance tomography. Part Part Syst Charact 17(3):96–104

13. Wang H, Li Y, Qiu G, Song G, Yang W (2014) Measurement of gas–solids flow in loop seal and external heat exchanger in a circulating fluidized bed. Powder Technol 266:249–261. https://doi.org/10.1016/j.powtec.2014.06.046
14. Warsito W, Marashdeh Q, Fan L-S (2007) Electrical capacitance volume tomography. IEEE Sensors J 7(4):525–535

Investigation the Application of Electrical Capacitance Tomography on Pipe Flow with Thick Wall

Shiguo Liang, Jiamin Ye, Hanqiao Che, and Haigang Wang

1 Introduction

Electrical capacitance tomography (ECT) is a relative mature visualization method applied in industrial process. ECT is attracting increasing attention with respect to the merits compared with other process tomography techniques, such as non-intrusive, non-radiative, and fast imaging speed [1]. ECT is widely used in the measurement of multiphase flow, i.e., gas-solid flow in fluidized beds [2, 3], gas-liquid flow in pipelines [4], and pharmaceutical fluidized bed for pellet coating and drying [5].

There are two challenges in the investigation and application of electrical capacitance tomography in real industry process. The first one is imaging the process with the wall thickness effect. Another one is imaging the process with high permittivity ratio media such as tap water and air. The stray capacitance and ill-posed problem becomes obvious when it comes to thick pipe and high dielectric constant materials. Yang [6] studied the effect of electrode number on ECT sensor with small pipe diameter and thick pipe wall. Based on an eight-electrode sensor on the coal delivery system, the sensitivity maps and image for different flow patterns were analyzed. In [7], ECT sensor was utilized on a bubble column apparatus to research the flow recognition in water.

S. Liang · H. Che · H. Wang
Institute of Engineering Thermophysics, Chinese Academy of Sciences, Beijing, China

University of Chinese Academy of Sciences, Beijing, China

J. Ye (✉)
Institute of Engineering Thermophysics, Chinese Academy of Sciences, Beijing, China
e-mail: yejiamin@iet.cn

M. Jiang et al. (eds.), *The Proceedings of the International Conference on Sensing and Imaging*, Lecture Notes in Electrical Engineering 506,
https://doi.org/10.1007/978-3-319-91659-0_31

The aim of this research is to study the effect of wall thickness on the image quality and sensitivity distribution. Simulation results will be given and analyzed.

2 Principal of ECT

Figure 1 shows the eight-electrode ECT sensor for the current study. The inner diameter of the pipe is 50 mm, and two kinds of pipe thickness are used for comparison, namely, 2 and 12 mm. To investigate the wall thickness effect, the relative pipe thickness is introduced, which represents the ratio of the pipe thickness and the outer radius of the pipe. The ratio is defined as

$$\delta = \frac{R_{\mathrm{o}} - R_i}{R_{\mathrm{o}}} \times 100\%. \tag{1}$$

Thus, the relative pipe thickness is 7.41% for the thin pipe and 32.43% for the thick pipe.

To visualize the objects in the sensing area, the permittivity vector is usually calculated with certain algorithms, the so-called inverse problem in ECT. Linear back project (LBP) [8] is the widely used image reconstruction algorithm, which can be expressed as

$$\mathbf{g} = \mathbf{S}^T \cdot \boldsymbol{\lambda} \tag{2}$$

where $\mathbf{g}$ is the gray level matrix, i.e., the normalized permittivity vector, $\boldsymbol{\lambda}$ is the normalized capacitance vector, and $\mathbf{S}$ is the sensitivity matrix in the sensing area.

With Landweber iteration, the quality of the reconstructed image can be improved. The Landweber iteration algorithm can be expressed as

$$\mathbf{g}^{(n+1)} = \mathbf{g}^{(n)} + \alpha \cdot \mathbf{S}^T \cdot \left(\boldsymbol{\lambda} - \mathbf{S}^T \cdot \mathbf{g}^{(n)}\right) \tag{3}$$

where α is the step length and the superscript n is the iteration number.

The LBP algorithm is non-iterative, simple, fast, and thus appropriate for online image reconstruction. The sensitivity matrix can be calculated as [9],

$$S_{ij}(x, y) = -\int\int_{p(x,y)} \frac{\nabla\varphi_i(x, y)}{V_i} \cdot \frac{\nabla\varphi_j(x, y)}{V_j} \mathrm{dxdy} \tag{4}$$

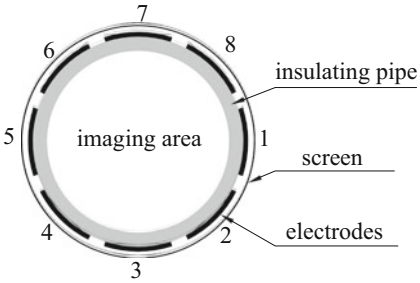

Fig. 1 ECT sensor with eight-electrode

where $S_{i,j}(x,y)$ is the sensitivity value between the ith electrode and the jth electrode in the pixel of (x,y) and $\varphi_i$is the potential distribution when the ith electrode is energized with voltage V_i .

The normalized capacitance vector can be written in the following expression:

$$\boldsymbol{\lambda} = \frac{\mathbf{C}_\mathrm{m} - \mathbf{C}_\mathrm{l}}{\mathbf{C}_\mathrm{h} - \mathbf{C}_\mathrm{l}} \tag{5}$$

where $\mathbf{C}_\mathrm{m}$ is the measurement capacitance and $\mathbf{C}_\mathrm{h}$ and $\mathbf{C}_\mathrm{l}$ represent the calibration capacitances when the pipe is filled with high permittivity and low permittivity medium, respectively.

3 Results and Analysis

The capacitance and sensitivity are two key factors for image reconstruction. In the following parts, the analysis of capacitance and sensitivity will be given and analyzed.

3.1 Capacitance

Figure 2 shows the capacitance distribution for annular flow distribution, where C_h is the capacitance when the sensor is filled with high permittivity media, C_l with low permittivity media, C_m the annular flow pattern, and $\boldsymbol{\lambda}$ is the normalized capacitance. Figure 2a, b is the capacitances for the relative pipe thickness of 7.41%. For the sensor with thin pipe, the measurement result indicates that the C_m is between C_h and C_l, except the capacitance for adjacent electrodes, i.e., those above 15 pF. For the sensor with relative pipe thickness of 32.43%, C_l is higher than that of high permittivity media. The results clearly show the difference between the thick and thin pipe.

3.2 Sensitivity Analysis

Figure 3 shows the sensitivity maps of different electrodes for the sensor with the relative pipe thickness of 7.41% and 32.43%, respectively. It is clear that the sensor with thin wall has higher sensitivity than that with thick wall. The sensitivity maps among different electrodes both for thin and thick wall have the same distributions, i.e., high sensitivity closed to the wall region and low value in the central area.

To further compare the differences of the sensitivity in the sensor with thin and thick wall, the sensitivity values along the dimensionless radial position (i.e., r/R) of the sensor are given in Fig. 4. In Fig. 4, the value of 0.5 indicates in the center, and 0, 1 indicate the positions closed to the wall.

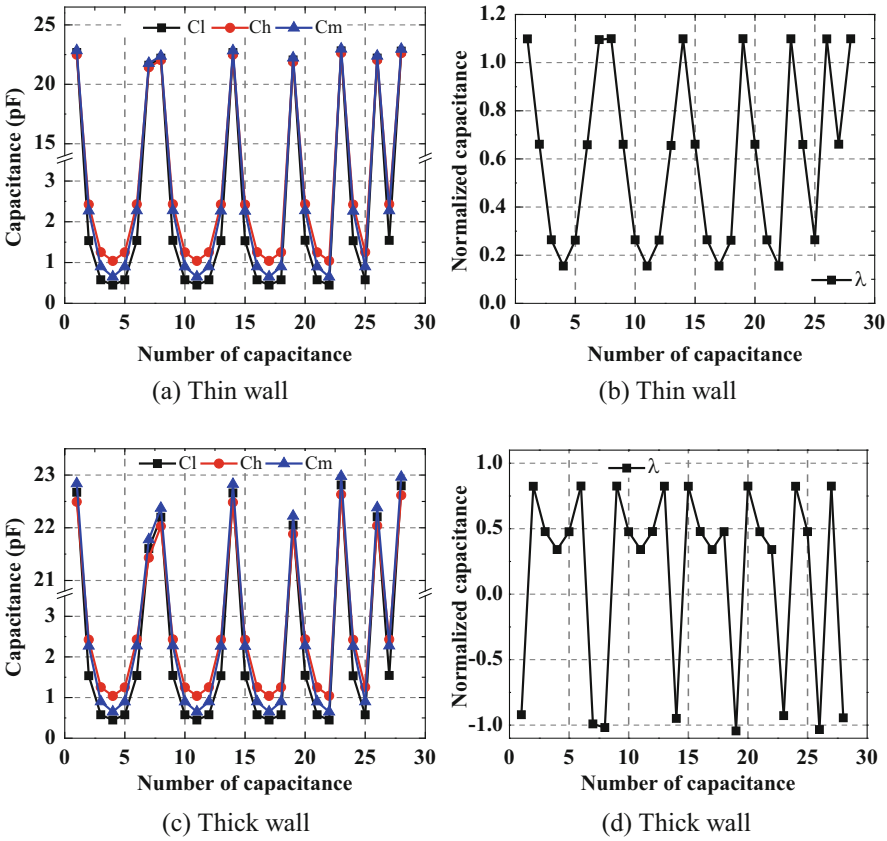

Fig. 2 Capacitances of annular flow distribution. (**a**) Thin wall. (**b**) Thin wall. (**c**) Thick wall. (**d**) Thick wall

For the sensitivity of adjacent electrodes, i.e., $S_{1,2}$, along the radial position, the sensitivity value with thick wall is lower than that with thin wall for the position far from the electrode (0–0.8), while for the position near the electrode (0.8–1), sensitivity value with thick wall is higher than that with thin wall. In other words, the area near the electrodes is more sensitive for the sensor with thick wall.

For $S_{1,3}$, the radial position is smaller than 0.87, the sensitivity value of sensor with thin wall is higher, after 0.87, the value goes down so rapidly that it is lower than the sensitivity value of sensor with thick wall.

For the sensitivity of opposite electrodes, $S_{1,5}$, along the x direction, the sensitivity value is minimum at the radial position of 0.5, which means the core area of the sensor is less sensitive. Besides, it can be seen in the Fig. 4c that the sensitivity value of sensor with thin wall is larger than thick wall in x direction. Yet, along the y direction, the sensitivity value is maximum at the radial position of 0.5.

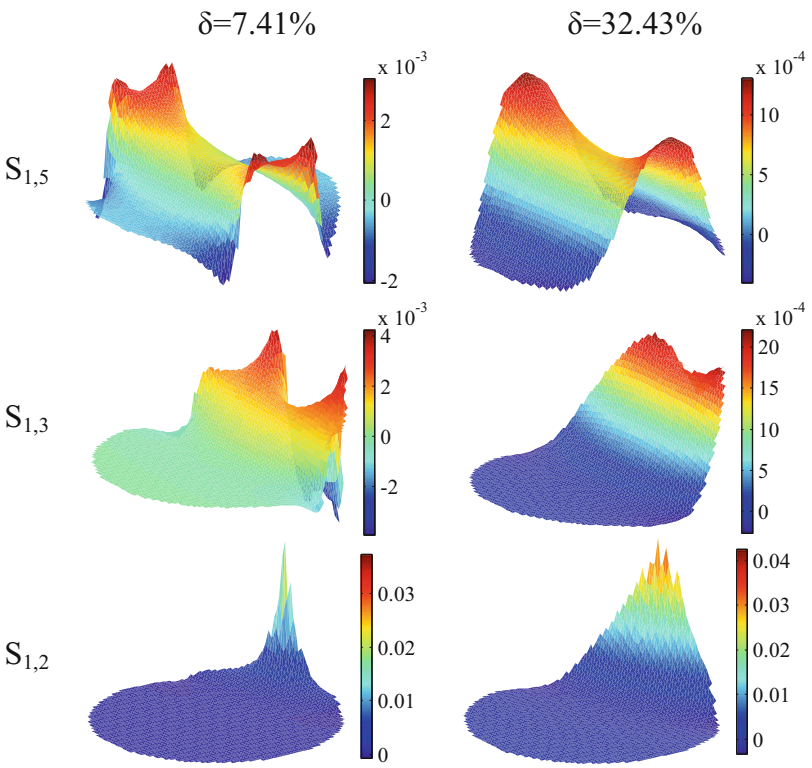

Fig. 3 Sensitivity maps for the sensor with thin and thick wall

3.3 Image Reconstruction

Figure 5 shows the real distribution of flow patterns and the corresponding reconstructed images for 7.41% and 32.43% thick pipe. It is noted that the capacitances with adjacent electrodes are rejected. The flow patterns are annular flow, bubbly flow, core flow, and stratified flow, represented and named as AF, BF, CF, and SF accordingly.

It can be seen from Fig. 5 that the reconstructed images of four flow patterns can reflect the real distributions well for the sensor with the relative pipe thickness of 7.41%. However, for the sensor with the relative pipe thickness of 32.43%, the images are seriously distorted, only the stratified flow can be reconstructed properly.

The capacitance distributions indicate that there is great difference between the thin and thick wall for the adjacent electrodes. One possible method is to reject the adjacent measurements of capacitance, and the reconstructed images are given in Fig. 5, as well.

It can be seen from Fig. 5 that the quality of the reconstructed images has been improved compared to the image in sensor with relative pipe thickness of 32.43%.

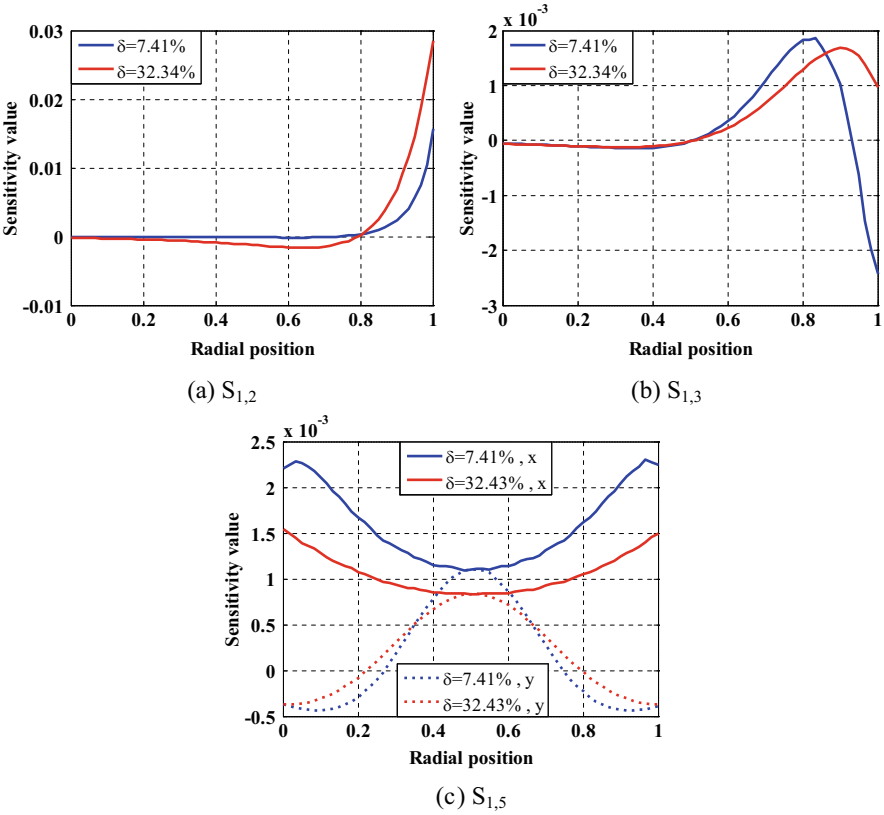

(a) $S_{1,2}$ (b) $S_{1,3}$

(c) $S_{1,5}$

Fig. 4 Sensitivity values on radial position of (**a**) $S_{1,2}$, (**b**) $S_{1,3}$, and (**c**) $S_{1,5}$

However, in terms of image reconstruction and normalized capacitance method, it needs to be investigated further to give high-quality images for the application of ECT in real industry pipeline process with thick wall.

Figure 6 shows that the images reconstructed with Landweber get improved for most images for both the thin wall and thick wall, compared with the images reconstructed with LBP. Besides, for the sensor with thickness of 32.43%, the images without adjacent capacitance are better than those with adjacent capacitance.

3.4 Relative Image Error

Figure 7 shows the relative image error of the four flow patterns compared to the real distributions. As shown in Fig. 7, the relative image error for the pipe of 32.43% is 40–60% larger than that of 7.41%. Except the stratified flow, the relative image

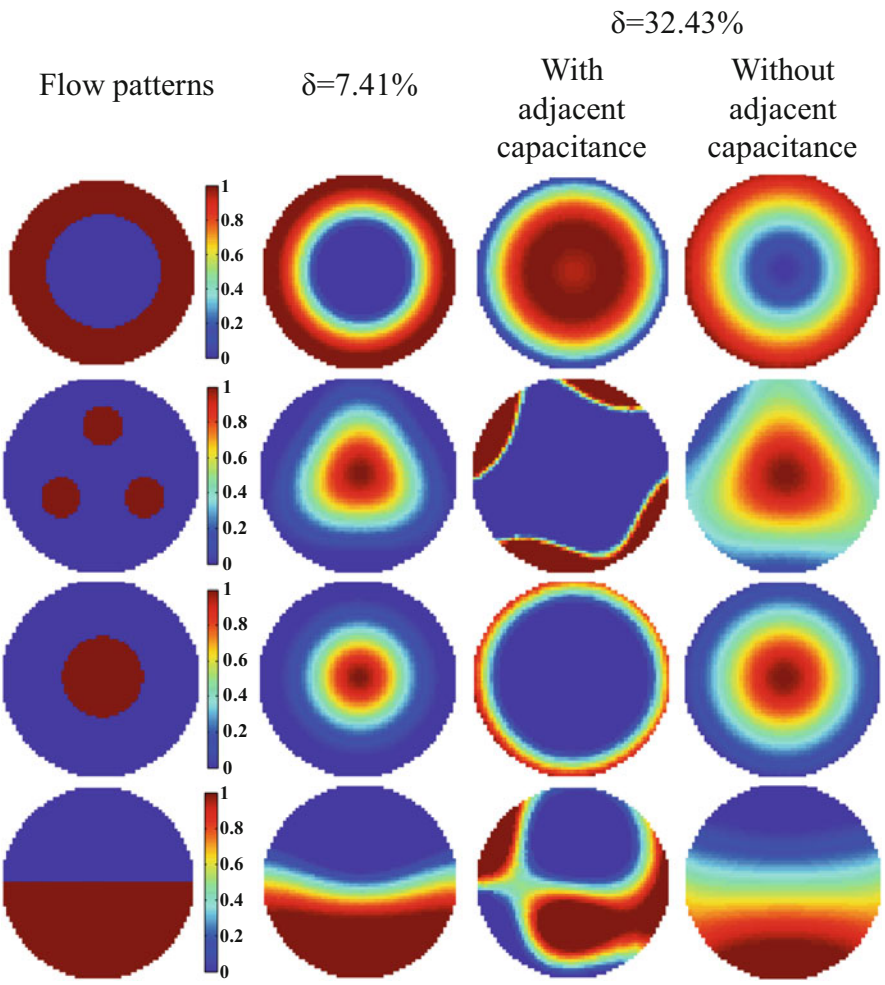

Fig. 5 Image reconstructed with LBP for different flow patterns

errors are 80% for the thick pipe. After the rejection of the adjacent capacitance, the relative image error drops 18–40%.

Figure 8 is the relative image error of the images reconstructed with Landweber. It can be seen that the relative image error is smaller when the Landweber algorithm is used, especially for the sensor with thickness of 32.43%. The error can also drop down when the adjacent capacitance is rejected.

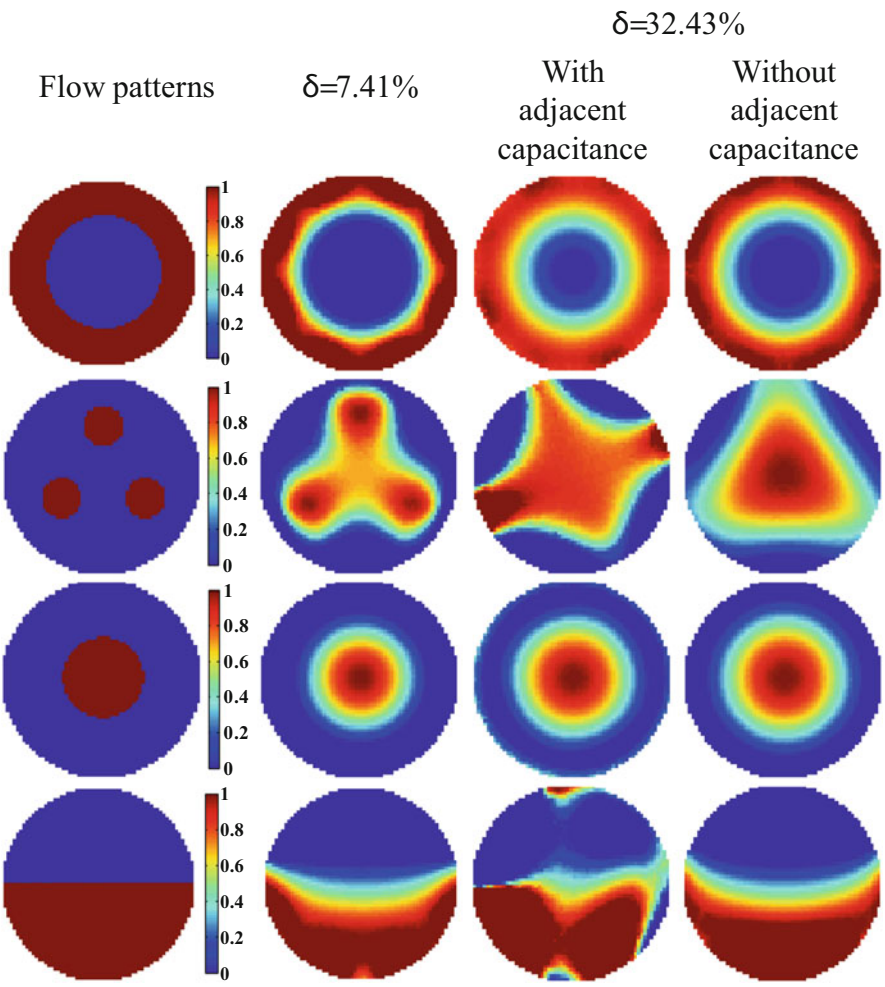

Fig. 6 Image reconstruction with Landweber for different flow patterns

4 Conclusions

This paper presents the application of electrical capacitance tomography in the pipe with the relative wall thickness of 7.41% and 32.43%. The research is based on numerical simulation. The flow patterns used for the simulation include annular flow, bubbly flow, core flow, and stratified flow. From the capacitance analysis of the annular flow, the main difference of capacitance in thick pipe is the adjacent capacitances. For 32.43% thick pipe, the low calibration capacitance is larger than the high calibration capacitance, which leads to the negative value of normalized capacitance. From the sensitivity analysis, it can be seen that the sensitivity maps in

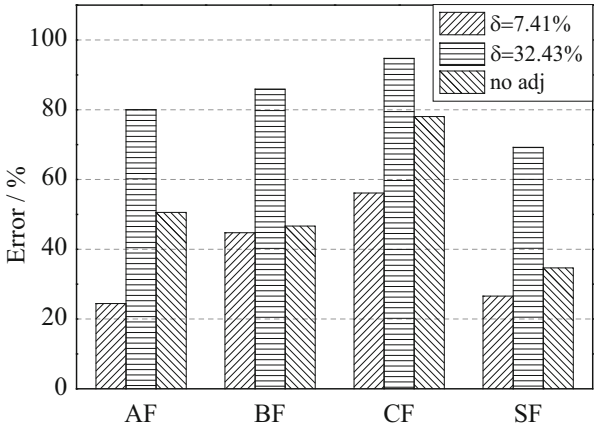

Fig. 7 Relative image error of the images reconstructed with LBP for different flow patterns

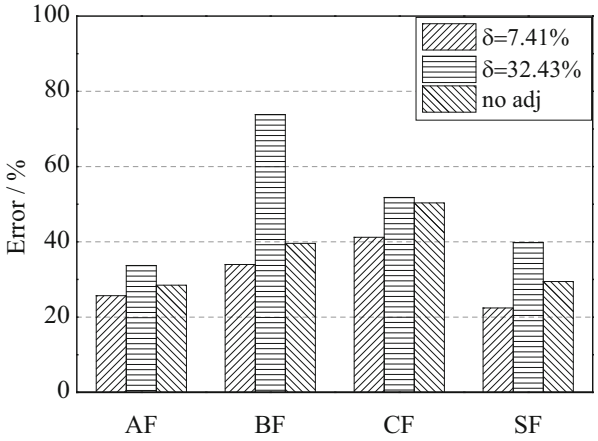

Fig. 8 Relative image error of the images reconstructed with Landweber for different flow patterns

the thick pipe are less sharp. The quality of image reconstructed in thin pipe is high, while the images in thick pipe are seriously distorted. The reconstructed images are improved greatly without the adjacent capacitance. The relative image error drops 18–40% compared the image reconstructed from full measured capacitance, when LBP is used for reconstruction.

Acknowledgments The National Natural Science Foundation of China (No. 61374018) is thanked for supporting this work.

References

1. Yang W (2010) Topical review: design of electrical capacitance tomography sensors. Measure Sci Technol 21:1–13
2. Liu S, Chen Q, Wang HG, Jiang F, Ismail I, Yang WQ (2005) Electrical capacitance tomography for gas-solids flow measurement for circulating fluidized beds. Flow Meas Instrum 16:135–144
3. Wang C, Lv Z, Li D (2008) Experimental study on gas–solids flows in a circulating fluidised bed using electrical capacitance tomography. Powder Technol 185(2):144–151
4. Ismail I, Gamio JC, Bukhari SFA, Yang WQ (2005) Tomography for multi-phase flow measurement in the oil industry. Flow Measure Instrument 16(2):145–155
5. Wang H, Yang W (2011) Scale-up of an electrical capacitance tomography sensor for imaging pharmaceutical fluidized beds and validation by computational fluid dynamics. Measure Sci Technol 22(10):104015
6. Yang DY, Zhou B, Xu CL, Wang SM (2011) Thick-wall electrical capacitance tomography and its application in dense-phase pneumatic conveying under high pressure. IET Image Process 5(5):513–522
7. Bennett MA, Luke SP, Jia X, West RM, Williams RA (1999) Analysis and flow regime identification of bubble column dynamics. In: Proc. of 1st world congress on industrial process tomography, Buxton, 14–17 April, vol 1999, pp 54–61
8. Xie CG, Huang SM, Hoyle BS, Thorn R (1992) Electrical capacitance tomography for flow imaging: system model for development of image reconstruction algorithms and design of primary sensors. Circ Dev Syst Iee Proceed G 139(1):89–98
9. Liu S, Yang WQ, Wang H, Jiang F, Su Y (2001) Investigation of square fluidized beds using capacitance tomography: preliminary results. Measure Sci Technol 12(12):1120

A New Method for Differential Phase-Contrast Imaging Without Phase Stepping

Jingzheng Wang and Jian Fu

1 Introduction

X-ray imaging is a popularly utilized tool in medical diagnosis and industrial nondestructive testing. X-ray imaging, with the absorbing information of the materials, cannot get good contrast when the sample is composed of elements of low atomic number, like soft tissues and organic materials. As X-rays are phase-shifted more than absorbed, phase information of these materials can further improve the imaging contrast [1–3]. So far, there are five common methods to retrieve phase information, namely, crystal interferometer-based imaging [4], propagation-based imaging [5, 6], diffraction-enhanced imaging [2, 7], grating-based interferometer imaging [8] (GBI), and speckle-based imaging [9, 10].

Grating-based interferometer imaging, which is also commonly called differential phase-contrast imaging (DPCI), has attracted many investigators in the recent years [11–22]. Conventional DPCI needs phase stepping procedure to retrieve the phase information, which is costing too much time during the scanning. Yongshuai Ge designed a new grating to replace the conventional absorption grating [23], which can achieve a single-shot image without phase stepping. Peiping Zhu used a method called "reverse projection" to acquire phase signal without phase stepping [24], but it needs the sample to rotate to a symmetrical position for resampling. Zanette demonstrated a method called interlaced stepping, which combined CT

J. Wang
School of Mechanical Engineering and Automation, Beihang University, Beijing, China

J. Fu (✉)
School of Mechanical Engineering and Automation, Beihang University, Beijing, China

Research center of Digital Radiation Imaging, Beihang University, Beijing, China
e-mail: fujian706@buaa.edu.cn

M. Jiang et al. (eds.), *The Proceedings of the International Conference on Sensing and Imaging*, Lecture Notes in Electrical Engineering 506,
https://doi.org/10.1007/978-3-319-91659-0_32

rotation step and phase step to reduce the scanning time [25]. Xin Liu proposed a method that needs movement of the phase grating [26]. It needs twice the movement of the phase grating and can easily retrieve the phase signal with good spatial resolution.

In this work, we present another solution to retrieve phase signal of the sample without phase stepping by designing a new absorption grating. Each column is the same as the conventional one, but it is shifted between adjacent columns. An experimental data supports this idea.

2 Methods

2.1 Configurations

This method we implement is based on the Talbot-Lau-type interferometer. Figure 1a depicts the DPCI setup of the conventional method. An X-ray beam generated by a laboratory tube is separated by grating G0 as several coherent linear X-ray sources. All X-ray beams penetrate the sample and then go through the phase grating G1 and the absorption grating G2. Finally, an X-ray pattern is recorded by the detector that is behind the G2. During this process, the G2 need to be moved M times transversely, which is called phase stepping procedure. And the detector captures projections after each movement of the G2 (Fig. 1c).

Figure 1b shows the configuration of the proposed method, which is almost the same in the setup as the conventional method. The only difference between these two methods is the G2. The proposed method just needs exposure once without phase stepping by using a new absorption grating G2 we designed (Fig. 1e), whereas the conventional method needs exposure several times with the phase stepping procedure at the G2.

2.2 New Grating Design

The main idea of this new grating is that intensity of four adjacent pixels in a row of a detector can be considered as the intensity of one detector's pixel in four different phase stepping positions of the normal G2, which means it only needs one exposure to retrieve phase-contrast signal. Any two adjacent grating columns have a relative offset of d, where d is $1/M$ of g2 and g2 is the period of absorption grating ($M = 4$ in this work). There are four pixels in the new G2 as an example, and pixel NO. i ($i = 1, 2, 3, 4$) in new grating is the same as in normal G2 in position NO. i. If considering the similarity among the intensity of these four adjacent pixels, then, pixel NO. i of new grating is the same as pixel NO. i of normal grating in position NO. i ($i = 1, 2, 3, 4$). It can be described mathematically as Eqs. 1–4:

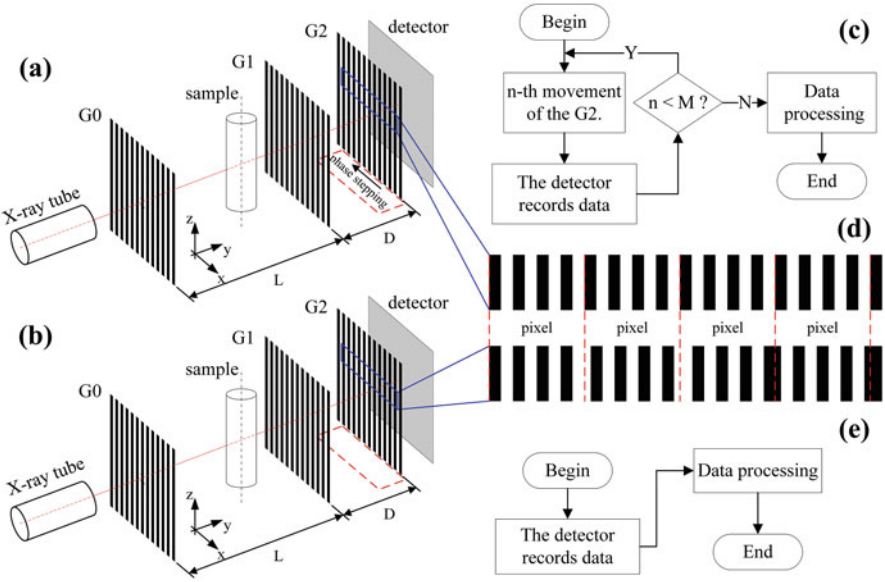

Fig. 1 DPCI configurations. (**a**) Shows the configuration of the conventional method, which needs a phase stepping procedure. (**b**) Shows the configuration of the proposed method, which does not need a phase stepping procedure by using a new grating. (**c**) Shows the phase retrieval steps of the conventional method. (**d**) Shows the grating comparison between the conventional method and the proposed method. (**e**) Shows the phase retrieval steps of the proposed method

$$I_1(x, z) = I(x - 1, z), \tag{1}$$

$$I_2(x, z) = I(x, z), \tag{2}$$

$$I_3(x, z) = I(x + 1, z), \tag{3}$$

$$I_4(x, z) = I(x + 2, z), \tag{4}$$

where I with subscript is intensity in four different positions in the conventional method and I without subscript is the original intensity of single-shot image taken from detector by the proposed method. Then, using the Fourier analysis method [23, 27, 28] to retrieve the phase-contrast signal.

For example, if there is a single-shot image captured by the detector, then we pick up four adjacent pixels in a row, marked as (a), (b), (c), and (d). Thus, these four pixels' values can be regarded as four values of pixel (b) in four different positions in the conventional method by Eqs. (1)–(4). Next, do signal extract procedure by a normal way. In addition, this method is just like a template, which slides in a row, and each pixel's phase signal can be calculated.

3 Experiments

An experiment was implemented by the conventional method. The image size is 307×652. The grating is stepped four times. The heights and periods of the grating structures were 35 and 10 μm for the source grating G0, 40 and 3.2 μm for the phase grating G1, and 25 and 4.8 μm for the analyzer grating G2, respectively. The source grating was placed 31 mm from the X-ray tube. The distance between G0 and G1 was 300 mm, whereas G1 and G2 were 145 mm apart, corresponding to the first fractional Talbot distance.

Due to the lack of designed grating, the acquired projection by the proposed method is made from the projections captured by the conventional method, which makes the projection perform like captured by using new grating, so that new grating we demonstrated can replace the phase stepping in the conventional method. We assume that the four projections in conventional method are marked as P_0, P_1, P_2, and P_3, and the projection in proposed method is marked as P_{new}. Then we set the value in column c of proposed projection to j-th projection of conventional method in the same position, where j is the remainder of c/4. This procedure can be mathematically described as:

$$P_{\text{new}}(x, z) = P_c(x, z), c = x \bmod 4, (x = 0, 1, 2, \ldots, W), \tag{5}$$

where W is the width of the projection and c refers to which projection in the conventional method.

And based on the projection image, we can extract signals shown in Fig. 2. The results of proposed method successfully show the structure of the sample compared with the conventional method. The intensity profile along the red line marked in Fig. 2 was plotted in Fig. 3, which shows the phase intensity of proposed method is along the conventional method. It proves that the image retrieved by proposed method is corresponding to conventional method. Furthermore, the proposed method provides a highly efficient way to retrieve phase-contrast images.

4 Conclusion

In this work, we demonstrate a new method by designing a new absorption grating, which effectively extracts the signals of sample and greatly reduces the exposure time and radiation dose as well. The experiment data in this work is taken from the conventional method, which can prove our idea in the rough. As the feasibility of the proposed method is proved, a proposed grating needs to be made, and another experiment using new grating needs to be carried out in the later work.

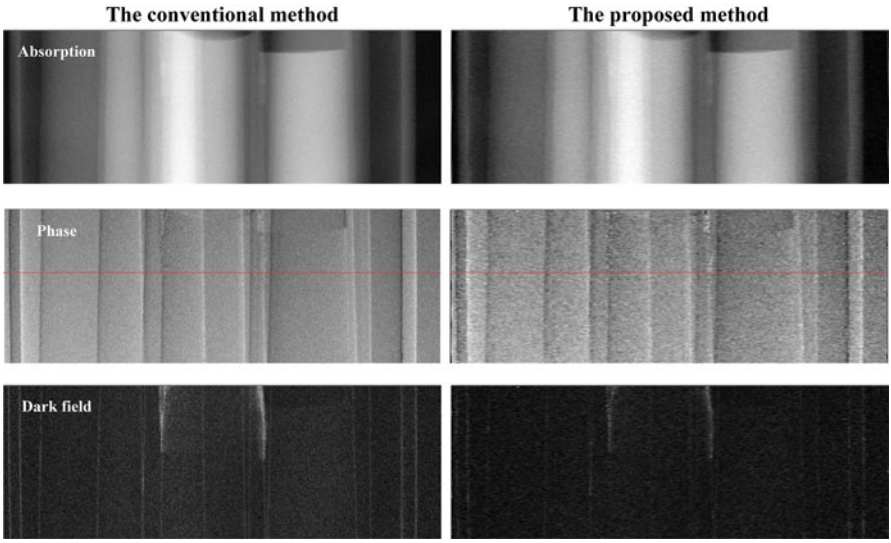

Fig. 2 Experiment results. Three signals of sample by the two methods

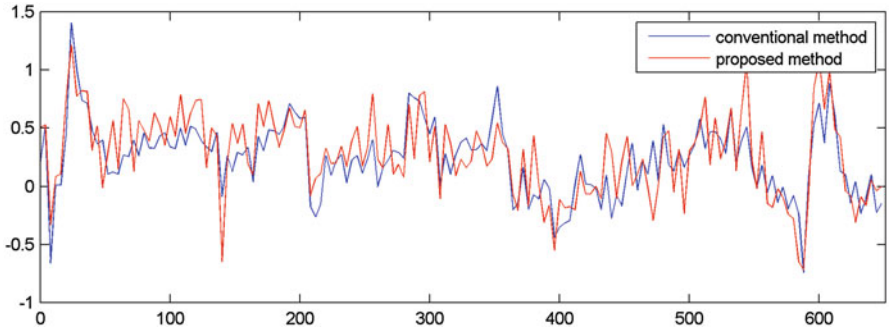

Fig. 3 Intensity profiles along the red lines in Fig. 2

Acknowledgments This work is supported by National Natural Science Foundation of China – Joint Scientific Fund Project of Chinese Academy of Sciences (No. 11179009, U1432101, 11574023), Beijing Natural Science Foundation Project (No.7152088), and Ministry of Education New Century Excellent Talents Program (No. NCET-13-0022).

References

1. Wilkins SW, Gureyev TE, Gao D, Pogany A, Stevenson AW (1996) Phase-contrast imaging using polychromatic hard X-rays. Nature 384(6607):335–338
2. Thomlinson W, Chapman D, Zhong Z, Johnston RE, Sayers D (1997) Diffraction enhanced x-ray imaging. Phys Med Biol 42(11):2015–2025

3. David C, Nohammer B, Solak HH, Ziegler E (2002) Differential x-ray phase contrast imaging using a shearing interferometer. Appl Phys Lett 81(17):3287–3289
4. Momose A (1995) Demonstration of phase-contrast X-ray computed tomography using an X-ray interferometer. Nucl Instr Meth Phys Res 352(3):622–628
5. Snigirev A, Snigireva I, Kohn V, Kuznetsov S, Schelokov I (1995) On the possibilities of x-ray phase contrast microimaging by coherent high energy synchrotron radiation. Rev Sci Instrum 66(12):5486–5492
6. Huang ZF, Kang KJ, Li Z, Zhu PP, Yuan QX, Huang WX, Wang JY, Zhang D, Yu AM (2006) Direct computed tomographic reconstruction for directional-derivative projections of computed tomography of diffraction enhanced imaging. Appl Phys Lett 89(4):041124 - 041124-041123
7. Dilmanian FA, Zhong Z, Ren B, Wu XY, Chapman LD, Orion I, Thomlinson WC (2000) Computed tomography of x-ray index of refraction using the diffraction enhanced imaging method. Phys Med Biol 45(4):933–946(914)
8. Weitkamp T, Diaz A, Nohammer B, Pfeiffer F, Rohbeck T, Cloetens P, Stampanoni M, David C (2004) Hard x-ray phase imaging and tomography with a grating interferometer. In: SPIE international symposium on optical science and technology, pp 626–630
9. Zanette I, Zhou T, Burvall A, Lundström U, Larsson DH, Zdora M, Thibault P, Pfeiffer F, Hertz HM (2014) Speckle-based x-ray phase-contrast and dark-field imaging with a laboratory source. Phys Rev Lett 112(25):253903–253903
10. Zhou T, Zanette I, Zdora MC, Lundström U, Larsson DH, Hertz HM, Pfeiffer F, Burvall A (2015) Speckle-based x-ray phase-contrast imaging with a laboratory source and the scanning technique. Opt Lett 40(12):2822–2825
11. Pfeiffer F, Weitkamp T, Bunk O, David C (2006) Phase retrieval and differential phase-contrast imaging with low-brilliance X-ray sources. Nat Phys 2(4):258–261. https://doi.org/10.1038/nphys265
12. Chen GH, Qi Z (2008) Image reconstruction for fan-beam differential phase contrast computed tomography. Phys Med Biol 53(4):1015–1025
13. M B THJ, R Fl OB, C D FP (2009) Soft-tissue phase-contrast tomography with an x-ray tube source. Phys Med Biol 54(9):2747–2753
14. Fu J, Hu X, Velroyen A, Bech M, Jiang M, Pfeiffer F (2015) 3D algebraic iterative reconstruction for cone-beam x-ray differential phase-contrast computed tomography. PLoS One 10(3):e0117502
15. Fu J, Li P, Wang QL, Wang SY, Bech M, Tapfer A, Hahn D, Pfeiffer F (2011) A reconstruction method for equidistant fan beam differential phase contrast computed tomography. Phys Med Biol 56(14):4529–4538
16. Fu J, Schleede S, Tan R, Chen L, Bech M, Achterhold K, Gifford M, Loewen R, Ruth R, Pfeiffer F (2012) An algebraic iterative reconstruction technique for differential X-ray phase-contrast computed tomography. Z Med Phys 23(3):186–193
17. Fu J, Velroyen A, Tan R, Zhang J, Chen L, Tapfer A, Bech M, Pfeiffer F (2012) A reconstruction method for cone-beam differential x-ray phase-contrast computed tomography. Opt Express 20(19):21512–21519
18. Fu J, Biernath T, Willner M, Amberger M, Meiser J, Kunka D, Mohr J, Herzen J, Bech M, Pfeiffer F (2014) Cone-beam differential phase-contrast laminography with x-ray tube source. Epl 106(6):68002
19. Fu J, Chen L (2014) Single-slice reconstruction method for helical cone-beam differential phase-contrast CT. Biomed Mater Eng 24(1):45–51
20. Fu J, Tan R, Chen L (2014) Analysis and accurate reconstruction of incomplete data in X-ray differential phase-contrast computed tomography. Anal Bioanal Chem 406(3):897–904
21. Fu J, Willner M, Chen L, Tan R, Achterhold K, Bech M, Herzen J, Kunka D, Mohr J, Pfeiffer F (2014) Helical differential X-ray phase-contrast computed tomography. Phys Med 30(3):374–379
22. Fu J, Hu X, Li C (2015) X-ray differential phase-contrast tomographic reconstruction with a phase line integral retrieval filter. Nucl Instr Meth Phys Res 778:14–19

23. Ge Y, Li K, Garrett J, Chen GH (2014) Grating based x-ray differential phase contrast imaging without mechanical phase stepping. Opt Express 22(12):14246–14252
24. Zhu P, Zhang K, Wang Z, Liu Y, Liu X, Wu Z, Mcdonald SA, Marone F, Stampanoni M (2010) Low-dose, simple, and fast grating-based X-ray phase-contrast imaging. Proc Natl Acad Sci 107(31):13576–13581
25. Zanette I, Weitkamp T (2012) Trimodal low-dose X-ray tomography. Proc Natl Acad Sci U S A 109(26):10199–10204
26. Liu X, Guo J-C, Lei Y-H, Li J, Niu H-B (2016) Simple phase extraction in x-ray differential phase contrast imaging. Chinese Phys B 25(2). https://doi.org/10.1088/1674-1056/25/2/028704
27. Bech M (2009) X-ray imaging with a grating interferometer. Neils Bohr Institute – University of Copenhagen:35–42
28. Hahn D (2014) Statistical iterative reconstruction for X-ray phase-contrast computed tomography. Technische Universität München:22–25

Automatic Liver Tumor Segmentation Based on Random Forest and Fuzzy Clustering

Jun Ma, Yuanqiang Li, Yuli Wu, Menglu Zhang, Jian He, Yudong Qiu, and Xiaoping Yang

1 Introduction

Accurate segmentation of the primary or secondary liver tumor in computed tomography (CT) has been an essential step to create precise liver tumor models for pre-procedural planning and precise treatment. Nowadays, two kinds of approaches have been mainly used in clinical workflow. One kind of approaches is manual segmentation. Although this method is relatively reliable, it is very labor-intensive to manually segment the whole slices of 3D CT images, and the segmentation results are subject to inter- and intra-observer variability. The other kind of approaches is interactive or semiautomatic segmentation. But the user assistance is still time-consuming for CT images with multiple tumors. Automatic segmentation is the most promising technique to handle the above problems. However, implementation of accurate and robust automatic segmentation for 3D liver CT datasets is challenging because of the high anatomical variability in patients, low signal-to-noise ratios, and similar intensities between targets and backgrounds (especially in non-contrast-enhanced CT images).

Almost all of existing methods typically employed semiautomatic methods for liver tumor segmentation. Häme et al. proposed a semiautomatic framework based on nonparametric intensity distribution estimation and a hidden Markov measure

J. Ma (✉) · Y. Li · Y. Wu · M. Zhang · X. Yang (✉)
Department of Mathematics, Nanjing University of Science and Technology, Nanjing, China
e-mail: junma@njust.edu.cn; yangxp@mail.njust.edu.cn

J. He
Department of Radiology, Nanjing Drum Tower Hospital, Nanjing, China

Y. Qiu
Department of Hepatopancreatobiliary Surgery, Nanjing Drum Tower Hospital, Nanjing, China

M. Jiang et al. (eds.), *The Proceedings of the International Conference on Sensing and Imaging*, Lecture Notes in Electrical Engineering 506,
https://doi.org/10.1007/978-3-319-91659-0_33

field model for liver lesion segmentation [4]. Linguraru et al. used shape analysis to segment liver at first, and then graph cuts were employed to segment hepatic tumors based on shape and enhancement constraints [7]. Level set methods were also modified to segment liver lesions [5, 6].

In this paper, we propose a novel framework to segment liver tumor from CT scans based on random forest and fuzzy clustering. For evaluation, segmentation experiments have been conducted on the liver tumor segmentation challenge testing datasets, resulting in promising results.

2 Data

CT scans provided by the challenge organizer were acquired from various clinical sites around the world [2]. Cases include a variety of liver tumors during clinical practice. The training and testing datasets contain 130 and 70 CT scans, respectively.

3 Method

The proposed automatic liver tumor segmentation consists of two phases: preprocessing and segmentation of liver tumor. In the preprocessing phase, the curvature filter is introduced to remove noise, and spatial regularization is employed by a trained mask. In the segmentation phase, we build a strong feature pool by features extraction and selection, and then efficient random forests are trained to classify each pixel into three categories: the liver, the tumor, and the background. After that, fuzzy clustering and morphological operators are used to deal with the under- and oversegmentation. A detailed description of each phase is given in the following sections.

3.1 Preprocessing

CT images are inevitably affected by noise in the acquisition process. In order to reduce the influence of noise over the course of feature extraction, we must denoise on the volumetric CT images. Even though many filtering techniques can be employed for CT images denoising, they are in general incapable of preserving the edges. The curvature filter removes the noise efficiently without generating artifacts and has no parameter to be tuned. Thus, we first introduce the curvature filter [3] to remove noise in preprocessing step (see Fig. 1b).

Moreover, in order to constrain the segmentation in a specific region and eliminate the interference of surrounding tissues, we employ a spatial regularization strategy, which is motivated by one of the “winning” algorithmic properties in

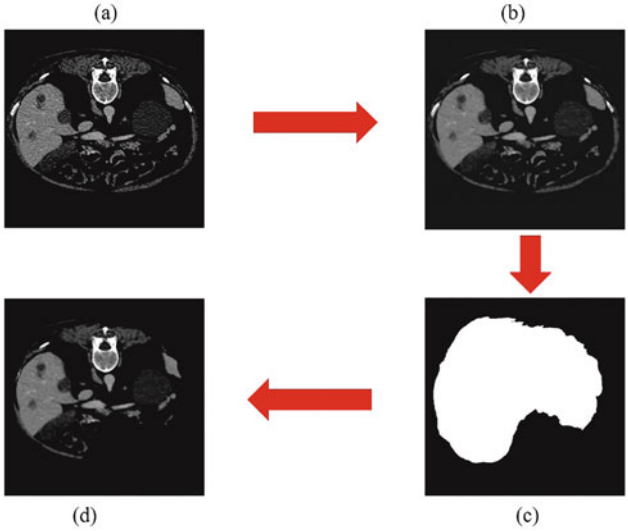

Fig. 1 Two main steps of the preprocessing. (**a**) Input image. (**b**) Curvature filter. (**c**) Liver mask. (**d**) Spatial regularization

BRATS [8]. Specifically, we make a mask for spatial regularization by taking the union of all the liver ground truth in the training dataset. By doing this, we can guarantee that the liver tumor is in the mask (Fig. 1c). Meanwhile, the computation cost can be reduced by segmenting only in the mask (Fig. 1d).

3.2 Random Forest Training

After preprocessing, we first classify the pixels into three categories, the liver, the tumor, and the background, by a statistical learning method. The basic assumption of all statistical learning methods is that the data have certain statistical rules. In LiTS, CT images vary greatly because the dataset was collected from six medical centers. Extracting features to train a classifier from all images may produce a weak classifier due to nonsignificant statistical rules of the dataset. Hence, we divide the 130 CT scans into 3 types by the gray level of livers in training dataset, namely, [20,70], [70,100], and [100,140]. Random forest is a commonly used learning-based method which combines bagging and fully-grown decision trees [1]. We train a random forest classifier for each type.

Features extraction and selection: Both intensity and texture features are calculated. The intensity features consist of the summation and average of local area gray intensity. The texture features include gray-level co-occurrence matrix, local binary pattern features, Gabor filter features, Robert features, Hog features, Haar-like features, local entropy, local range, and local standard deviation of the image. In order to incorporate features in different scales, all the features are extracted in both 5×5 and 11×11 patches. Table 1 shows the parameters of each feature set.

Table 1 Parameters of each feature set (Scales:5,11)

Feature	Parameters	Number
GLCM	Num. of properties: 3	90
LBP	Num. of neighbors: 8	118
Gabor	Num. of orientations: 4	16
Robert	Patch size: 3×3	2
HOG	Patch size: 3×3; 9 orientations	144
Haar-like	Calculated edge feature template by integral image	2
Sum	Patch size: $5 \times 5, 11 \times 11$	2
Average	Patch size: $5 \times 5, 11 \times 11$	2
Local entropy	Patch size: $5 \times 5, 11 \times 11$	2
Local range	Patch size: $5 \times 5, 11 \times 11$	2
Local standard deviation	Patch size: $5 \times 5, 11 \times 11$	2

In 3D volumetric images, a large amount of features can be extracted. In order to reduce the influence of redundant features on the classifier, Yaqub et. al [9] made a feature pool with fewer "good" features by feature scoring and selection. In our work, we calculate 382 features from the training data as a main feature pool as shown in Table 1. Then 116 features are chosen from the main feature pool as the strong feature pool according to the information gain ratio, including the summation and average of local area gray intensity, gray-level co-occurrence matrix, Gabor filter features, local entropy, local range, and local standard deviation of the image.

Random forest training: For each case, we divide all the pixels into three classes: the liver, the tumor, and the background. In order to select the appropriate number of trees, 70% of the samples are randomly selected for training, and the remaining 30% of the samples are used as testing data. We train the random forest from 1 tree to 20 trees and choose the random forest which has the highest test accuracy of testing data. The final random forest classifier we use contains 15 randomly trained trees, and the maximum tree depth is 12. We also find that even if increasing the number of trees and the maximum tree depth in the forest, there is only a slight improvement in the accuracy of the testing data.

3.3 Tumor Segmentation

Before segmentation, we skim through the whole volume to confirm a few parameters. The number of images per case varies from a few dozen to more than one thousand in the LiTS datasets. Many images without liver are also included in the CT scans. Segmenting the entire volume will increase computation cost and make no sense. Therefore, we go through the volume data before performing random forest classification, which coincides with the clinical workflow. During this process, we find out the slice range of the plausible liver tumor as well as decide the range of the image intensity and the corresponding random forest. In addition, since for each case, liver orientation may be different, the direction of the liver mask is also determined.

After confirming the above parameters, the procedure of tumor segmentation is totally automatic. First, each pixel in the mask is classified by the random forest. In this way, most of the tumor and normal liver are separated from the original images. However, there are many over segmentation in the current results due to the surrounding similar tissues. Since it is well known that the liver is the largest organ in the abdomen, in the second step, the maximum connected region is extracted as region of interest (ROI) from the combination of the tumor and normal liver segmentation results. This can eliminate the interference of similar tissues outside the liver. Subsequently, in order to include the tumors that are not classified by the random forest, closing operation is applied to fill small holes in the ROI. The structuring element of closing operation is set as a 10×10 square.

Finally, the obtained ROI contains normal liver and tumor (Fig. 2b). Due to the different gray level, normal liver and tumor in the ROI can be separated by fuzzy clustering method. The class with small intensity is taken as tumor from the clustering results (Fig. 2c). Additionally, in order to remove isolate points and make the segmentation results smooth, we apply an opening operation with a square structuring element whose width is 3 pixels to refine the tumor segmentation (Fig. 2d).

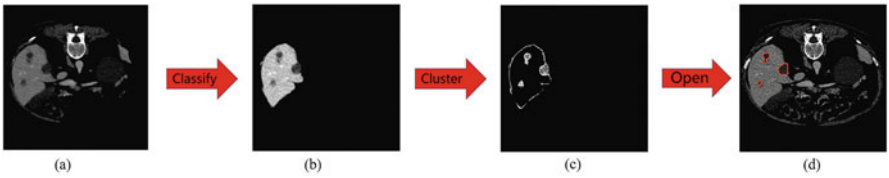

Fig. 2 The procedure of the tumor segmentation. (**a**) Preprocessed image. (**b**) Classification result. (**c**) Clustering result. (**d**) Final result

Table 2 Evaluation of the proposed method

Metric	Score
Dice	0.47
Volume Overlap Error	0.65
Relative Volume Difference	− 0.35
Average symmetric surface distance	11.49
Maximum symmetric surface distance	64.31

4 Experiments and Results

The proposed method is tested on the liver tumor segmentation challenge(LiTS). All the experiments are run on a PC with 8G RAM i7-core with MATLAB 2015b. The training times for all random forests are about 5 minutes. The average processing time for segmenting a CT scan with 120 slices is about an hour and a half. Table 2 lists the quantitative evaluation of the proposed method in the testing data.

The calculated mean scores of Dice, volume of overlap error (VOE), relative volume difference (RVD), average symmetric surface distance (ASD), and maximum symmetric surface distance (MSD) are 0.47, 0.65, −0.35, 11.49, and 64.31, respectively. Figure 3 shows six tumor segmentation results in the short axis view.

Besides, we compare the accuracy of four classifiers on the feature set. Specifically, random forest, SVM (Gaussian kernel), SVM (quadratic kernel), and K-nearest neighborhood are used to classify the feature set into three categories: the background, the liver, and the tumor. Each classifier uses threefold cross validation scheme. Table 3 shows the classification results of these classifiers. It can be seen that random forest shows better performance as compared to other classifiers by achieving maximum recall and precision.

5 Discussion and Conclusion

An automatic method for segmentation of the liver tumor in CT scans using random forest and fuzzy clustering has been presented. The proposed method has three main highlights. Firstly, the curvature filter is introduced as a preprocessing step for noise removal to reduce the variance of the CT datasets. Secondly, a spatial regularization strategy is employed as a region constraint to narrow the segmentation range and reduce the computation cost. Finally, the combination of random forest and fuzzy clustering is used to segment liver tumor efficiently, where both intensity and texture features are utilized.

There are a few limitations that are worth noting. The first one is that most of the undersegmentation errors occur in the unclear or small tumors, which the random forest cannot recognize. In addition, most of the oversegmentation errors take place in the gallbladder surrounded by the liver which is classified as tumor. Finally, our implementation works under the assumption that the intensity of the liver and tumor

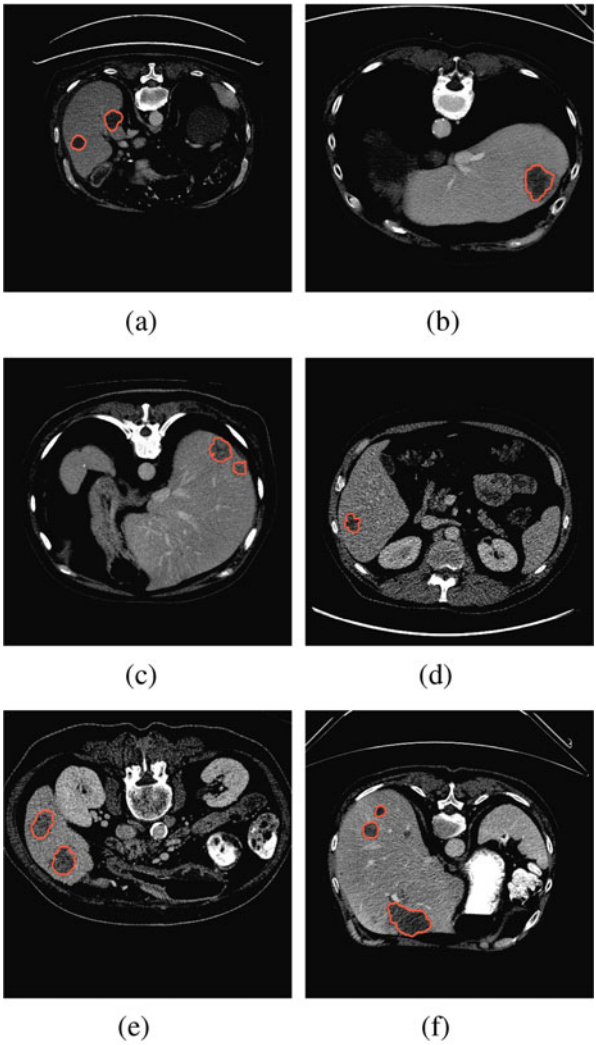

Fig. 3 The results of proposed segmentation method. (**a**) Case 3, Slice 164. (**b**) Case 19, Slice 74. (**c**) Case 27, Slice 74. (**d**) Case 33, Slice 493. (**e**) Case 48, Slice 265. (**f**) Case 56, Slice 378

Table 3 Classification accuracy of different classifiers

Classifier	Recall	Precision
Random Forest	0.88	0.65
SVM (Gaussian Kernel)	0.86	0.60
SVM (Quadratic Kernel)	0.81	0.59
K Nearest Neighborhood	0.77	0.53

have certain statistical rules in the datasets, which is valid in most cases. However, we find that the tumor is whitened in some cases, such as case 52 and case 63 in the testing data. Therefore, these lesions cannot be identified either.

In the future, our method can be further improved as follows: (1) adding more classes (e.g., gallbladder) to the random forest classifier can identify the interference tissue; (2) using more training cases might improve the accuracy of the segmentation results; and (3) the processing time can be reduced by parallel computing in classification.

Acknowledgements This study was supported by National Nature Science Foundation of China for funding (Grant Nos. 11531005). Thanks to the organizers of the LiTS Challenge for the public liver tumor dataset.

References

1. Breiman L (2001) Random forests. Mach Learn 45:5–32. https://doi.org/10.1023/A:1010933404324
2. Christ P (2017) LiTS – liver tumor segmentation challenge. http://competitions.codalab.org/competitions/15595
3. Gong Y, Sbalzarini IF (2017) Curvature filters efficiently reduce certain variational energies. IEEE Trans Image Process 26(4):1786–1798
4. Häme Y, Pollari M (2012) Semi-automatic liver tumor segmentation with hidden Markov measure field model and non-parametric distribution estimation. Med Image Anal 16(1):140–149
5. Hoogi A, Beaulieu CF, Cunha GM, Heba E, Sirlin CB, Napel S, Rubin DL (2017) Adaptive local window for level set segmentation of CT and MRI liver lesions. Med Image Anal 37:46–55
6. Hoogi A, Subramaniam A, Veerapaneni R, Rubin DL (2017) Adaptive estimation of active contour parameters using convolutional neural networks and texture analysis. IEEE Trans Med Imaging 36(3):781–791. https://doi.org/10.1109/TMI.2016.2628084
7. Linguraru MG, Richbourg WJ, Liu J, Watt JM, Pamulapati V, Wang S, Summers RM (2012) Tumor burden analysis on computed tomography by automated liver and tumor segmentation. IEEE Trans Med Imaging 31(10):1965–1976. https://doi.org/10.1109/TMI.2012.2211887
8. Menze BH, Jakab A, Bauer S, Kalpathy-Cramer J et al (2015) The multimodal brain tumor image segmentation benchmark (brats). IEEE Trans Med Imaging 34(10):1993–2024. https://doi.org/10.1109/TMI.2014.2377694
9. Yaqub M, Javaid MK, Cooper C, Noble JA (2014) Investigation of the role of feature selection and weighted voting in random forests for 3-D volumetric segmentation. IEEE Trans Med Imaging 33(2):258–271. https://doi.org/10.1109/TMI.2013.2284025

Using Electrically Tunable Lens to Improve Axial Resolution and Imaging Field in Light Sheet Fluorescence Microscope

Muyue Zhai, Xiaoshuai Huang, Heng Mao, Qiudong Zhu, and Shanshan Wang

1 Introduction

The light sheet microscope is the primary tool for three-dimensional imaging in the life sciences. It uses a thin sheet of light to illuminate biological samples, which will reduce the luminous flux on the biological sample, thereby reducing phototoxicity and light bleaching. In addition, since only the focal plane of the detection objective is excited, the influence of the fluorophore out of focus on the contrast of the image will be reduced too.

Conventionally, biological samples have a certain thickness, so the traditional coaxial lighting method in the imaging of biological samples has a great limitation. For example, the image contrast decreases with the increasing of the imaging depth, and the fluorescent markers of biological samples were quickly bleached. Confocal microscopy is a common method for increasing the axial resolution, but this approach still has a greater phototoxicity on biological samples. In 2004, Huisken et al. reported the first modern light sheet microscope in the journal *Science* named the selective plane illumination microscopy (SPIM) [1]. The SPIM forms a Gaussian light through a cylindrical lens and excitation objective to selectively excite the specific plane of the biological sample. All the fluorescence emitted from

M. Zhai · Q. Zhu · S. Wang (✉)
Beijing Key Lab. for Precision Optoelectronic Measurement Instrument and Technology, School of Opto-Electronics, Beijing Institute of Technology, Beijing, China
e-mail: 2120160609@bit.edu.cn; zqd@bit.edu.cn; wshan@bit.edu.cn

X. Huang
Institute of Molecular Medicine, Peking University, Beijing, China

H. Mao
LMAM, School of Mathematical Sciences, Peking University, Beijing, China
e-mail: heng.mao@pku.edu.cn

M. Jiang et al. (eds.), *The Proceedings of the International Conference on Sensing and Imaging*, Lecture Notes in Electrical Engineering 506,
https://doi.org/10.1007/978-3-319-91659-0_34

the excited sample surface is collected by the detection objective and the camera. From then on, the light sheet microscope has been widely used in the field of life sciences because of its high axial resolution and low light toxicity.

We hope that the LSFM's light sheet is thinner to increase the axial resolution and imaging contrast as more as possible, and we hope that the illumination of the light sheet will be wider and longer for high-speed large FOV imaging. However, subject to physical laws, the two aspects are contradictory, so we cannot get very thin, very wide, and long light sheet at the same time, so that we can only make a choice. We optimize the lighting conditions in the part the FOV – through the cylindrical lens and high NA excitation light [2] – to obtain a thinner sheet in the region and then use the ETL to enlarge the FOV by temporal multiplexing [3, 4]. After splicing the image regions, we can obtain a large FOV, high-resolution image. The short time response of the ETL ensures the temporal resolution of the system; the high NA of the excitation light enables thinner light sheet illumination in the specific region to ensure axial resolution [5] and image contrast. By temporal multiplexing of the regions, we achieve the large FOV imaging.

2 Theory

The LSFM produces a light sheet illumination on the sample through the cylindrical lens and the excitation objective. The thickness of the light sheet is limited by the diffraction limit. According to the Rayleigh criterion (Eq. 1), the thickness of the light sheet is inversely proportional to the effective numerical aperture (NA) of the objective.

$$\omega_0 = \frac{1.4\lambda f}{2D_{\text{lens}}} \tag{1}$$

where ω_0 is the beam waist thickness, f is the focal length of the excitation optics, λ is the wavelength of the excitation light, and D_{lens} is the diaphragm of the excitation optics.

Just as shown in Fig. 1, the Rayleigh length of the Gaussian beam [6] is proportional to the square of the light sheet's thickness (Eq. 2). In order to ensure a sufficiently large FOV, the usual LSFM will limit the excitation NA to about 0.10, which will increase the thickness of the light sheet.

$$Z_R = \frac{\pi\omega_0^2}{\lambda} \tag{2}$$

where Z_R represents the Rayleigh length, λ is the wavelength of the laser, and ω_0 is the beam waist.

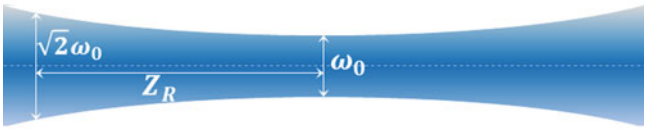

Fig. 1 Base-mode Gaussian beam parameters

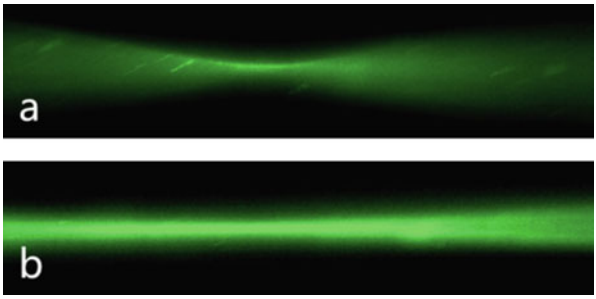

Fig. 2 Light sheet beam shapes of different NA. (**a**) The light sheet beam of NA 0.3. (**b**) The light sheet beam of NA 0.1

These equations are for characterizing light sheets propagating in air (refractive index $n = 1.0$); in a medium of refractive index n, the confocal parameter becomes:

$$b_n = 2nZ_R \tag{3}$$

where n is the refractive index of the medium and b_n denotes the confocal parameter in medium with refractive index n (Fig. 2).

However, the NA of the detection objective is usually above 0.4, so the thickness of the light sheet is thicker than the depth of focus [7] of the detection objective (Eq. 4).

$$d_{\text{tot}} = \frac{\lambda \cdot n}{\text{NA}^2} + \frac{n}{M \cdot \text{NA}} \cdot e \tag{4}$$

where d_{tot} represents the depth of field, λ is the wavelength of excitation light, n is the refractive index of the medium between the object and the objective front lens element, and NA equals the objective numerical aperture. The variable e is the smallest distance that can be resolved by a detector that is placed in the image plane of the microscope objective, whose lateral magnification is M.

The light outside the depth of focus of the detection objective enters the objective, reducing the imaging contrast. And the plane selection will get worse simultaneously. We raise the excitation NA to 0.25, which greatly reduces the thickness of the light sheet, but this also leads to a reduction in the illumination field of the light sheet. By the axial scanning of the excitation light using ETL,

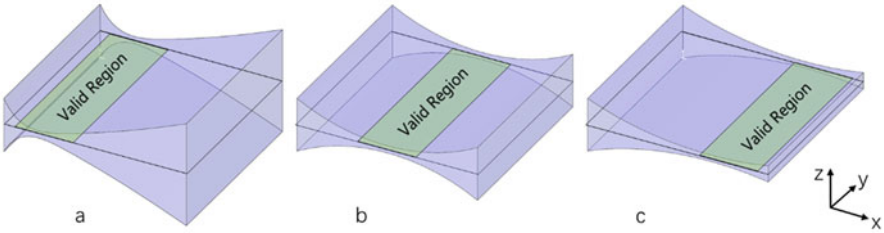

Fig. 3 The data collection and processing. (**a**) The frame when the light sheet is near the excitation objective. (**b**) The frame when the light sheet is on the focus point of the excitation objective. (**c**) The frame when the light sheet is away from the excitation objective

we get several regions of thin light sheet illumination. Then we combine the several high-contrast images to get a high-contrast and large FOV image.

As shown in the Fig. 3, the focus line will move along the x-axis during the zoom process of ETL. When the focus lines are in the following positions, three images are acquired. Capture the effective region for each image, and combine them to get a complete high-resolution and high-contrast image.

3 System Description

3.1 Temporal Multiplexing LFSM

We first proposed an experiment for principle demonstration to verify the effectiveness of temporal multiplexing LFSM. The schematic diagram is shown in Fig. 4; the laser beam emitted from the fiber is collimated by a collimator objective. Then the laser beam passes through the ETL. The laser beam aperture is limited to 6 mm by the aperture stop so as to match the ETL's aperture. The light sheet was produced by a cylindrical lens, and then it was again imaged on the sample surface by a tube lens and a water-dipping exposure objective. The effective illumination NA of the excitation objective is 0.25. The ETL and the exit pupil of the excitation objective are conjugated.

The signals are collected at right angles to the illumination sheet via a water-dipping detection objective. The transverse magnification of the detection optical path is 40X, and the unit pixel that corresponds to the size of the object is 6.5 um/40 = 162.5 nm.

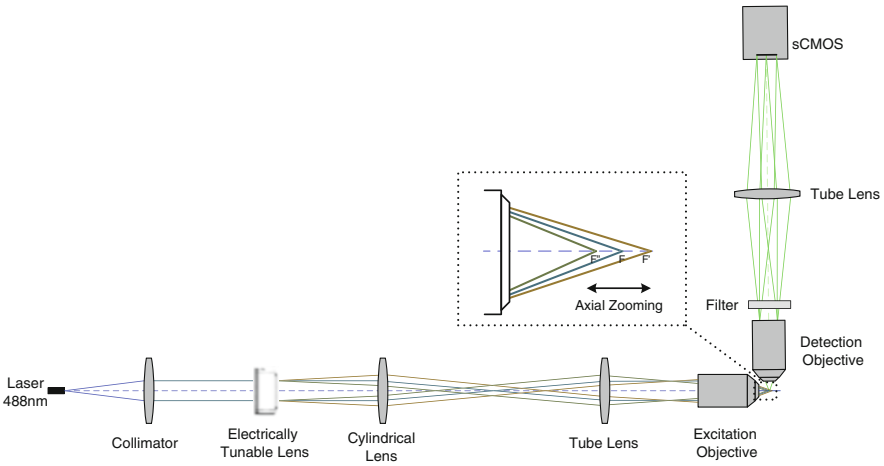

Fig. 4 Light sheet fluorescence microscope schematic diagram

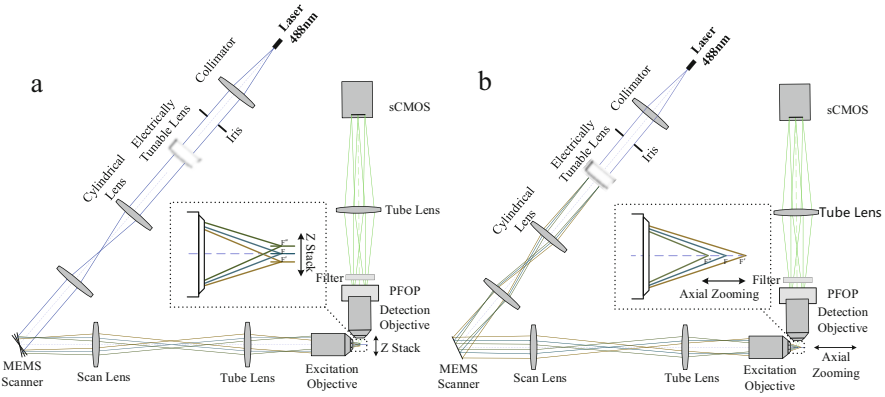

Fig. 5 LSFM volumetric imaging system schematic diagram. (**a**) MEMS scanning view. (**b**) ETL working view

3.2 LSFM Volumetric Imaging System

Subsequently, according to the above temporal multiplexing LFSM, we develop the LSFM volumetric imaging system by using Piezo Focus Objective Positioner and MEMS scanner. The implementation process is shown in the schematic diagram. This imaging system enhances axial resolution and contrast by temporal multiplexing, and it has the capability of volumetric imaging, which is similar to the confocal microscope (Fig. 5).

Figure 6 is its hardware connection diagram. Its workflow is shown in Fig. 7. The ETL performs an axial zooming driven by the precise control signal provided by the FPGA controller, changing the focus position of the excitation light. And after each

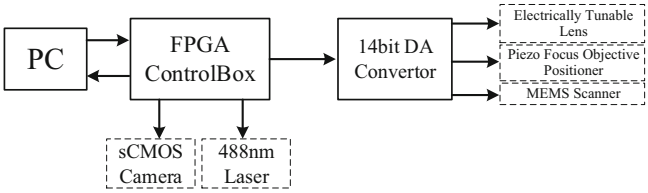

Fig. 6 LSFM volumetric imaging system hardware connection diagram

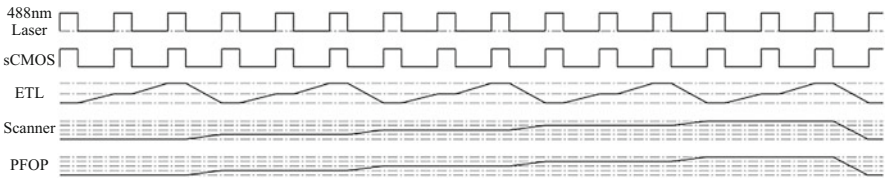

Fig. 7 LSFM volumetric imaging system timing diagram

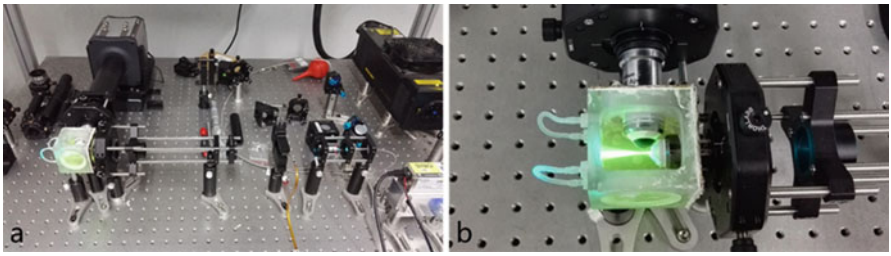

Fig. 8 Light sheet fluorescence microscope experimental setup

step of the zooming process, the image is acquired by the sCMOS to complete the large field of view and high-axial-resolution imaging. Then, the MEMS scanner and the PFOP move synchronized for the Z-Stack, driven by the FPGA controller. Subsequently, the above two processes are repeated to complete the volumetric imaging of the organism.

4 Experiment

We set up an experimental system for principle demonstration, as shown in Fig. 8. Fluorescent beads whose diameter is 20 nm evenly spread in the chamber. The actual output power of the laser is 10 mW. The sCMOS camera (Andor Neo) uses the global shutter mode to acquire the fluorescence signal. ETL (Optotune, EL-6-15) uses the Optotune Driver4 controller to manually control its zooming process. And the cylindrical lens is placed on the rotating frame so as to adjust the direction of the cylindrical lens to make the plane of light sheet and the detection objective coincide.

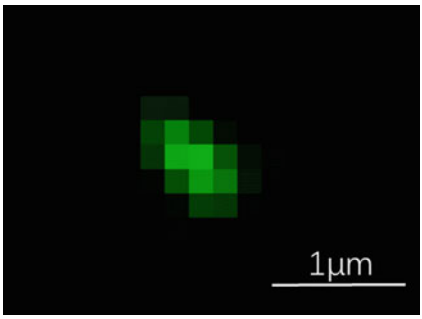

Fig. 9 The partial magnification image of the fluorescent beads

4.1 PSF Calibration

The effective illumination NA of the excitation objective (Olympus 20X, 0.5 NA) is 0.25, which can obtain the light sheet with the thinnest thickness of 1.2 um in the z-axis direction. This can effectively increase the image contrast and obtain the image near the diffraction limit. As shown in the Fig. 9, under the condition of exposure time of 1 ms and laser power of 10 mW, we obtain the high-contrast and high-spatial-resolution images when imaging the fluorescent beads by a water-dipping detection objective (Nikon 40X,0.8 NA). The beads are moved irregularly with the flow, and the oblique elongation of the PSF shown in the figure is due to the unavoidable motion blur in the exposure process.

4.2 Performance Evaluation

The laser beam width is limited to 6 mm by the aperture stop, and a sheet having a width greater than 400 μm is produced in the y-axis direction by a cylindrical lens (*Daheng*, $f_x = 100\ mm$), a tube lens (*Thorlabs*, $f = 80\ mm$), and an excitation objective ($20X\ @\ f_{Tube-Lens} = 180\ mm$). Control the ETL for x-axis zooming; thus the focus line will move along the x-axis; then get three images continuously. The valid regions of each image are shown in Fig. 10. Through the ETL zooming, expand the x-axis length of the FOV to 300 um, which can cover about 0.12 mm ^{2} in the objective space.

To analyze the imaging performance quantitatively, we calculated the ratio of the average area of beads inside and outside the valid region.

The ratio of the average area of beads inside and outside the valid region of the images can be obtained by calculating the average area of beads inside and outside the valid region of 100 images. The calculation process is shown in Eq. 5. The result demonstrates that the above method of increasing the axial resolution by using large NA excitation illumination is effective.

$$\text{Ratio}_{\text{Area}} = \frac{\text{Area}_{\text{Beads in\_valid\_region}}}{\text{Area}_{\text{Beads out\_of\_valid\_region}}} = \frac{196\text{pixel}^2}{256\text{pixel}^2} = 76.6\% \tag{5}$$

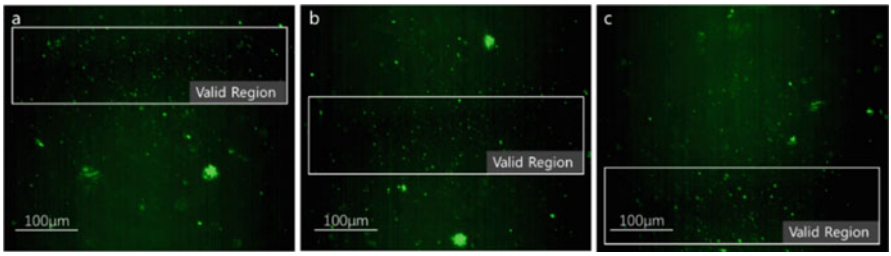

Fig. 10 The image of the fluorescent beads during the zooming process. (**a**) The ETL is at the negative diopters (current = 103 mA). (**b**) The ETL is at the zero diopters (current = 110 mA). (**c**) The ETL is at the positive diopters (current = 118 mA)

The other comparison criterion is RMS contrast, which is defined as geometrical mean of all pixel intensities after subtracting the mean of these intensities (Eq. 6):

$$\text{RMS Contrast} = \sqrt{\frac{1}{MN}\sum_{n=1}^{N}\sum_{m=1}^{M}\left(I\left(m,n\right)-\overline{I}\right)^2} \tag{6}$$

We calculated the RMS contrast inside and outside the valid region of 100 images. And the following results were obtained. The image contrast in the valid area is significantly higher than the area outside the valid area from the results.

$$\text{RMS Contrast}_{\text{In\_valid\_region}} = 18.47 \tag{7}$$

$$\text{RMS Contrast}_{\text{Out\_of\_valid\_region}} = 9.20 \tag{8}$$

5 Conclusion and Discussion

The operability of the proposed scheme is verified by preliminary experiments. It is proved by experiment that the axial resolution and contrast of the imaging are improved by using the large NA excitation illumination. With the ETL's axial zooming and temporal multiplexing, the image FOV has also been ensured.

A larger excitation field can be obtained for high-speed imaging using a cylindrical lens to produce a light sheet under low NA condition. But the axial resolution of the LSFM is relatively poor under the condition of low excitation NA. Increasing the NA of the excitation light means that the thickness of the light sheet is reduced. The light sheet is thinner, so the fluorescence image contrast is significantly increased by the reduction of the emitted light outside the depth of focus of the detection objective. At the same time, the Rayleigh length of the Gaussian beam is proportional to the square of the light sheet's thickness, resulting in a decrease of the

effective illumination region. Using the ETL, the x-axis fast push-up of the high NA excitation light is achieved. This technique can reduce the thickness of light sheet and increase the axial resolution significantly.

However, with the decrease of the thickness of the light sheet, the inhomogeneity of the refractive index of the sample has a greater effect on the fluorescence imaging, so it is necessary to add the adaptive optics system in the excitation light path. We plan to further optimize the excitation light by using AO system in the future work to achieve better image quality.

References

1. Huisken J, Swoger J, Del Bene F et al (2004) Optical sectioning deep inside live embryos by selective plane illumination microscopy[J]. Science 305(5686):1007–1009
2. Ritter JG, Spille JH, Kaminski T et al (2011) A cylindrical zoom lens unit for adjustable optical sectioning in light sheet microscopy[J]. Biomed Opt Express 2(1):185–193
3. Fu Q, Martin BL, Matus DQ et al (2016) Imaging multicellular specimens with real-time optimized tiling light-sheet selective plane illumination microscopy[J]. Nat Commun 7
4. Chmielewski AK, Kyrsting A, Mahou P et al (2015) Fast imaging of live organisms with sculpted light sheets[J]. Sci Rep 5
5. Engelbrecht CJ, Stelzer EH (2006) Resolution enhancement in a light-sheet-based microscope (SPIM)[J]. Opt Lett 31(10):1477–1479
6. Yan J. Principle and technology of laser[M]. Higher Education Press
7. Spring KR, Davidson MW. The depth of field and the depth of focus. https://www.microscopyu.com/microscopy-basics/depth-of-field-and-depth-of-focus

Index

M. Jiang et al. (eds.), *The Proceedings of the International Conference on Sensing and Imaging*, Lecture Notes in Electrical Engineering 506,
https://doi.org/10.1007/978-3-319-91659-0

M